Appraisal of Core Analysis Methods against Zero-Power Experiments on Full-Scale BWR Fuel Assemblies

THÈSE N^{O} 5257 (2012)

PRÉSENTÉE LE 20 JANVIER 2012
À LA FACULTÉ DES SCIENCES DE BASE
LABORATOIRE DE PHYSIQUE DES RÉACTEURS ET DE COMPORTEMENT DES SYSTÈMES
PROGRAMME DOCTORAL EN ENERGIE

ÉCOLE POLYTECHNIQUE FÉDÉRALE DE LAUSANNE

POUR L'OBTENTION DU GRADE DE DOCTEUR ÈS SCIENCES

PAR

Flavio Dante GIUST

acceptée sur proposition du jury:

Prof. L. Rivkin, président du jury
Prof. R. Chawla, directeur de thèse
Dr S.-Ö. Lindahl, rapporteur
Dr G. Perret, rapporteur
Dr T. Williams, rapporteur

ÉCOLE POLYTECHNIQUE
FÉDÉRALE DE LAUSANNE
Suisse
2012

Abstract

The present doctoral research aims at the appraisal of nodal core simulators used for the calculation of commercial boiling water reactor (BWR) cores, against measurements carried out at the Paul Scherrer Institute under the LWR-PROTEUS experimental programme. The research focuses mainly on the prediction of radial and axial total-fission rate (i.e. power) distributions in the vicinity of core heterogeneities, caused by features such as the presence of control blades, enrichment boundaries or partial length rods. As such, this thesis complements previous validation work performed for LWR calculational methods on the basis of integral experiments in zero-power research reactors, the latter corresponding largely to the validation of two-dimensional, reflected fuel-assembly calculations.

Two commercial code systems have been investigated currently: HELIOS/PRESTO-2, presently used for core monitoring at the Leibstadt Nuclear Power Plant (Switzerland), and CASMO-5/SIMULATE-5, which represents the most recent generation of the widely applied CASMO/SIMULATE system. Six different LWR-PROTEUS configurations have been modelled, for which the nodal reconstructed total-fission rate distributions have been compared against experimental results, as well as against reference, three-dimensional whole-reactor Monte Carlo calculations using the MCNPX code.

To start with, a methodology has been developed and tested for appropriate representation of the multi-zone experimental configurations, as employed in the LWR-PROTEUS programme, by means of reduced-geometry models set up using the investigated nodal code systems. The approach adopted has been to apply, in each case, case-dependent three-dimensional boundary conditions to the nodal code's modelling of the 3x3 array of BWR assemblies constituting the LWR-PROTEUS test zone. This has been done in terms of so-called Partial Current Ratios (PCRs), which describe the relation between the incoming and outgoing neutron currents across the test-zone boundary. These PCRs have been derived from the fore-mentioned MCNPX calculation of the multi-zone PROTEUS reactor, thus allowing for the adequate description of the three-dimensional effects associated with the interaction between the test zone and its surroundings.

The results obtained for the reference LWR-PROTEUS configuration, with a test zone consisting of an unperturbed regular array of identical, axially uniform BWR fuel assemblies (of type SVEA-96+), showed that both the investigated nodal methodologies reproduce the experimental total-fission rate distribution with very good accuracy, equivalent to that achievable with high-order transport calculations. This has provided adequate indication that the developed methodology of using three-dimensional PCRs, calculated by means of an appropriate whole-reactor MCNPX model, offers a reliable platform for the desired validation.

The full insertion of a L-shaped hafnium control blade, especially fabricated for the LWR-PROTEUS programme, has permitted the study of the behaviour of calculated total-fission rate distributions in the presence of strong radial and azimuthal flux gradients. In this case, the use of reflective boundary conditions in the lattice calculations, combined with the azimuthal non-uniformity of the currents that couple the test zone with the outer zones of the reactor, produce systematic deviations which, together, lead to some loss of accuracy in comparison with the regular, uncontrolled case.

The three-dimensional effects of the changes in enrichment and gadolinium content between two different axial sections of the fuel assembly have also been studied. In this case, the calculations of the axial total-fission rate distributions are seen to generally reproduce the experimental data with good accuracy, although certain systematic effects are observed. In particular, at local level, and very near the strong axial heterogeneity caused by the enrichment boundary, relatively large deviations have been found to occur. However, due to their very local character, these deviations are not considered to represent a relevant issue in connection with power reactor monitoring and design.

Also for the demanding case of the LWR-PROTEUS configuration with a partially inserted control blade, the results obtained in this thesis show a very good behaviour. As in the boundary enrichment case, however, some very localized deviations occur in the vicinity of the strong axial flux gradients.

In a separate phase of the LWR-PROTEUS programme, BWR assemblies with partial length rods (PLRs), viz. of type SVEA-96 Optima2, were studied in the central test zone. The results of the comparisons made currently for the corresponding LWR-PROTEUS configurations have shown that, also for fuel assemblies with axial heterogeneities of this type, the performance of both the investigated nodal methodologies is very satisfactory for predicting the global distribution of the total-fission rate. The local three-dimensional effects caused by the PLRs are also predicted with good accuracy, similar, in fact, to that obtained with high-order three-dimensional transport calculations.

The present research shows that the two nodal code systems investigated – HELIOS/ PRESTO-2 and CASMO-5/SIMULATE-5 – reproduce the LWR-PROTEUS experimental results with high accuracy, both for the radial and the three-dimensional (i.e. at pellet level) comparisons. Significant deviations occur almost exclusively within a short distance from the nodal interface, in cases featuring strong gradients across the core midplane. The axial and radial shapes of the total-fission rate distributions are well predicted in most cases, which represents an important observation concerning the monitoring of operational limits in power reactor cores.

Thus, overall – within the range of applicability of the experimental conditions studied in the LWR-PROTEUS programme – the results of the comparisons performed in this thesis confirm that nodal methodologies with pin-power reconstruction have a very high level of performance. In fact, the accuracy that they can achieve for the assembly-internal total-fission rate distribution is, in general, higher than that practically achievable in an operating nuclear power plant. This is due to unavoidable, additional uncertainties in the characterisation of a BWR core under power reactor conditions.

Finally, the present research has provided quantitative insights into the applicability of integral data, produced in critical facilities such as PROTEUS, for validating the calculation of power-reactor core heterogeneities. One has thus been able to demonstrate that the experimental evidence from the LWR-PROTEUS programme indeed constitutes a very valuable basis for the validation and appraisal of three-dimensional nodal methodologies with pin-power reconstruction.

Keywords: Nodal methods, pin-power reconstruction, core heterogeneities, boiling water reactor (BWR), zero-power research reactor, experimental validation, total-fission rate, neutron, current, three-dimensional distribution, LWR-PROTEUS experimental programme, HELIOS, PRESTO-2, CASMO-5, SIMULATE-5, MCNPX.

Kurzfassung

Ziel der vorliegenden Doktorarbeit ist die Beurteilung der Rechengenauigkeit von nodalen Kernsimulatoren, welche für die Berechnung kommerzieller Siedewasserreaktoren (SWR) konzipiert sind, gegenüber Messungen, die im experimentellen Programm LWR-PROTEUS am Paul Scherrer Institut vorgenommen wurden. Die Forschung konzentriert sich hauptsächlich auf die Vorhersage der radialen und axialen Verteilungen der totalen Spaltrate (d.h. der Leistung) in der Nähe von Heterogenitäten des Kerns, die durch die Anwesenheit von Kontrollstäben, Anreicherungsgrenzen oder teillangen Brennstäben verursacht werden. Somit ergänzt diese Dissertation frühere Validierungsarbeiten im Bereich von LWR-Rechenmethoden auf der Basis von integralen Experimenten in Nullleistungs-Forschungsreaktoren, welche hauptsächlich auf die Validierung von zweidimensionalen Brennelementrechnungen bezogen sind.

Zwei kommerzielle Codesysteme sind untersucht worden: HELIOS/PRESTO-2, welches gegenwärtig für die Kernüberwachung des Kernkraftwerks Leibstadt (Schweiz) eingesetzt wird, und CASMO-5/SIMULATE-5, das die neueste Generation des weit verbreitet angewandten Systems CASMO/SIMULATE repräsentiert. Sechs verschiedene LWR-PROTEUS-Konfigurationen sind modelliert worden. Für diese wurden die rekonstruierten Spaltratenverteilungen gegenüber experimentellen Ergebnissen und, als Ergänzung, dreidimensionalen Monte-Carlo-Berechnungen des ganzen Reaktors mit dem Code MCNPX verglichen.

Als erster Schritt wurde eine Methodik entwickelt und getestet, um eine geeignete Darstellung der experimentellen LWR-PROTEUS-Mehrzonenkonfigurationen zu ermöglichen. Dabei sind nodale Modellierungen der Testzone mit den zu studierenden Codesystemen vorgenommen worden. Für diesen Zweck wurden von der jeweiligen Kernkonfiguration abhängige dreidimensionale Randbedingungen für die aus 3x3 SWR-Brennelementen bestehende Testzone eingeführt, welche auf der Verwendung von sogenannten PCRs (Partial Current Ratios) basieren, welche das Verhältnis zwischen den über der Testzonen-Grenzfläche eintretenden und austretenden Neutronen-Strömen beschreiben. Diese PCRs wurden durch die oben erwähnten MCNPX-Berechnungen für den Mehrzonen-Reaktor PROTEUS ermittelt, was eine geeignete Beschreibung der mit dem Zusammenspiel zwischen der Testzone und seiner Umgebung verbundenen dreidimensionalen Effekte erlaubt.

Die Ergebnisse der Untersuchungen zeigen, dass für den LWR-PROTEUS-Referenzfall einer regelmässigen Anordnung von identischen, axial gleichförmigen Brennelementen (vom Typ SVEA-96+) beide untersuchten nodalen Methoden die experimentellen Spaltratenverteilungen mit einer sehr guten Genauigkeit wiedergeben, die der mit Transportberechnungen hoher Ordnung erreichbaren entspricht. Des Weiteren zeigen diese Ergebnisse, dass die entwickelte Methodologie der Verwendung von dreidimensionalen PCRs, mit geeigneten MCNPX-Berechnungen erstellt, eine zuverlässige Plattform für die angestrebte Validierung bietet.

Der Einsatz eines L-förmigen Hafnium-Kontrollstabs mit voller Höhe, welcher speziell für das experimentelle Programm LWR-PROTEUS hergestellt wurde, hat die Studie des Verhaltens der berechneten Spaltratenverteilung in Anordnungen mit starken radialen und azimutalen Flussgradienten ermöglicht. In diesem Fall erzeugt die Anwendung von reflektierten Randbedingungen für die Gitterberechnungen und auch die azimutale Ungleichförmigkeit der Ströme, welche die Testzone mit den äusseren Zonen des Reaktors verbinden, systematische Abweichungen, die zusammen betrachtet zu einem gewissen Verlust an Genauigkeit im Vergleich zum gleichförmigen, nicht kontrollierten Fall führen.

Die dreidimensionalen Effekte der Änderungen der Anreicherung und des Gadolinium-Gehalts zwischen zwei verschiedenen axialen Zonen des Brennelements wurden ebenfalls untersucht. In diesem Fall geben die Berechnungen die experimentellen Werte im Allgemeinen mit guter Genauigkeit wieder, obwohl einige systematische Effekte zu sehen sind. Insbesondere können in unmittelbarer Nähe der starken axialen Heterogenität infolge der Anreicherungsgrenze relativ grosse Abweichungen beobachtet werden. Diese Abweichungen werden jedoch wegen ihres sehr lokalen Charakters nicht als relevantes Problem im Zusammenhang mit der Überwachung und Auslegung von Leistungsreaktoren betrachtet.

Auch für den anspruchsvollen Fall eines teilweise eingefahrenen Kontrollstabs zeigen die in dieser Doktorarbeit erzielten Ergebnisse ein sehr gutes Verhalten, trotz einiger sehr lokaler Abweichungen, die wie für den Fall der Anreicherungsgrenze in Gebieten mit starken axialen Flussgradienten vorkommen.

In einer getrennten Phase des LWR-PROTEUS-Programms sind SWR-Brennelemente vom Typ SVEA-96 Optima2, mit teillangen Brennstäben (PLRs), studiert worden. Die Ergebnisse der Vergleiche haben auch für diesen Fall gezeigt, dass das Verhalten der beiden nodalen Methoden bezüglich der Voraussage der globalen Verteilung der Spaltrate sehr zufriedenstellend ist. Sie spiegeln auch die durch die teillangen Stäbe verursachten lokalen dreidimensionalen Effekte mit guter Genauigkeit wieder, ähnlich dem Einsatz von Transportrechnungen hoher Ordnung.

Die vorliegende Arbeit zeigt, dass die zwei untersuchten nodalen Codesysteme – HELIOS/PRESTO-2 und CASMO-5/SIMULATE-5 – die experimentellen Ergebnisse von LWR-PROTEUS mit guter Genauigkeit wiedergeben, sowohl für die radialen als auch für die dreidimensionalen (d.h. mit einer Auflösung entsprechend der Brennstofftablettengrösse) Vergleiche. Bedeutende Abweichungen kommen fast ausschliesslich innerhalb einer kurzen Entfernung von der Knotengrenze in Fällen vor, die starke Gradienten an der Kern-Mittelebene zeigen. Die axialen und radialen Profile der Spaltratenverteilung werden in den meisten Fällen mit einer guten Genauigkeit vorausgesagt, was eine wichtige Feststellung in Bezug auf die Überwachung von betrieblichen Grenzwerten in Leistungsreaktorkernen darstellt.

Die Ergebnisse der in dieser Doktorarbeit durchgeführten Vergleiche bestätigen, innerhalb des Anwendungsbereichs der untersuchten experimentellen Bedingungen, dass nodale Methoden mit Rekonstruktion der Stableistungen die Spaltratenverteilung innerhalb des Brennelements mit sehr hoher Genauigkeit voraussagen können. Tatsächlich ist diese Genauigkeit im Allgemeinen höher als die, die wegen unvermeidlicher zusätzlicher Unsicherheiten in der Charakterisierung des unter Leistungsbedingungen stehenden SWR-Kerns in einem Kernkraftwerk praktisch erreichbar ist.

Schliesslich gibt die vorliegende Dissertation Einblicke in die Anwendbarkeit integraler experimenteller Daten, die in Nullleistungs-Forschungsanlagen wie PROTEUS gewonnen wurden, für die Validierung von Berechnungen zu Heterogenitäten in Leistungsreaktorkernen. Es konnte dabei gezeigt werden, dass die im experimentellen Programm LWR-PROTEUS erhaltenen Ergebnisse eine sehr wertvolle Basis für die Validierung und Bewertung von dreidimensionalen nodalen Methoden mit Rekonstruktion der Stableistungen darstellen.

Schlüsselwörter: Nodale Methoden, Rekonstruktion der Stableistung, Kernheterogenitäten, Siedewasserreaktor (SWR), Nullleistungs-Forschungsreaktor, experimentelle Validierung, Spaltrate, Neutron, Strom, dreidimensionale Verteilung, LWR-PROTEUS experimentelles Programm, HELIOS, PRESTO-2, CASMO-5, SIMULATE-5, MCNPX.

Contents

List of Abbreviations

2D	Two-Dimensional
3D	Three-Dimensional
BA	Burnable Absorber
BWR	Boiling Water Reactor
C5	CASMO-5 - 2D lattice code
C5/S5	CASMO-5/SIMULATE-5 (programme system)
CB	Control Blade
CCCP	Collision Probabilities with Current Coupling
C/E	Ratio of Calculated over Measured Value
CP	Collision Probabilities
CPR	Critical Power Ratio
CPU	Central Processing Unit
DO	Dry-Out
ENDF	Evaluated Nuclear Data File
FD	Finite Differences (method)
FE	Finite Elements (method)
FLPD	Fraction of Limiting Power Density
FLR	Full Length Rod
FR	Fast Reactor
HE	HELIOS - 2D lattice code
HE/P2	HELIOS/PRESTO-2 (programme system)
k-effective	Effective Multiplication Factor
k-infinity	Infinite Multiplication Factor
KKL	Kenrkraftwerk Leibstadt (Switzerland)
LHGR	Linear Heat Generation Rate
LHS	Left Hand Side
LPRM	Local Power Range Monitor
LWR	Light Water Reactor
MC	Monte Carlo
MFLCPR	Maximum Fraction of Limiting Critical Power Ratio
MFLPD	Maximum Fraction of Limiting Power Density
mfp	Mean Free Path
MOC	Method of Characteristics
NPP	Nuclear Power Plant
P2	PRESTO-2 - 3D core simulator
PCR	Partial Current Ratio
PE	Polyethylene
PLR	Partial Length Rod
PMCF	Pin Map Correction Factor
PPM	Pin-Power Map
PPR	Pin-Power Reconstruction

PWR	Pressurised Water Reactor
RHS	Right Hand Side
RI	Resonance Integral
S5	SIMULATE-5 - 3D core simulator
SDM	Shut-Down Margin
SPP	Studsvik Scandpower AB
TIP	Traversing In-Core Probe
TMOL	Thermal Mechanical Operating Limit
TZ	Test Zone
XS	Cross-Section
XSDB	Cross-Section Data Bank

Chapter 1

Introduction

Uranium was discovered in 1789 by Martin Klaproth, a German chemist, and named after the planet Uranus.

This opening chapter first provides a general introduction to nuclear fission as energy source in Section 1.1, to light water reactors (LWRs) as the most common nuclear power plants in Section 1.2, as also to the role of calculations and experiments in LWR operations in Section 1.3. The motivation and objectives of the present doctoral research are presented in Section 1.4, while an outline of the thesis is given in Section 1.5.

1.1 Nuclear fission as source of energy

Already in very early times, mankind understood that energy represented an essential resource for mastering the daily challenges of life. The discovery of fire and the knowledge of how to handle it allowed a quantum jump in life expectancy, life quality and technical development. Besides the sun and a few natural sources of hot water, chemical combustion was for centuries the only process that could provide heat to human beings. It was also the only known way of bringing light into the dark. Apart from his own muscle power, the only sources of mechanical energy available to man were domestic animals, wind and water. Later, the invention of the steam machine and the internal combustion engine extended the applicability of chemical combustion to the production of mechanical power. At the same time, the discovery of electricity and the development of technologies to handle it allowed the transport and distribution of energy on a large scale. Since then, the conversion of hydraulic and thermal energy into electricity represents an extremely relevant aspect in the development of human society.

Although thermal energy can be released from exothermic chemical reactions such as combustion in an engine, it may also be released from processes that do not concern the chemical bindings of atoms in matter. In 1905, Albert Einstein theoretically put forward the equivalence between mass and energy, governed by one of the most elegant and famous equations in physics, namely $E=mc^2$, c being the speed of light in vacuum. This universal relation implies that whenever mass is reduced in a process of any kind, that process leads to an energy release. Naturally, this relation applies to chemical reactions as well.

In 1939, Otto Frisch confirmed experimentally what Lise Meitner and he himself, working together with Niels Bohr, had predicted before, namely that the fission of a uranium nucleus leads to an energy release of about 200 MeV (3.2×10^{-11} Joule). This was the first experimental confirmation of Albert Einstein's special theory of relativity. Otto Hahn and Fritz Strassman showed that fission not only released a large amount of energy, but that it also released additional neutrons which could cause fission in other uranium nuclei and possibly a self-sustaining chain reaction. The same year, Bohr proposed that fission was much more likely to occur in the ^{235}U isotope than in ^{238}U and that fission would occur more effectively with slow neutrons than with fast neutrons. Also in Russia, 1940 saw great advances being made in the understanding of nuclear fission, including the possibility of a chain reaction. Prominent Russian physicists, among them Kirill Sinelnikov, Pyotr Kapitsa, Vladimir Vernadsky and Igor Kurchatov, worked in the field.

The key facts concerning nuclear fission chain reactions started to be known, and the possible use of their enormous potential was taken into consideration. The British MAUD reports, issued in 1941, suggested the feasibility of a nuclear device with gigantic destruction power and, at the same time, also that of a "uranium boiler" for the production of heat.

In December 1942, Enrico Fermi achieved at the University of Chicago, USA, the first self-sustained nuclear chain reaction. His experimental natural uranium fuelled, graphite moderated pile was shut down under controlled conditions after having demonstrated that the reaction could have been maintained for an infinite period.

The Chicago Pile Number One, CP-1, was constructed under an abandoned football stadium at the University campus. On December 2, 1942, first criticality was achieved. The self-sustained nuclear chain reaction having been demonstrated, Fermi's pile was shut-down after reaching 0.5 watt of power. (Source: World Nuclear Association, http://www.world-nuclear.org/info).

In the 1950's, the interest in developing nuclear devices for electrical energy production grew dramatically. The first nuclear reactor to produce electricity (albeit a trivial amount) was the small Experimental Breeder Reactor (EBR-1) in Idaho, USA, which started up in December 1951. After that, several reactor concepts were developed on both sides of the iron curtain, the new focus being on demonstrating the suitability of nuclear energy for producing steam and electricity [1].

Today, with an overall installed capacity of about 380'000 MWe, nuclear power plants (NPP) generate about 14% of the world's electricity demand. After a stagnation period that started in the 1980's, the industry is now showing signs of recovery, manifested through on-going new builds in several countries around the world.

1.2 Light water reactors

More than 80% of the world's operating NPPs, as well as the majority of the projected new installations, are powered by Light Water Reactors (LWRs). In this kind of plant, the fuel consists of low enriched uranium in the form of uranium dioxide (UO_2) pellets loaded into zircalloy tubes (cladding) and arranged in regular assemblies. The slowing down process (moderation) needed to reduce the energy of the neutrons, thus increasing significantly their ability to produce fissions and hence to generate power, takes place in the light (ordinary) water that flows between the fuel rods. This water also accomplishes the important task of removing the heat generated in the fuel and transporting it out of the reactor core.

Depending on the heat transmission process employed, two kinds of LWRs are clearly distinguished. If the heat transfer takes place in the liquid phase only, the plant is referred to as a Pressurised Water Reactor (PWR). If, on the other hand, a phase change (boiling) is used as heat transfer mechanism in addition to the single phase heat transfer, the device is called a Boiling Water Reactor (BWR). In any case, the ultimate design criterion is the ability to cool the fuel under normal, abnormal and potential accidental conditions. This criterion, in turn, is a condition to guarantee fuel integrity. Thus, the design and operation of LWRs relies on two fundamental aspects: one is the accurate knowledge of the three dimensional (3D) neutron field and the associated power distribution, and the other is the determination of the temperature and density of the reactor core materials, in particular the fuel and the moderator (water or mixture of water and steam). These two aspects concern two important areas of reactor engineering: neutronics and thermal-hydraulics, respectively. Recalling that the neutron flux distribution depends on the properties of the fuel and moderating materials, and that the temperature and density of these materials depend on the power distribution, it becomes evident that these two aspects are closely coupled by feedback mechanisms.

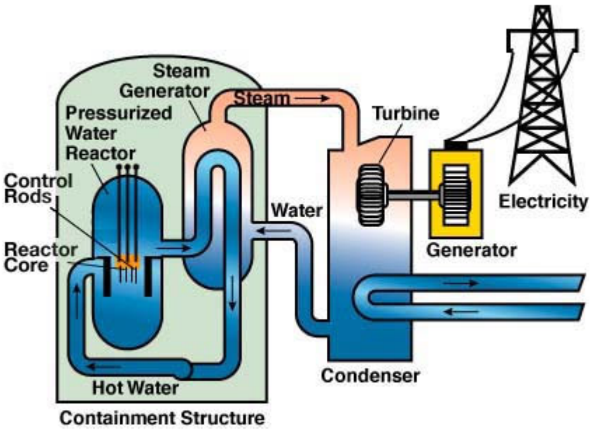

Schematic view of a Pressurised Water Reactor (PWR). The pressure in the primary loop is such that no boiling occurs (ca. 150 bar). The steam to drive the turbine is generated in steam generators which transfer the heat from the primary to the secondary loop. (Source: http://www.oncor.com).

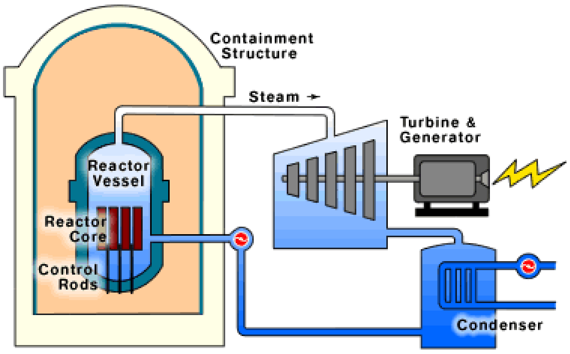

Schematic view of a Boiling Water Reactor (BWR). Boiling occurs in the reactor core and the steam is conducted to the turbine after being separated from the liquid and dried. The pressure in the reactor vessel is approx. 70 bar. (Source: http://www.solcomhouse.com).

1.3 The role of calculations and experiments

Since the pioneering use of nuclear fission for power production, scientists and engineers have been faced with the challenge of obtaining the highest possible energy output while ensuring at the same time the integrity of the reactor. At the very beginning, only poor information about the power distribution in the core could be retrieved. Although the global power level could be deduced from ex-core detector readings and heat balance measurements, an accurate knowledge of the local power developed by the fuel remained impossible. This lack of information had in many cases important consequences on the integrity of the fuel and the safety of the plant. It was therefore evident that a better determination of the core local power distribution was of fundamental importance.

For several reasons, a direct measurement of the 3D local power distribution at fuel pellet level in an operating LWR is not possible. In particular, it is not possible to locate fixed neutron or gamma detectors inside the fuel elements, since these are loaded, shuffled or discharged during every core reload. Also the amount of cabling which would be necessary to retrieve the detector signals required for a detailed flux mapping would be prohibitively large. Thus, in power reactor cores, only global and regional measurements are made. In PWRs, ex-core detectors are placed in the shield that surrounds the core, while movable detectors such as in-core fission chambers or aero-ball activation probes are regularly (for example once a month) driven along specific fuel assembly guide tubes at selected core positions to produce a 3D regional power map. In BWRs, Traversing In-Core Probes (TIPs) are used, and local power range monitors (LPRMs) are fixed at specific axial positions (normally 4 along the core height) in the water gap between the fuel elements at specific core positions.

Because of the constraints mentioned above, it becomes evident that the detailed local power distribution at fuel pellet level can only be known through calculations. Of course, in order to demonstrate that the calculated local power distribution has sufficient accuracy for the purpose of thermal limit monitoring, adequate agreement needs to be guaranteed between the calculated and measured global power distributions. For instance, at regular periods (normally once per month) the 3D flux (or power) is measured using movable detectors like those mentioned above. In a BWR, this 3D measured power distribution is used basically for the two following purposes (in a PWR for the second one only):

1) To calibrate the local power range monitors (LPRMs).
2) To verify that the calculated 3D power distribution complies with the pre-defined accuracy requirements.

The LPRMs allow the BWR reactor operators to have a continuous picture of the global 3D power distribution in the core[1]. The surveillance of the thermal margins, on the other hand, must rely on the results of the 3D core simulator. At regular intervals, for example every five minutes, the local power distribution is calculated according to the reactor conditions at that particular moment. Two approaches may then be used:

1) Adjustment of the calculated 3D power distribution against the detector readings (e.g. LPRMs in a BWR) before the local power is used for evaluation of the thermal margins (adaptive method).
2) Evaluation of the thermal margins using the calculated local power directly.

Both approaches are used in the industry. The adaptive method is preferred in cases where the accuracy of the 3D core simulator is not sufficient to allow the direct use of the calculated local power. In modern core monitoring systems, however, the preferred strategy is to let the

---

[1] For BWR cores, the surveillance of the 3D power distribution is more important than for PWRs, where the axial component plays a secondary role and is mostly monitored through the core axial offset.

calculated local power distribution build the basis for the surveillance of the thermal limits. The measurement campaigns are then used to verify the 3D simulator results. This methodology is applied, for example, at the Leibstadt NPP (KKL) in Switzerland [2].

In all cases, for the on-line monitoring of the plant, it is required that the 3D core calculations are performed in relatively short time, normally less than 30 seconds. It is in this context that the availability of qualified, reliable and fast computational tools for reactor physics calculations plays a fundamental role in the safe and economical operation of modern nuclear power plants.

These computational tools, however, can only be trusted if the results they deliver are supported by experimental evidence. Of course, important evidence is provided by the flux measurements done during plant operation. Further validation may be done using gamma-scan measurements of irradiated fuel in the reactor fuel pond. Nevertheless, experimental programmes involving critical facilities and hot laboratories play a crucial role in the investigation of specific effects. In particular, although plant measurements reflect the real operation environment, they cannot describe the detailed response to particular "clean" conditions. It is in this respect that experiments that are especially designed for the investigation of particular effects or phenomena are irreplaceable tools for the assessment of calculation schemes.

Thus, to pursue the ultimate goal of safe and economical nuclear power production, two areas of research must be closely and continuously addressed:

1) The development of analytical and numerical methodologies for the accurate calculation of the neutron flux distribution in the core.
2) The deployment of appropriate experimental facilities, in conjunction with the application of suitable measurement techniques, to assess the accuracy of the calculated values.

The most challenging questions in connection with these two areas of research are: first, how can the conditions occurring in the power reactor core be simulated in an experiment in order to retrieve data applicable to the proposed verification and, second, how can the experimental evidence gained under the particular conditions of the experiment be reliably used to assess the performance of the calculation methods in the real power reactor core environment.

While the calculation methods are designed to account as much as possible for the conditions occurring in the power reactor, it is not possible to design experiments that reproduce exactly (or in many cases even approximately) those conditions. For example, a realistic distribution of temperature, power density and exposure is very difficult to reproduce in an experimental setup designed for high precision nuclear measurements. Moreover, the geometry of the power reactor core can obviously be only partially reproduced in an experimental setup. Thus, measurements must be made under conditions that are achievable within the constraints imposed by the experiment, and these may differ significantly from those occurring in the power reactor core.

Despite these unavoidable constraints, experiments can be designed to reflect as closely as possible certain conditions that are relevant for the particular phenomena to be investigated. For instance, in the LWR-PROTEUS programme performed at PSI, full-size BWR fuel assemblies were used to obtain valuable information about pellet-wise, three-dimensional total-fission distributions in a realistic assembly geometry and composition.

PROTEUS is a zero power critical facility especially designed to offer high flexibility concerning the configuration used in the central measurement region, the so called test zone. The facility is located at the Paul Scherrer Institute in Switzerland, and has been in operation since 1968. Starting in 1998, the LWR-PROTEUS experimental programme [3], [4], [5] was developed with the aim of providing measurements of total-fission and ^{238}U capture rate distributions, as well as pin removal reactivity effects, in full-size BWR fuel assemblies. The measurements performed constitute a large collection of valuable experimental evidence for the validation of LWR neutronics codes, as applied to current-day, highly heterogeneous fuel assembly designs. More details concerning the PROTEUS reactor and the LWR-PROTEUS experimental programme are given in Section 2.5.

The next section briefly describes the application of the LWR-PROTEUS experimental database for the appraisal of core calculation methodologies, the main goal of the present doctoral research.

1.4 Motivation and objectives of this doctoral research

The main targets set for the present research are the development and application of a methodology aimed at the optimal use of LWR-PROTEUS experimental results for the appraisal and assessment of 3D power reactor calculation tools, as also the identification of trends, strengths and weaknesses related to them. Thereby, focus is set on the assessment of methodologies used to determine the power distribution in BWR fuel assemblies using fixed moderating conditions. Thus, it is mainly neutronics aspects that are addressed, the reactor thermal-hydraulics being considered as providing fixed boundary conditions.

The principal aims addressed in this thesis are:

1) To propose and apply an effective methodology for comparing the results of local (fuel pellet level) power distributions obtained with industrial core monitoring and design calculational schemes, against experimental evidence from the LWR-PROTEUS programme.
2) To demonstrate the applicability of LWR-PROTEUS data for the appraisal and validation of nodal codes. Complementary, quantitative insights which could impact the design of future experiments could be obtained at this stage.
3) To assess the capability of the reference calculational schemes to reproduce the experimental results, identifying strengths, weaknesses and trends and analysing their sensitivity to changes in relevant parameters.
4) To derive conclusions about the impact of the observed behaviour on real BWR core monitoring and design issues.

In the past few years, a considerable amount of effort has been spent on the validation of a range of 2D assembly codes by using LWR-PROTEUS results, and also 2D comparisons against Monte Carlo calculations have been done [6], [7], [8]. On the other hand, less attention has been paid to the field of validation and appraisal of codes used for the design and simulation of LWR cores, in particular three-dimensional nodal core simulators. Early radial and axial comparisons of nodal, pin reconstructed results with LWR-PROTEUS experiments were published in [9], where a simple approach for the description of the test-zone boundary was used. Independently from LWR-PROTEUS, axial comparisons of nodal reconstructed power profiles with Monte Carlo results focusing on the control blade tip region have been reported in [10], where different void fractions were analysed. In this context, the study of 3D heterogeneities such as partially inserted control rods, part-length rods and axial enrichment boundaries represents a topic of particular importance.

Thus, the area of interest for the application of nodal core simulators in the analysis of LWR-PROTEUS measurements concerns the radial and axial heterogeneities occurring in different test-zone configurations. The heterogeneities studied in the horizontal plane include fully inserted absorber blades and channel-bowing effects investigated by observing the impact of inter-assembly gap variations. Concerning axial heterogeneities, variations of fuel rod enrichments and burnable absorber concentrations, as well as the presence of part-length fuel rods and/or of a partly-inserted control blades have been studied.

The present doctoral research aims at the assessment of modern whole-core simulation methodologies for BWRs via a systematic utilisation of a variety of integral measurements conducted in the LWR-PROTEUS Phases I and III. Issues of interest include:

- Analysis of the 3D flux behaviour in the vicinity of interfaces and core discontinuities.
- Definition and assessment of the boundary conditions used to represent the interaction between the calculated system and its surroundings.
- Study of the impact of parameter variations on the total-fission rate. Parameters of interest concern the lattice modelling, the coupling between test-zone and driver zones and the 3D nodal representation of the fuel.
- Identification of strengths and weaknesses that are implicit in the methodologies.

The investigations performed in this thesis provide information about the level of accuracy that may be expected for the determination of the pellet-level power distribution in a power reactor. The accuracy of the calculated local power is one of the most important aspects to be considered in the determination of limit values for safety relevant parameters such as the linear power density. Subordinate to this, improvements in fuel utilization and operational flexibility could also be achieved through a better knowledge of the local power distribution in the core.

At this point, it is important to bear in mind that the moderator materials used in the individual LWR-PROTEUS configurations investigated (see Table 1) were uniformly distributed over the entire test zone. They were selected to represent the special cases of cold zero power (Phase I) and hot zero power (Phase III), respectively. Particular sources of uncertainty existing in real production applications, such as temperature and moderator density distributions, have not been accounted for. However, it is indeed in this frame where the value of the LWR-PROTEUS programme in terms of providing a set of "clean experiments" must be underlined.

The present research also contributes to the understanding of the strengths and weaknesses of LWR-PROTEUS-type experiments for validating the modelling of LWR core heterogeneities.

The calculation schemes used have been set up using two reactor physics code systems that are designed for power plant core simulation. These systems are HELIOS/PRESTO-2 (HE/P2), presently used in the Leibstadt Nuclear Power Plant (KKL) and CASMO-5/SIMULATE-5 (C5/S5), which is the latest generation of codes offered by the nuclear software producer Studsvik Scandpower (SSP). In order to allow an accurate representation of the interaction of the test-zone with its surroundings, Monte Carlo (MCNPX) models have been employed for the determination of boundary conditions between the central 3x3 array of BWR fuel assemblies and the outer PROTEUS reactor regions. The calculation schemes are configured to reflect as much as possible the modality of use applied in production calculations. For instance, nuclear parameter data banks for reflected single assemblies have been generated, as it is the case in power reactor applications. These data banks contain the cross-sections, discontinuity factors and 2D pin-power distributions needed in the 3D nodal calculation with pin-power reconstruction. The nodalisation adopted for the 3D nodal calculation is similar to that used for power reactor cores. The calculation schemes have been set up such as to allow sensitivity studies concerning geometrical, spectral, and diffusion or transport theory parameters. These include, for instance, the impact of fuel assembly displacements (channel bowing or sub-assembly pressing), which are significant sources of uncertainty in power reactor calculations. Axial heterogeneities, such as enrichment boundaries, partially inserted control blades or the tips of partial length rods (PLRs), are modelled without adapting the axial nodalisation to the particular discontinuity being studied. This has been done intentionally in order to reflect the real situation occurring in production applications, where the nodalisation is uniform over the whole core. For the same reason, spacers are described as branch-off cases leading to delta-cross-sections, and not as particular nodes with a special set of cross-sections. The effect of different modelling aspects concerning the representation of the test-zone surroundings by means of boundary conditions, are also analysed.

In accordance with the mentioned scope, the LWR-PROTEUS configurations that have been investigated in this thesis were selected such as to allow the appraisal of the nodal methodologies with regard to different types of radial and axial heterogeneities. These configurations are listed in Table 1.

Table 1 LWR-PROTEUS configurations studied in this thesis. In Phase I, the test zone was loaded with SVEA-96+ fuel elements, in which two axial segments (upper and lower) with different nuclear designs (enrichment and gadolinium content) are present. In Phase III, SVEA-96 Optima2 fuel assemblies were investigated. These assemblies contain partial length rods (PLRs) of two different lengths.

Conf.	Moderator	Axial Region	Heterogeneity (direction)
I-1A	Light water	Lower	None
I-1C	Light water	Boundary lower/upper	Enrichment boundary (axial)
I-2A	Light water	Lower	Hafnium blade (radial)
I-6A	Light water	Lower	Hf Blade, partly inserted (radial+axial)
III-1	66.3% H_2O + 33.7% D_2O	Tip of 1/3-length PLR	Partial Length Rods at lattice corners (axial)
III-2	66.3% H_2O + 33.7% D_2O	Tip of 2/3-length PLR	Partial Length Rods adjacent to central water canal (axial)

1.5 Thesis outline

This thesis is structured in 9 chapters, which are summarised below:

In the present chapter, **Chapter 1**, some general aspects concerning nuclear energy and the motivation and aims of the present research have been discussed.

Chapter 2 presents a review of the methodologies used in the industry for the monitoring and design of power reactor cores. The relevant aspects of the calculation chains and the approximations and limitations arising from their use are discussed. Further, the concept of nodal diffusion theory methods with pin-power reconstruction is introduced, and a general description of the programme systems HELIOS/PRESTO-2 (HE/P2) and CASMO-5/SIMULATE-5 (C5/S5) is provided. The state of knowledge concerning the assessment of such methodologies is reviewed from the point of view of comparisons against high-order transport results, which is a validation procedure widely used, but also considering the use of experimental data, which is the main objective of this thesis. The experimental data used belongs entirely to the LWR-PROTEUS programme, the main characteristics of which are also summarised in this chapter.

Chapter 3 discusses the methodology used to model the LWR-PROTEUS test zone using the programme systems HE/P2 and C5/S5. The fundamental aspects of the lattice calculations, the determination of the necessary test-zone boundary conditions and the modelling issues concerning the solution of the 3D problem by means of the nodal diffusion method are presented in this section. In particular, the assumptions needed to represent the experimental setup with the input capabilities of the specific programmes are discussed. The methodology focuses on preserving the modelling approaches used in production calculations for power reactors, while at the same time describing the particularities of the LWR-PROTEUS configurations as accurately as possible. In this context, the fundamental issue of representing the surroundings of the test zone by means of appropriate boundary conditions is addressed in detail.

Chapter 4 discusses the case of a uniform system consisting of an array of fuel elements (SVEA-96+) with identical fuel design (pin layout) and uniform axial composition (Configuration I-1A). In the absence of leakage and considering nominal geometry, this would correspond to an infinite array of identical fuel assemblies. Thus, this case is especially suited to serve as a reference for studying the impact of different types of heterogeneities, both in the radial and axial directions. In addition to the standard case, for which the modelling options were intentionally kept as close as possible to those used in production calculations at KKL, the sensitivities to variations in parameters for the lattice calculation and for the representation of the test-zone boundary are also investigated. These sensitivity calculations give a picture of the importance of the different modelling aspects on the pin-power distribution.

Chapter 5 addresses the impact of a fully inserted control blade (CB) on the radial power distribution (Configuration I-2A). Due to the strong flux gradients present, the calculation of the pin-power distribution in the presence of a control blade is one of the most significant challenges for the pin-power reconstruction methodology. In particular, the constraints imposed by the use of a L-shaped control blade (half of a cruciform-shaped BWR-CB) and the consequences of the use of reflected symmetry in the lattice calculations are discussed. As in Chapter 4, the sensitivity to different modelling options is investigated.

Chapter 6 concerns the case of axial changes in enrichment and gadolinium content (Configuration I-1C). Axially varying fuel is commonly used in BWR cores, where the axial power profile is an important criterion for design. This produces significant changes in the axial distribution of the pin-wise fission rate, mainly in the immediate vicinity of the interface between two lattice types.

Chapter 7 treats the effects of the strong axial heterogeneity occurring at the end of a partially inserted control blade (Configuration I-6A). These effects occur in the presence of the strong radial perturbations discussed in Chapter 5. The partial insertion of a CB thus leads to significantly skewed 3D fission rate distributions, which are particularly demanding for the nodal methodologies.

Chapter 8 analyses the case of fuel with partial length rods (SVEA-96 Optima2, Configurations III-1 and III-2). This design feature finds wide application in modern BWR cores due to its improved characteristics concerning critical power ratio and shut-down margin.

However, the axial transition between fuel, fission gas plenum and moderator imposes additional challenges for the determination of the local power, mainly in the axial direction.

Concluding this thesis, **Chapter 9** recalls the main aim of the present research and summarises the principal messages, presenting the most relevant results in a compact manner. Complementing this discussion, the advantages and limitations of using the LWR-PROTEUS experimental database for the assessment of industrial 3D nodal codes are discussed. Furthermore, attention is paid to the applicability of the results obtained in this research to the situation occurring in actual BWR cores. Despite the fact that the present experimental comparisons have been made for very specific conditions, the observed behaviour can be extended to a larger application domain. In this context, observations are made about the calculational accuracies achievable in the surveillance and design of power reactor cores. Finally, closing the chapter, suggestions are made for further investigations in the present field of research.

Chapter 2

Reactor physics calculations and experiments

In 1932, the British physicist James Chadwick discovered the neutron.

The general methodologies for steady-state reactor physics calculations in nuclear power plant (NPP) applications are first outlined in Section 2.1. Nodal methods for core analysis are discussed in more specific terms in Section 2.2, while Section 2.3 provides further details about such methods in the context of pin-power reconstruction. The calculation chain and the individual neutronics codes used in the present research are outlined in Section 2.4. Finally, Section 2.5 presents details about the LWR-PROTEUS programme and the experimental configurations considered currently for validation of the calculation chain.

2.1 Steady-state reactor physics calculations for nuclear power plants

The basic goal of reactor physics calculations applied to nuclear power plants is the determination of the various nuclear reaction rates, i.e. the number of nuclear reactions of different types occurring per unit volume and unit time at any given point in the reactor core. From the total-fission rate, the power developed in the fuel can be derived. Since neutrons interact with matter, and matter undergoes changes caused by these interactions, the phenomena affecting the neutron distribution in the reactor core are closely coupled also to fuel composition changes caused by neutron absorption. Basically, the determination of the neutron density is governed by two general relations, expressed by the Boltzmann and the Bateman equations. The first describes the neutron distribution in space, direction, energy and time when the properties of the interacting medium are known. The second describes the changes of the medium caused by neutron interaction. This feedback process is depicted in Figure 1.

2.1.1 The Boltzmann and the Bateman equations

Let $N(\vec{r},\vec{\Omega},E,t)d\vec{r}d\vec{\Omega}dE$ be the number of neutrons present at time t in the phase space interval $d\vec{r}d\vec{\Omega}dE$, where $\vec{r}$ is the position vector, $\vec{\Omega}$ the direction vector and E the energy. Then, denoting with v the speed of neutrons having energy E,

$$\Phi(\vec{r},\vec{\Omega},E,t)d\vec{r}d\vec{\Omega}dE = vN(\vec{r},\vec{\Omega},E,t)d\vec{r}d\vec{\Omega}dE \qquad \{1\}$$

is the total distance travelled per second by the neutrons present at time t in the phase space interval $d\vec{r}d\vec{\Omega}dE$. This magnitude, called the angular flux, is the unknown variable in the general Boltzmann equation for the transport of neutrons:

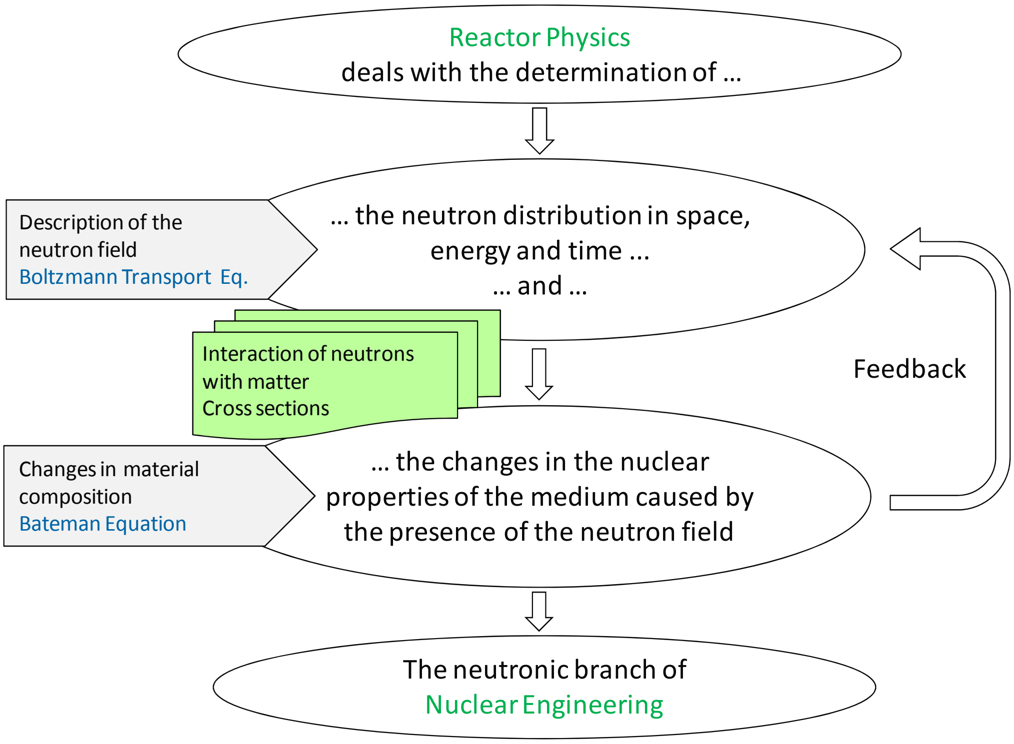

Figure 1 The scope of reactor physics. Basically, the determination of the neutron distribution in the reactor core and the changes in material composition due to interactions with neutrons are governed by the Boltzmann and the Bateman equations, respectively.

$$\frac{1}{v}\frac{\partial \Phi}{\partial t} + \vec{\Omega}\cdot\vec{\nabla}\Phi + \Sigma_t\Phi = \int_{4\pi} d\,\vec{\Omega}' \int_0^{\infty} \Sigma_s\left(E' \to E, \vec{\Omega}' \to \vec{\Omega}\right)\Phi' dE' + S \qquad \{2\}$$

where, for clarity, the independent variables have been omitted, Σ_t and Σ_s denote the total and scattering macroscopic cross-sections and S represents the source term.

This general integral-differential equation describes the balance between neutrons entering and leaving a specific point in the phase-space. On the left hand side (removals), the first term represents the variation of the angular flux in time, the second gives the streaming or leakage out of the differential volume in question, while the third term quantifies the neutrons that are physically removed from the system (absorption)[2] or are scattered to other energies and directions. On the right hand side (appearances), the first term accounts for the neutrons that are scattered from any direction and energy into the interval $(\vec{\Omega} + d\vec{\Omega}, E + dE)$, while the second represents the source neutrons entering the system (fission and external sources).

The macroscopic cross-sections depend on the properties of the matter and the numerical density of the nuclei present. Thus, for a material composed of J isotopes j:

$$\Sigma(\vec{r}, E) = \sum_{j=1}^{J} N_j(\vec{r})\sigma_j(\vec{r}, E) \qquad \{3\}$$

---

[2] In this context, absorption means the disappearance of the neutron in question, i.e. it consists of radiative capture and fission.

where $\sigma_j(\vec{r}, E)$ is a particular type of microscopic cross-section of isotope j, whose units are cm^2. Integrating the angular flux {1} over all directions of neutron motion gives the scalar flux (also simply called flux):

$$\phi(\vec{r}, E, t) = \int_{4\pi} \Phi(\vec{r}, \vec{\Omega}, E, t)\, d\vec{\Omega} \tag*{\{4\}}$$

The product of the macroscopic cross-section and the flux gives the reaction rate, the various reaction rates being basic parameters needed for the design and monitoring of nuclear reactor cores:

$$RR_x(\vec{r}, E, t) = \Sigma_x(\vec{r}, E) \cdot \phi(\vec{r}, E, t) \tag*{\{5\}}$$

where the subscript x denotes the type of reaction, e.g. fission, absorption, capture, scattering, etc. Thus, the reaction rates describe the production and removal of nuclei in matter (with the exception of scattering, which does not change the nuclear properties of the interacting nucleus). Recalling that nuclei are also transmuted by means of decay, leads to the Bateman equation in its general form:

$$\frac{dN_i}{dt} = -\lambda_i N_i - r_i N_i + \sum_{j \neq i} N_j(\lambda_{j\to i} + r_{j\to i}) + \Gamma_i \tag*{\{6\}}$$

where λ_i is the decay constant and r_i the absorption rate per nucleus of isotope i:

$$r_i = \int_{4\pi} d\vec{\Omega} \int_0^\infty \sigma_{a,i} \Phi dE \tag*{\{7\}}$$

Analogously, $r_{j\to i}$ symbolises the production rate of isotope i due to neutron reactions in one nucleus of isotope j, while Γ_i represents the yield of isotope i due to fission:

$$\Gamma_i = \sum_{j=1}^{N_{fis}} \int_{4\pi} d\vec{\Omega} \int_0^\infty \gamma_{j\to i} \sigma_{f,j} N_j \Phi dE \tag*{\{8\}}$$

In words, the Bateman equation states that the rate of change of the number density of isotope i is given by the sum of four contributions: first, the decay rate of the nucleus, second, its removal rate (due to capture and/or fission), third, the production of isotope i due to decay and/or capture in other isotopes, and fourth, the fission yield.

2.1.2 Solution of the Boltzmann transport equation

We shall now focus on the methods of solution of the Boltzmann transport equation. The composition changes described by the Bateman equation are usually accounted for by a quasi-stationary approach, in which the matter is depleted using the flux solution of a specific step, giving the system composition for the next step (burnup calculation). Although the accurate determination of the fuel depletion is an extremely important aspect in reactor physics applied to power reactors, its study lies beyond the scope of this thesis and will not be discussed further.

Thus, from now on and for the particular case of the studies concerning this thesis, the properties of matter are assumed to be known and remain unchanged in time. This assumption is well supported by the two following facts: first, the fuel used in the LWR-PROTEUS phases I and III is fresh (not irradiated) and contains exclusively enriched uranium gained from natural ore (no reprocessed uranium or plutonium). This means that, for practical purposes, the nuclear properties of the fuel can be considered constant in time. The second fact concerns the very low power level at which the LWR-PROTEUS experiments were performed (ca. 100 W), which leads to a negligible depletion of the fuel.

Returning to the general Boltzmann equation for the transport of neutrons {2}, one important fact can be readily observed, namely that no terms describing collisions between neutrons are present. Even in very high flux reactors the neutron density is much lower than the number density of nuclei in the matter. Hence, interactions between neutrons can be neglected, which renders the Boltzmann transport equation for neutrons linear. However, and despite this important simplification, the exact numerical resolution of the general transport equation for the angular flux, with its seven independent variables $\left(\vec{r},\vec{\Omega},E,t\right)$[3], is very difficult, being analytically feasible under a number of simplifying assumptions and in very simple geometries only.

Before addressing the methodologies used to solve the Boltzmann equation, one important aspect must be mentioned, viz. the characterisation of the various interactions of neutrons with matter. This very vast research area is in fact a particular branch of neutron physics and will not be addressed here. For our discussion, it is important to emphasise that the knowledge of the microscopic cross-sections and other basic parameters describing each type of nuclear reaction is a common pre-requisite to all calculation methods, both stochastic and deterministic. These basic cross-sections are compiled in so called Evaluated Nuclear Data Files (ENDFs), and are independent of the system to which they are to be applied. For all discussions made in this thesis, the ENDFs are given and no consideration is made regarding their content other than the impact they show on the final results.

Figure 2 briefly depicts the role played by the ENDFs in the calculation chain. The determination of the ENDFs is based on general physical principles (measurements and models). As mentioned, they are independent of the system to be calculated.

Stochastic, also known as Monte Carlo (MC) methods, make use of these data files almost directly, taking advantage of their continuous energy representation. MC methods allow one to obtain very accurate solutions of the neutron transport equation, with practically no constraints on the geometry and composition of the system. Unfortunately, these methodologies demand enormous amounts of computer resources, which makes them inadequate for production calculations related to the core design and monitoring of nuclear power plants.

Thus, for industrial applications, where the 3D flux distribution at pellet level − including the iterations needed to account for the thermal-hydraulic, thermal-mechanic and xenon feedback effects − must be known for the complete core in the time-frame of seconds, only deterministic methods are able to provide the necessary computational speed. In the deterministic approach, the solution of the problem is a function of the independent variables. In the case we are considering, this means that the angular flux must be expressed as a continuous, well behaved function of $\vec{r},\vec{\Omega},E$ and t in the whole problem domain. Unfortunately, the exact analytical solution of the general Boltzmann equation {2} in a real, heterogeneous geometry such as the

---

[3] The space vector has three components, the directional vector has two.

reactor core is not possible. Even the numerical solution of the general equation in such systems is very cumbersome and, observed from a practical point of view, unfeasible. Thus, approximations must be made to simplify the general equation, taking advantage of the characteristics of the nuclear systems encountered in practice. These approximations allow the development of numerical schemes that are suitable to be programmed into computer codes.

A first simplification consists in recognising the degree of time dependence of the problem. Transient calculations require the explicit inclusion of the time variable, and this is mandatory for the analysis of fast transients, like for example the sudden ejection of a control rod. On the other hand, normal plant operation and slow transients can be described by stationary or quasi-stationary schemes. Here, the partial derivatives with respect to time are set to zero, and slow variations in the properties of matter, and consequently in the neutron flux, are accounted for by successive solutions of the stationary problem. This is, for example, the case in fuel depletion calculations, control rod position adjustments and/or xenon transients. In the particular case of this thesis, only the stationary case is relevant. All measurements and calculations correspond to critical configurations and are therefore independent of time.

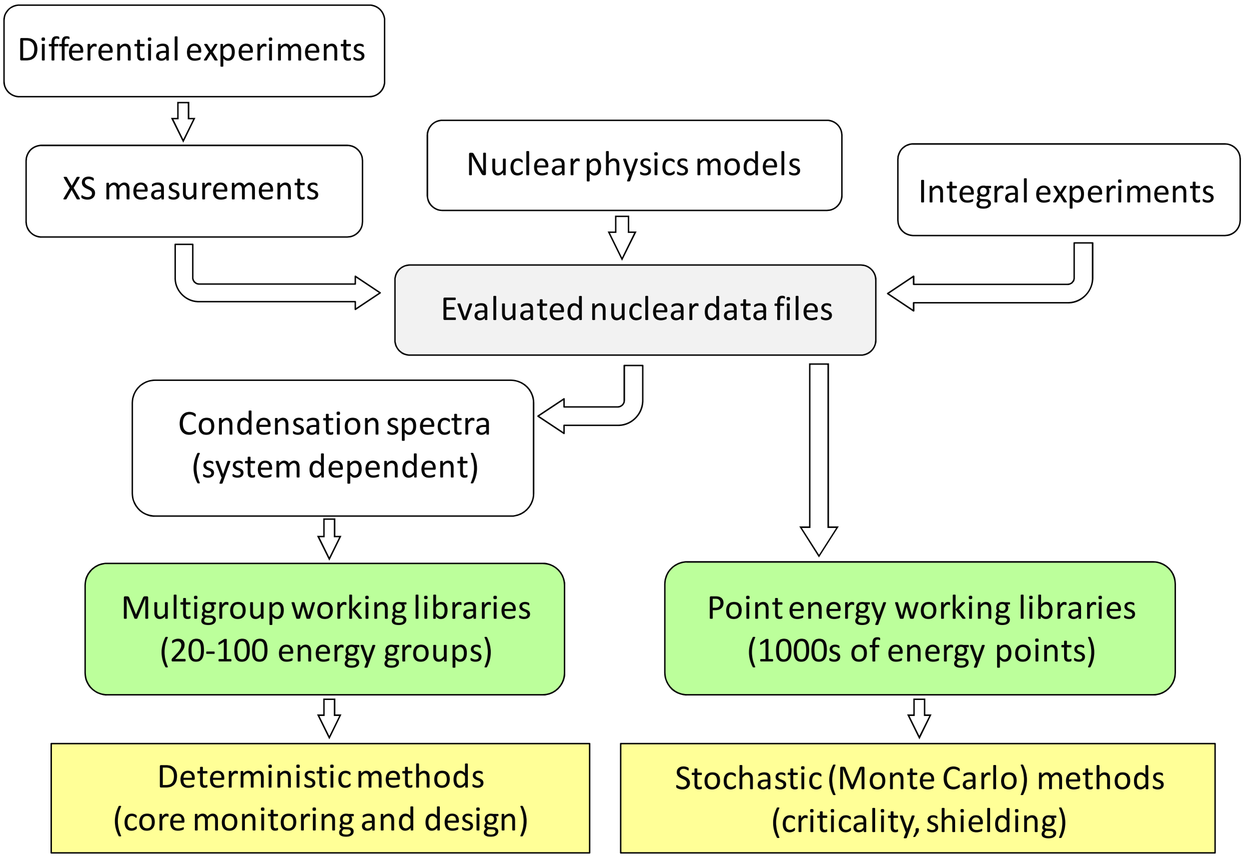

Figure 2 Schematic view of the role played by the evaluated nuclear data files in the calculation chain. Stochastic (MC) methods use the ENDFs directly, while for deterministic methods so-called working libraries are created as an intermediate step. In these libraries, the energy is discretised in intervals or groups, making them dependent on the condensation spectra.

Even for deterministic calculations in steady-state, the determination of the 3D angular flux in the whole reactor with fuel pellet detail and with the needed energy resolution would require an enormous amount of computational effort. Thus, a second important simplification is made. It consists in the subdivision of the calculational process into two main levels: lattice and core calculations. These are described below.

2.1.3 Lattice calculations

In the first level, called lattice or assembly calculation, 2D transport methods like collision probabilities (CP) or method of characteristics (MOC) [11], [12] are used. This calculation is generally performed without knowledge of the composition and operating conditions outside the system under consideration. In most practical cases, this system comprises a small portion of the reactor core (usually one fuel assembly with its corresponding half-gaps) and is described with high space and neutron energy resolution, usually few millimetres and 20-100 energy groups, respectively. The lattice surroundings being unknown, they are usually assumed to be identical to the lattice itself. Thus, the system is modelled imposing zero-net-current (reflective) boundary conditions to the calculation domain.

Figure 3 depicts the lattice calculation process. If possible, symmetry is accounted for in order to save calculational effort, for example by solving only one half of a BWR fuel assembly by cutting it along the NW-SE diagonal with a reflective boundary condition.

The multiplication factor (eigenvalue) of such a system is the infinite multiplication factor (no leakage) k_∞, and the corresponding spectrum (eigenvector) also reflects this no-leakage situation. Normally, this spectrum differs from the criticality spectrum at $k = 1$. In an operating reactor, on the other hand, each region of the core satisfies the balance between production, removal and leakage. Therefore, each subsystem may be regarded as being critical. Deviations are compensated by out-leakage or in-leakage, depending on the sign of $(k_\infty - 1)$. It is this leakage effect which causes the criticality flux (or criticality spectrum)[4] to be different from the infinite medium flux. The criticality or leakage-corrected flux is also referred to as the fundamental flux, which is the result of fundamental mode (leakage) calculations performed at lattice level, for instance by means of the B_n method [11], [13].

The (deterministic) lattice calculations require the existence of pre-calculated multigroup working libraries. These working libraries are closely coupled to the lattice codes that use them, and are therefore prepared by the code developers and delivered together with the programmes. In these libraries, that are created starting from the general ENDFs, the energy is discretised in intervals or groups, making them dependent on the condensation spectra. This means, for example, that while an ENDF may be equally used on a thermal or a fast system, a multigroup working library created for LWR applications will not be suitable for fast reactor (FR) calculations.

Lattice calculations are performed for every lattice design present in the core and for any condition potentially occurring in it (burnup, moderator density and temperature, fuel temperature, xenon concentration and presence of control elements, among others). The results of these calculations are assembly-averaged (homogenized) cross-sections (XS), pin-power maps (PPM) and discontinuity factors (DF) representing a particular operational state. These data are then grouped and parameterised (in the form of tables or polynomial coefficients) in so called Cross-Section Data Banks (XSDB), which act as data sources for the 3D core calculations.

---

[4] This is the energy dependence of the flux, which is relevant for the leakage or fundamental mode calculation.

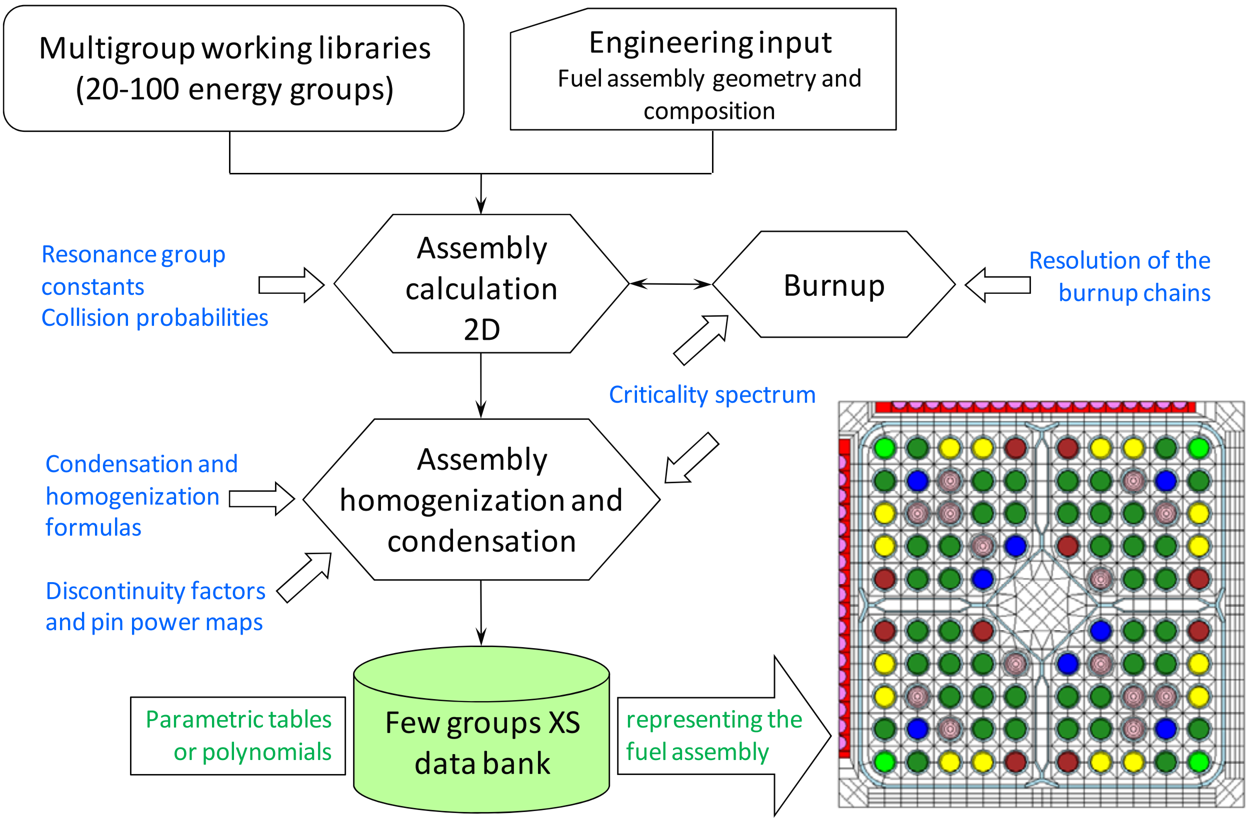

Figure 3 Schematic representation of the lattice calculation process. In this example, a BWR fuel assembly of type SVEA-96+, used in Phase I of the LWR-PROTEUS experiments, is shown.

2.1.4 Core calculations

In the second level, usually called core calculation, the 3D problem is solved for the whole core, in some cases including the reflector. At this level, and with the main goal of saving computer resources, the spatial and energetic discretisation is much coarser than those used in the lattice calculation. The core is subdivided into sub-regions, widely known as nodes, which usually have the radial dimensions of one fuel assembly with its corresponding half-gaps (BWRs), or in some cases 1/4 assembly with half-gaps (PWRs). Axially, the number of nodes is chosen so that their shape is approximately cubic (ca. 25 in BWRs and ca. 18 in PWRs).

As result, the neutron flux distribution over the whole reactor core is obtained, constituting the basis for the determination of the parameters needed for the design and monitoring of the power plant. These are, for instance, nodal power and burnup, pin power and burnup, margin to thermal limits and core reactivity (k-effective). The determination of the 3D power distribution is in addition essential for the calculation of the thermal-hydraulic parameters governing the reactivity feedback effects occurring in the core. The core calculation process is depicted in Figure 4.

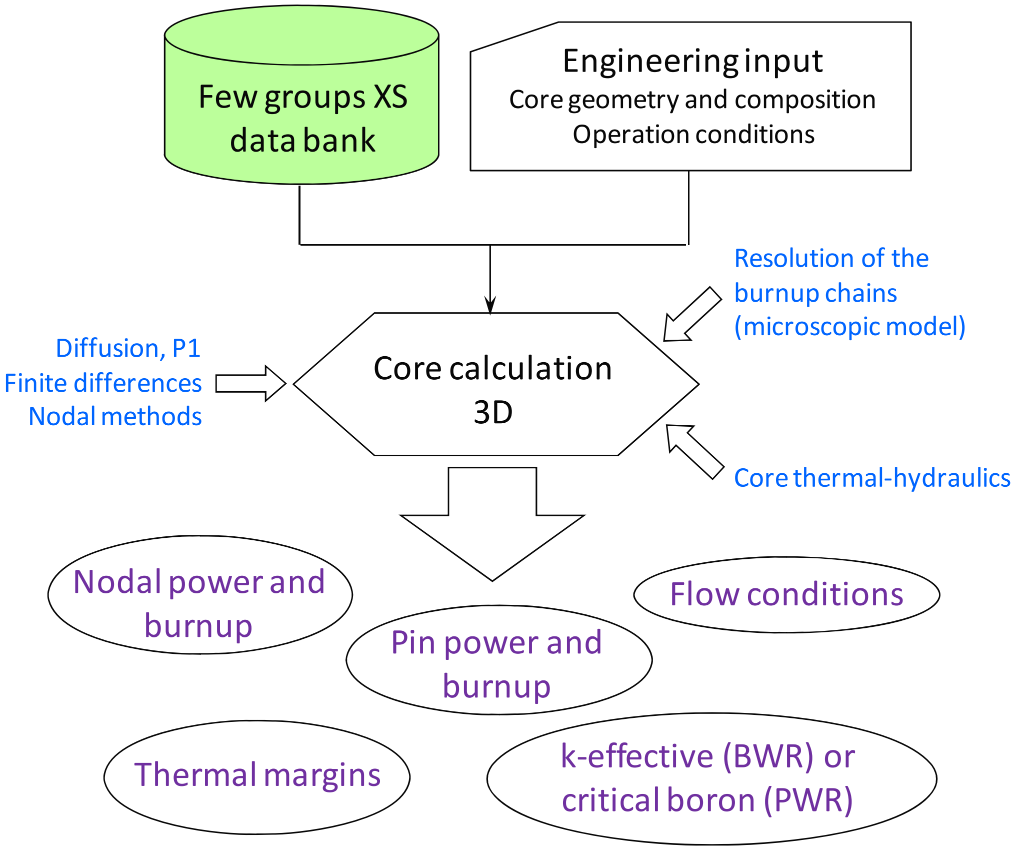

Figure 4 Schematic view of the core calculation step. Nodal methods, solving the diffusion equation and including pin reconstruction capabilities, represent the methodology most commonly applied to power plant design and monitoring.

2.2 The nodal methodology for core analysis

Referring to the steady-state methodologies applied to the design and monitoring of power reactor cores, we mentioned two important simplifications: one is the elimination of the time dependence from the basic equations, the second is the subdivision of the deterministic calculation process in two well-defined steps. During this presentation, we mentioned methods that are used at lattice calculation level. However, while CP and MOC are well suited for the calculation of the micro-flux inside the fuel assembly with high energy resolution, their application in the whole core 3D case would require an unacceptable amount of computer resources.

In the nodal methodology, the core is subdivided, as mentioned earlier, into relatively large volumes (nodes) of preferably cubic shape. These nodes are neutronically coupled, leading to the global solution of the 3D problem in the reactor core while considering the relevant boundary conditions. Taking advantage of the homogenisation and condensation process applied to the cross-sections generated during the lattice calculation, three further approximations, leading to the P_1 and the diffusion equations, are imposed to the stationary Boltzmann transport equation. These approximations are discussed in the following. It should be mentioned that nodal diffusion methods, i.e. methods based on diffusion theory, represent the methodology most commonly applied to power plant design and monitoring. However, nodal methods based on P_1 and/or P_3 theory exist as well, although they are mostly applied in non-conventional situations.

2.2.1 The P1 and diffusion approximations

To begin with, one important simplifying fact must be mentioned: although the neutron flux in the reactor core is not exactly isotropic, the directional dependence of the angular flux is relatively weak. In other words, it is not far from reality to assume that, at any given point in the core, the number of neutrons travelling in one specific direction is not extremely different from the number of neutrons travelling in other directions. Naturally, this assumption is less valid in the presence of strong absorbers or at the core boundary. However, for the calculation of the flux distribution, and consequently the reaction rates in the power reactor core, this assumption is acceptably accurate.

Now, the angular flux, being a well behaved function of the directional variable $\vec{\Omega}$, can be expanded in spherical harmonics. Assuming that the anisotropy is weak, the expansion can be truncated, without a significant loss of accuracy, keeping the terms $l \leq 1$ only:

$$\Phi(\vec{r}, E, \vec{\Omega}) \cong \frac{1}{4\pi} \phi(\vec{r}, E) + \frac{3}{4\pi} \vec{\Omega} \cdot \vec{J}(\vec{r}, E) \qquad \{9\}$$

One may note here that, in the particular case of isotropic flux, the net current $\vec{J}$ is equal to zero and the integral over $d\vec{\Omega}$ in equation {4} is trivial:

$$\Phi(\vec{r}, E, \vec{\Omega}) = \frac{1}{4\pi} \phi(\vec{r}, E) \qquad \{10\}$$

Equation {9}, known as the weak anisotropy approximation, is the first of the three approximations mentioned above and allows the decoupling of the higher order terms occurring in the streaming term of the Boltzmann equation, leading to the stationary P1 equations (from which the partial time derivatives have already been eliminated) [14]:

$$\begin{cases} \vec{\nabla} \cdot \vec{J} + \Sigma_t(\vec{r}, E)\, \phi = \displaystyle\int_0^\infty \Sigma_{s0}\,(\vec{r}, E' \to E)\, \phi(\vec{r}, E')\, dE' + S_0(\vec{r}, E) & \{11\} \\ \dfrac{1}{3} \vec{\nabla} \phi + \Sigma_t(\vec{r}, E)\, \vec{J} = \displaystyle\int_0^\infty \Sigma_{s1}\,(\vec{r}, E' \to E)\, \vec{J}(\vec{r}, E')\, dE' + \vec{S}_1(\vec{r}, E) & \{12\} \end{cases}$$

Note that, in {11} and {12}, the angular flux does not appear. Instead, the net current $\vec{J}(\vec{r}, E)$, has been introduced:

$$\vec{J}(\vec{r}, E) = \int_{4\pi} \Phi(\vec{r}, E, \vec{\Omega})\, \vec{\Omega}\, d\,\vec{\Omega} \qquad \{13\}$$

The second assumption concerns the anisotropic source $\vec{S}_1(\vec{r}, E)$ in {12}. This term represents neutrons that are born in preferred directions, contributing to the anisotropy of the angular flux. In a nuclear reactor core, however, most neutrons are produced by isotropic processes (fission, neutron emission by gamma capture, neutron emission by decay). Some reactions, such as (n,2n), may have anisotropic components, but in most power plant applications these can be neglected. Hence, for our purposes, $\vec{S}_1(\vec{r}, E)$ may be considered to be equal to zero and can therefore be eliminated.

The third assumption postulates that the neutron absorption in the materials present in the system is relatively weak. This is of course not valid inside a fuel pin or inside a control blade, but these strong heterogeneities have been already correctly treated during the lattice calculation and properly smoothed out (homogenisation) for the creation of the cross-section data bank, as depicted in Figure 3. Thus, when solving the 3D problem in the whole core, using homogenised nodal cross-sections, it is permissible to assume that the anisotropic components of the in-scattering and out-scattering terms are balanced, leading to what is known as the weak absorption approximation:

$$\int_0^{\infty} \Sigma_{s1}\,(E' \rightarrow E)\,\vec{J}(E')\,dE' \cong \int_0^{\infty} \Sigma_{s1}\,(E \rightarrow E')\,\vec{J}(E)\,dE' \qquad \{14\}$$

Introducing the two latter approximations into the P1 equations {11} and {12} leads to one of the most widely used equations in reactor physics, namely the diffusion equation:

$$-\vec{\nabla} \cdot D(\vec{r},E)\,\vec{\nabla}\phi + \Sigma_t(\vec{r},E)\,\phi = \int_0^{\infty} \Sigma_{s0}\,(\vec{r},E' \rightarrow E)\,\phi(\vec{r},E')\,dE' + S_0(\vec{r},E) \qquad \{15\}$$

A new parameter, the diffusion coefficient, has appeared in the streaming term of {15} (the first term on the left hand side). After some algebra, it can be shown that this is given by [14]:

$$D(\vec{r},E) = \frac{1}{3[\Sigma_t(\vec{r},E) - \bar{\mu}_0(\vec{r},E)\,\Sigma_{s0}(\vec{r},E)]} \equiv \frac{1}{3\,\Sigma_{tr}(\vec{r},E)} \qquad \{16\}$$

where $\bar{\mu}_0$ is the mean value of the cosine of the scattering angle and $\Sigma_{tr}(\vec{r},E)$ is the transport cross-section.

One important issue is still to be mentioned. Since we have eliminated the time variable, aiming to restrict the analysis to the steady-state case, equations {11}, {12} and {15} are only valid for a critical system, i.e. when the number of neutrons being produced and removed per unit time exactly matches. To force this balance, the source term is divided by the system multiplication factor k, whose value is exactly 1 for a critical system. Thus, disregarding the presence of external sources (which is an accurate assumption for a reactor at power), the source term $S_0(\vec{r},E)$ contains only the fission source and is given by:

$$S_0(\vec{r},E) = \frac{1}{k}\chi(E)\int_0^{\infty} \nu(E')\,\Sigma_f\,(\vec{r},E')\phi(\vec{r},E')dE' \qquad \{17\}$$

Here, $\nu(E')$ is the mean number of neutrons emitted per fission and $\chi(E)$ is their energy spectrum.

Finally, introducing {17} into {15} and discretising the energy variable into groups, leads to the multigroup form of the stationary neutron diffusion equation:

$$-\vec{\nabla} \cdot D_g\,\vec{\nabla}\phi_g + \Sigma_{r,g}\,\phi_g = \sum_{g' \neq g} \Sigma_{s,g' \rightarrow g}\phi_{g'} + \frac{1}{k}\chi_g \sum_{g'} \nu\Sigma_{f,g'}\phi_{g'} \qquad \{18\}$$

in which, for simplicity, the argument $\vec{r}$ has been dropped. Note that, on the LHS of equation $\{18\}$, the removal cross-section $\Sigma_{r,g}$ has replaced the Σ_t of $\{12\}$, since in the multigroup representation the self-scattering cancels and has been removed from both sides of the equation. Thus, $\Sigma_{r,g}\phi_g$ represents the removal rate of neutrons being either absorbed or scattered outside the energy group g.

Equation $\{18\}$ builds the basis for nodal diffusion, which is the most widely used method for the calculation of the flux distribution in large power reactor cores. In the following subsection, the main aspects of this methodology are outlined.

2.2.2 Solution of the diffusion equation

At the beginning of the application of computer technology to reactor physics, the finite differences (FD) method was the commonly applied approach to solve the 3D neutron diffusion equation. In this method, the leakage term is described by a low-order difference representation of the flux gradient [11]. This results in a system of equations coupled by the leakage between adjacent meshes only. Besides its simplicity, the main advantage of the FD method is that it converges to the exact solution of the multigroup diffusion equations in the limit of an infinitely fine mesh [15], [16]. However, the low computational efficiency of this method and the relatively limited and expensive computer availability in the past turned the solution of design and safety problems into a difficult and costly process. For instance, to achieve a reasonable accuracy, the application of finite differences schemes to a typical LWR requires mesh sizes in the order of 2 or 3 cm, or even smaller. This leads to more than 10^6 mesh points, i.e. 10^6 unknowns per energy group. An even finer mesh is required to achieve acceptable accuracy in regions where the neutron flux shows strong gradients, like near water structures in a LWR. The need for fine meshes translates into a large number of unknowns in the resulting system of equations, making this method impractical for the fast calculation of large reactor cores.

Finite element (FE) techniques have been proposed in an attempt to reduce the number of meshes needed. In this method, the spatial shapes of the multigroup fluxes are represented as polynomials over large homogenized regions [15]. Like in the FD method, the FE solution converges to the exact analytical solution if the mesh is infinitely fine. Although in the FE method the number of unknowns is substantially reduced compared with the FD method, the complexity of the coupling between the resulting equations increases, leading to no significant reduction of the computational effort.

Nodal diffusion methods were first proposed in the 1970's as a response to the increased need of computer-efficient calculational tools capable of providing acceptably accurate answers to the increasingly demanding safety and operation issues. Physicists and engineers started then to investigate numerical solutions of the diffusion equation that would be more affordable than the traditional FD or FE schemes. The main concept behind these efforts was the reduction of the number of unknowns for the resolution of the 3D flux equations.

Basically, nodal methods are characterised by the following properties:

1) Each node is represented by one unknown or nodal variable.
2) In the nodal equations, each node is only coupled with its direct neighbours.

3) The nodal XS and albedos define, in a unique way, the coupling coefficients, which may even depend on the solution.
4) The average flux per node and the net leakage to the reflector must be readily and uniquely correlated to the nodal solution.

In 1971, Børresen [17] proposed a so-called 1.5 group coarse-mesh nodal model that still can be regarded as one the fastest existing methods to solve the 3D diffusion problem in a LWR. At the time when computer availability was relatively restricted and very expensive, his method offered an enormous pay-off in terms of accuracy and speed. In the 1.5 group methodology, use is made of the fact that in LWRs the mean free path (mfp) of epithermal neutrons is 3 to 5 times as long as the mfp at thermal energies. In addition, the typical nodal dimensions are very large compared to the thermal mfp. Hence, the inter-nodal coupling is mainly caused by epithermal neutrons and the thermal flux can be derived in a second step. These facts are exploited in the 1.5 group models by using two-group data for the nodal cross-sections, but describing the global coupling as a one-group coupling for the epithermal group only. Owing to a number of elegant approximations, Børresen's method leads to a system of equations in which there is just one unknown per node. In addition, the iteration matrix obtained has a very simple structure, permitting the use of efficient solvers like the power iteration method with Chebysheb polynomial acceleration [11].

As already mentioned, the ultimate goal of reactor physics calculations applied to LWR cores is to allow the optimal utilization of the nuclear fuel while assuring, at the same time, the safety of the plant. To achieve this, the best possible knowledge of the local, pellet-wise power distribution in the whole core is of primary importance. The power per unit length developed in the fuel rods, the Linear Heat Generation Rate (LHGR), is a crucial parameter affecting the fuel mechanical behaviour. Related to the fuel rod burnup, the LHGR constitutes one of the limiting parameters that must be constantly monitored in normal operation. Thus, it is not sufficient for today's design and operation requirements to know the nodal-averaged values of the power distribution. Instead, a detailed characterisation of the neutron flux inside the nodes is required. To achieve this, nodal methods are enriched with two important features: first, the smooth variation of the flux inside the node is determined by expanding the flux in functions (e.g. exponentials), their coefficients carrying information about the inter-nodal leakage. The result is the so-called homogeneous (or asymptotic) flux. Second, the fine structure of the transport solution obtained in the lattice calculation, in the form of 2D pin-power maps, is superimposed on the homogeneous flux, resulting in the desired fine-structured 3D solution, also called the heterogeneous flux. The methodology of determining the local power distribution by means of this procedure is usually referred to as pin-power reconstruction.

Nodal diffusion with pin-power reconstruction is at present the most commonly applied methodology for the surveillance of the local heat generation rate in nuclear power reactor cores. These methods deliver a high level of accuracy at a relatively low computational cost. This high computational efficiency is an important requirement in modern on-line core supervision systems, where a complete 3D core simulation is performed typically every five minutes (in the case of operational manoeuvres, even more frequently). A short execution time is therefore a pre-requisite for this kind of application.

In the next section, a brief description of the nodal methodology with pin-power reconstruction, based on the PRESTO-2 model, is presented.

2.3 Example of a nodal method with pin-power reconstruction

At present, computer availability permits one to increase dramatically the complexity of the numerical solutions at a relatively low cost. At the same time, the requirements of optimal fuel utilisation and uncompromised reactor safety have led in the past 20 years to a large number of new developments. For instance, full two-group models with intra-nodal flux-shape and pin-power reconstruction capability are now applied in commercial codes, e.g. PRESTO-2, SIMULATE-3, POLCA-7, PRISM and MICROBURN-B2, among many others. In the latest generation of 3D nodal diffusion codes, the two-group scheme was abandoned in favour of a multigroup approach, as is the case for example in SIMULATE-5.

In this illustration of the basic aspects of the nodal methodology, we will restrict the discussion to the two-energy-group model of PRESTO-2. The extension to a larger number of groups relies on the same principles. A well structured description of the PRESTO-2 method is given in [18]. Basic considerations about multigroup nodal methods are presented in [15]. Basically, the problem of determining the detailed, local flux distribution can be split in two main parts: the first part is the determination of a global flux solution that satisfies the neutron balance in the whole core, taking into account the inter-nodal leakage to define the "smooth" or "asymptotic" intra-nodal flux shape. In the second part, "fine structure" information obtained in the multigroup transport (assembly) calculation is used to impose flux continuity at the node boundaries and to reconstruct the local (pin level) flux shape. The result of the first step is the global, so-called "homogeneous" flux ϕ^{hom}, the second delivers the fine-structured or "heterogeneous" flux ϕ^{het}. In the following subsections, these two calculational steps are described separately.

2.3.1 The homogeneous flux solution

Rewriting the multigroup diffusion equation {18} for two groups, and denoting with $\Sigma_{1\to2}$ the down-scattering cross-section from group 1 into group 2, we get:

$$\begin{cases} D_1\nabla^2\phi_1 - (\Sigma_{a1} + \Sigma_{1\to2})\phi_1 + \dfrac{1}{k_{eff}}(\nu\Sigma_{f1}\phi_1 + \nu\Sigma_{f2}\phi_2) = 0 & \{19\} \\ D_2\nabla^2\phi_2 - \Sigma_{a2}\phi_2 + \Sigma_{1\to2}\phi_1 = 0 & \{20\} \end{cases}$$

which can be expressed in compact matrix form as:

$$\bar{\bar{D}}\nabla^2\bar{\phi}(\vec{r}) + \bar{\bar{\Sigma}}(\vec{r})\bar{\phi}(\vec{r}) = 0 \qquad \{21\}$$

where:

$$\bar{\phi} = \begin{bmatrix} \phi_1 \\ \phi_2 \end{bmatrix} \qquad \{22\}$$

$$\bar{\bar{D}} = \begin{bmatrix} D_1 & 0 \\ 0 & D_2 \end{bmatrix} \qquad \{23\}$$

$$\bar{\bar{\Sigma}} = \begin{bmatrix} \frac{1}{k_{eff}}\nu\Sigma_{f1} - \Sigma_{a1} - \Sigma_{1\to 2} & \frac{1}{k_{eff}}\nu\Sigma_{f2} \\ \Sigma_{1\to 2} & -\Sigma_{a2} \end{bmatrix} \qquad \{24\}$$

In equation {21}, the variable $\vec{r}$ has been restored to emphasise that $\bar{\phi}$ and $\bar{\bar{\Sigma}}$ may vary within the node, while $\bar{\bar{D}}$ is assumed to be uniform within it. Integrating {21} over $\vec{r}$ and recalling Fick's law:

$$J = -D\nabla\phi \qquad \{25\}$$

we get a neutron balance equation that can be used for the global coupling of the nodes:

$$\sum_{m=1}^{6} \frac{1}{h_{nm}}\bar{J}_{nm} - \bar{\bar{\Sigma}}_n^{hom}\bar{\phi}_n^{ave} = 0 \qquad \{26\}$$

In {26}, h_{nm} is the node size in direction nm, while $\bar{J}_{nm}$ is the net average current (leakage) from node n to node m, where n and m are neighbours, as depicted in Figure 5. $\bar{\phi}_n^{ave}$ is the average flux in node n and $\bar{\bar{\Sigma}}_n^{hom}$ is the homogenised cross-section matrix in the same node.

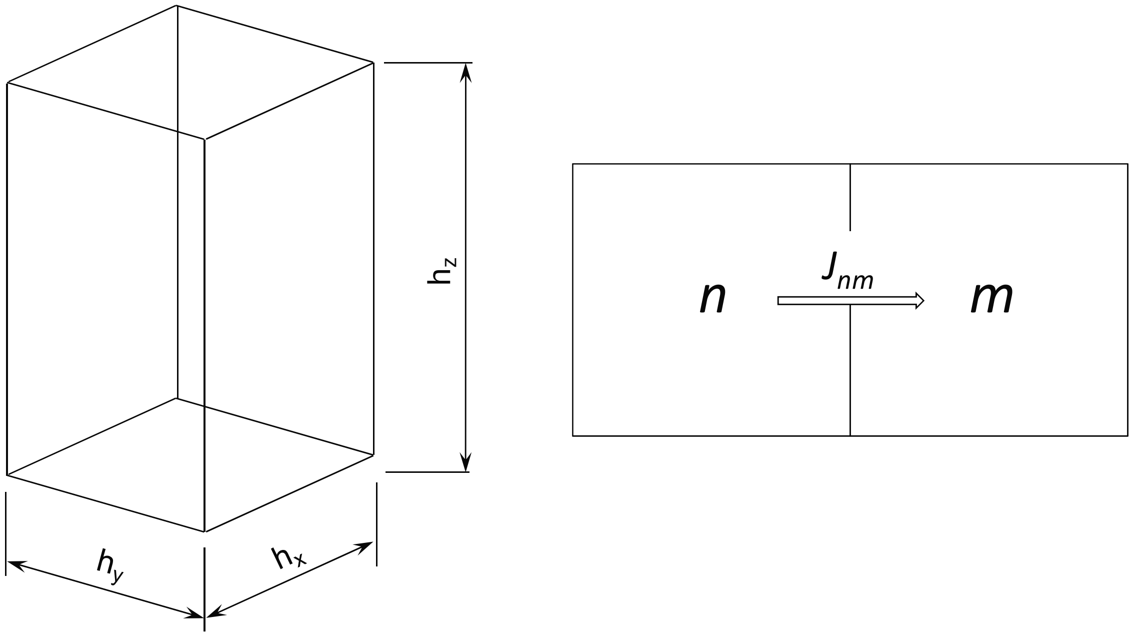

Figure 5 Node dimensions (left) and current coupling between two neighbouring nodes (right).

Equation {26} contains two unknown variables, $\bar{J}_{nm}$ and $\bar{\phi}_n^{ave}$. By deriving a relation between the net current and the average flux, $\bar{J}_{nm}$ can be eliminated from the balance equation. It is the purpose of the detailed nodewise analysis of the multigroup (in this particular case two-group) diffusion formulation to arrive at such a relation.

Equation {26} can be solved in an iterative manner. Having an estimate of the flux distribution, improved evaluations of the average cross-section can be made. Note that we have reduced the problem of finding the global flux distribution to the solution of a system of equations in which there is one unknown per node, namely $\bar{\phi}_n^{ave}$. As already mentioned in Section 2.2, this is one of the main characteristics of the nodal methodology.

Naturally, the determination of the local power at pellet level requires more detail than the global profile described by $\bar{\phi}_n^{ave}$. Thus, inside each node, the flux is represented by a combination of exponential shape functions in the x-, y- and z-directions. The shape functions are the solutions of the diffusion equation inside the node. The local problem, i.e. the flux variation inside the node, is solved by handling coupled sets of differential equations. This is done by decomposing the diffusion problem into two non-homogeneous wave equations, the so-called modal representation. With this formalism, it is possible to determine the flux in the sides of each node, which in turn permits to obtain the intra-nodal profile that satisfies, through the inter-nodal leakage, the global solution in the whole domain, i.e. the reactor core. These smooth functions describing the 3D coupled intra-nodal solution are known as the homogeneous flux, and represent the solution of the nodal problem where the cross-sections, although keeping a weak spatial dependency, were homogenised in each node. A detailed account of the cross-section homogenisation methodology and the mathematical derivation of the equations leading to the node side fluxes, and finally to the homogeneous flux, would be too extensive to be included in the present description. For further information related to PRESTO-2, the interested reader may consult the code documentation [18], which provides a complete description of the specific methodology used.

Now, we can assume that the coupled set of differential equations has been solved for the whole core, considering of course the boundary conditions imposed at the core periphery, and that the homogeneous flux in every node is known. As already mentioned, the solution of equation {26}, with known homogenised cross-sections Σ_a^{ave} and $\nu\Sigma_f^{ave}$, results in the homogeneous flux ϕ^{hom}. This yields the "exact" solution concerning global parameters like k_{eff}, nodal average fluxes and nodal average currents. A detailed treatment of these global conservation aspects will not be made here. The interested reader may consult Section 2.2 of [19], where the conservation aspects of the homogenisation methodology, due to Koebke [20], are described.

2.3.2 The heterogeneous flux solution

Although the homogeneous flux solution satisfies the global neutron balance in the core, it does not contain the detailed, fine-structure spatial information which is needed to characterise the local flux distribution at pellet level. In particular, the spatial detail obtained in the multigroup transport calculation at assembly level has been lost during the homogenisation process applied to generate the nodal cross-sections. Further, the homogeneous flux, being represented by a combination of smooth (exponential) functions, will not describe exactly the spatial shape near the node boundaries, where it is not even required to be continuous. In fact, the homogeneous flux at the node boundary is discontinuous by the ratio of the discontinuity factors of the two nodes, as expressed by equation {28} below.

Thus, to obtain the desired fine-structure flux shape, additional spatial information must be imposed on the homogeneous flux. To achieve this, two corrections are applied to ϕ^{hom}, viz.:

1) the application of discontinuity factors to the node-face fluxes
2) the superposition of 2D transport pin-power maps (pin-power reconstruction)

The result is the so-called heterogeneous flux ϕ^{het}. This flux corresponds to the solution we would obtain by solving the multigroup 3D-transport problem in the whole core, with pellet-level detail, by means of a high order deterministic transport method (e.g. MOC) or eventually by means of a Monte Carlo calculation.

In the present case, and for the reasons explained in Section 2.1, the calculation is split into two main steps: a 2D multigroup transport (lattice) calculation and the subsequent solution of the 3D nodal problem. Thus, the transport information must be gathered from the solution of the 2D lattice problem and used together with the 3D nodal diffusion solution to deliver the final ϕ^{het}.

The correlation between homogeneous and heterogeneous flux in the core is depicted in Figure 6. The discontinuity factors are applied to the node-face averaged fluxes and are defined as the ratio between the heterogeneous and the homogeneous fluxes:

$$f_{n,si} = \frac{\phi_{n,si}^{het}}{\phi_{n,si}^{hom}} \qquad \{27\}$$

Thus, the continuity of the heterogeneous flux is imposed by multiplying the homogeneous flux by the discontinuity factor on both sides of the nodal interface:

$$f_{n,si}\phi_{n,si}^{hom} = f_{n+1,si-1}\phi_{n+1,si-1}^{hom} = \phi_{n,si}^{het} = \phi_{n+1,si-1}^{het} \qquad \{28\}$$

where n denotes the node and si the face (in Figure 6, $si = s1, s2$ corresponds to the left and right side, respectively).

It is evident, from the above discussion, that equation {28} is only exact if the "true" heterogeneous flux is known. As mentioned before, this is not exactly the case, since normally only the single-assembly solution of the lattice calculation is available. In fact, the "true" core transport flux may deviate strongly from the idealised lattice solution, as can occur in cases where strong global gradients are present. The reason why the use of discontinuity factors obtained from reflected assembly calculations is still justified is that, as can be seen from equation {28}, only the ratio $f_{n,si}/f_{n+1,si-1}$ is of importance. This ratio turns out to be relatively insensitive to actual core conditions [18]. Hence, the use of discontinuity factors obtained in reflected-assembly calculations relies on the assumption that the ratio between the discontinuity factors of two adjacent nodes in the lattice case ($\phi^{hom} \equiv uniform$) and in the "true" (unknown) case is similar. The correlation between the homogeneous and the heterogeneous fluxes obtained in the lattice calculation is depicted in Figure 7. In this case, due to the zero-net-current assumption, the homogeneous flux is uniform.

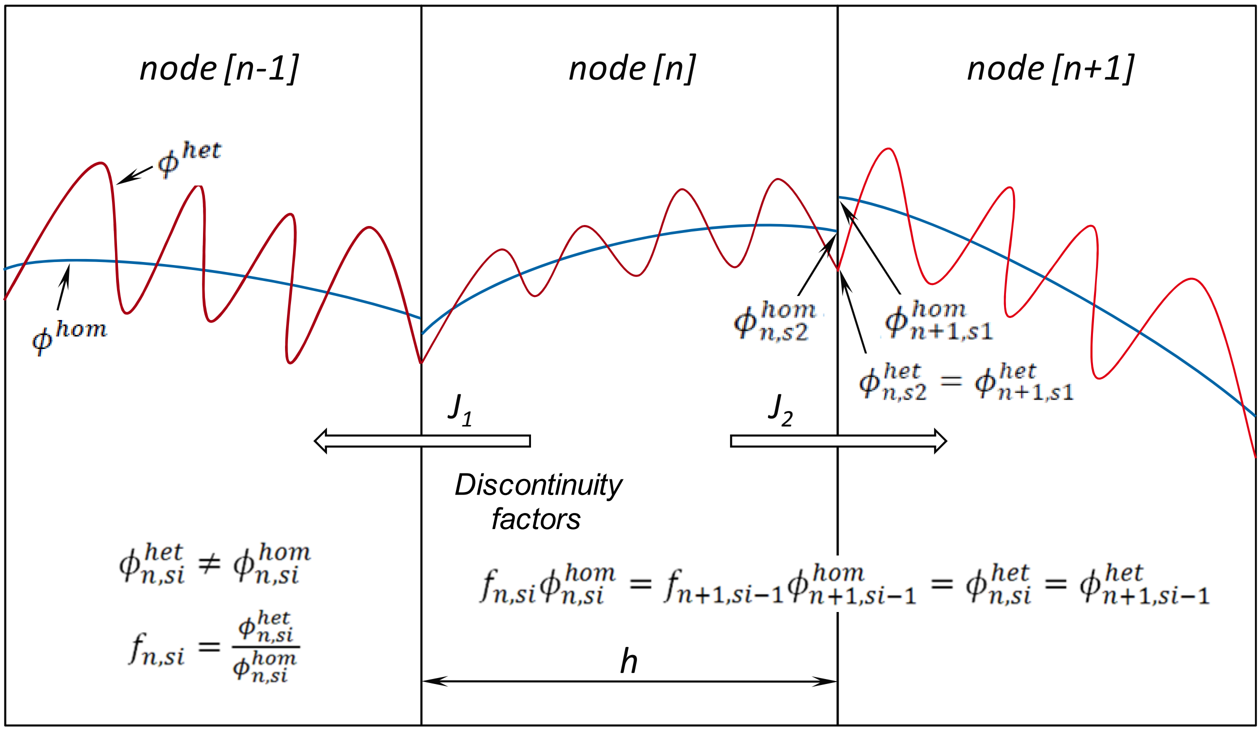

Figure 6 The heterogeneous "exact" and the homogeneous "nodal" flux solutions in the core. The homogeneous flux carries the information of the inter-nodal leakage. The use of these fluxes is equivalent to using the net currents at the sides (J_i) as boundary conditions between the nodes. Note that $\phi_{n,si}^{hom}$ is not continuous, but satisfies the global neutron balance in the core.

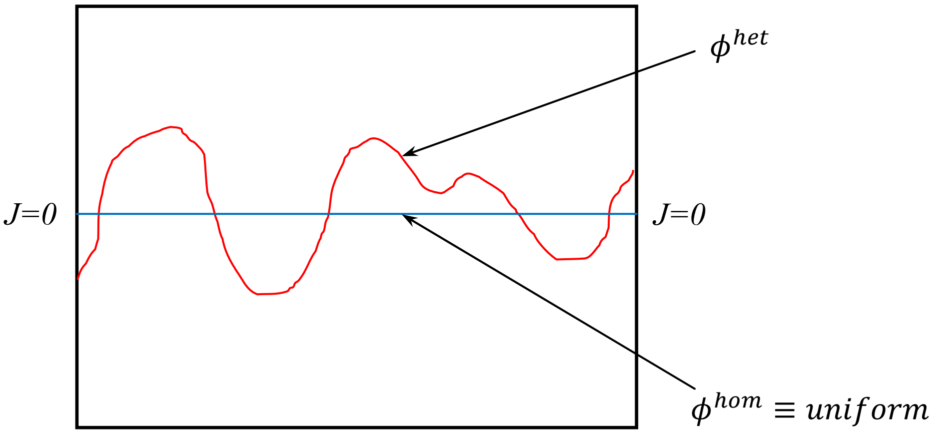

Figure 7 The heterogeneous and the homogeneous flux in the lattice (reflected) case. Due to the zero-net-current assumption, the homogeneous flux is uniform.

The use of discontinuity factors was proposed by Koebke [20] in his homogenisation method, in which the continuity of the homogeneous flux at nodal interfaces is not required, and the discontinuity is accounted for by means of appropriate homogenisation parameters. These homogenisation parameters consist of cross-sections, diffusion coefficients (for each direction) and heterogeneity factors, here referred to as discontinuity factors. Koebke's equivalence theory allows one to define the system of homogenised equations that reproduces all the desired global quantities of the heterogeneous problem (k_{eff}, nodal average fluxes and nodal average currents). This is independent of the number of energy groups. Formally (the "true" heterogeneous core solution must be known), it would be possible to define "exact" homogenised parameters via equivalence theory with only one energy group.

The second aspect to be accounted for in the determination of the core heterogeneous flux is the superposition of the local flux profile obtained in the assembly 2D-transport calculations. This process, usually known as Pin-Power Reconstruction (PPR), permits the determination of the local (pellet level) flux with good accuracy without the need of solving the 3D-transport problem. Thus, the 2D-transport and the 3D homogeneous solutions are combined to give the final 3D heterogeneous flux:

$$\phi^{het}(x,y,z) = S_{rad}(x,y) \cdot S_{axi}(z) \cdot \phi^{hom}(x,y,z) \qquad \{29\}$$

where:

$S_{rad}(x,y)$	is the radial fine-structure shape function (one value per pin cell) carried over from the lattice code evaluation.
$S_{axi}(z)$	is the axial fine-structure shape function, which accounts for axial heterogeneities like spacers, control blade tips and material composition discontinuities (enrichment or burnable absorber content).
$\phi^{hom}(x,y,z)$	is the homogeneous flux distribution inside a node obtained from the solution of the 3D diffusion problem, with smoothly varying cross-sections inside the nodes. It accounts for smooth, global power tilts caused by uneven leakage of neutrons between nodes.

Equation {29} makes the basic assumption that the heterogeneous dependence is separable into a radial component (S_{rad}) and an axial component (S_{axi}). Furthermore, a directional separation is also assumed in the calculation of the intra-nodal homogeneous solution, the homogeneous flux inside a node being given by:

$$\phi^{hom}(x,y,z) = \psi(x,y) + \xi(z)$$

Thus, the spatial dependence of the heterogeneous flux inside a node is separated in the radial and axial directions and, therefore, the pin power axial dependence is correct only in average.

$$\phi^{het}(x,y,z) = S_{rad}(x,y) \cdot S_{axi}(z) \cdot [\psi(x,y) + \xi(z)] \qquad \{30\}$$

Equation {30} puts in evidence one important limitation of this methodology: inside one node, the flux in all fuel pins has a separable axial dependence, while $S_{axi}(z)$ and $\xi(z)$ vary piecewise from node to node along the fuel element. Hence, the continuity of the heterogeneous flux in the axial direction cannot be granted for all pins. In particular, significant discontinuities may occur in nodes showing skewed flux shapes in the radial direction, for example in the case of a partially inserted control blade.

2.3.3 Axial heterogeneities

As discussed in Subsection 2.3.2, the heterogeneous flux inside the node is calculated as the combination of radial and axial shape functions as indicated in equation {30}.

To account for axial heterogeneities, the 1D diffusion equation is solved by subdividing the assembly into sub-nodes such that cross-sections are constant within each sub-node. Thus, the boundaries of the sub-nodes coincide with those of the original nodes, plus axial discontinuities such as the top of a control blade or the interface between two fuel pin material compositions. The resulting flux profiles $S_{axi}(z)$ (see equation {29}) are then used to define the weights, axial discontinuity factors and shape functions needed to homogenise the core nodes and determine their internal axial profile. This methodology allows the use of a uniform nodalisation in the axial direction, which is mandatory for power reactor calculations.

2.4 The calculation chain and the programmes used

As discussed in Section 2.1, the determination of the 3D flux distribution in the reactor core is performed following two well defined steps: the lattice calculation and the core calculation.

The neutronic properties of the fuel and the core structural components are described in the core calculation in terms of homogenised, few-(usually two)-group parameters (macroscopic cross-sections, flux discontinuity factors), calculated by a lattice physics programme. The lattice calculation also delivers the fine structured, pin-wise form functions (in the form of 2D pin-power maps) needed for the determination of the heterogeneous flux. These data are passed to the core simulator in the form of tables or polynomials that are functions of several variables. Thus, a transport calculation is performed for each combination of variables of interest, followed by a depletion calculation when needed. As we have mentioned in Section 2.1, these parameterised lattice data are stored in databases that are input to the 3D nodal code.

There is a close connection between the form in which the lattice data is produced and stored, and how it is used by the 3D core simulator. Hence, in most cases, the lattice programme and the 3D simulator constitute a code system that functions as a single unit. In this thesis, the two following code systems have been used:

- HELIOS/PRESTO-2 (HE/P2)
- CASMO-5/SIMULATE-5 (C5/S5).

The two code systems are depicted in Figure 8. HELIOS and CASMO-5 are 2D transport codes for lattice calculations. PRESTO-2 and SIMULATE-5 are 3D nodal diffusion codes with pin-power reconstruction capability. The creation of the database that links the two calculation levels is done by the auxiliary programmes TABGEN and CMSLINK, respectively.

In the following subsections, a brief description of these two programme systems is made.

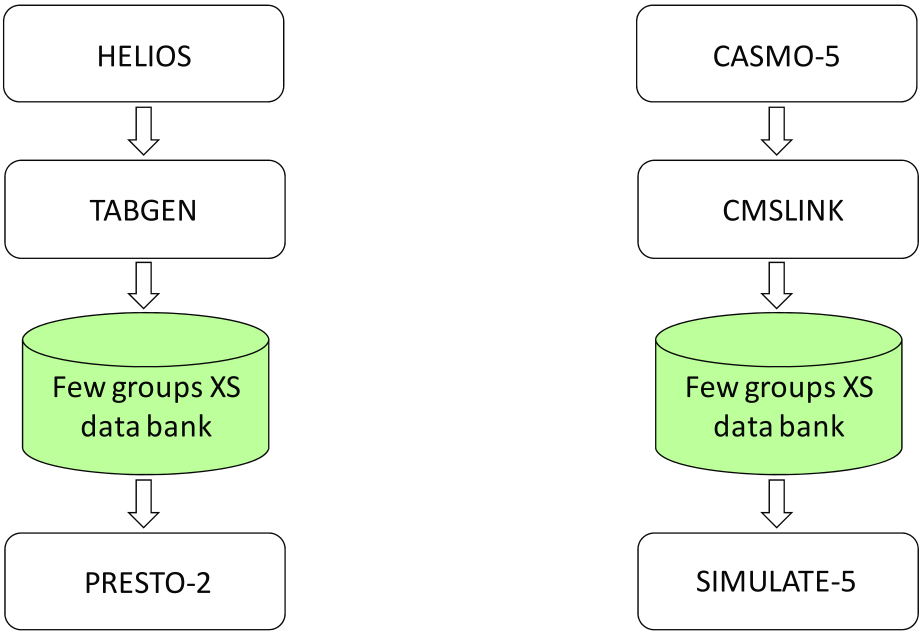

Figure 8 The HELIOS/PRESTO-2 (left) and CASMO-5/SIMULATE-5 (right) code systems. HELIOS and CASMO-5 are 2D transport codes for lattice calculations. PRESTO-2 and SIMULATE-5 are 3D nodal diffusion codes with pin-power reconstruction capability.

2.4.1 Lattice code HELIOS

HELIOS is a 2D lattice code with general geometry capabilities [21]. The neutron transport equation is solved by the Coupled Current Collision Probability (CCCP) method. In this method, the system (in our case the lattice) is subdivided into space elements in which collision probabilities (CPs) are applied. Typical space elements are, for example, a pin cell (a fuel pin with its associated surrounding coolant) or a part of a water structure (for example, the central water canal in the SVEA-96 fuel assembly). Space elements are built from structures, which in turn are subdivided into regions. Regions may be polygons or circular sectors. Within these, the material properties are uniform, and the flux and sources are assumed to be flat (basic assumptions of the CP method). To build space elements, structures are connected by exact coupling, which means, CPs are applied over the whole space element. Neighbouring space elements are coupled by currents, which in turn may be discretised in angular sectors in order to capture the flux anisotropy. The coupling of all space elements, together with the system boundary conditions, define the problem domain.

As mentioned in Section 2.1, deterministic 2D lattice calculations use multigroup XS working libraries. In these libraries, the energy dependence of the cross-sections, which is continuous in the ENDFs, has been discretised by dividing the energy range of interest, from 20 MeV to 10^{-4} eV, into a number of broad groups g. These XSs have been obtained by flux-averaging using typical reactor spectra according to {31}, u denoting lethargy and a absorption.

$$\sigma_{a,g} = \frac{\int_g \sigma_{\mathrm{a}}(u)\,\phi(u)\,du}{\int_g \phi(u)\,du} \qquad \{31\}$$

The groups and the spectra are chosen such as to make the XSs insensitive to variations of the flux solution in their anticipated range of application. Unfortunately, this procedure is impractical for the resonance isotopes in the range from about 100 keV to about 1 eV. In this range, the XSs exhibit many resonances, and thousands of groups would be required to achieve a satisfactory accuracy. The use of XS libraries with that many groups would make reactor design calculations prohibitively slow and expensive.

Thus, resonance-shielded effective microscopic cross-sections must be calculated before the transport equation is solved. Basically, this is done by solving equation {31} over the corresponding energy range. The difficulty arises from the fact that, due to the presence of resonances, the weighting function, i.e. the flux, shows strong variations depending on the characteristics of the problem to be solved. For instance, at and near the energy of a resonance, $\phi(u)$ exhibits a dip that depends on the material composition, not only through the concentration of the resonance isotope in question but also due to the interaction with resonances of other isotopes occurring at similar energies. Thus, accounting appropriately for the lattice characteristics, effective XSs for the resonance isotopes, in all the regions where they occur and in all the resonance groups, need to be evaluated. In HELIOS, this is done by means of the subgroup method [21], which applies the Lebesgues-Stieltjes conversion to express the resonance integrals as quadratures in σ_a. The effective XSs can then be obtained from:

$$\sigma_a = \frac{\sum_n w_n \sigma_n \phi_n}{\sum_n w_n \phi_n} \qquad \{32\}$$

For heterogeneous systems, this allows an evaluation of the group-averaged absorption XSs in all regions by calculating the fluxes ϕ_n, thus allowing the calculation of effective resonance cross-sections in any arbitrary geometry.

Once the equivalent cross-sections are known, the multigroup transport problem can be solved. Owing to the linear character of the Boltzmann transport equation applied to neutrons or gamma particles (no interaction between particles take place), the flux in a specific region i can be expressed as a linear combination of source and in-current contributions [11], [22]:

$$\phi_i = \sum_{j=1}^{I} X_{ij} Q_j + \sum_{s=1}^{S} \Upsilon_{is} j_s^- \qquad \{33\}$$

Knowing the sources Q_j, the currents j_s^- and the response fluxes X_{ij} and Υ_{is} , the flux in each region of the space element ϕ_i can be evaluated. The response fluxes depend on the first-flight collision probabilities p_{ij}, which in turn depend on the material properties and the system geometry.

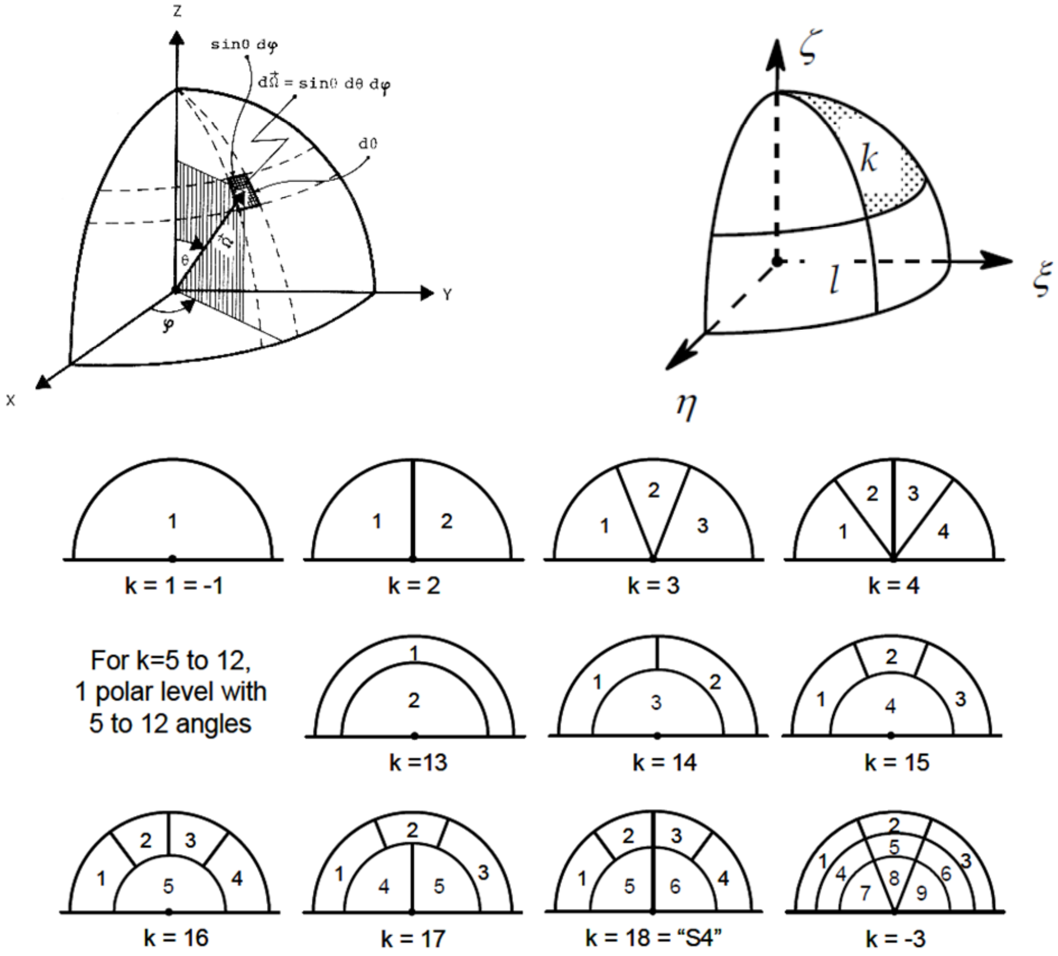

Figure 9 Top left: one octant of the directional sphere, showing the directional vector $\vec{\Omega}$ with its polar and azimuthal angles θ and φ. Source: [11]. Top right: angular sectors in the current coupling. Bottom: options for the current coupling in HELIOS. k=0 means "exact" coupling, which implies that the coupled space elements form a new space element, inside which CPs apply. Source: [21].

Between space elements, the coupling is accomplished by partial currents. The angular dependence of the interface or coupling currents can be discretised with several levels of detail. This is done by partitioning the directional half-sphere into a number of polar levels θ, and each θ level into a number of azimuthal φ intervals, as shown in Figure 9. The sectors are defined such that, for the current caused by an isotropic flux (cosine current), the same number of neutrons pass through each sector. Moreover, inside each sector, cosine currents are assumed.

The one-group transport problem is solved for every energy group, and the groups are coupled by the source terms (scattering and fission). The multigroup iteration process is depicted in Figure 10. For groups with energy below the threshold $E_{(gc)}$, additional iterations are made. In this energy region, where up-scattering occurs, the source term depends also on groups with lower energy. The fundamental mode rebalancing consists of a group-wise normalisation that accelerates the convergence process in the thermal energy region [21].

Once the outer (also called eigenvalue) iterations have converged, the flux in all regions of the system (lattice) is known, together with the multiplication factor *k*. This neutron-transport multiplication factor (or eigenvalue) corresponds to the situation where no leakage occurs (reflected assembly), and the associated eigenvector, the neutron spectrum, also reflects this no-leakage situation. Thus, the spectrum obtained in the solution of the transport problem generally differs from the criticality spectrum for *k=1*.

In the reflected lattice calculation, it is assumed that the 2D spatial shape of the transport solution, in each one of the fine-structure (library) energy groups, is not influenced by the leakage of neutrons streaming into or out of the lattice when it forms part of the core. In other words, global flux tilts, as they occur in a core composed of different assemblies surrounded by a core reflector, are not accounted for. The only way of including global leakage information in the solution of the transport problem at lattice level is to include more of the surroundings in the system, or to specify boundary conditions that approximately describe their presence.

However, while preserving the reflected-lattice boundary condition, leakage adjustments to the transport solution that only affect the energy spectrum can be made. These adjustments are made by simulating a spatially independent (mainly axial) leakage. Obviously, these spectrum adjustments do not influence the cross-sections per library group, but they become important when few-group XSs are evaluated. Thus, this is important for the collapsing of XSs into fewer energy groups for use in the 3D core simulator, or when the XSs are integrated over the entire spectrum to obtain the effective reaction rates for burnup calculations.

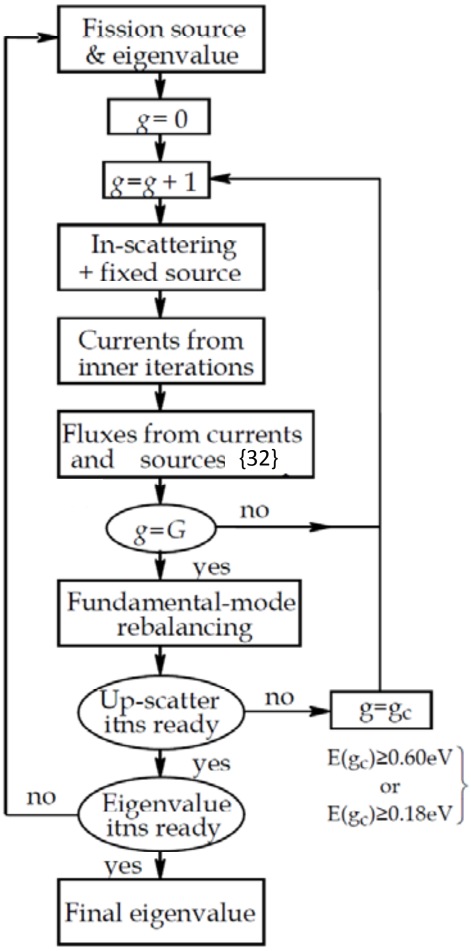

Figure 10 The multigroup iteration scheme in HELIOS [21].

Because the spatial solutions are frozen, the system can be homogenized per group, preserving its reaction and boundary-leakage rates. Thus, for a system composed of *I* regions *i* containing *J* isotopes *j*, the homogenized macroscopic XS in each library group is given by:

$$\Sigma = \frac{\sum_i^I \sum_j^J N_i^j \sigma_i^j \phi_i V_i}{\sum_i^I \phi_i V_i} \qquad \{34\}$$

where N_i^j is the numerical density of istope j in region i of volume V_i and σ_i^j is the corresponding microscopic cross-section. In this way, the system can be represented by a homogenised material with a set of group XSs and a global flux spectrum. The global spectrum, together with the homogenized XSs, still yields the multiplication factor k of the transport calculation.

Thus, the leakage is sought which makes this system critical. The criticality spectrum that corresponds to this leakage is more suitable for XS condensation (group collapsing) and burnup than the no-leakage spectrum of the transport calculation. Unless explicitly requested, which may be the case for scoping studies for example, it is this criticality spectrum that is finally enforced on the spatial transport solution. The concepts of homogenisation and condensation are depicted in Figure 11.

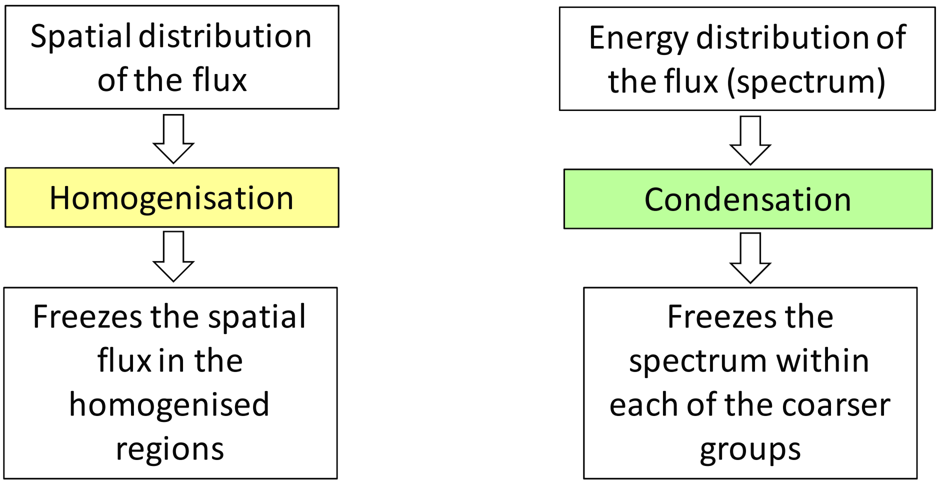

Figure 11 The cross-section homogenisation and condensation processes.

If not specified otherwise, HELIOS uses the B_1 method for the determination of the critical spectrum. In this method, the angular flux is assumed to be expressible as a modal expansion, in which the modes have been separated into a spatial and an angle-energy dependent mode:

$$\Phi(\vec{r},\vec{\Omega},E)=\sum_{n}\phi_n(\vec{r})\psi_n(\vec{\Omega},E) \qquad \{35\}$$

where $\vec{r}$ and $\vec{\Omega}$ are the space and angular coordinates and E is the energy variable.

The spatial modes of the expansion {35}, $\phi_n(\vec{r})$, are solutions of the Helmholtz or wave equation:

$$\nabla^2\phi_n+B_n^2\phi_n=0 \qquad \{36\}$$

while the angular dependence of $\psi_n(\vec{\Omega},E)$ may be expanded in Legendre polynomials and the energy dependence may be discretised into groups to yield, after some algebra, the B_1 equations in their multigroup form [11]:

$$\begin{cases} \Sigma_g\psi_g \pm iBJ_g=\sum_{g'}\Sigma_{0,g'\to g}\psi_{g'}+\chi_g \\ \pm iB\psi_g+3\alpha_g(B)\Sigma_gJ_g=3\sum_{g'}\Sigma_{1,g'\to g}J_{g'} \end{cases} \qquad \{37\}$$

In {37}, α_g[5] is a function of the buckling B and J is the net current. These equations can be solved in an iterative way, varying the value of the buckling B until the critical condition $k=1$ is

---

[5] This function has no physical meaning, being equal to 1 in the case of the P_1 equations.

reached. The spectrum ψ_g corresponding to this situation is the desired criticality spectrum. A detailed derivation of the B_1 equations and the iterative method of solution is given in [11]. Another well structured discussion about the criticality spectrum calculation can be found in [13].

Once the criticality spectrum $\psi_g(B)$ is known, the cross-sections can be collapsed to the number of groups needed for the core calculation according to:

$$\Sigma_G = \frac{\sum_{g\in G} \Sigma_g \psi_g}{\sum_{g\in G} \psi_g} \qquad \{38\}$$

Finally, a set of macroscopic few-group cross-sections, discontinuity factors (as defined in Subsection 2.3.2) and pin-power maps (relative distribution of pin power corresponding to the transport solution of the reflected lattice) are stored in a database, as input for the 3D nodal calculation. In the case of a power reactor, these sets of data are calculated for different conditions (e.g. coolant density, fuel temperature, xenon concentration) and as a function of burnup. For each state and burnup step, one transport calculation is needed. The resulting data are stored in tables that cover the whole range of variation of each free variable. By means of interpolation from these tables[6], the 3D core simulator finds the parameters corresponding to the conditions at each node in the core.

In the particular case of the LWR-PROTEUS experiments, only one element of the case matrix is needed, viz. that corresponding to zero burnup and full moderator density at room temperature and without xenon.

2.4.2 Core simulator PRESTO-2

PRESTO-2 is a three-dimensional code for simulating the neutronic, thermal and hydraulic behaviour of a LWR core. PRESTO-2 solves the coupled two-group neutron diffusion / thermal-hydraulics problem. The core power distribution is computed down to the pellet level. Thus, one can compute not only the bundle-average values of important parameters, but also their within-bundle distributions. A summary of the methodology employed in PRESTO-2 for the nodal solution of the diffusion equation has been presented in Section 2.3. In the present subsection, emphasis is placed on the PRESTO-2 representation of the reactor core from a general point of view. Specific issues concerning the modelling of LWR-PROTEUS with PRESTO-2 will be discussed in Chapter 3.

In the following, the discussion is restricted to BWR cores. This corresponds to the fact that, in the LWR-PROTEUS configurations analysed in this thesis, the measurements were done on BWR assemblies[7].

For the solution of the 3D diffusion problem, the core is subdivided into nodes. In the radial direction, one node corresponds to one fuel element and its corresponding half-gaps. For power

---

[6] In some code systems, also polynomials are used.

[7] In LWR-PROTEUS Phase II, a PWR type of lattice was placed in the centre of the test zone to investigate segments of burnt fuel. The investigations performed in this thesis, however, refer exclusively to Phases I and III, where the measurements were made in the central assembly of a 3x3 configuration of BWR fuel assemblies of type SVEA-96+ (Phase I) and SVEA-96 Optima2 (Phase III).

reactor applications, PRESTO-2 simulations may be performed in a domain comprising the active core and the reflector. The side reflector is modelled as a layer of nodes with appropriate cross-sections, as depicted in Figure 12.

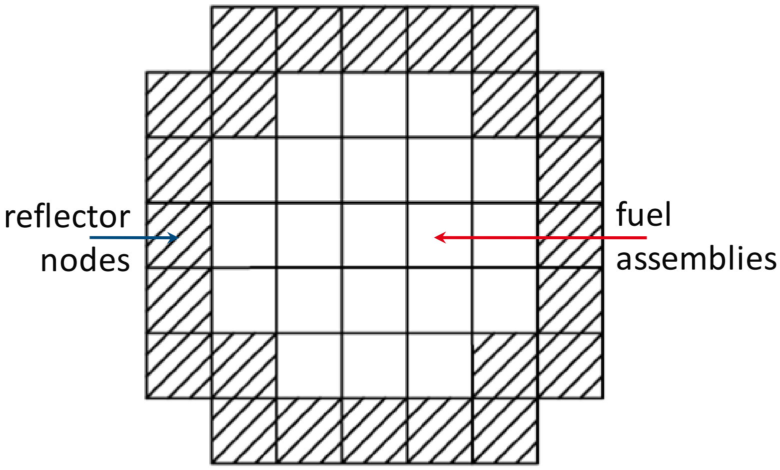

Figure 12 The reflector surrounding the core may be represented by an additional row of nodes. Although this approach can be successfully applied to large power reactor cores, it is not suitable in the case of LWR-PROTEUS. Source: [18].

Alternatively, PRESTO-2 allows the specification of the core boundary conditions by means of radial and axial albedo matrices. These are defined as:

$$\bar{\bar{a}} = \begin{bmatrix} a_{11} & - \\ a_{21} & a_{22} \end{bmatrix} \qquad \{39\}$$

where the group albedo

$$a_{gg'} = \frac{j_g^-}{j_{g'}^+} \; for \; g, g' = 1, 2 \qquad \{40\}$$

represents the number of neutrons entering the core in group g relative to those having leaked from it in group g'. Note that the up-scattering component a_{12} is not explicitly given. Instead, the a_{21} component of the albedo matrix is assumed to represent an effective down-scattering term, calculated such that the up-scattering is subtracted from the true down-scattering to yield an effective value.

The albedo matrices {39} can be specified for the top, bottom and side boundaries of the core. While the top and bottom surfaces are planar and therefore the definition of their albedo matrices is straightforward, for the side albedos three situations may be identified (planar, outer corner and inner corner), as depicted in Figure 13.

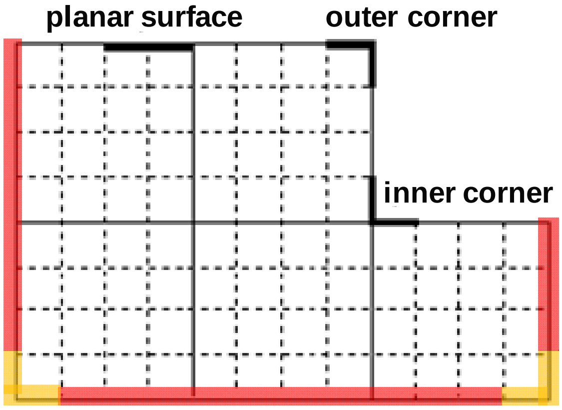

Figure 13 The three types of side albedos defined in PRESTO-2. The size of the corner surfaces corresponds to 1/4 of the assembly pitch.

The fuel assembly faces are divided into 4 segments. According to its position with respect to the inner and outer corners, the corresponding albedo matrix is assigned to each segment. One important limitation is that all planar, outer corner or inner corner albedo matrices must be the same, irrespective of their position along the core periphery. Although this is a good assumption for power reactor cores, it may be insufficient for the modelling of the LWR-PROTEUS test zone using PRESTO-2, particularly in cases where the flux profile is skewed in the radial direction.

To capture axial variations in the radial boundary conditions, PRESTO-2 allows the specification of a different albedo matrix at each core level (each level having the height of one node). This is an important feature when the axial profile of the flux is of interest, particularly in the case of relatively small domains like the LWR-PROTEUS test zone.

The characterisation of the fuel assembly is done in PRESTO-2 by specifying the axial segments that compose it and their corresponding lengths. A set of cross-sections, discontinuity factors and pin-power maps, as stored in the XSDB, is assigned to each segment. In considering the loading of the assemblies in the reactor core, they are oriented according to their relative position with respect to the control blades.

For every fuel rod in the core, PRESTO-2 calculates the LHGR at 1cm intervals in the axial direction. With this, the detailed 3D power profile can be obtained.

2.4.3 Lattice code CASMO-5

CASMO is a multigroup two-dimensional transport theory code for lattice calculations on BWR and PWR fuel assemblies or on simple pin cells. It has been available for nuclear reactor calculations for more than 30 years. Since the first versions were released, improvements in computer availability have permitted reductions in the number and severity of physical approximations, and the implementation of more direct and detailed algorithms. Thus, the evolution from CASMO-3 [23] to CASMO-4 [24] was characterised by improvements in the spatial modelling, mainly concerning the change from a 2D-transport solution based on homogenized pin cells to a 2D-transport solution with full heterogeneous geometry. Following this evolution, CASMO-5 has been conceived to add, among other improvements, further detail in the energy treatment [25]. With this purpose, CASMO-5 is coupled to a 586-group XS data library.

The code handles a geometry consisting of cylindrical fuel rods of varying composition in a square pitch. In this respect, it does not feature the same generality as HELIOS, which can virtually handle any 2D geometry. Instead, CASMO-5 is tailored to PWR and BWR applications, which allows for relatively simple input decks, one important advantage for industrial applications. However, the fact that many features concerning the system geometry are hardwired in the programme sets restrictions to the applicability of CASMO-5 in special cases that differ from power reactor cores. As we will see later, this affects the application of CASMO-5 to the LWR-PROTEUS controlled configurations.

For solution of the two-dimensional transport problem CASMO-5, uses the Method of Characteristics (MOC). In this method, the integral transport equation is solved by tracking the neutrons born and colliding along specific paths or directions, which are swept to cover the entire space [13].

CASMO-5 uses a cross-section library based on the ENDF/B-VII nuclear data file. The working library contains 586 neutron and 18 gamma groups. The XS for SIMULATE-5 (see below) can be generated in any sub-set of these. SIMULATE-5 will then solve the nodal diffusion problem in the given number of energy groups.

2.4.4 Core simulator SIMULATE-5

SIMULATE-5 is a three-dimensional code for simulating the neutronic, thermal, and hydraulic behaviour of PWR and BWR cores. Thus, its application field is the same as that of PRESTO-2. SIMULATE-5 is planned to succeed the widely used SIMULATE-3 code [26]. Like SIMULATE-3 and also PRESTO-2, SIMULATE-5 solves the nodal diffusion problem in the 3D domain composed of core and reflector.

Particular to SIMULATE-5 is the capability to solve the 3-D nodal diffusion problem using an arbitrary number of energy groups. When a multigroup library generated by CASMO-5 is detected, SIMULATE-5 automatically uses the given group structure for the solution of the nodal problem. Apart from computer memory and computer runtime, there is no limit on the number of energy groups. This capability has been used in this thesis to study the impact of varying the energy detail at core calculation level. At this moment, the SIMULATE-5 programme documentation is being completed, a summary of the programme capabilities being given in [27].

As in the case of PRESTO-2, the core surroundings may be represented in SIMULATE-5 by means of a layer of reflector nodes or by using reflector albedos[8]. Like CASMO-5, SIMULATE-5 was designed with focus on PWR and BWR applications. Although this feature simplifies the input preparation process, it may lead to difficulties in the modelling of untypical cases like LWR-PROTEUS. For instance, the definition of BWR control blades in a PWR configuration (which is the case with the 3x3 array of LWR-PROTEUS) is not possible. SIMULATE-5 makes use of the fact that all BWR cores have an even number of rows, while in PWR cores the number

---

[8] The standard version of SIMULATE-5 allows for axially uniform radial albedos only. For use in this thesis, a special version accepting axial-layer dependent radial albedos was produced by Studsvik Scandpower. Further details about the spatial distribution of the PRESTO-2 and SIMULATE-5 albedo inputs are given in Chapter 3, Section 3.6.

of rows is always odd. Due to this feature, together with the limitation in CASMO-5 mentioned in Subsection 2.4.3, the investigation of LWR-PROTEUS configurations where the L-shaped control blade is inserted has not been possible with the CASMO-5/SIMULATE-5 route.

2.4.5 Monte Carlo code MCNPX

The basic principle of the Monte Carlo (MC) method is straightforward. The life of a single particle (for example a neutron) is simulated from its initial emission (from fission or from a fixed source) until it disappears from the system (by absorption or leakage). Random numbers are used to define the free variables that characterise the location of the particle in the phase space (position, direction and energy), and also to define the optical path that the particle will follow until its first interaction. The frequency and outcome of the various interactions occurring during the particle life are simulated according to cross-sections and collision laws, and are sampled (tallied) to build a statistical solution of the transport problem.

The Monte Carlo method is mostly used to study complicated geometries and non-standard situations. It is particularly suitable for the validation of deterministic results, principally when a high level of detail in space and energy is required. Hence, MC is a very suitable method to calculate the 3D-transport solution in the PROTEUS reactor, defining a reference for comparison against 3D deterministic calculations.

Taking advantage of the above mentioned properties, the Monte Carlo particle transport code MCNPX has been used in this thesis for two purposes:

1) The determination of boundary conditions for the test zone, which are needed in the nodal calculation to represent the surroundings.
2) The determination of local fission rates in all pins with fine axial detail, as reference solution to complement the experimental database in those positions where no measurement was made.

MCNPX is a general purpose, Monte Carlo radiation transport code that can track nearly all types of particles at nearly all energies. For this thesis, however, only neutrons with energy below 20 MeV are of interest. Thus, the same calculations could have been done using several versions of the MCNP code. The use of MCNPX was motivated by the participation of the author as beta-tester for the version that was under development when this thesis was started in the year 2007. This particular version, MCNPX-2.6b, has been kept throughout the doctoral research. However, similar results can be expected using, for example, the officially distributed version MCNPX-2.5.0 [28], or recent versions of the code MCNP. All MCNPX calculations presented in this thesis have been performed using the JEFF-3.1 nuclear data library.

2.5 The LWR-PROTEUS experimental programme

The PROTEUS reactor is a zero-power critical facility consisting of a central test zone, in which the measurements are made, surrounded by a buffer region and two driver zones (D_2O and graphite moderated) that render the system critical. The reactor's safety and control rods are located in the outer regions, and criticality is achieved by adjusting the fuel loading in the D_2O and graphite drivers. The buffer zone consists of natural uranium metal rods and provides a certain spectral decoupling of the test and driver zones.

In the LWR-PROTEUS reactor configuration, the test zone consisted of a square tank within which an array of 3x3 BWR fuel assemblies was located. The fuel assemblies were provided by the Leibstadt Nuclear Power Plant (KKL), having been taken from production reload batches for use in the LWR-PROTEUS experimental programme. Since the assemblies are 4.5 m in length and the active height of the PROTEUS driver regions is about 1 m, the test tank could be moved axially to enable step-wise investigations along the whole length of the test assemblies. Thus, it has been possible to study the axial power profile variation across axial heterogeneities such as enrichment boundaries or the tips of partial length rods. A schematic view of the PROTEUS reactor with its test zone configured for the LWR-PROTEUS experimental programme is shown in Figure 14, a horizontal section of the test zone and its surroundings being depicted in Figure 15.

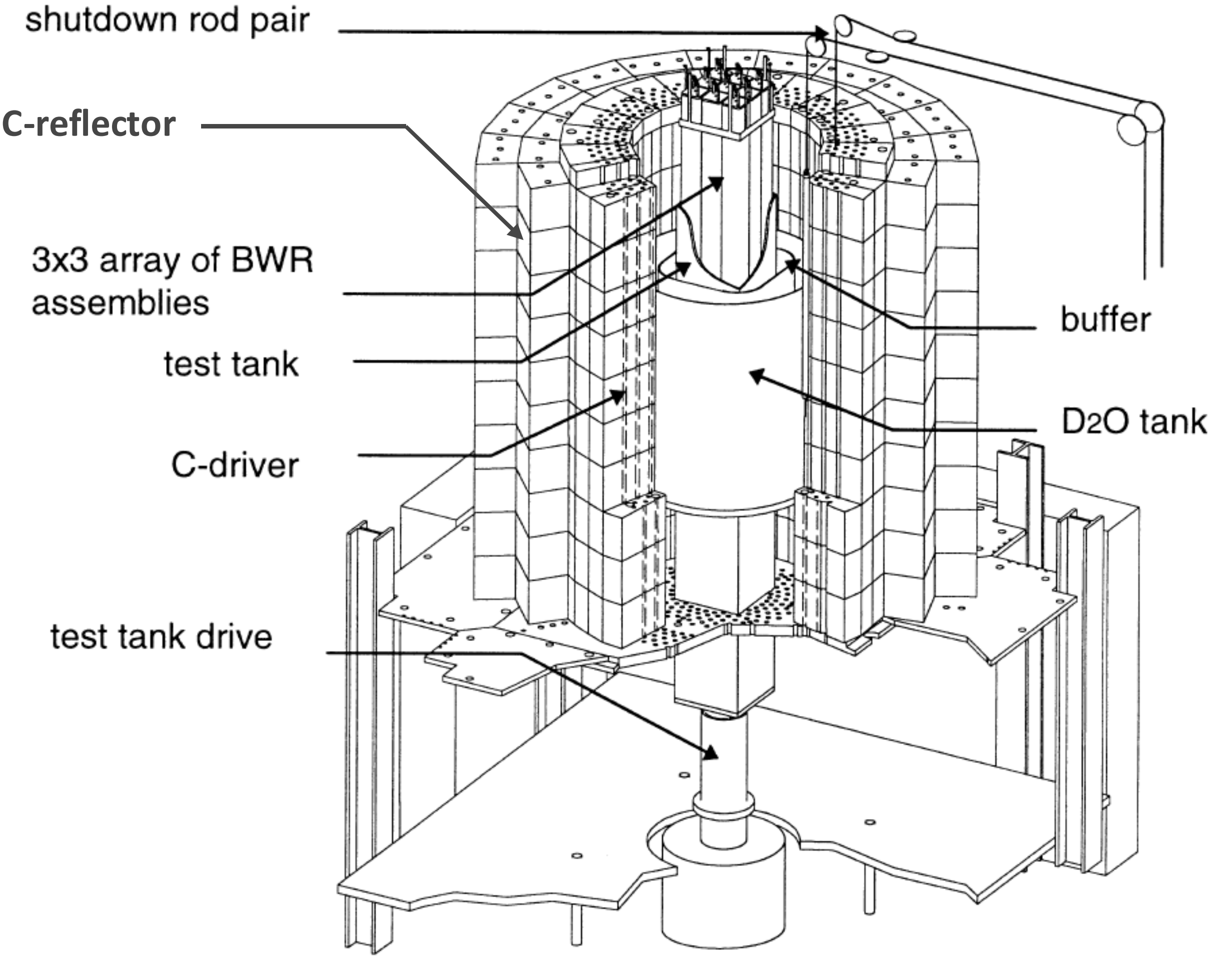

Figure 14 Schematic view showing the main components of the PROTEUS reactor as configured for the LWR-PROTEUS experimental programme. Source: PSI.

In Phase I, the test zone was loaded with nine identical fuel assemblies of type SVEA-96+, fabricated by Westinghouse. The fuel assemblies featured axially varying nuclear designs, concerning pin enrichment and gadolinium content. The test tank was filled with light water at 20ºC for neutron moderation, but polyethylene inserts (thin rods and plates) were also used to study the impact of variations in the moderator density. In Phase I, pin-wise radial and axial reaction rate distributions of total-fission and capture in ^{238}U were measured. For this, following irradiation, selected fuel pins were removed from the central fuel assembly and placed in a fully automated gamma-scanning device, where the delayed gamma activity was measured. For each fuel pin, the activity of several different fission products was measured, batches of up to ten fuel pins being analysed each time. In addition, pin-removal reactivity measurements were made. After completing the measurements of Phase I, the nine SVEA-96+ fuel assemblies were returned to KKL to be loaded into the core.

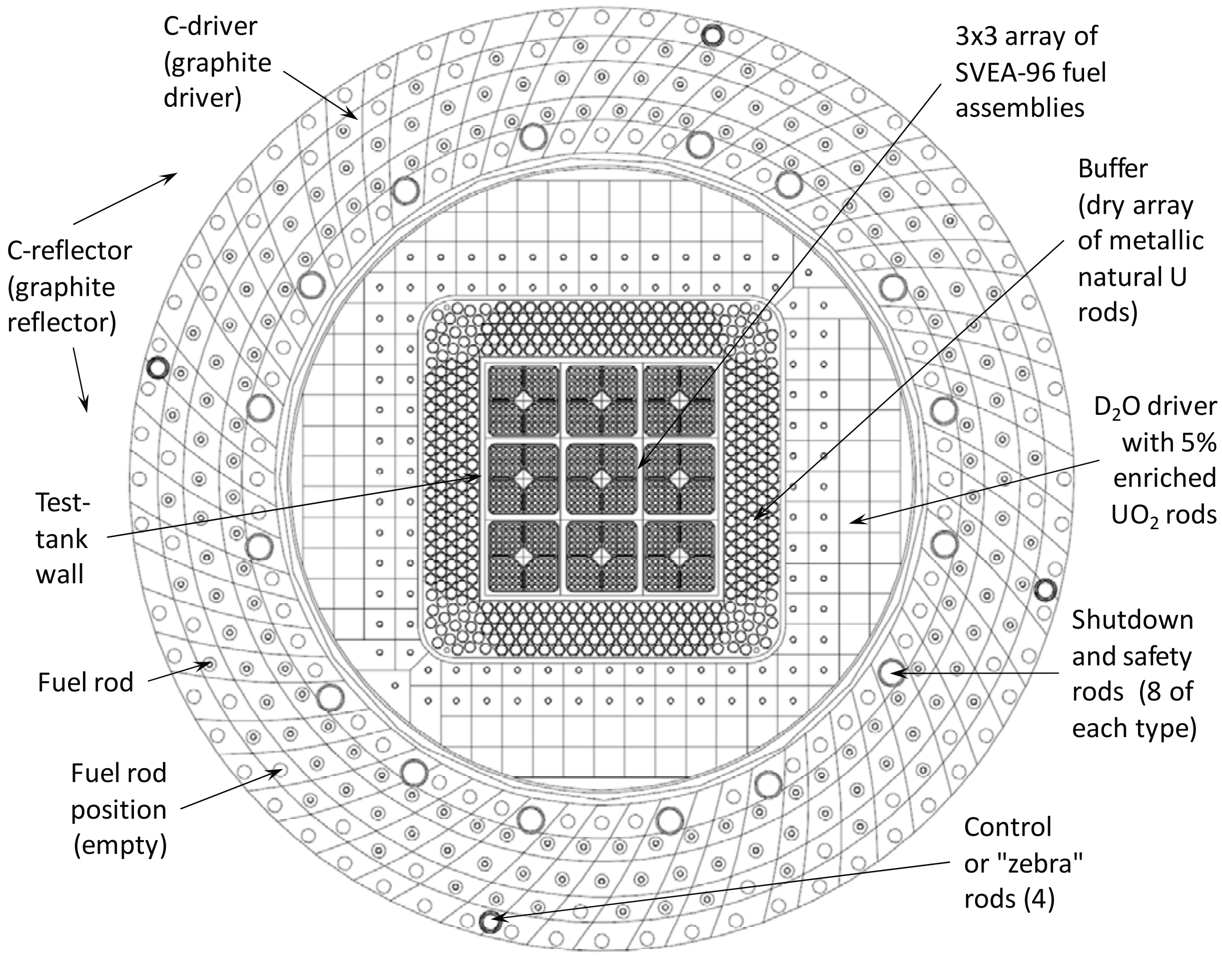

Figure 15 MCNPX plot showing the horizontal section of the LWR-PROTEUS reactor (up to the graphite driver region) in Configuration I-1A. The fuel loading in the D_2O and graphite drivers for each test-zone configuration is such as to achieve criticality. Small reactivity deviations are compensated by the movement of the four control rods (also called "zebra" rods).

Phase II of the LWR-PROTEUS programme focused on the reactivity effects of burnup. Measurements involving PWR and BWR pin segments irradiated to high exposure in Swiss NPPs were made. The depleted samples were placed in the central lattice position of a PWR mock-up loaded in the centre of the test zone's 3x3 array. The eight fuel assemblies surrounding the PWR mock-up were of type SVEA-96 Optima2 (KKL reload e18-1), the same as used in Phase III.

In Phase III, nine Westinghouse fuel assemblies of type SVEA-96 Optima2, also provided by KKL, were loaded in the test zone. This fuel element design features Partial Length Rods (PLRs) with 1/3 and 2/3 of the full-assembly length, with the main purpose of improving Shut-Down Margin (SDM) and Dry-Out (DO) performance. PLRs introduce axial heterogeneities in the assembly geometry, whose study was one of the main purposes of the Phase III experiments.

A second set of experiments performed during Phase III was related to the investigation of the effect of heterogeneous coolant voiding, simulated by the insertion of a steel tank containing different mixtures of light and heavy water in the active zone of the assembly.

The three phases constituting the LWR-PROTEUS experimental programme are depicted in Table 2. The present thesis concerns a subset of the measurements performed in Phases I and III. In particular, the total-fission rates in cases where radial and axial heterogeneities play an important role are of interest for this research. Complete lists of the experimental configurations investigated during Phases I and III of the LWR-PROTEUS experimental programme are presented in Table 3 and Table 4, respectively. In both tables, the configurations that are investigated in this doctoral research, already mentioned in Section 1.4, are highlighted with a grey background.

Table 2 The three phases of the LWR-PROTEUS experimental programme.

	Fuel	Moderator	Investigated phenomena
Phase I	9 x SVEA 96+	Light water or thin polyethylene rods and plates	Radial and axial pin-wise reaction rate distributions (total-fission and capture in ^{238}U) Effect of pin removal on reactivity
Phase II	8 x SVEA 96 Optima2 1 x PWR mock-up containing 1 PWR or BWR burned segment	H_2O, mixture of H_2O and D_2O or borated H_2O in different configurations H_2O in the outer fuel assemblies in all configurations	Reactivity changes due to burnup Measurements involving pin segments irradiated to high exposure in Swiss NPPs (PWR and BWR)
Phase III	9 x SVEA 96 Optima2	Mixture of H_2O (66.3%) and D_2O (33.7%)	Effect of heterogeneous coolant voiding and 3D effects near partial length rods

The SVEA-96 BWR fuel design features a 10x10 square lattice. It consists of four sub-assemblies separated by four internal bypass channels (water wings). The four central lattice positions are occupied by a square-formed, 45° rotated water canal. The four sub-assemblies are physically separated by the water wings, but openings at regular elevations allow the hydraulic communication and pressure equalisation between them. In the SVEA-96+ design, all fuel rods have the full assembly length. In the SVEA-96 Optima2 design, the four corner rods and the eight rods adjacent to the water canal are partial length rods (PLRs), having approximately 1/3 and 2/3 of the full assembly length, respectively. A schematic view of the SVEA-96 BWR fuel design is shown in Figure 16.

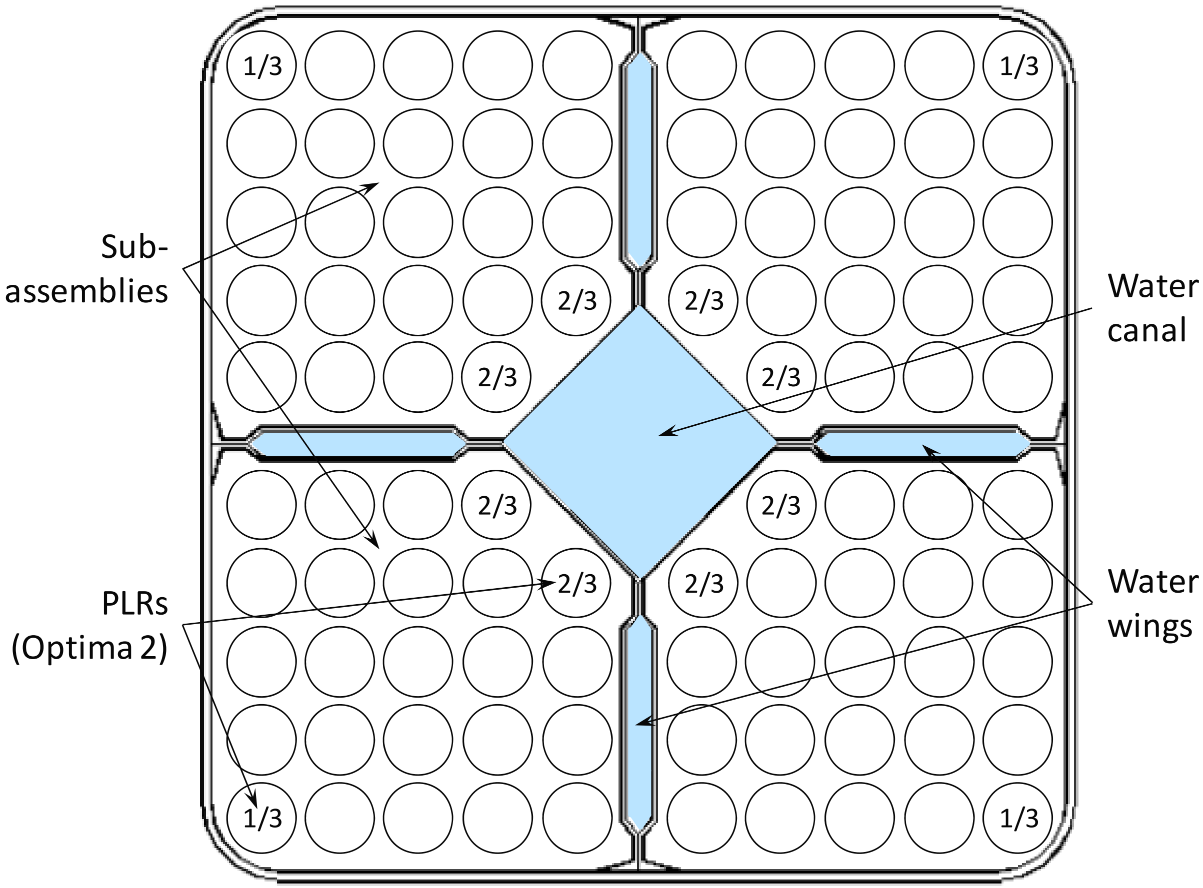

Figure 16 Schematic view of a SVEA-96 BWR design, showing in particular the water structures and the four sub-assemblies with 24 fuel pin positions each. In the Optima2 design, the 1/3-length and 2/3-length PLRs occupy the positions marked with the corresponding fractions.

The SVEA-96+ fuel assemblies used in Phase I (KKL reload e14-2) contain three axial zones with different enrichment and gadolinium contents. These axial zones were designed in order to optimise the axial power profile in the BWR core. Their average enrichments and their gadolinium contents are[9]:

• blanket:	natural uranium (15 cm).	Lattice KKL032.
• upper segment:	enrichment: 3.70, Gd: 14 x 3.95 + 2 x 2.0.	Lattice KKL060.
• lower segment:	enrichment: 4.02, Gd: 14 x 3.95.	Lattice KKL061.

The selection of the axial zone to be measured was made by adjusting the axial position of the test tank by means of the test-tank drive mechanism. Figure 18 shows the three axial positions corresponding to the Phase I configurations 1A, 1B and 1C.

---

[9] The enrichments shown are lattice-average values expressed in percent weight (w/o) ^{235}U with respect to the total heavy metal mass (^{235}U+^{238}U). The gadolinium contents are fuel pin values expressed in w/o Gd_2O_3 (all Gd isotopes plus oxygen) with respect to the total fuel mass (UO_2+Gd_2O_3).

The SVEA-96 Optima2 fuel assemblies measured in Phase III feature a uniform enrichment and gadolinium layout throughout the length of each fuel rod, but they are axially heterogeneous due to the presence of PLRs. The assemblies belong to the KKL reloads e18-1 (eight peripheral) and e20-2 (central). Their axial composition is depicted in Figure 17. Also in this case, the measurements at the segment boundaries were performed by adjusting the test-tank axial position accordingly.

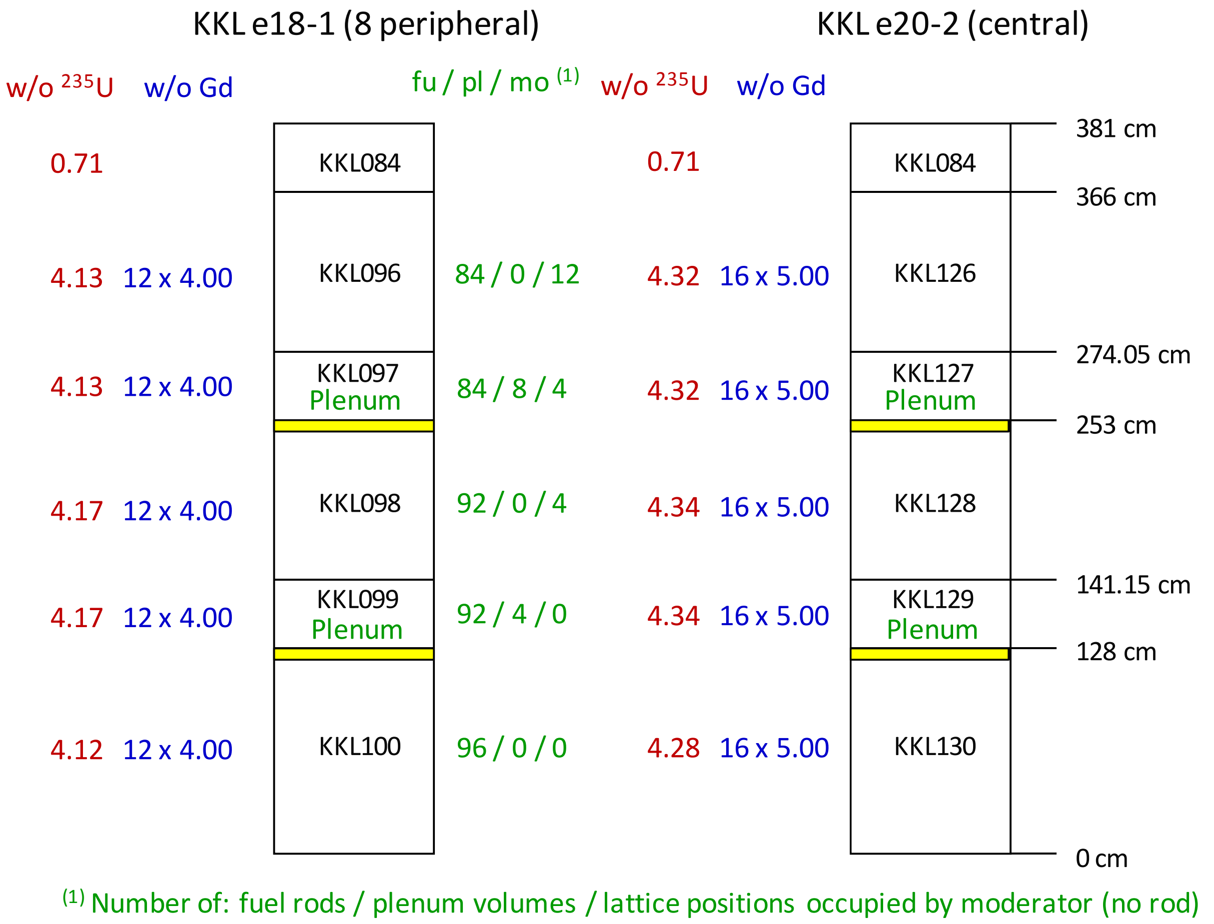

Figure 17 Axial composition of the SVEA-96 Optima2 assemblies used in the LWR-PROTEUS Phase III experiments (figure not to scale). The plenum regions above the PLRs and the two natural uranium pellets at the top of the PLR active length (yellow shaded segments, 2 cm long) have been explicitly modelled. The names of the lattices follow the nomenclature used in the KKL production data bank.

Due to the size of the test zone, the use of a real cross-shaped BWR control blade was not possible. Instead, L-shaped control blades (half of a normal blade), one containing Hf and one containing B_4C as absorber material, were especially fabricated for use in the LWR-PROTEUS programme. The geometry and position of the L-shaped control blades are depicted in Figure 19. Further details of the PROTEUS reactor and the LWR-PROTEUS experimental programme can be found in [4] and [5].

Table 3 Test zone configurations investigated during Phase I of the LWR-PROTEUS experimental programme. The configurations that are considered in this thesis are highlighted with a grey background.

Configuration	Moderator	Axial Zone	Type of Heterogeneity
1A	Light water	Lower	None
1B	Light water	Upper	None
1C	Light water	Boundary	Enrichment boundary (axial)
2A	Light water	Lower	Hafnium blade (radial)
2B	Light water	Upper	Hafnium blade (radial)
2C	Light water	Lower	B_4C blade (radial)
3A	Polyethylene	Lower	None (moderator in form of PE thin rods)
3B	Polyethylene	Upper	None (moderator in form of PE thin rods)
3D	Polyethylene	Boundary	Enrich. bound. (axial) (mod. PE thin rods)
4A	L.water + Polyeth.	Lower	None (LW mod. mixed with PE thin rods)
5A	Polyethylene	Lower	Hf blade (radial) (mod. PE thin rods)
6A	Light water	Lower	Hf blade, partly inserted (radial+axial)
7A	Light water	Lower	Central assembly displaced (radial)

Table 4 Test zone configurations investigated during Phase III of the LWR-PROTEUS experimental programme. The configurations that are considered in this thesis are highlighted with a grey background.

Configuration	Moderator	Axial Zone	Type of Heterogeneity
III-1	Mixture of H_2O (66.3%) and D_2O (33.7%)	Boundary	PLRs at lattice corners (axial)
III-2	Mixture of H_2O (66.3%) and D_2O (33.7%)	Boundary	PLRs adjacent to central water canal (axial)
III-3	Special tanks with different mixtures of H_2O and D_2O for the simulation of void effects	Central	Moderator density

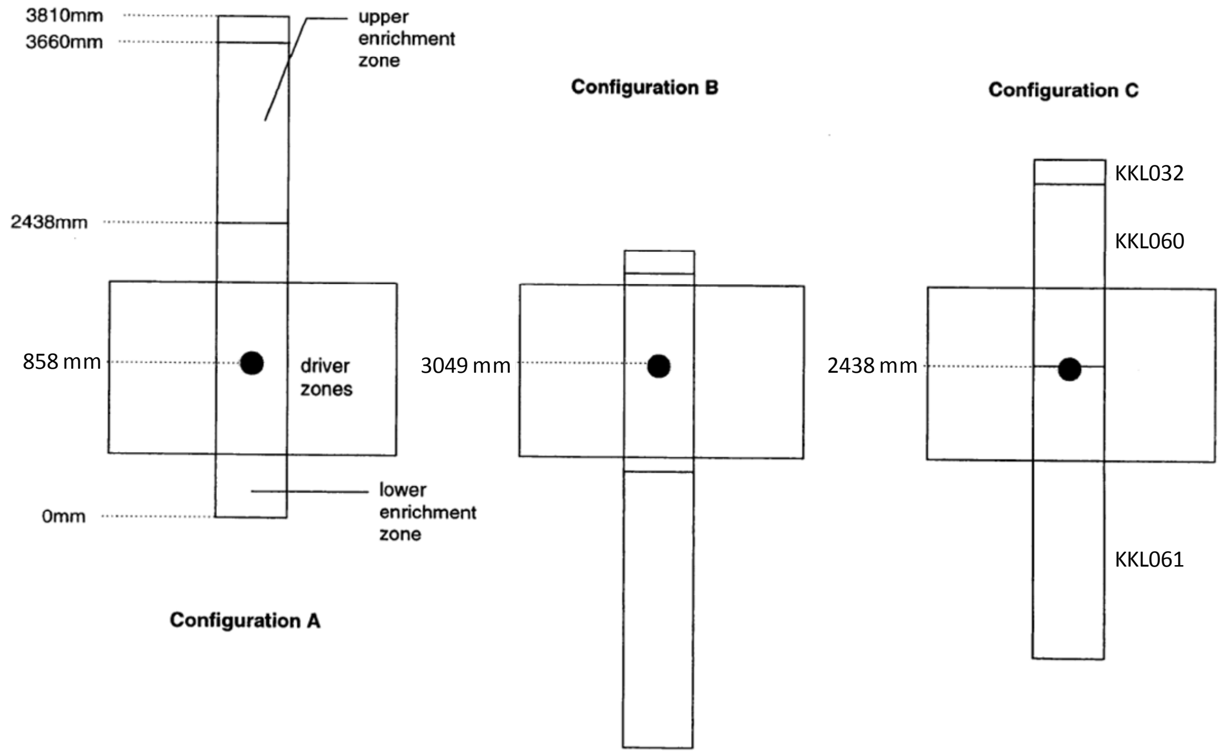

Figure 18 The three different axial positions of the test tank used during the Phase I experiments. Figure based on PSI drawing.

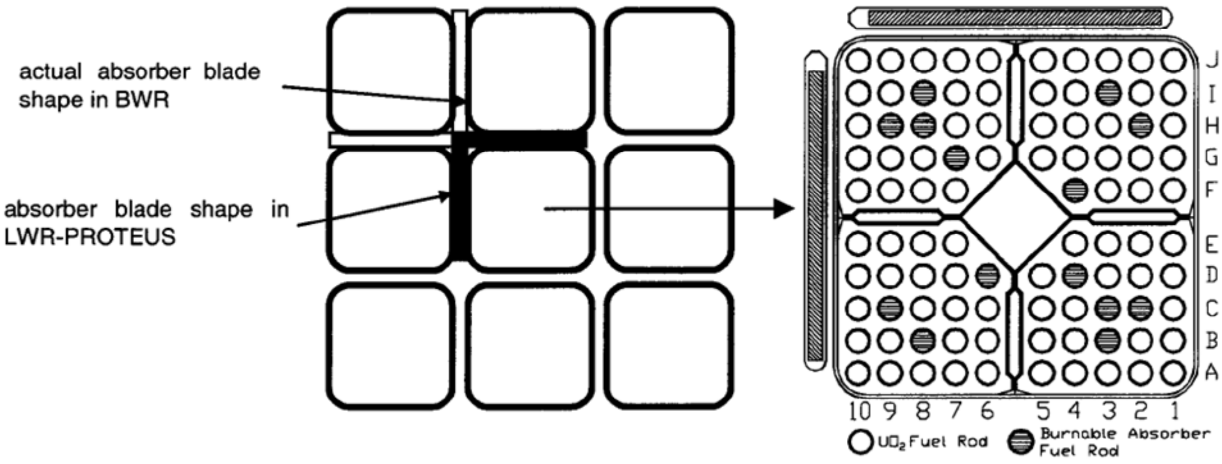

Figure 19 Form and position of the L-shaped control blades used in the Phase I experiments. Source: PSI.

Chapter 3

Synopsis of the modelling methodology

> *In 1935, Enrico Fermi found that a large variety of artificial radionuclides could be formed by bombarding atoms with neutrons. Using uranium as target, even some much lighter ones.*

The modelling of LWR-PROTEUS using power reactor core-monitoring and design tools is discussed in this chapter. The global concept behind the calculational model is depicted in Section 3.1. Section 3.2 describes the lattice modelling using HELIOS, while the associated PRESTO-2 core calculation model is described in Section 3.3. The lattice modelling with CASMO-5 and the SIMULATE-5 core model are described in Sections 3.4 and 3.5, respectively. Finally, Section 3.6 addresses the definition of the boundary conditions used to represent the test-zone surroundings in the 3D nodal calculation.

3.1 General considerations

The accuracy of a given methodology in solving a specific problem is closely related to the modelling features used for its application. For instance, in 3D core calculations, a refinement of the spatial mesh or an increase of the number of energy groups would lead to more accurate results. However, in practical applications, there are a number of constraints that must be accounted for. These constraints prescribe how the methodology can or should be applied to a particular system. For example, an extremely fine nodalisation or the use of a multi-assembly transport solution for the generation of nodal cross-sections could be used in a small domain such as the 3x3 LWR-PROTEUS test zone, but this would not be applicable to a large BWR core.

In the present research, aimed at the assessment of core calculation methodologies using experimental data from the LWR-PROTEUS programme, focus is set on the modelling of the experimental set-up using features and options that are similar to those used in production applications for power reactor cores. This is important in order to derive conclusions that are applicable to the power reactor environment. For instance, lattice data need to be produced in reflected assembly calculations, and the results stored in cross-section data banks accessed by the 3D core simulator. The core calculations, in turn, should be performed using a nodalisation equivalent to that normally applied to power reactor cores.

Particularly important in the LWR-PROTEUS modelling is the representation of the reactor regions surrounding the test zone. Thus, the buffer and driver zones are strongly coupled with the test zone by partial currents carrying significant spectral information. Due to the strongly heterogeneous nature of these surrounding regions, their representation by means of a layer of reflector nodes is not possible. Instead, the interaction between the test zone and the rest of the reactor can be accurately described by ratios of partial currents crossing the test-zone boundary.

The main purpose of this chapter is to describe the modelling features and approximations used in the calculation of the LWR-PROTEUS distributions of total-fission rates by means of the programme systems HELIOS/PRESTO-2 and CASMO-5/SIMULATE-5. In the following sections, the fundamental aspects of the three main calculation steps, namely the lattice modelling, the core modelling and the representation of the test-zone boundary are addressed. Focus is set here on the general modelling aspects that are common to all cases investigated, the specific features and approximations concerning each particular test-zone configuration being discussed in detail in Chapters 4 to 8.

3.2 Lattice calculations - HELIOS model

The 2D transport code HELIOS, with its ENDF/B-VI based cross-section library [29], is the programme system presently used at Axpo[10] for the cross-section generation for the Leibstadt Nuclear Power Plant (KKL). The programme version used in this thesis is HELIOS-1.9. One of the most significant virtues of HELIOS is the high level of flexibility it permits in the geometrical description of the lattice. In principle, any reactor design can be modelled with HELIOS, which makes it suitable for the calculation of systems that deviate significantly from the typical lattice designs used in LWRs. Particularly important for the studies performed in this thesis is the capability of HELIOS to model the singularities occurring in the LWR-PROTEUS test-zone configurations. For instance, to study the impact of irregular inter-assembly gaps, the normal assumption of half-symmetry in the lattice calculation has been intentionally abandoned in several cases. Another example of special modelling is the representation of the L-shaped control blade, in contrast with the regular BWR case of cruciform blades.

In this research, HELIOS is used for the generation of the two-group cross-sections, discontinuity factors and pin total-fission rate maps required by the core simulator PRESTO-2. In the following subsections, the general aspects concerning the modelling of the various LWR-PROTEUS configurations investigated in this thesis are presented and discussed.

3.2.1 Description of the lattice

From the user's point of view, the preparation of the HELIOS input is a relatively demanding process. In principle, no *a priori* assumption is made concerning the system geometry, composition and physical modelling. Instead, a number of operators with specific functions are provided, which the user may combine to build the system to be calculated. This architecture offers a high degree of freedom, but at the same time requires significant experience and physical understanding.

The description of the SVEA-96+ and SVEA-96 Optima2 lattices investigated in this thesis is largely based on the inputs used for the production calculations at the Leibstadt NPP. As discussed before, this has been done intentionally in order to reproduce the production calculation environment as closely as possible. However, some particular features of the LWR-PROTEUS configurations need to be accounted for.

Cross-section calculations for power reactors are performed in single-assembly reflected geometry. This means that zero net currents are assumed at the system boundaries or, in other

---

[10] Axpo AG is the Swiss energy concern owning the Beznau NPP (KKB) and 23% of the Leibstadt NPP (KKL). Axpo Kernenergie is a 100% daughter of Axpo AG, being responsible for the fuel cycle activities concerning both NPPs.

words, that the entire space is being filled with identical lattices. In addition, use is made of the fact that all BWR lattice designs feature diagonal symmetry with respect to the diagonal passing through the centre of the control blade. Thus, the transport problem is solved for one half of the lattice, with specular reflection along the mentioned diagonal, and the solution is later expanded to the full system. Furthermore, the nominal gap size resulting from the assembly pitch of the core is used.

In LWR-PROTEUS, due to experimental constraints[11], the fuel assemblies were not located at the exact positions corresponding to the nominal inter-assembly gaps. Thus, the experimental gap sizes showed small deviations with respect to a regular 3x3 test-zone arrangement. As part of the characterisation of the experiment, the inter-assembly gaps were measured for each configuration. The sizes of the measured gaps are given in the chapters dedicated to the individual cases, viz. Chapters 4 to 8.

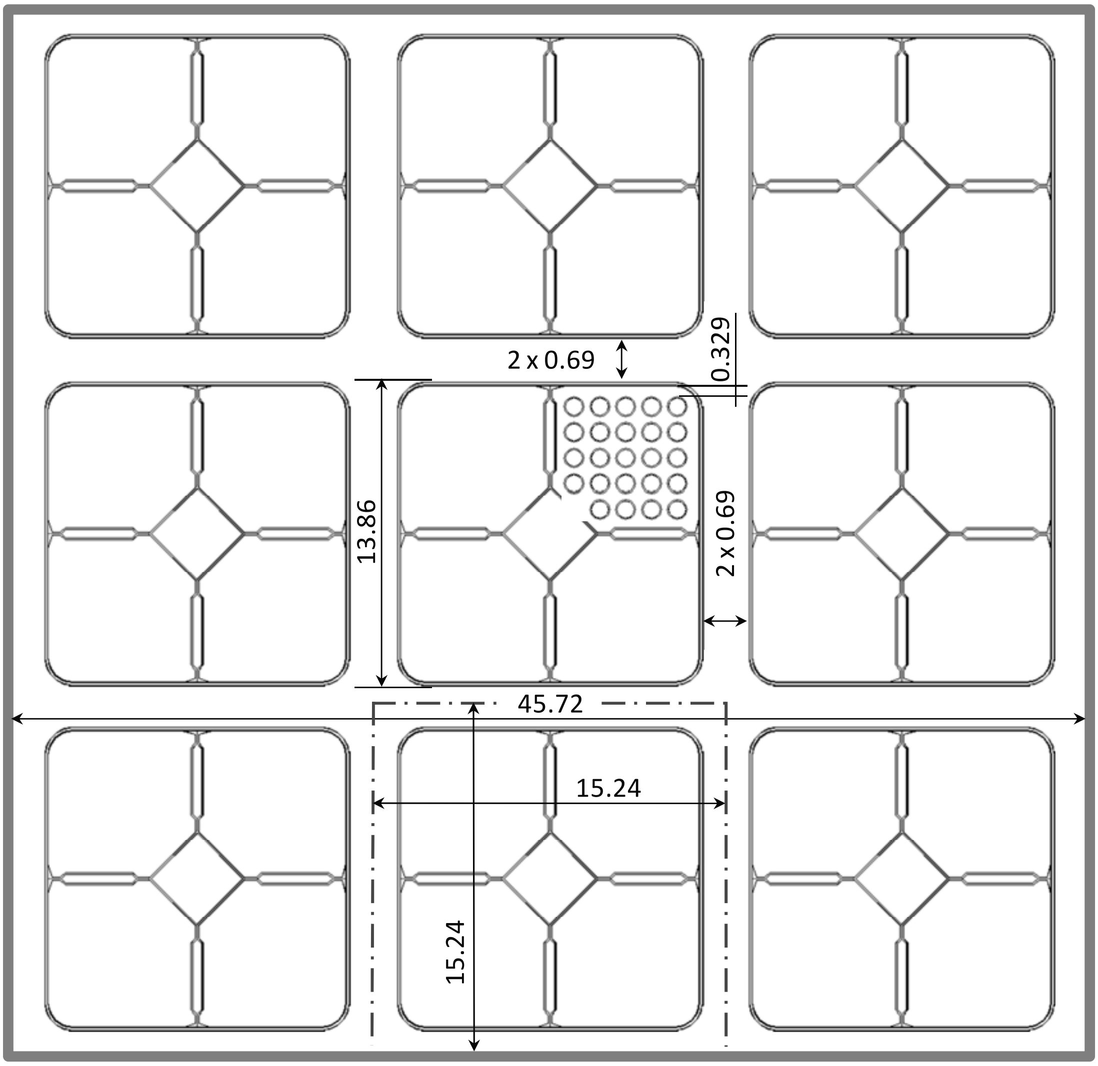

Figure 20 Nominal dimensions of the LWR-PROTEUS 3x3 test-zone array. The half-gap size is 0.69 cm for all gaps. The nominal distance (no sub-assembly pressing) between the outer surface of the cladding of the peripheral pins and the inner wall of the fuel box is 0.329 cm (SVEA-96+).

---

[11] The assembly channels, even when freshly manufactured, are not perfectly straight. Thus, even if the assemblies could have been placed exactly at the nominal positions by means of the top and bottom grids, the gap widths at the elevation of the measurements would deviate from the nominal values.

The LWR-PROTEUS test zone, showing the nominal dimensions, is depicted in Figure 20. The regular lattice has a side length equal to 15.24 cm, comprising two equal half-gaps of 0.69 cm each, the fuel box external width being 13.86 cm. Thus, for the case of nine identical fuel assemblies, the nominal geometry could be exactly represented by one single set of lattice parameters.

The situation is different when the real LWR-PROTEUS test-zone geometry is modelled. In this case, due to the irregular gap sizes, the nominal, infinitely reflected lattice does not represent the system exactly. Particularly important is the relative position of the fuel pins with respect to the inter-assembly gaps surrounding the central assembly, where the measurements were done. In the Phase I experiments (see Table 3 in Section 2.5), the central assembly was modelled using reflective boundary conditions, in full geometry and with the measured gap sizes. Furthermore, in order to account for the influence of the eight peripheral fuel assemblies with highest possible detail, each one of them was calculated with its own gap sizes, instead of the nominal values. The modelling particularities of each Phase I configuration are presented in Chapters 4 to 7.

Thus, effectively, for the Phase I configurations, lattice calculations were performed for each fuel assembly with its measured gaps. In Configurations I-1A and I-2A, this corresponds to nine cross-section sets per case. In Configurations I-1C and I-6A, both featuring axial heterogeneities, different cross-section sets are required for each axial zone (see also Sections 6.2 and 7.2). Thus, in total, 42 (2x9+12+12) different data sets were stored in the reference cross-section data bank for Phase I. Furthermore, additional sets were calculated in connection with sensitivity studies in Configurations I-1A and I-2A. These are described in Chapters 4 and 5, respectively.

In the calculations for Phase III (see Table 4 in Section 2.5), a different approach was used. Here, the central assembly was calculated in half-symmetry using averaged measured gaps for the central assembly, while nominal gaps were used for the peripheral ones. To describe the SVEA-96 Optima2 fuel elements used in this phase, seven cross-section sets are needed per fuel assembly type (three axial segments, two lattices representing the plenum volume of the PLRs and two additional lattices to model the natural uranium tip (2 cm) at the top of the PLR's pellet columns). With the central and peripheral assemblies having different nuclear designs (KKL e20-2 and KKL e18-1 respectively), 14 different lattices are effectively needed to describe the test zone in Configurations III-1 and III-2 (see also Figure 17). This issue will be discussed in detail in Chapter 8, where the modelling and results for Phase III are presented.

In order to simulate the internal displacement of the SVEA-96 sub-assemblies, which according to the fuel vendor Westinghouse occurs in the power reactor due to the forces induced by the coolant flow, the four sub-assemblies in each of the nine test-zone assemblies were pressed towards the centre of the assembly by means of polypropylene wires. This displacement, which in the case of LWR-PROTEUS Phase I is 0.051 cm in the x and y directions, leads to a change in the distance between the outer surface of the first-pin cladding and the inner wall of the fuel box. Thus, in the nominal case, shown in Figure 20, this distance is 0.329 cm, while in the experiment, due to the sub-assembly pressing, it is 0.380 cm, as shown in Figure 35 in Chapter 4. These experimental pin positions have been used in the HELIOS model, the corresponding pin coordinates being automatically transferred to PRESTO-2 via the cross-section data bank. For Phase III, where SVEA-96 Optima2 fuel assemblies were used, the sub-assembly displacements were slightly different. These are given in Chapter 8, where the details and results for Configurations III-1 and III-2 are presented and discussed.

With the exception of sensitivity cases featuring an increased number of rings in the fuel pins (see Chapters 4 and 5), the mesh used in the HELIOS model is identical to that used in the production calculations at KKL. The same concerns all HELIOS model and running options, which have been preserved in the reference calculations. It is only when running certain sensitivity cases that modified options have been considered. Thus, unless otherwise specified, for all calculations presented in this thesis, the fuel assembly (including gaps) was modelled using the mesh depicted in Figure 21.

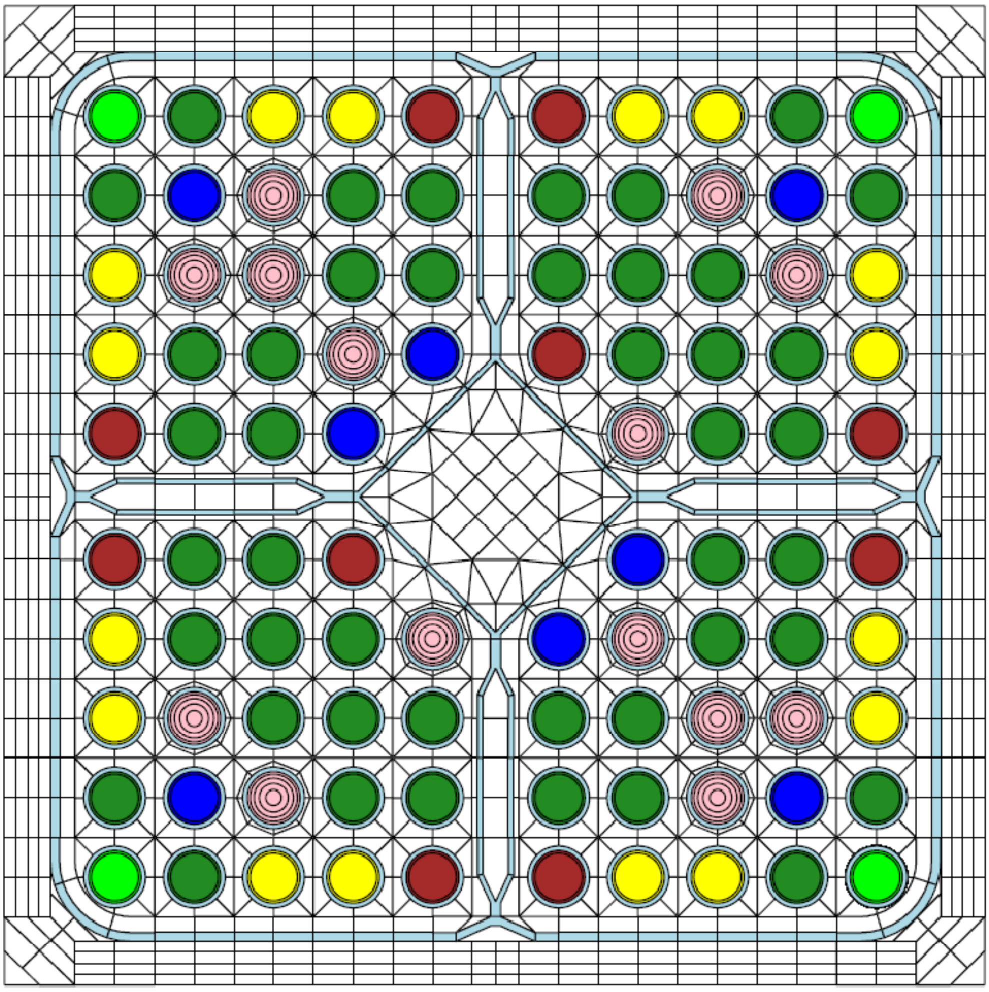

Figure 21 Mesh used in the HELIOS lattice calculations. The colours that fill the fuel pins represent different enrichments. The pins containing gadolinium can be identified by the presence of additional rings inside the pin volumes. Each polygon or circular region constitutes a flat-flux region in the transport calculation. This figure depicts the lower section of the SVEA-96+ assembly.

The mesh may vary slightly between different lattice designs, for example to represent the water volume above the PLRs in the SVEA-96 Optima2 assembly.

In all lattice calculations, the fuel assemblies were represented using the same orientation, i.e. with the wide-wide gap (vertex of the control blade) located in the north-west corner. For the core calculations, the assemblies were rotated according to their orientation in the test-zone, as depicted in Figure 22.

For configurations where the control blade is inserted, specific calculations were made for the central fuel assembly and the two neighbours sharing the control blade. As shown in Figure 22, the L-shaped control blade used in LWR-PROTEUS cannot be represented by a reflected lattice. Moreover, in the controlled state, assembly 4 cannot be represented by a rotation of assembly 2 (see also Figure 23). Hence, both assemblies had to be modelled explicitly.

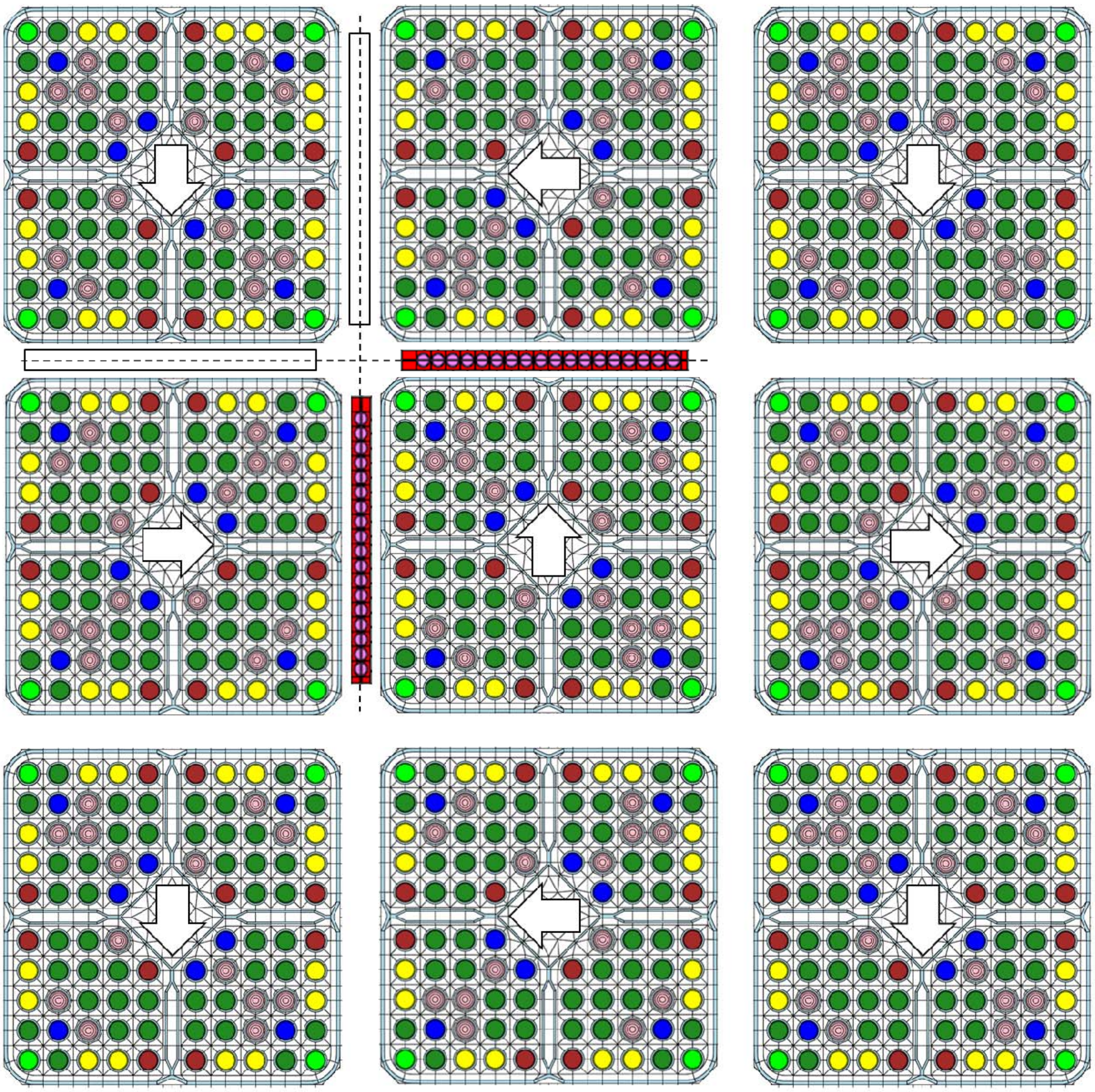

Figure 22 Fuel assembly orientation in the test-zone (example of Phase I). The arrows point towards the north edge of the lattice (HELIOS calculation). The L-shaped control blade used in Configurations I-2A and I-6A is placed in the north-west gap of the central fuel assembly. The two missing blades, which would complete a real BWR control blade, are represented by white rectangles.

3.2.2 Cross-section data bank

All calculations correspond to fresh fuel and zero (very low) power. In the case of LWR-PROTEUS, the lattice calculations deliver three sets of data:

1) Basic cross-sections
2) Discontinuity factors
3) Pin-power maps

The pellet densities and enrichments have been provided by the fuel vendor (Westinghouse). The moderator temperatures were as measured during the experiments. In analogy with the production cross-section data bank at KKL, the effect of spacers has been included, when applicable, by means of delta XSs and delta pin-power maps. These deltas are applied by the 3D simulator PRESTO-2 to the basic parameters at the elevations where spacers are present[12].

For the modelling of the L-shaped control blade (CB) used in Configurations I-2A and I-6A, on the other hand, the methodology of delta-parameters[13] used in the production XSDB has been abandoned in favour of an explicit set of controlled lattice parameters. Thus, the controlled assemblies are described as independent lattices, i.e. by a complete set of lattice parameters. In addition to the central assembly, which is controlled by both wings of the CB, the northern and western neighbours are also controlled, but with only one wing, as depicted in Figure 23.

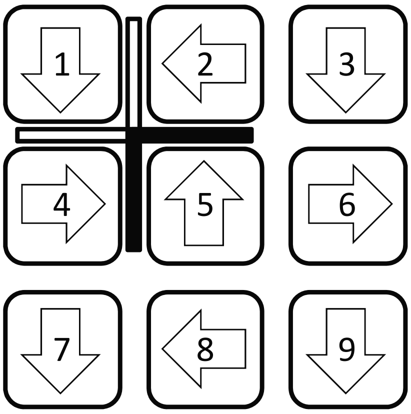

Figure 23 HELIOS modelling of the LWR-PROTEUS L-shaped control blade.

Thus, to describe the controlled test-zone, four basic lattice calculations are needed: a) no CB (assemblies 1, 3, 6, 7, 8 and 9), b) one blade on the west side (assembly 2), c) one blade on the north side (assembly 4), and d) two blades, on the north and west sides (assembly 5). In particular, it can be seen that assemblies 2 and 4 cannot be interchanged by a rotation. As in a power reactor core, the north-west corner of the lattice always coincides with the vertex of the CB.

Another important aspect to be considered for the LWR-PROTEUS applications is the deactivation of the gamma-smearing calculation. In power reactors, the pin-power distribution is affected by the gamma absorption in the fuel. Thus, a fraction of the power developed in a given fuel pin is not due to fissions occurring in it but is produced by the absorption of gamma-rays originated in other pins. In the case of LWR-PROTEUS, total-fission rates were measured by means of post-irradiation gamma-scans based on the induced fission-product activity. Thus, for the studies presented in this thesis, the gamma-smearing component must be excluded from the

---

[12] In this thesis, depending on the configuration under investigation, different approaches were used concerning the effect of spacers. Specific details are given in Chapters 4 to 8, where the specific configurations are discussed.

[13] In power reactor cores, any assembly type may be controlled by any control blade type. Therefore, for production XSDBs, branch-off calculations are done for each lattice combined with each control rod segment. For relevant parameters such as basic cross-sections, discontinuity factors and pin-power maps, delta-parameters are calculated as differences between the controlled and uncontrolled states and stored in the XSDB. For controlled nodes, and accounting for the CB fraction when the CB covers only part of the node, PRESTO-2 adds these deltas to the basic parameters to obtain the controlled values.

pin-power maps[14]. In HE/P2, this is done by modifying the input to the post-processor ZENITH appropriately.

Moreover, since the LWR-PROTEUS experimental data used in this thesis concerns total-fission reactions, the energy per fission must be set to 1 for the calculation of the pin-power maps. This is done by using Σ_f instead of $\kappa \cdot \Sigma_f$ in the pin-power calculation performed by the post-processor ZENITH.

For use with PRESTO-2, the cross-sections and discontinuity factors have been collapsed to two energy groups. The thermal cut-off energy used in the KKL production data bank, 1.84 eV, has been used in most calculations of Phase I. Sensitivity cases were also done using 0.625 eV as thermal cut-off energy. In the calculations for Phase III, only 0.625 eV has been used.

The lattice data have been stored in cross-section data banks by means of the interface programme TABGEN, which belongs to the HELIOS system. TABGEN reads the data created by HELIOS and organizes them in tables that can be read by the 3D simulator PRESTO-2.

3.3 Core calculations - PRESTO-2 model

As discussed in Chapter 2, the main advantage of nodal diffusion in comparison with other methodologies used to solve the diffusion problem, such as finite differences or finite elements, is the significant reduction in computational effort needed to achieve a specific accuracy. This is due to the ability of nodal schemes to deliver accurate results using a relatively coarse space discretisation. Thus, parallelepipedal nodes covering one fuel assembly plus half-gaps in the radial direction are normally used in power reactor cores. In the KKL plant, for instance, with an assembly pitch equal to 15.24 cm and an active core height equal to 381 cm, 25 axial levels are used, which results in cubical nodes of 15.24 cm side length.

Theoretically, the nodal height does not need to be uniform, i.e. it could be adjusted in order to match the axial heterogeneities occurring in the core. This would avoid the appearance of discontinuities within the nodes. In real cases, however, this adaptive nodalisation is not practicable. This is due to several reasons. In the power reactor core, there is a mixture of different fuel assembly designs, which normally have different axial zones. Since the axial nodalisation must be the same for the complete core, the requirement of making nodal boundaries coincident with material regions would result in an unnecessarily large number of (small) nodes. Furthermore, since the core loading changes from cycle to cycle, the nodalisation would need to be changed cycle-wise as well. In addition, there are many data handling steps in the production calculation chain that depend on the nodalisation. Also for this reason, it is important (actually mandatory) that the nodalisation remains constant throughout the reactor cycles. Finally, the upper ends of the control blades, which in BWRs are used during a large fraction of the operation cycle to control reactivity, may not be coincident with the node boundaries.

Thus, the normal situation is that axial heterogeneities, such as enrichment boundaries, partially inserted control blades or PLRs, do not necessarily coincide with the boundaries of the nodes. Nodal simulators include models to capture this effect, and it is important, for the

---

[14] For simplicity, the classical denomination "pin power map" is widely used in this thesis. Strictly speaking, however, in the case of LWR-PROTEUS, the denomination "total-fission rate map" should be used instead.

assessment performed in this research, to show how these situations are handled by the tested codes.

For calculating the LWR-PROTEUS test zone, consisting of the 3×3 array of BWR fuel assemblies, a fixed nodalisation has been used with PRESTO-2 to reflect the typical case of a power reactor core. Thus, the axial boundaries of the model have been chosen to be equidistant from the centre plane of the reactor driver, with the upper boundary lying 6.65 cm below the test tank water level. This setup results in a 123 cm high core, i.e. with axial boundaries located at ±61.5 cm with respect to the driver midplane. The core is subdivided into 10 axial levels, resulting in uniform nodes with dimension 15.24 x 15.24 x 12.3 cm. The resulting test-zone nodalisation is depicted in Figure 24.

The core midplane, which by definition coincides with the midplane of the buffer and driver zones, defines the interface between the 5th and 6th axial layers. In the axially heterogeneous experiments, however, the core midplane does not always coincide with the axial heterogeneity. For instance, in Configuration I-6A, the tip of the control blade is located 0.54 cm above the core mid plane, while in Configurations III-1 and III-2 it is the interface between the enriched and the natural uranium pellets of the PLRs which coincides with the core midplane, the end of the pellet column (where the plenum starts) lying 2 cm inside the 6th axial node.

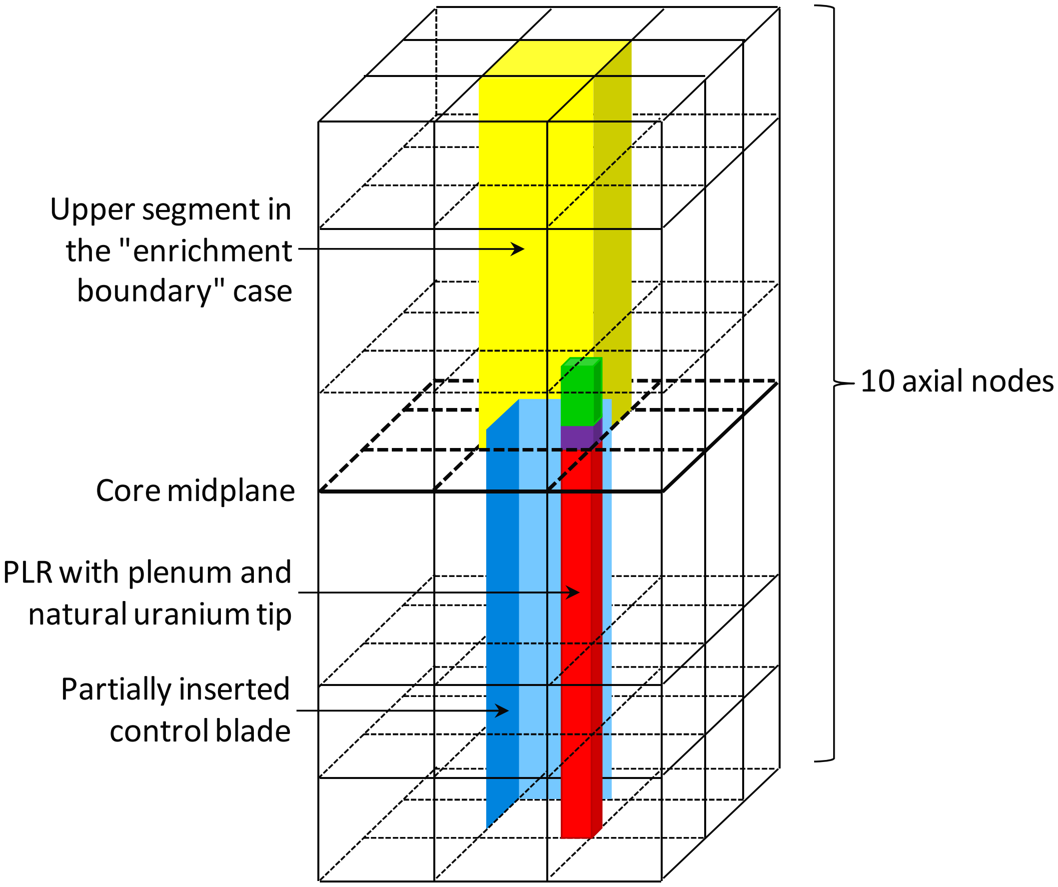

Figure 24 Nodalisation of the LWR-PROTEUS test zone. In the radial direction, each node comprises one fuel assembly with its associated half gaps, while there are 10 nodes in the axial direction. The upper segment in the "enrichment boundary" case (Configuration I-1C), the partially inserted control blade (Configuration I-6A) and a partial length rod plus plenum and natural uranium tip (Configurations III-1 and III-2) are schematically represented. The axial discontinuities in the latter three configurations do not coincide with the nodal interface at the core midplane.

As already mentioned in Section 3.2, the cross-sections, discontinuity factors and pin-power maps used in PRESTO-2 were obtained from HELIOS reflected assembly calculations, in which the wide-wide gap was always located at the north-west corner of the lattice. For the modelling of the test zone, the assemblies have been rotated accordingly to their "as loaded" positions.

3.3.1 Pin positions

Due to the use of measured gaps, the size of the reflected lattice modelled with HELIOS may differ from the radial size of the test-zone nodes modelled with PRESTO-2. This is because the latter always have the nominal value corresponding to the assembly pitch, 15.24 cm, while the sum of the sizes of the fuel box and two half-gaps may differ from this value. Although the use of measured gaps in the lattice calculation leads to the best estimation of the 2D pin-power maps and discontinuity factors, the pin coordinates will then deviate slightly from those finally assumed in PRESTO-2, which assumes that the assembly pitch has been used as external lattice dimension in both directions (x and y). Thus, when the pin-power maps are superimposed onto the asymptotic solution (see Subsection 2.3.2), all pins will have a displacement with respect to the positions they would occupy in the nominal case. To illustrate this, one may consider the case of Configuration I-1A, which will be discussed in Chapter 4. Reference is made to Figure 35 of Section 4.1, which shows the radial dimensions measured in the experimental setup. The coordinates that the fuel pins have in the experiment must be compared with the values they get in the PRESTO-2 model.

For the calculation, the central assembly is assumed to be placed in the exact centre of the test zone[15]. Thus, as can be seen in Figure 35, the geometrical centre of the central assembly is located at 22.86 cm from the inner walls of the test tank, the inner dimension of the test tank being 45.72 cm (2 x 22.86 cm). It should be noted here that 1/3 of 45.72 cm is the nominal lattice pitch, i.e. 15.24 cm. This means that in the PRESTO-2 model the pins would be placed exactly at their experimental positions if the centre of the lattice calculated with HELIOS coincides with the centre of the PRESTO-2 nodes used in the test-zone representation. Thus, knowing the coordinates of each pin with respect to the centre of the lattice and placing the centre of the lattice at the centre of the node, the pins occupy their correct positions.

To place the lattice in the node, PRESTO-2 uses the coordinates of the north-west corner of the lattice measured from its centre. In the HELIOS/PRESTO-2 model used at KKL, these coordinates are called XNWCRNR and YNWCRNR, for the x and y directions, respectively. ZENITH, the HELIOS post-processor, calculates XNWCRNR and YNWCRNR as one half of the length of the north side of the lattice.

In production lattice calculations, the nominal gap size is used and the length of the lattice side always matches the size of the core node. In this way, the correct (nominal) position of the pins is always preserved. For the LWR-PROTEUS investigations performed in this thesis, on the other hand, the lattice calculations have been performed using the measured gaps, in order, as discussed, to account for the effect of the gap size on the pin-power maps. Thus, for the

---

[15] In fact, the exact position of the central assembly with respect to the test-zone walls is not known. For the characterisation of the experiment, only the distances between the central assembly and its nearest neighbours were measured. Thus, it is also an assumption that the peripheral assemblies are exactly aligned with the central one, as indicated for example in Figure 35 for Configuration I-1A.

particular case of Configuration I-1A, and referring again to Figure 35, the following coordinates for the north-west corner of the lattice are obtained:

$$XNWCRNR = YNWCRNR = -\frac{0.7185 + 13.86 + 0.6865}{2} = -7.6325\,cm$$

To determine the positions of the pins in the node, PRESTO-2 sets the north-west corner of the lattice coincident with the north-west corner of the node. Hence, if the lattice size does not match the size of the node, a displacement occurs. This situation is depicted in Figure 25. On the left hand side, the nominal lattice dimensions lead to the centred positioning of the lattice in the node. In the case of LWR-PROTEUS, shown on the right hand side for Configuration I-1A, a displacement of 0.0125 cm occurs in both directions (x and y).

One way to correct for this effect is to set manually the coordinates to their nominal values, i.e.:

$$XNWCRNR = YNWCRNR = -7.6200\,cm$$

In this way, PRESTO-2 will place the centre of the lattice coincident with the centre of the node, which is the real situation in the LWR-PROTEUS test zone.

However, it needs to be noted that the impact of such a displacement on the calculated pin fission rates is very small, the artificial intervention being thus, in fact, unnecessary. In order to confirm this statement, calculations for configurations I-1A and I-2A were made using both sets of coordinates. Even in the especially challenging case of Configuration I-2A (control blade inserted), the differences were found not to exceed 0.27% of the C/E values, while in Configuration I-1A the effects lay below 0.12%.

The reason for this small impact can be explained as follows. The positioning of the pins inside the nodes is needed in the pin-power reconstruction process for the superposition of the 2D pin-power maps, calculated by HELIOS, onto the asymptotic flux solution of PRESTO-2. Thus, due to the relatively smooth behaviour of the asymptotic flux, a small displacement of the pin position, in the order of 0.1 mm, as shown above, does not affect the reconstructed pin-powers significantly.

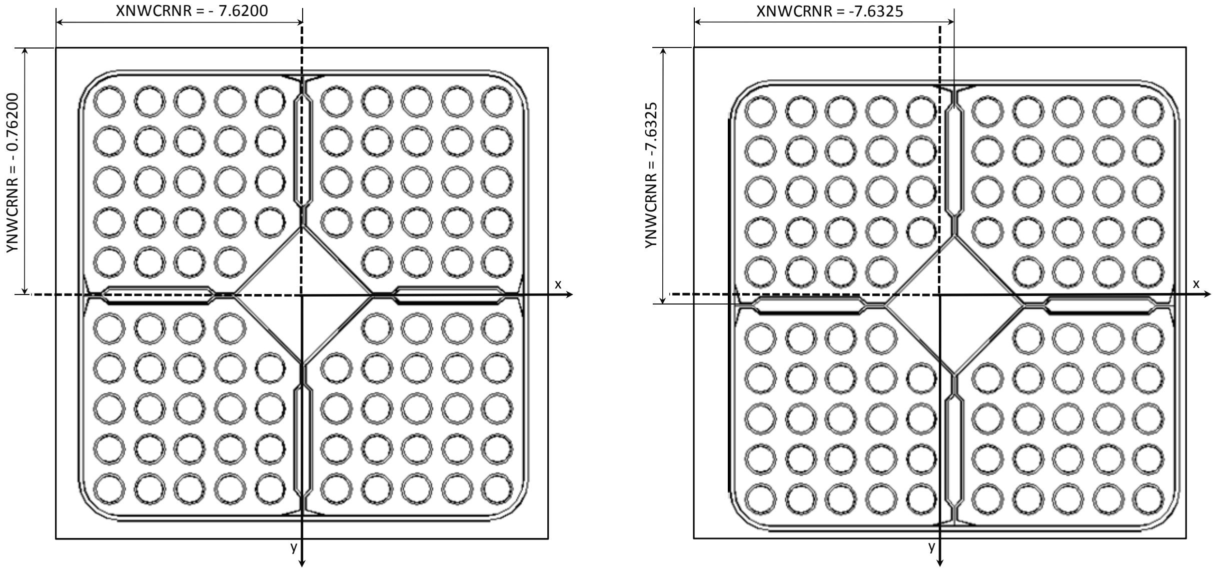

Figure 25 Position of the lattice in the core node. The coordinates XNWCRNR and YNWCRNR are calculated in ZENITH as 1/2 of the length of the north side. For the nominal case (left), the lattice is exactly centred in the node. If the gaps deviate from the nominal values (right), the lattice is slightly displaced. All dimensions are given in cm.

On the other hand, it needs to be remembered that, in the lattice calculation, the relative positions of the pins with respect to the inter-assembly gaps are much more important. In this case, the transport calculation captures the real heterogeneous nature of the flux, where small variations in the moderator volume may have a significant effect. Thus, although the use of the experimental gap sizes in the lattice calculation is important, the positioning of the lattice in the core node plays a much less significant role. Although a correction of this effect is possible with HELIOS/PRESTO-2, the manipulation was not considered necessary for the purpose of this research.

3.3.2 Axial heterogeneities and axial nodalisation

As discussed in Chapter 2, Subsection 2.3.3, axial heterogeneities are treated by the nodal programme by subdividing the assembly into sub-nodes, whose boundaries coincide with those of the original nodes plus the axial-discontinuity boundaries such as the top of a control blade or the interface between two different fuel-pin material compositions. For the modelling of the axially heterogeneous configurations investigated in this thesis, and for the reasons explained earlier, no special nodalisation was used in order to force the node boundaries to be coincident with the axial heterogeneities (spacers, enrichment boundaries, gas plenum regions in the PLRs, tip of the PLRs or tip of the CB). Instead, the same axial nodalisation (10 nodes, each 12.3 cm high) was used for all configurations investigated. Thus, the detailed axial distributions obtained in this research are the result of the intra-nodal, pellet-level reconstruction capabilities of PRESTO-2 and SIMULATE-5 and not the product of a finer, ad-hoc nodalisation of each individual axial heterogeneity considered.

3.4 Lattice calculations - CASMO-5 model

The 2D transport code CASMO-5 with its ENDF/B-VII based cross-section library [31] is a further development of the widely established CASMO-4 code. CASMO-5, complemented with the interface programme CMSLINK, prepares the cross-section data for the 3D simulator SIMULATE-5.

Differently from HELIOS, for which the user models the lattice geometry by means of general operators, CASMO-5 requires almost exclusively engineering data as input. This leads to very compact input decks and facilitates significantly the input preparation process. Although this is a welcomed feature in industrial applications, it may lead to limitations in special cases.

In the case of the LWR-PROTEUS calculations performed in this thesis, two main problems arise, viz.:

1) The deviation of the gap sizes with respect to the nominal values.
2) The use of the L-shaped control blade.

3.4.1 Energy group structure

SIMULATE-5 can, unlike PRESTO-2, solve the nodal diffusion problem in an arbitrary number of energy groups. For the calculation of the lattice parameters for SIMULATE-5, CASMO-5 uses a 586-group cross-section library based on the ENDF/B-VII.0 data file.

CASMO-5 calculates the necessary data, provided the appropriate condensation structure is selected by the user. In standard applications for power reactors, the CASMO-5 transport calculation is performed in a condensed structure of 19 groups [31]. For special applications, however, the energy condensation may need to be done in a different structure, including the group boundaries defined in SIMULATE-5. In this thesis, for instance, in order to match the group boundaries used for the determination of the Partial Current Ratios (see Table 7), the number of groups used for the transport calculation and for the editing of the lattice parameters in CASMO-5 was increased to 22 (including the 19 standard groups mentioned above). The group structures used for the CASMO-5 and SIMULATE-5 calculations are shown in Table 5.

Table 5 Group structures used in the CASMO-5/SIMULATE-5 calculations. For the two-group calculations, the thermal cut-off energy was set at 0.625 eV (1.84 eV in HELIOS/PRESTO-2).

CASMO-5 library group	CASMO-5 condensed	SIMULATE-5	Upper limit	Lower limit	Width	Unit
1	1	1	20.00000	4.96590	15.03410	MeV
32	2		4.96590	1.00000	3.96590	
63	3		1.00000	0.82085	0.17915	
67	4	2	820.84998	19.30500	801.54498	keV
125	5		19.30500	9.11880	10.18620	
129	6	3	9.11880	5.53080	3.58800	
133	7		5.53080	0.14870	5.38210	
162	8		148.70000	47.90000	100.80000	eV
167	9		47.90000	27.70000	20.20000	
168	10		27.70000	16.00000	11.70000	
169	11		16.00000	6.82500	9.17500	
297	12		6.82500	6.52500	0.30000	
309	13		6.52500	4.00000	2.52500	
410	14		4.00000	2.00000	2.00000	
490	15		2.00000	1.85000	0.15000	
496	16	4	1.85000	0.62500	1.22500	
545	17	5	0.62500	0.35000	0.27500	
556	18		0.35000	0.30000	0.05000	
558	19		0.30000	0.19000	0.11000	
563	20		0.19000	0.10000	0.09000	
572	21		0.10000	0.03000	0.07000	
581-586	22		0.03000	0.00000	0.03000	

3.4.2 Inter-assembly gaps

As discussed in Subsection 3.2.1 for the HELIOS case, the modelling of the measured inter-assembly gaps requires a full-geometry representation of the lattice. In addition, the size of the lattice does not match the size of the core nodes, which leads to the considerations made in Subsection 3.3.1 for the case of PRESTO-2.

With CASMO-5 as well, the lattice can be modelled in full geometry, which allows the specification of the measured gap size on each side of the lattice. In this way, the transport calculation correctly considers the relative position of the pins with respect to the neighbouring assemblies. However, the calculation chain CASMO-5/CMSLINK/SIMULATE-5 does not allow for this special situation. Attempts to produce data for SIMULATE-5 using full-geometry lattice calculations with CASMO-5 failed[16]. The reason for this is that the use of measured gaps in CASMO-5 leads to a lattice size that is slightly different from the nominal lattice pitch in the test zone. The same effect occurs in the HELIOS/PRESTO-2 calculation, but in this case the programme system allows for the mentioned deviation. The effect of this approximation has been discussed for the HELIOS/PRESTO-2 situation in Subsection 3.3.1.

Thus, for the CASMO-5/SIMULATE-5 calculations, the following procedure was adopted: the lattices were modelled in half-symmetry, as usually done for production calculations, but using, for both the wide and narrow gaps, the average of the measured values instead of the nominal ones. For each assembly, the gaps used in CASMO-5 are then given by:

$$wide\ gap = \frac{north\ gap + west\ gap}{2} \qquad narrow\ gap = \frac{south\ gap + east\ gap}{2}$$

As an example, the gaps used in Configuration I-1A are shown in Figure 52 of Chapter 4. In this way, the effect of the gap size could at least be partially accounted for, although not as exactly as in the case of a full-geometry lattice calculation.

3.4.3 Rotation of the SVEA-96 water canal by 45°

The central water canal in the SVEA-96 assembly design has a square cross-section that occupies 4 lattice positions, its sides forming a 45° angle with respect to the fuel box surfaces, as

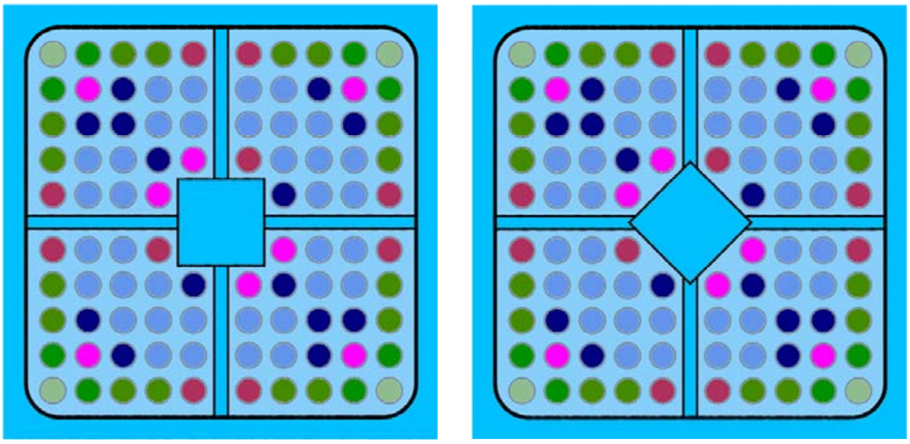

Figure 26 Effect of the use of option DIA in CASMO-5. On the left hand side, the standard CASMO-4 representation with the sides of the water canal being parallel to the fuel box sides. On the right hand side, the water canal is rotated 45° by means of the inclusion of the input card DIA. The pictures were created by including card TIF in the CASMO-5 input deck.

---

[16] According to the code provider Studsvik Scandpower (SSP), an option is now available in SIMULATE-5 that allows the user to specify a displacement of the assembly with respect to the nominal core pitch. This can be used, for example, to study the effect of channel bowing in BWRs. In the calculations performed during this thesis, however, this option was not used.

shown in Figure 16. As a default, CASMO-5 models the water canal with its sides parallel to the fuel box, as shown on the left hand side of Figure 26[17]. Optionally, the water canal may be rotated 45° when specifying the input card DIA, reflecting more accurately the real geometry (right hand side of Figure 26). This option was used in all CASMO-5 calculations presented in this thesis.

3.4.4 Sub-assembly compression

As in the case of HELIOS/PRESTO-2, the sub-assembly compression was accounted for in CASMO-5 by the displacement of the pin coordinates as shown, for the particular case of Configuration I-1A [32], in Figure 27[18]. It can be seen, that this displacement differs from the previously mentioned compression (see Subsection 3.2.1). The measured value, 0.051 cm, is the displacement derived from the distance between the cladding of the peripheral pins and the inner

```
LDX  * Layout of pin off-centre displacement towards East
 0.0375
 0.0375  0.0375
 0.0375  0.0375  0.0375
 0.0375  0.0375  0.0375  0.0375
 0.0375  0.0375  0.0375  0.0375     0
    0       0       0       0       0    0
 0.0375  0.0375  0.0375  0.0375     0    0    0
 0.0375  0.0375  0.0375  0.0375  0.0375  0 -0.0375 -0.0375
 0.0375  0.0375  0.0375  0.0375  0.0375  0 -0.0375 -0.0375 -0.0375
 0.0375  0.0375  0.0375  0.0375  0.0375  0 -0.0375 -0.0375 -0.0375 -0.0375
 0.0375  0.0375  0.0375  0.0375  0.0375  0 -0.0375 -0.0375 -0.0375 -0.0375 -0.0375

LDY  * Layout of pin off-centre displacement towards North
-0.0375
-0.0375 -0.0375
-0.0375 -0.0375 -0.0375
-0.0375 -0.0375 -0.0375 -0.0375
-0.0375 -0.0375 -0.0375 -0.0375     0
    0       0       0       0       0    0
 0.0375  0.0375  0.0375  0.0375     0    0    0
 0.0375  0.0375  0.0375  0.0375  0.0375  0  0.0375  0.0375
 0.0375  0.0375  0.0375  0.0375  0.0375  0  0.0375  0.0375  0.0375
 0.0375  0.0375  0.0375  0.0375  0.0375  0  0.0375  0.0375  0.0375  0.0375
 0.0375  0.0375  0.0375  0.0375  0.0375  0  0.0375  0.0375  0.0375  0.0375  0.0375
```

Figure 27 Displacement of the pin coordinates in CASMO-5 to describe the sub-assembly compression in the x (upper map) and y (lower map) directions.

---

[17] This is the only option available in CASMO-4.

[18] The same displacements are valid for all LWR-PROTEUS Phase I configurations.

wall of the fuel box. For the nominal lattice (see Figure 20), this distance is 0.329 cm, while the measured value is 0.380 cm (see Figure 35). In CASMO-5, pin displacements are specified by means of the LDX and LDY cards, these input parameters representing the offsets, in x and y directions respectively, of the pin centres with respect to the centres of the lattice cells. The latter, in turn, are defined such that the boundaries of the cells that are adjacent to the water cross coincide with the boundary of the slab region representing it. Due to the fact that the measured lattice pitch (1.237 cm) also differs from the nominal value (1.240 cm), the peripheral pins are already shifted 4.5 x 0.003 = 0.0135 cm towards the water cross. Thus, the LDX and LDY inputs must only account for the remaining displacement, i.e. 0.051 – 0.0135 = 0.0375 cm.

3.4.5 Cross-section data bank

As mentioned before, the CASMO-5/SIMULATE-5 system is designed to require a minimum of physical inputs from the user. Contrary to HELIOS, for which the structure of the cross-section data bank must be programmed by means of input operators, CASMO-5 requires one single instruction (S5C), that may be complemented by several options, in order to create a suitable case matrix for SIMULATE-5. This philosophy has significant advantages in production applications for power plants, not only from the point of view of the engineering resources needed to perform the calculations but also concerning the quality assurance of the input decks. However, as mentioned before, input simplifications are necessarily coupled with compromises in the programme system flexibility. Thus, in the case of LWR-PROTEUS, certain special C5 features need to be activated in order to produce a suitable case matrix, from which basically the cold condition at zero burnup is needed. In any case, since S5 requires a minimal matrix to work with, a relative large number of non-used cases must be calculated, which in principle has no other disadvantage than a somewhat longer execution time and larger data files. The C5 cross-section data bank generation instructions used in this thesis are shown in Table 6.

Table 6 CASMO-5 cross-section data bank generation instructions.

XPO 'FISS'	Edit the total-fission rate distribution.
THE 0	No thermal expansion.
XEN 0	^{135}I and ^{135}Xe concentration equal to 0.0.
INC 'CR/control-rods.inc'	Include control rod data (required but not used).
TFU= 760 TMO= 560	Fuel and moderator temperature. The S5 case matrix requires a realistic (power case) fuel temperature, the 20°C condition being automatically included in the XSDB. The actual moderator temperature is input to S5.
PDE 30 'WGU'	Power density in W/gHM (HM = Heavy Metal Initial). As in the case of TFU, S5 requires a realistic (power case) power density. The zero power condition is specified in the core calculation.
DEP -20	Maximum exposure in MWd/kgHM. Intermediate steps are selected by C5. Although only zero burnup cases are run, a depletion path is required by S5.
GAM -80	Gamma calculations at all exposure points. For completeness, S5 requires gamma data to be included in the XS data library. To be suppressed, the gamma smearing calculation must be explicitly switched off in S5.
S5C	Create the complete case matrix for S5.

3.4.6 Interface CASMO-5/SIMULATE-5 - CMSLINK

CMSLINK is the interface programme between CASMO-5 and SIMULATE-5. It post-processes the data created by CASMO-5 and creates the cross-section data libraries needed by SIMULATE-5. Through it, the group structure to be used in SIMULATE-5 is defined, as well as the creation of a full-power or a zero-power data library. For the LWR-PROTEUS calculations, only the zero-power (also called "cold") data library is needed, the group structure being the one shown in Table 5.

3.5 Core calculations - SIMULATE-5 model

The SIMULATE-5 model of the test zone uses the same nodalisation as the PRESTO-2 model, shown in Figure 24. Also as in the PRESTO-2 case, the test-zone surroundings are modelled by Partial Current Ratios (PCRs), instead of defining a set of reflector nodes. The boundary conditions for the nodal domain will be discussed in detail in Section 3.6.

3.5.1 Group structure

The group structure used for the nodal diffusion calculation is automatically defined by the structure stored in the cross-section data libraries created by CMSLINK (see Subsection 3.4.6 and Table 5). The PCRs describing the boundary conditions, however, must be given in the same group structure. This aspect will be discussed in Section 3.6.

3.5.2 Gamma smearing

In the CASMO-5/SIMULATE-5 system, the calculated pin-powers are automatically corrected by the power generated by gamma capture in the fuel pins. This process accounts, as discussed earlier, for the fact that the power being developed in each pin is affected by fissions occurring in other pins of the core. This leads to a somewhat smoother power shape. Especially affected are the fuel pins containing gadolinium, in which the fission rate is significantly lower but the gamma capture component is equally strong, or even stronger, due to the captures in Gd, than in regular pins.

Since in the LWR-PROTEUS experiments the measured parameter is the total-fission rate, the gamma capture correction must be switched off for the core calculations, as in the case of PRESTO-2, in order to allow a correct comparison. This is done by activating the SIMULATE-5 option 'COR.GAM' 0.0. Without this option, the gamma-smearing would be performed even if the energy per fission is set to a constant value (total-fission rate edit), which would lead to erroneous results.

3.5.3 Pin Positions

As in the case of HELIOS/PRESTO-2, and as discussed in Subsection 3.4.2, the measured gap sizes are used in the CASMO-5/SIMULATE-5 calculations. This leads to a lattice size that is slightly different from the node size in the test zone. In Subsection 3.3.1, the details of this mismatch were discussed for the case of HELIOS/PRESTO-2, the impact on the total-fission rate distribution being found to be very small. Similar conclusions can be applied to the CASMO-5/ SIMULATE-5 case, where the pin-power reconstruction methodology of superimposing the 2D transport solution to the asymptotic nodal profile builds upon the same principles. Thus, also in this case, the impact of the lattice size mismatch can be neglected.

3.6 Boundary conditions for the test zone

The solution of the nodal diffusion problem in the core domain requires the knowledge of the boundary conditions that represent the core surroundings. As mentioned in Chapter 2, when introducing the code PRESTO-2 (see Subsection 2.4.2), these boundary conditions can be specified in two different ways, namely:

1) Extending the calculated domain beyond the active core, by means of the definition of one or more layers of reflector nodes, with a black boundary (zero incoming current) constraint at the outer surface.
2) Representing the interaction with the universe that surrounds the calculated domain by means of partial (incoming and outgoing) currents.

Although both methodologies are physically founded, their range of applicability differs. For instance, the use of reflector nodes is a suitable procedure in the case of large power reactor cores. In this case, the core is surrounded by non-multiplicative materials such as light water and steel. In the reflector region, the neutron flux rapidly decreases, and the assumption of zero incoming current at the outer surface is justified. Eventually, neutrons returning to the system after having escaped the reflector can be accounted for by a non-zero boundary albedo at the outer reflector surface.

Power reactor cores, for which the nodal methodology was principally developed, contain a relatively large number of fuel elements (in the order of 500-800 for a BWR). As an example, Figure 28 shows a schematic representation of the reactor core at the Leibstadt Nuclear Power Plant (KKL). The core contains 648 fuel assemblies, 149 cruciform control blades and 39 detector (LPRM and TIP) strings. In the illustrated KKL case, the core reflector can be modelled, for example, by means of an extra row of 80 nodes per axial level. Doing so, the number of nodes to be calculated increases from 16'200 (=648x25) to 18'200 (=728x25), which can be correlated with an increase of approximately 12% in the computational effort needed for the 3D flux calculation.

The second methodology for the modelling of the core surroundings is the use of partial currents to describe the reflector response. In power reactor applications, and recalling the non-multiplicative character of the reflector materials, this can be done by means of albedo matrices applied directly to the core boundary. This means, neutrons leaking out of the core may partly return to it, the ratio between the incoming and outgoing partial currents being given by the value of the albedo. As shown in Figure 13 of Chapter 2, three particular situations can be identified: planar surfaces, outer corners and inner corners. In the case of planar surfaces and outer corners, neutrons may only return to the core after having collided in the reflector material. On the other hand, for re-entrant surfaces (inner corners), leaking neutrons have in addition the possibility to re-enter the core uncollided (first-fly transmission).

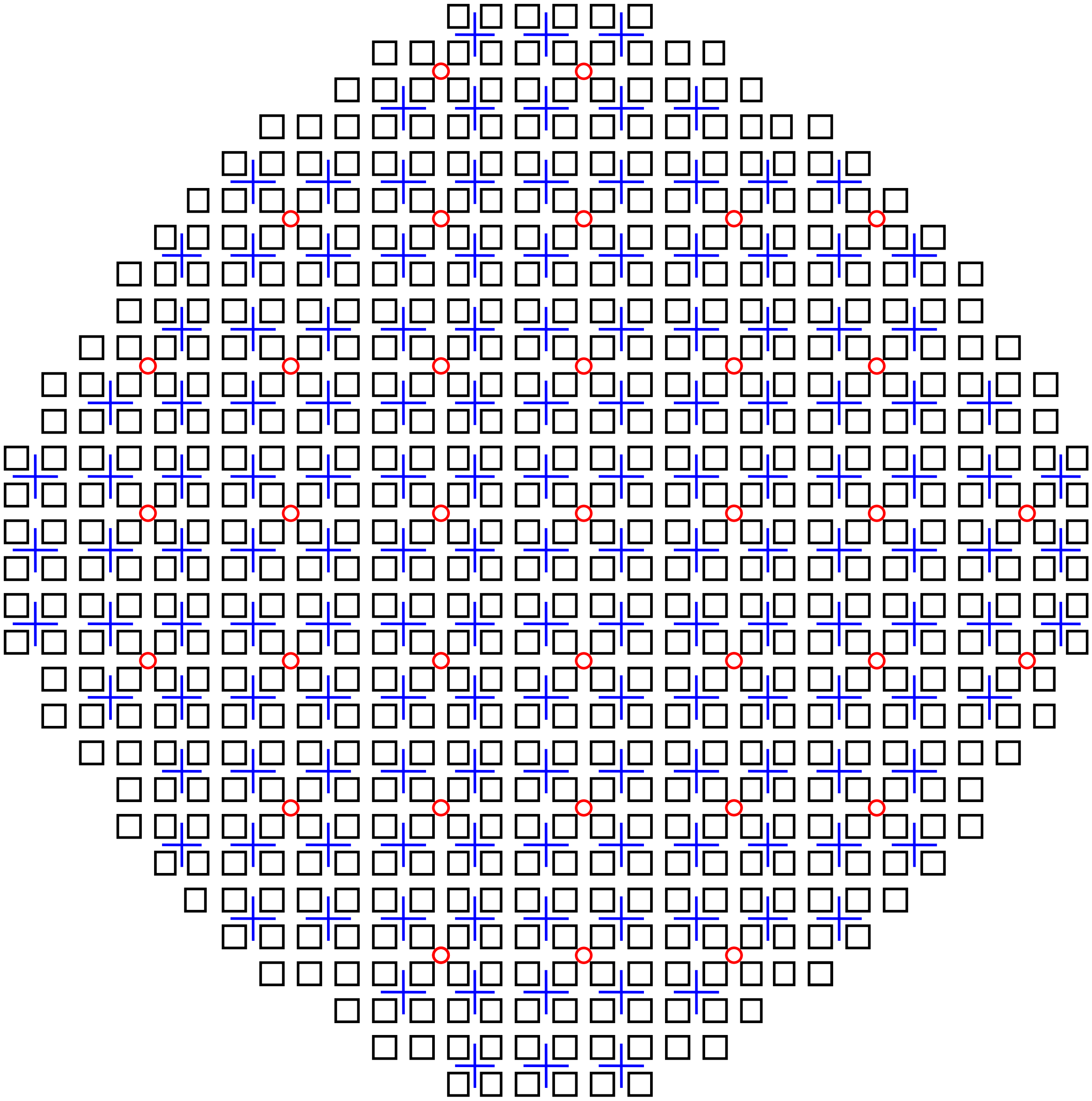

Figure 28 Schematic representation of the reactor core at the Leibstadt NPP (KKL). The figure shows the 648 fuel assemblies, the 35 detector strings (red circles) and the 149 control blades (blue crosses).

For each albedo type depicted in Figure 13, an albedo matrix, the order of which is equal to the number of energy groups used in the nodal diffusion calculation, can be defined, the general form of these matrices being given by equation {40} of Subsection 2.4.2, which is rewritten here for the general case of G energy groups:

$$a_{gg'} = \frac{j_g^-}{j_{g'}^+} \; for \; g, g' = 1, \ldots, G \qquad \{41\}$$

Thus, the nodal diffusion problem can be closed if the ratios {41} are known over the entire core boundary.

It should be noted that, strictly speaking, the $a_{gg'}$ depend on the core conditions too. The reason is that the spectrum of the outgoing current depends on the fuel composition and coolant density in the peripheral channels, and the probability of a leaking neutron to return to the core with a specific energy depends on this spectrum. For practical applications, however, a distinction concerning the fuel composition is not needed. The properties of the peripheral assemblies (normally highly depleted) can be assumed to be similar, and for each axial level the use of just three sets of radial albedo matrices, as described before, is sufficient for power reactor cores.

On the other hand, since the coolant density varies over the length of the fuel assemblies (most significantly in BWRs), the albedos will change as a function of the elevation. Furthermore, since the coolant density profile depends on the operational conditions of the core, a fixed set of axially varying albedos may not be sufficient to describe the system accurately. In some industrial core simulators, such as PRESTO-2, this problem is solved by introducing polynomial functions that account for the dependence of the $a_{gg'}$ on the coolant density.

For determination of the $a_{gg'}$ for power reactor cores, use is made of the fact that the materials in the reflector region are non-multiplicative. Hence, it is sufficient to perform a 2D transport calculation (deterministic or stochastic) in order to calculate the partial currents at the core-reflector interface using a typical core loading and a representative reflector composition. The albedos $a_{gg'}$ obtained in this form, are valid for any core loading and may be considered as reactor dependent data.

However, one problem still remains: in its general form given by {41}, the albedo matrix contains non-diagonal elements representing the up- and down-scattering of neutrons in the reflector. For calculations in two energy groups, as in the case of PRESTO-2, the thermal cut-off is selected such that the up-scattering from group 2 into group 1 is zero, leading to the albedo matrix {39} of Subsection 2.4.2. However, a down-scattering component exists, representing the contribution of neutrons that are slowed down in the reflector after having left the core with epithermal energy. In multigroup nodal diffusion, as in the case of SIMULATE-5, depending on the group structure used, even up-scattering terms may occur.

The problem with the non-diagonal terms of the albedo matrix is that it is not possible to derive them from ratios of partial currents obtained from criticality calculations. For instance, using deterministic eigenvalue calculations or stochastic fission-source (kcode)[19] calculations, the origin of the neutrons contributing to the incoming partial currents in each energy group cannot be determined. Thus, from such calculations, only the diagonal terms of the albedo matrix can be obtained.

To evaluate the non-diagonal terms, the original energy group of the outgoing neutrons that contribute to the incoming current in each group must be known. This can only be done by means of fixed-source calculations, for example using MCNPX. Fixing the energy of the source neutrons (whose spatial distribution must correspond to that of the fission source), the number of neutrons re-entering the core in each energy group can be determined. Varying the source energy to cover each emission group, the in- and out-currents can be evaluated, hence yielding all components $a_{gg'}$ of the matrix. Although cumbersome, this methodology allows one to define full, and thus less case dependent, albedo matrices.

---

[19] In MCNP or MCNPX, kcode is the calculation mode in which the fission source is re-evaluated based on the flux solution of a previous generation of particles. After a sufficient number of cycles, the final flux is obtained (criticality calculation).

In the particular case of LWR-PROTEUS, special considerations need to be made. In this case, the representation of the test-zone surroundings by means of an extra layer of reflector nodes, as done for power reactor cores, is not possible. The D_2O and graphite driver zones are multiplicative and contribute significantly to the reactor criticality, while the buffer located between the D_2O driver and the test zone produces a strong incoming current of epithermal neutrons. Thus, the test-zone is strongly coupled with the rest of the reactor. Rigorously, this coupling can be represented by the currents that leave and enter the test zone through any point at its interface with the surroundings, more precisely by the ratios j_g^-/j_g^+, i.e. the diagonal terms a_{gg} of the albedo matrix {41}.

Several methodologies could be applied to determine these partial currents. In all cases, however, it is required that the surroundings are included in the calculation. For instance, 2D transport calculations over the complete LWR-PROTEUS reactor can deliver sets of PCRs that are valid for each different axial composition segment in the test zone. This method has the disadvantage, however, that the axial variation of the PCRs is not correctly accounted for. Even though for axially uniform cases, such as Configurations I-1A or I-2A, this may seem an acceptable approximation, it will be shown later (see Subsection 6.3.3) that this procedure may be insufficient in cases with axial heterogeneities. Furthermore, the PCRs obtained from 2D transport calculations do not include axial leakage information, this aspect having a significant impact on the magnitude of the PCRs (see also Section 4.4).

A more accurate procedure is to determine the partial currents by means of 3D transport calculations over the complete reactor. This approach, although expensive in computer resources, offers the most accurate description of the coupling between test zone and the outer reactor regions. In this thesis, 3D full-reactor MCNPX calculations have been used to determine the test-zone boundary conditions for each studied configuration. For this purpose, the partial currents (incoming and outgoing) were tallied at the inner surface of the test tank wall, in 12 segments per side for each axial level. The top and bottom surfaces each obtained a single set of partial currents. Details of these calculations are given in Subsection 3.6.1.

It must be underlined here, that due to their particular character, the current ratios j_g^-/j_g^+ do not represent albedos in the normal sense of non-multiplicative reflectors as discussed earlier. Therefore, the denomination Partial Current Ratios (PCRs) is used instead. It should also be borne in mind that the PCRs are closely related to the specific configuration of the test and outer zones. In other words, a set of PCRs representing the boundary conditions of the test zone for a specific LWR-PROTEUS configuration is valid for that particular configuration only. However, once known, the PCRs allow one to decouple the calculation of the test zone from the rest of the reactor, thus enabling the application of standard nodal diffusion methodologies to the core (test zone) domain.

In the following subsection, a methodology for deriving configuration-dependent PCRs, based on MCNPX calculations, is presented. An alternative approach, using a 2D whole-reactor HELIOS model of LWR-PROTEUS, is discussed in Subsection 3.6.2.

3.6.1 Configuration dependent PCRs - 3D full-reactor MCNPX model

For the determination of the PCRs, the perimeter of the test zone is subdivided into 12 segments per side, each being 3.81 cm wide. This corresponds to 1/4 of the node width (which in turn is equal to the nominal assembly pitch). Axially, the test zone is subdivided into 10 layers which are 12.3 cm high. Figure 29 depicts the nodalisation of the LWR-PROTEUS test zone and the discretisation of the test-zone boundary. A detailed view of the azimuthal discretisation is shown in Figure 30.

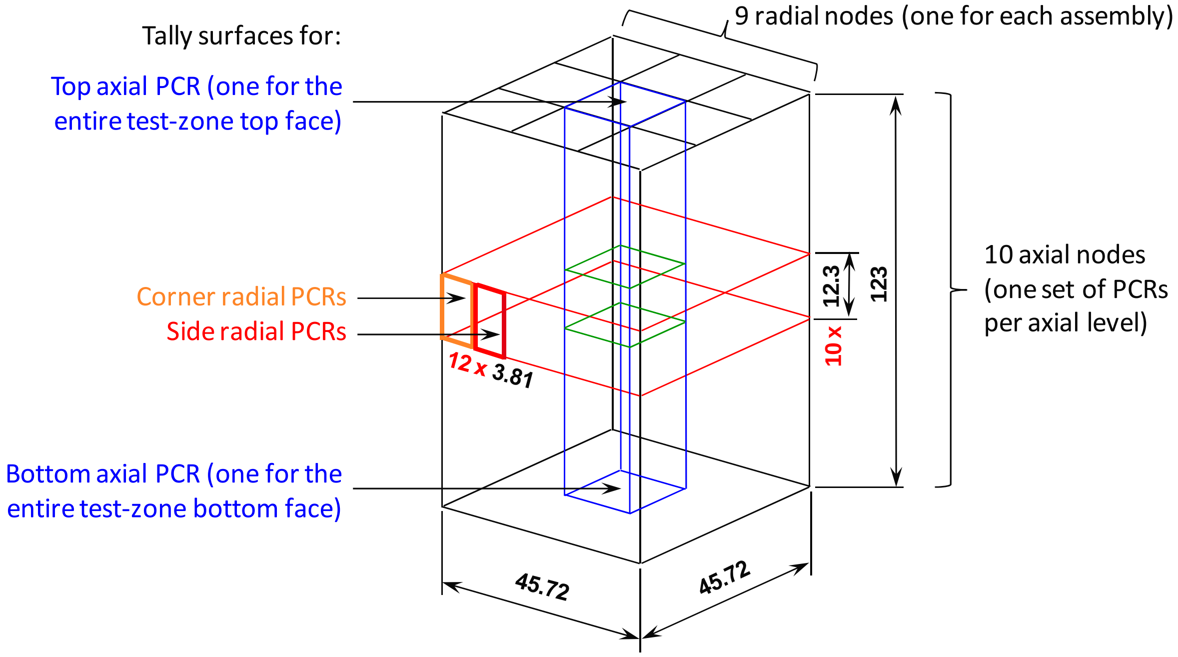

Figure 29 Nodalisation of the LWR-PROTEUS test zone and discretisation of the test-zone boundary for the calculation of the PCRs (dimensions in cm).

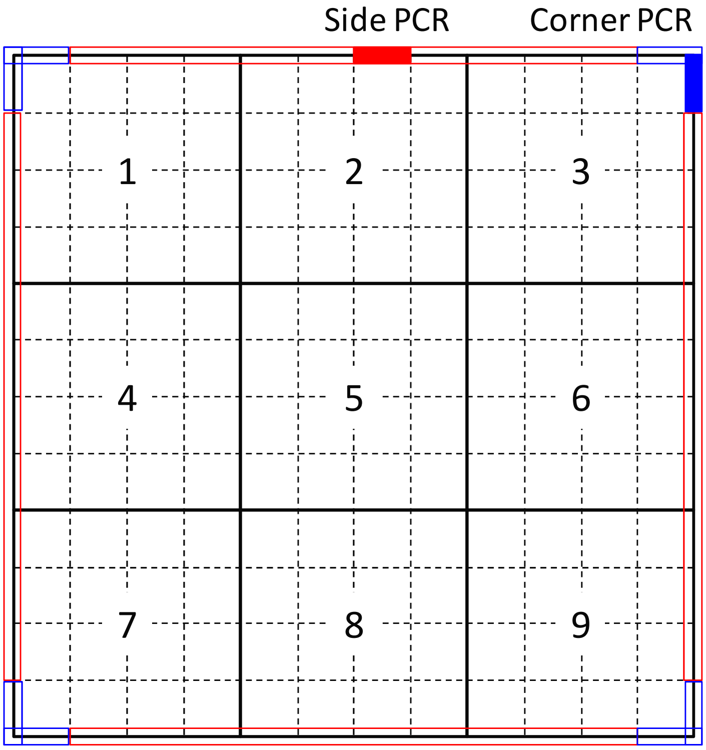

Figure 30 Discretisation of the LWR-PROTEUS test-zone boundary surfaces. The size of the tally segments corresponds to 1/4 of the assembly pitch (red and blue filled lines). In PRESTO-2, PCR matrices can be defined for sides (non-filled red) and corners (non-filled blue) at each axial level. In SIMULATE-5, if axial dependence is specified, only one PCR matrix per axial level is possible (sides and corners are lumped together).

The 3D MCNPX model of the PROTEUS reactor used in this thesis for the calculation of the PCRs is largely based on the developments previously done in the frame of the LWR-PROTEUS experimental programme [33]. In PROTEUS, MCNPX is used not only for the modelling of experiments but also for operational support, for example in connection with the determination of the critical fuel loading of the driver zones. The MCNPX model is thus very well validated and can be regarded as a reliable numerical tool for flux and reactivity calculations for the PROTEUS reactor.

Axial and radial views of the MCNPX whole-reactor model are shown in Figure 31. The test-zone and the outer regions are modelled with a high level of detail. In particular, the pin-wise modelling of the fuel assemblies allows the calculation of detailed 3D total-fission rate distributions that can be compared against the reconstructed pin-powers obtained with the nodal calculations, as will be presented and discussed in the following chapters.

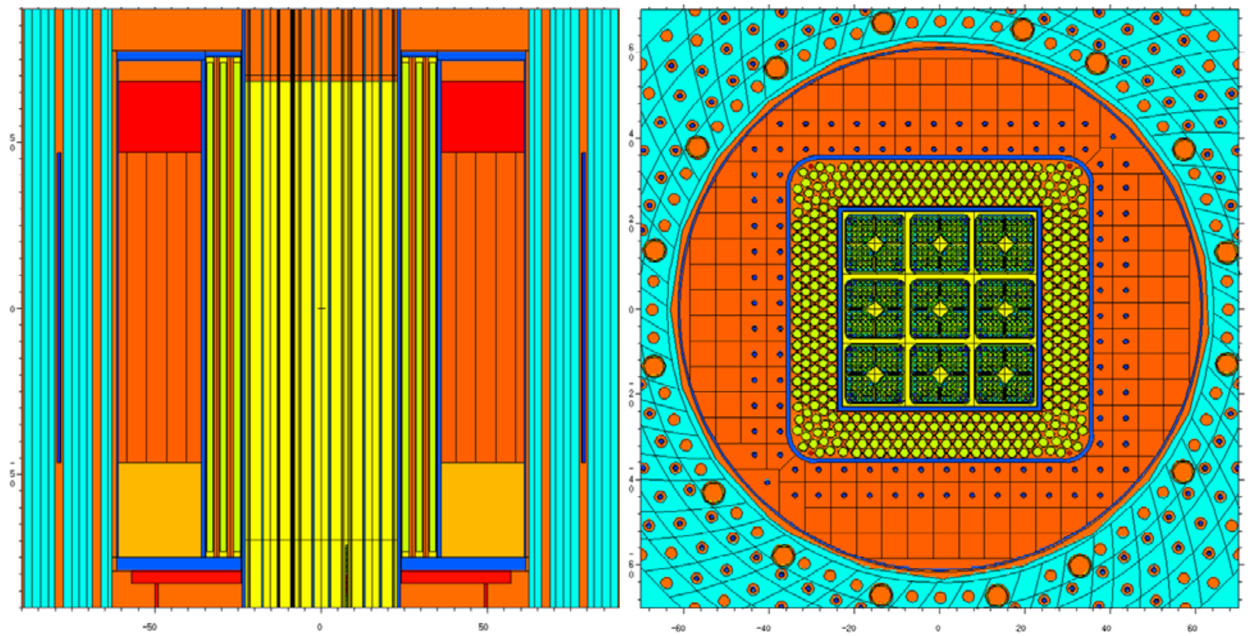

Figure 31 Axial and radial views of the 3D MCNPX model of LWR-PROTEUS. The pictures have been truncated to enhance the level of detail in the most relevant regions.

The definition of 12 segments per face (48 segments along the test-zone perimeter) was selected for compatibility with the PRESTO-2 input modality. In it, the albedo matrices, through which the PCRs are given as input, are defined for two geometric types, sides and corners, as shown in Figure 30. Thus, at each axial level, two PCR matrices can be defined: a corner matrix, representing the 8 boundary segments coloured in blue, and a side matrix, coloured in red, which comprises the remaining 40 segments. Unfortunately, PRESTO-2 does not allow the specification of particular PCR values for each corner or side, which leads to a loss of azimuthal information. This is not important for power reactor cores but may be of significance in the case of LWR-PROTEUS, especially in cases showing a strong azimuthal asymmetry such as Configuration I-2A, which will be discussed in Chapter 5.

Concerning SIMULATE-5, the standard version of the programme (which the software producer Studsvik Scandpower kindly supplied specifically for use in this thesis) allows the input of side and corner PCRs, but for one axial level only. Kindly responding to the author's request, Studsvik Scandpower created a special version of the programme with the capability of accepting the input of axially varying PCR matrices for the radial direction[20]. Although this option only allows for the definition of a single PCR per axial level (separate side and corner matrices can only be specified if the standard whole-core-length input is used), it is essential for the modelling of LWR-PROTEUS.

Regarding energy, the tallies were subdivided in five bins, as shown in Table 7. This was done for two reasons: first, to study the spectral behaviour of the PCRs, and second, to define five-group PCRs for the multigroup nodal diffusion calculation with SIMULATE-5. For use in PRESTO-2 (and also for certain SIMULATE-5 cases), the currents were collapsed to two groups, as indicated in the table.

Table 7 Energy group structure used for the PCRs

5 groups	2 groups cut-off 1.84	2 groups cut-off 0.625	Upper limit [eV]
1	1	1	20×10^6
2			0.82085×10^6
3			9.1188×10^3
4	2		1.84
5		2	0.625

In MCNPX, the in- and out-currents were tallied for all axial levels (10), all peripheral segments (48), and all energy groups (5), from which the detailed PCRs could be calculated. Thus, 480 current (F1) tallies were used to calculate the partial currents at the test-zone boundary. For this purpose, two cosine bins (-1 to 0 and 0 to 1) were used at each surface, to integrate the incoming and outgoing currents.

The tallies were then summed over corners and sides, as shown in Figure 30, to yield two incoming and two outgoing currents per axial level (only one in the case of SIMULATE-5). Finally, the components of the PCR diagonal matrices were calculated according to {42}.

$$PCR_{gg} = \frac{j_g^-}{j_g^+}\ for\ g = 1, \ldots, G\ with\ G = 2\ or\ 5 \qquad \{42\}$$

We recall here that PCR_{gg} does not represent a diagonal albedo in the classical sense, as is the case for a power reactor where a non-multiplicative, diffusive medium surrounds the reactor core. In the case of LWR-PROTEUS, the PCRs describe the coupling between the test zone and the driver and buffer regions, which are multiplicative too. Thus, the PCRs, since they depend on the test zone configuration and the fuel loading in the outer regions, are, as mentioned earlier, only valid for the particular case for which they have been calculated.

---

[20] Studsvik Scandpower's support, in particular from Dr. Sten-Örjan Lindahl, is gratefully acknowledged.

3.6.2 Configuration dependent PCRs - 2D whole-reactor HELIOS model

As an alternative method to calculate the PCRs at the LWR-PROTEUS test-zone boundary, a 2D whole-reactor calculation can be performed using a deterministic lattice code with flexible geometry capabilities, such as HELIOS. From this calculation, the partial currents needed to determine the PCRs can be obtained with the desired space and energy discretisation. A partial view of the HELIOS whole-reactor model is shown in Figure 32, in which the outer regions of the graphite reflector have been cut off to allow a better resolution of the inner parts of the reactor.

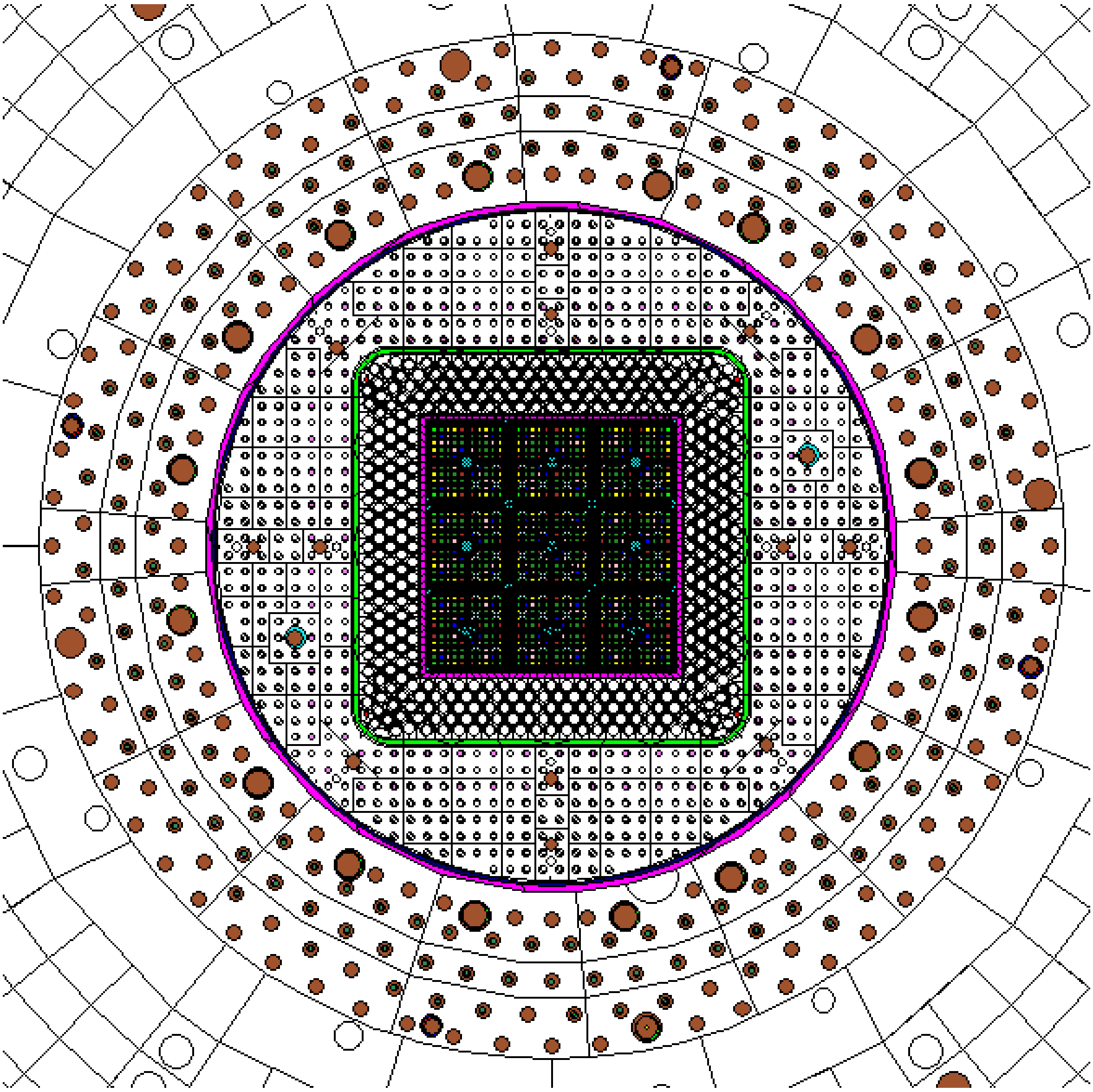

Figure 32 Partial view of the LWR-PROTEUS reactor in Configuration I-1A, as modelled with HELIOS.

The HELIOS whole-reactor model has been developed for the LWR-PROTEUS project by Studsvik Scandpower in collaboration with PSI. In this thesis, this model was taken over, having been slightly modified to deliver the required PCRs. This was done with the sole purpose of assessing the applicability of 2D PCRs to describe the test-zone boundary in LWR-PROTEUS, instead of the 3D PCRs provided by MCNPX.

To determine the partial currents j_g^- and j_g^+ across the test-zone boundary, the coupling between the outer surface of the test tank and the buffer (see Figure 14 and Figure 32), must be done by currents. In the case of the HELIOS calculations performed in this thesis, the current coupling order used was *k=4* (see Figure 9 in Subsection 2.4.1 for a description of the current coupling order in the CCCP method of HELIOS). The test-zone boundary was subdivided appropriately, to allow the determination of the side and corner PCRs for PRESTO-2 as depicted in Figure 30.

Results of the PCR calculations performed with HELIOS are presented and discussed, for Configurations I-1A and I-2A, in Chapters 4 and 5, respectively.

3.6.3 Calculation of pin map correction factors (PMCFs) with HELIOS

The spatial and energetic discretisation of the PCRs calculated with MCNPX (48 segments over the test-zone perimeter and 5 energy groups, respectively) was intentionally introduced to capture the effect of the non-uniformity (space) and the spectrum (energy) of the test-zone partial currents on the total-fission rate distribution of the central assembly. However, as discussed before, the albedo input in PRESTO-2 does not allow for the same level of spatial and energetic detail. Thus, in order to study the effect of the variation of the PCRs over the test-zone perimeter, as also of the number of energy groups used in their definition, so-called pin map correction factors (PMCFs) have been determined on the basis of 2D HELIOS calculations comprising the whole test zone (3x3 array of fuel assemblies). In this model, albedo conditions (instead of reflected) were imposed on the system boundary (test-zone inner walls). These albedos correspond to the PCRs calculated using the 3D MCNPX model described in Subsection 3.6.1, and were utilized to determine the PMCFs by means of two different HELIOS calculations. The first calculation (48/05) describes the test-zone boundary using 5-group PCRs in 12 segments per face, as calculated with MCNPX. The second calculation (02/02) uses the condensed (2 groups) and spatially averaged (one value for the four faces and one value for the four out-corners) PCRs that are used in PRESTO-2. The pin map correction factors (PMCFs) are then defined as:

$$(n/m)PMCF = \frac{HELIOS\ Fission\ Rate\ (n/m)}{HELIOS\ Fission\ Rate\ (02/02)} \qquad \{43\}$$

where the notation *(n/m)* symbolises the number of subdivisions along the test zone perimeter *(n)* and the number of energy groups *(m)*. Thus, for the case mentioned above, *n=48* and *m=05*. The procedure is repeated at each axial level corresponding to the core nodalisation.

To provide complementary information, a third HELIOS calculation, using spatially averaged PCRs in 5 groups (02/05), has been used to separate the effects of energy condensation and spatial averaging of the PCRs on the pin-wise fission rate distribution. The HELIOS model employed is depicted in Figure 33. The outer boundary of the system, on which the PCRs are calculated, corresponds to the inner walls of the test tank, in agreement with the PRESTO-2 representation of the test zone.

Finally, the PMCFs are applied to the pin-power maps obtained with PRESTO-2 {44}, the results being affected, in some cases significantly, by the variation of the PCRs and their spectra along the test-zone periphery.

$$P2(n/m)PinPow = P2(02/02)PinPow \cdot (n/m)PMCF \qquad \{44\}$$

The impact of the PMCFs has been investigated for the axially uniform configurations, i.e. Configurations I-1A and I-2A. The correction was found to be especially important in the controlled case (Configuration I-2A), which will be discussed in Chapter 5. In this configuration, the azimuthal asymmetries observed in the PCRs have a significant impact on the pin total-fission rates, even for the central fuel assembly, where the measurements were done. On the other hand, for configurations with no significant azimuthal asymmetry, the PMCFs do not play an important role. In Chapter 4, this expected behaviour is numerically demonstrated for Configuration I-1A.

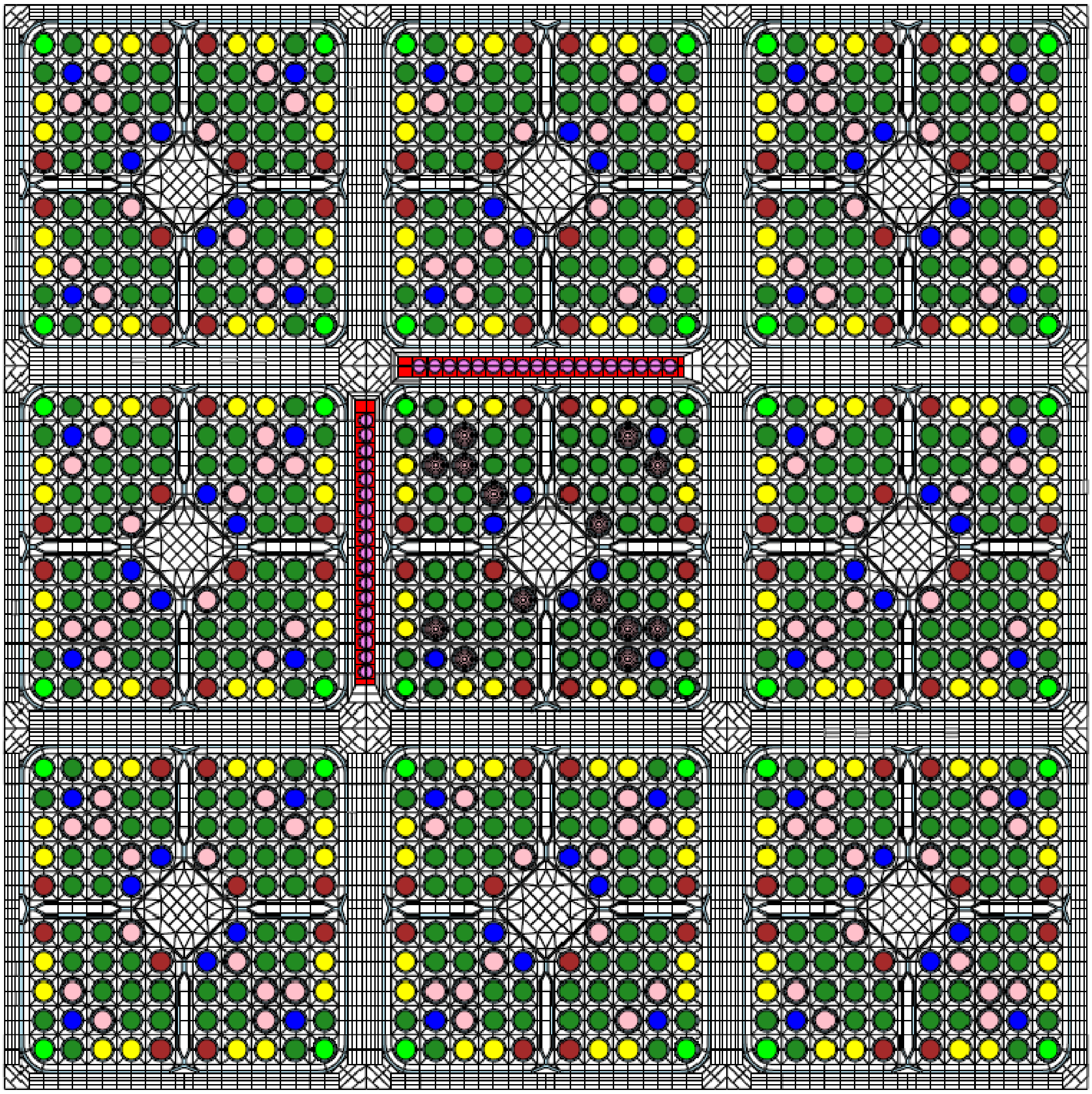

Figure 33 HELIOS model of the test zone, used for the determination of the PMCFs (pin map correction factors). The picture shows the controlled case (Configuration I-2A). The same model, with the control blades removed, was used for Configuration I-1A. For these 3x3 transport calculations, the Gd pins in the peripheral assemblies were modelled with two concentric rings instead of five, which reduces the execution time without noticeably affecting the results.

Chapter 4

Uniform case - Configuration I-1A

In 1941, it was suggested that the controlled fission of uranium could be used to provide energy in the form of heat for use in machines.

This chapter presents the modelling details and results of the comparisons with experiment performed for LWR-PROTEUS Configuration I-1A, in which the test zone is constituted by the regular 3x3 configuration corresponding to the lower axial zone of the SVEA-96+ assemblies.

Section 4.1 describes the experimental set-up, while the particularities of the lattice modelling with HELIOS are presented in Section 4.2. In Section 4.3, the representation of the test-zone boundary by means of partial currents obtained from 3D MCNPX whole-reactor calculations is addressed. The alternative method for determining the test-zone boundary PCRs, based on 2D HELIOS whole-reactor modelling, is described in Section 4.4. Section 4.5 presents the results of the radial comparisons of total-fission rates using HELIOS/PRESTO-2. The modelling and the results of the total-fission comparisons using CASMO-5/SIMULATE-5 are presented in Sections 4.6 and 4.7, respectively. Section 4.8 shows the verification of the axial flux profile in the test zone, while a discussion about the k-effective values obtained in the different calculations presented in this chapter is given in Section 4.9. Finally, the main messages from the chapter are summarized in Section 4.10.

4.1 Description of the test zone

In order to investigate the performance of any given computational methodology, it is always useful to first apply it to simple cases which may be used as a reference. Excluding the purely academic case of a homogeneous parallelepipedal reactor with albedo boundary conditions, which can be solved analytically, a regular array of reflected fuel assemblies constitutes the next simplest case one may consider. If this array extends to infinity, then the flux shows no global curvature and the fine-structure flux is identical to that obtained in a reflected single-assembly 2D calculation. Note that in the case of an infinite array of fuel elements of finite height, the impact of the axial leakage on the cross-section condensation can be accounted for by adding an external buckling [11]. In the real case of a finite reactor, the radial leakage imposes a global curvature to the flux. Thus, the real flux can be considered to be the combination of two components: the homogeneous or asymptotic flux, which has a smooth character and carries the leakage-related information, and the fine-structure flux or micro-flux, which represents the strong local variations. The superposition of these two components delivers the real, heterogeneous flux. As discussed in Chapter 2 (Section 2.3), nodal methodologies with pin-power reconstruction make use of this separation.

From the point of view of the global or asymptotic flux, a 3x3 array of identical fuel assemblies would resemble the case of a homogeneous parallelepipedal reactor. Strictly seen, this is only true if the lattice is symmetrical along both diagonals, which for the SVEA-96+

assemblies used in the LWR-PROTEUS Phase I experiments is not the case (see, for example, Figure 21 in Chapter 3). However, the above mentioned array represents the closest one can get to a "uniform" system, with no radial or axial heterogeneities. The characterisation of such a system is the main purpose of Configuration I-1A.

In this configuration, the test tank is filled with light water at room temperature (23°C), the nine SVEA-96+ fuel assemblies being rotated according to the orientation they would have in a power reactor core. The orientation of the fuel assemblies and the relative positions of the fuel pins are shown in Figure 34, where the colours that fill the fuel pins represent different enrichments. The pins containing gadolinium can be identified by the additional rings inside the pin volumes. The nominal pitch of the assemblies in the test tank is 15.24 cm, equal to the assembly pitch in the KKL core. KKL is a General Electric BWR-6 plant, the core having a S-type arrangement (the wide and narrow gaps have the same nominal size)[21]. In this core geometry, the fuel elements are arranged in a uniform pattern, the distances between fuel assemblies being equal in both directions throughout the core. The external size of the fuel box being 13.86 cm, this defines a nominal distance between fuel boxes equal to 1.38 cm, i.e. the half-gap size is 0.69 cm.

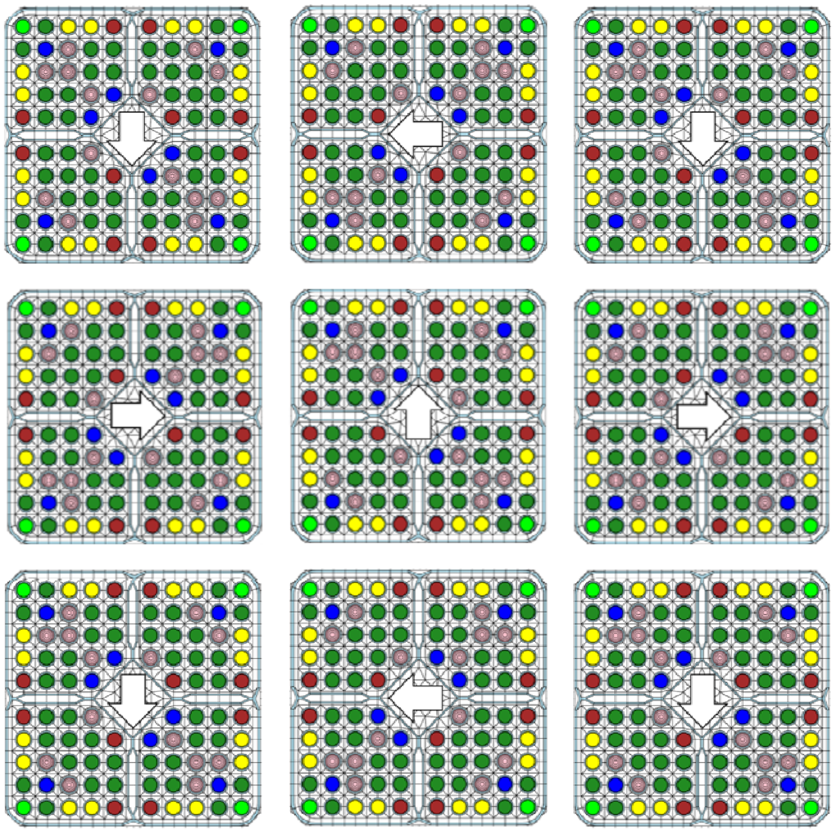

Figure 34 Arrangement of fuel assemblies in the test zone of Configuration I-1A. BWR fuel assemblies are always symmetric with respect to the NW-SE diagonal, the NW corner being coincident with the centre of the control blade cell. In LWR-PROTEUS, the central assembly has a zero-degree rotation, the peripheral assemblies being rotated as shown through the arrows in the central canals. Note that due to the lattice symmetry, this arrangement corresponds to the case of reflected symmetry along the inter-assembly gap midlines.

---

[21] The General Electric lattice types are: D lattice: BWR/2-4 plants, S lattice: BWR/6 plants (KKL), and C lattice: BWR/4-5 plants. The S and C lattices are symmetric, while D is asymmetric (larger control blade side gaps).

Thus, the test tank in LWR-PROTEUS is designed to accommodate a 3x3 array of elements with a cross-section of 15.24 x 15.24 cm. This nominal geometry was depicted earlier in Figure 20, in connection with the lattice description made in Subsection 3.2.1.

As mentioned before (see Subsections 3.2.1 and 3.3.1), it was not possibly to place the fuel assemblies in the exact nominal positions. Instead, after the fuel elements have been fixed in the test-tank, the resulting inter-assembly distances were measured in order to provide a best-estimate description of the geometry. Furthermore, the sub-assemblies (pin clusters that occupy each quadrant of the fuel assembly) were pressed, in x and y directions, 0.051 cm towards the central water canal. This pressing was intentionally introduced in order to simulate the displacement of the sub-assemblies that, according to the fuel manufacturer, occurs in a power reactor due to the forces imposed by the coolant flow. The experimental inter-assembly distances and the cladding-to-box distance (0.38 cm), corresponding to Configuration I-1A, are shown in Figure 35.

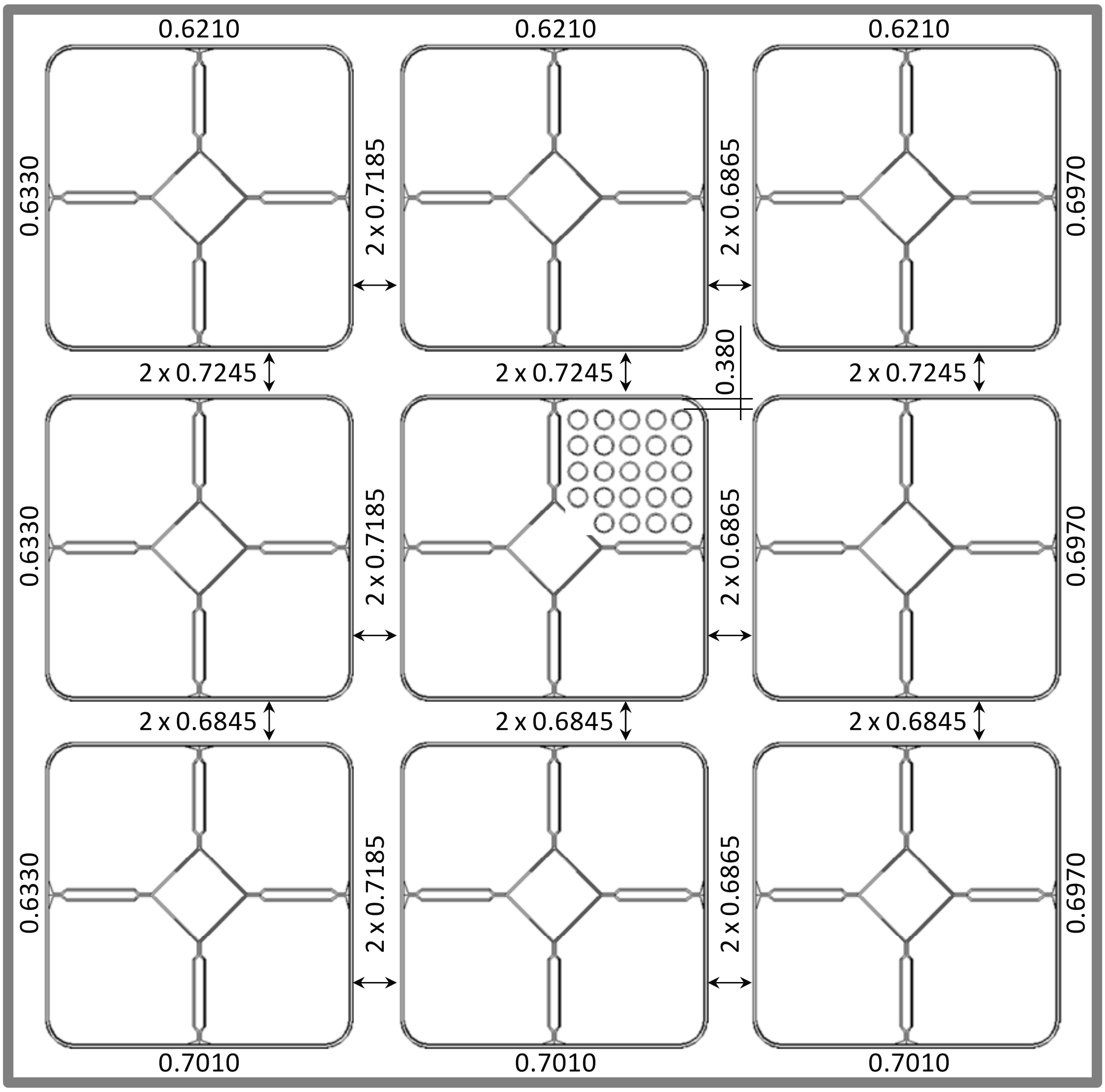

Figure 35 Measured dimensions in Configuration I-1A. The distance between the outer surface of the cladding of the peripheral pins and the inner wall of the fuel box is 0.380 cm (sub-assembly pressed 0.051 cm towards the central canal).

4.2 Lattice calculations - HELIOS modelling

Lattice data were obtained from HELIOS calculations following the same general methodology applied for production calculations at KKL. As discussed in Section 3.2, three exceptions were made in order to describe specific features of the LWR-PROTEUS experiments: 1) the suppression of the gamma-absorption effect on the pin powers, 2) the calculation of pin total-fission rates instead of pin powers and 3) the use of measured inter-assembly gaps. The two first exceptions are common to all the LWR-PROTEUS configurations and have been consistently applied to the HELIOS calculations performed in this thesis. The measured gaps, on the other hand, depend on the configuration being analysed.

Thus, nine lattices were calculated for Configuration I-1A, each with its corresponding measured gaps, as shown in Figure 35. These nine sets of lattice data (cross-sections, discontinuity factors and pin-power maps) were stored in a XSDB, which together with the PCRs describing the test-zone surroundings, discussed in Section 4.3, have formed the basis for the PRESTO-2 core calculations for Configuration I-1A.

Taking advantage of the axial uniformity of Configuration I-1A, which can be described by a single set of cross-sections for the complete test-zone length, several parameters in the lattice calculation were varied to study the sensitivity of the total-fission rates to changes in the lattice modelling. As a complement, also the changes in the system multiplication factor k-effective were analysed. Further, to investigate the impact of these changes on cases with strong radial heterogeneities, the same was done for Configuration I-2A, which will be discussed in Chapter 5.

The relevant characteristics of the basic lattice calculation, the reference case, are depicted in Subsection 4.2.1. The changes introduced to define each sensitivity case are described in Subsection 4.2.2.

4.2.1 The reference case

The reference case features the standard modelling options used at KKL and serves as basis for the analysis of the sensitivity of the reconstructed pin-power results to changes in the lattice parameters and modelling options. In the reference case, the reflected assembly calculations are characterised by:

1) Use of the standard HELIOS cross-section library [29]. This library is based on ENDF/B-VI.1, with some data from revisions VI.3 and VI.8. It includes an adjustment to the resonance integral (RI) of ^{238}U that leads to a reduction of 3.4% in its resonance capture. This adjustment is introduced to compensate a bias observed in the comparisons against the 101 critical experiments of Strawbridge and Barry [34]. The library contains 47 neutron energy groups and is the standard HELIOS library for production calculations at KKL.
2) Condensation spectrum: HELIOS solves the transport problem in the group structure of the cross-section library (i.e. 47 groups). The data needed for the 3D nodal calculation is subsequently obtained by homogenisation of the whole reflected system and condensation into two energy groups. The condensation process is performed using the critical spectrum calculated with the B1-method [29], instead of the zero-leakage spectrum of the reflected case. This accounts for the fact that the calculated reflected lattice is in reality part of a critical system.

3) Current coupling: in HELIOS, the transport problem is solved using the CCCP (Current Coupling Collision Probabilities) method [29]. The space elements, which are calculated with collision and transmission probabilities, are coupled by currents across their boundaries. These currents are discretised in the azimuthal and polar directions in a variable number of angular sectors (see Figure 9). The recommended discretisation for normal LWR calculations is in terms of four azimuthal and one polar sector. This is called coupling order k=4 in HELIOS terminology.
4) The fuel pins are subdivided into 2 rings (uranium pins) and 5 rings (pins containing gadolinium). With *rf* being the radius of the fuel pellet, the sizes of the rings are, in fractions of *rf*, 0.9 and 1.0 (uranium), and 0.3, 0.55, 0.75, 0.9 and 1.0 (gadolinium). The rings define the flat-flux regions for the collision probability calculation.
5) The boundary between the thermal and fast groups is set to 1.84 eV. This is the value used in the standard HELIOS/PRESTO-2 model at the Leibstadt NPP.

4.2.2 The sensitivity cases

To evaluate the impact on k-effective and the pin-wise fission rate distribution, sensitivity cases were run modifying selected parameters in the 2D lattice calculation, while keeping all the others unchanged. These cases are:

1) A 190-group library without adjustment to the ^{238}U resonance integral was used. This library is based on the same ENDF/B-VI data as the 47-group library used in the reference case. This sensitivity case aims at showing the impact of the group structure and the RI adjustment used in the reference case.
2) The infinite medium spectrum (B^2=0) was used for condensation. This is the spectrum obtained from the transport solution of the reflected case, i.e. with no leakage. In principle, the use of the infinite medium spectrum for the condensation of cross-sections is not adequate since it ignores the leakage that renders the system critical. The aim of this sensitivity case is to show the impact of the condensation spectrum on the homogenised 2-group cross-sections, pin total-fission maps and discontinuity factors used in PRESTO-2.
3) The use of current coupling between space elements was suppressed (coupling order k=0), leading to a system defined by a single space element throughout, to which collision probabilities are applied. This eliminates the angular redistribution inherent to coupling with interface currents, and represents the highest accuracy obtainable with a particular spatial mesh and energy discretisation. The large amount of computer resources needed renders this option impractical for production applications.
4) The number of subdivisions (rings) in the fuel pins was increased to 5 (uranium pins) and 9 (gadolinium pins). The radii correspond to regions of equal volume, the respective fractions of *rf* are: 0.45, 0.63, 0.77, 0.89 and 1.0 (uranium) and 0.33, 0.47, 0.58, 0.67, 0.75, 0.82, 0.88, 0.94 and 1.0 (gadolinium).
5) A thermal cut-off of 0.625 eV was used for the nodal calculations.

4.3 Test-zone boundary conditions using the 3D MCNPX model

PCRs representing the test-zone surroundings were calculated using a 3D MCNPX model of LWR-PROTEUS for Configuration I-1A, following the methodology described in Subsection 3.6.1.

An example of the tally discretisation is given in Figure 36, which shows the partial currents and corresponding PCRs at the 5th axial level (node layer immediately below the core midplane) in energy group 2 (between 9.12 keV and 0.82 MeV, Table 7). The large PCR values occurring in this energy group are due to the strong fast current entering the test zone (see also Subsection 4.3.4). The MCNPX calculations were performed using 200'000 particles and 250 cycles, i.e. 50x10^6 histories.

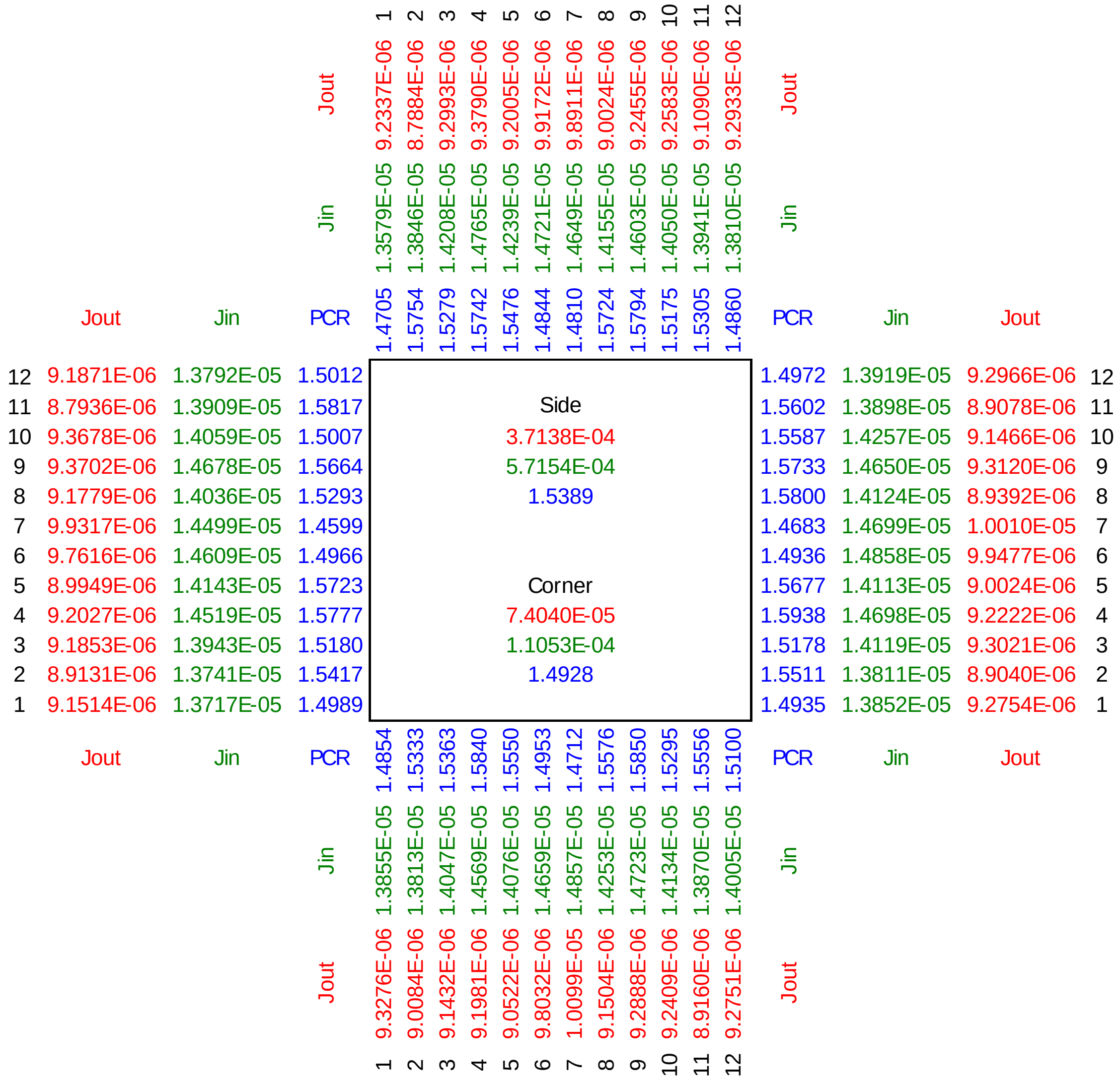

Figure 36 Example of partial currents entering and leaving the test zone (green and red colour, respectively) and PCRs (blue) for Configuration I-1A, at axial level 5 in energy group 2 (9.12 keV to 0.82 MeV). The picture shows the spatial detail used for the MCNPX tallies. The side and corner values, as depicted in Figure 30, are shown inside the square representing the test-zone perimeter. These are calculated by integrating the partial currents over the corresponding segments.

Corresponding to the above scheme, the PCRs were evaluated for the 10 axial levels of the test zone (see Figure 29), in the 2 and 5 energy group structures described in Table 7.

4.3.1 PCRs for PRESTO-2

For the calculation of the radial PCRs needed for PRESTO-2, the partial currents were first integrated along the test-zone sides and corners, as depicted in Figure 30. The PCRs were then calculated as the ratio of the integrated currents. The results corresponding to the 5th axial level and 2nd energy group are shown inside the square representing the test-zone perimeter in Figure 36. Furthermore, for the PRESTO-2 application, the PCRs were collapsed to two energy groups. The collapsing was done by integrating the currents over each macro-group and then taking the ratio j_g^-/j_g^+. The same procedure was used for the calculation of the axial PCRs at the top and bottom core boundaries. In this case, the partial currents were tallied over the $(45.72\ \mathrm{cm})^2$ horizontal planes located at ±61.5 cm from the core midplane (see Figure 29).

The PCRs for PRESTO-2 in Configuration I-1A, for 1.84 eV thermal cut-off energy, are shown in Table 8, the approximate 1σ statistical (relative) errors in % being indicated in brackets[22].

Table 8 PCRs for PRESTO-2 in Configuration I-1A, derived from the partial currents obtained in the 3D whole-reactor MCNPX calculation. The figures in brackets are the approximate 1σ statistical (relative) errors in %. As in the case of production applications at KKL, the HELIOS/PRESTO-2 calculations were performed using a thermal cut-off energy of 1.84 eV.

Configuration I-1A Upper limit (eV)	PCR_{11} $20\mathrm{x}10^6$		PCR_{22} 1.84	
Axial direction at top	0.770 (0.05)		0.937 (0.1)	
Radial direction 1σ error (%)	Side (0.05)	Corner (0.3)	Side (0.2)	Corner (1.0)
Axial level 10	0.985	1.025	0.387	0.421
Axial level 9	0.990	1.029	0.385	0.419
Axial level 8	0.995	1.036	0.383	0.415
Axial level 7	0.997	1.041	0.381	0.411
Axial level 6	0.994	1.040	0.380	0.410
Axial level 5	0.993	1.036	0.380	0.411
Axial level 4	0.994	1.037	0.381	0.411
Axial level 3	0.994	1.037	0.382	0.409
Axial level 2	0.990	1.035	0.383	0.408
Axial level 1	0.979	1.029	0.384	0.414
Axial direction at bottom	0.836 (0.05)		0.958 (0.1)	

4.3.2 PCRs for SIMULATE-5

Analogously to PRESTO-2, SIMULATE-5 allows the specification of albedo boundary conditions at the core boundary. As mentioned in Subsection 3.6.1, a special code version allowing the input of axial-level dependent PCRs for the sides was created by SSP for use in this

---

[22] The PCR relative errors are propagated from the 1σ statistical uncertainties of the MCNPX current tallies. Although these uncertainties are slightly dependent on the axial level, a common approximate value, representing all levels, has been defined to characterise the accuracy of the calculated PCRs.

thesis. Thus, integrating the partial currents over the complete test-zone perimeter at each axial level, the PCRs for SIMULATE-5 shown in Table 9 could be obtained. Aiming at the use of the multigroup nodal diffusion capability of SIMULATE-5, the PCRs are defined in five energy groups, in addition to the classical 2-group structure (in this case with a cut-off energy of 0.625 eV). The boundaries of the energy groups correspond to those of Table 7, Chapter 3.

Table 9 PCRs for SIMULATE-5 in Configuration I-1A, derived from the partial currents obtained in the 3D whole-reactor MCNPX calculation[23]. The PCRs are given in the five and two energy group structures shown in Table 7.

Configuration I-1A		5 energy groups					2 energy groups	
		PCR_{11}	PCR_{22}	PCR_{33}	PCR_{44}	PCR_{55}	PCR_{11}	PCR_{22}
Upper limit (eV)		$20\text{x}10^6$	$821\text{x}10^3$	9119	1.84	0.625	$20\text{x}10^6$	0.625
Axial dir. at top		0.676	0.824	0.875	0.866	0.915	0.788	0.915
Radial direction	Axial level 10	0.713	1.521	0.642	0.631	0.348	0.979	0.348
	Axial level 9	0.715	1.527	0.649	0.634	0.344	0.983	0.344
	Axial level 8	0.716	1.535	0.659	0.640	0.341	0.989	0.341
	Axial level 7	0.715	1.540	0.662	0.640	0.338	0.991	0.338
	Axial level 6	0.711	1.536	0.663	0.639	0.337	0.988	0.337
	Axial level 5	0.710	1.531	0.663	0.642	0.337	0.987	0.337
	Axial level 4	0.710	1.533	0.663	0.644	0.337	0.988	0.337
	Axial level 3	0.711	1.533	0.662	0.640	0.339	0.988	0.339
	Axial level 2	0.710	1.529	0.656	0.635	0.340	0.984	0.340
	Axial level 1	0.701	1.515	0.646	0.636	0.342	0.974	0.342
Axial dir. at bottom		0.783	0.864	0.901	0.903	0.947	0.848	0.947

4.3.3 Axial behaviour of the radial PCRs

In all nodal calculations of the LWR-PROTEUS test zone presented in this thesis, the axial dependence of the radial PCRs, calculated with the 3D MCNPX model, has been explicitly accounted for. However, as can be seen from Table 8 and Table 9, for axially uniform cases, such as Configuration I-1A, this axial dependence is relatively weak. This can also be observed in Figure 37, where the PCR values corresponding to Table 8 are presented graphically. Since in Configuration I-1A only the radial comparison of calculational and experimental results is of interest (all reaction rate measurements having been performed at the core midplane), the use of axially-uniform radial PCRs, obtained for example from 2D calculations by means of a HELIOS whole-reactor model, can also be justified. This alternative method will be discussed in Section 4.4, the corresponding results being presented in Subsection 4.5.3.

---

[23] The PCRs for SIMULATE-5 were obtained from a separate MCNPX calculation with 800x10^6 instead of 50x10^6 histories. As normally done in CASMO/SIMULATE production applications, the two-group SIMULATE-5 calculations were performed using a thermal cut-off energy of 0.625 eV.

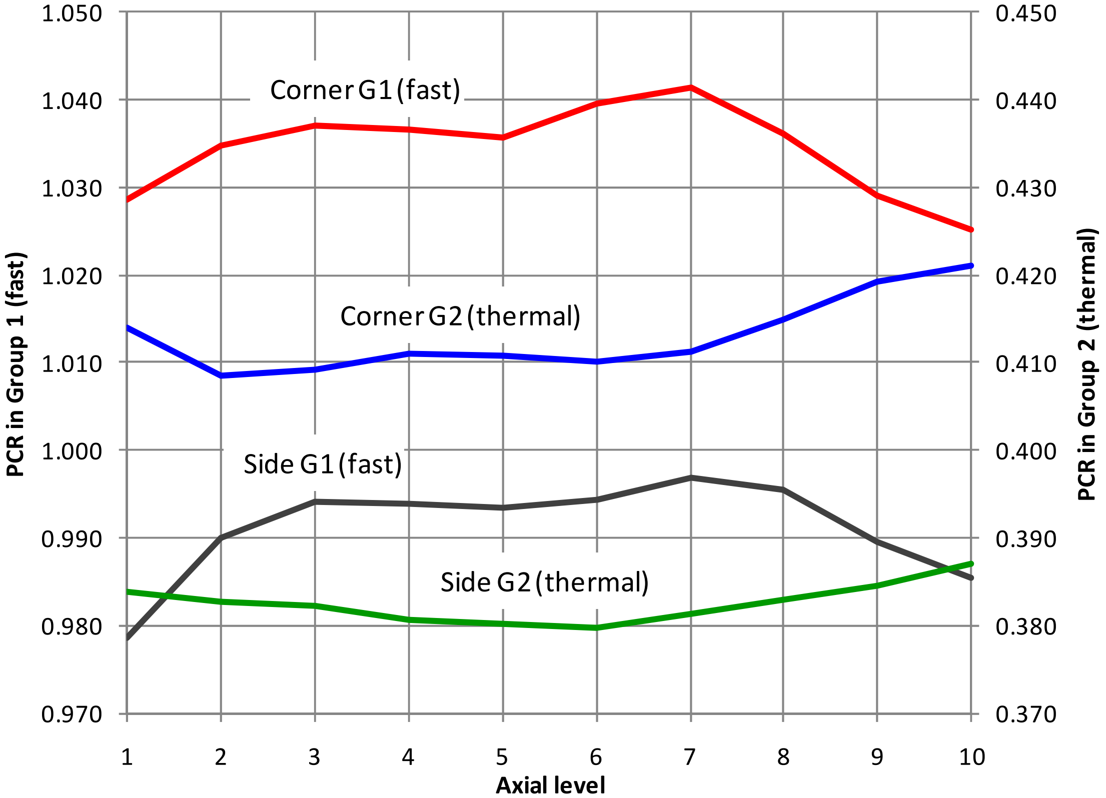

Figure 37 Axial variation of the radial PCRs in Configuration I-1A, as derived from the partial currents obtained in the 3D whole-reactor MCNPX calculation. The numerical values are shown in Table 8.

4.3.4 Energy dependence of the partial currents and PCRs

To illustrate the energy dependence of the partial currents crossing the test-zone boundary, Figure 38 shows the relative intensities of the incoming and outgoing currents in Configuration I-1A at axial level 5 (just below the core midplane) in five energy groups. The corresponding PCRs, calculated according to equation {42}, are included in the same figure. The upper boundaries of the five energy groups are shown in Table 7. For producing the figure, the partial currents calculated with the 3D MCNPX model were integrated over the complete test-zone boundary, i.e. by summing over all sides and corners, and over all axial levels.

It can be seen from Figure 38, that there is a strong current entering the test zone in group 2, i.e. between 9.12 keV and 0.82 MeV. This current is caused by fission neutrons undergoing inelastic scattering in the metallic uranium rods of the buffer zone. In this energy group, the PCR is significantly larger than one (see also Table 9) reflecting the role of the PROTEUS buffer as a source of fast neutrons for the test zone. At thermal energies, the relatively small magnitude of the currents with energies between 0.625 eV and 1.84 eV (group 4) suggests that the change in thermal cut-off energy should not have a strong impact on the description of the boundary conditions for the test zone.

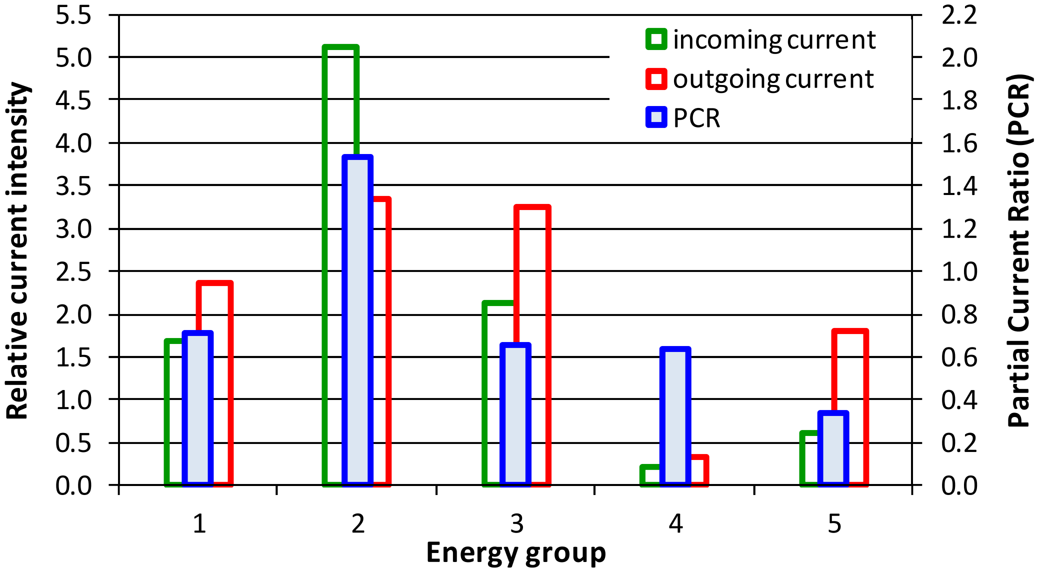

Figure 38 Energy dependence of the radial currents (arbitrary units) and PCRs in Configuration I-1A in five energy groups, derived from the partial currents obtained in the 3D whole-reactor MCNPX calculation. The partial currents were integrated over the complete test-zone boundary, i.e. by summing over all sides and corners, and over all axial levels.

4.4 Test-zone boundary conditions using the 2D HELIOS model

As mentioned in Subsection 4.3.3 the radial PCRs can also be determined via an alternative procedure, viz. by using the 2D HELIOS model of the whole LWR-PROTEUS reactor described in Subsection 3.6.2. This approach was applied in a previously published study on Configuration I-1C [9], in which two PCR-matrices were used to characterise the test-zone boundary for the upper and lower enrichment zones.

Although the results reported in [9] were quite promising, it will be shown in Chapter 6 that, for axially heterogeneous systems such as Configuration I-1C, the lack of axial dependence in the radial PCRs has a significant impact on the axial behaviour of the neutron flux. Thus, the use of PCRs obtained from 2D whole-reactor transport calculations does not appear to be quite adequate for representing the test-zone boundary in cases where the axial profile is of interest.

However, in the case of axially uniform configurations such as I-1A and I-2A (the latter being discussed in Chapter 5), the use of PCRs obtained from 2D reactor calculations can indeed be justified. In these cases, as mentioned, the measurements were made over the horizontal plane located at core mid-height, the axial curvature of the neutron flux being of no consequence for the radial behaviour of the total-fission rate. Moreover, as discussed in Subsection 4.3.3, the axial dependence of the radial PCRs calculated with the 3D MCNPX model is relatively weak, confirming the lack of importance of considering 3D effects.

The radial PCRs obtained with the 2D HELIOS full-reactor model are shown in Table 10. In the axial direction (top and bottom boundaries of the test zone), the MCNPX PCRs were retained.

It can be seen in Table 10 that the PCRs in the 2D HELIOS case are larger than those obtained with the 3D MCNPX model, the effect being more pronounced at epithermal energies.

The most significant difference between the MCNPX and HELIOS two-group PCRs occurs in the fast group, in which the PCRs calculated with HELIOS are 4% to 5% higher than those obtained with MCNPX. One important contribution to this difference is the axial leakage, which is properly accounted for in the 3D MCNPX calculation, while in the 2D HELIOS calculation all neutrons contribute to the partial current at the test-zone boundary, even those travelling almost parallel to the axial direction. This geometrical effect is depicted in Figure 39, where the blue and red arrows together represent the neutrons entering the test zone in the 2D representation, while the red arrows alone symbolise the 3D case. Since the axial leakage in the light water moderated test zone is smaller than in the surrounding buffer and drivers, the incoming current is overestimated in relation to the outgoing current, leading to an overestimation of the PCR.

In this context, it should be noted that, since the outer reactor regions in LWR-PROTEUS are neutronically more diffusive than the test zone, they have a higher axial leakage, which is not taken into account in the HELIOS transport calculation (2D). This applies to the buffer, and to the D_2O and graphite driver zones. For instance, the migration area in the buffer is approximately 2.5 times larger than in the test zone, while in the D_2O driver it is about 7 times larger [35]. One is recalling in this discussion a well known result of nuclear reactor theory, from which the migration area is related to the distance travelled by the neutrons, in a supposedly infinite medium, from their emission to their absorption. In classical notation, the migration area is given by:

$$M^2 = \tau + L^2 \qquad \{45\}$$

where τ is the neutron (Fermi) age and L the thermal diffusion length, given, in turn, by:

$$\tau = \frac{D_1}{\Sigma_r + \Sigma_{a1}} \qquad L^2 = \frac{D_2}{\Sigma_{a2}} \qquad \{46\}$$

In equation {46}, for the fast (1) and thermal (2) groups, D is the diffusion coefficient and Σ the macroscopic cross-section, while r and a mean removal and absorption, respectively. Thus, in equation {45}, $\sqrt{\tau}$ describes the distance travelled by neutrons until they reach thermal energies, while L represents their diffusion as thermal neutrons.

Finally, it can be mentioned that due to the less important axial leakage of the thermal neutrons, the thermal PCRs calculated in 3D with MCNPX and in 2D with HELIOS do not differ significantly.

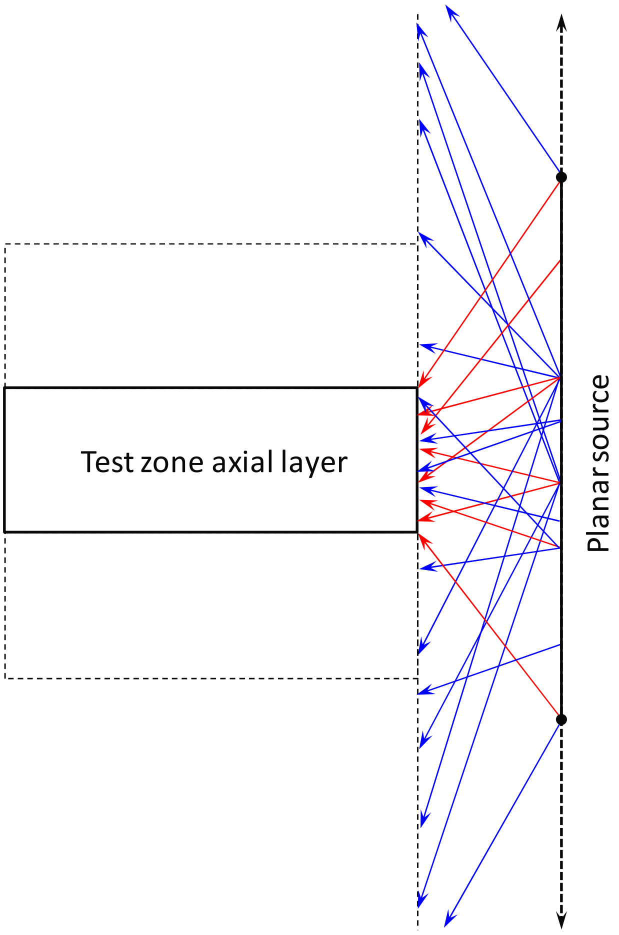

Figure 39 Schematic view of a planar neutron source placed outside the test zone. In the 2D representation, the source extends to ±∞ and all neutrons travelling to the left cross the side face of a particular test-zone layer, thus contributing to the partial current (blue and red arrows). In the 3D case, only the neutrons having directions that intersect the face under consideration contribute (red arrows only).

Table 10 Radial PCRs for PRESTO-2 in Configuration I-1A, derived from the partial currents obtained in the 2D whole-reactor HELIOS calculation. For comparison, the axially averaged PCRs, calculated by integrating over all axial levels the partial currents obtained with MCNPX, are shown in brackets. The last row shows the relative differences (HELIOS/MCNPX−1.0), expressed in %. The thermal cut-off energy is 1.84 eV.

	PCR_{11}		PCR_{22}	
Group upper limit (eV)	$20x10^6$		1.84	
	Side	Corner	Side	Corner
HELIOS PCRs in radial direction	1.038	1.058	0.386	0.421
Axially averaged MCNPX PCRs	(0.992)	(1.036)	(0.382)	(0.412)
HELIOS/MCNPX−1.0	4.6%	2.1%	1.0%	2.2%

4.5 Radial comparisons of total-fission rates - HELIOS/PRESTO-2

Due to the axially uniform character of Configuration I-1A, the experimental investigations were focused on the radial distribution of the pin-by-pin total-fission rate. The measurements were performed at the core midplane, in order to minimise the influence of the top and bottom core boundaries. In total, 61 pins were measured. The experimental values (E) were normalised to 1.0, as were the corresponding calculated values (C). The latter may be considered, as discussed below, either as axial averages (over the entire test-zone length), or as core-midplane results. Thus, each distribution was divided by its own average value according to:

$$\tilde{x}_i = x_i/\bar{x} \quad \text{with} \quad \bar{x} = n^{-1}\sum x_i \qquad \{47\}$$

where n=61 is the number of measured pins. The C/E values were then obtained as the ratio between the corresponding components of each distribution. It should be noted that, since both sets of total-fission rate values (calculated and measured) are normalized to 1.0, the average C/E ratio will slightly differ from 1.0.

In cases where the core is axially uniform, the normalised axial average and core-midplane values of the pin-wise fission rate distribution are almost equal. For instance, for Configuration I-1A, this ratio, as calculated with PRESTO-2, lies within the band 0.998 to 1.002 for the 96 fuel pins of the central assembly. In particular, within each node, all pins show similar axial profiles and the PRESTO-2 intra-nodal variable separation of the 3D heterogeneous flux, represented by equation {30}, is very accurate. In the case of MCNPX, the ratio as defined above varies over a somewhat wider range, viz. between 0.982 and 1.021. This is mainly due to the larger statistical fluctuation of the tally that covers the small pin segment centred at the core midplane (1.23 cm length), compared with the sum of the 100 tallies contained over the full pin length[24]. However, it must be mentioned that small physical differences do occur in the axial flux curvature of different fuel pins along the core height. The pin-by-pin comparisons between the normalised axial averages and the normalised core midplane values of the pin-wise fission rates calculated with PRESTO-2 and MCNPX are shown in Figure 40.

---

[24] In the MCNPX calculations, the 100 tallies per fuel rod used to determine the 3D total-fission distribution have a 1σ statistical uncertainty of ca. 0.8%, that of the axially averaged value being then 0.8/100^0.5=0.08%.

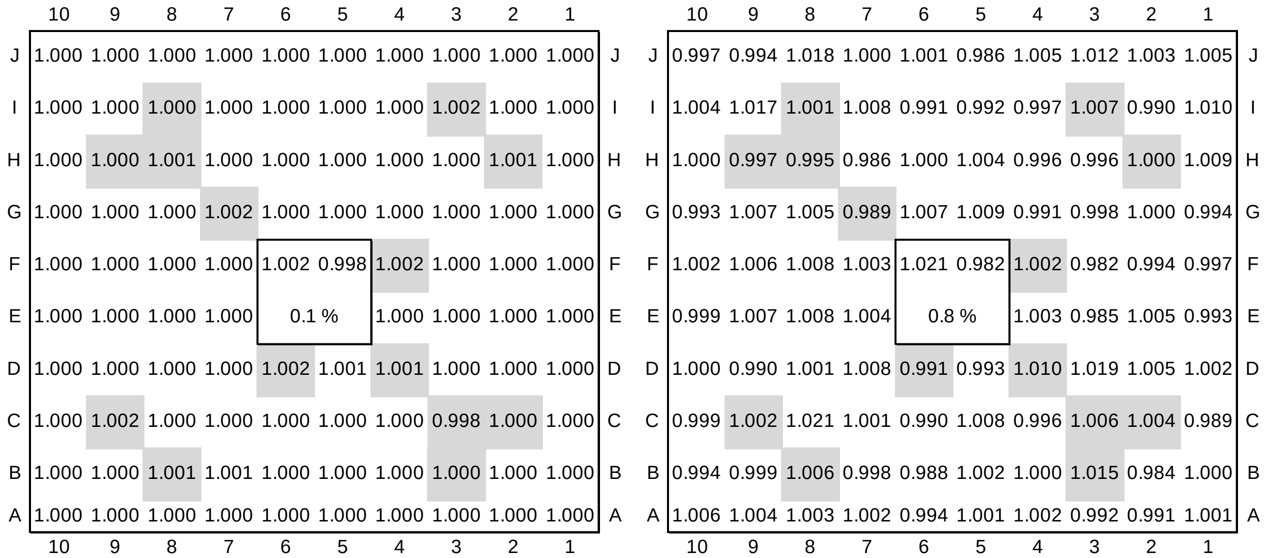

	10	9	8	7	6	5	4	3	2	1	
J	1.000	1.000	1.000	1.000	1.000	1.000	1.000	1.000	1.000	1.000	J
I	1.000	1.000	1.000	1.000	1.000	1.000	1.000	1.002	1.000	1.000	I
H	1.000	1.000	1.001	1.000	1.000	1.000	1.000	1.000	1.001	1.000	H
G	1.000	1.000	1.000	1.002	1.000	1.000	1.000	1.000	1.000	1.000	G
F	1.000	1.000	1.000	1.000	1.002	0.998	1.002	1.000	1.000	1.000	F
E	1.000	1.000	1.000	1.000	0.1 %		1.000	1.000	1.000	1.000	E
D	1.000	1.000	1.000	1.000	1.002	1.001	1.001	1.000	1.000	1.000	D
C	1.000	1.002	1.000	1.000	1.000	1.000	1.000	0.998	1.000	1.000	C
B	1.000	1.000	1.001	1.001	1.000	1.000	1.000	1.000	1.000	1.000	B
A	1.000	1.000	1.000	1.000	1.000	1.000	1.000	1.000	1.000	1.000	A
	10	9	8	7	6	5	4	3	2	1	

	10	9	8	7	6	5	4	3	2	1	
J	0.997	0.994	1.018	1.000	1.001	0.986	1.005	1.012	1.003	1.005	J
I	1.004	1.017	1.001	1.008	0.991	0.992	0.997	1.007	0.990	1.010	I
H	1.000	0.997	0.995	0.986	1.000	1.004	0.996	0.996	1.000	1.009	H
G	0.993	1.007	1.005	0.989	1.007	1.009	0.991	0.998	1.000	0.994	G
F	1.002	1.006	1.008	1.003	1.021	0.982	1.002	0.982	0.994	0.997	F
E	0.999	1.007	1.008	1.004	0.8 %		1.003	0.985	1.005	0.993	E
D	1.000	0.990	1.001	1.008	0.991	0.993	1.010	1.019	1.005	1.002	D
C	0.999	1.002	1.021	1.001	0.990	1.008	0.996	1.006	1.004	0.989	C
B	0.994	0.999	1.006	0.998	0.988	1.002	1.000	1.015	0.984	1.000	B
A	1.006	1.004	1.003	1.002	0.994	1.001	1.002	0.992	0.991	1.001	A
	10	9	8	7	6	5	4	3	2	1	

Figure 40 Ratio of the axially averaged and core-midplane values of the pin-by-pin total-fission rate distributions in Configuration I-1A, corresponding to PRESTO-2 (left) and MCNPX (right). In the place occupied by the central water hole, the maximum, minimum and standard deviation of the corresponding distribution are shown[25]. It can be seen that in the deterministic case (PRESTO-2) both distributions are practically identical, which indicates that the axial profile is the same for all pins (the separation of the z variable is in this case almost exact). In the stochastic calculation (MCNPX), a larger dispersion (within ~ ±2%) occurs. This is mainly due to the statistical fluctuations in the small tally volumes at core midplane.

The percental statistical uncertainties of the experimental values lay between 1.1% and 0.4%. For the calculation/experiment comparisons, no error band is assigned to the PRESTO-2 results. This means, the uncertainties corresponding to the input data used in the deterministic nodal calculation (e.g. dimensions, compositions, temperatures, etc.) are not accounted for. Hence, the C/Es reflect the ratio between the most probable values of the calculated and measured total-fission rates, with an absolute error band resulting from the propagation of the experimental percental relative error ε_E of each measured pin. Thus, for each pin, the absolute error band of the C/E ratio is given by:

$$e_{\left(\tilde{C}/_{\tilde{E}}\right)} = 0.01 \cdot \varepsilon_E \cdot \tilde{C}/\tilde{E} \tag{48}$$

As already mentioned, the calculations were performed preserving the modelling features used in the production applications at KKL. A reference case, described in Subsection 4.2.1, was set up to determine the agreement of the production model with the LWR-PROTEUS experimental data. In addition, the reference case serves as a comparison basis for several sensitivity studies, described in Subsection 4.2.2. These have been carried out with the purpose of quantifying the impact of changes in the lattice modelling on the local total-fission rate. Furthermore, the sensitivity of the results to certain changes in the description of the test-zone boundary has been analysed (Subsection 4.5.3), as has also the impact of the pin coordinates in PRESTO-2 (Subsection 4.5.4), the inter-assembly gap size (Subsection 4.5.5) and the sub-assembly pressing (Subsection 4.5.6).

---

[25] This convention has been used in figures of this type throughout the thesis.

4.5.1 The reference case - PRESTO-2 and MCNPX C/E results

Figure 41 shows the calculation-to-experiment ratio (C/E), corresponding to the PRESTO-2 and MCNPX results obtained for the reference case in Configuration I-1A. The results of both calculations correspond to the axial average over the core axial length. As discussed above, this is equivalent to considering the core midplane values in PRESTO-2. In the case of MCNPX, on the other hand, it gives a smoother radial distribution. The numbers indicated under each C/E value represent the absolute error band, according to {48}, expressed in permille.

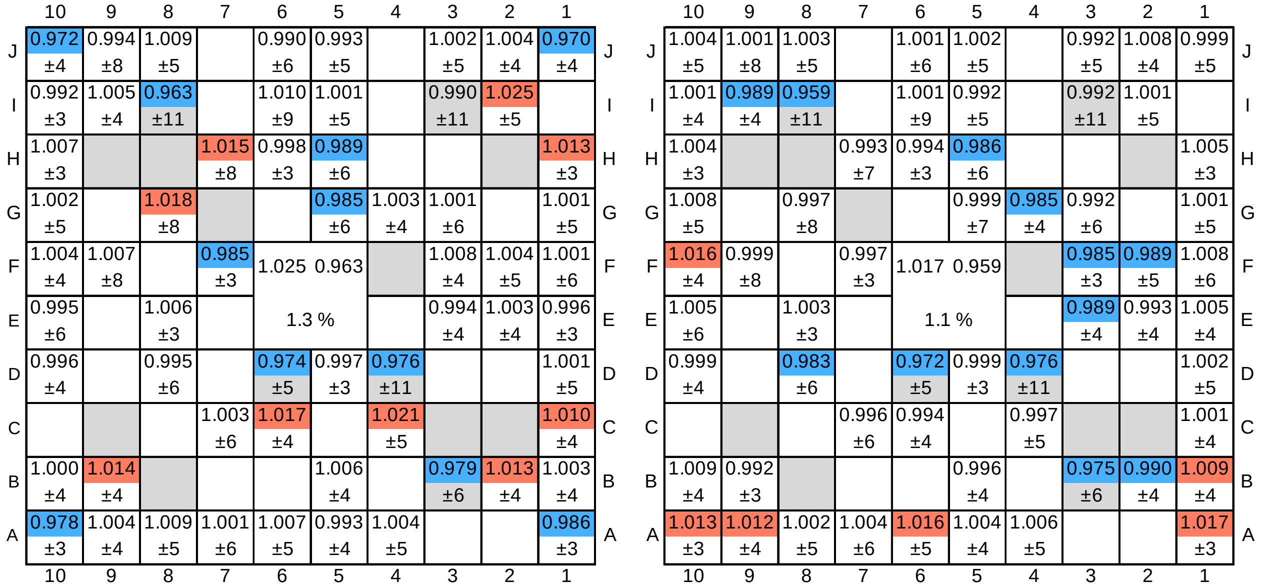

	10	9	8	7	6	5	4	3	2	1
J	0.972 ±4	0.994 ±8	1.009 ±5		0.990 ±6	0.993 ±5		1.002 ±5	1.004 ±4	0.970 ±4
I	0.992 ±3	1.005 ±4	0.963 ±11		1.010 ±9	1.001 ±5		0.990 ±11	1.025 ±5	
H	1.007 ±3			1.015 ±8	0.998 ±3	0.989 ±6				1.013 ±3
G	1.002 ±5		1.018 ±8			0.985 ±6	1.003 ±4	1.001 ±6		1.001 ±5
F	1.004 ±4	1.007 ±8		0.985 ±3	1.025	0.963		1.008 ±4	1.004 ±5	1.001 ±6
E	0.995 ±6		1.006 ±3		1.3 %			0.994 ±4	1.003 ±4	0.996 ±3
D	0.996 ±4		0.995 ±6		0.974 ±5	0.997 ±3	0.976 ±11			1.001 ±5
C				1.003 ±6	1.017 ±4		1.021 ±5			1.010 ±4
B	1.000 ±4	1.014 ±4				1.006 ±4		0.979 ±6	1.013 ±4	1.003 ±4
A	0.978 ±3	1.004 ±4	1.009 ±5	1.001 ±6	1.007 ±5	0.993 ±4	1.004 ±5			0.986 ±3

	10	9	8	7	6	5	4	3	2	1
J	1.004 ±5	1.001 ±8	1.003 ±5		1.001 ±6	1.002 ±5		0.992 ±5	1.008 ±4	0.999 ±5
I	1.001 ±4	0.989 ±4	0.959 ±11		1.001 ±9	0.992 ±5		0.992 ±11	1.001 ±5	
H	1.004 ±3			0.993 ±7	0.994 ±3	0.986 ±6				1.005 ±3
G	1.008 ±5		0.997 ±8			0.999 ±7	0.985 ±4	0.992 ±6		1.001 ±5
F	1.016 ±4	0.999 ±8		0.997 ±3	1.017	0.959		0.985 ±3	0.989 ±5	1.008 ±6
E	1.005 ±6		1.003 ±3		1.1 %			0.989 ±4	0.993 ±4	1.005 ±4
D	0.999 ±4		0.983 ±6		0.972 ±5	0.999 ±3	0.976 ±11			1.002 ±5
C				0.996 ±6	0.994 ±4		0.997 ±5			1.001 ±4
B	1.009 ±4	0.992 ±3				0.996 ±4		0.975 ±6	0.990 ±4	1.009 ±4
A	1.013 ±3	1.012 ±4	1.002 ±5	1.004 ±6	1.016 ±5	1.004 ±4	1.006 ±5			1.017 ±3

Figure 41 Configuration I-1A, reference case. C/E values (top number in each cell) corresponding to PRESTO-2 (left) and MCNPX (right), along with the experimental error band expressed in permille (bottom number). The C values correspond to the axial average of the calculated 3D distributions over each individual rod. The red colour indicates positions where C/E minus the absolute error exceeds 1.005. The blue colour indicates positions where the C/E plus the absolute error is less than 0.995. The pin cells containing gadolinium are identified by a grey background. The statistical uncertainty of MCNPX (about 0.08%) was intentionally not included to make the ranges for the colour assignment comparable in both pictures.

It can be seen from Figure 41 that the reconstructed total-fission rates calculated by PRESTO-2 agree well with the measurements. Some general trends can be identified, but these are of the same order as the deviations previously observed in comparisons with transport calculations [6]. In general, the fission rates in pins containing gadolinium tend to be underestimated, most strongly in position I8 (3.7%)[26]. Also systematically underestimated are the corner pins, between 2 and 3%. Moreover, some underestimation of the fission rate in pins adjacent to the central water canal can be observed. For instance, in pins G5 and F7, which do not contain gadolinium, HE/P2 underestimates the measurements by 1.5%. All these deviations originate in the HELIOS calculations and do not relate, in a significant manner, to the 3D solution presented. In general, it can be concluded that 3D nodal diffusion in 2 groups, with pin reconstruction, delivers accurate results for the test assembly in the regular configuration I-1A. The impact of the surroundings in this central region is small, so that the use of reflected

---

[26] It is interesting to note that a similar systematic underestimation of the total-fission rate in the pins containing gadolinium is also observed in MCNPX (for pin I8, for instance, it is 4.1%). This indicates that the origin of these deviations could lie in the basic cross-sections of the gadolinium isotopes, as investigated further in [36].

symmetry in the 2D transport calculation, for the cross-section and pin-power map generation, is quite adequate.

Even though the axial average and midplane results for the calculated pin-wise fission rate distribution are very similar (as can be seen, especially for the deterministic case, in Figure 40), it is worth comparing the values at core midplane against the experimental results directly. As discussed earlier, this leads to a somewhat larger standard deviation in the case of MCNPX, while for PRESTO-2 it does not represent a significant change. The results of the comparisons using the calculated values at core midplane are shown in Figure 42. The corresponding PRESTO-2 C/E distribution (left hand side of the figure) will be used as reference for the comparisons related to the sensitivity cases. For each of the latter, it is again the calculated core midplane values which have been used. The results of these comparisons are discussed in the following subsections.

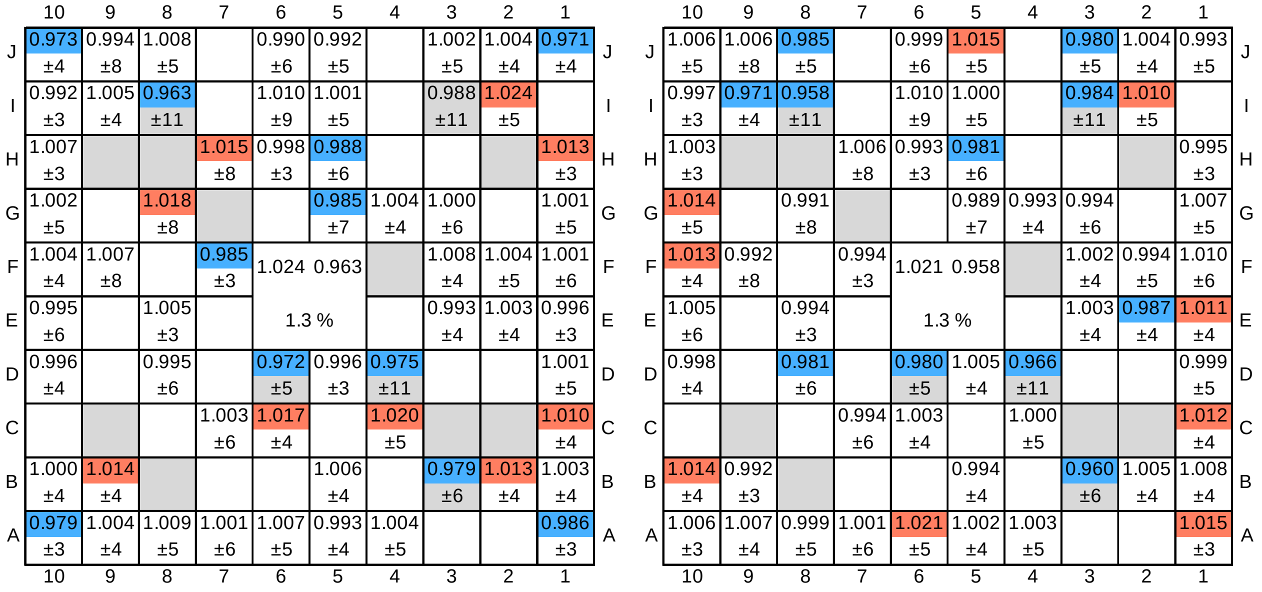

	10	9	8	7	6	5	4	3	2	1	
J	0.973 ±4	0.994 ±8	1.008 ±5		0.990 ±6	0.992 ±5		1.002 ±5	1.004 ±4	0.971 ±4	J
I	0.992 ±3	1.005 ±4	0.963 ±11		1.010 ±9	1.001 ±5		0.988 ±11	1.024 ±5		I
H	1.007 ±3			1.015 ±8	0.998 ±3	0.988 ±6				1.013 ±3	H
G	1.002 ±5		1.018 ±8			0.985 ±7	1.004 ±4	1.000 ±6		1.001 ±5	G
F	1.004 ±4	1.007 ±8		0.985 ±3	1.024	0.963		1.008 ±4	1.004 ±5	1.001 ±6	F
E	0.995 ±6		1.005 ±3		1.3 %			0.993 ±4	1.003 ±4	0.996 ±3	E
D	0.996 ±4		0.995 ±6		0.972 ±5	0.996 ±3	0.975 ±11			1.001 ±5	D
C				1.003 ±6	1.017 ±4		1.020 ±5			1.010 ±4	C
B	1.000 ±4	1.014 ±4				1.006 ±4		0.979 ±6	1.013 ±4	1.003 ±4	B
A	0.979 ±3	1.004 ±4	1.009 ±5	1.001 ±6	1.007 ±5	0.993 ±4	1.004 ±5			0.986 ±3	A
	10	9	8	7	6	5	4	3	2	1	

	10	9	8	7	6	5	4	3	2	1	
J	1.006 ±5	1.006 ±8	0.985 ±5		0.999 ±6	1.015 ±5		0.980 ±5	1.004 ±4	0.993 ±5	J
I	0.997 ±3	0.971 ±4	0.958 ±11		1.010 ±9	1.000 ±5		0.984 ±11	1.010 ±5		I
H	1.003 ±3			1.006 ±8	0.993 ±3	0.981 ±6				0.995 ±3	H
G	1.014 ±5		0.991 ±8			0.989 ±7	0.993 ±4	0.994 ±6		1.007 ±5	G
F	1.013 ±4	0.992 ±8		0.994 ±3	1.021	0.958		1.002 ±4	0.994 ±5	1.010 ±6	F
E	1.005 ±6		0.994 ±3		1.3 %			1.003 ±4	0.987 ±4	1.011 ±4	E
D	0.998 ±4		0.981 ±6		0.980 ±5	1.005 ±4	0.966 ±11			0.999 ±5	D
C				0.994 ±6	1.003 ±4		1.000 ±5			1.012 ±4	C
B	1.014 ±4	0.992 ±3				0.994 ±4		0.960 ±6	1.005 ±4	1.008 ±4	B
A	1.006 ±3	1.007 ±4	0.999 ±5	1.001 ±6	1.021 ±5	1.002 ±4	1.003 ±5			1.015 ±3	A
	10	9	8	7	6	5	4	3	2	1	

Figure 42 Configuration I-1A, reference case. C/E values (top number in each cell) corresponding to PRESTO-2 (left) and MCNPX (right), along with the experimental error band expressed in permille (bottom number). In this case, the C values correspond to the core midplane point of the calculated 3D distributions in each individual rod. The colour convention is the same as in Figure 41. The statistical uncertainty of MCNPX (about 0.8%) was intentionally not included to make the ranges for the colour assignment comparable in both pictures.

4.5.2 Sensitivity cases concerning the lattice modelling

As mentioned before, the aim of the sensitivity calculations is to show how modelling factors impact the total-fission C/E results. This subsection presents, in comparison with the reference case defined in Subsection 4.2.1, the results for the five sensitivity cases concerning the lattice modelling (see Subsection 4.2.2). As shown below, the impact of the changes considered for the lattice sensitivity is in general small, the most important effects, in a relative sense, being those of the condensation spectrum and the current coupling (see below).

Cross-section library

Using the 190-group HELIOS cross-section library, the C/Es improve by 0.3% in the corner pins and by 0.4% in the gadolinium pins close to the central water canal[27] (see Figure 43). There is no change in the other gadolinium pins, in the remaining pins adjacent to the inter-assembly gaps or in the uranium pins adjacent to the water canal. Small improvements can be observed, however, in the inner part of the lattice. The maximum, minimum and standard deviation of the C/Es are 1.023, 0.963 and 1.2%, respectively, representing only a marginal improvement with respect to the reference case, shown on the left hand side of Figure 42.

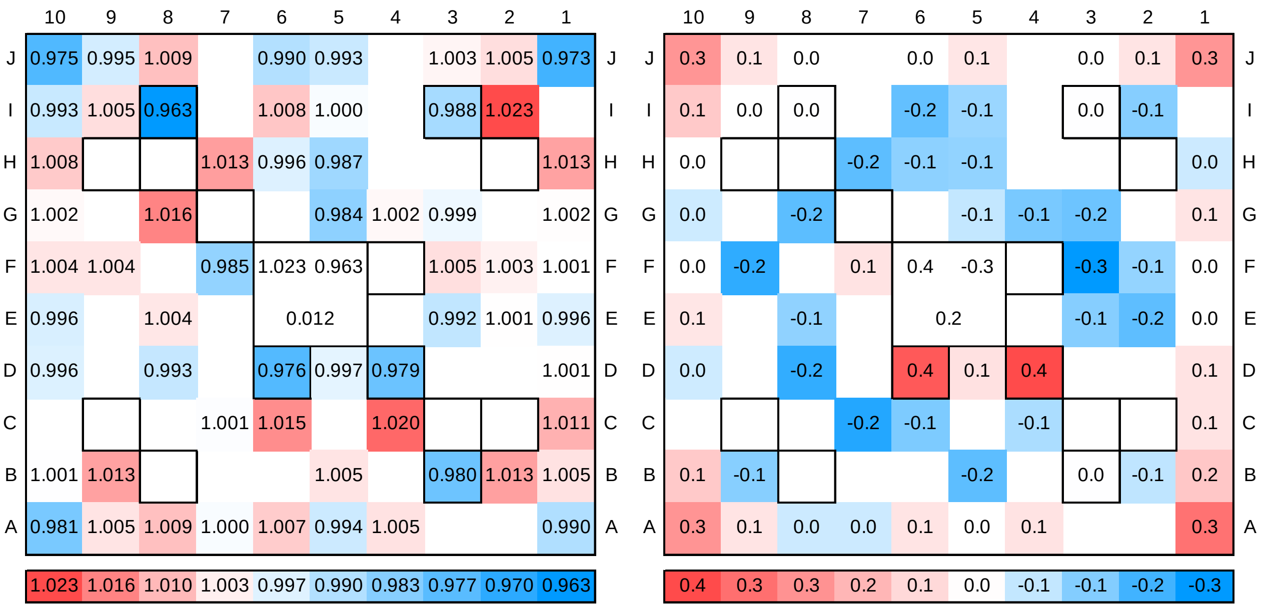

	10	9	8	7	6	5	4	3	2	1	
J	0.975	0.995	1.009		0.990	0.993		1.003	1.005	0.973	J
I	0.993	1.005	0.963		1.008	1.000		0.988	1.023		I
H	1.008			1.013	0.996	0.987				1.013	H
G	1.002		1.016			0.984	1.002	0.999		1.002	G
F	1.004	1.004		0.985	1.023	0.963		1.005	1.003	1.001	F
E	0.996		1.004		0.012			0.992	1.001	0.996	E
D	0.996		0.993		0.976	0.997	0.979			1.001	D
C				1.001	1.015		1.020			1.011	C
B	1.001	1.013				1.005		0.980	1.013	1.005	B
A	0.981	1.005	1.009	1.000	1.007	0.994	1.005			0.990	A
	1.023	1.016	1.010	1.003	0.997	0.990	0.983	0.977	0.970	0.963	

	10	9	8	7	6	5	4	3	2	1	
J	0.3	0.1	0.0		0.0	0.1		0.0	0.1	0.3	J
I	0.1	0.0	0.0		-0.2	-0.1		0.0	-0.1		I
H	0.0			-0.2	-0.1	-0.1				0.0	H
G	0.0		-0.2			-0.1	-0.1	-0.2		0.1	G
F	0.0	-0.2		0.1	0.4	-0.3		-0.3	-0.1	0.0	F
E	0.1		-0.1		0.2			-0.1	-0.2	0.0	E
D	0.0		-0.2		0.4	0.1	0.4			0.1	D
C				-0.2	-0.1		-0.1			0.1	C
B	0.1	-0.1				-0.2		0.0	-0.1	0.2	B
A	0.3	0.1	0.0	0.0	0.1	0.0	0.1			0.3	A
	0.4	0.3	0.3	0.2	0.1	0.0	-0.1	-0.1	-0.2	-0.3	

Figure 43 Configuration I-1A, sensitivity case concerning the HELIOS cross-section library. The C/E values corresponding to the 190-group library are shown on the left hand side. The right picture shows the absolute differences, expressed in percent, with respect to the reference case (pert.-ref.)x100. The colour convention has only a relative meaning, in which warmer colours represent higher values.

Condensation spectrum

The results of this sensitivity case are shown in Figure 44. In Configuration I-1A, the use of the zero-leakage (infinite-medium) condensation spectrum decreases the fission rate in the gadolinium pins by approximately 1%. The non-gadolinium pins remain practically unchanged. As k-infinity >1, the zero-leakage spectrum is softer than the critical spectrum, which increases the probability of neutrons to be captured by the gadolinium nuclei. Hence, compared with the reference case, the fission rate in pins containing gadolinium is slightly reduced. In pin I8, the difference reaches -1.7%.

---

[27] This corresponds to the absolute value of the difference of the C/E ratios between the perturbed and the reference cases expressed in percent, i.e. (perturbed-reference)x100. Note that the differences are not divided by the absolute value of the reference C/Es, as should be the case according to the definition of relative differences. This was intentionally done in order to avoid the modulation effect caused by the different C/E values, as a consequence of which pins with low C/Es would be assigned increased differences, the opposite being the case for pins showing high C/Es.

It will be shown later in Chapter 5, where the case of a totally inserted control blade is investigated, that with the central assembly having a k-infinity <1, the effect of using the zero-leakage spectrum for the cross-section condensation increases the fission rate in the gadolinium pins. This is because, in the controlled case, the spectrum is harder if the leakage is not accounted for. This behaviour underlines the importance of using the criticality spectrum for the cross-section condensation to pass from the group structure used for the lattice transport calculation to that required by the core simulator. However, even though the effect of the leakage on the few-group cross-sections is more evident for the gadolinium pins, it actually affects the power distribution over the entire assembly. Using the infinite-medium spectrum for the XS condensation, the maximum, minimum and standard deviation of the C/Es are 1.024, 0.946 and 1.4%, respectively.

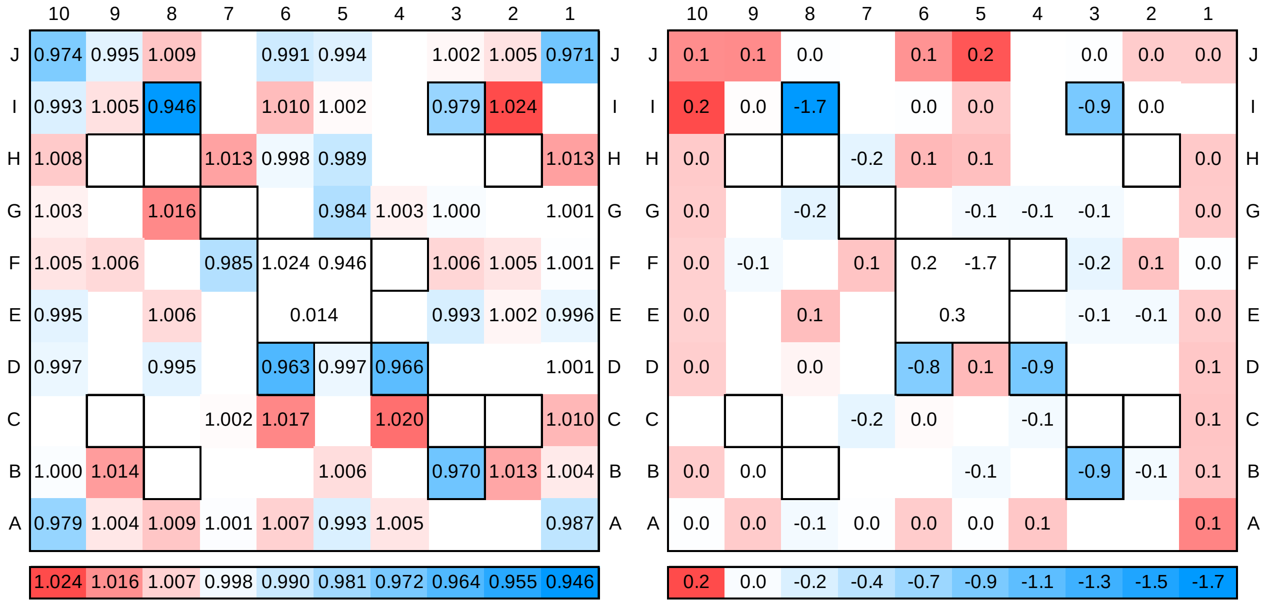

	10	9	8	7	6	5	4	3	2	1	
J	0.974	0.995	1.009		0.991	0.994		1.002	1.005	0.971	J
I	0.993	1.005	0.946		1.010	1.002		0.979	1.024		I
H	1.008			1.013	0.998	0.989				1.013	H
G	1.003		1.016			0.984	1.003	1.000		1.001	G
F	1.005	1.006		0.985	1.024	0.946		1.006	1.005	1.001	F
E	0.995		1.006		0.014			0.993	1.002	0.996	E
D	0.997		0.995		0.963	0.997	0.966			1.001	D
C				1.002	1.017		1.020			1.010	C
B	1.000	1.014				1.006		0.970	1.013	1.004	B
A	0.979	1.004	1.009	1.001	1.007	0.993	1.005			0.987	A

1.024	1.016	1.007	0.998	0.990	0.981	0.972	0.964	0.955	0.946

	10	9	8	7	6	5	4	3	2	1	
J	0.1	0.1	0.0		0.1	0.2		0.0	0.0	0.0	J
I	0.2	0.0	-1.7		0.0	0.0		-0.9	0.0		I
H	0.0			-0.2	0.1	0.1				0.0	H
G	0.0		-0.2			-0.1	-0.1	-0.1		0.0	G
F	0.0	-0.1		0.1	0.2	-1.7		-0.2	0.1	0.0	F
E	0.0		0.1		0.3			-0.1	-0.1	0.0	E
D	0.0		0.0		-0.8	0.1	-0.9			0.1	D
C				-0.2	0.0		-0.1			0.1	C
B	0.0	0.0				-0.1		-0.9	-0.1	0.1	B
A	0.0	0.0	-0.1	0.0	0.0	0.0	0.1			0.1	A

0.2	0.0	-0.2	-0.4	-0.7	-0.9	-1.1	-1.3	-1.5	-1.7

Figure 44 Configuration I-1A, sensitivity case concerning the condensation spectrum. Left picture: C/E values corresponding to the infinite-medium (zero-leakage) spectrum. Right picture: percental differences with respect to the reference case, (pert.-ref.)x100.

Collision probabilities with no current coupling

By not using current coupling (i.e. by solving the full system using collision probabilities), an improvement in the C/Es is observed in most pins, but the small magnitude of this improvement confirms that the current coupling with four azimuthal angular sectors (k=4) is a good approximation in reflected lattice calculations. The effect can be observed comparing Figure 45 with Figure 42 (reference case). Using k=0, the standard deviation of the C/Es slightly improves from 1.3% to 1.2%. The maximum and minimum values of the C/Es distribution are 1.019 and 0.963, respectively.

Physically, the use of k=0 eliminates the limitations introduced by the current coupling method in the description of strong flux gradients which lead to anisotropic currents. Unfortunately, k=0 calculations require much larger computer resources so that, considering the marginal impact on the results, the use of k=0 is not justified for production calculations. For instance, the CPU time needed to perform a reflected assembly calculation in full geometry using k=0 is about 1'000 times longer than using k=4[28]. Taking into account the fact that the number of calculations needed to create a cross-section data bank for production applications is relatively large (in the case of HELIOS/PRESTO-2, it comprises several thousands of reactivity points per lattice), the computational effort saving caused by the use of current coupling (k=4) is very significant.

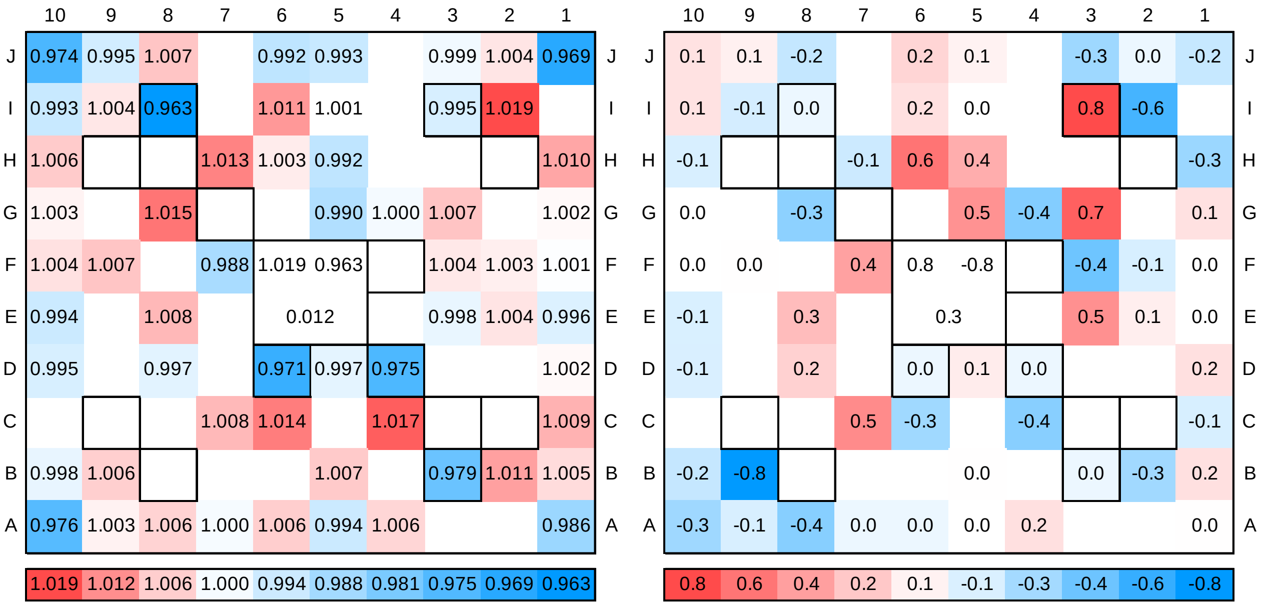

	10	9	8	7	6	5	4	3	2	1	
J	0.974	0.995	1.007		0.992	0.993		0.999	1.004	0.969	J
I	0.993	1.004	0.963		1.011	1.001		0.995	1.019		I
H	1.006			1.013	1.003	0.992				1.010	H
G	1.003		1.015			0.990	1.000	1.007		1.002	G
F	1.004	1.007		0.988	1.019	0.963		1.004	1.003	1.001	F
E	0.994		1.008		0.012			0.998	1.004	0.996	E
D	0.995		0.997		0.971	0.997	0.975			1.002	D
C				1.008	1.014		1.017			1.009	C
B	0.998	1.006				1.007		0.979	1.011	1.005	B
A	0.976	1.003	1.006	1.000	1.006	0.994	1.006			0.986	A

1.019	1.012	1.006	1.000	0.994	0.988	0.981	0.975	0.969	0.963

	10	9	8	7	6	5	4	3	2	1	
J	0.1	0.1	-0.2		0.2	0.1		-0.3	0.0	-0.2	J
I	0.1	-0.1	0.0		0.2	0.0		0.8	-0.6		I
H	-0.1			-0.1	0.6	0.4				-0.3	H
G	0.0		-0.3			0.5	-0.4	0.7		0.1	G
F	0.0	0.0		0.4	0.8	-0.8		-0.4	-0.1	0.0	F
E	-0.1		0.3		0.3			0.5	0.1	0.0	E
D	-0.1		0.2		0.0	0.1	0.0			0.2	D
C				0.5	-0.3		-0.4			-0.1	C
B	-0.2	-0.8				0.0		0.0	-0.3	0.2	B
A	-0.3	-0.1	-0.4	0.0	0.0	0.0	0.2			0.0	A

0.8	0.6	0.4	0.2	0.1	-0.1	-0.3	-0.4	-0.6	-0.8

Figure 45 Configuration I-1A, sensitivity case concerning the use of current coupling. Left picture: C/E values corresponding to the transport (CP) calculation over the whole system (k=0). Right picture: percental differences with respect to the reference case, (pert.-ref.)x100.

Mesh size in the fuel pins

A finer radial subdivision of the fuel pins has no significant effect. The mesh used in the reference case (2 and 5 rings in uranium and gadolinium pins, respectively) is well suited for all calculations. The external ring in the regular uranium pins allows an accurate description of the plutonium build-up process, while the five rings used in the gadolinium pins permit an adequate modelling of the flux-depression caused by the strong thermal absorption occurring in the BA.

For special applications, however, a finer subdivision may be necessary. This is the case, for example, in the investigation of the detailed behaviour of the neutron flux and the isotopic composition inside the fuel pins [37].

Thermal cut-off energy

The two-group lattice parameters, i.e. the cross-sections and discontinuity factors, depend on the group structure. Thus, they are affected by the change in the thermal cut-off energy. Furthermore, as shown in Figure 38, the PCRs show a significant spectral dependence and are therefore also sensitive to changes in the thermal cut-off energy. Table 11, for instance, shows

---

[28] On the Linux server where the calculations were made, one lattice calculation ran in 0.23 CPU minutes using k=4, while for k=0 the elapsed CPU time was 219 minutes.

the 2-group PCRs for a thermal cut-off energy of 0.625 eV. It can be seen, that these PCRs differ slightly from those corresponding to 1.84 eV, presented in Table 8.

It will be shown later, in Section 4.9, that changing the thermal cut-off energy from 1.84 eV to 0.625 eV produces an increase of 220 pcm in k-effective. This difference confirms the known fact that a 2-group representation cannot capture spectral effects exactly. On the other hand, the relatively moderate change in k-effective also shows that, by consistently changing the group structure used in the nodal calculation and in the representation of the boundary conditions, the use of either of the two thermal cut-off energies investigated in this thesis is well justified.

Table 11 PCRs for PRESTO-2 in Configuration I-1A, derived from the partial currents obtained in the 3D whole-reactor MCNPX calculation. The PCRs correspond to a thermal cut-off energy of 0.625 eV.

Configuration I-1A	PCR_{11}		PCR_{22}	
Upper limit (eV)	$20x10^6$		0.625	
Axial direction at top	0.773		0.944	
Radial direction	Side	Corner	Side	Corner
Axial level 10	0.972	1.013	0.344	0.373
Axial level 9	0.977	1.017	0.341	0.370
Axial level 8	0.982	1.023	0.337	0.364
Axial level 7	0.984	1.029	0.335	0.357
Axial level 6	0.981	1.027	0.334	0.355
Axial level 5	0.981	1.023	0.334	0.357
Axial level 4	0.981	1.024	0.334	0.357
Axial level 3	0.981	1.024	0.336	0.355
Axial level 2	0.977	1.022	0.337	0.357
Axial level 1	0.966	1.016	0.339	0.364
Axial direction at bottom	0.839		0.964	

In contrast to the two-group parameters, the 2D pin-power maps from the lattice calculation, which are a result of the integration of the fission rate over the entire energy range, are insensitive to the thermal cut-off energy. This implies that the changes in the reconstructed total-fission rate are only due to changes in the solution of the nodal diffusion problem. Since these are, as discussed above, relatively small, the use of 0.625 eV instead of 1.84 eV as thermal cut-off energy must have a low impact on the fission rate distribution.

As mentioned, this was confirmed by the C/E comparisons. Differences with respect to the reference case were found to lie within the band ±0.4%, the maximum, minimum and standard deviation of the C/E distribution in this sensitivity case being 1.025, 0.959 and 1.3%, respectively.

4.5.3 Sensitivity cases concerning the test-zone boundary conditions

One of the important design criteria for the LWR-PROTEUS experimental programme was a weak influence of the outer zones of the reactor on the region where the measurements were made. For this reason, all measurements were performed in pins belonging to the central assembly[29], the eight surrounding assemblies acting as an efficient decoupling layer. This spectral decoupling of the outer reactor regions plays a key role in the robustness of the experimental results, i.e. their relative independence from the multi-zone nature of the LWR-PROTEUS critical facility.

One way to evaluate this lack of significant dependence is to study the impact of changes in the test-zone boundary conditions on the total-fission C/Es. This has been accomplished by performing sensitivity studies related to the space and energy dependence of the test-zone PCRs. These are described in the following subsections.

Impact of the subdivision of the PCRs in space and energy

Due to the coupling between the test zone and its surroundings, the PCRs depend on the case under consideration. In fact, the reactor being made critical by adjusting the fuel loading in the D_2O- and C-drivers (cf. Figure 15), significant variations of the partial currents crossing the test tank occur, depending on the reactivity of the test-zone configuration. In addition, these currents show variations in space (axially and azimuthally) and energy. For the characterisation of the test-zone surroundings, however, it is the ratio between incoming and outgoing currents, i.e. the PCR, which is important.

As mentioned before, the axial variation of the radial PCRs is accounted for. However, for each axial node level, a single PCR matrix is used for all four faces, and another one for all four outer corners forming the test zone perimeter (see Figure 30). This is because PRESTO-2 requires the same albedo matrix on all surfaces facing the surroundings that belong to the same category among the following three surface types: “flat”, “inner corner” or “outer corner” (see Figure 13). As described in Chapter 3, Subsection 3.6.3, pin map correction factors (PMCFs) have been defined to study the effect of the spatial variation of the PCRs along the four test-zone faces, as also of the number of energy groups used in their definition. The PMCFs were calculated, for each axial level, from the ratio between two 2D HELIOS calculations for a model of the 3x3 test zone (Figure 33) with albedo boundary conditions (instead of reflected): one calculation (48/05) describes the test zone boundary by 5-group PCRs in 12 segments per face, as calculated with MCNPX. The other calculation (02/02) uses the condensed (2 groups) and spatially averaged (one value for the four faces and one value for the four out-corners) PCRs that are used in PRESTO-2. The PMCFs are then defined by equation {43}. To investigate the impact of the space and energy discretization on the fission rate distribution, the following two cases have been evaluated:

1) The PMCFs were applied to the reconstructed pin fission rate maps to account for the differences between cases 48/05 and 02/02, as regards the pin-wise fission rate distribution. This corresponds to the most detailed representation of the test zone boundary that can be made with the present methodology.
2) PMCFs were applied to the reconstructed pin fission rate maps to account for the differences between the “intermediate” case 02/05 and the PRESTO-compatible case 02/02. Here, the PMCFs represent the effects of only changing the number of energy groups in which the boundary PCRs are defined (5 instead of 2), the spatial distribution of the PCRs being kept the same.

---

[29] There were also other practical reasons. For example, the spacers in the measured assembly had to be relaxed in order to facilitate the extraction of the fuel pins for the gamma scanning.

In the particular case of Configuration I-1A, the azimuthal variation of the PCRs along the test zone perimeter is relatively weak. Thus, in this case, the PRESTO-2 restriction of uniform side and corner albedos does not represent a severe limitation. This can also be concluded from the quadrant deviations depicted in Table 12. This table shows the percental deviation δ of the PCR for each quadrant of the test zone boundary, with respect to the mean value for all four quadrants. For this purpose, the PCR for each quadrant a_i has been calculated from equation {42} using the partial currents integrated along the two half-sides of the test zone perimeter which converge to the respective corner. For this comparison, the currents were also integrated over the whole test-zone length. It can be seen, that the partial current distribution is practically symmetric in the azimuthal direction (the deviations are smaller than 1%). This result reflects the azimuthally uniform character of Configuration I-1A.

Table 12 Configuration I-1A. Percental deviation δ of the PCRs for each quadrant of the test zone boundary with respect to the mean value for all four quadrants ($\Sigma_1^4\ \delta=0$). The energy groups are defined in Table 7.

$$\delta = \left[\frac{a_i}{\frac{1}{4}\Sigma_1^4\, a_i} - 1\right] \cdot 100$$

Energy Group	NW	NE	SW	SE
1	-0.77	0.54	0.05	0.18
2	-0.37	0.14	-0.03	0.26
3	0.03	0.11	-0.09	-0.06
4	0.01	-0.34	0.43	-0.10
5	0.24	0.23	0.12	-0.59

Application of the 48/05 PMCFs

The PMCFs are applied by simply multiplying the calculated total-fission rate distribution by the PMCF map. On the left, Figure 46 shows the result of the application of the 48/05 PMCFs to the reference case (Figure 42) and, on the right, the corresponding PMCF map at the 5th axial level.

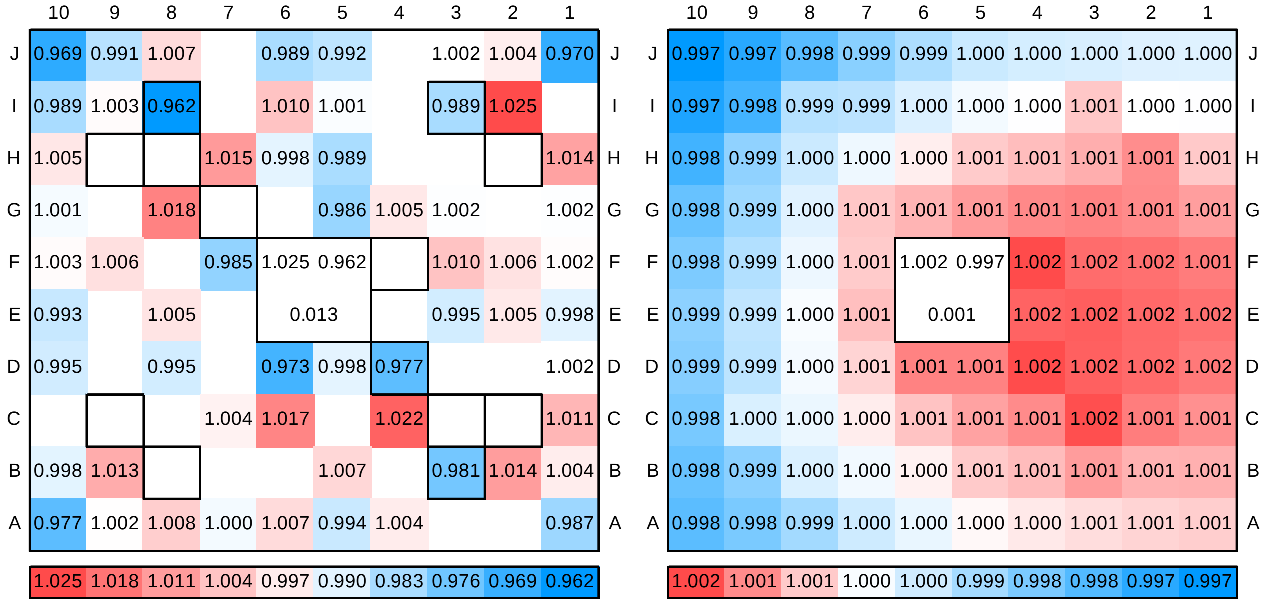

	10	9	8	7	6	5	4	3	2	1	
J	0.969	0.991	1.007		0.989	0.992		1.002	1.004	0.970	J
I	0.989	1.003	0.962		1.010	1.001		0.989	1.025		I
H	1.005			1.015	0.998	0.989				1.014	H
G	1.001		1.018			0.986	1.005	1.002		1.002	G
F	1.003	1.006		0.985	1.025	0.962		1.010	1.006	1.002	F
E	0.993		1.005		0.013			0.995	1.005	0.998	E
D	0.995		0.995		0.973	0.998	0.977			1.002	D
C				1.004	1.017		1.022			1.011	C
B	0.998	1.013				1.007		0.981	1.014	1.004	B
A	0.977	1.002	1.008	1.000	1.007	0.994	1.004			0.987	A

1.025	1.018	1.011	1.004	0.997	0.990	0.983	0.976	0.969	0.962

	10	9	8	7	6	5	4	3	2	1	
J	0.997	0.997	0.998	0.999	0.999	1.000	1.000	1.000	1.000	1.000	J
I	0.997	0.998	0.999	0.999	1.000	1.000	1.000	1.001	1.000	1.000	I
H	0.998	0.999	1.000	1.000	1.000	1.001	1.001	1.001	1.001	1.001	H
G	0.998	0.999	1.000	1.001	1.001	1.001	1.001	1.001	1.001	1.001	G
F	0.998	0.999	1.000	1.001	1.002	0.997	1.002	1.002	1.002	1.001	F
E	0.999	0.999	1.000	1.001	0.001		1.002	1.002	1.002	1.002	E
D	0.999	0.999	1.000	1.001	1.001	1.001	1.002	1.002	1.002	1.002	D
C	0.998	1.000	1.000	1.000	1.001	1.001	1.001	1.002	1.001	1.001	C
B	0.998	0.999	1.000	1.000	1.000	1.001	1.001	1.001	1.001	1.001	B
A	0.998	0.998	0.999	1.000	1.000	1.000	1.000	1.001	1.001	1.001	A

1.002	1.001	1.001	1.000	1.000	0.999	0.998	0.998	0.997	0.997

Figure 46 Configuration I-1A, sensitivity case concerning the use of the 48/05 PMCFs. The left picture shows the C/E values corresponding to the reference case multiplied by the PMCFs, which are shown (for the 5th axial level) in the right picture.

It can be seen that the PMCFs are very close to 1. However, a small tilt can be observed, the PMCFs being slightly lower on the west side, mainly near the NW corner. This can be correlated to the deviations shown in Table 12, where the high-energy PCRs (groups 1 and 2) calculated over the NW quadrant are lower than those corresponding to the SE quadrant. The 48/05 PMCFs in Configuration I-1A are spatially distributed as shown on the right hand side of Figure 46. It will be shown later, in Chapter 5, that the insertion of a control blade imposes a strong tilt on the global flux in the test zone, leading to a much more skewed distribution of PMCFs.

As discussed, employment of just the central assembly for the LWR-PROTEUS measurements provided an effective way of minimising the impact of the test-zone surroundings on the measured pin-wise reaction rates. In this frame, the central assembly can be considered, approximately, as belonging to an "infinite" array of identical assemblies. The weak spatial dependence of the PMCFs in Configuration I-1A, shown in Figure 46, supports this statement. In the eight peripheral assemblies, however, the total-fission rate distribution is strongly affected by the finite character of the test zone. To illustrate this, the relative pin-power distribution over the 9 fuel assemblies constituting the test zone, as calculated by PRESTO-2, is shown in Figure 47.

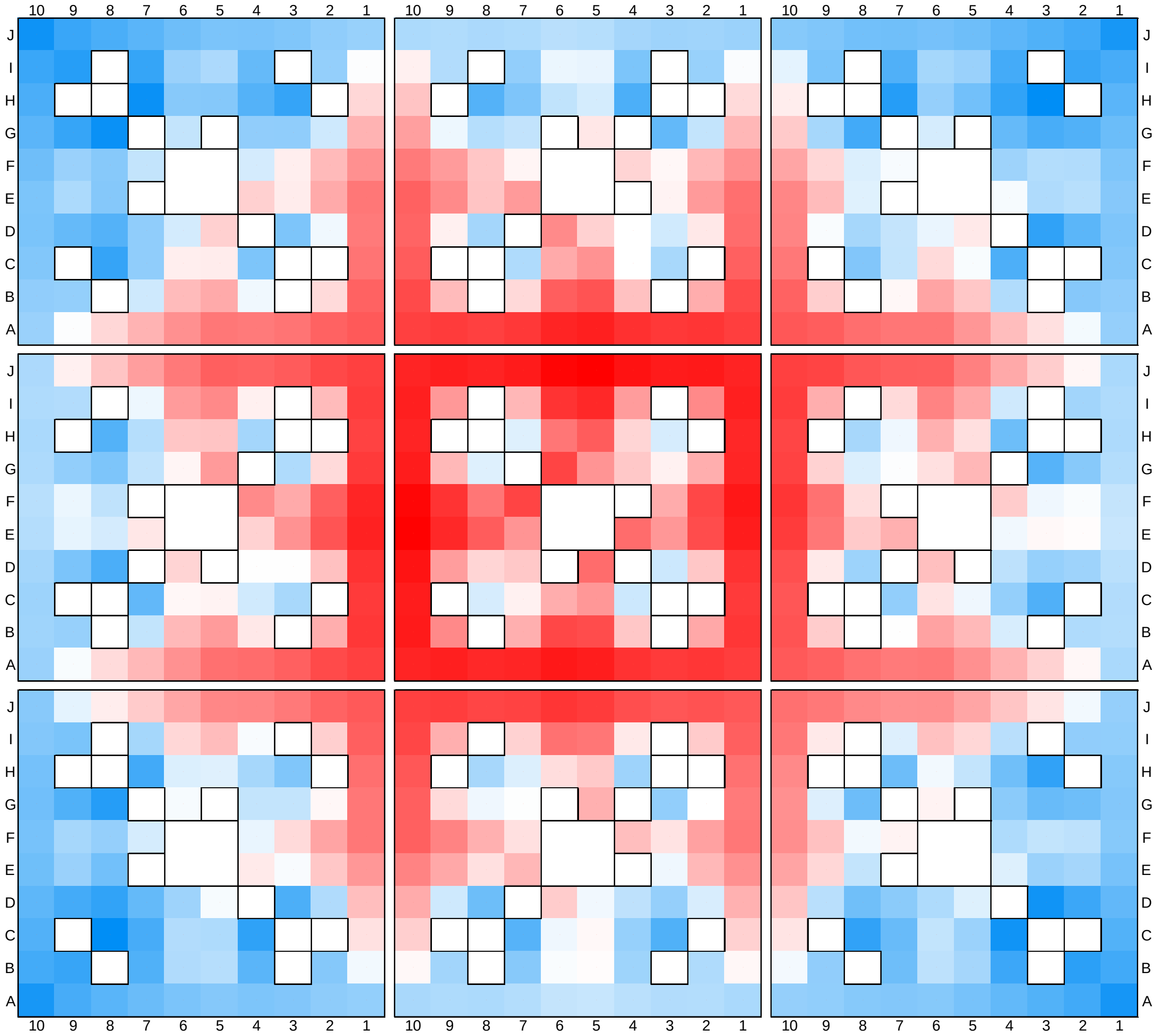

Figure 47 Configuration I-1A, reference case: relative total-fission rate distribution in the nine assemblies of the LWR-PROTEUS test zone, as calculated with PRESTO-2. A warm-cold colour scale, from which the gadolinium pins have been excluded, has been used to allow the visualisation of the flux radial shape. The relative total-fission rate distribution being normalised to 1.0 for the 3x3 configuration, the scale covers the range ~0.6 to ~1.7, warmer colours indicating higher values.

In Figure 47, the effect of the inter assembly gaps, which increases the power in the adjacent pins due to the increased moderation, can be clearly seen. Furthermore, the boundary effect at the test-zone perimeter, where the thermal flux is low compared with its value at the test-zone centre, can also be clearly identified.

Application of the 02/05 PMCFs

This case is introduced with the purpose of separating the effects of the space and energy subdivision of the PCRs. In the 02/05 case, the spatial variation of the PCRs used in the 3x3 HELIOS calculation matches that of the PRESTO-2 PCRs. Hence, it is only the spectral information contained in the five-group PCRs which causes the PCRs to deviate from 1.0. The results of this comparison are shown in Figure 48. As before, the PMCFs are applied by simply multiplying the calculated total-fission rate distribution by the PMCF map.

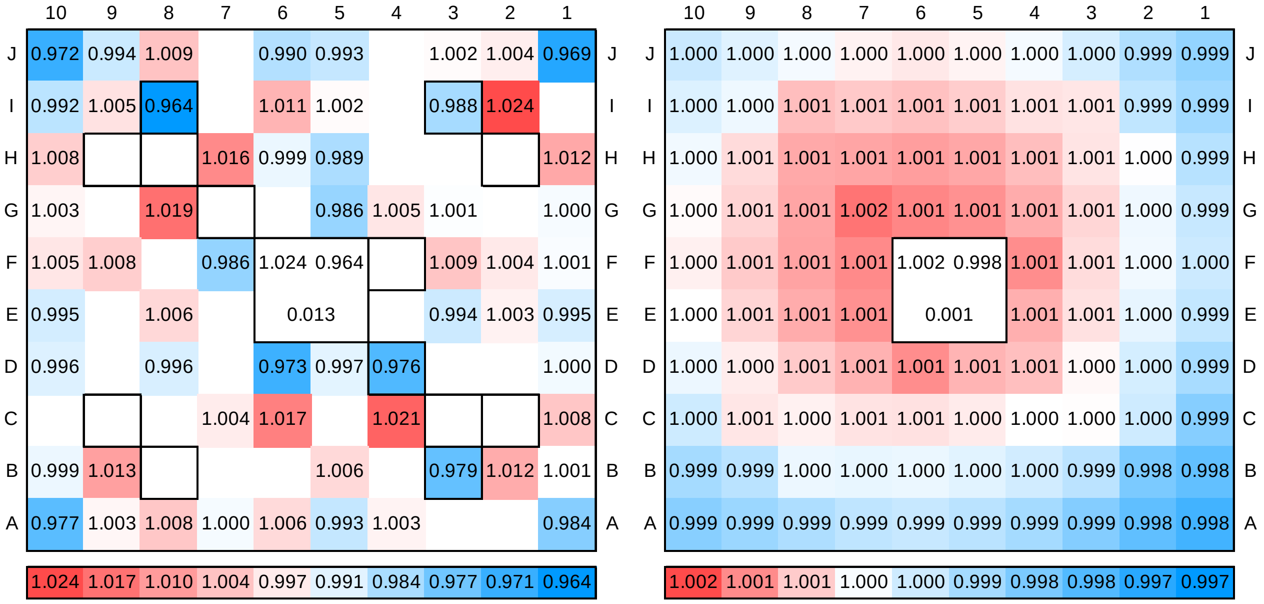

	10	9	8	7	6	5	4	3	2	1	
J	0.972	0.994	1.009		0.990	0.993		1.002	1.004	0.969	J
I	0.992	1.005	0.964		1.011	1.002		0.988	1.024		I
H	1.008			1.016	0.999	0.989				1.012	H
G	1.003		1.019			0.986	1.005	1.001		1.000	G
F	1.005	1.008		0.986	1.024	0.964		1.009	1.004	1.001	F
E	0.995		1.006		0.013			0.994	1.003	0.995	E
D	0.996		0.996		0.973	0.997	0.976			1.000	D
C				1.004	1.017		1.021			1.008	C
B	0.999	1.013				1.006		0.979	1.012	1.001	B
A	0.977	1.003	1.008	1.000	1.006	0.993	1.003			0.984	A

1.024	1.017	1.010	1.004	0.997	0.991	0.984	0.977	0.971	0.964

	10	9	8	7	6	5	4	3	2	1	
J	1.000	1.000	1.000	1.000	1.000	1.000	1.000	1.000	0.999	0.999	J
I	1.000	1.000	1.001	1.001	1.001	1.001	1.001	1.001	0.999	0.999	I
H	1.000	1.001	1.001	1.001	1.001	1.001	1.001	1.001	1.000	0.999	H
G	1.000	1.001	1.001	1.002	1.001	1.001	1.001	1.001	1.000	0.999	G
F	1.000	1.001	1.001	1.001	1.002	0.998	1.001	1.001	1.000	1.000	F
E	1.000	1.001	1.001	1.001	0.001		1.001	1.001	1.000	0.999	E
D	1.000	1.000	1.001	1.001	1.001	1.001	1.001	1.000	1.000	0.999	D
C	1.000	1.001	1.000	1.001	1.001	1.000	1.000	1.000	1.000	0.999	C
B	0.999	0.999	1.000	1.000	1.000	1.000	1.000	0.999	0.998	0.998	B
A	0.999	0.999	0.999	0.999	0.999	0.999	0.999	0.999	0.998	0.998	A

1.002	1.001	1.001	1.000	1.000	0.999	0.998	0.998	0.997	0.997

Figure 48 Configuration I-1A, sensitivity case concerning the use of the 02/05 PMCFs. The left picture shows the C/E values corresponding to the reference case multiplied by the PMCFs, which are shown on the right picture.

In brief, it has been shown that both energy and spatial refinements have little impact on the total-fission rate in the central assembly. It will be shown in Section 4.9, however, that the energy refinement does affect the neutron balance, and hence the system reactivity, in a significant manner.

Use of 2D PCRs calculated with HELIOS

Taking advantage of the high flexibility that HELIOS offers for detailed 2D geometrical descriptions, a 2D HELIOS model of the complete PROTEUS reactor was used to evaluate the in- and out-currents at the test zone boundary (see Subsection 3.6.3 and Section 4.4). The radial PCRs were then calculated according to equation {42} and used in place of the MCNPX PCRs, described in Subsection 3.6.1 and Section 4.3. As done in the MCNPX case, the partial currents were integrated along the four sides and four corners of the test zone perimeter. Here, however, since the calculation is performed in 2D, the same PCRs were used for all 10 axial levels. The resulting PCRs are shown in Table 10. In the axial direction (top and bottom boundary of the test zone), the MCNPX PCRs were kept.

The C/E values corresponding to the PRESTO-2 calculation that uses the 2D HELIOS PCRs are shown, together with their differences with respect to the reference case, in Figure 49.

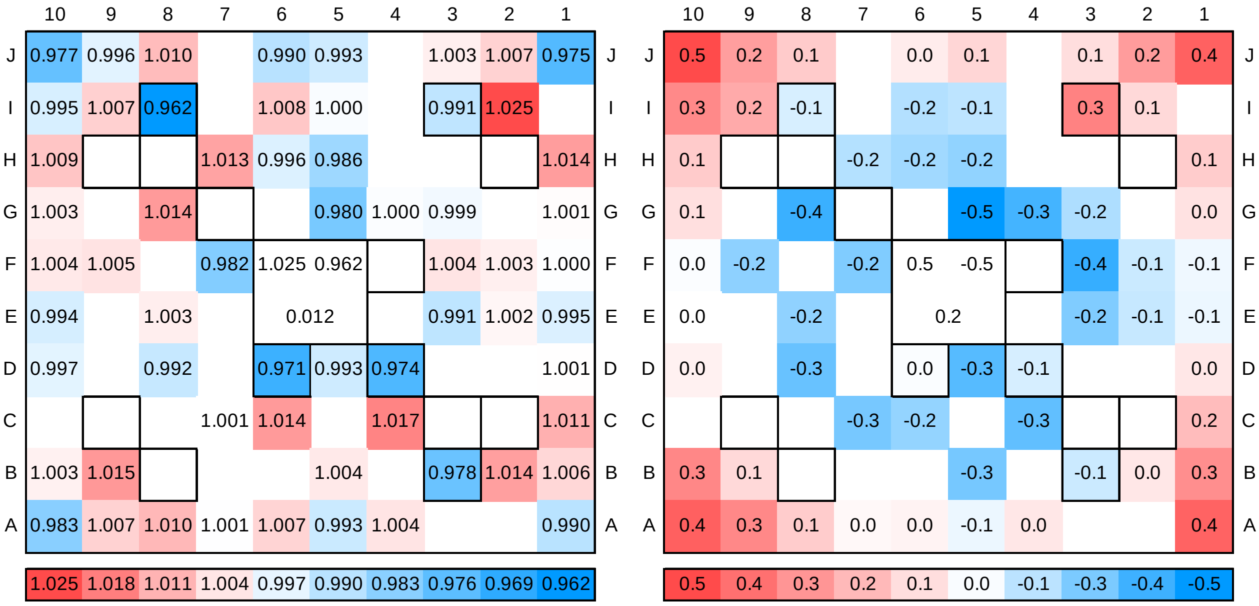

	10	9	8	7	6	5	4	3	2	1	
J	0.977	0.996	1.010		0.990	0.993		1.003	1.007	0.975	J
I	0.995	1.007	0.962		1.008	1.000		0.991	1.025		I
H	1.009			1.013	0.996	0.986				1.014	H
G	1.003		1.014			0.980	1.000	0.999		1.001	G
F	1.004	1.005		0.982	1.025	0.962		1.004	1.003	1.000	F
E	0.994		1.003		0.012			0.991	1.002	0.995	E
D	0.997		0.992		0.971	0.993	0.974			1.001	D
C				1.001	1.014		1.017			1.011	C
B	1.003	1.015				1.004		0.978	1.014	1.006	B
A	0.983	1.007	1.010	1.001	1.007	0.993	1.004			0.990	A

1.025	1.018	1.011	1.004	0.997	0.990	0.983	0.976	0.969	0.962

	10	9	8	7	6	5	4	3	2	1	
J	0.5	0.2	0.1		0.0	0.1		0.1	0.2	0.4	J
I	0.3	0.2	-0.1		-0.2	-0.1		0.3	0.1		I
H	0.1			-0.2	-0.2	-0.2				0.1	H
G	0.1		-0.4			-0.5	-0.3	-0.2		0.0	G
F	0.0	-0.2		-0.2	0.5	-0.5		-0.4	-0.1	-0.1	F
E	0.0		-0.2		0.2			-0.2	-0.1	-0.1	E
D	0.0		-0.3		0.0	-0.3	-0.1			0.0	D
C				-0.3	-0.2		-0.3			0.2	C
B	0.3	0.1				-0.3		-0.1	0.0	0.3	B
A	0.4	0.3	0.1	0.0	0.0	-0.1	0.0			0.4	A

0.5	0.4	0.3	0.2	0.1	0.0	-0.1	-0.3	-0.4	-0.5

Figure 49 Configuration I-1A, sensitivity case concerning the use of PCRs obtained with the 2D HELIOS whole-reactor model. Left picture: C/E values. Right picture: percental differences with respect to the reference case, (pert.-ref.)x100.

As discussed in Section 4.4, the 2D HELIOS full-reactor model leads to larger PCRs in the epithermal energy range compared with the 3D MCNPX model. It will be shown later, in Section 4.9, that this has a significant effect on the LWR-PROTEUS whole-reactor k-effective value. On the other hand, the impact on the fission rate distribution is relatively small, the fission rates of the corner pins being increased by about 0.5%. This confirms that the influence of the test zone surroundings on the central assembly is weak, which gives the experimental results the desired robustness. However, the effects of the boundary conditions are systematic and therefore need to be borne in mind. Thus, compared to MCNPX, the larger HELIOS PCRs (see discussion in Section 4.4) increase the fission rate in the outer assemblies, leading to slightly higher fission rates at the periphery of the central assembly and to lower values at its centre.

Impact of the corner PCRs

The above results suggest that, in the case of Configuration I-1A, the azimuthal distribution of the PCRs over the test-zone periphery plays no significant role for the determination of the total-fission rate distribution in the central assembly. Even the separation between corner and side PCRs, allowed by PRESTO-2 and depicted in Figure 30, has a very small impact. In fact, using azimuthally uniform radial PCRs in PRESTO-2, i.e. one PCR per axial level, does not change the results. This was confirmed by running a case in which the PCRs given in Table 8 were replaced by PCRs obtained from the integration of the partial currents over the whole perimeter. Using the latter, which are shown in Table 13 below, the C/Es were found to be practically identical (differences smaller than 0.1%) to their reference-case equivalents shown in Figure 42.

Table 13 Radial PCRs for PRESTO-2 in Configuration I-1A, derived from the partial currents obtained in the 3D whole-reactor MCNPX calculation, using a thermal cut-off energy of 1.84 eV. Differently from the PCRs of Table 8, these were obtained by current integration over the whole test-zone perimeter.

Configuration I-1A	PCR_{11}	PCR_{22}
Upper limit (eV)	$20x10^6$	1.84
Axial level 10	0.991	0.392
Axial level 9	0.996	0.389
Axial level 8	1.002	0.387
Axial level 7	1.004	0.385
Axial level 6	1.001	0.384
Axial level 5	1.000	0.384
Axial level 4	1.000	0.385
Axial level 3	1.001	0.386
Axial level 2	0.997	0.386
Axial level 1	0.986	0.388

4.5.4 Impact of the pin coordinates on the map reconstruction in PRESTO-2

As discussed in Chapter 3, Subsection 3.3.1, the use of measured inter-assembly gaps in HELIOS leads to a slight misalignment of the pin coordinates in PRESTO-2 when the 2D pin-power maps are superimposed onto the asymptotic flux solution. In the particular case of Configuration I-1A, the displacement is $7.6325 - 7.6200 = 0.0125\ cm$. The situation has been depicted in Figure 25.

One way to correct for this effect in the HE/P2 calculation is to modify the parameters *XNWCRNR* and *YNWCRNR* in the XDSB (TABGEN file) in order to reflect the exact positions of the central assembly pins with respect to the node boundaries. Figure 35 shows the dimensions that were measured in the experimental set-up for Configuration I-1A. The distance between the west and north walls of the test zone and the midpoint of the central assembly are, respectively:

$$0.6330 + 2x0.7185 + 1.5x13.86 = 22.86\ cm\ (x\text{-direction})$$

$$0.6210 + 2x0.7245 + 1.5x13.86 = 22.86\ cm\ (y\text{-direction})$$

where 13.86 cm is the fuel box outer dimension and 22.86 cm is exactly one half of the test-zone wall-to-wall inner distance. Thus, the central assembly is assumed to occupy the nominal position in the test-zone assembly lattice, and, as discussed in Subsection 3.3.1, by setting:

$$XNWCRNR = YNWCRNR = -7.6200\ cm$$

PRESTO-2 will locate the fuel pins in their correct positions with respect to the node boundaries. At the same time, since the lattice has been modelled in HELIOS using the measured gaps, the 2D transport pin power maps also correspond to the experimental dimensions.

Even though the above procedure leads to the most accurate modelling of the LWR-PROTEUS geometry with PRESTO-2, the modification of the corner coordinates *XNWCRNR* and *YNWCRNR* requires a manual intervention in the XSDB. However, as mentioned before, this thesis principally focuses on the appraisal of the methodologies used for production calculations keeping the special adjustments needed to reproduce the experimental conditions at a reasonable minimum. Therefore, it turns out to be more interesting to keep the standard procedure for all calculations and study in one particular case the impact that the above modification has on the results. This has been done here, i.e. for Configuration I-1A.

For the reference case of Subsection 4.5.1, the *XNWCRNR* and *YNWCRNR* coordinates in the XSDB were manually fixed at −7.6200 cm, as indicated above. The changes in the pin-wise total-fission rate distribution (see Figure 42) were found to lie between +0.12% and −0.06% for all pins. Thus, the effect can indeed be neglected. Since the deviations of the gap size with respect to the nominal dimensions are similar for all the LWR-PROTEUS configurations analysed in this thesis, the standard procedure for the determination of the pin coordinates in the HE/P2 XSDB can thus be considered quite adequate and has, consequently, been used in all calculations.

4.5.5 Impact of the inter-assembly gap size

Here, the sensitivity to employment of measured gap sizes, instead of nominal values, is considered as such. Thus, instead of using the measured gap sizes as done for the reference case of Subsection 4.5.1, lattice calculations were performed with HELIOS using the nominal half-gap size. The sizes of the measured and nominal half-gaps are summarised in Table 14. The results obtained for the total-fission rate distribution are shown in Figure 50.

Table 14 Nominal and measured half-gaps (cm) corresponding to the central assembly in Configuration I-1A.

		North	East	South	West
Nominal	(perturbed case)	0.6900	0.6900	0.6900	0.6900
Measured	(reference case)	0.7245	0.6865	0.6845	0.7185
Difference	(perturbed-reference)	−0.0345	0.0035	0.0055	−0.0285

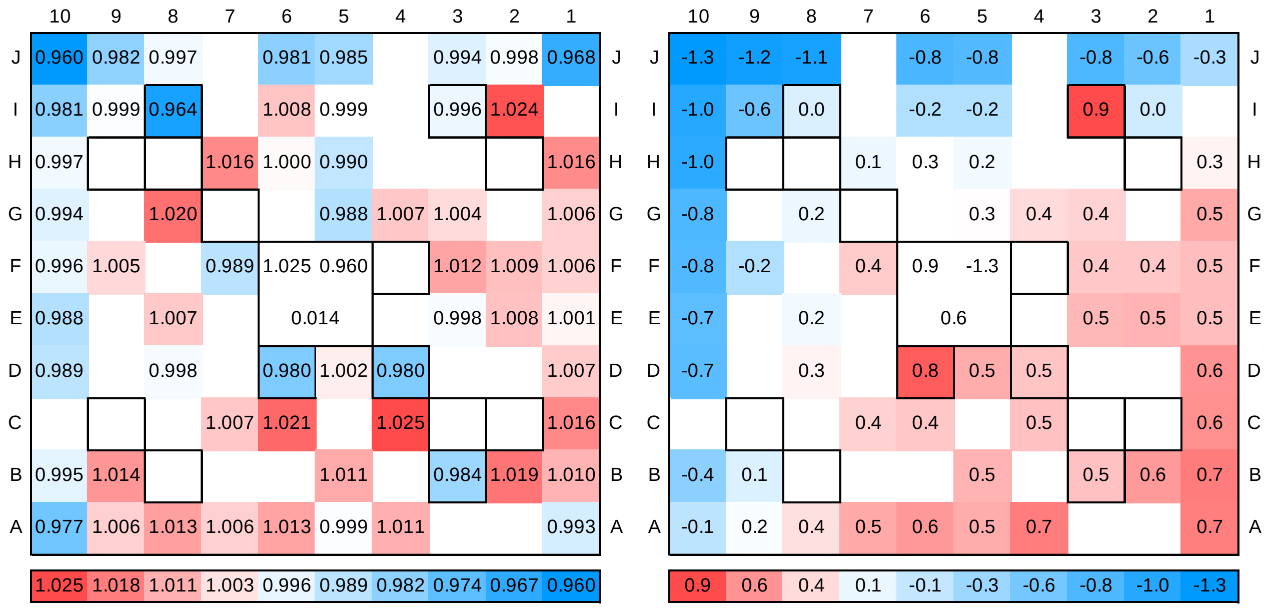

	10	9	8	7	6	5	4	3	2	1	
J	0.960	0.982	0.997		0.981	0.985		0.994	0.998	0.968	J
I	0.981	0.999	0.964		1.008	0.999		0.996	1.024		I
H	0.997			1.016	1.000	0.990				1.016	H
G	0.994		1.020			0.988	1.007	1.004		1.006	G
F	0.996	1.005		0.989	1.025	0.960		1.012	1.009	1.006	F
E	0.988		1.007		0.014			0.998	1.008	1.001	E
D	0.989		0.998		0.980	1.002	0.980			1.007	D
C				1.007	1.021		1.025			1.016	C
B	0.995	1.014				1.011		0.984	1.019	1.010	B
A	0.977	1.006	1.013	1.006	1.013	0.999	1.011			0.993	A

1.025	1.018	1.011	1.003	0.996	0.989	0.982	0.974	0.967	0.960

	10	9	8	7	6	5	4	3	2	1	
J	-1.3	-1.2	-1.1		-0.8	-0.8		-0.8	-0.6	-0.3	J
I	-1.0	-0.6	0.0		-0.2	-0.2		0.9	0.0		I
H	-1.0			0.1	0.3	0.2				0.3	H
G	-0.8		0.2			0.3	0.4	0.4		0.5	G
F	-0.8	-0.2		0.4	0.9	-1.3		0.4	0.4	0.5	F
E	-0.7		0.2		0.6			0.5	0.5	0.5	E
D	-0.7		0.3		0.8	0.5	0.5			0.6	D
C				0.4	0.4		0.5			0.6	C
B	-0.4	0.1				0.5		0.5	0.6	0.7	B
A	-0.1	0.2	0.4	0.5	0.6	0.5	0.7			0.7	A

0.9	0.6	0.4	0.1	-0.1	-0.3	-0.6	-0.8	-1.0	-1.3

Figure 50 Configuration I-1A, impact of the inter-assembly gap size. The C/E values corresponding to the nominal gaps are given in the left map. On the right hand side, the (pert.-ref.)x100 values are shown. The effect of the north- and west-gap narrowing caused by the use of the nominal dimensions instead of the measured ones can be clearly seen.

It is seen that the impact of the assembly positions in the test zone is indeed quite significant, the reaction rates in the pins adjacent to the modified water gaps being affected most. For instance, on the north and west sides, a gap reduction of ~0.3 mm reduces the fission rate by ~1%, as shown in the right hand side of Figure 50. In the NW corner pin, the difference reaches 1.3%. The global tilt along the NW-SE diagonal, caused by the changes in the gap sizes (see Table 14), can be clearly identified. Using nominal gaps, the maximum, minimum and standard deviation of the C/Es are 1.025, 0.960 and 1.4%, respectively.

4.5.6 Impact of the sub-assembly pressing

As described in Section 4.1, the four sub-assemblies in the central fuel element were pressed 0.51 mm towards the central water canal in the x and y directions. The intention has been to simulate the displacement of the sub-assemblies that, according to the fuel manufacturer, occurs in a power reactor due to the forces imposed by the coolant flow. In the lattice calculations for production applications, however, this displacement is not modelled, the nominal lattice positions being used instead. One reason for this is the dependence on the coolant flow, due to which the exact value of the displacement is hardly predictable. Another reason is the axial variation of the lattice displacement, which also adds uncertainty in the determination of the pin coordinates at each axial level in the core.

It is clearly of interest to investigate the impact of the sub-assembly pressing on the pin-power results. This has been done by re-calculating the HELIOS XSDB using the nominal pin coordinates and comparing the PRESTO-2 reconstructed total-fission rate distribution with the experimental results. The corresponding C/E comparison is shown in Figure 51.

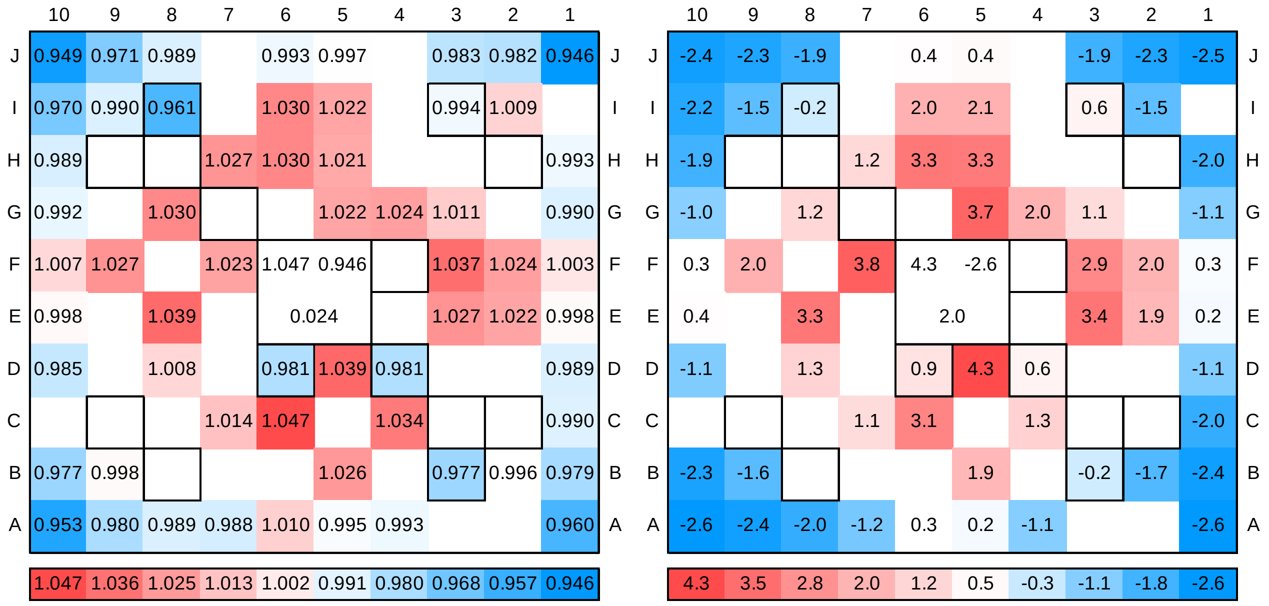

	10	9	8	7	6	5	4	3	2	1	
J	0.949	0.971	0.989		0.993	0.997		0.983	0.982	0.946	J
I	0.970	0.990	0.961		1.030	1.022		0.994	1.009		I
H	0.989			1.027	1.030	1.021				0.993	H
G	0.992		1.030			1.022	1.024	1.011		0.990	G
F	1.007	1.027		1.023	1.047	0.946		1.037	1.024	1.003	F
E	0.998		1.039		0.024			1.027	1.022	0.998	E
D	0.985		1.008		0.981	1.039	0.981			0.989	D
C				1.014	1.047		1.034			0.990	C
B	0.977	0.998				1.026		0.977	0.996	0.979	B
A	0.953	0.980	0.989	0.988	1.010	0.995	0.993			0.960	A
	1.047	1.036	1.025	1.013	1.002	0.991	0.980	0.968	0.957	0.946	

	10	9	8	7	6	5	4	3	2	1	
J	-2.4	-2.3	-1.9		0.4	0.4		-1.9	-2.3	-2.5	J
I	-2.2	-1.5	-0.2		2.0	2.1		0.6	-1.5		I
H	-1.9			1.2	3.3	3.3				-2.0	H
G	-1.0		1.2			3.7	2.0	1.1		-1.1	G
F	0.3	2.0		3.8	4.3	-2.6		2.9	2.0	0.3	F
E	0.4		3.3		2.0			3.4	1.9	0.2	E
D	-1.1		1.3		0.9	4.3	0.6			-1.1	D
C				1.1	3.1		1.3			-2.0	C
B	-2.3	-1.6				1.9		-0.2	-1.7	-2.4	B
A	-2.6	-2.4	-2.0	-1.2	0.3	0.2	-1.1			-2.6	A
	4.3	3.5	2.8	2.0	1.2	0.5	-0.3	-1.1	-1.8	-2.6	

Figure 51 Configuration I-1A, impact of the 0.51 mm sub-assembly pressing towards the central canal. Left picture: C/E values corresponding to the nominal pin coordinates. Right picture: percental differences with respect to the reference case, (pert.-ref.)x100.

It can be seen that the sub-assembly pressing produces a considerable perturbation in the total-fission rate map. Compared with the reference case, the use of nominal pin coordinates moves each sub-assembly 0.51 mm in both directions (x and y) away from the fuel element centre, producing a reduction of the moderation effect in the pins near the assembly corners, and hence reducing their power. On the other hand, pins surrounding the water canal and water wings experience increased moderation, which increases the power of these pins. From these results, it can be concluded that, for fuel elements of type SVEA-96 under full moderation conditions, a 0.051 cm displacement of the sub-assemblies affects the pin-powers by as much as about -2.6% to 4.3%.

It is important to note that the use of nominal pin coordinates, as is done in standard lattice calculations for power reactors, tends to reduce the fission rate in the pins near the lattice corners. For fresh fuel, as can be seen in Figure 47, it is the peripheral pins which develop the largest power, and may thus become limiting as regards pin-power related thermal parameters such as LHGR. Thus, the standard use of nominal pin coordinates in production calculations is seen to be somewhat non-conservative under these conditions. Inversely, if the limiting pins are located in the central part of the lattice, the situation is reversed, the use of nominal coordinates being conservative in this case.

The maximum, minimum and standard deviation of the C/E distribution in Figure 51 are 1.047, 0.946 and 2.4%, respectively. Compared with the reference case, the increase of the standard deviation from 1.3% to 2.4% clearly reflects the effect of the pin displacement caused by the sub-assembly pressing.

4.6 CASMO-5/SIMULATE-5 - Nodal diffusion in 2 and 5 groups

In addition to the HELIOS/PRESTO-2 calculations reported in the previous sections, the LWR-PROTEUS test zone has been modelled using the programme system CASMO-5/ SIMULATE-5. Also in this case, the modelling was done while keeping, as much as possible, the standard procedures that are applied in power reactor applications. A particular feature of SIMULATE-5 is the capability of solving the nodal diffusion problem in any number of energy groups. This feature has been used to investigate the effect of increasing the number of groups from two to five in the core calculation, which was not possible using the HE/P2 system.

4.6.1 Lattice calculations

Differently from the HELIOS case, the lattice calculations were performed with CASMO-5 using half-lattice geometry. This option was selected in order to preserve the procedure used in power reactor calculations. However, the displacement of the fuel assemblies, with respect to their nominal positions in the test zone (see Figure 35), was approximately accounted for by defining average wide and narrow gaps. The resulting half-gap sizes are shown, for the nine fuel assemblies, in Figure 52. The differences with respect to the values used in the HELIOS full-geometry calculation are shown, for the central assembly, in Table 15.

Table 15 Half-gaps used in the HELIOS and CASMO-5 lattice calculations for Configuration I-1A.

Half-gaps (cm)	West	North	South	East
HELIOS full-geometry	0.7185	0.7245	0.6845	0.6865
CASMO-5 half-geometry	0.7215	0.7215	0.6855	0.6855
Difference (C5-HE)	0.003	-0.003	0.001	-0.001

The differences shown in Table 15 suggest that approximation of the measured gaps by defining appropriate wide and narrow average values should not introduce any significant inaccuracy. This is indeed seen to be the case when one considers the analysis performed with HE/P2 concerning the gap size, presented in Subsection 4.5.5. According to this, a gap size variation of ~0.03 mm can be correlated with a change of about 0.1% in the calculated pin total-fission rate, which lies well within the experimental uncertainty band.

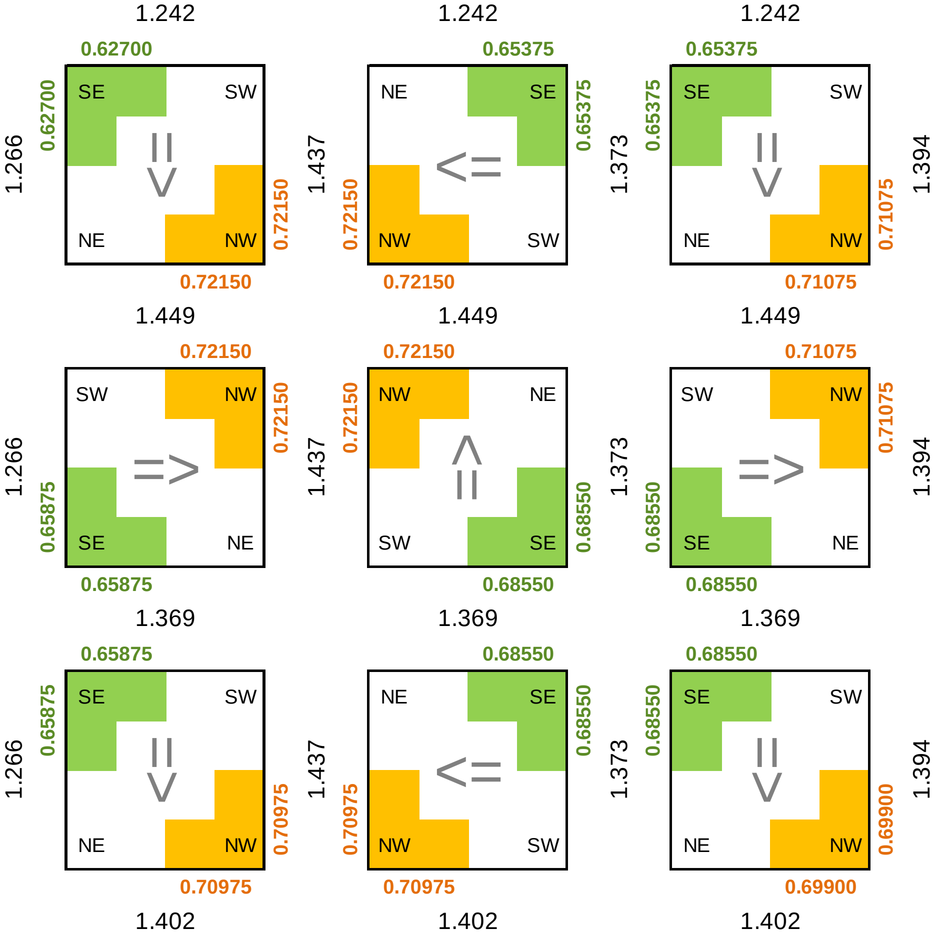

Figure 52 Gap sizes used in the CASMO-5 model for Configuration I-1A. For each assembly, the measured north and west half-gaps are averaged to give the wide half-gap size (orange numbers). Analogously, the experimental south and east values define the CASMO-5 narrow half-gap (green numbers). The black numbers between assemblies are the box-to-box distances, while those at the periphery represent twice the distance between the corresponding fuel box and the test-tank wall. All values are given in cm.

For the investigation of Configuration I-1A using C5/S5, two cross-section libraries were created, one with 2 and one with 5 energy groups. The 2-group library has a thermal cut-off energy of 0.625 eV, the group structure of the 5-group library being shown in Table 5, Subsection 3.4.1. For the latter, the group boundaries were defined in consistency with the 5-group structure of the PCRs, shown in Table 7, Subsection 3.6.1.

4.6.2 Core calculations

For the core calculations, the same nodalisation has been used for the test zone as in the HE/P2 case (see Figure 24). Furthermore, the test-zone boundary conditions, described by means of radial and axial PCRs, were analogous to those used in the HE/P2 calculations, depicted in

Figure 29. However, due to the fact that the SIMULATE-5 version used for this study only accepts a single PCR value per axial level, i.e. the sides and corners are not separated, the PCRs were calculated by integrating the partial currents over the whole test-zone perimeter. The PCRs used in the C5/S5 calculations for Configuration I-1A are shown in Table 9.

As discussed in Subsection 4.5.3, the impact of explicitly modelling the corner and side PCRs is very small. Thus, it can be said that, in Configuration I-1A, the radial albedo (PCR) input of S5 provides sufficient accuracy for the description of the test-zone boundary.

While the radial PCRs can be directly applied to the test-zone boundary by setting the number of reflector node layers to zero[30], the same cannot be done in the axial direction, since SIMULATE-5 expects one top and one bottom reflector layer. In the model used in this thesis, this input requirement was satisfied by defining two thin extra nodes (0.5 cm high each), with the lattice composition of the fuel, at the test-zone top and bottom faces. Thus, the top and bottom axial PCRs, shown in Table 9, were applied to the outer surfaces of the two thin extra nodes.

The SIMULATE-5 sub-nodalisation, by which the nodes are internally subdivided to better describe the intra-nodal radial flux shape, was kept at the standard value of 5 (i.e. 5 subdivisions in the x and y directions).

4.7 Radial comparisons of total-fission rates - CASMO-5/SIMULATE-5

For Configuration I-1A, C/E comparisons have been made using the C5/S5 model described above, while employing two and five energy groups. The results of these comparisons are shown in the following subsections.

4.7.1 Calculation in 2 energy groups

The C/Es obtained with SIMULATE-5 in 2 energy groups are shown on the left hand side of Figure 53, while the percental differences with respect to the PRESTO-2 reference case are presented on the right hand side. The reconstructed total-fission rates calculated with SIMULATE-5 agree well with the measurements. The maximum, minimum and standard deviation of the C/Es are 1.021, 0.968 and 1.1%, respectively, which are similar to the values obtained with PRESTO-2, presented in Figure 42 in Subsection 4.5.1 (1.024, 0.963 and 1.3%, respectively). In fact (see Figure 53), the C5/S5 and HE/P2 results agree within ~1% for all pins. As in the case of HE/P2, the fission rate in pins containing gadolinium is underestimated, most strongly in position I8 (3.2%). As is the case for HELIOS, these deviations originate in the CASMO-5 calculation and do not relate, in a significant manner, to the 3D nodal solution.

However, certain trends that are specific to the C5/S5 code system can be identified. In the C5/S5 case, the fission rates of the corner pins are ~1% closer to the measured values than for HE/P2, the maximum deviation being -2.0% in pin J1, while in HE/P2 the C/E deviation in the same pin reaches -2.9%. On the other hand, as was the case also for HE/P2, some underestimation of the total-fission rate in pins adjacent to the central water canal can be

---

[30] In SIMULATE power reactor models, the reflector region is described by an extra layer of nodes. In the case of SIMULATE-5, in addition, albedo boundary conditions can be defined at the outer surface of the reflector. In the LWR-PROTEUS model, no reflector nodes were defined in the radial direction, the PCRs being applied directly to the test-tank inner walls.

observed. For instance, in pins G5, F7 and D5, which do not contain gadolinium, C5/S5 underestimates the measurements by between 1.2% and 1.8%, the same pins being underestimated in the HE/P2 case by 0.4% to 1.5%, i.e. somewhat less strongly.

As with HE/P2, the C5/S5 calculations show that 3D nodal diffusion in 2 energy groups, with pin reconstruction, delivers accurate results for the test assembly in the regular Configuration I-1A.

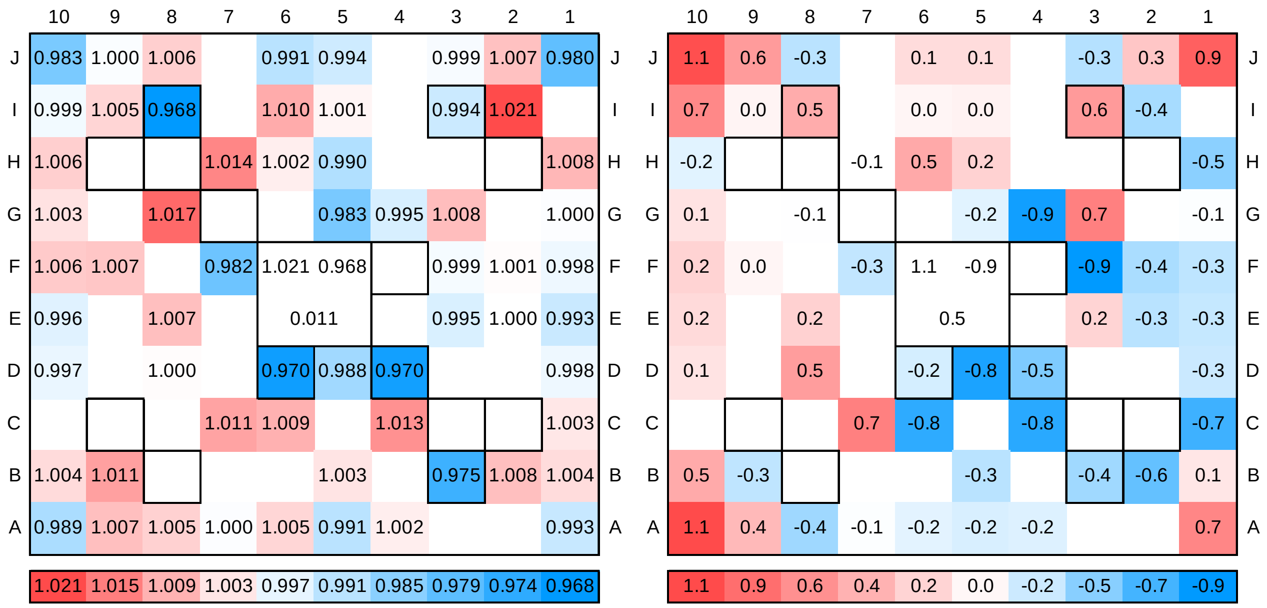

	10	9	8	7	6	5	4	3	2	1	
J	0.983	1.000	1.006		0.991	0.994		0.999	1.007	0.980	J
I	0.999	1.005	0.968		1.010	1.001		0.994	1.021		I
H	1.006			1.014	1.002	0.990				1.008	H
G	1.003		1.017			0.983	0.995	1.008		1.000	G
F	1.006	1.007		0.982	1.021	0.968		0.999	1.001	0.998	F
E	0.996		1.007		0.011			0.995	1.000	0.993	E
D	0.997		1.000		0.970	0.988	0.970			0.998	D
C				1.011	1.009		1.013			1.003	C
B	1.004	1.011				1.003		0.975	1.008	1.004	B
A	0.989	1.007	1.005	1.000	1.005	0.991	1.002			0.993	A

1.021	1.015	1.009	1.003	0.997	0.991	0.985	0.979	0.974	0.968

	10	9	8	7	6	5	4	3	2	1	
J	1.1	0.6	-0.3		0.1	0.1		-0.3	0.3	0.9	J
I	0.7	0.0	0.5		0.0	0.0		0.6	-0.4		I
H	-0.2			-0.1	0.5	0.2				-0.5	H
G	0.1		-0.1			-0.2	-0.9	0.7		-0.1	G
F	0.2	0.0		-0.3	1.1	-0.9		-0.9	-0.4	-0.3	F
E	0.2		0.2		0.5			0.2	-0.3	-0.3	E
D	0.1		0.5		-0.2	-0.8	-0.5			-0.3	D
C				0.7	-0.8		-0.8			-0.7	C
B	0.5	-0.3				-0.3		-0.4	-0.6	0.1	B
A	1.1	0.4	-0.4	-0.1	-0.2	-0.2	-0.2			0.7	A

1.1	0.9	0.6	0.4	0.2	0.0	-0.2	-0.5	-0.7	-0.9

Figure 53 Configuration I-1A, SIMULATE-5 calculation in 2 energy groups. Left picture: C/E values. Right picture: percental differences with respect to the PRESTO-2 reference case, (S5-P2ref.)x100.

4.7.2 Calculation in 5 energy groups

Figure 54 shows the C/E results of SIMULATE-5 in the 5 energy-group case. On the right hand side, the percental differences with respect to the 2 energy-group case are shown.

In general terms, it can be said that increasing the number of groups used for the solution of the nodal diffusion problem has a small impact on the C/E results for Configuration I-1A. The maximum, minimum and standard deviation of the C/Es are 1.020, 0.967 and 1.1%, respectively, very similar to the results obtained with 2 energy groups.

However, a clear systematic trend can be observed. Compared with the 2-group case, the total-fission rate at the corner with larger gaps (NW) is increased by 0.2% while it is decreased by a similar amount (0.3%) at the opposite corner. Since the only difference between both calculations is the number of groups used in S5 and the corresponding PCR matrices, the tilt observed can only be caused by spectral effects. Furthermore, the comparisons presented in Subsection 4.5.3, where the 02/05 PMCFs are applied to the HE/P2 results, show that only changing the number of groups used for the PCRs produces a small tilt in the same direction. As shown in Figure 48, the 02/05 PMCFs are 0.2% lower in the SE corner than in the NW corner. Thus, the 0.5% tilt observed in Figure 54, right hand side map, when passing from 2 to 5 energy groups, may be subdivided into two contributions: one is the use of 5-group PCRs (an effect of

~0.2%), the other is the application of 5-group nodal diffusion (~0.3%)[31]. Furthermore, the underestimation observed in pins G5, F7 and D5, discussed in Subsection 4.7.1, is reduced by 0.2% to 0.3% when passing from 2 to 5 energy groups.

Thus, it can be concluded that, although the differences between the 2-group and the 5-group calculations are small, the use of 5 energy groups leads to certain specific improvements in the C/E comparison. However, due to their small magnitude, these improvements do not affect the standard deviation of the C/Es, which remains at 1.1%.

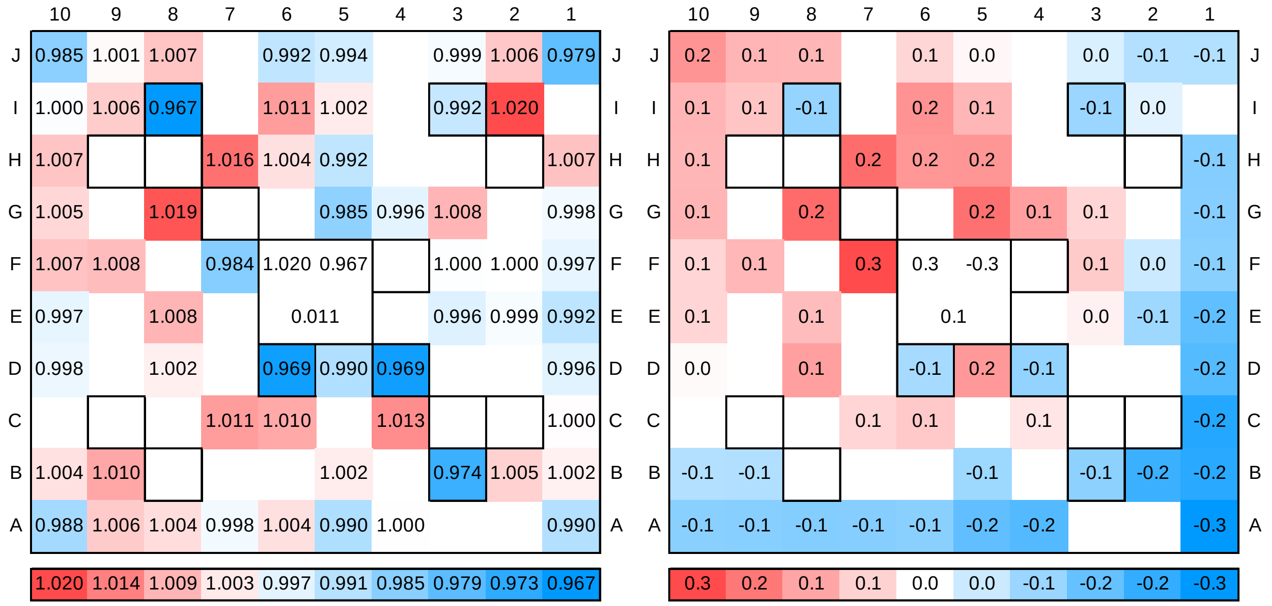

	10	9	8	7	6	5	4	3	2	1	
J	0.985	1.001	1.007		0.992	0.994		0.999	1.006	0.979	J
I	1.000	1.006	0.967		1.011	1.002		0.992	1.020		I
H	1.007			1.016	1.004	0.992				1.007	H
G	1.005		1.019			0.985	0.996	1.008		0.998	G
F	1.007	1.008		0.984	1.020	0.967		1.000	1.000	0.997	F
E	0.997		1.008		0.011			0.996	0.999	0.992	E
D	0.998		1.002		0.969	0.990	0.969			0.996	D
C				1.011	1.010		1.013			1.000	C
B	1.004	1.010				1.002		0.974	1.005	1.002	B
A	0.988	1.006	1.004	0.998	1.004	0.990	1.000			0.990	A

1.020	1.014	1.009	1.003	0.997	0.991	0.985	0.979	0.973	0.967

	10	9	8	7	6	5	4	3	2	1	
J	0.2	0.1	0.1		0.1	0.0		0.0	-0.1	-0.1	J
I	0.1	0.1	-0.1		0.2	0.1		-0.1	0.0		I
H	0.1			0.2	0.2	0.2				-0.1	H
G	0.1		0.2			0.2	0.1	0.1		-0.1	G
F	0.1	0.1		0.3	0.3	-0.3		0.1	0.0	-0.1	F
E	0.1		0.1		0.1			0.0	-0.1	-0.2	E
D	0.0		0.1		-0.1	0.2	-0.1			-0.2	D
C				0.1	0.1		0.1			-0.2	C
B	-0.1	-0.1				-0.1		-0.1	-0.2	-0.2	B
A	-0.1	-0.1	-0.1	-0.1	-0.1	-0.2	-0.2			-0.3	A

0.3	0.2	0.1	0.1	0.0	0.0	-0.1	-0.2	-0.2	-0.3

Figure 54 Configuration I-1A, SIMULATE-5 calculation in 5 energy groups. Left picture: C/E values. Right picture: percental differences with respect to the 2 energy-group case, (S5_5g-S5_2g)x100.

4.8 Verification of the axial flux curvature

Figure 55 shows the comparison, between MCNPX, PRESTO-2, SIMULATE-5[32] and experiment, of the axial fission rate distribution in pin position E2. For this measurement, the fuel pin was replaced by a stainless steel guide tube, inside which a miniature fission chamber was moved axially over the core height. A total of 22 points were measured between -30 and 60 cm relative to the core midplane. The experimental results are normalized to 1.0, and the calculated values are scaled to give the same average for the measured axial positions. It should be mentioned that two spacers, each 2.6 cm high, were located within the active height of the test zone, at approximately ±30 cm with respect to the core midplane. The effect of these spacers can be seen in the MCNPX and measured fission rate profiles, in the form of two small depressions at the corresponding positions. Since the C/E comparisons only concern the radial distribution at

---

[31] The trends being relatively weak, this division may appear a bit speculative. However, it is clear that the trend is qualitatively similar, but more pronounced, in the SIMULATE-5 5-group calculation than when alone the 02/05 PMCFs are applied.

[32] The SIMULATE-5 results shown here correspond to the 2-group calculation. The differences with respect to the 5-group case are negligible.

core midplane, the spacers were not included in the HE/P2 and C5/S5 models for Configuration I-1A. Concerning the verification of the axial flux curvature, it is observed from the MCNPX results that the spacer effect is small and has no significant impact on the comparison of the overall axial profiles. The standard deviations of the differences between calculation and measurement for the axial profile are 2.1%, 2.2% and 2.1% for MCNPX, PRESTO-2 and SIMULATE-5, respectively.

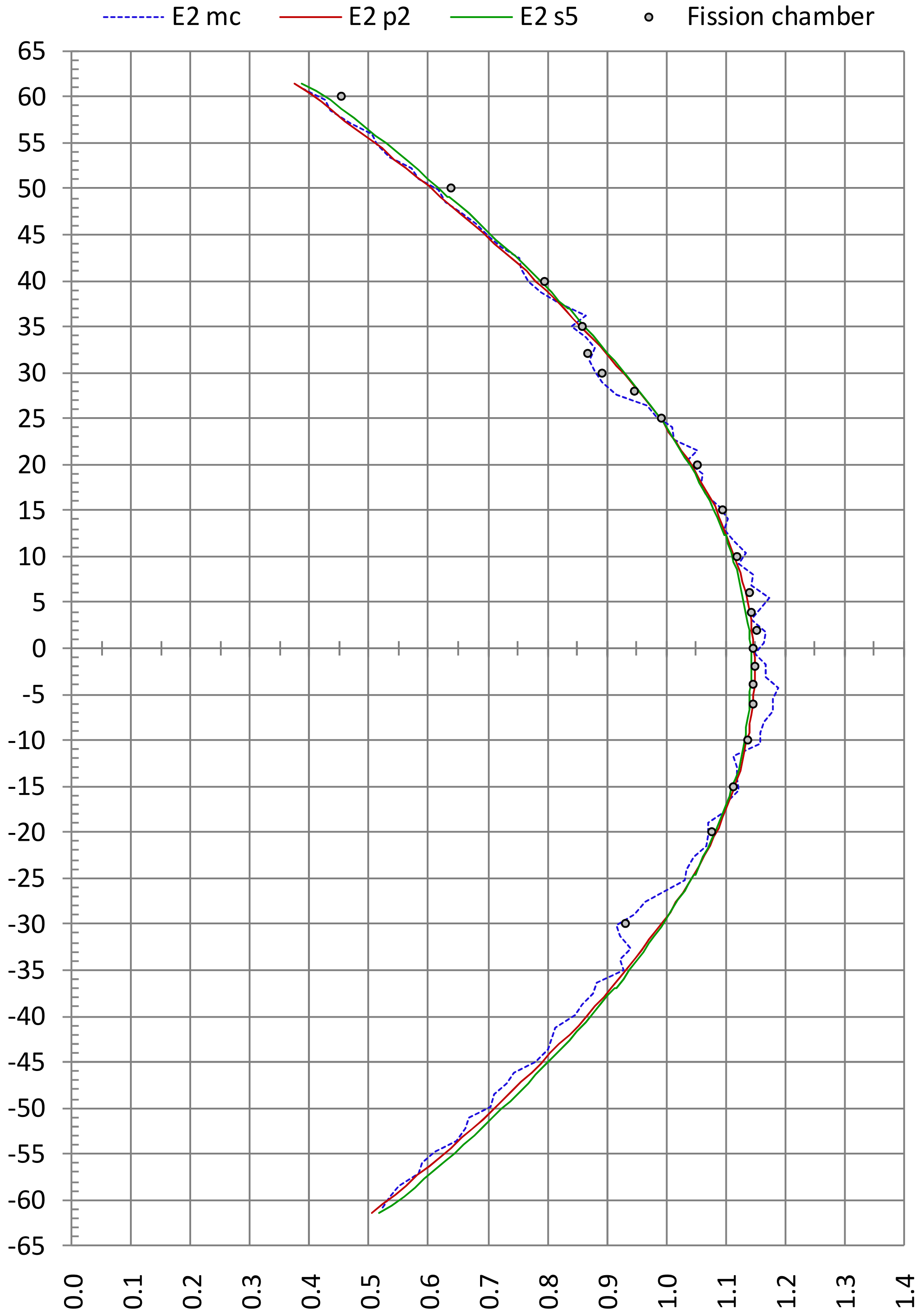

Figure 55 Configuration I-1A - Axial comparison of calculated total-fission rates with measured fission chamber results at pin position E2, for MCNPX (blue dashed line), PRESTO-2 (red line) and SIMULATE-5 with 2 energy groups (green line). All distributions were normalised to 1.0 over the 22 measured points.

4.9 k-effective

Although the LWR-PROTEUS whole-reactor k-effective values do not constitute the primary experimental evidence needed for validating pin-power reconstruction methodologies, they do provide a useful consistency check.

4.9.1 Principal results

Table 16 shows the k-effective values for Configuration I-1A corresponding to various calculated cases described in this chapter, together with the differences, in pcm, with respect to the MCNPX whole-reactor calculation and the PRESTO-2 reference case.

Table 16 The first column of numbers shows the PRESTO-2 (rows 2 to 10) and SIMULATE-5 (rows 11 and 12) k-effective results for Configuration I-1A. Column 2 shows the differences (expressed in pcm) with respect to MCNPX, the k-effective value for which is given in the first row of Column 1, followed in brackets by its 1σ uncertainty (in pcm). Column 3 shows the differences (in pcm), for all calculations with respect to the PRESTO-2 reference case.

	Calculated	Differences (pcm) with respect to	
	k-effective	MCNPX	P2 ref. case
MCNPX-2.6b with JEFF-3.1 library	1.00120 (12)	0	-1046
P2 reference case (ENDF/B-VI v1 and v3)	1.01166	1046	0
P2 190 groups "unadjusted" library	1.00821	701	-345
P2 infinite medium (B^2=0) spectrum	1.01210	1090	44
P2 collision probabilities k=0	1.01238	1118	72
P2 finer pin subdivision	1.01179	1059	13
P2 thermal cut-off 0.625 eV	1.01386	1266	220
P2 HELIOS whole-reactor PCRs (radial)	1.02839	2719	1673
P2 nominal gaps (0.6900 cm)	1.01146	1026	-20
P2 no sub-assembly pressing	1.01463	1343	297
S5 two energy groups	1.01082	962	-84
S5 five energy groups	1.00825	705	-341

It can been seen that the k-effective values obtained with PRESTO-2 and SIMULATE-5, using the radial and axial PCRs calculated with MCNPX, are significantly higher than those obtained in the 3D MCNPX calculation. For the P2 reference case, the difference is 1046 pcm, while for S5 it is 962 and 705 pcm for the cases with 2 and 5 energy groups, respectively.

Part of these differences can be attributed to the cross-section library. The MCNPX calculations were made using JEFF-3.1, while the multigroup library used in HELIOS is based on ENDF/B-VI.1, VI.3 and VI.8, and includes an adjustment (reduction) in the resonance integral (RI) of ^{238}U. Using the unadjusted 190-group library in HELIOS (first sensitivity case), the k-effective is reduced by 345 pcm, so that the corresponding PRESTO-2 - MCNPX difference becomes 701 pcm. In a further step, the combined effect of the ^{238}U RI reduction and the number of energy groups was split into its two components by using a 47-group library analogous to that used in the reference case but without adjustment. This comparison showed that the RI adjustment alone reduces the k-effective by 228 pcm. Ignoring the second-order effects caused by the simultaneous application of both modifications, the further reduction due to the increase in the number of energy groups from 47 to 190 may thus be deduced as 117 pcm.

As mentioned in Subsection 3.4.1, CASMO-5 uses, for the calculation of the lattice parameters for SIMULATE-5, a 586-group cross-section library based on the ENDF/B-VII.0 data file. In the case of C5/S5, the overestimation of k-effective in comparison with MCNPX is somewhat smaller than in the case of HE/P2, the 5-group SIMULATE-5 calculation being 257 pcm closer to MCNPX than the 2-group case.

MCNPX calculations with ENDF/B-VI.1 have not been performed in the frame of this thesis, but previous MCNPX results for Configurations I-1A and I-2A using different nuclear data libraries [38] showed that ENDF/B-VI.2 delivers k-effective values which are very similar to (~40 pcm lower than) the present JEFF-3.1 results.

Another aspect to be considered in the comparison of k-effective values between P2, S5 and MCNPX is the description of the spacers. As mentioned in Section 4.8, two inconel spacer grids lie inside the modelled part of the test zone. In the P2 and S5 calculations for Configuration I-1A, the effect of these spacers was not accounted for. In the 3D MCNPX model, however, these have been included. To evaluate the impact of the spacers on the core reactivity, a parallel calculation including the two spacers was made with HE/P2, the combined effect of the two spacers being found to be -145 pcm.

From the above discussion, it can be concluded that the systematic overestimation of k-effective in the 3D nodal calculations is not caused by the nuclear data library or by spacer modelling alone. On the other hand, the modelling of the interaction between the test zone and the outer reactor regions, which is a very important factor in the context of the multi-zone layout of the PROTEUS reactor, plays an important role in the determination of k-effective. For example, only a 1.5% reduction in the fast PCR a_{11} is needed to reduce the k-effective calculated by P2 or S5 to the level of MCNPX.

4.9.2 Effect of the energy dependence of the PCRs

Due to the significantly different spectra occurring in the test zone and in the buffer, the partial currents at the boundary between them show a strong energy dependence. In the test zone, the neutron spectrum in the high energy range has a shape similar to the fission spectrum, whereas in the buffer the spectrum has a peak at around 0.5 MeV, below the threshold for inelastic scattering in the metallic fuel (no light isotopes are present in this region). For instance, for the 5-group structure shown in Table 7, the radial PCRs in group 2 (9.1 keV to 0.8 MeV) are significantly larger than one (see Table 9). This indicates that a strong incoming current occurs in this energy range. Hence, collapsing the partial currents into two groups (with a cut-off energy of 1.84 eV or 0.625 eV) leads to an overestimation of the importance of the incoming neutrons on the system reactivity, since the 0.5 MeV peak is distributed throughout the fast group and the probability of causing fission is larger in the low energy part of this group. The calculations performed with HELIOS on the 3x3 test zone, used for the determination of the PMCFs, show that the multiplication factor increases significantly when the test zone PCRs are described in two groups instead of five. This can be seen in Table 17, where the differences in k-effective calculated with the 2D HELIOS 3x3 test-zone model using different boundary conditions are shown[33]. The first column corresponds to two different spatial discretisation schemes with the same group structure, while the second column shows the impact of changing the number of groups without changing the spatial description. In the third column, both effects are combined.

Table 17 Configuration I-1A, k-effective changes in pcm caused by the PCR discretisation used in the 2D HELIOS calculation of the 3x3 test zone. The suffixes "s" and "g" denote perimeter segments and energy groups, respectively.

	48s/05g-02s/05g	02s/05g-02s/02g	48s/05g-02s/02g
Δ k-effective (pcm)	15	−691	−676

While the energy discretisation of the PCRs plays a significant role in the determination of k-effective, the spatial discretisation is practically irrelevant. As seen from Table 17, the impact of changing from 2 to 48 azimuthal segments per axial level affects the k-effective value by 15 pcm only. In principle, this result can be attributed to the azimuthally uniform character of Configuration I-1A. However, as will be shown in Chapter 5, Subsection 5.8.2, even for the case of the fully inserted control blade (Configuration I-2A), i.e. a case with strong azimuthal heterogeneity, the impact of the spatial discretisation of the PCRs on k-effective is quite small.

4.9.3 Effect of using PCRs from the 2D HELIOS whole-reactor model

This is a specific effect presented in Table 16, which merits separate discussion. Thus, it is seen from the table that, in comparison with the reference case, the usage of HELIOS PCRs yields a higher (1673 pcm) k-effective value. This is caused by an overestimation of the partial currents entering the test zone. As discussed in Section 4.4, the most significant difference between the MCNPX and HELIOS two-group PCRs occurs in the fast group, in which the PCRs calculated with HELIOS are 4% to 5% higher than those obtained with MCNPX, the axial leakage being the main responsible for this behaviour. The axial leakage of thermal neutrons being much lower, the impact of the thermal PCRs on the k-effective differences is less important.

4.9.4 Effect of the number of energy groups used in the C5/S5 calculations

A second specific effect seen in Table 16, which is of particular interest, is the comparison of the SIMULATE-5 k-effective results obtained with 2 and 5 energy groups. These k-effective values correspond to the calculations presented in Subsections 4.7.1 and 4.7.2, respectively.

As can be seen from Table 18, increasing the number of groups from 2 to 5 reduces the k-effective obtained with SIMULATE-5 by 257 pcm. Considered alone, this trend agrees with previous calculations performed by Studsvik Scandpower on KRITZ critical experiments [39], where the average k-effective over 10 cases was evaluated with SIMULATE-5[34] using different numbers of energy groups. In [39], the reported k-effective reduction when passing from a

---

[33] These differences correspond to the HELIOS cases run using the PCRs at the 5th axial level, i.e. the calculations from which the PMCFs were derived.

[34] At the time when the results were published, the name of the code was SIMULATE-4.

2-group model to an 8-group model, in both cases using the standard sub-mesh model of S5, is 445 pcm.

Table 18 k-effective values corresponding to the CASMO-5/SIMULATE-5 calculations performed in 2 and 5 energy groups for Configuration I-1A.

2 groups (cut-off 0.625 eV)	5 groups	Difference (5g-2g) (pcm)
1.01082	1.00825	−257

However, one important consideration must be made here. The KRITZ experiments consisted of a 4x4 array of 8x8 BWR fuel assemblies in different configurations, placed inside a square vessel filled with water at different temperatures [40]. Briefly described, this vessel was surrounded by a pressure tank, the space between them being filled with steam. For the experiments reported in [39], criticality was achieved by adjusting the boron concentration in the moderator. In contrast to LWR-PROTEUS, the 4x4 core in the KRITZ reactor was a single-zone critical configuration, i.e. there were no driver regions outside the 4x4 experimental zone. Hence, the core surroundings can, in this case, be approximately represented by black (zero incoming current) boundary conditions.

Thus, in the case of KRITZ, the k-effective comparisons show the pure effect of the number of groups on the nodal diffusion solution and its ability to predict the leakage in the small 4x4 core. In the case of LWR-PROTEUS, on the other hand, the additional effect of the test-zone surroundings, described by the PCRs, must be accounted for. Thus, the change in k-effective can be considered to be composed of two contributions: one originated in the nodal diffusion calculation, the other caused by the energy discretisation of the PCRs describing the test-zone boundary.

As discussed in Subsection 4.9.2, passing from 2 to 5 groups for the energy discretisation of the PCRs, reduces k-effective, in the case of the 2D HELIOS 3x3 test zone model, by 691 pcm (see Table 17). One is tempted to assume, that the energy discretisation of the PCRs has a similar impact on the k-effective calculated with S5. If this were the case, the impact of the nodal diffusion calculation alone could be estimated by subtracting the effect of the PCRs from the total k-effective change, i.e.

$$\Delta\, keff_{nodal\, diffusion} = \Delta\, keff_{total} - \Delta\, keff_{PCR}$$

$$(-257 + 691)\, pcm = 434\, pcm$$

Hence, the above assumption would lead to the conclusion that, compared with the 2-group case, the use of 5 groups in the nodal diffusion calculation increases the k-effective level by ~430 pcm, contradicting the evidence obtained in the KRITZ benchmark exercise reported in [39].

In consequence, the SIMULATE-5 k-effective results discussed here for LWR-PROTEUS indicate that the combined effect of group number on multigroup nodal diffusion and multigroup PCRs is in fact weaker than the corresponding effect on the 2D transport solution for the 3x3 test zone discussed in Subsection 4.9.2. The moderate combined effect on k-effective (257 pcm) also shows that, if the PCRs correctly describe the neutron balance across the test zone and its surroundings, the 2-group representation provides an adequate estimation of the reactivity of the system.

As shown in Subsections 4.7.1 and 4.7.2, the impact of the number of energy groups used in the nodal calculation on the pin-wise total-fission rate distribution is relatively small, which constitutes a relevant conclusion of this doctoral research. In this light, a deeper analysis of the PROTEUS whole-reactor k-effective behaviour, although an interesting aspect as such, clearly falls outside the scope of the present research, and will therefore not be further pursued.

4.10 Chapter summary and principal messages

This chapter was dedicated to the investigation of the capability of nodal methodologies with pin-power reconstruction to predict the radial distribution of pin-wise total-fission in a uniform array of 3x3 full-scale BWR fuel elements. For this purpose, results of the 3D nodal diffusion codes PRESTO-2 and SIMULATE-5 were compared against experimental evidence gained for Configuration I-1A during Phase I of the LWR-PROTEUS experimental programme. As a complement, transport results obtained with the stochastic programme MCNPX were also included in the comparisons.

For a uniform test zone arrangement such as that of Configuration I-1A, the use of reflected symmetry in the assembly calculations leads to very satisfactory results in the reconstructed pin-power map. The systematic underestimation observed in the corner and gadolinium pins stems mainly from the 2D transport calculation. The PMCFs are, in this case, very close to 1.0, indicating that the test zone boundary representation using uniform PCRs is quite adequate.

The agreement of radial total-fission rate distributions of both PRESTO-2 and SIMULATE-5 with experiment is good, as is also the agreement of MCNPX, the standard deviations of the C/Es being 1.3%, 1.1% (2 energy groups) and 1.1%, respectively. In the case of SIMULATE-5, the use of 5 energy groups for the nodal diffusion calculation leads to small improvements in the C/E values. However, due to the small magnitude of these improvements, the standard deviation of the C/Es remains 1.1%. In the axial direction, the global curvature of the flux across the test zone is accurately predicted by all three codes.

The sensitivity cases considered in relation to the assembly lattice description have shown that the effects on the C/E values are of relatively minor importance in general, suggesting that the models used in the transport calculation do not have a significant impact on the total-fission rate distribution. Among the individual effects considered, the most important have been found to be the assumed gap size between neighbouring assemblies and the consideration of the sub-channel pressing. In general, the cases investigated show that, under full moderation conditions at room temperature, a gap reduction of ~0.3 mm reduces the fission rate by ~1% in the pins facing the gap, while a displacement of the sub-assemblies by as little as ~0.5 mm away from the centre of the assembly affects the pin-powers by between −2.6% and 4.3%, depending on the lattice position and with a clearly systematic pattern.

From the investigations presented in this chapter, it can be concluded that the developed methodology of using 3D PCRs, calculated with a whole-reactor MCNPX model, offers a suitable platform for the utilisation of LWR-PROTEUS experimental results for the assessment of nodal methodologies with pin-power reconstruction, in regular fuel assembly arrays such as the test zone of Configuration I-1A. Furthermore, the observed relatively weak dependence on the accuracy of the applied test-zone boundary conditions has underlined the robustness of the considered experimental data.

Chapter 5

Full control blade insertion - Configuration I-2A

Westinghouse designed the first fully commercial PWR, Yankee Rowe, which started up in 1960 having an electrical power of 250 MWe. The plant operated until 1992.

This chapter presents the modelling details and results of the comparisons with experiment performed for LWR-PROTEUS Configuration I-2A, in which a L-shaped hafnium control blade is fully inserted at the north-west corner of the test zone's central SVEA-96+ assembly.

Section 5.1 describes the experimental set-up, while in Section 5.2 the particularities of the lattice modelling with HELIOS are presented. Section 5.3 addresses the representation of the test-zone boundary by means of partial currents obtained from 3D MCNPX whole-reactor calculations. As in the previous chapter, an alternative method for determining the test-zone boundary PCRs, based on a 2D HELIOS whole-reactor model has been considered, and this is described in Section 5.4. The results of the radial comparisons of total-fission rates using HELIOS/PRESTO-2 are presented and discussed in Section 5.5. As mentioned previously (Subsection 2.4.4), the CASMO-5/SIMULATE-5 route could not be applied to LWR-PROTEUS configurations with the L-shaped control blade inserted, and the corresponding reasons for having to omit the C5/S5 analysis of Configuration I-2A are recalled in Section 5.6. The verification of the axial flux profile in the test zone is presented in Section 5.7, while a discussion on the k-effective values obtained in the different calculations presented in this chapter is given in Section 5.8. Finally, the principal messages from the chapter are summarized in Section 5.9.

5.1 Description of the test zone

In Configuration I-2A, a fully inserted, L-shaped hafnium control blade (half of a real cruciform blade) is located at the north-west corner of the central fuel assembly. The aim of this experiment is the investigation of the radial and azimuthal heterogeneity caused by the presence of the control blade. The fuel elements, the axial position of the test-tank and the moderator (light water at room temperature) are the same as in Configuration I-1A.

Apart from the presence of the L-shaped control blade, the only difference between Configurations I-1A and I-2A is the size of the inter-assembly gaps. The measured gaps corresponding to Configuration I-2A are shown in Figure 56. The position of the L-shaped control blade was such that its wings were not exactly centred in their respective gaps. Thus, the thickness of the blade being 0.805 cm, the distance between its central plane and the central assembly fuel box is 0.805/2+0.275 = 0.6775 cm for the north gap and 0.805/2+0.285 = 0.6875 cm for the west gap. This means that, with respect to the gap midplane, the central plane of the control blade is displaced towards the central fuel assembly by 0.7245−0.6775 = 0.047 cm for the north gap and by 0.7185−0.6875 = 0.031 cm for the west gap. However, since all lattice calculations performed in this thesis were made in single-assembly reflected geometry (see

Subsection 3.2.1), these displacements cannot be modelled if the size of the gaps is to be preserved. In fact, keeping the measured distances between control blade and assembly box, the gaps would be narrower than the real gap by 0.047x2=0.094 cm (north) and 0.031x2=0.062 cm (west). Since it is not possible to satisfy both conditions simultaneously, the preservation of the gap sizes was selected as modelling option, such that the control blade wings are always placed in the centre of the gap.

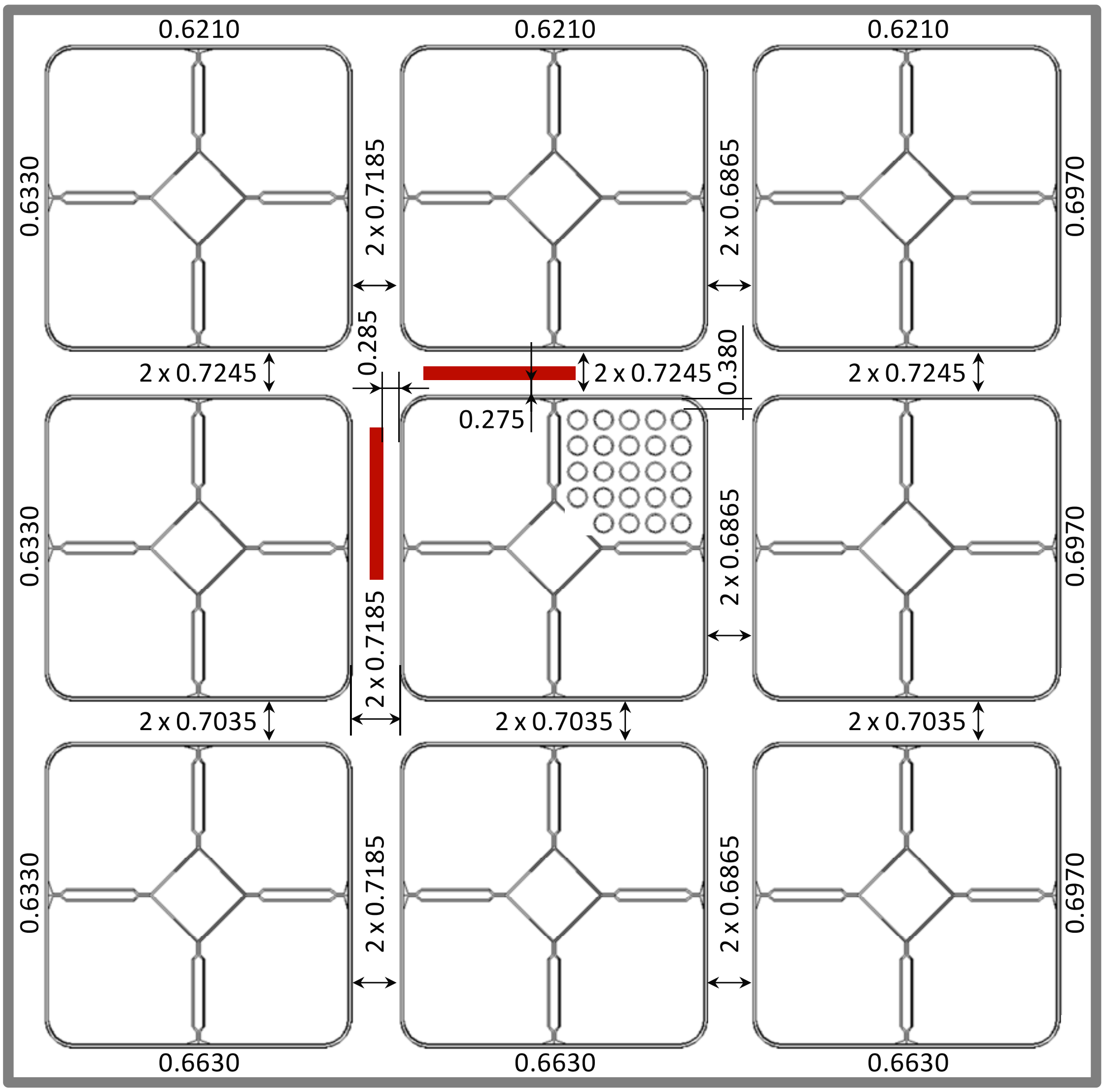

Figure 56 Measured dimensions in configuration I-2A. The distance between the outer surface of the cladding of the peripheral pins and the inner wall of the fuel box is 0.380 cm (sub-assembly pressed 0.051 cm towards the central canal). The wings of the control blade are separated from the outer surface of the central assembly fuel box by 0.275 cm and 0.285 cm for the north gap and the west gap, respectively.

5.2 Lattice calculations - HELIOS model

As for Configuration I-1A, the measured inter-assembly distances are accounted for by means of nine different sets of cross-sections, discontinuity factors and pin fission-rate maps, one for each of the nine fuel assemblies in the test zone. In Configuration I-2A, in addition, the central assembly is modelled with two control blade (CB) wings forming an "L" at the north-west corner. Its nearest neighbours, on the north and west sides, have one CB wing each. As shown in Figure 23 (see Subsection 3.2.2), this eliminates the fictitious CB wings that a full-blade representation would introduce in assemblies 2 and 4. Figure 57 shows the HELIOS models for the four basic lattice calculations which are needed: a) no CB (assemblies 1,3,6,7,8 and 9), b) one blade on the west side (assembly 2), c) one blade on the north side (assembly 4), d) two blades, on the north and west sides, respectively (assembly 5).

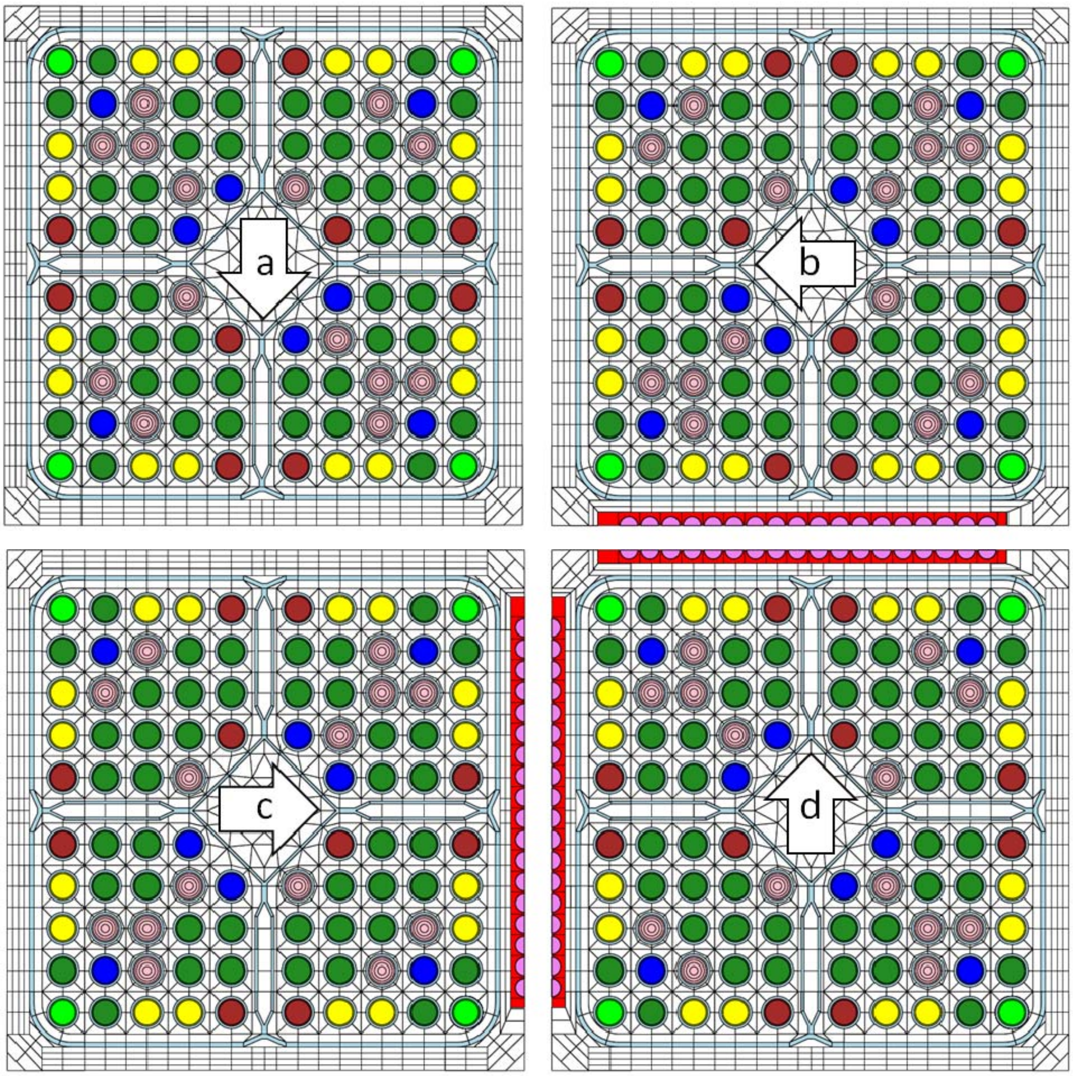

Figure 57 HELIOS models for the four basic lattice calculations needed in Configuration I-2A. Following the numbering depicted in Figure 23, these are: a) no CB (assemblies 1,3,6,7,8 and 9), b) one blade on the west side (assembly 2), c) one blade on the north side (assembly 4), d) two blades, on the north and west sides, respectively (assembly 5). Note: the denominations N, S, E, W refer always to the standard orientation used in the lattice calculation, i.e. with the vertex of the CB in the top-left (NW) corner.

5.2.1 Reference and sensitivity cases

Analogously to Configuration I-1A, a reference case, featuring the standard modelling options used at KKL, has been used as basis for the analysis of a number of sensitivity cases. The general characteristics of the reference case and the different sensitivity calculations are the same as those corresponding to Configuration I-1A, described in Subsections 4.2.1 and 4.2.2, respectively.

5.3 Test-zone boundary conditions using the 3D MCNPX model

The test-zone boundary conditions were determined using a 3D MCNPX model of Configuration I-2A, in full analogy with the procedure used for Configuration I-1A, described in Section 4.3. In the controlled case, however, the presence of the control blade produces a larger impact on the azimuthal distribution of the PCRs across the test-zone perimeter.

Analogously to Figure 36 for the case without CB, an example of the tally discretisation showing the partial currents and corresponding PCRs at the 5th axial level (node layer immediately below the core midplane) in energy group 2 (between 9.12 keV and 0.82 MeV) is shown in Figure 58. As in the case of Configuration I-1A (Section 4.3), the large PCR values occurring in this energy group are due to the strong fast current entering the test zone (see Subsection 5.3.3).

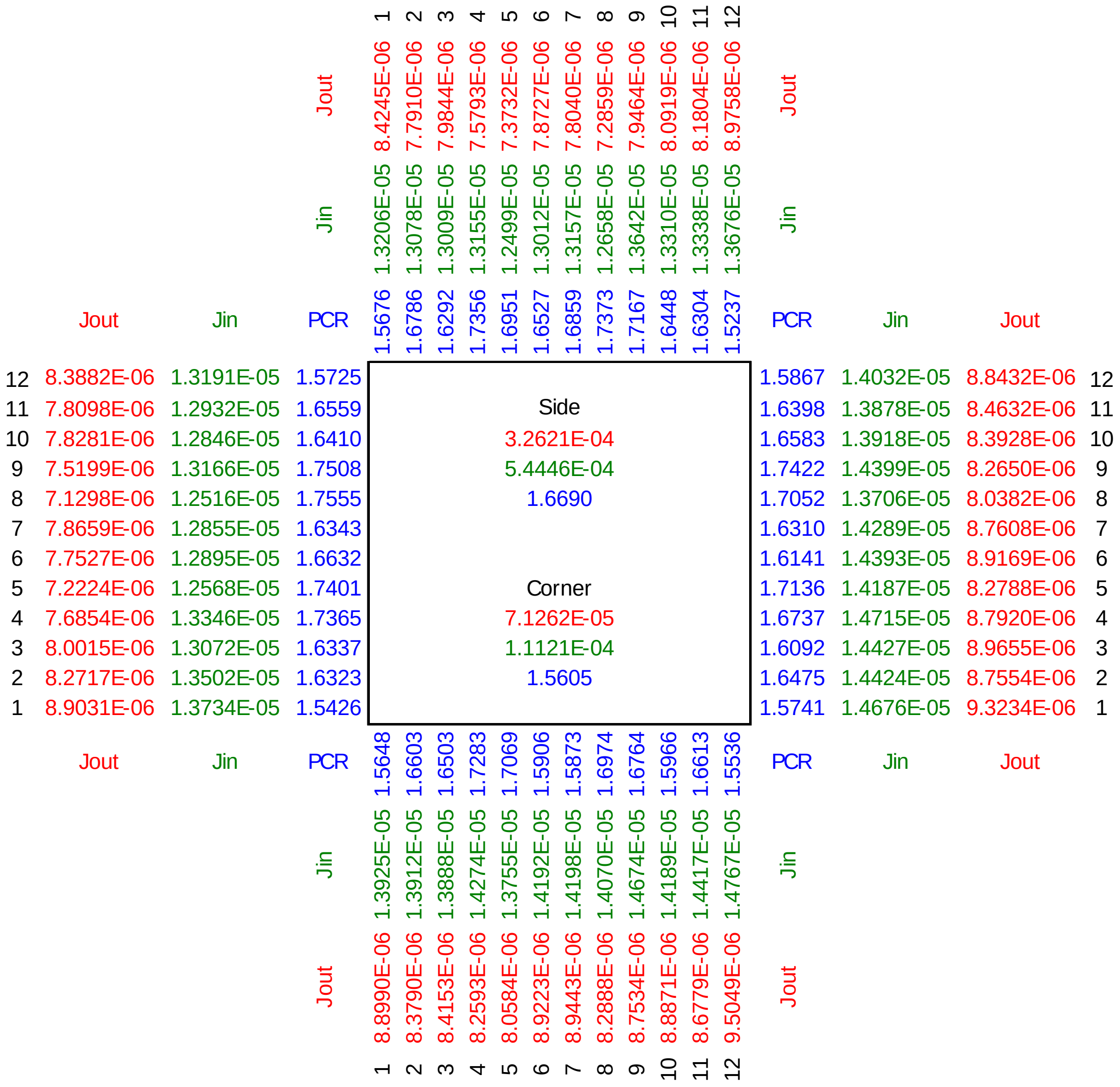

	PCR	Jin	Jout
1	1.5676	1.3206E-05	8.4245E-06
2	1.6786	1.3078E-05	7.7910E-06
3	1.6292	1.3009E-05	7.9844E-06
4	1.7356	1.3155E-05	7.5793E-06
5	1.6951	1.2499E-05	7.3732E-06
6	1.6527	1.3012E-05	7.8727E-06
7	1.6859	1.3157E-05	7.8040E-06
8	1.7373	1.2658E-05	7.2859E-06
9	1.7167	1.3642E-05	7.9464E-06
10	1.6448	1.3310E-05	8.0919E-06
11	1.6304	1.3338E-05	8.1804E-06
12	1.5237	1.3676E-05	8.9758E-06

	Jout	Jin	PCR
12	8.3882E-06	1.3191E-05	1.5725
11	7.8098E-06	1.2932E-05	1.6559
10	7.8281E-06	1.2846E-05	1.6410
9	7.5199E-06	1.3166E-05	1.7508
8	7.1298E-06	1.2516E-05	1.7555
7	7.8659E-06	1.2855E-05	1.6343
6	7.7527E-06	1.2895E-05	1.6632
5	7.2224E-06	1.2568E-05	1.7401
4	7.6854E-06	1.3346E-05	1.7365
3	8.0015E-06	1.3072E-05	1.6337
2	8.2717E-06	1.3502E-05	1.6323
1	8.9031E-06	1.3734E-05	1.5426

Side
3.2621E-04
5.4446E-04
1.6690

Corner
7.1262E-05
1.1121E-04
1.5605

PCR	Jin	Jout	
1.5867	1.4032E-05	8.8432E-06	12
1.6398	1.3878E-05	8.4632E-06	11
1.6583	1.3918E-05	8.3928E-06	10
1.7422	1.4399E-05	8.2650E-06	9
1.7052	1.3706E-05	8.0382E-06	8
1.6310	1.4289E-05	8.7608E-06	7
1.6141	1.4393E-05	8.9169E-06	6
1.7136	1.4187E-05	8.2788E-06	5
1.6737	1.4715E-05	8.7920E-06	4
1.6092	1.4427E-05	8.9655E-06	3
1.6475	1.4424E-05	8.7554E-06	2
1.5741	1.4676E-05	9.3234E-06	1

	PCR	Jin	Jout
1	1.5648	1.3925E-05	8.8990E-06
2	1.6603	1.3912E-05	8.3790E-06
3	1.6503	1.3888E-05	8.4153E-06
4	1.7283	1.4274E-05	8.2593E-06
5	1.7069	1.3755E-05	8.0584E-06
6	1.5906	1.4192E-05	8.9223E-06
7	1.5873	1.4198E-05	8.9443E-06
8	1.6974	1.4070E-05	8.2888E-06
9	1.6764	1.4674E-05	8.7534E-06
10	1.5966	1.4189E-05	8.8871E-06
11	1.6613	1.4417E-05	8.6779E-06
12	1.5536	1.4767E-05	9.5049E-06

Figure 58 Example of partial currents entering and leaving the test zone (green and red colour respectively) and PCRs (blue) for Configuration I-2A at axial level 5 in energy group 2 (9.12 keV to 0.82 MeV). The picture shows the spatial detail used for the MCNPX tallies. The side and corner values, as depicted in Figure 30, are shown inside the square representing the test-zone perimeter. These are calculated by integrating the partial currents over the corresponding segments.

Also in this case, the MCNPX calculations were performed using 200'000 particles and 250 cycles, i.e. 50×10^6 histories.

Following the same procedure as before, the PCRs were evaluated for the 10 axial levels of the test zone, depicted in Figure 29, and in the 2 and 5 energy group structures described in Table 7.

5.3.1 PCRs for PRESTO-2

The procedure used for the calculation of the radial PCRs needed for the PRESTO-2 modelling of Configuration I-2A is identical to that described in Subsection 4.3.1 for the case of Configuration I-1A. The results corresponding to the 5th axial level and 2nd energy group are shown inside the square representing the test-zone perimeter in Figure 58. As before, the PCRs were collapsed to two energy groups. Also for the calculation of the axial PCRs at the top and bottom core boundaries, the same procedure was used.

The PCRs for PRESTO-2 in Configuration I-2A, for 1.84 eV thermal cut-off energy, are shown in Table 19, the approximate 1σ statistical (relative) errors in % being indicated in brackets[35].

Table 19 PCRs for PRESTO-2 in Configuration I-2A, derived from the partial currents obtained in the 3D whole-reactor MCNPX calculation. The figures in brackets are the approximate 1σ statistical (relative) errors in %. As in the case of production applications at KKL, the HELIOS/PRESTO-2 calculations were performed using 1.84 eV as thermal cut-off energy.

Configuration I-2A Upper limit (eV)	PCR_{11} 20×10^6		PCR_{22} 1.84	
Axial direction at top	0.800 (0.05)		0.942 (0.1)	
Radial direction 1σ error (%)	Side (0.05)	Corner (0.3)	Side (0.2)	Corner (1.0)
Axial level 10	1.072	1.084	0.406	0.435
Axial level 9	1.079	1.085	0.406	0.435
Axial level 8	1.089	1.094	0.406	0.431
Axial level 7	1.094	1.099	0.405	0.430
Axial level 6	1.093	1.097	0.406	0.431
Axial level 5	1.093	1.094	0.405	0.432
Axial level 4	1.095	1.095	0.403	0.433
Axial level 3	1.094	1.095	0.404	0.432
Axial level 2	1.088	1.090	0.404	0.432
Axial level 1	1.074	1.080	0.406	0.439
Axial direction at bottom	0.841 (0.05)		0.960 (0.1)	

---

[35] The PCR relative errors are propagated from the 1σ statistical uncertainties of the MCNPX current tallies. Although these uncertainties slightly dependent on the axial level, a common approximate value, representing all levels, is defined to characterise the accuracy of the calculated PCRs.

5.3.2 Axial behaviour of the radial PCRs

As in the case of Configuration I-1A (see Subsection 4.3.3), the axially uniform character of Configuration I-2A leads to a relatively weak axial variation of the radial PCRs. This can be seen from Table 19 and in Figure 59, where the corresponding PCR values are presented graphically. Since in Configuration I-2A only the radial comparison of calculational and experimental results is of interest (all reaction rate measurements having been performed at the core midplane), the use of axially-uniform radial PCRs, obtained for example from 2D calculations by means of a HELIOS whole-reactor model, can also be justified. This alternative method will be discussed in Section 5.4, the corresponding results being presented in Subsection 5.5.3.

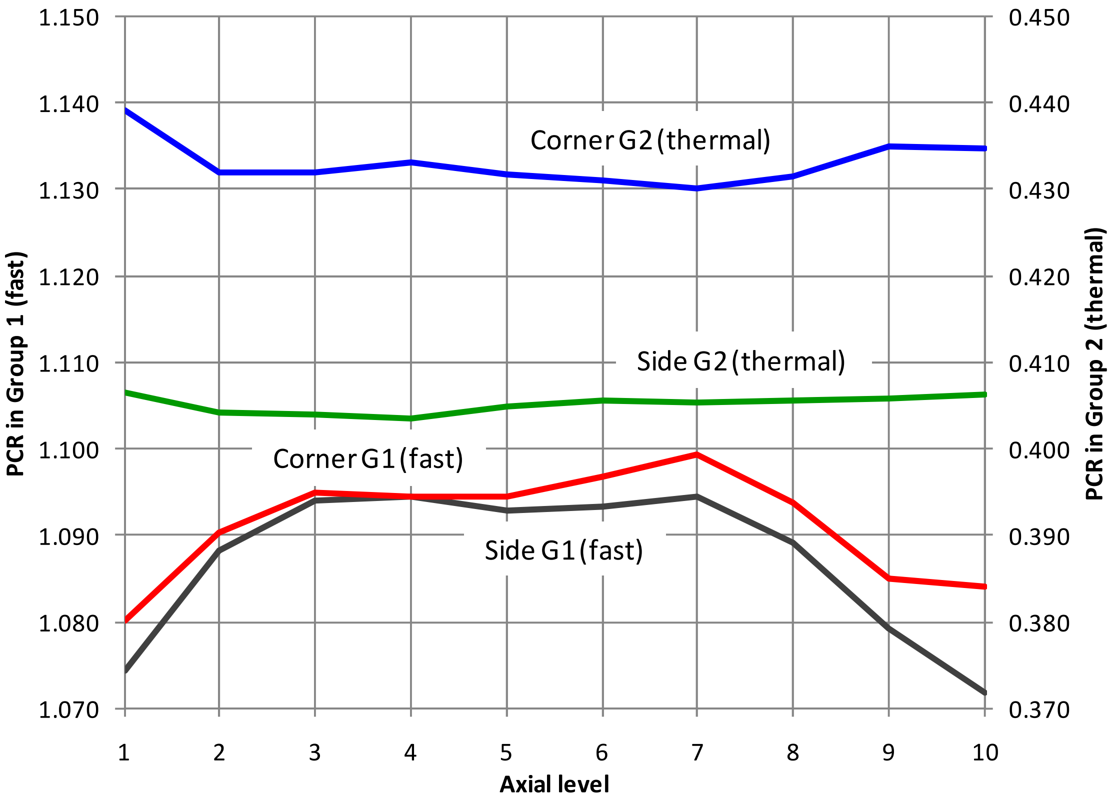

Figure 59 Axial variation of the radial PCRs in Configuration I-2A, as derived from the partial currents obtained in the 3D whole-reactor MCNPX calculation. The numerical values are shown in Table 19.

Comparing Figure 59 with Figure 37, between which the scale on the left only differs in terms of a shift of 0.1, it can be observed that the impact of the control blade insertion on the PCRs is smaller at the corners than along the sides. This is a geometrical effect that can be easily correlated to the relative distances of the perturbation (introduced by the control blade) to the surfaces forming the sides and corners, respectively (compare Figure 57 with Figure 30, Subsection 3.6.1).

Finally, one should point out the rather weak axial dependence of the radial PCRs in Configurations I-1A and I-2A. The fact that the epithermal PCRs have a somewhat more pronounced dependence reflects the different axial curvatures for the epithermal and thermal energy groups. For the former, the PCRs are larger in the central part of the test zone and decrease slightly towards the top and bottom regions of the core, while for the latter, a more uniform behaviour is observed.

5.3.3 Energy dependence of the partial currents and PCRs

Due to the presence of the control blade, the test zone is less reactive in Configuration I-2A than in Configuration I-1A, the driver zones (D_2O and graphite) thus playing a larger role in the system criticality. As to be expected, in order to set the reactor critical, a larger fuel loading is needed in the driver zones for Configuration I-2A than for Configuration I-1A.

As a consequence, the PCRs increase for the case with inserted control blade. The reason for this behaviour can be traced back to the changes affecting the partial currents crossing the test-zone radial boundary. Thus, while the outgoing currents significantly decrease due to the reduction of the fission rate caused by the presence of the control blade, the incoming currents, consisting of neutrons born in the buffer and driver regions, remain almost unchanged. Comparing the 2-group PCRs obtained in the controlled case (I-2A) with those corresponding to the case without control blade (I-1A) − Table 19 and Table 8, respectively − it can be seen that with the control blade insertion the epithermal PCRs (group 1) increase by about 10% for the sides and by 5.5% for the corners. In turn, the thermal PCRs (group 2) increase by 6% and 5% for the sides and corners, respectively.

As previously done in Subsection 4.3.4 for Configuration I-1A, Figure 60 shows the relative intensity of the partial currents in Configuration I-2A, calculated with the 3D MCNPX model in five energy groups, integrated over the complete test-zone radial boundary, i.e. summing over all sides and corners and over all axial levels, together with the corresponding PCRs. The reduction of the outgoing currents can be observed by comparing Figure 60 with Figure 38, where the partial currents and PCRs in Configuration I-1A are shown. To facilitate the comparison, the numerical values plotted in Figure 38 and Figure 60 are presented in Table 20.

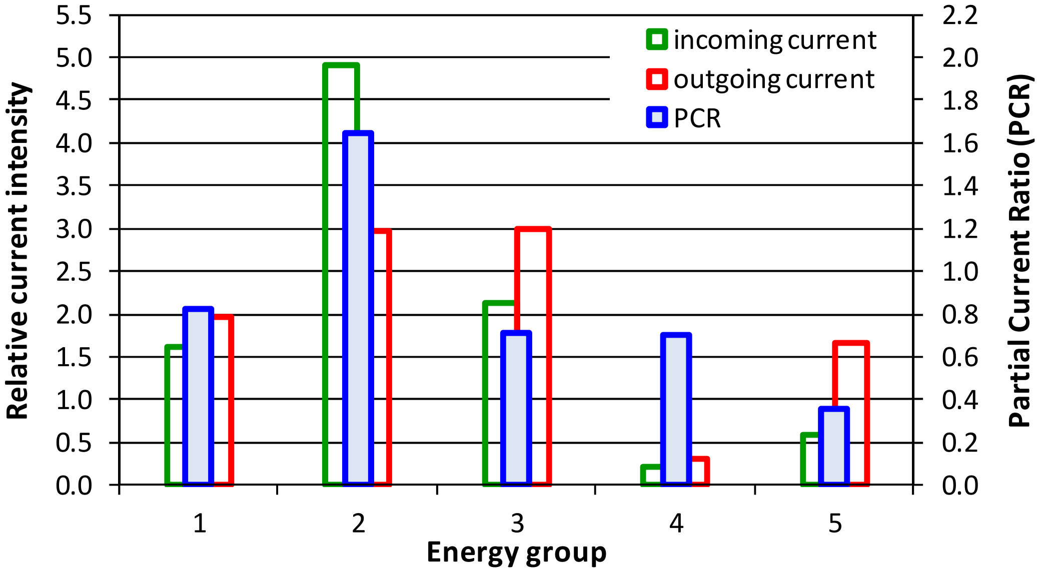

Figure 60 Energy dependence of the radial currents and PCRs in Configuration I-2A in five energy groups, derived from the partial currents obtained in the 3D whole-reactor MCNPX calculation. The partial currents were integrated over the complete test-zone boundary, i.e. by summing over all sides and corners and over all axial levels.

From Table 20, it can be seen that the increase of the PCRs due to the control blade insertion is more pronounced at higher energies. This is due to the longer mean free path (mfp) of higher energy neutrons, for which the coupling between different parts of the system is stronger.

Table 20 Partial currents and PCRs corresponding to the entire test-zone radial boundary in Configurations I-1A and I-2A, derived from the partial currents obtained in the 3D whole-reactor MCNPX calculation. The PCRs are given for the five and two (cut-off 1.84 eV) energy group structures shown in Table 7. The absolute and relative differences of the PCRs in Configurations I-1A and I-2A are given in the two bottom rows.

	5 energy groups					2 energy groups	
	Group 1	Group 2	Group 3	Group 4	Group 5	Group 1	Group 2
Upper limit (eV)	$20\text{x}10^6$	$821\text{x}10^3$	9119	1.84	0.625	$20\text{x}10^6$	1.84
Incoming Curr. I-1A Incoming Curr. I-2A	1.674 1.612	5.122 4.908	2.139 2.123	0.213 0.216	0.612 0.594	8.935 8.643	0.825 0.809
Outgoing Curr. I-1A Outgoing Curr. I-2A	2.353 1.968	3.345 2.977	3.247 2.984	0.333 0.308	1.806 1.671	8.945 7.928	2.138 1.979
PCR I-1A PCR I-2A	0.711 0.819	1.531 1.649	0.659 0.711	0.639 0.700	0.339 0.355	0.999 1.090	0.386 0.409
$\text{PCR I-2A} - \text{PCR I-1A}$	0.108	0.118	0.052	0.061	0.016	0.091	0.023
$\frac{\text{PCR I-2A}}{\text{PCR I-1A}} - 1$	15.2%	7.7%	7.9%	9.5%	4.7%	9.1%	6.0%

5.4 Test-zone boundary conditions using the 2D HELIOS model

Due to the axially uniform character of Configuration I-2A, the alternative procedure used to determine the radial PCRs by means of a 2D HELIOS model of the whole LWR-PROTEUS reactor (described for Configuration I-1A in Section 4.4) could also be applied in this case. The PCRs obtained with the 2D HELIOS whole-reactor model are shown in Table 21. In the axial direction (top and bottom boundaries of the test zone), the MCNPX PCRs were kept.

Table 21 Radial PCRs for PRESTO-2 in Configuration I-2A, derived from the partial currents obtained in the 2D whole-reactor HELIOS calculation. For comparison, the axially averaged PCRs, calculated by integrating over all axial levels the partial currents obtained with MCNPX, are shown in brackets. The last row shows the relative differences (HELIOS/MCNPX−1.0), expressed in %. The thermal cut-off energy is 1.84 eV.

	PCR_{11}		PCR_{22}	
Group upper limit (eV)	$20\text{x}10^6$		1.84	
	Side	Corner	Side	Corner
HELIOS PCRs in radial direction Axially averaged MCNPX PCRs	1.141 (1.090)	1.122 (1.093)	0.413 (0.405)	0.444 (0.433)
HELIOS/MCNPX−1.0	4.7%	2.7%	2.0%	2.5%

Comparing Table 21 with Table 10, it can be seen that in the controlled case the PCRs obtained with the 2D HELIOS model differ from those obtained with the 3D MCNPX model to about the same degree as in the case of Configuration I-1A. However, a small systematic increase in the relative differences (4.7% vs. 4.6%, 2.7% vs. 2.1%, 2.0% vs. 1.0% and 2.5% vs. 2.2%) is observed. This can be correlated to the larger contribution of the outer PROTEUS reactor regions to the neutron balance in the test zone when the control blade is inserted, due to which the axial leakage effect discussed in Section 4.4 gains importance.

5.5 Radial comparisons of total-fission rates - HELIOS/PRESTO-2

With the L-shaped hafnium control blade being totally inserted in the test zone, Configuration I-2A is axially uniform. Thus, as in the case of Configuration I-1A, the measurements in the central SVEA-96+ assembly were focused on the radial distribution of the pin-by-pin fission rate and were performed at the core midplane, thus minimising the influence of the top and bottom test-zone boundaries. In total, 64 pins were measured. The normalisation of the experimental and calculated total-fission rate distributions was done following the same procedure as in the case of Configuration I-1A (see Chapter 4, Section 4.5). Also in this case, for the calculated distributions, both axial averages over the entire active pin length and core midplane values were determined.

In Configuration I-2A, as expected for an axially uniform configuration, the ratio between the normalized axial average and core midplane values of the pin total-fission rates calculated with PRESTO-2 were found to lie within a narrow band, viz. between 0.999 and 1.003, for all 96 fuel pins of the central assembly. Thus, in the presence of a fully inserted control blade, the intra-nodal variable separation of the 3D heterogeneous flux, represented by equation {30}, shows the same level of accuracy as for the uncontrolled case, discussed in Section 4.5. Also, as expected and as discussed earlier, the same ratio (i.e. axial-average to midplane values) varies over a somewhat wider range in the case of MCNPX, viz. between 0.974 and 1.031. As in the case of Configuration I-1A, this is largely due to the statistical fluctuations of the tallies that cover the small pin segments centred at the core midplane. The pin-by-pin comparison between the normalised axial average and the normalised core midplane values of the pin-wise fission rates calculated with PRESTO-2 and MCNPX is shown in Figure 61.

As done for Configuration I-1A, a reference case, with the general characteristics described in Subsection 4.2.1, was set up to determine the agreement of the production model with the LWR-PROTEUS experimental data. The percental statistical uncertainties of the experimental values lay between 0.96% and 0.35%. As discussed in Section 4.5, the absolute error band of the C/E ratio is given for each pin by equation {48}.

As before, the reference case serves as a basis of comparison for the sensitivity studies, described in Subsection 4.2.2, with the purpose of quantifying the impact of changes in the lattice modelling, now in the presence of the hafnium control blade. Finally, the sensitivity of changes in the description of the test-zone boundary is also analysed. The results of these comparisons are presented in the following subsections.

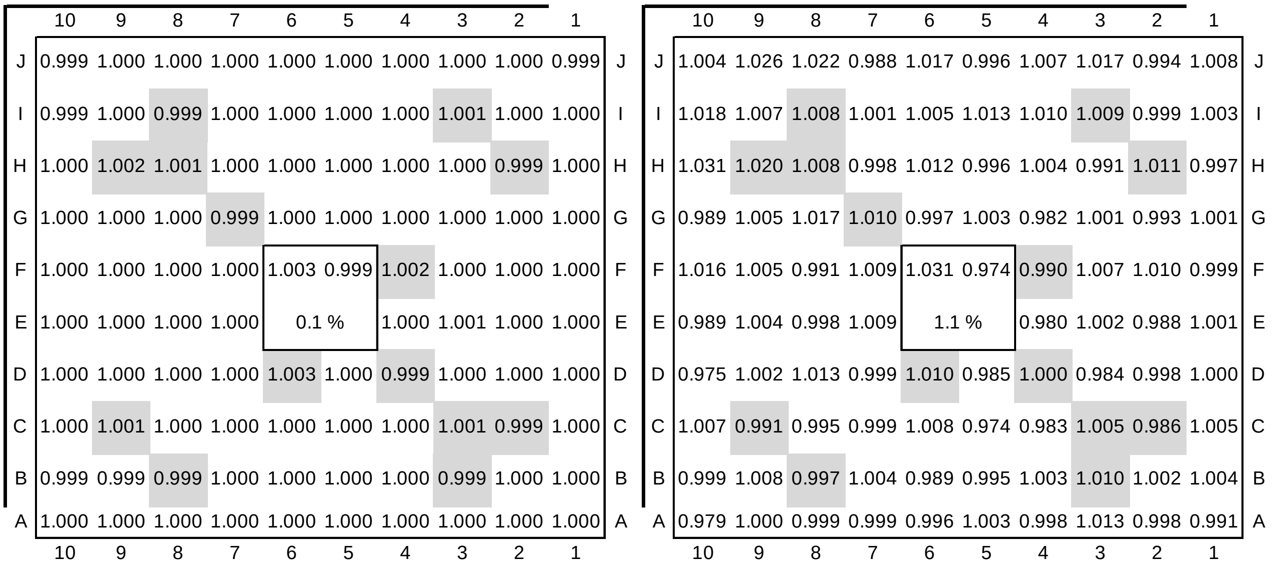

	10	9	8	7	6	5	4	3	2	1	
J	0.999	1.000	1.000	1.000	1.000	1.000	1.000	1.000	1.000	0.999	J
I	0.999	1.000	0.999	1.000	1.000	1.000	1.000	1.001	1.000	1.000	I
H	1.000	1.002	1.001	1.000	1.000	1.000	1.000	1.000	0.999	1.000	H
G	1.000	1.000	1.000	0.999	1.000	1.000	1.000	1.000	1.000	1.000	G
F	1.000	1.000	1.000	1.000	1.003	0.999	1.002	1.000	1.000	1.000	F
E	1.000	1.000	1.000	1.000	0.1 %		1.000	1.001	1.000	1.000	E
D	1.000	1.000	1.000	1.000	1.003	1.000	0.999	1.000	1.000	1.000	D
C	1.000	1.001	1.000	1.000	1.000	1.000	1.000	1.001	0.999	1.000	C
B	0.999	0.999	0.999	1.000	1.000	1.000	1.000	0.999	1.000	1.000	B
A	1.000	1.000	1.000	1.000	1.000	1.000	1.000	1.000	1.000	1.000	A
	10	9	8	7	6	5	4	3	2	1	

	10	9	8	7	6	5	4	3	2	1	
J	1.004	1.026	1.022	0.988	1.017	0.996	1.007	1.017	0.994	1.008	J
I	1.018	1.007	1.008	1.001	1.005	1.013	1.010	1.009	0.999	1.003	I
H	1.031	1.020	1.008	0.998	1.012	0.996	1.004	0.991	1.011	0.997	H
G	0.989	1.005	1.017	1.010	0.997	1.003	0.982	1.001	0.993	1.001	G
F	1.016	1.005	0.991	1.009	1.031	0.974	0.990	1.007	1.010	0.999	F
E	0.989	1.004	0.998	1.009	1.1 %		0.980	1.002	0.988	1.001	E
D	0.975	1.002	1.013	0.999	1.010	0.985	1.000	0.984	0.998	1.000	D
C	1.007	0.991	0.995	0.999	1.008	0.974	0.983	1.005	0.986	1.005	C
B	0.999	1.008	0.997	1.004	0.989	0.995	1.003	1.010	1.002	1.004	B
A	0.979	1.000	0.999	0.999	0.996	1.003	0.998	1.013	0.998	0.991	A
	10	9	8	7	6	5	4	3	2	1	

Figure 61 Ratio of the axially averaged and core midplane values of the pin-by-pin total-fission rate distributions in Configuration I-2A, corresponding to PRESTO-2 (left) and MCNPX (right). In the stochastic calculation (MCNPX), a relatively large dispersion (within ~ ±3%) occurs. This is mainly due to the statistical fluctuations in the small tally volumes at core midplane.

5.5.1 The reference case - PRESTO-2 and MCNPX C/E results

Figure 62 shows the calculation-to-experiment ratios (C/E), corresponding to the PRESTO-2 and MCNPX results obtained for the reference case in Configuration I-2A. The results of both calculations correspond to the axial average over the core axial length. The numbers indicated under each C/E value represent the absolute error band, according to equation {48}, expressed in permille.

As for Configuration I-1A, it is worth comparing the values at core midplane against the experimental results directly. The results of the comparisons using the calculated values at core midplane are shown in Figure 63. The corresponding PRESTO-2 C/E distribution (left hand side of the figure) will be used as reference for the comparisons related to the sensitivity cases, for which the calculated core midplane values have also been used.

Observing the C/Es corresponding to PRESTO-2 (left hand side of Figure 62 and Figure 63), a clear deviation caused by the presence of the control blade can be identified. In Configuration I-2A, the reflected geometry used in the lattice calculations leads to systematic underestimations of the total-fission rate in pins adjacent to the tip and vertex of the control blade. This is due to the fact that the reflected-assembly model implicitly places a complete cruciform control blade (four wings) adjacent to the north-west corner of the central assembly, as also in all adjacent control cells. Low total-fission rates at these locations are transferred to PRESTO-2, via the pin-wise maps, and thus affect the reconstructed local total-fission rate distribution.

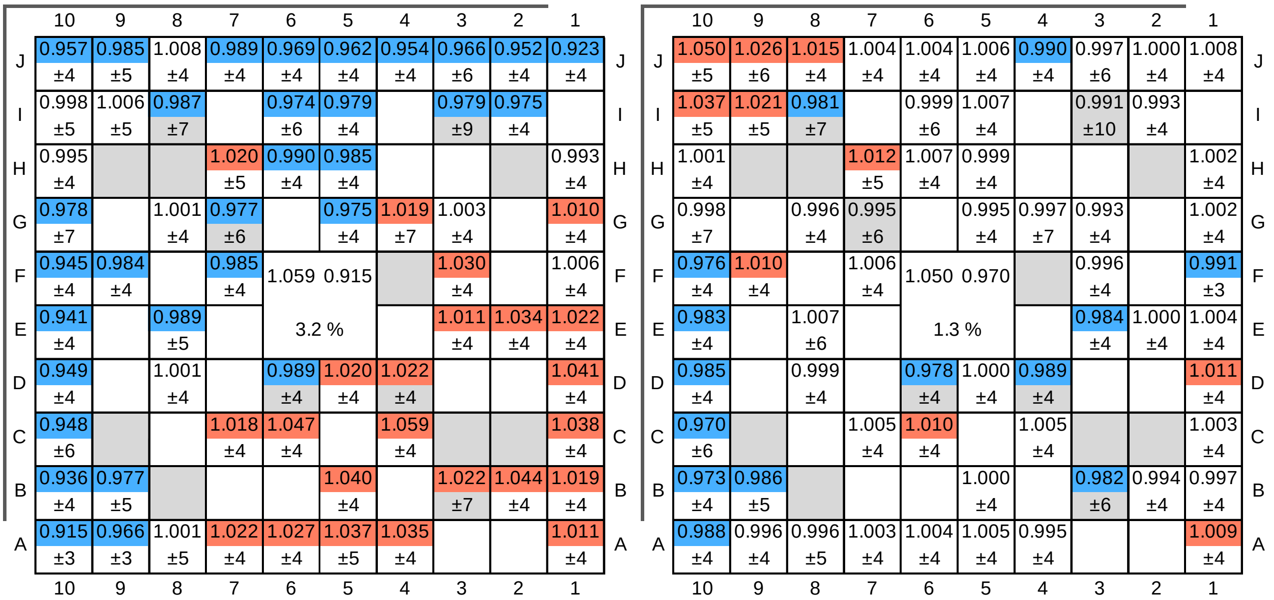

	10	9	8	7	6	5	4	3	2	1	
J	0.957 ±4	0.985 ±5	1.008 ±4	0.989 ±4	0.969 ±4	0.962 ±4	0.954 ±4	0.966 ±6	0.952 ±4	0.923 ±4	J
I	0.998 ±5	1.006 ±5	0.987 ±7		0.974 ±6	0.979 ±4		0.979 ±9	0.975 ±4		I
H	0.995 ±4			1.020 ±5	0.990 ±4	0.985 ±4				0.993 ±4	H
G	0.978 ±7		1.001 ±4	0.977 ±6		0.975 ±4	1.019 ±7	1.003 ±4		1.010 ±4	G
F	0.945 ±4	0.984 ±4		0.985 ±4	1.059	0.915		1.030 ±4		1.006 ±4	F
E	0.941 ±4		0.989 ±5		3.2 %			1.011 ±4	1.034 ±4	1.022 ±4	E
D	0.949 ±4		1.001 ±4		0.989 ±4	1.020 ±4	1.022 ±4			1.041 ±4	D
C	0.948 ±6			1.018 ±4	1.047 ±4		1.059 ±4			1.038 ±4	C
B	0.936 ±4	0.977 ±5				1.040 ±4		1.022 ±7	1.044 ±4	1.019 ±4	B
A	0.915 ±3	0.966 ±3	1.001 ±5	1.022 ±4	1.027 ±4	1.037 ±5	1.035 ±4			1.011 ±4	A
	10	9	8	7	6	5	4	3	2	1	

	10	9	8	7	6	5	4	3	2	1	
J	1.050 ±5	1.026 ±6	1.015 ±4	1.004 ±4	1.004 ±4	1.006 ±4	0.990 ±4	0.997 ±6	1.000 ±4	1.008 ±4	J
I	1.037 ±5	1.021 ±5	0.981 ±7		0.999 ±6	1.007 ±4		0.991 ±10	0.993 ±4		I
H	1.001 ±4			1.012 ±5	1.007 ±4	0.999 ±4				1.002 ±4	H
G	0.998 ±7		0.996 ±4	0.995 ±6		0.995 ±4	0.997 ±7	0.993 ±4		1.002 ±4	G
F	0.976 ±4	1.010 ±4		1.006 ±4	1.050	0.970		0.996 ±4		0.991 ±3	F
E	0.983 ±4		1.007 ±6		1.3 %			0.984 ±4	1.000 ±4	1.004 ±4	E
D	0.985 ±4		0.999 ±4		0.978 ±4	1.000 ±4	0.989 ±4			1.011 ±4	D
C	0.970 ±6			1.005 ±4	1.010 ±4		1.005 ±4			1.003 ±4	C
B	0.973 ±4	0.986 ±5				1.000 ±4		0.982 ±6	0.994 ±4	0.997 ±4	B
A	0.988 ±4	0.996 ±4	0.996 ±5	1.003 ±4	1.004 ±4	1.005 ±4	0.995 ±4			1.009 ±4	A
	10	9	8	7	6	5	4	3	2	1	

Figure 62 Configuration I-2A, reference case. C/E values (top number in each cell) corresponding to PRESTO-2 (left) and MCNPX (right), along with the experimental error band expressed in permille (bottom number). The C values correspond to the axial average of the calculated 3D distributions over each individual rod. The colour convention is identical to that used in Figure 41. The presence of the control blade is symbolised by bars adjacent to the north and west faces of the lattice.

In addition to this, a global tilt in the NW-SE direction is observed. This tilt, characterised by an underestimation of the fission rate at the NW corner and an overestimation at the SE corner, is partially caused by the non-uniformity of the PCRs at the outer edge of the test zone, which cannot be explicitly accounted for in the PRESTO-2 model. As will be shown later in Subsection 5.5.3, the tilt is significantly reduced through the application of the 48/05 PMCFs. Thus, the global NW-SE tilt, being principally caused by the lack of spatial detail in the test-zone boundary representation, is an effect which can be considered to be a consequence of the application of PRESTO-2 to LWR-PROTEUS, and should not be expected to occur in the modelling of a real BWR core.

It must also be underlined that the L-shaped control blade is a special feature of the LWR-PROTEUS experiments. Configuration I-2A, in this respect, is more challenging for the nodal and reconstruction methods than an actual BWR core, where the cruciform control blade is correctly represented by the reflected assembly lattice calculation. On the other hand, since during operation of a BWR only few control blades are inserted into the core, the reflection of these into the adjacent control cells is expected to underestimate the pin-power at the NE and SW corners as observed in the experimental configuration.

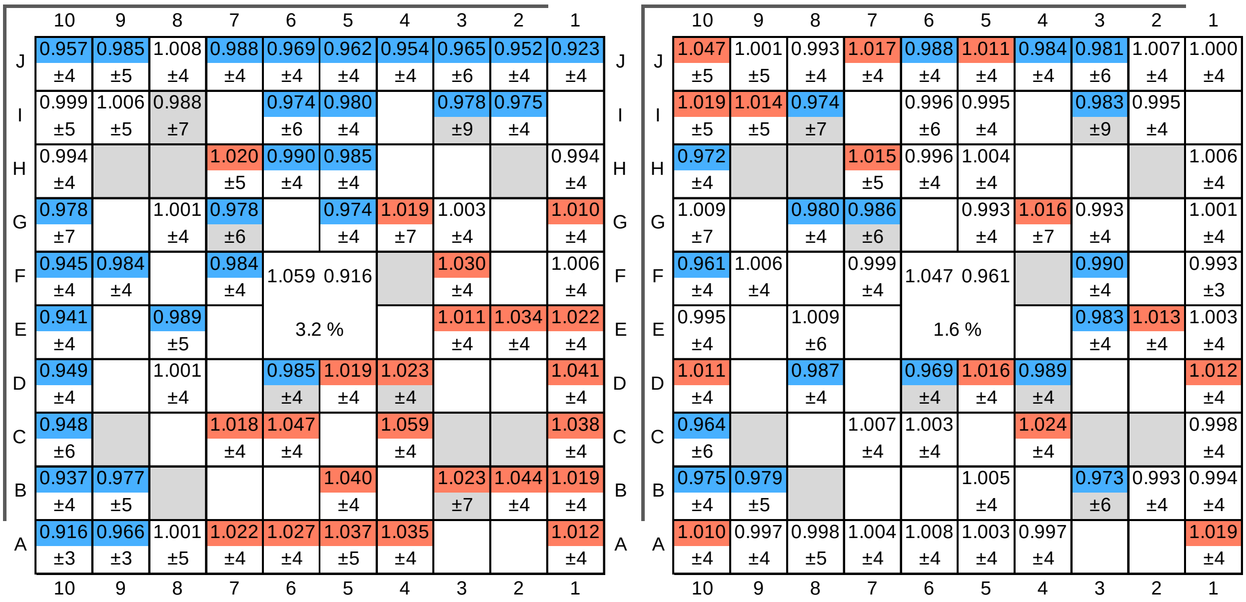

	10	9	8	7	6	5	4	3	2	1
J	0.957 ±4	0.985 ±5	1.008 ±4	0.988 ±4	0.969 ±4	0.962 ±4	0.954 ±4	0.965 ±6	0.952 ±4	0.923 ±4
I	0.999 ±5	1.006 ±5	0.988 ±7		0.974 ±6	0.980 ±4		0.978 ±9	0.975 ±4	
H	0.994 ±4			1.020 ±5	0.990 ±4	0.985 ±4				0.994 ±4
G	0.978 ±7		1.001 ±4	0.978 ±6		0.974 ±4	1.019 ±7	1.003 ±4		1.010 ±4
F	0.945 ±4	0.984 ±4		0.984 ±4	1.059	0.916		1.030 ±4		1.006 ±4
E	0.941 ±4		0.989 ±5		3.2 %			1.011 ±4	1.034 ±4	1.022 ±4
D	0.949 ±4		1.001 ±4		0.985 ±4	1.019 ±4	1.023 ±4			1.041 ±4
C	0.948 ±6			1.018 ±4	1.047 ±4		1.059 ±4			1.038 ±4
B	0.937 ±4	0.977 ±5				1.040 ±4		1.023 ±7	1.044 ±4	1.019 ±4
A	0.916 ±3	0.966 ±3	1.001 ±5	1.022 ±4	1.027 ±4	1.037 ±5	1.035 ±4			1.012 ±4

	10	9	8	7	6	5	4	3	2	1
J	1.047 ±5	1.001 ±5	0.993 ±4	1.017 ±4	0.988 ±4	1.011 ±4	0.984 ±4	0.981 ±6	1.007 ±4	1.000 ±4
I	1.019 ±5	1.014 ±5	0.974 ±7		0.996 ±6	0.995 ±4		0.983 ±9	0.995 ±4	
H	0.972 ±4			1.015 ±5	0.996 ±4	1.004 ±4				1.006 ±4
G	1.009 ±7		0.980 ±4	0.986 ±6		0.993 ±4	1.016 ±7	0.993 ±4		1.001 ±4
F	0.961 ±4	1.006 ±4		0.999 ±4	1.047	0.961		0.990 ±4		0.993 ±3
E	0.995 ±4		1.009 ±6		1.6 %			0.983 ±4	1.013 ±4	1.003 ±4
D	1.011 ±4		0.987 ±4		0.969 ±4	1.016 ±4	0.989 ±4			1.012 ±4
C	0.964 ±6			1.007 ±4	1.003 ±4		1.024 ±4			0.998 ±4
B	0.975 ±4	0.979 ±5				1.005 ±4		0.973 ±6	0.993 ±4	0.994 ±4
A	1.010 ±4	0.997 ±4	0.998 ±5	1.004 ±4	1.008 ±4	1.003 ±4	0.997 ±4			1.019 ±4

Figure 63 Configuration I-2A, reference case. C/E values (top number in each cell) corresponding to PRESTO-2 (left) and MCNPX (right), along with the experimental error band expressed in permille (bottom number). In this case, the C values correspond to the core midplane point of the calculated 3D distributions in each individual rod. The colour convention is identical to that used in Figure 41.

While for Configuration I-1A (Figure 41 and Figure 42) the C/Es obtained with PRESTO-2 and MCNPX show practically the same level of accuracy, the situation changes when a strong radial and azimuthal heterogeneity, such as the L-shaped control blade in Configuration I-2A, is introduced. Thus, and due to the effects discussed above, the standard deviation of the C/Es calculated with PRESTO-2 increases from 1.3% (I-1A) to 3.2% (I-2A).

As expected, the MCNPX results, which correspond to a high-order transport solution of the whole reactor, show approximately the same accuracy in both configurations[36]. Worth mentioning, however, is the overestimation observed in the pins near the control blade vertex (which is most clearly visible in the right hand side picture of Figure 62). This behaviour could be caused by the existence of small deviations in the ratio of water to structural material volumes in the control blade central-piece modelling.

5.5.2 Sensitivity cases concerning the lattice modelling

Also in Configuration I-2A, the impact of the changes considered for the study of the sensitivity to the lattice modelling have generally been found to be small, the results of the comparisons being shown in the following paragraphs. As in the case of Configuration I-1A, the most important effects, in a relative sense, are those related to the condensation spectrum and the current coupling.

---

[36] A small change is nevertheless observed. For the axially averaged case, the standard deviations of the C/Es are 1.1% and 1.3% for Configurations I-1A (Figure 41) and I-2A (Figure 62), respectively. For the core-midplane case, these are 1.3% and 1.6% for Configurations I-1A (Figure 42) and I-2A (Figure 63), respectively.

Cross-section library

The effect of using the 190-group HELIOS cross-section library is very similar to that observed in Configuration I-1A. The C/Es improve by 0.3% in the corner pins adjacent to the control blade and by 0.4% in the gadolinium pins close to the central water canal. There is no change in the other gadolinium pins, in the remaining pins adjacent to the inter-assembly gaps or in the uranium pins adjacent to the water canal. Also as before, small improvements occur in the inner part of the lattice. The maximum, minimum and standard deviation of the C/Es are 1.057, 0.919 and 3.1%, respectively, representing only a marginal improvement with respect to the reference case, shown on the left hand side of Figure 63. This result is as expected, confirming that the standard 47-group library correctly accounts for the spectral differences between the controlled and uncontrolled cases.

Condensation spectrum

The results corresponding to the use of the zero-leakage spectrum for the XS condensation in Configuration I-2A are shown in Figure 64. The maximum, minimum and standard deviation of the C/Es are 1.057, 0.918 and 3.3%, respectively.

As discussed in Subsection 4.5.2, since k-infinity > 1 in the uncontrolled configuration, the zero-leakage (infinite-medium) condensation spectrum in the case of Configuration I-1A decreases the fission rate in the gadolinium pins by approximately 1%, while the non-gadolinium pins remain practically unchanged. In the controlled case of Configuration I-2A, the central assembly has k-infinity < 1, so that use of the zero-leakage option for the cross-section condensation leads to a harder spectrum, which increases the fission rate in the gadolinium pins. As seen in Figure 64, this behaviour is manifested through positive differences occurring in the gadolinium pins (between +0.3 and +0.7%). The opposite behaviour in the regular and controlled cases underlines the importance of using the critical spectrum for the cross-section condensation.

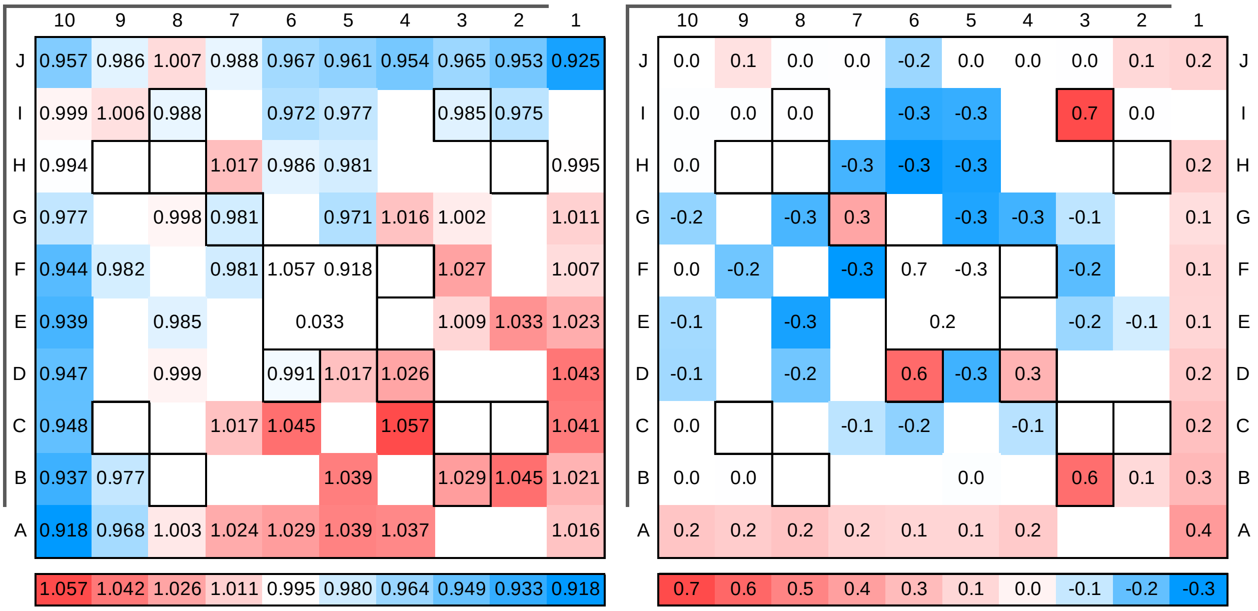

	10	9	8	7	6	5	4	3	2	1
J	0.957	0.986	1.007	0.988	0.967	0.961	0.954	0.965	0.953	0.925
I	0.999	1.006	0.988		0.972	0.977		0.985	0.975	
H	0.994			1.017	0.986	0.981				0.995
G	0.977		0.998	0.981		0.971	1.016	1.002		1.011
F	0.944	0.982		0.981	1.057	0.918		1.027		1.007
E	0.939		0.985		0.033			1.009	1.033	1.023
D	0.947		0.999		0.991	1.017	1.026			1.043
C	0.948			1.017	1.045		1.057			1.041
B	0.937	0.977				1.039		1.029	1.045	1.021
A	0.918	0.968	1.003	1.024	1.029	1.039	1.037			1.016

1.057	1.042	1.026	1.011	0.995	0.980	0.964	0.949	0.933	0.918

	10	9	8	7	6	5	4	3	2	1	
J	0.0	0.1	0.0	0.0	-0.2	0.0	0.0	0.0	0.1	0.2	J
I	0.0	0.0	0.0		-0.3	-0.3		0.7	0.0		I
H	0.0			-0.3	-0.3	-0.3				0.2	H
G	-0.2		-0.3	0.3		-0.3	-0.3	-0.1		0.1	G
F	0.0	-0.2		-0.3	0.7	-0.3		-0.2		0.1	F
E	-0.1		-0.3		0.2			-0.2	-0.1	0.1	E
D	-0.1		-0.2		0.6	-0.3	0.3			0.2	D
C	0.0			-0.1	-0.2		-0.1			0.2	C
B	0.0	0.0				0.0		0.6	0.1	0.3	B
A	0.2	0.2	0.2	0.2	0.1	0.1	0.2			0.4	A

0.7	0.6	0.5	0.4	0.3	0.1	0.0	-0.1	-0.2	-0.3

Figure 64 Configuration I-2A, sensitivity case concerning the condensation spectrum. Left picture: C/E values corresponding to the infinite-medium (zero-leakage) spectrum. Right picture: percental differences with respect to the reference case, (pert.-ref.)x100.

Collision probabilities with no current coupling

The results for this sensitivity case are shown in Figure 65. Using k=0, the standard deviation of the C/Es slightly worsens from 3.2% to 3.4%, the maximum and minimum values of the C/Es distribution being 1.056 and 0.904, respectively.

Compared with Configuration I-1A, the use of k=0 in the controlled case produces a slightly stronger effect on the fission rate distribution, particularly at the pins near the vertex and the tips of the control blade. In particular, the underestimation of the NW quadrant observed in the reference case, especially in the pins near the control blade vertex, tends to be reduced. However, at the control blade tips (e.g. pins A10 and J1), the underestimation is even stronger than in the reference case. This suggests that the more accurate transport solution accentuates the effect of the reflected lattice calculation, discussed in Subsection 5.5.1.

Overall, the results of this sensitivity case do, however, confirm that, also in the presence of a fully inserted control blade, the current coupling with four azimuthal angular sectors (k=4) is a good approximation in reflected lattice calculations.

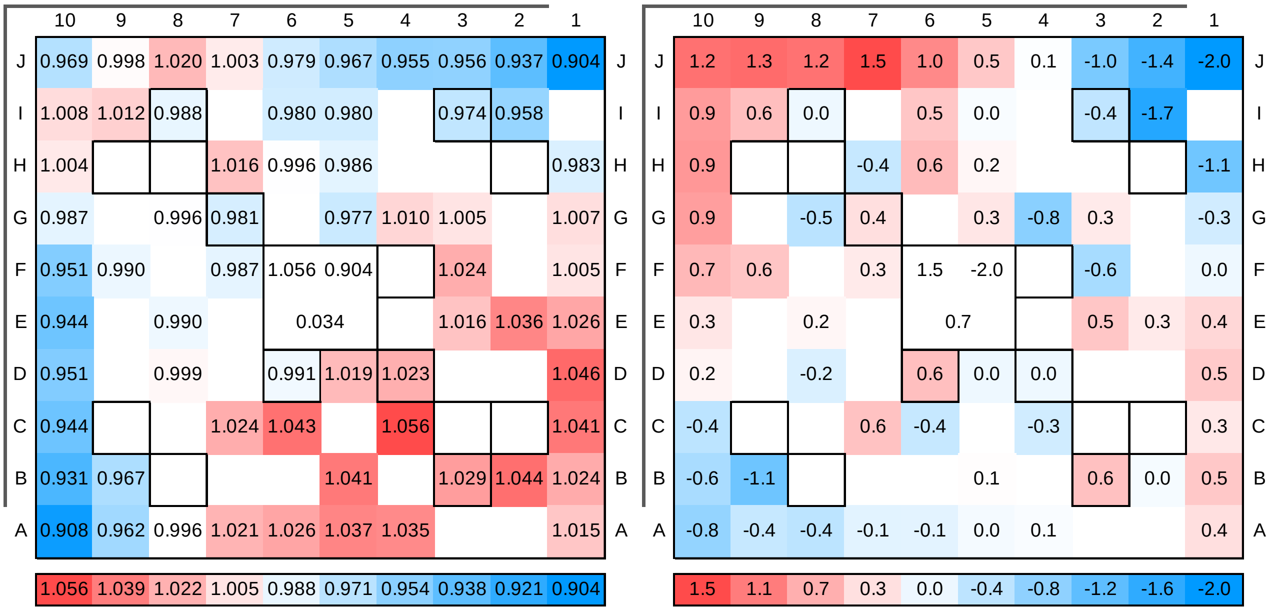

	10	9	8	7	6	5	4	3	2	1	
J	0.969	0.998	1.020	1.003	0.979	0.967	0.955	0.956	0.937	0.904	J
I	1.008	1.012	0.988		0.980	0.980		0.974	0.958		I
H	1.004			1.016	0.996	0.986				0.983	H
G	0.987		0.996	0.981		0.977	1.010	1.005		1.007	G
F	0.951	0.990		0.987	1.056	0.904		1.024		1.005	F
E	0.944		0.990		0.034			1.016	1.036	1.026	E
D	0.951		0.999		0.991	1.019	1.023			1.046	D
C	0.944			1.024	1.043		1.056			1.041	C
B	0.931	0.967				1.041		1.029	1.044	1.024	B
A	0.908	0.962	0.996	1.021	1.026	1.037	1.035			1.015	A
	1.056	1.039	1.022	1.005	0.988	0.971	0.954	0.938	0.921	0.904	

	10	9	8	7	6	5	4	3	2	1	
J	1.2	1.3	1.2	1.5	1.0	0.5	0.1	-1.0	-1.4	-2.0	J
I	0.9	0.6	0.0		0.5	0.0		-0.4	-1.7		I
H	0.9			-0.4	0.6	0.2				-1.1	H
G	0.9		-0.5	0.4		0.3	-0.8	0.3		-0.3	G
F	0.7	0.6		0.3	1.5	-2.0		-0.6		0.0	F
E	0.3		0.2		0.7			0.5	0.3	0.4	E
D	0.2		-0.2		0.6	0.0	0.0			0.5	D
C	-0.4			0.6	-0.4		-0.3			0.3	C
B	-0.6	-1.1				0.1		0.6	0.0	0.5	B
A	-0.8	-0.4	-0.4	-0.1	-0.1	0.0	0.1			0.4	A
	1.5	1.1	0.7	0.3	0.0	-0.4	-0.8	-1.2	-1.6	-2.0	

Figure 65 Configuration I-2A, sensitivity case concerning the use of current coupling. Left picture: C/E values corresponding to the transport (CP) calculation over the whole system (k=0). Right picture: percental differences with respect to the reference case, (pert.-ref.)x100.

Mesh size in the fuel pins

Also in Configuration I-2A, as expected, the finer radial subdivision of the fuel pins has no significant effect on the calculated fission rate distribution. As for the reference case, the maximum, minimum and standard deviation of the C/Es are 1.059, 0.916 and 3.2%, respectively.

Thermal cut-off energy

As discussed in Subsection 4.5.2 for Configuration I-1A, the cross-sections and discontinuity factors, as well as the PCRs, have a spectral dependence and are therefore sensitive to changes in the thermal cut-off energy. In Table 22, the 2-group PCRs are shown for a thermal cut-off energy

0.625 eV. It can be seen that these PCRs differ slightly from those corresponding to 1.84 eV, presented in Table 19.

It will be shown later, in Section 5.8, that changing the thermal cut-off energy from 1.84 eV to 0.625 eV produces an increase of 312 pcm in k-effective. As in the case of Configuration I-1A (220 pcm), this difference confirms that a 2-group representation does not capture the spectral effects exactly. The larger change in k-effective occurring in Configuration I-2A also shows that the spectral effects are even more important in the controlled case. However, also in this case, the relatively moderate impact on k-effective suggests that the use of any of the two thermal cut-off energies investigated in this thesis is justified.

Table 22 PCRs for PRESTO-2 in Configuration I-2A, derived from the partial currents obtained in the 3D whole-reactor MCNPX calculation. The PCRs correspond to a thermal cut-off energy of 0.625 eV.

Configuration I-2A	PCR_{11}		PCR_{22}	
Upper limit (eV)	$20x10^6$		0.625	
Axial direction at top	0.803		0.948	
Radial direction	Side	Corner	Side	Corner
Axial level 10	1.057	1.071	0.359	0.381
Axial level 9	1.064	1.072	0.357	0.379
Axial level 8	1.074	1.080	0.353	0.370
Axial level 7	1.080	1.086	0.352	0.365
Axial level 6	1.079	1.084	0.352	0.368
Axial level 5	1.078	1.082	0.351	0.368
Axial level 4	1.079	1.082	0.350	0.371
Axial level 3	1.079	1.082	0.351	0.371
Axial level 2	1.073	1.077	0.352	0.371
Axial level 1	1.060	1.067	0.357	0.382
Axial direction at bottom	0.843		0.968	

As discussed in Subsection 4.5.2 for the uncontrolled case, the 2D pin-power maps, being a result of the integration of the fission rate over the entire energy range, are insensitive to the thermal cut-off energy. This implies that, also in Configuration I-2A, the changes in the reconstructed total-fission rate are only due to changes in the nodal flux solution in the test zone. Since these are, as discussed above, relatively small, the use of 0.625 eV instead of 1.84 eV as thermal cut-off energy indeed has little influence on the fission rate distribution. However, in relative terms and as suggested by the somewhat larger impact on k-effective, the flux solutions for each of the two thermal cut-off energies can be expected to differ more in the controlled case than in the case without control blade. This interpretation was supported by the results of the C/E comparisons, which showed differences with respect to the reference case lying within the band +0.4% to −0.9% (±0.4% in Configuration I-1A), while the maximum, minimum and standard deviation of the C/E distribution were the same as in the reference case, viz. 1.059, 0.916 and 3.2%, respectively.

5.5.3 Sensitivity cases concerning the test-zone boundary conditions

Due to the azimuthally asymmetric character of Configuration I-2A, which becomes evident considering the location of the L-shaped hafnium control blade in the test zone (see, for example, Figure 19), the impact of the spatial distribution of the PCRs is significantly stronger in this case than in the case of the uncontrolled, thus azimuthally uniform, Configuration I-1A. The results of the sensitivity cases concerning the test-zone boundary representation in Configuration I-2A are presented in the following subsections.

Impact of the subdivision of the PCRs in space and energy

As for Configuration I-1A (see Subsection 4.5.3), PMCFs were calculated from the ratio between two 2D HELIOS calculations for the 3x3 test zone model of Configuration I-2A. Again, albedo boundary conditions (instead of reflected) were used. Thus, 48/05 and 02/05 PCRs were derived from MCNPX whole-reactor calculations, so as to describe the test zone boundary in 5 energy groups and in 48 or 2 azimuthal segments per axial level, respectively. As before, the Pin Map Correction Factors (PMCFs) are defined by equation {43}. Thus, also for Configuration I-2A, the two following cases were evaluated:

1) Application of the 48/05 PMCFs to the reconstructed pin fission rate maps, leading to the most detailed representation of the test zone boundary that can be made with the present methodology.
2) Application of the 02/05 PMCFs, to account for the differences caused by only changing the number of energy groups (5 instead of 2), thus allowing the separation of the spatial and spectral effects.

In Configuration I-2A, the azimuthal variation of the PCRs along the test zone perimeter is much stronger than in Configuration I-1A. Therefore, in this case, the PRESTO-2 restriction of uniform side and corner albedos, represents a more important limitation. In analogy with Table 12 (Configuration I-1A), Table 23 shows, for Configuration I-2A, the percental deviation δ of the PCR for each quadrant of the test-zone boundary, with respect to the mean value for all four quadrants. In this case, it can be seen that the partial current distribution is quite asymmetric in the azimuthal direction (the deviations reach more than 2%). This clearly reflects the azimuthally heterogeneous character of Configuration I-2A.

Table 23 Configuration I-2A. Percental deviation δ of the PCRs for each quadrant of the test zone boundary with respect to the mean value for all four quadrants ($\Sigma_1^4\ \delta=0$). The energy groups are defined in Table 7.

$$\delta = \left[\frac{a_i}{\frac{1}{4}\sum_1^4 a_i} - 1\right] \cdot 100$$

Energy Group	NW	NE	SW	SE
1	1.97	0.43	-0.22	-2.19
2	0.86	0.23	0.01	-1.11
3	0.84	0.02	0.12	-0.99
4	0.99	0.10	0.06	-1.15
5	1.16	0.05	0.14	-1.35

Application of the 48/05 PMCFs

As before, the PMCFs are applied by simply multiplying the calculated total-fission rate distribution by the PMCF map. The left picture in Figure 66 shows the result of the application of the 48/05 PMCFs to the reference case (Figure 63) while, on the right hand side, the corresponding PMCF map at the 5th axial level is shown.

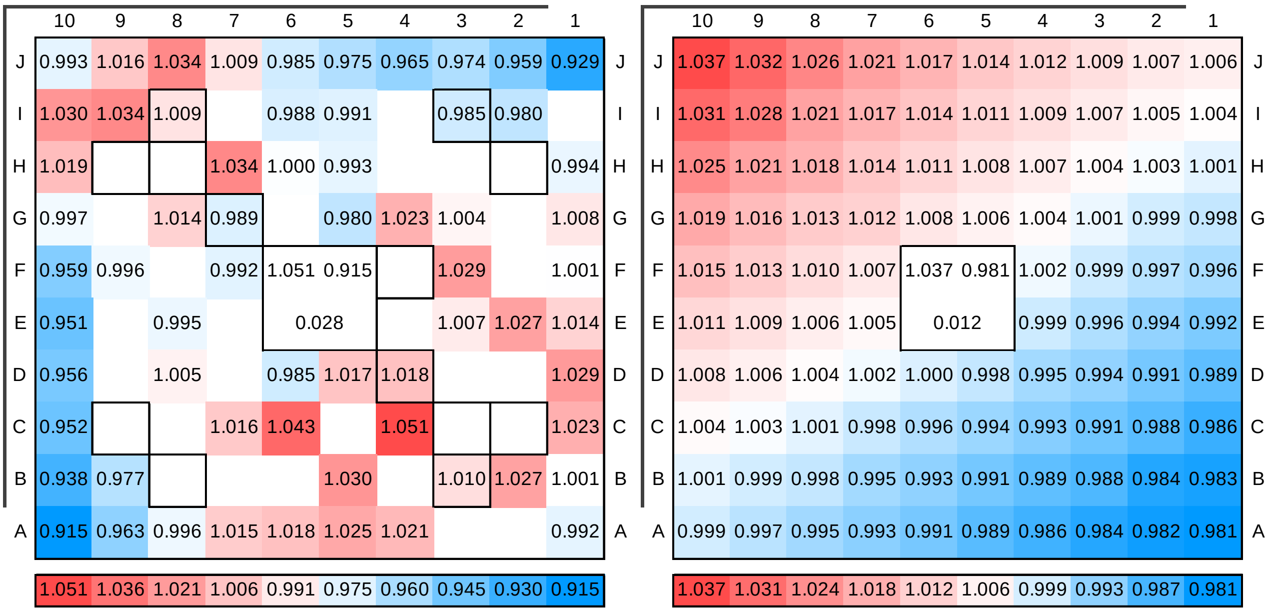

	10	9	8	7	6	5	4	3	2	1	
J	0.993	1.016	1.034	1.009	0.985	0.975	0.965	0.974	0.959	0.929	J
I	1.030	1.034	1.009		0.988	0.991		0.985	0.980		I
H	1.019			1.034	1.000	0.993				0.994	H
G	0.997		1.014	0.989		0.980	1.023	1.004		1.008	G
F	0.959	0.996		0.992	1.051	0.915		1.029		1.001	F
E	0.951		0.995		0.028			1.007	1.027	1.014	E
D	0.956		1.005		0.985	1.017	1.018			1.029	D
C	0.952			1.016	1.043		1.051			1.023	C
B	0.938	0.977				1.030		1.010	1.027	1.001	B
A	0.915	0.963	0.996	1.015	1.018	1.025	1.021			0.992	A

1.051	1.036	1.021	1.006	0.991	0.975	0.960	0.945	0.930	0.915

	10	9	8	7	6	5	4	3	2	1	
J	1.037	1.032	1.026	1.021	1.017	1.014	1.012	1.009	1.007	1.006	J
I	1.031	1.028	1.021	1.017	1.014	1.011	1.009	1.007	1.005	1.004	I
H	1.025	1.021	1.018	1.014	1.011	1.008	1.007	1.004	1.003	1.001	H
G	1.019	1.016	1.013	1.012	1.008	1.006	1.004	1.001	0.999	0.998	G
F	1.015	1.013	1.010	1.007	1.037	0.981	1.002	0.999	0.997	0.996	F
E	1.011	1.009	1.006	1.005	0.012		0.999	0.996	0.994	0.992	E
D	1.008	1.006	1.004	1.002	1.000	0.998	0.995	0.994	0.991	0.989	D
C	1.004	1.003	1.001	0.998	0.996	0.994	0.993	0.991	0.988	0.986	C
B	1.001	0.999	0.998	0.995	0.993	0.991	0.989	0.988	0.984	0.983	B
A	0.999	0.997	0.995	0.993	0.991	0.989	0.986	0.984	0.982	0.981	A

1.037	1.031	1.024	1.018	1.012	1.006	0.999	0.993	0.987	0.981

Figure 66 Configuration I-2A, sensitivity case concerning the use of the 48/05 PMCFs. The left picture shows the C/E values corresponding to the reference case multiplied by the PMCFs, which are shown in the right picture.

It can be seen that the control blade imposes a clear tilt on the PMCFs, whose values vary from 0.981 at the SE corner of the lattice to 1.037 at the NW corner. This tilt again reflects the azimuthally asymmetric character of Configuration I-2A, compensating, to a large extent, the systematic trend observed in the C/Es calculated with PRESTO-2. Thus, the use of the 48/05 PMCFs in the controlled configuration improves the C/E map significantly, as can be seen from the comparison of the left hand sides of Figure 63 and Figure 66, the standard deviation of the C/E distribution decreasing from 3.2% to 2.8%. However, it is worth noting that the underestimation observed near the control blade tips (NE and SW corners of the lattice) is not corrected by the use of the PMCFs. In fact, this effect is caused by the reflective boundary condition used in the lattice calculation (see also Subsection 5.5.1) and, as such, remains insensitive to the PMCFs.

As done in Figure 47 for Configuration I-1A, the relative pin-power distribution over the nine fuel assemblies that constitute the test-zone, as calculated by PRESTO-2, is depicted for Configuration I-2A in Figure 67. Also here, a warm-cold colour scale, from which the gadolinium pins have been excluded, has been used to allow the visualisation of the radial flux shape. The pin-power depression caused by the presence of the L-shaped control blade can be clearly seen.

The challenge that Configuration I-2A imposes on the test-zone boundary conditions can be evaluated observing the power distribution over the pins facing the test-tank wall. For instance, the total-fission rate in pin J10 of assembly 1[37] is 30% lower than in pin A1 of assembly 9. This clearly suggests that the radial albedo input capability of PRESTO-2, which permits only one

---

[37] Assembly numbers according to Figure 23.

side and corner value per axial level (see also Subsection 3.6.1), is somewhat insufficient for an accurate representation of the test-zone boundary in the controlled case, thus explaining the positive impact that the application of the 48/05 PMCFs has on the C/E distribution in the central assembly.

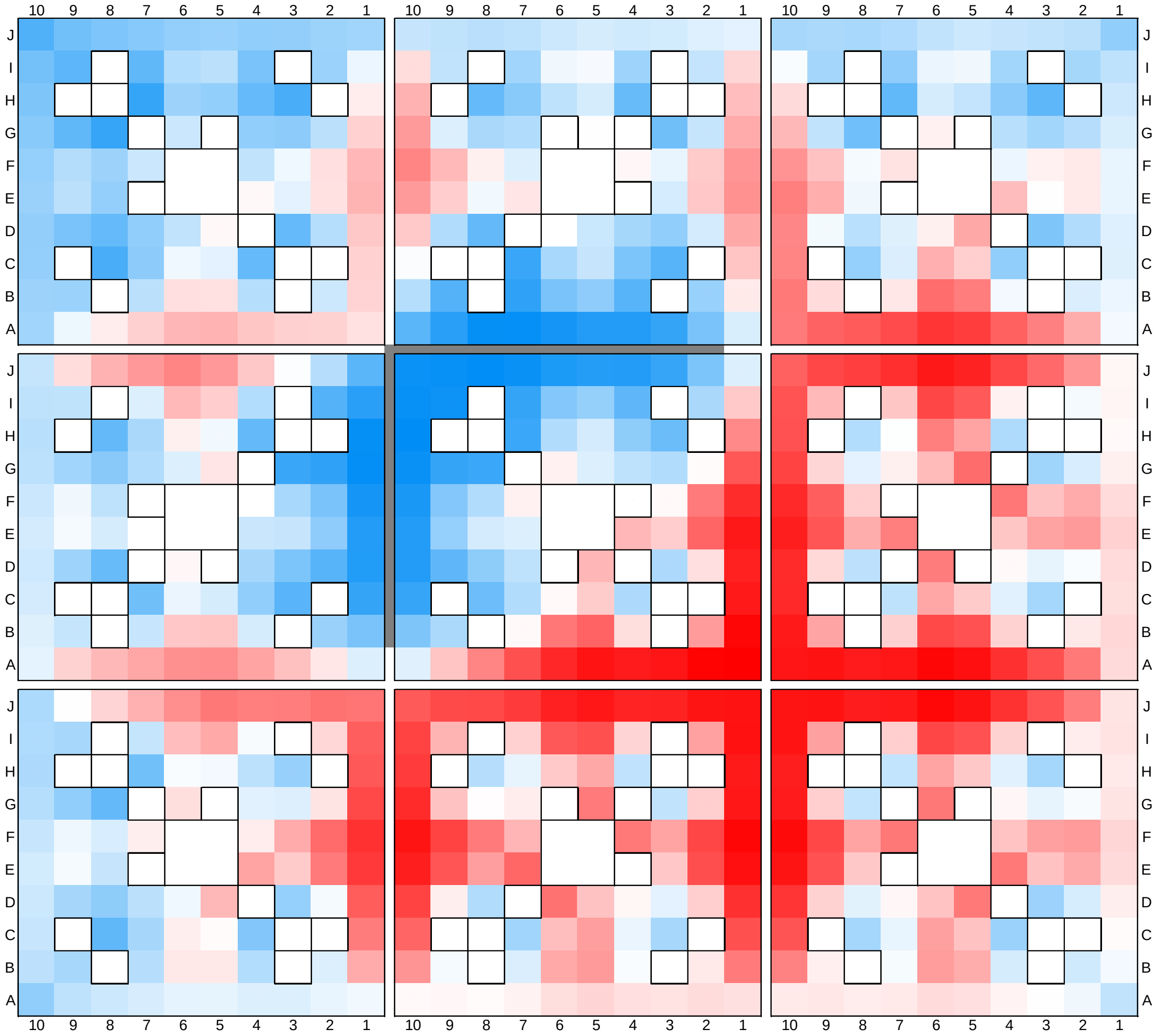

Figure 67 Configuration I-2A, reference case: relative total-fission rate distribution in the nine assemblies of the LWR-PROTEUS test zone, as calculated with PRESTO-2. A warm-cold colour scale, from which the gadolinium pins have been excluded, has been used to allow the visualisation of the flux radial shape. The relative total-fission rate distribution being normalised to 1.0 for the 3x3 configuration, the scale covers the range ~0.5 to ~1.7, warmer colours indicating higher values.

Application of the 02/05 PMCFs

As for the uncontrolled configuration, this case is introduced to separate the effects of the space and energy subdivision of the PCRs. In the 02/05 case, the spatial discretisation of the PCRs used in the 3x3 HELIOS calculation is the same as in PRESTO-2. The effect of the spectral information contained in the five-group PCRs can then be observed clearly. The results of this comparison are shown in Figure 68.

As was the case in Configuration I-1A, also for the controlled case the refinement in the energy discretisation of the PCRs has a very small effect on the total-fission rate distribution in the central assembly. However, it significantly affects the system reactivity. This aspect will be discussed later in Section 5.8.

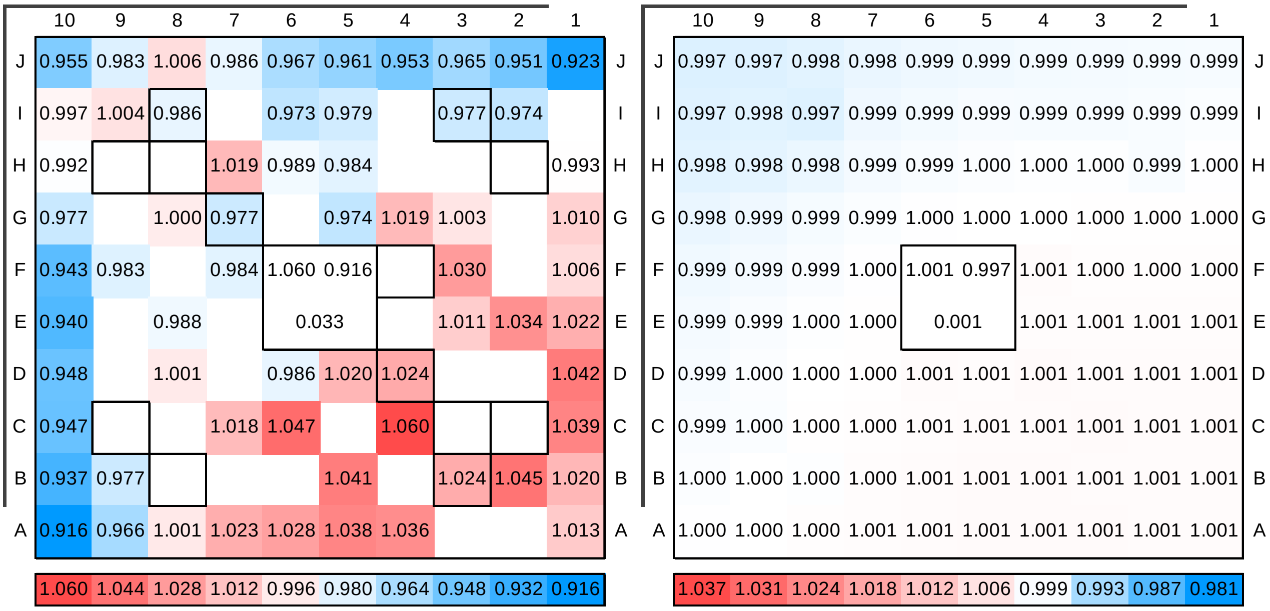

	10	9	8	7	6	5	4	3	2	1	
J	0.955	0.983	1.006	0.986	0.967	0.961	0.953	0.965	0.951	0.923	J
I	0.997	1.004	0.986		0.973	0.979		0.977	0.974		I
H	0.992			1.019	0.989	0.984				0.993	H
G	0.977		1.000	0.977		0.974	1.019	1.003		1.010	G
F	0.943	0.983		0.984	1.060	0.916		1.030		1.006	F
E	0.940		0.988		0.033			1.011	1.034	1.022	E
D	0.948		1.001		0.986	1.020	1.024			1.042	D
C	0.947			1.018	1.047		1.060			1.039	C
B	0.937	0.977				1.041		1.024	1.045	1.020	B
A	0.916	0.966	1.001	1.023	1.028	1.038	1.036			1.013	A

1.060	1.044	1.028	1.012	0.996	0.980	0.964	0.948	0.932	0.916

	10	9	8	7	6	5	4	3	2	1	
J	0.997	0.997	0.998	0.998	0.999	0.999	0.999	0.999	0.999	0.999	J
I	0.997	0.998	0.997	0.999	0.999	0.999	0.999	0.999	0.999	0.999	I
H	0.998	0.998	0.998	0.999	0.999	1.000	1.000	1.000	0.999	1.000	H
G	0.998	0.999	0.999	0.999	1.000	1.000	1.000	1.000	1.000	1.000	G
F	0.999	0.999	0.999	1.000	1.001	0.997	1.001	1.000	1.000	1.000	F
E	0.999	0.999	1.000	1.000	0.001		1.001	1.001	1.001	1.001	E
D	0.999	1.000	1.000	1.000	1.001	1.001	1.001	1.001	1.001	1.001	D
C	0.999	1.000	1.000	1.000	1.001	1.001	1.001	1.001	1.001	1.001	C
B	1.000	1.000	1.000	1.000	1.001	1.001	1.001	1.001	1.001	1.001	B
A	1.000	1.000	1.000	1.001	1.001	1.001	1.001	1.001	1.001	1.001	A

1.037	1.031	1.024	1.018	1.012	1.006	0.999	0.993	0.987	0.981

Figure 68 Configuration I-2A, sensitivity case concerning the use of the 02/05 PMCFs. The left picture shows the C/E values corresponding to the reference case multiplied by the PMCFs, which are shown on the right picture. The colour scale at the bottom of the latter was intentionally made equal to that of Figure 66 to facilitate the visual comparison.

Use of 2D PCRs calculated with HELIOS

As described in Section 5.4, a 2D HELIOS model of the complete LWR-PROTEUS reactor, including the L-shaped control blade, was used to evaluate the in- and out-currents at the test zone boundary in Configuration I-2A. From these partial currents, the radial PCRs were calculated and used in place of the MCNPX PCRs. Also here, as required by PRESTO-2, the partial currents were integrated along the four sides and four corners of the test zone perimeter. As before, since the calculation is performed in 2D, the same PCRs were used for all 10 axial levels.

As seen in Table 21, the 2D HELIOS full-reactor model leads to larger PCRs compared with the 3D MCNPX model. It will be shown later, in Section 5.8, that this has a significant effect on the LWR-PROTEUS test-zone k-effective value calculated with PRESTO-2. As was also the case in Configuration I-1A, the impact on the fission rate distribution is relatively small, but in this case the values for the pins near the NW corner of the assembly are increased by up to 1.0% (see Figure 69). As in the case of Configuration I-1A, (see Subsection 4.5.3), the larger HELIOS PCRs (compared to MCNPX) increase the fission rate in the outer assemblies, leading to slightly higher fission rates at the periphery of the central assembly and to lower values at its centre.

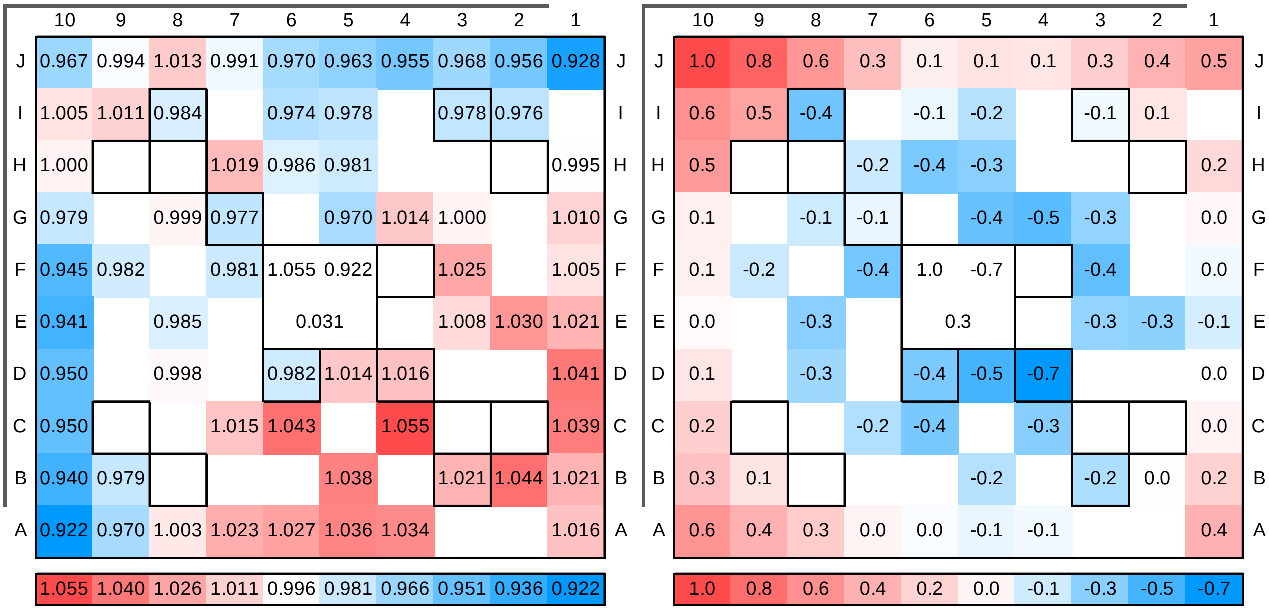

	10	9	8	7	6	5	4	3	2	1	
J	0.967	0.994	1.013	0.991	0.970	0.963	0.955	0.968	0.956	0.928	J
I	1.005	1.011	0.984		0.974	0.978		0.978	0.976		I
H	1.000			1.019	0.986	0.981				0.995	H
G	0.979		0.999	0.977		0.970	1.014	1.000		1.010	G
F	0.945	0.982		0.981	1.055	0.922		1.025		1.005	F
E	0.941		0.985		0.031			1.008	1.030	1.021	E
D	0.950		0.998		0.982	1.014	1.016			1.041	D
C	0.950			1.015	1.043		1.055			1.039	C
B	0.940	0.979				1.038		1.021	1.044	1.021	B
A	0.922	0.970	1.003	1.023	1.027	1.036	1.034			1.016	A

1.055	1.040	1.026	1.011	0.996	0.981	0.966	0.951	0.936	0.922

	10	9	8	7	6	5	4	3	2	1	
J	1.0	0.8	0.6	0.3	0.1	0.1	0.1	0.3	0.4	0.5	J
I	0.6	0.5	-0.4		-0.1	-0.2		-0.1	0.1		I
H	0.5			-0.2	-0.4	-0.3				0.2	H
G	0.1		-0.1	-0.1		-0.4	-0.5	-0.3		0.0	G
F	0.1	-0.2		-0.4	1.0	-0.7		-0.4		0.0	F
E	0.0		-0.3		0.3			-0.3	-0.3	-0.1	E
D	0.1		-0.3		-0.4	-0.5	-0.7			0.0	D
C	0.2			-0.2	-0.4		-0.3			0.0	C
B	0.3	0.1				-0.2		-0.2	0.0	0.2	B
A	0.6	0.4	0.3	0.0	0.0	-0.1	-0.1			0.4	A

1.0	0.8	0.6	0.4	0.2	0.0	-0.1	-0.3	-0.5	-0.7

Figure 69 Configuration I-2A, sensitivity case concerning the use of PCRs obtained with the 2D HELIOS whole-reactor model. Left picture: C/E values. Right picture: percental differences with respect to the reference case, (pert.-ref.)x100.

5.5.4 Impact of the pin coordinates on the map reconstruction in PRESTO-2

As discussed in Chapter 3, Subsection 3.3.1, the use of measured inter-assembly gaps in HELIOS leads to a slight misalignment of the pin coordinates in PRESTO-2 when the 2D pin-power maps are superimposed onto the asymptotic flux solution. This situation has been depicted in Figure 25.

The size of the north and west gaps being the same in both configurations, the misalignment in Configuration I-2A is the same as in Configuration I-1A (see Subsection 4.5.4). Thus, changing the coordinates XNWCRNR and YNWCRNR in the XSDB as discussed in Subsection 4.5.4, the differences with respect to the reference case (Figure 63) can be calculated. These were found to lie between +0.27% and −0.17% for all pins, with the extreme values being found for pins facing the control blade. Thus, even in the more challenging case of Configuration I-2A (in which strong gradients occur in the vicinity of the control blade), the effect is small. Hence, also in this case, the standard procedure for the determination of the pin coordinates in the HE/P2 XSDB is considered adequate.

5.5.5 Impact of the inter-assembly gap size

The sensitivity of the total-fission rate distribution to the inter-assembly gap sizes in Configuration I-2A was investigated in analogy to the case of Configuration I-1A, presented in Subsection 4.5.5. The nominal and measured dimensions of the inter-assembly gaps that surround the central assembly in Configuration I-2A are shown in Figure 20 and Figure 56, respectively, the sizes of the half-gaps being summarised in Table 24.

Table 24 Nominal and measured half-gaps (cm) corresponding to the central assembly in Configuration I-2A.

		North	East	South	West
Nominal	(perturbed case)	0.6900	0.6900	0.6900	0.6900
Measured	(reference case)	0.7245	0.6865	0.7035	0.7185
Difference	(perturbed-reference)	−0.0345	0.0035	−0.0135	−0.0285

In Configuration I-2A, a reduction of ~0.3 mm in the north and west gaps reduces the total-fission rate in the pins facing the control blade by ~2%, as shown on the right hand side of Figure 70. Thus, compared with Configuration I-1A, for which the corresponding total-fission rate reduction is about 1% (see Figure 50), the impact of the gap reduction on the pins facing the north and west gaps is strengthened. This larger impact is caused by the fact that the gap reduction moves the fuel pins closer to the strongly absorbing control blade. For pin J10, however, the impact of the gap reduction is similar in both configurations (−1.3% in I-1A and −1.2% in I-2A). This particular behaviour can be explained by observing the detailed geometry of the control blade vertex (see Figure 57). It can be seen, that reducing both gaps simultaneously, the distance between pin J10 and the CB absorber pins experiences a smaller change compared to other pins facing the gap.

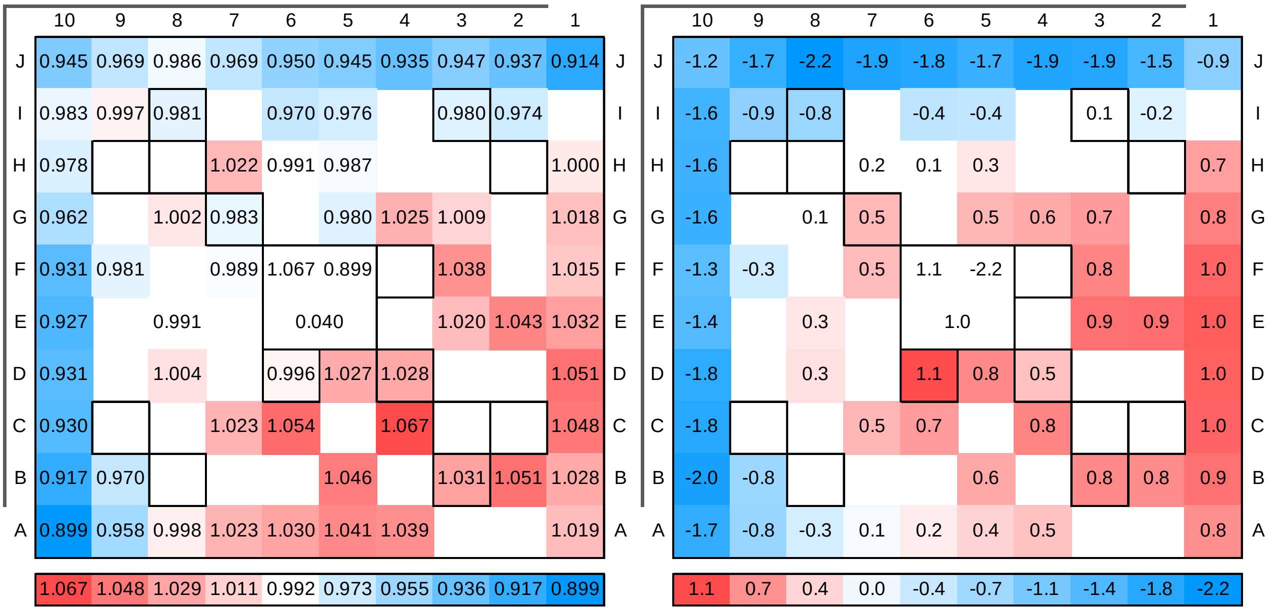

	10	9	8	7	6	5	4	3	2	1	
J	0.945	0.969	0.986	0.969	0.950	0.945	0.935	0.947	0.937	0.914	J
I	0.983	0.997	0.981		0.970	0.976		0.980	0.974		I
H	0.978			1.022	0.991	0.987				1.000	H
G	0.962		1.002	0.983		0.980	1.025	1.009		1.018	G
F	0.931	0.981		0.989	1.067	0.899		1.038		1.015	F
E	0.927		0.991		0.040			1.020	1.043	1.032	E
D	0.931		1.004		0.996	1.027	1.028			1.051	D
C	0.930			1.023	1.054		1.067			1.048	C
B	0.917	0.970				1.046		1.031	1.051	1.028	B
A	0.899	0.958	0.998	1.023	1.030	1.041	1.039			1.019	A
	1.067	1.048	1.029	1.011	0.992	0.973	0.955	0.936	0.917	0.899	

	10	9	8	7	6	5	4	3	2	1	
J	-1.2	-1.7	-2.2	-1.9	-1.8	-1.7	-1.9	-1.9	-1.5	-0.9	J
I	-1.6	-0.9	-0.8		-0.4	-0.4		0.1	-0.2		I
H	-1.6			0.2	0.1	0.3				0.7	H
G	-1.6		0.1	0.5		0.5	0.6	0.7		0.8	G
F	-1.3	-0.3		0.5	1.1	-2.2		0.8		1.0	F
E	-1.4		0.3		1.0			0.9	0.9	1.0	E
D	-1.8		0.3		1.1	0.8	0.5			1.0	D
C	-1.8			0.5	0.7		0.8			1.0	C
B	-2.0	-0.8				0.6		0.8	0.8	0.9	B
A	-1.7	-0.8	-0.3	0.1	0.2	0.4	0.5			0.8	A
	1.1	0.7	0.4	0.0	-0.4	-0.7	-1.1	-1.4	-1.8	-2.2	

Figure 70 Configuration I-2A, impact of the inter-assembly gap size. The C/E values corresponding to the nominal gaps are given in the left map. On the right hand side, the (pert.-ref.)x100 values are shown.

An additional effect, also observed in Configuration I-1A (see Subsection 4.5.5), can be seen in Figure 70. The reduction of the total-fission rate in the pins facing the north and west gaps, caused by the reduction of the gap sizes when the nominal dimensions are used, produces a tilt that increases the total-fission rate in the pins facing the east and south gaps. However, this increase is stronger for the east than for the south gap, which in turn is due to the superposition of the effects of the increase in the size of the east gap and the decrease for the south gap (see Table 24).

Using nominal gap values, the maximum, minimum and standard deviation of the C/Es are 1.067, 0.899 and 4.0%, respectively.

5.5.6 Impact of the sub-assembly pressing

As done for Configuration I-1A (see Subsection 4.5.6), the impact of the 0.51 mm pressing of the four sub-assemblies in the central fuel assembly was also investigated in Configuration I-2A. As before, the impact of the pin displacement on the pin-power results, now in the presence of the L-shaped control blade, has been evaluated by re-calculating the HELIOS XSDB using the nominal pin coordinates and comparing the PRESTO-2 reconstructed total-fission rate distribution with the experimental results. The C/E values obtained in this comparison are shown in Figure 71.

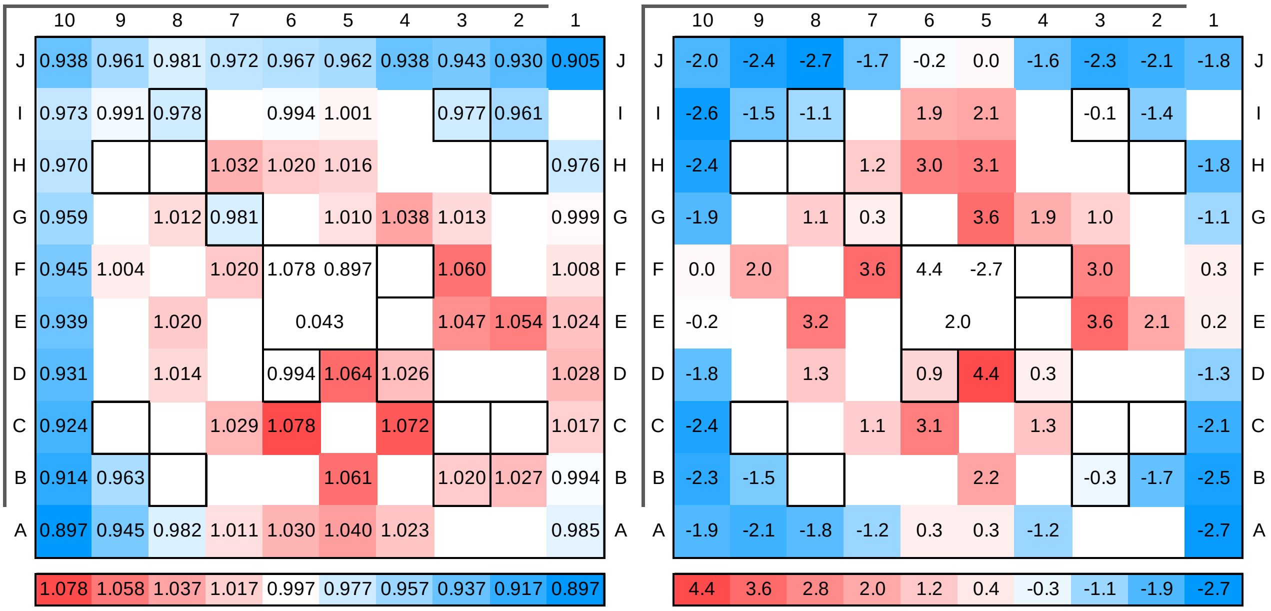

	10	9	8	7	6	5	4	3	2	1
J	0.938	0.961	0.981	0.972	0.967	0.962	0.938	0.943	0.930	0.905
I	0.973	0.991	0.978		0.994	1.001		0.977	0.961	
H	0.970			1.032	1.020	1.016				0.976
G	0.959		1.012	0.981		1.010	1.038	1.013		0.999
F	0.945	1.004		1.020	1.078	0.897		1.060		1.008
E	0.939		1.020		0.043			1.047	1.054	1.024
D	0.931		1.014		0.994	1.064	1.026			1.028
C	0.924			1.029	1.078		1.072			1.017
B	0.914	0.963				1.061		1.020	1.027	0.994
A	0.897	0.945	0.982	1.011	1.030	1.040	1.023			0.985
	1.078	1.058	1.037	1.017	0.997	0.977	0.957	0.937	0.917	0.897

	10	9	8	7	6	5	4	3	2	1
J	-2.0	-2.4	-2.7	-1.7	-0.2	0.0	-1.6	-2.3	-2.1	-1.8
I	-2.6	-1.5	-1.1		1.9	2.1		-0.1	-1.4	
H	-2.4			1.2	3.0	3.1				-1.8
G	-1.9		1.1	0.3		3.6	1.9	1.0		-1.1
F	0.0	2.0		3.6	4.4	-2.7		3.0		0.3
E	-0.2		3.2		2.0			3.6	2.1	0.2
D	-1.8		1.3		0.9	4.4	0.3			-1.3
C	-2.4			1.1	3.1		1.3			-2.1
B	-2.3	-1.5				2.2		-0.3	-1.7	-2.5
A	-1.9	-2.1	-1.8	-1.2	0.3	0.3	-1.2			-2.7
	4.4	3.6	2.8	2.0	1.2	0.4	-0.3	-1.1	-1.9	-2.7

Figure 71 Configuration I-2A, impact of the 0.51 mm sub-assembly pressing towards the central canal. Left picture: C/E values corresponding to the nominal pin coordinates. Right picture: percental differences with respect to the reference case, (pert.-ref.)x100.

As in the case of Configuration I-1A (see Figure 51), the sub-assembly pressing produces a significant perturbation of the total-fission rate map. The use of nominal pin coordinates moves each sub-assembly away from the fuel element centre in both directions (x and y), producing a reduction of the moderation in the pins near the assembly corners, hence reducing their power. At the same time, pins surrounding the water canal and water wings experience increased moderation, which increases the power of these pins. However, while away from the control blade the impact of removing the sub-assembly pressing is very similar to that observed in the uncontrolled case (see Figure 51), a small additional reduction in the total-fission rates of the pins which are facing the control blade can be observed in the controlled configuration. As in the case of the change in the gap sizes, discussed in Subsection 5.5.5, this behaviour can be attributed to the reduction of the distance to the absorber rods. Also, for the same reasons discussed earlier, the impact on pin J10 is not larger (the effect of the pressing removal is in fact 0.4% smaller than for Configuration I-1A). Interesting to see is that, in the present case, the reduction of the total-fission rate for pins J1 and A10 is significantly smaller than in the case of Configuration I-1A. For these pins, the elimination of the sub-bundle pressing leads in fact to an increase of the distance to the absorber rods (see Figure 57) which, in turn, due to the normalisation of the total-fission rate distribution, produces a relative increase in their values.

Considering all pins, it can be concluded that for fuel elements of type SVEA-96 under full moderation conditions and in the presence of a control blade[38], a 0.51 mm displacement of the sub-assemblies affects the pin-powers by ca. -2.7% to 4.4%, this result being very similar to that of the uncontrolled case (Configuration I-1A, viz. ca. -2.6% to 4.3%).

In controlled assemblies, as can be seen in Figure 67, it is the peripheral pins distant from the control blade which develop the largest power, and thus have the potential for becoming limiting with respect to the power peaking factor. However, since the assembly-averaged power is low, the effect is less crucial as regards thermal parameters than for uncontrolled cases.

The maximum, minimum and standard deviation of the C/E distribution of Figure 71 are 1.078, 0.897 and 4.3%, respectively. Comparing with the reference case, the effects of the sub-assembly pressing on the total-fission rate distribution are clearly reflected by the increase of the standard deviation from 3.2% to 4.3%.

5.6 Omission of the CASMO-5/SIMULATE-5 calculations

As mentioned in Subsection 2.4.4, the LWR-PROTEUS test-zone could not be modelled with the CASMO-5/SIMULATE-5 route for configurations in which the L-shaped control blade was inserted, viz. I-2A and I-6A. The main reason for this is that for an odd number of fuel assembly rows, such as the 3x3 array in LWR-PROTEUS, SIMULATE-5 automatically assumes the modelling of a PWR core. In this kind of reactor, the control elements are clusters of absorber rods that enter specific lattice positions in the fuel assembly (see Figure 72). Since SIMULATE-5 does not allow the definition of BWR control blades in an array consisting of an odd number of assembly rows, the CASMO-5/SIMULATE-5 calculations in this thesis could only be performed on configurations in which the L-shaped control blade was not present.

---

[38] It should be underlined that, even though the investigated L-shaped control blade differs from the real cruciform blades, the present findings are basically applicable to the case of BWR core geometries, the discussions made here being extendable to such configurations.

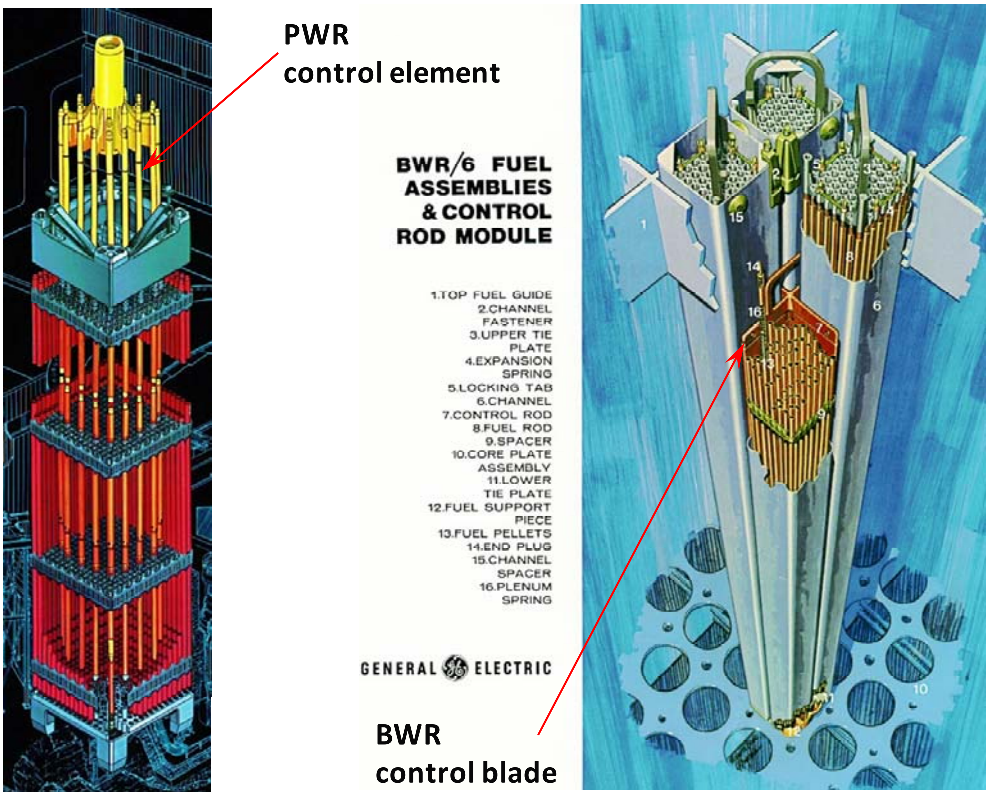

Figure 72 Differences in PWR and BWR control element designs. On the left, a PWR fuel assembly with partially inserted control rods and, on the right, a BWR control cell consisting of four fuel elements with cruciform control blade partially inserted. (By courtesy of Westinghouse and General Electric. Source: www.nucleartourist.com/systems/pwrfuel1.htm). SIMULATE-5 modelling of an odd-number of assembly rows automatically assumes PWR control element geometry.

5.7 Verification of the axial flux curvature

To characterise the axial fission rate distribution in Configuration I-2A, two axial measurements were done. In the first, pin J1, after an irradiation, was gamma-scanned over the range −54 cm to +56 cm (with respect to the core midplane). In the second measurement, a Geiger-Müller tube (simulating a gamma Traversing In-Core Probe (TIP)) was moved along the TIP location at the south-east corner of the central assembly, i.e. closest to the A1 fuel pin. The measurement range, in this case, was from −60 cm to +50 cm, relative to the core midplane. Both measurements provide information about the axial curvature of the flux.

Figure 73 shows the comparison of the measurements with MCNPX and PRESTO-2 results for pins J1 and A1. (The procedure used for normalization of the axial profiles is completely analogous to that employed in Figure 55 for Configuration I-1A).

As in the case of Configuration I-1A, the effect of the two spacers, located at approximately ±30 cm with respect to the core midplane, can be seen in the MCNPX fission rate profile, in the form of two small depressions at the corresponding positions. Also in this case, since the C/E comparisons only concern the radial distribution at core midplane, the spacers were not included in the HE/P2 model.

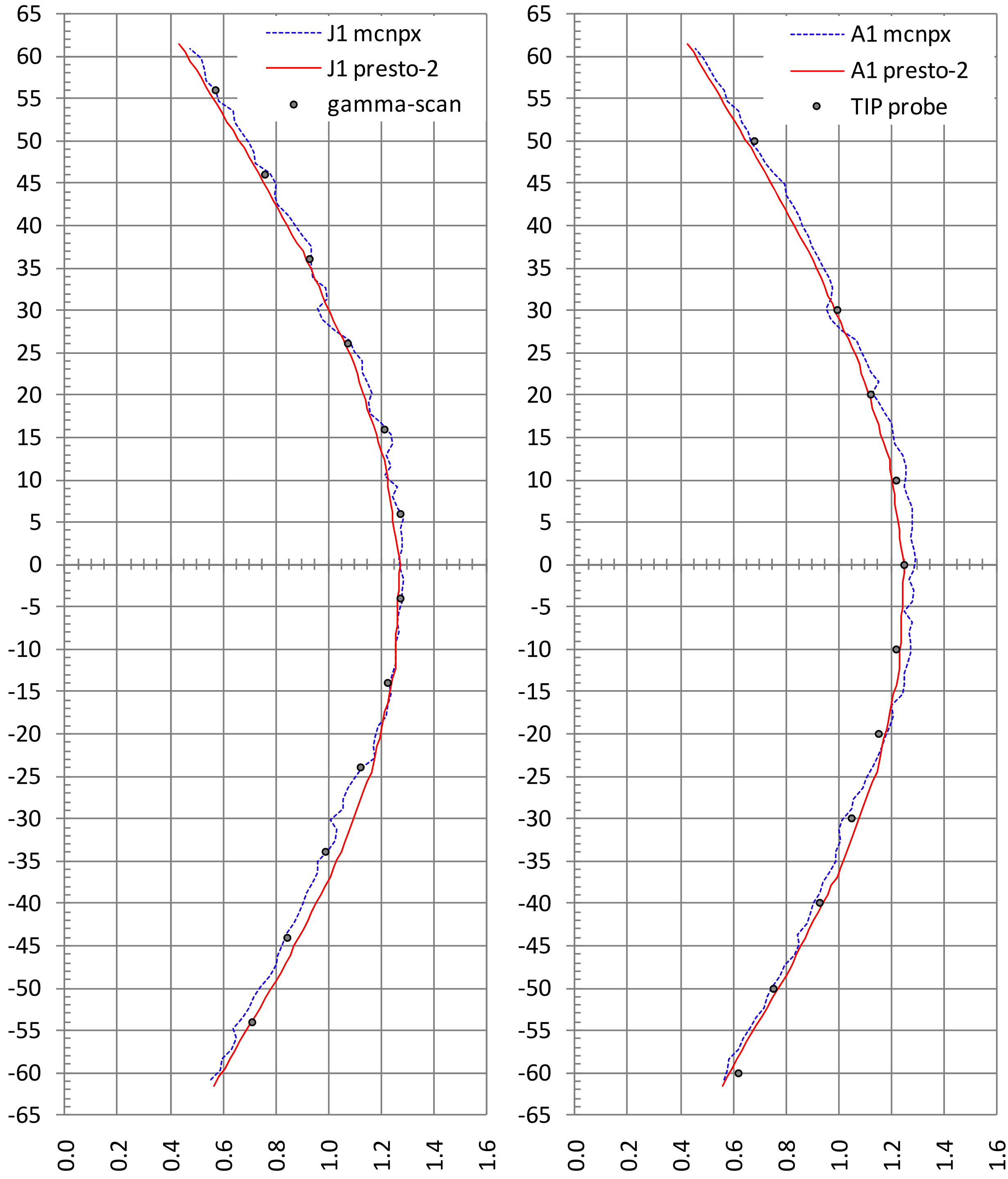

Figure 73 Configuration I-2A - Axial comparison of MCNPX (blue dashed line) and PRESTO-2 (red line) total-fission rates with gamma-scan measurements on pin J1 (left hand side) and with signals of a TIP probe facing pin position A1 (right hand side). All distributions are normalized to 1.0 over the corresponding set of measured points (12 and 11, respectively).

For both pin positions, the agreement between calculation and measurement is good. For the gamma-scan (pin J1), the standard deviations of the differences are 1.8% and 3.3% for MCNPX and PRESTO-2, respectively. For the simulated TIP probe (closest to pin A1), the corresponding values are 3.7% and 2.1%, respectively.

Viewed together, the axial comparisons for Configurations I-1A (Section 4.8) and I-2A thus show that, for axially uniform cases, the applied methodology predicts the global flux curvature in the test zone of LWR-PROTEUS with good accuracy.

5.8 k-effective

Also for Configuration I-2A, the comparison of the whole-reactor k-effective values obtained for the different sensitivity cases is of interest.

5.8.1 Principal results

Table 25 shows the results corresponding to various PRESTO-2 cases considered in Section 5.5, together with the differences (in pcm) with respect to the MCNPX whole-reactor calculation and the PRESTO-2 reference case.

Table 25 The first column of numbers shows the PRESTO-2 (rows 2 to 10) k-effective results for Configuration I-2A. Column 2 shows the differences (expressed in pcm) with respect to MCNPX, the k-effective value for which is given in the first row of Column 1, followed in brackets by its 1σ uncertainty (in pcm). Column 3 shows the differences (in pcm), for all calculations with respect to the PRESTO-2 reference case.

	Calculated k-effective	Differences (pcm) with respect to MCNPX	P2 ref. case
MCNPX-2.6b with JEFF-3.1 library	1.00472 (10)	0	-1075
P2 reference case (ENDF/B-VI v1 and v3)	1.01547	1075	0
P2 190 groups "unadjusted" library	1.01274	802	-273
P2 infinite medium (B^2=0) spectrum	1.01506	1034	-41
P2 collision probabilities k=0	1.01624	1152	77
P2 finer pin subdivision	1.01560	1088	13
P2 thermal cut-off 0.625 eV	1.01859	1387	312
P2 HELIOS whole-reactor PCRs (radial)	1.04312	3840	2765
P2 nominal gaps (0.6900 cm)	1.01462	990	-85
P2 no sub-assembly pressing	1.01930	1458	383

As in the case of Configuration I-1A (see Section 4.9), the k-effective values obtained with PRESTO-2 in Configuration I-2A, using the radial and axial PCRs calculated with MCNPX, are significantly higher than those obtained in the 3D MCNPX calculation. The difference is 1075 pcm for the reference case, being reduced to 802 pcm if the 190-group unadjusted library of HELIOS is used (first sensitivity case). Thus, changing the HELIOS library, the k-effective is reduced by 273 pcm with respect to the reference case. Now, using the 47-group library without RI adjustment (see also Section 4.9), it is found that the elimination of the RI adjustment alone reduces the k-effective by 234 pcm. As before, ignoring the second-order effects caused by the simultaneous application of both modifications, the further reduction due to the increase in the number of energy groups from 47 to 190 may thus be deduced as 39 pcm.

5.8.2 Effect of the energy dependence of the PCRs

The considerations made in Subsection 4.9.2 for Configuration I-1A can also be applied here. The differences in k-effective calculated with the 2D HELIOS 3x3 test zone model using different boundary conditions are shown in Table 26. As in Table 17, the first column corresponds to two different spatial discretisation schemes with the same group structure, while the second column shows the impact of changing the number of groups but keeping the spatial detail. In the third column, both effects are combined.

Table 26 Configuration I-2A, k-effective changes in pcm caused by the PCR discretisation used in the 2D HELIOS calculation of the 3x3 test zone. The suffixes "s" and "g" denote perimeter segments and energy groups, respectively.

	02s/05g-48s/05g	02s/02g-02s/05g	02s/02g-48s/05g
Δ k-effective (pcm)	-27	606	579

As for Configuration I-1A, the impact of the spatial discretisation on k-effective is very small (27 pcm), while the impact of refining the discretisation in energy is much more significant. On the other hand, as shown in Subsection 5.5.3, the pin fission rate distribution is significantly affected by the spatial discretisation of the PCRs, while the number of energy groups plays an almost negligible role.

5.8.3 Effect of using PCRs from the 2D HELIOS whole-reactor model

Again, this is a specific effect presented in Table 25, which merits separate discussion. Thus, it is seen from the table that, compared with the reference case, using HELIOS PCRs yields a higher (2765 pcm) k-effective value. This difference is even higher than that observed in Configuration I-1A (1673 pcm; see Subsection 4.9.3). Thus, the same axial leakage related effect discussed in Section 4.4 occurs also here, but with even greater intensity than in Configuration I-1A. Considering the discussion made in Subsection 5.3.3, this effect can be correlated, in the case of Configuration I-2A, to the higher incoming epithermal current entering the test zone from its surroundings.

5.9 Chapter summary and principal messages

Two main effects have been identified for LWR-PROTEUS cases with strong radial and azimuthal non-uniformities, such as those caused by the insertion of a control blade in Configuration I-2A. First, the total-fission rate distribution shows a significant radial tilt across the test zone and, in particular, across the central fuel assembly, where the measurements were made. Second, the zero-current assumption, implicit in the 2D reflected assembly calculation, leads to systematic local deviations in the pin-wise distribution. These deviations are caused by the presence of fictitious blades due to the reflective boundary condition and the consequent failure to account correctly for the surroundings of the central assembly.

Because of the first effect, the PRESTO-2 requirement of azimuthally uniform Partial Current Ratios (PCRs) leads to systematic variations in the C/E distribution along the NW-SE assembly diagonal. This has been investigated through the use of pin map correction factors

(PMCFs; see Subsection 3.6.3), derived from 2D (HELIOS) transport calculations of the test zone. The application of PMCFs to the nodal reconstructed total-fission distribution leads to a significant improvement in the agreement with experiment. Thus, the tilt of ~±3% observed for the reference case is practically compensated (in a global sense) when the 48/05 PMCFs are applied.

Concerning the second effect, a systematic underestimation has been observed for the total-fission rates in pins that are near the control blade tips. These deviations, which are approximately −9% for the corner pins J1 and A10, are inherent to the use of reflected geometry in the lattice calculations and cannot be avoided.

For the reference case, the radial comparison of PRESTO-2 with the experiment results in a C/E standard deviation of 3.2%, which is reduced to 2.8% when the 48/05 PMCFs are used. The fact that the agreement is not as good as in the case of Configuration I-1A (the standard deviation of the PRESTO-2 C/Es was 1.3% for that case) shows that the strong radial and azimuthal asymmetry imposed by the control blade, as also the local effects near the absorber, are not completely captured by the nodal methodology.

As expected, the systematic deviations mentioned above are not observed in the comparisons of MCNPX with experiment. The standard deviation of the C/Es in this case is 1.3% (using the axial average of the calculated 3D distributions over each individual rod), while the corresponding value for Configuration I-1A was 1.1%.

As in the case of the uncontrolled configuration, the sensitivity cases corresponding to the assembly lattice description show only a minor impact on the total-fission rate distribution, while the impact of the pin displacements (due to changes in the gap size or in the sub-bundle pressing) is somewhat intensified by the absorbing effect of the control blade. Thus, a gap reduction of ~0.3 mm reduces the fission rate by ~2% in the pins facing the control blade, while a displacement of ~0.5 mm of the sub-assemblies affects the pin-powers by between −2.7% and 4.4%, i.e. slightly more than in the case of Configuration I-1A.

The investigations presented in this chapter show that the proposed methodology is globally quite suitable for the radial assessment of nodal codes using LWR-PROTEUS experimental results in cases including control blades, such as Configuration I-2A. However, significant modelling approximations are needed to represent the 3x3 array of fuel assemblies in the presence of the L-shaped control blade, since this arrangement differs substantially from standard BWR core geometry. For instance, the use of the code system CASMO-5/ SIMULATE-5 was not possible for Configuration I-2A, due to the odd number of assembly rows in the test zone and the particular geometry of the L-shaped control blade.

Chapter 6

Axial changes in nuclear design - Configuration I-1C

The BWR was developed by the Argonne National Laboratory and the first plant, Dresden-1, of 250 MWe, was designed by General Electric and started up in 1960.

In this chapter, the modelling details and results of the comparisons with experiment are presented for LWR-PROTEUS Configuration I-1C, in which the axial effects of the enrichment boundary of the SVEA-96+ assembly were investigated.

Section 6.1 describes the experimental set-up, while the characteristics of the calculational models are presented in Section 6.2 (for HELIOS and PRESTO-2, as well as for CASMO-5 and SIMULATE-5). In Section 6.3, the representation of the test-zone boundary by means of partial currents obtained from 3D MCNPX whole-reactor calculations is addressed, while the limitations concerning the use of 2D PCRs are discussed in Section 6.4. Section 6.5 presents the results of the 3D total-fission C/E comparisons using MCNPX, HELIOS/PRESTO-2 and CASMO-5/SIMULATE-5, about which general remarks are made in Section 6.6. In Section 6.7, results obtained with the latest available PRESTO-2 version, viz. 1.15, released shortly before the conclusion of this research, are shown. The k-effective results obtained in the different calculations presented in this chapter are discussed in Section 6.8. To conclude, Section 6.9 summarizes the principal messages arising from the study of the present configuration.

6.1 Description of the test zone

Viewed axially (and apart from a short, natural uranium blanket region), the SVEA-96+ assemblies used in the LWR-PROTEUS experiments contain two different lattice designs. These two lattices have different enrichments in some of the fuel pins. Moreover, two pins contain gadolinium in the upper lattice only. The transition between two enrichment zones produces strong axial gradients in the neutron flux, which imposes an additional challenge to the pin-power reconstruction capability of the nodal codes.

The axial effect of the enrichment boundary on the neutron flux has been investigated in Configuration I-1C. As in all cases presented in this thesis, this is currently done by comparing the relative pin total-fission rate distributions, as measured by gamma scanning, with the calculated values. For the experimental set-up in PROTEUS, the test tank was axially displaced, making the elevation of the axial change in lattice design of the SVEA-96+ assemblies coincident with the test-zone midplane (see Figure 18 in Section 2.5). The measurements were carried out in 9 different fuel pins, with 17 experimental points per pin, axially distributed over the range −60 cm to +40 cm. The 4th and 5th spacers of the SVEA-96+ bundles (counted from the bottom) were located at −10.66 cm and +28.64 cm with respect to the test-zone midplane, respectively.

As in the case of Configurations I-1A and I-2A, the test tank was filled with light water at room temperature. The sub-assembly pressing, described in Section 4.1, was also the same. The experimental inter-assembly distances in Configuration I-1C are shown in Figure 74.

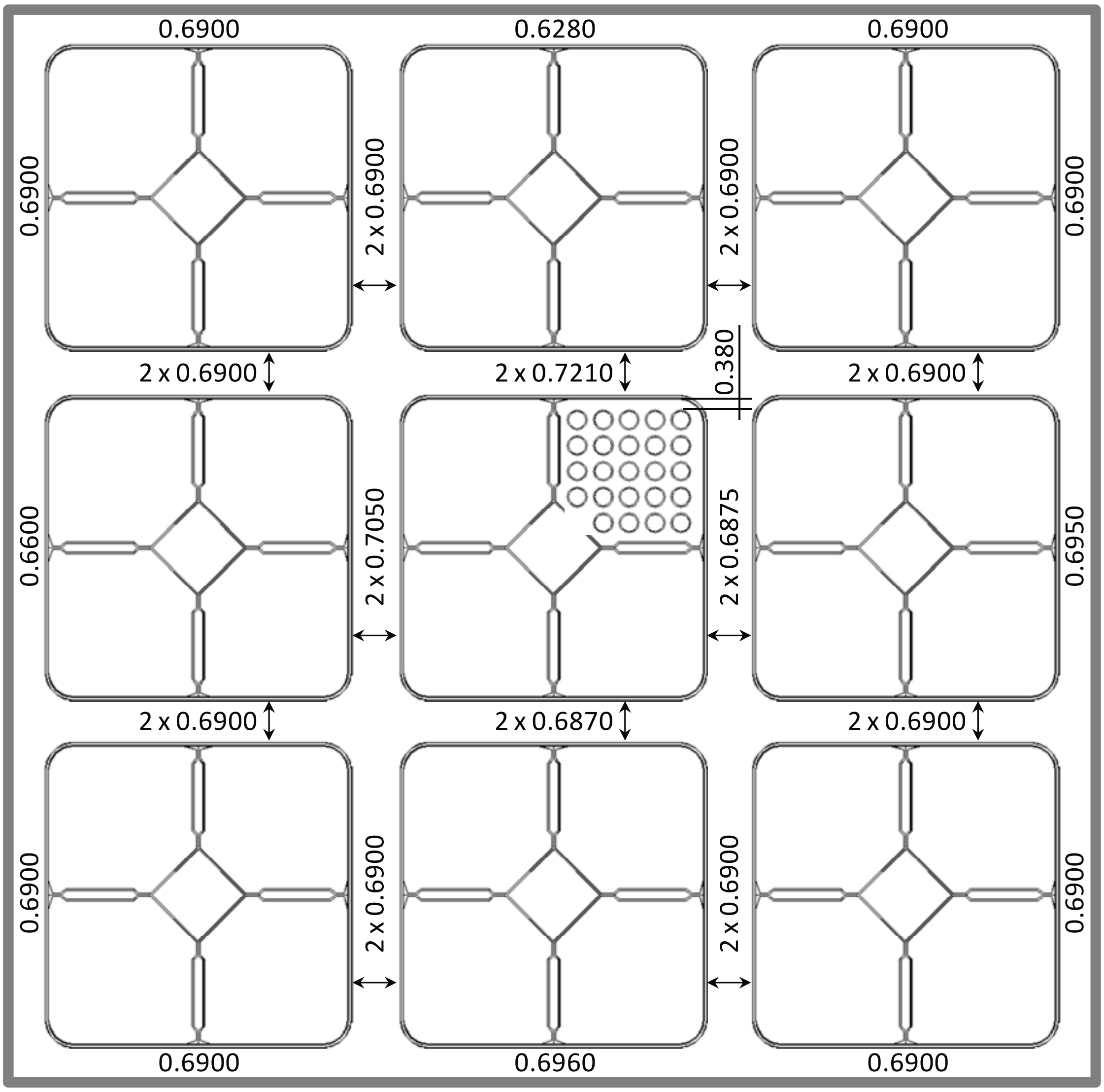

Figure 74 Measured dimensions in Configuration I-1C. The distance between the outer surface of the cladding of the peripheral pins and the inner wall of the fuel box is 0.380 cm (sub-assembly pressed 0.051 cm towards the central canal).

6.2 Characteristics of the calculational models

6.2.1 Lattice calculations - HELIOS model

The lattice calculations were performed with HELIOS using the modelling features corresponding to the reference case, described in Subsection 4.2.1. In the case of Configuration I-1C, two sets of cross-sections, one for the upper part and one for the lower part of the test zone, are needed. Thus, for this configuration, the XSDB contains the data for the corresponding 12 lattices[39]. Furthermore, the assessment of the axial profile being of primary importance, the spacers were modelled explicitly[40]. This has been done following the methodology used in power reactor calculations, i.e. by defining delta parameters representing the spacer (see also Subsection 3.2.2).

6.2.2 Core calculations - PRESTO-2 model

The PRESTO-2 model for the test zone in Configuration I-1C is analogous to that used for Configurations I-1A and I-2A, its fundamental aspects being discussed in Section 3.3. In the present case, the fuel region consists of two segments with an active length of 61.5 cm each, the core midplane being located at the interface between them. The elevations of the centre of the 4th and 5th spacers, with respect to the beginning of the active length in the SVEA-96+ fuel assemblies, are 233.14 cm and 272.44 cm, respectively, while the core midplane is at 243.8 cm (see Figure 18). Thus, the elevations of the spacers with respect to the bottom of the test zone, as specified in PRESTO-2, are:

$$4^{\text{th}} \text{ spacer: } 233.14 - (243.8\text{-}61.5) = 50.84 \text{ cm}$$

$$5^{\text{th}} \text{ spacer: } 272.44 - (243.8\text{-}61.5) = 90.14 \text{ cm}$$

which correspond to −10.66 cm and +28.64 cm with respect to the core midplane, respectively.

As discussed in Subsection 3.3.2, the axial nodalisation of the test zone is kept independent of the spacer positions. The heterogeneous flux solution, as described in Subsection 2.3.2, accounts for the perturbation of the intra-nodal axial flux profile caused by the spacers.

6.2.3 Lattice calculations - CASMO-5 model

As in the case of Configuration I-1A, the CASMO-5 calculations were done using a half-geometry description of the lattices. As before, the displacement of the fuel assemblies, with respect to their nominal positions in the test zone (see Figure 74), was approximately accounted for by defining average wide and narrow gaps. The resulting half-gap sizes are shown, for the nine fuel assemblies, in Figure 75. The differences with respect to the values used in the HELIOS full-geometry calculations are shown, for the central assembly, in Table 27.

Table 27 Half-gaps (cm) used in the HELIOS and CASMO-5 lattice calculations for Configuration I-1C.

Half-gaps	West	North	South	East
HELIOS full-geometry	0.70500	0.72100	0.68750	0.68700
CASMO-5 half-geometry	0.71300	0.71300	0.68725	0.68725
Difference (C5-HE)	0.008	-0.008	-0.00025	0.00025

---

[39] In fact, 12 lattices (instead of 18) are sufficient, since the four corner assemblies (1, 3, 7 and 9) have nominal gaps (see Figure 74) and only need to be calculated once.

[40] As mentioned in Sections 4.8 and 5.7, the spacers were not modelled in the nodal calculations for the axially uniform configurations (I-1A and I-2A). The reason for this is that they do not affect the radial distribution of the total-fission rate at core midplane, which was the subject of investigation in those cases.

According to Table 27, the west half-gap in CASMO-5 is 0.08 mm wider, while the north half-gap is 0.08 mm narrower, compared with the HELIOS full-geometry model. These differences can introduce small deviations in the calculated fission rates, of the order of 0.2% to 0.3% (see also Subsection 4.5.5, where it was found, for Configuration I-1A, that a gap size variation of ~0.03 mm produces a change of about 0.1% in the calculated pin total-fission rate). It must be recalled here that the experimental uncertainty in the total-fission measurements is about 0.5%, so that the definition of wide and narrow average gap widths does not introduce significant additional inaccuracy.

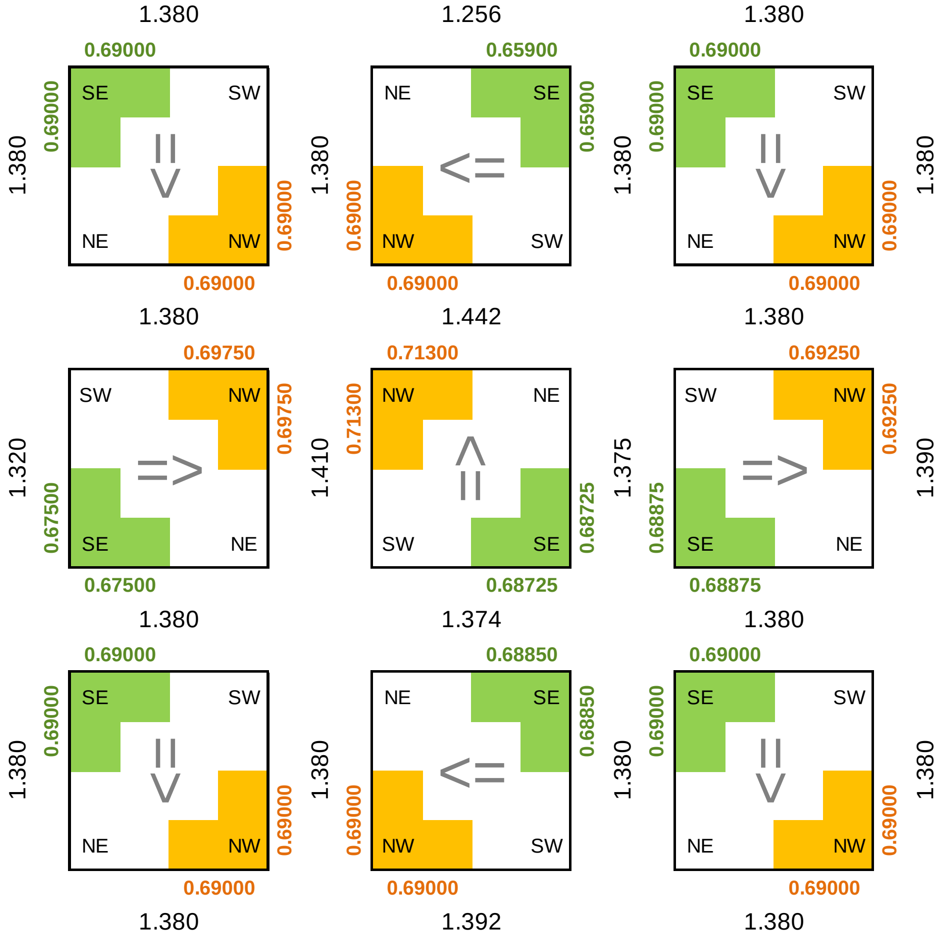

Figure 75 Gap sizes used in the CASMO-5 model for Configuration I-1C. For each assembly, the measured north and west half-gaps are averaged to give the wide half-gap size (orange numbers). Analogously, the experimental south and east values define the CASMO-5 narrow half-gap (green numbers). The black numbers between assemblies are the box-to-box distances, while those at the periphery represent twice the distance between the corresponding fuel box and the test-tank wall. All values are given in cm.

As done before for Configuration I-1A, CASMO-5 cross-section libraries with 2 and 5 energy groups were created for the investigation of Configuration I-1C. The 2-group library has a thermal cut-off energy of 0.625 eV, the group structure of the 5-group library being shown in Table 5, Subsection 3.4.1.

6.2.4 Core calculations - SIMULATE-5 model

The SIMULATE-5 model for Configuration I-1C is basically the same as that used for Configuration I-1A, its fundamental aspects being discussed in Section 3.5. As in the case of

PRESTO-2, the axial composition of the fuel and the spacer positions were specified explicitly. As before, the calculations were performed in 2 and 5 energy groups.

6.3 Test-zone boundary conditions using the 3D MCNPX model

PCRs representing the test-zone surroundings were calculated using a 3D MCNPX model of LWR-PROTEUS for Configuration I-1C, following the methodology described in Subsection 3.6.1. As in the case of Configurations I-1A and I-2A, the MCNPX calculations were performed using 200'000 particles and 250 cycles, i.e. 50x10^6 histories[41].

6.3.1 PCRs for PRESTO-2

The procedure used for calculation of the radial PCRs needed for PRESTO-2 in Configuration I-1C was identical to that described in Subsection 4.3.1 for the case of Configuration I-1A. The results (for 1.84 eV thermal cut-off energy) are shown in Table 28, the approximate 1σ statistical relative errors in % being shown in brackets[42].

Table 28 PCRs for PRESTO-2 in Configuration I-1C, derived from the partial currents obtained in the 3D whole-reactor MCNPX calculation. The figures in brackets are the approximate 1σ statistical relative errors in %. As in the case of production applications at KKL, the HELIOS/PRESTO-2 calculations were performed using a thermal cut-off energy of 1.84 eV.

Configuration I-1C	PCR$_{11}$		PCR$_{22}$	
Upper limit (eV)	20x10^6		1.84	
Axial direction at top	0.796 (0.05)		0.944 (0.1)	
Radial direction	Side	Corner	Side	Corner
1σ error (%)	(0.05)	(0.3)	(0.2)	(1.0)
Axial level 10	1.114	1.111	0.409	0.451
Axial level 9	1.119	1.115	0.409	0.446
Axial level 8	1.125	1.121	0.408	0.436
Axial level 7	1.123	1.121	0.406	0.430
Axial level 6	1.104	1.111	0.401	0.430
Axial level 5	1.068	1.091	0.396	0.429
Axial level 4	1.036	1.072	0.391	0.423
Axial level 3	1.016	1.056	0.386	0.417
Axial level 2	1.004	1.042	0.384	0.419
Axial level 1	0.992	1.032	0.386	0.427
Axial direction at bottom	0.849 (0.05)		0.956 (0.1)	

---

[41] However, for the comparison of the total-fission rate, discussed in Section 6.5 and its subsections, the number of particles and cycles was increased to 10^6 and 800, respectively. This was done to improve the statistical accuracy in the small volumes used to tally the total-fission rate at pellet level.

[42] The PCR relative errors are propagated from the 1σ statistical uncertainties of the MCNPX current tallies. Although these uncertainties slightly dependent on the axial level, a single approximate value, representing all levels, is indicated to characterise the calculational accuracy.

6.3.2 PCRs for SIMULATE-5

The procedure used for the calculation of the radial PCRs needed for SIMULATE-5 in Configuration I-1C was identical to that described in Subsection 4.3.2 for the case of Configuration I-1A. Also here, aiming at use of the multigroup nodal diffusion capability of SIMULATE-5, the PCRs have been defined in five energy groups, in addition to the classical 2-group structure (in this case with a cut-off energy of 0.625 eV). The boundaries of the energy groups correspond to those of Table 7 (Chapter 3). The PCRs are shown in Table 29.

Table 29 PCRs for SIMULATE-5 in Configuration I-1C, derived from the partial currents obtained in the 3D whole-reactor MCNPX calculation[43]. The PCRs are given in the five and two-energy-group structures shown in Table 7.

Configuration I-1C		5 energy groups					2 energy groups	
		PCR_{11}	PCR_{22}	PCR_{33}	PCR_{44}	PCR_{55}	PCR_{11}	PCR_{22}
Upper limit (eV)		20x10^{6}	821x10^{3}	9119	1.84	0.625	20x10^{6}	0.625
Axial dir. at top		0.702	0.851	0.895	0.877	0.927	0.815	0.927
Radial direction	Axial level 10	0.878	1.688	0.687	0.670	0.369	1.097	0.369
	Axial level 9	0.875	1.698	0.696	0.685	0.366	1.102	0.366
	Axial level 8	0.876	1.706	0.708	0.690	0.361	1.108	0.361
	Axial level 7	0.870	1.704	0.710	0.688	0.358	1.106	0.358
	Axial level 6	0.845	1.681	0.704	0.687	0.354	1.089	0.354
	Axial level 5	0.801	1.631	0.693	0.676	0.350	1.057	0.350
	Axial level 4	0.763	1.588	0.681	0.661	0.347	1.028	0.347
	Axial level 3	0.739	1.562	0.671	0.649	0.342	1.009	0.342
	Axial level 2	0.727	1.545	0.662	0.644	0.342	0.997	0.342
	Axial level 1	0.720	1.528	0.652	0.642	0.346	0.985	0.346
Axial dir. at bottom		0.796	0.876	0.911	0.917	0.946	0.859	0.946

6.3.3 Axial behaviour of the radial PCRs

As discussed in Subsections 4.3.3 and 5.3.2, for axially uniform cases, such as Configurations I-1A and I-2A, the axial dependence of the radial PCRs is relatively weak. In the case of Configuration I-1C, on the other hand, the different nuclear designs of the lattices below and above the core midplane lead to a significant axial dependence of the radial PCRs. This can be observed in Table 28 and Table 29, and also in Figure 76, where the PCR values corresponding to Table 28 are presented graphically.

---

[43] The PCRs for SIMULATE-5 were obtained from a separate MCNPX calculation with 800x10^{6} (instead of 50x10^{6}) histories.

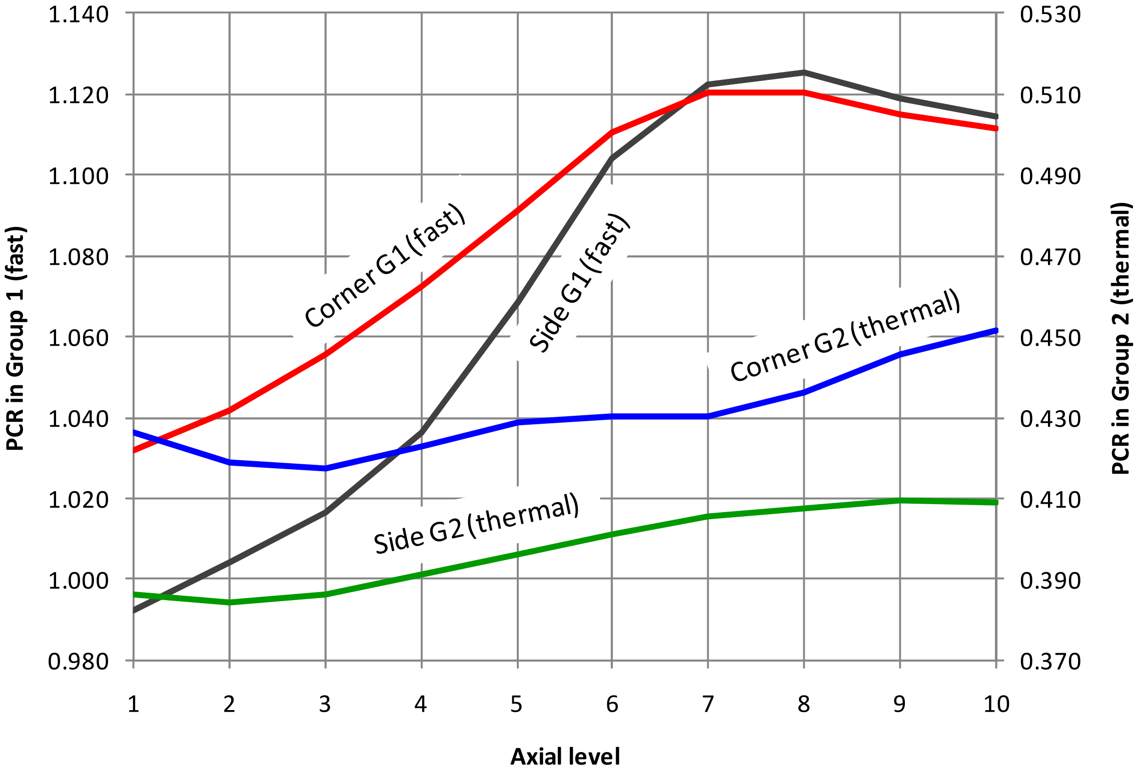

Figure 76 Axial variation of the radial PCRs in Configuration I-1C, as derived from the partial currents obtained in the 3D whole-reactor MCNPX calculation. The numerical values are shown in Table 28.

The axial variation of the PCRs in Configuration I-1C reflects the different k-infinity values of the two lattices constituting the test zone. For instance, for lattice KKL061 (below the core midplane), the k-infinity calculated by HELIOS for assembly 5 is 1.11358, while for lattice KKL060 (above the core midplane) it is 1.04861, i.e. as much as ~6500 pcm lower. Thus, the contribution of the PROTEUS driver zones to the neutron balance in the test zone is significantly stronger in the region above the core midplane, which results in larger radial PCRs for that region, mainly in the epithermal energy group.

Contrary to the case of the axially uniform configurations (I-1A and I-2A), where the use of axially uniform PCRs can be justified (see Sections 4.4 and 5.4), Figure 76 suggests that accounting for the axial dependence of the PCRs in axially heterogeneous cases, such as Configuration I-1C, is very important.

6.3.4 Energy dependence of the partial currents and PCRs

As previously done in Subsections 4.3.4 and 5.3.3 for Configurations I-1A and I-2A, respectively, Figure 77 shows the relative intensity of the partial currents in Configuration I-1C, calculated with the 3D MCNPX model in five energy groups. The results have been obtained by integrating over the complete test-zone radial boundary, i.e. summing over all sides and corners and over all axial levels. Also shown in the figure are the corresponding PCRs.

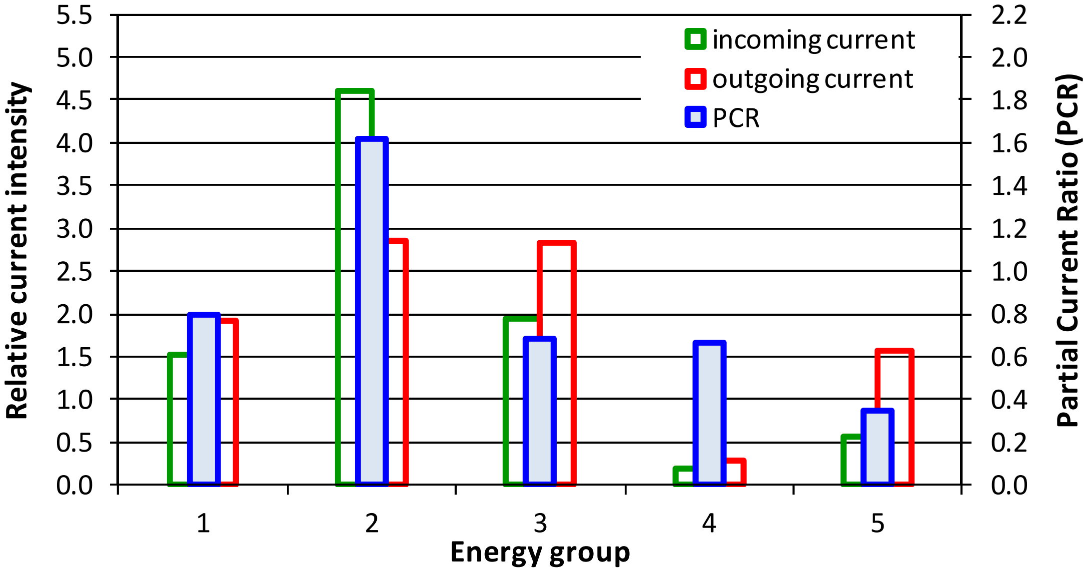

Figure 77 Energy dependence of the radial currents and PCRs in Configuration I-1C in five energy groups, derived from the partial currents obtained in the 3D whole-reactor MCNPX calculation. The partial currents were integrated over the complete test-zone boundary, i.e. were summed over all sides and corners and over all axial levels.

As mentioned before, the axial dependence of the partial currents, and hence the PCRs, is very important in Configuration I-1C. In this frame, it is useful to compare the axial variation of the radial coupling in five energy groups. For instance, Figure 78 and Figure 79 show the relative partial currents and the PCRs at axial levels 8 and 3, respectively, the numerical values of the PCRs having been presented in Table 29. From these pictures, it can be seen that the coupling between the test zone and the surrounding buffer and driver zones is stronger in the upper part of the core (larger PCRs), particularly for the first two groups. As discussed in Subsection 6.3.3, this can be attributed to the lower reactivity of the upper lattice.

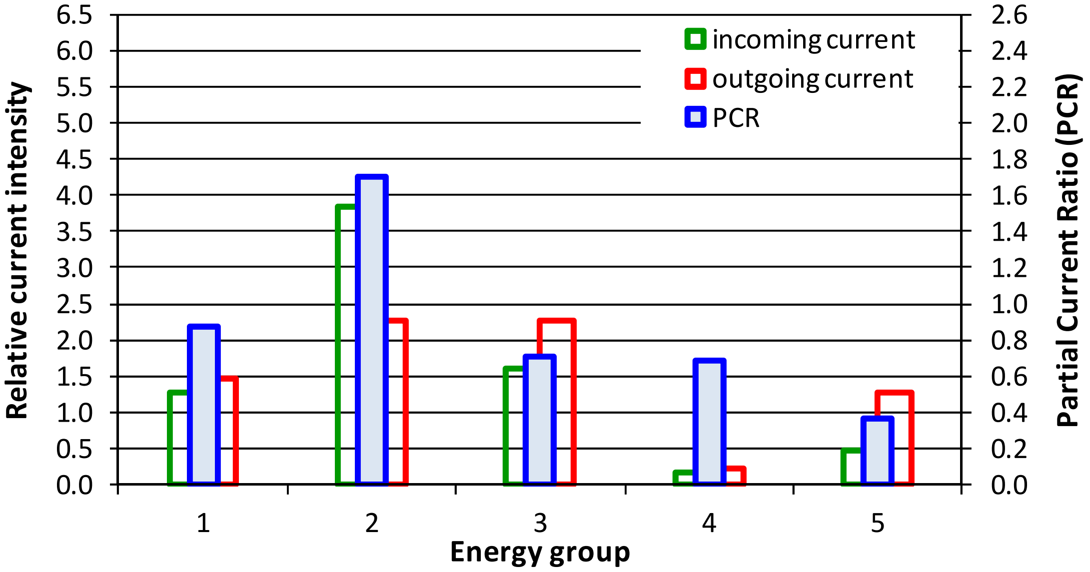

Figure 78 Energy dependence of the radial currents and PCRs in Configuration I-1C in five energy groups, at axial level 8 (middle of the test-zone upper half).

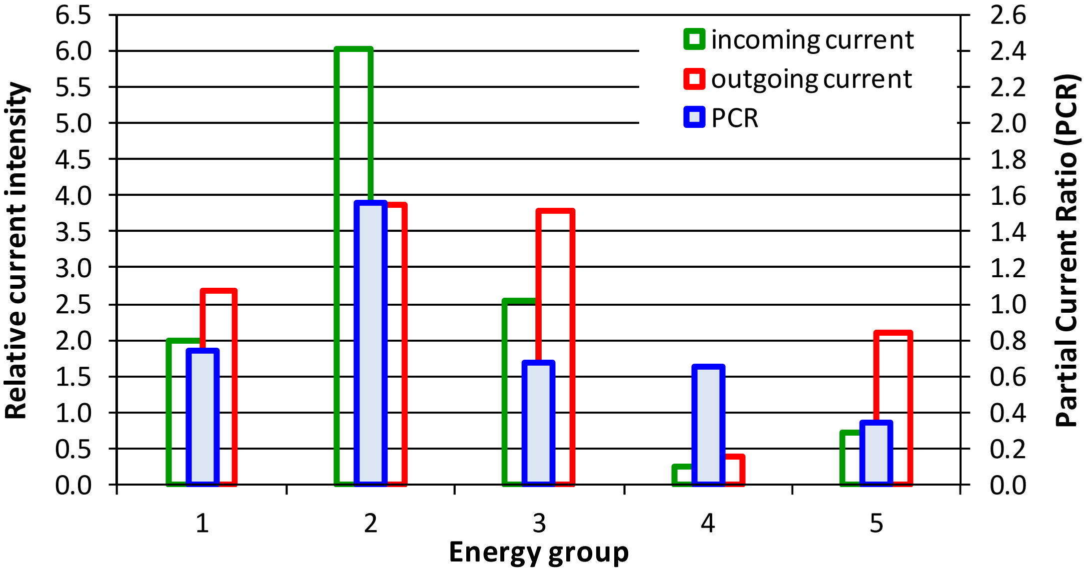

Figure 79 Energy dependence of the radial currents and PCRs in Configuration I-1C in five energy groups, at axial level 3 (middle of the test-zone lower half).

As further illustration, the axial profiles of the partial currents crossing the radial boundary of the test zone, in two energy groups with 0.625 eV cut-off, are shown in Figure 80. It can be seen that the partial current profiles peak in the bottom part of the core.

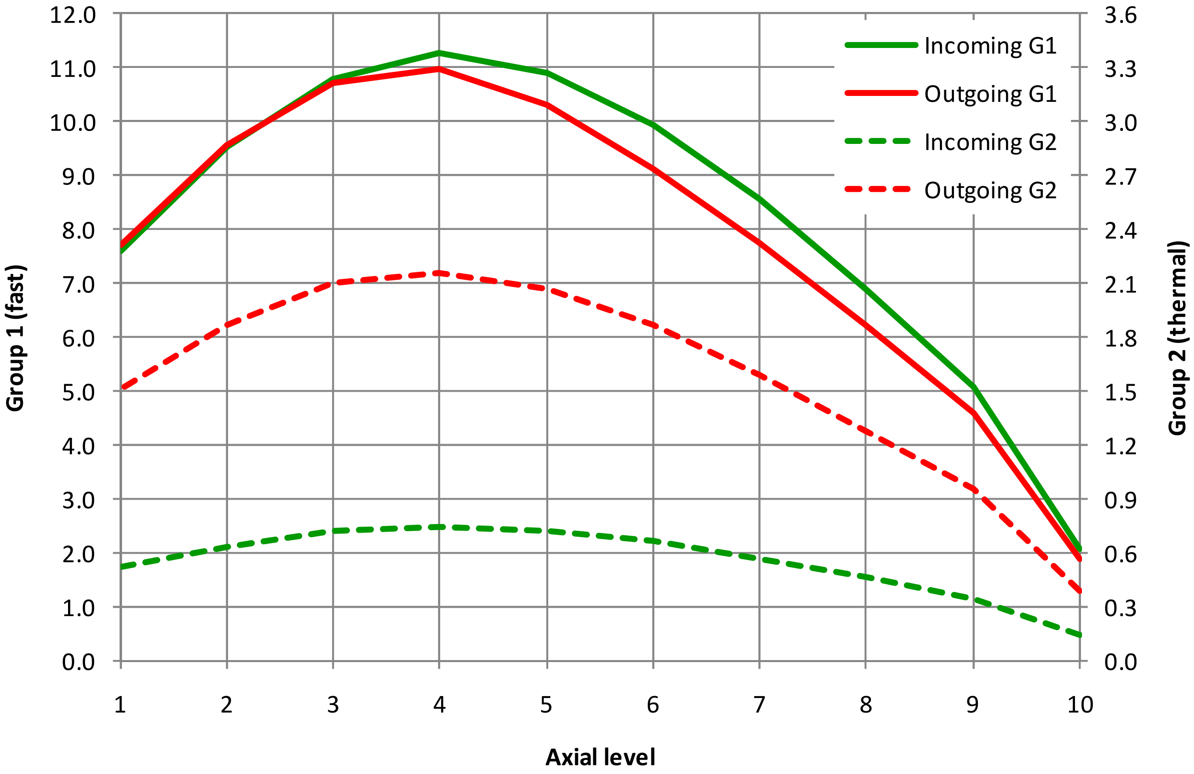

Figure 80 Axial profile of the radial currents in Configuration I-1C in two groups with 0.625 eV cut-off energy. The partial currents were integrated over the test-zone boundary at each axial level, i.e. were summed over all sides and corners.

As could be observed in Figure 76, the axial variation of the epithermal (fast) PCRs shows a smooth increase in the lower part of the core, rather than a steep gradient near the interface between the two enrichment zones at the test-zone midplane. This behaviour can be explained by looking at the axial variation of the partial currents in Figure 80, which shows that, between the bottom of the test-zone and the 6th axial level, approximately, the ratio of the epithermal incoming current to the corresponding outgoing current increases as a function of the elevation. This is consistent with the fact that the outer regions of the reactor are axially uniform, in contrast to the fuel assemblies in the test zone, leading to a more axially uniform profile of the incoming current. The increase of the epithermal PCR from the test-zone bottom to approximately axial level 6 in Figure 76 can be attributed to this effect. In the upper part of the core, beyond the 7th axial level, the impact of the change in the lattice properties vanishes and the PCR varies little with height, finally showing slightly lower values at levels 9 and 10.

6.4 Use of 2D test-zone boundary conditions

In Configuration I-1C, for the reasons discussed in Subsection 6.3.3, axially averaged PCRs cannot be used over the whole test-zone length without the loss of valuable information about the radial leakage. On the other hand, two different sets of PCRs, one for the upper part and one for the lower part of the test zone, respectively, could be derived using the corresponding 2D HELIOS models of the whole LWR-PROTEUS reactor, as done for the full test-zone length PCRs in Configurations I-1A and I-2A (see Subsections 4.5.3 and 5.5.3, respectively).

This 2D approach for the representation of the test-zone surroundings has been applied in a previous publication related to Configuration I-1C [9]. In this earlier work, which is the only existing report of nodal reconstructed C/E results for axial fission rate distributions in the LWR-PROTEUS experiments, the use of two sets of 2D PCRs (referred to as albedos in the publication), derived from HELIOS whole-reactor calculations, was the only means available for representing the test-zone surroundings. Furthermore, due to the lack of 3D information, axial PCRs representing the top and bottom boundaries of the test zone could not be determined. Instead, the nodal domain was modelled as a core extending from the beginning of the fuel assembly active length at the bottom to the test-tank water level at the top, assuming zero incoming currents at both axial boundaries ($PCR_{axial}=0.0$). The length of the test zone (140 cm) was finally fixed by imposing zero radial incoming currents ($PCR_{radial}=0.0$) to the core region extending beyond −70 cm, measured from the test-zone midplane.

In this thesis, the modelling of Configuration I-1C is focussed on the use of 3D PCRs obtained from MCNPX whole reactor calculations. As previously discussed, and with the constraints imposed by the space and energy discretisation, this provides the most accurate description of the test-zone surroundings that can be used for the assessment of nodal methodologies with pin-power reconstruction based on LWR-PROTEUS experimental results.

6.5 3D comparisons of total-fission rates

In Configuration I-1C, the measurements of total-fission were made in 9 fuel pins, at 17 elevations, covering the range −60 cm to +40 cm with respect to the core midplane. The pins were selected to facilitate the investigation of the axial effects of the assembly's enrichment boundary. The lattice positions of the measured pins and their enrichments in % weight ^{235}U are shown in Figure 81, the values being summarised in Table 30.

For the comparisons presented in this section, the 3D set of 9*17=153 experimental points has been normalized to 1.0, as have also the calculated values from MCNPX, PRESTO-2 and SIMULATE-5 for the same set of measured positions. This 3D normalisation has the advantage of allowing a simultaneous visualisation of the axial and radial behaviours[44]. Furthermore, the use of MCNPX as reference (3D transport) calculation allows one to extend the assessment of the two nodal codes beyond the measured domain. Thus, the pellet-level total-fission distribution obtained in the nodal calculations can also be compared in pins and at axial levels for which no measurements exist.

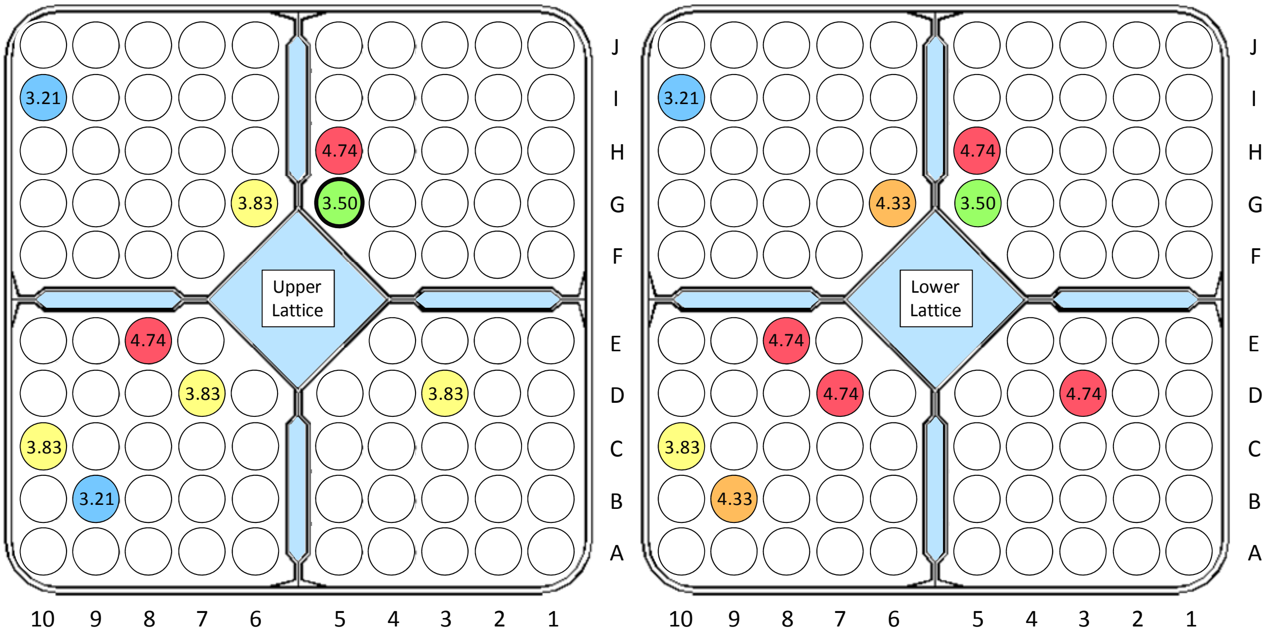

Figure 81 Measured pins in Configuration I-1C. For the upper (left) and lower (right) lattices, the enrichments are given in weight % ^{235}U. Pin G5 contains 2% weight Gd_2O_3 in the upper lattice. Different colours indicate different enrichments, while a thick pin-border indicates the presence of gadolinium.

Table 30 Enrichments (in weight % ^{235}U) and gadolinium contents (in weight % Gd_2O_3) of the measured pins for the upper and lower lattices in Configuration I-1C.

	C10	D3	D7	G6	I10	E8	G5	B9	H5
w/o upper	3.83	3.83	3.83	3.83	3.21	4.74	3.50	3.21	4.74
w/o lower	3.83	4.74	4.74	4.33	3.21	4.74	3.50	4.33	4.74
Gd upper	*0.00*	*0.00*	*0.00*	*0.00*	*0.00*	*0.00*	***2.00***	*0.00*	*0.00*
Gd lower	*0.00*	*0.00*	*0.00*	*0.00*	*0.00*	*0.00*	*0.00*	*0.00*	*0.00*

The C/Es corresponding to MCNPX, PRESTO-2 and SIMULATE-5 are presented and discussed in Subsections 6.5.1 to 6.5.3, respectively, while plots showing the total-fission distribution calculated with the three methodologies, together with the LWR-PROTEUS experimental results, are presented in Subsection 6.5.4. For the plots, the data sets were

---

[44] Using a different approach, two kinds of comparisons were done in [9]. First, the calculated and measured values were normalized considering all (9) measured pins at each axial level independently, thus providing information about the radial behaviour at each position. In a second comparison, each pin was normalized separately, using all (17) measured axial levels, giving in this case information about the axial variation in each pin. The two comparisons effectively reflect, in different ways, the same qualitative behaviour of the transition zone. The 3D normalization employed in this thesis is complementary to the comparison procedure applied in [9], having the advantage of allowing a direct global (axial and radial) comparison.

normalized as described above, the same scale being used in all the graphics in order to facilitate the visual comparison.

6.5.1 C/Es for MCNPX calculated total-fission distribution

The C/E values corresponding to the 153 measurement points, normalised as described earlier, are shown in Table 31. In the last three rows, the maximum, minimum and standard deviation ($\sigma = \sqrt{1/(n-1) \cdot \sum (C/E - \overline{C/E})^2}$) of the C/Es corresponding to each individual pin are shown, the values corresponding to all (153) measurements considered together being given in the last column. The MCNPX calculation was performed using 800 x 10^6 neutron histories.

Table 31 C/E values corresponding to MCNPX for the 153 points (9 pins and 17 axial levels) measured in Configuration I-1C. In the last three rows, the maximum, minimum and standard deviation of the C/Es for each pin (columns 2 to 10) and for all the measurements considered together (last column) are shown. The 13 C/Es with the largest differences from 1.0 are marked with a grey background.

Elev.	C10	D3	D7	G6	I10	E8	G5	B9	H5	All
40	1.046	1.024	1.015	1.019	1.037	1.060	0.980	1.067	1.050	
10	1.043	1.001	1.005	1.010	1.044	1.031	0.932	1.033	0.991	
4	1.039	0.982	0.979	1.001	1.037	1.016	0.931	1.017	1.005	
2	1.033	0.980	0.966	0.987	1.015	1.029	0.904	1.025	1.005	
1	1.016	0.977	0.979	1.003	1.026	1.037	0.950	0.987	1.030	
0	1.031	1.022	1.089	1.022	1.022	1.055	1.881	1.010	1.051	
-1	1.032	1.024	1.088	1.030	1.013	1.046	1.533	1.033	1.045	
-2	1.028	0.986	1.005	1.023	1.021	1.043	1.066	1.035	1.041	
-4	1.011	0.982	1.003	0.995	1.033	1.013	0.992	1.021	1.009	
-6	1.021	0.990	0.994	0.971	1.023	1.035	0.983	1.017	1.007	
-9	0.991	0.994	0.965	0.982	1.013	1.017	0.969	1.023	0.968	
-12	1.007	0.991	0.958	0.976	1.005	1.020	0.973	1.007	0.984	
-16	1.004	0.978	0.969	0.982	1.006	0.984	0.961	1.006	0.983	
-20	1.007	0.976	0.972	0.976	0.984	0.991	0.952	0.991	0.970	
-24	0.991	0.968	0.963	0.963	0.990	1.010	0.958	0.997	0.972	
-40	0.965	0.956	0.959	0.949	0.958	0.966	0.940	0.943	0.950	
-60	0.901	0.848	0.882	0.888	0.905	0.893	0.870	0.894	0.846	
Max	1.046	1.024	1.089	1.030	1.044	1.060	1.881	1.067	1.051	1.881
Min	0.901	0.848	0.882	0.888	0.905	0.893	0.870	0.894	0.846	0.846
StD	0.035	0.039	0.048	0.034	0.034	0.040	0.260	0.039	0.049	0.094

Considering the 153 measured points, the standard deviation of the C/Es is 9.4%, which indicates a relatively good agreement with experiment. However, some points near the strong gradients occurring at level 0 (core midplane) show larger deviations. This is specially the case for pins D7 and G5, which show the two strongest axial steps. In addition, for the bottom-most measurement (−60 cm), the C/Es are particularly low, which can be attributed to their proximity to the boundary of the test zone. If the 13 mentioned points (marked in Table 31 with a grey background) are eliminated from the statistics, the standard deviation of the remaining 140 C/Es is reduced to 3.1%, which represents a very good agreement. Thus, overall, the comparison of the MCNPX results with the LWR-PROTEUS experimental database confirms the ability of the model to adequately predict the total-fission distribution in the central assembly of the test zone. Consequently, the MCNPX results can be used as a reference for carrying out comparisons against other calculations (e.g. P2 and S5) also for pins that were not measured, thus indirectly extending the range of application of the experimental database.

6.5.2 C/Es for PRESTO-2 calculated total-fission distribution

The C/E values corresponding to the PRESTO-2 calculation are depicted in Table 32 analogously to the MCNPX results of Table 31. Considering the 153 measured points, the standard deviation of the C/Es is 11.5%. Remarkably, the 13 points showing the largest deviations (marked with a grey background) are the same ones as in the case of MCNPX. Removing these 13 points from the statistics, the standard deviation of the remaining 140 C/Es is reduced to 4.3%, which for the nodal calculation can be considered as good agreement with experiment. It should be mentioned here that, in the case of PRESTO-2, the standard deviation is affected more strongly by the systematic underestimation observed in the bottom part of the test zone (below −20 cm), which can be observed in the axial plots presented later in Subsection 6.5.4. For instance, excluding in addition the elevations −40 and −24 cm, the standard deviation of the PRESTO-2 C/Es is further reduced to 3.5%. For comparison, for the same set of 122 points, the standard deviation of the MCNPX C/E distribution is 2.9%.

Table 32 C/E values corresponding to PRESTO-2 for the 153 points (9 pins and 17 axial levels) measured in Configuration I-1C. The 13 C/Es with the largest differences from 1.0 are marked with a grey background.

Elev.	C10	D3	D7	G6	I10	E8	G5	B9	H5	All
40	1.061	1.027	1.061	1.015	1.048	1.069	0.994	1.066	1.059	
10	1.056	1.031	1.047	1.010	1.040	1.067	0.959	1.061	1.039	
4	1.056	1.025	1.038	1.011	1.033	1.062	0.940	1.062	1.032	
2	1.052	1.021	1.034	0.990	1.030	1.052	0.924	1.058	1.027	
1	1.048	1.027	1.027	0.995	1.036	1.038	0.925	1.039	1.023	
0	1.038	1.052	1.145	1.022	1.017	1.087	2.010	1.034	1.059	
-1	1.012	1.033	1.147	1.033	0.995	1.095	1.639	1.025	1.067	
-2	1.016	0.997	1.042	1.007	1.000	1.047	1.062	1.028	1.036	
-4	1.011	1.002	1.000	0.988	1.000	1.017	0.969	1.028	0.995	
-6	1.013	1.001	0.994	0.972	1.002	1.017	0.961	1.031	0.998	
-9	1.026	1.018	1.012	0.996	1.017	1.034	0.972	1.041	1.009	
-12	1.027	1.012	1.008	0.989	1.020	1.035	0.971	1.039	1.011	
-16	0.995	0.985	0.980	0.962	0.984	0.996	0.935	1.011	0.974	
-20	0.982	0.971	0.968	0.950	0.971	0.983	0.926	0.998	0.958	
-24	0.970	0.966	0.963	0.937	0.957	0.979	0.912	0.988	0.951	
-40	0.920	0.918	0.922	0.895	0.911	0.928	0.871	0.943	0.905	
-60	0.832	0.832	0.832	0.813	0.835	0.840	0.792	0.865	0.819	
Max	1.061	1.052	1.147	1.033	1.048	1.095	2.010	1.066	1.067	2.010
Min	0.832	0.832	0.832	0.813	0.835	0.840	0.792	0.865	0.819	0.792
StD	0.058	0.053	0.074	0.054	0.053	0.063	0.306	0.050	0.063	0.115

6.5.3 C/Es for SIMULATE-5 calculated total-fission distribution

Table 33 shows the C/E values corresponding to the SIMULATE-5 calculation with 5 energy groups. Considering the 153 measured points, the standard deviation of the C/Es is 10.5%. Also in this case, the 13 points showing the largest deviations (marked with a grey background) are the same ones as with MCNPX. Removing these 13 points from the statistics, the standard deviation of the remaining 140 C/Es is reduced to 3.2%, which for the nodal calculation can be regarded as good agreement with experiment. Compared with PRESTO-2, SIMULATE-5 shows a significantly smaller underestimation of the measurements in the bottom part of the test zone, while agreeing very well with MCNPX (see also the axial plots presented in

Subsection 6.5.4). Thus, when excluding the elevations −40 and −24 cm, the standard deviation of the SIMULATE-5 C/Es remains practically at the same level, viz. 3.3% in this case.

In summary, keeping in mind the 3D character of the distributions being compared, the C/E standard deviations obtained, while excluding the 13 most challenging points, indicate good agreement with experiment of not only the MCNPX results (3.1%) but also of the two nodal calculations, viz. PRESTO-2 (4.3%) and SIMULATE-5 (3.2%).

In the following subsections, plots corresponding to the 3D normalised total-fission rate distributions are shown, providing a visual complement to the numerical results presented in Table 31, Table 32 and Table 33.

Table 33 C/E values corresponding to SIMULATE-5 for the 153 points (9 pins and 17 axial levels) measured in Configuration I-1C. The 13 C/Es with the largest differences from 1.0 are marked with a grey background.

Elev.	C10	D3	D7	G6	I10	E8	G5	B9	H5	All
40	0.979	0.947	0.969	0.942	0.974	0.988	0.914	0.982	0.979	
10	1.016	0.993	0.997	0.979	1.009	1.032	0.925	1.021	1.003	
4	1.026	0.997	0.998	0.989	1.013	1.035	0.914	1.032	1.006	
2	1.026	0.995	0.997	0.971	1.013	1.030	0.899	1.031	1.004	
1	1.024	1.003	0.993	0.977	1.022	1.017	0.904	1.015	1.002	
0	1.026	1.040	1.126	1.014	1.014	1.081	2.006	1.022	1.053	
-1	1.010	1.030	1.142	1.032	1.001	1.102	1.645	1.022	1.073	
-2	1.015	0.995	1.036	1.006	1.006	1.053	1.065	1.025	1.042	
-4	1.008	0.998	0.994	0.986	1.006	1.022	0.971	1.025	0.999	
-6	1.008	0.994	0.985	0.966	1.004	1.018	0.960	1.025	1.000	
-9	0.985	0.974	0.966	0.964	0.985	0.998	0.942	0.997	0.974	
-12	0.992	0.974	0.968	0.962	0.995	1.005	0.946	1.000	0.982	
-16	1.002	0.989	0.983	0.969	0.998	1.010	0.946	1.016	0.988	
-20	1.000	0.986	0.981	0.966	0.996	1.006	0.946	1.014	0.980	
-24	0.998	0.991	0.987	0.964	0.992	1.014	0.942	1.015	0.984	
-40	0.978	0.973	0.976	0.952	0.977	0.992	0.929	1.000	0.967	
-60	0.919	0.920	0.919	0.902	0.929	0.936	0.882	0.954	0.912	
Max	1.026	1.040	1.142	1.032	1.022	1.102	2.006	1.032	1.073	2.006
Min	0.919	0.920	0.919	0.902	0.929	0.936	0.882	0.954	0.912	0.882
StD	0.026	0.027	0.055	0.029	0.022	0.037	0.304	0.020	0.036	0.105

6.5.4 3D comparisons

Measured pins I10 and C10

Figure 82 shows the axial comparison of MCNPX, PRESTO-2, SIMULATE-5 and experiment for pins I10 and C10. Both pins are axially uniform, but differ in their enrichments (3.21% and 3.83%, respectively). Despite this difference, the power level in both pins is almost identical, which is an indication of a successful nuclear design[45].

The agreement between measurement and calculation for these pins is, in general, very satisfactory. In the region of greatest interest, i.e. between the axial levels −20 cm and +10 cm

---

[45] One of the main targets of the lattice designer is the minimisation of the peaking factor, i.e. the pin enrichments are selected such as to obtain a pin-power distribution which is as flat as possible.

with respect to the core midplane, where most measurements were done, MCNPX, PRESTO-2 and SIMULATE-5 agree very well with experiment. The depression caused by the spacer located at −10.66 cm is well predicted by MCNPX and SIMULATE-5. PRESTO-2, however, does not capture this effect correctly. It will be shown, in Section 6.7, that this aspect improves when the latest available PRESTO-2 version, viz. 1.15, is used.

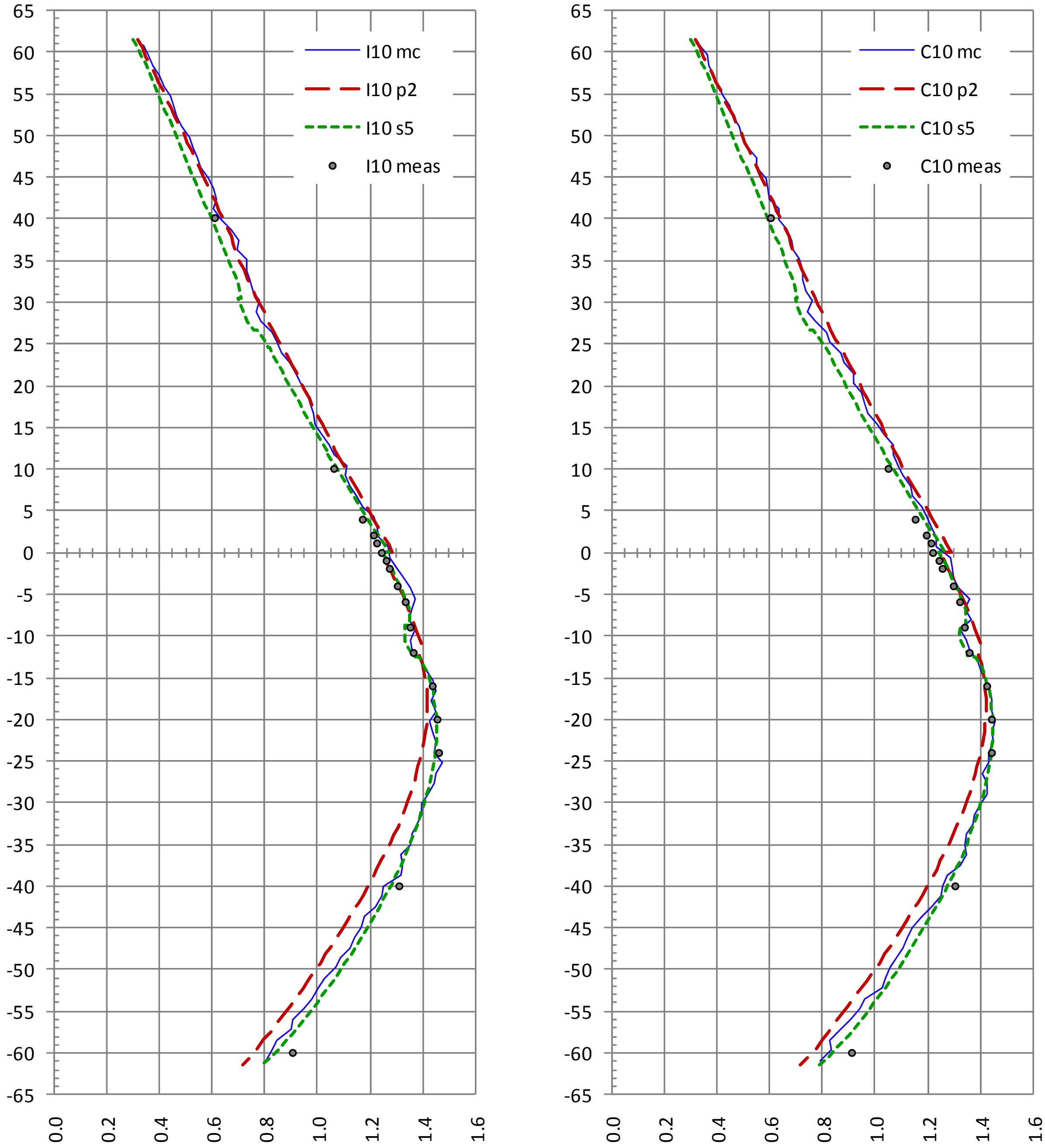

Figure 82 Configuration I-1C: 3D comparison of calculated and measured total-fission rates in pins I10 and C10 (both axially uniform, with 3.21% and 3.83% enrichment, respectively) for MCNPX (blue line), PRESTO-2 (red dashed line) and SIMULATE-5 (green dotted line). All distributions are normalized to 1.0 over the complete 3D set of 153 measured points.

The transition between axial nodes 5 and 6 (whose interface coincides with the core midplane) shows a singular behaviour (~4% step) in PRESTO-2 and, although with lower intensity (~1%), also in SIMULATE-5. This unphysical behaviour is caused by the combined effect of the variable separation of the flux (equation {30}) and the use of 2D pin-power maps for the pin-power reconstruction (see also Section 6.6).

Away from the core midplane, the agreement is also satisfactory. MCNPX and SIMULATE-5 show a very good agreement with experiment in the axial range ±40 cm, while both codes slightly underestimate the lowermost measurement, at −60 cm, by about 10% and 8%, respectively. In the bottom part of the test zone, PRESTO-2 systematically underestimates the measurements, the deviation of the C/E reaching ~17% at −60 cm.

The standard deviations of the C/Es for pin I10 are, for MCNPX, PRESTO-2 and SIMULATE-5, 3.4%, 5.3% and 2.2%, respectively. For pin C10, these are 3.5%, 5.8% and 2.6%, respectively.

Measured pins E8 and H5

Figure 83 shows the axial comparison of MCNPX, PRESTO-2, SIMULATE-5 and experiment for pins E8 and H5, which are uniformly enriched (4.74%). Since these two pins occupy symmetrical positions far from the inter-assembly gaps, the deterministic calculations give almost identical results[46].

In this case, however, significant composition changes occur in neighbouring pins[47]. Due to this, and despite the axially uniform composition of the two investigated pins, the nodal reconstructed total-fission profile shows, for both PRESTO-2 and SIMULATE-5, a step at core midplane. This behaviour is caused by the 2D character of the pin-power maps used in the pin-power reconstruction process. As mentioned in Subsection 2.3.2, the final, heterogeneous flux is obtained by superposition of the homogeneous solution (corrected by the discontinuity factors) and the 2D relative pin-power distribution, obtained from the lattice calculation. Since the lattice transport calculation is performed in 2D, it does not account for the local effect of the axial heterogeneity. Thus, even though the homogeneous flux solution reproduces well the global intra-nodal axial profile, the 3D transport information needed to describe the axial gradient in the vicinity of the lattice interface is not available. In addition, the variable separation embodied in equation {30} does not allow for the introduction of pin-wise axial corrections to the heterogeneous flux (see also the discussion in Section 6.6). The combination of these two limitations produces, as can be seen in Figure 83, somewhat larger deviations with respect to the experimental results very close to the core midplane. A similar behaviour is observed in all pins showing steep gradients at core midplane, as will be shown further below. The MCNPX results, on the other hand, accurately reproduce the smooth gradient evidenced by the measurements. This result confirms the ability of the high-order transport calculation to accurately describe the 3D flux gradients occurring in the vicinity of axial heterogeneities.

Despite the above discussed effect, which is inherent to the pin-power reconstruction methodology, the agreement between calculation and measurement in the central region of the test zone is, in general, good. Away from the core midplane, MCNPX and SIMULATE-5 show very good agreement with experiment in the axial range ±40 cm, while both codes underestimate the lowermost measurement, at −60 cm, by about 11% and 7%, respectively, for pin E8.

---

[46] In the case of symmetrical gaps, the deterministic calculations would have given exactly identical results.

[47] In fact, pins E7 and G5 show very steep axial variations of the fission rate, caused by the presence of gadolinium in their upper halves.

PRESTO-2, in this case, systematically underestimates the measurements in the bottom part of the test zone, with the C/E deviation reaching about 16% at −60 cm for pin E8.

The standard deviations of the C/Es for pin E8 are, for MCNPX, PRESTO-2 and SIMULATE-5, 4.0%, 6.3% and 3.7%, respectively, while for pin H5 these are 4.9%, 6.3% and 3.6%, respectively.

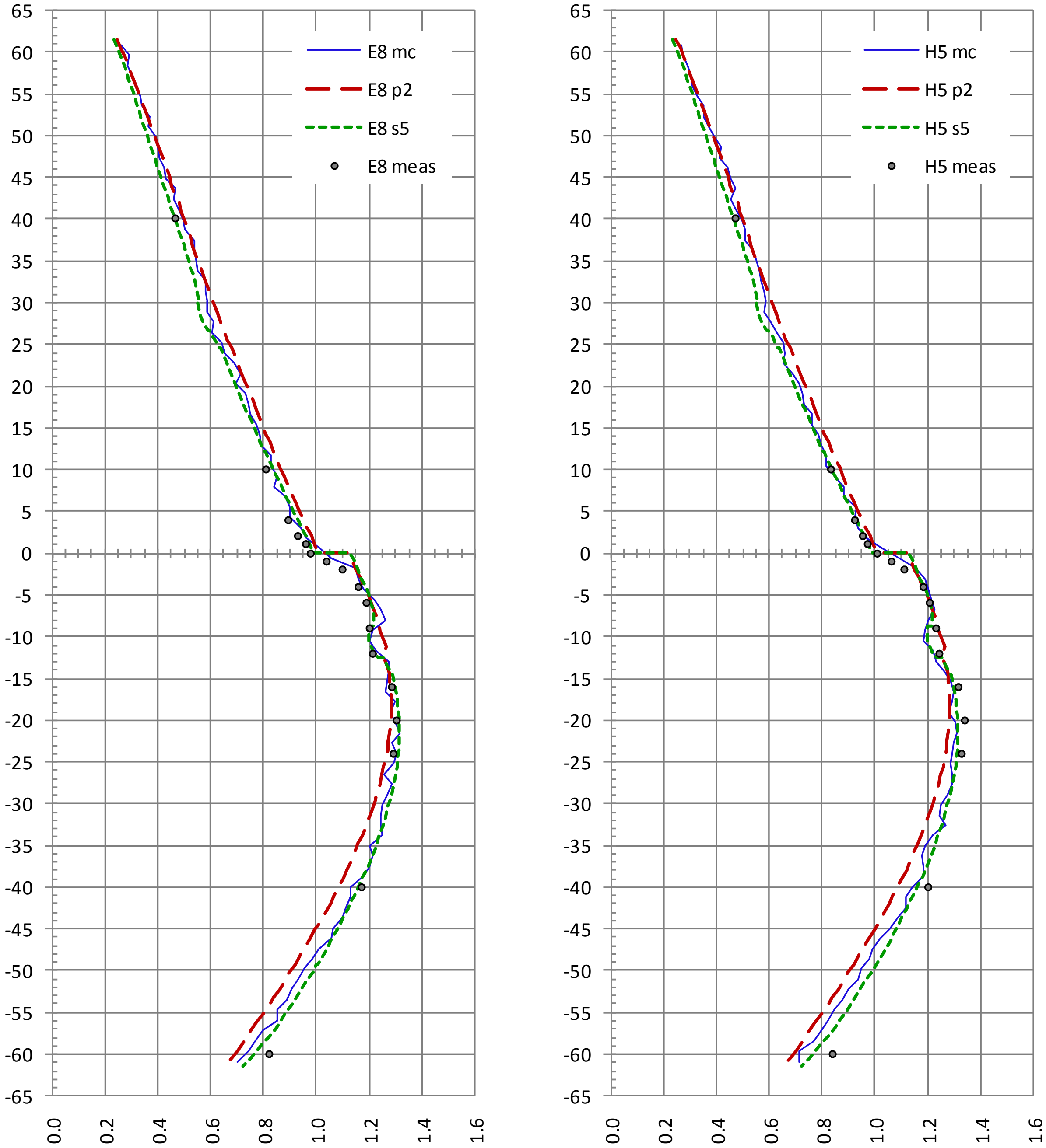

Figure 83 Configuration I-1C: 3D comparison of calculated and measured total-fission rates in pins E8 and H5 for MCNPX (blue line), PRESTO-2 (red dashed line) and SIMULATE-5 (green dotted line). These two pins occupy symmetrical positions, are axially uniform and have 4.74% enrichment.

Measured pins D7 and D3

These two pins feature a fuel composition change (the ^{235}U enrichment being 3.83% above, and 4.74% below, the core midplane). The total-fission comparisons are shown in Figure 84. Also in this case, and for the same reasons as mentioned earlier, the axial flux gradient occurring very close to the core midplane is not completely captured by the nodal calculations, while MCNPX reproduces the experimental results with good accuracy. In pin D7, the stronger flux depression caused by the gadolinium present in the upper part of the neighbouring pin E7 can be clearly observed.

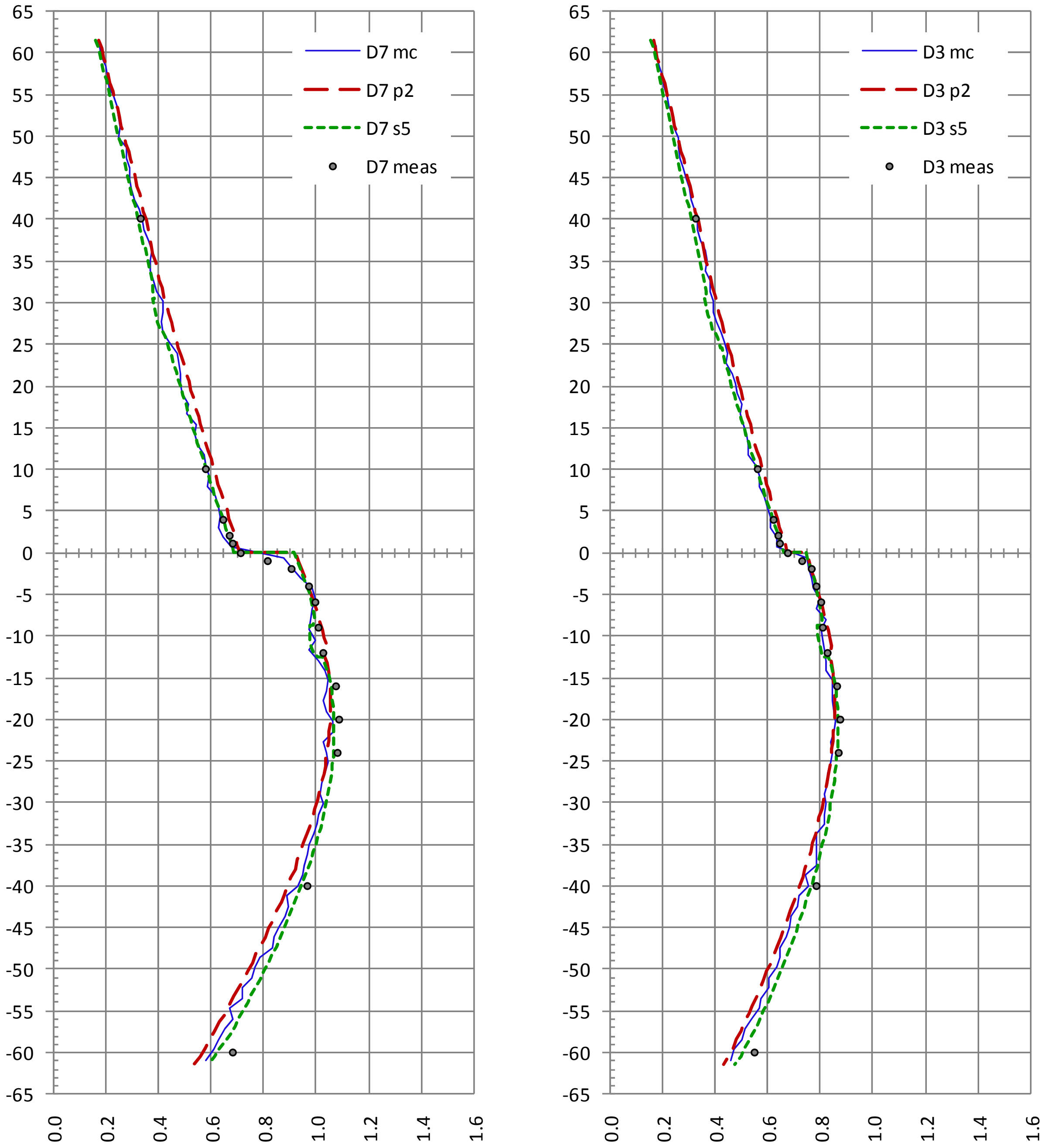

Figure 84 Configuration I-1C: 3D comparison of calculated and measured total-fission rates in pins D7 and D3 for MCNPX (blue line), PRESTO-2 (red dashed line) and SIMULATE-5 (green dotted line). These two pins are of 3.83% enrichment in the upper part and 4.74% in the lower part.

One particularity of these two pins is that they are not facing water regions (water cross, water wing or inter-assembly gap). The agreement between PRESTO-2 and MCNPX for the bottom part of the test zone is better than in the previously discussed cases.

The standard deviations of the C/Es for pin D7 are 4.8%, 7.4% and 5.5% for MCNPX, P2 and S5, respectively, while for pin D3 the corresponding values are 3.9%, 5.3% and 2.7%.

Measured pins B9 and G6

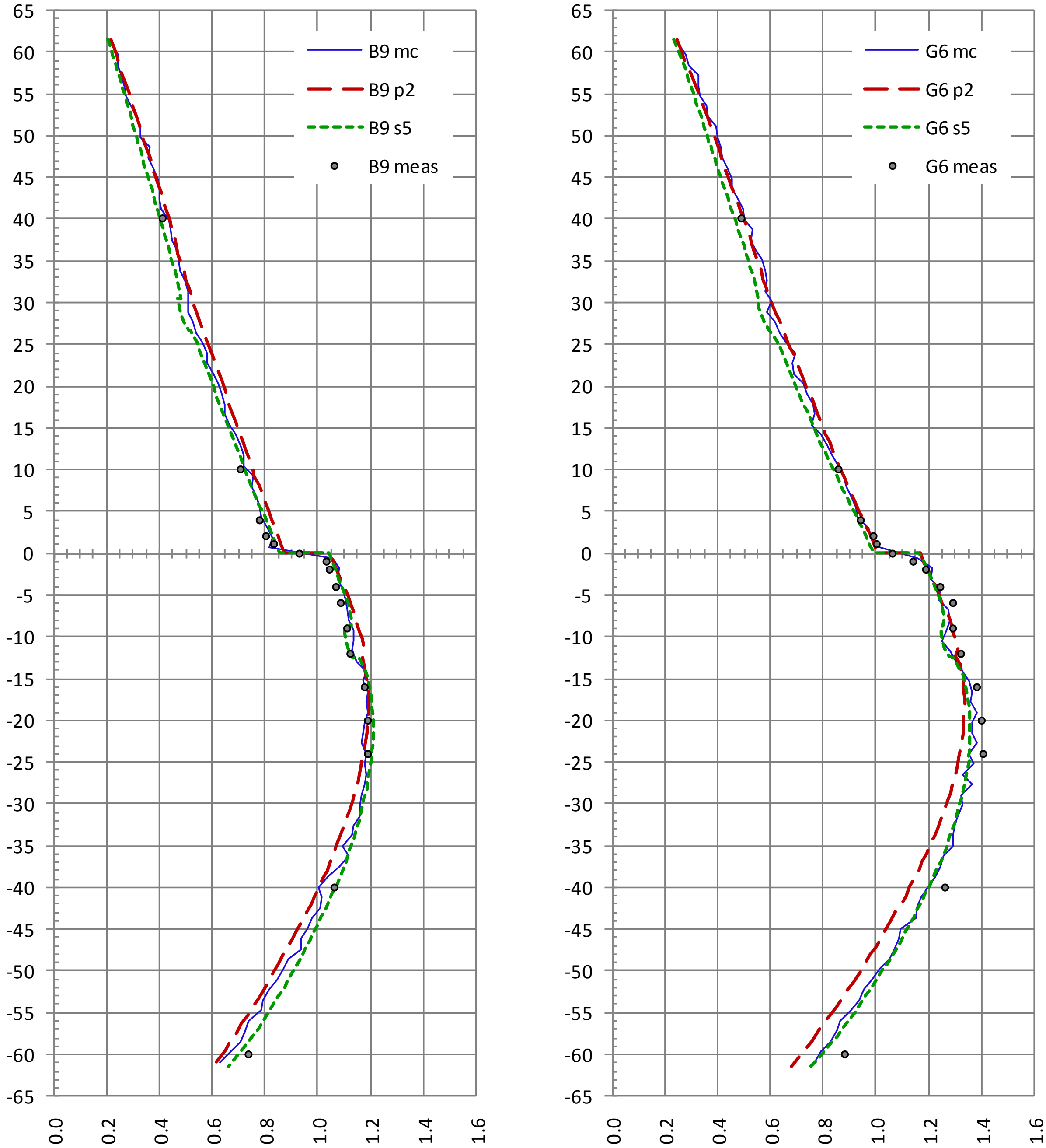

Figure 85 Configuration I-1C: 3D comparison of calculated and measured total-fission rates in pins B9 and G6 for MCNPX (blue line), PRESTO-2 (red dashed line) and SIMULATE-5 (green dotted line). In the upper part, pin B9 has 3.21% enrichment and pin G6 3.83%, both having 4.33% enrichment in the lower part.

The results for these pins are shown in Figure 85. The same behaviour and trends discussed earlier are also observable in these pins. In particular, the effects of the water structures (cross and wing) adjacent to pin G6 can be seen. As mentioned before, for pins that are far from water volumes (e.g. D7, D3 and B9), the global agreement in the bottom part of the test zone is better than for pins that are adjacent to them. For the latter, all calculations tend to underestimate the measurements more strongly, the deviation being most pronounced in the case of PRESTO-2.

The standard deviations of the C/Es for pin B9 are, for MCNPX, PRESTO-2 and SIMULATE-5, 3.9%, 5.0% and 2.0%, respectively, while for pin G6 these are 3.4%, 5.4% and 2.9%, respectively.

Measured pin G5

The most pronounced axial gradient occurs in pin G5, in which the upper part has a gadolinium content of 2%. This can clearly be seen in Figure 86. Due to the large gradient, the differences between calculation and experiment are relatively large very near the core midplane. Also for the remaining measurements in the bottom half of the test zone, the agreement of all three calculations with experiment is worse than for other pins. Here, the calculations are systematically lower than the measurements at all points, except at 0, −1 and −2 cm (at 0 cm, the results of the nodal calculations are not well defined, since this point coincides exactly with the node boundary and the profile is not continuous).

Thus, considering all the 17 measured points, the standard deviations of the C/Es for pin G5 are 26.0%, 30.6% and 30.4%, for MCNPX, PRESTO-2 and SIMULATE-5, respectively. However, excluding from the statistics the three above mentioned points, the standard deviations are drastically reduced to 3.3%, 5.1% and 2.5%, respectively.

This suggests that excluding the elevations 0, −1 and −2 cm from the normalisation process could affect the overall agreement of the 3D distribution. However, normalizing the measured and calculated results over the set of 9 x 14 = 126 points leads to practically unchanged results. This is due to the fact that among the 27 ignored points, only 4 (see Table 32 and Table 33) show very large deviations.

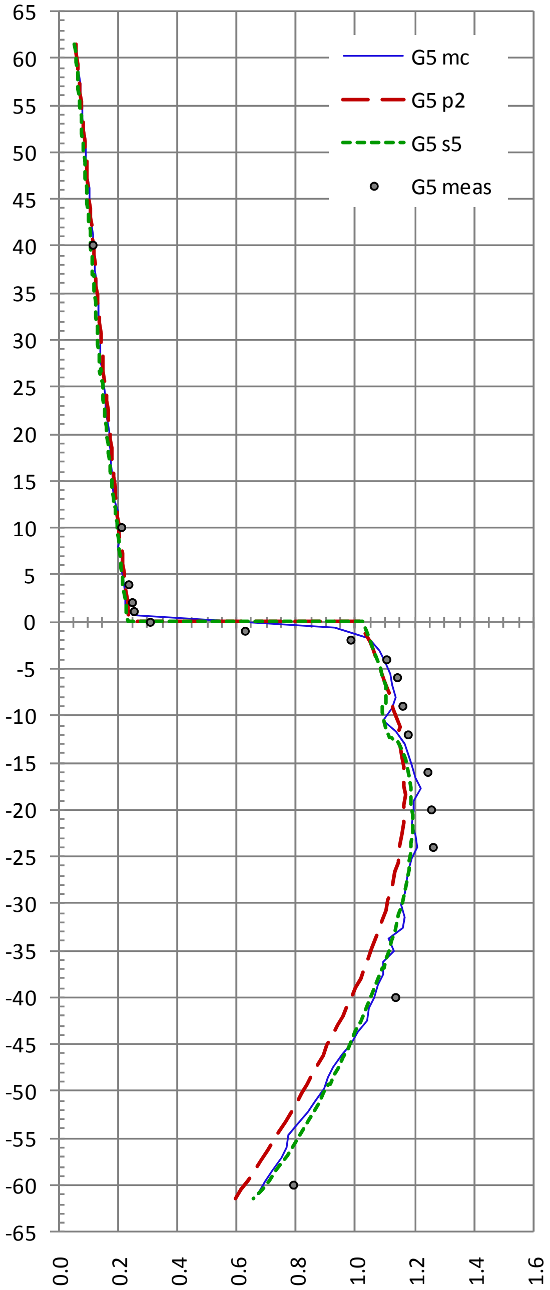

Figure 86 Configuration I-1C: 3D comparison of calculated and measured total-fission rates in pin G5. The enrichment is uniformly 3.50%. In the upper part, the pellets contain 2% gadolinium.

6.6 General remarks concerning the 3D comparisons in Configuration I-1C

In this configuration, the composition (enrichment and/or gadolinium concentration) of several fuel pins is axially non-uniform. In the transition region (±4 cm from core midplane), the variable separation represented by equation {30} of Subsection 2.3.2, whereby all pins receive the same axial dependence for the asymptotic flux inside the node, and the approximation embodied in the use 2D pin-power maps for the determination of the heterogeneous flux, lose accuracy. The small, unphysical step observed in the PRESTO-2 and SIMULATE-5 results for pins I10 and C10 at core midplane (see Figure 82), reflects this effect. For these pins, which are axially uniform and mostly surrounded by uniform neighbours, the combined effects of the differences between the 2D pin-power maps of the upper and lower lattices and the use of a radially uniform $\xi(z)$ for the asymptotic flux, lead to this unphysical behaviour (which is observed in neither the measurements nor in the MCNPX results).

Pins affected by axial heterogeneities, on the other hand, show large fission rate gradients at the core midplane. This is the case, for example, of pin G5, shown in Figure 86, and pins B9 and E8, shown in Figure 85 and Figure 83, respectively. For these pins, the step occurring at the nodal interface coincident with the core midplane is mainly caused by the differences between the 2D pin-power maps corresponding to the upper and lower lattices. Pin G5 contains gadolinium above the core midplane only. Pin B9 has an enrichment discontinuity and is surrounded by an almost axially uniform neighbourhood, while pin E8 is axially uniform but is surrounded by several pins with axial discontinuities.

Focusing the discussion on the range ±15 cm, and ignoring the immediate vicinity of the core midplane (measurements at 0, −1 and −2 cm), the comparison of the three calculations with experiment shows in general good agreement.

Concerning the immediate vicinity of the core midplane, the gradual transition, well predicted by MCNPX, is described by PRESTO-2 and SIMULATE-5 as a pronounced step. Here, the effect of the composition change cannot be correctly accounted for by the function $\xi(z)$, describing the axial dependence of the asymptotic flux, since this is a global dependence valid for all pins. In addition, with $\xi(z)$ being a combination of exponential shape functions (see Subsection 2.3.1), the strong gradients occurring at the node boundaries coincident with the axial discontinuity cannot be captured completely. Furthermore, as already mentioned in Subsection 6.5.4, the 2D character of the pin-power maps used in the reconstruction process plays a fundamental role. In this frame, the lack of 3D transport information at pellet level, which cannot be compensated due to the unavailability of radially dependent $\xi(z)$ functions, contributes significantly to the deviations observed very near the axial discontinuity.

When interpreting the results in the vicinity of the core midplane, however, there is one observation that should be made concerning the axial position of the enrichment boundary. Due to the pre-defined dimension of the fuel pellets, it is possible that the real position of the interface between two different enrichments slightly differs from its nominal value. Due to the fabrication tolerances, this difference may even vary among the pins. Uncertainties of some few millimetres due to these effects must therefore be expected, which is especially important when the results in the vicinity of very steep gradients are compared. For instance, observing the axial profiles in the 3D comparisons of MCNPX with experiment for pins E8, H5, D7, D3 and G5, it seems to be quite plausible that the enrichment boundaries are located slightly below (about 1cm) the nominal elevation (which is coincident with the test-zone midplane). These displacements, moreover, may be different in the individual pins (consider, for instance, the axial plots for pins B9 and G6, from which hardly any displacement can be inferred).

The agreement of SIMULATE-5 with MCNPX is very good over the whole test-zone length and for all pins (this is also true for pins that have not been measured). PRESTO-2, on the other hand, agrees well with MCNPX in the upper half of the test zone (which has a lower k-infinity than the lower half). Far below the core midplane, PRESTO-2 tends to deliver lower values than MCNPX for pins that are adjacent to water structures (internal bypasses or inter-assembly gaps). At the lowest levels, all calculations tend to underestimate the experiment, the differences being larger with PRESTO-2 than with MCNPX and SIMULATE-5.

As mentioned earlier, the only previous detailed reporting of nodal reconstructed results for axial total-fission rate distributions in the LWR-PROTEUS experiments has been in [9], and that has been for this particular test-zone configuration. Despite the significant differences in the description of the test-zone surroundings, as also in the normalization procedure adopted, the observations made regarding the pin-power reconstruction results have been similar.

In brief, since the axial heterogeneity in Configuration I-1C is related to the changes in fuel pin compositions, the impact on the fission rate is mainly local and can be well described by the pin-power reconstruction process, except very close to the enrichment boundary. This results in acceptable values for the standard deviations of the ratios between calculation and experiment, which significantly improve if the most challenging points, at levels 0, −1 and −2 cm, are not included in the statistics (see also Table 34).

Table 34 Standard deviations of C/E values, in %, for the 3D pin-wise total-fission rate distribution in Configuration I-1C. The individual C and E distributions have each been normalized to 1.0 over the whole set of 153 measured points. In the first three rows, the standard deviation for each pin has been calculated while including all the 17 measured elevations, while in the last three rows the most challenging levels (0, −1 and −2 cm) have been excluded from the statistics (only 14 points are considered).

		C10	D3	D7	G6	I10	E8	G5	B9	H5	All
17 axial points	MCNPX	3.5	3.9	4.8	3.4	3.4	4.0	26.0	3.9	4.9	9.5
	PRESTO-2	5.8	5.3	7.4	5.4	5.3	6.3	30.6	5.0	6.3	11.6
	SIMULATE-5	2.6	2.7	5.5	2.9	2.2	3.7	30.4	2.0	3.6	10.6
14 axial points	MCNPX	3.8	4.0	3.2	3.3	3.8	4.1	3.3	4.2	4.8	4.2
	PRESTO-2	6.4	5.6	6.0	5.6	5.9	6.3	5.2	5.6	6.4	6.2
	SIMULATE-5	2.8	2.3	2.1	2.2	2.3	2.5	2.5	2.1	2.4	3.3

It can be seen, from these results, that the steep gradient occurring in pin G5 is the main single factor responsible for the relatively high standard deviations calculated over all (153) points (last column, three first rows in Table 34).

6.7 Use of PRESTO-2-1.15

It should be recalled here that, as long as nothing else is explicitly mentioned, all PRESTO-2 calculations presented in this thesis correspond to the code version that was available when the thesis started, in the year 2007, viz. PRESTO-2-1.13. In 2008, version 1.14 was released, but the changes included in it did not affect the results of the flux calculation. Recently, SSP released a new code version, viz. PRESTO-2-1.15. In it, several improvements concerning the axial homogenisation methodology have been introduced. In particular, the ability to model local axial discontinuities, such as for example spacers or the tip of a control rod, has been enhanced. As mentioned in Subsection 6.5.4, PRESTO-2-1.13 does not capture the effect of the spacers on the total-fission profile correctly. To show the effect of the above code modifications, the PRESTO-2 calculations were repeated using the new programme version. As an example, Figure 87 shows the results for pins B9 and G6. As can be seen by comparing the plots with those of Figure 85, there is a considerable improvement, the presence of the spacers now being captured by corresponding flux depressions at −10.66 cm and +28.64 cm with respect to the core midplane.

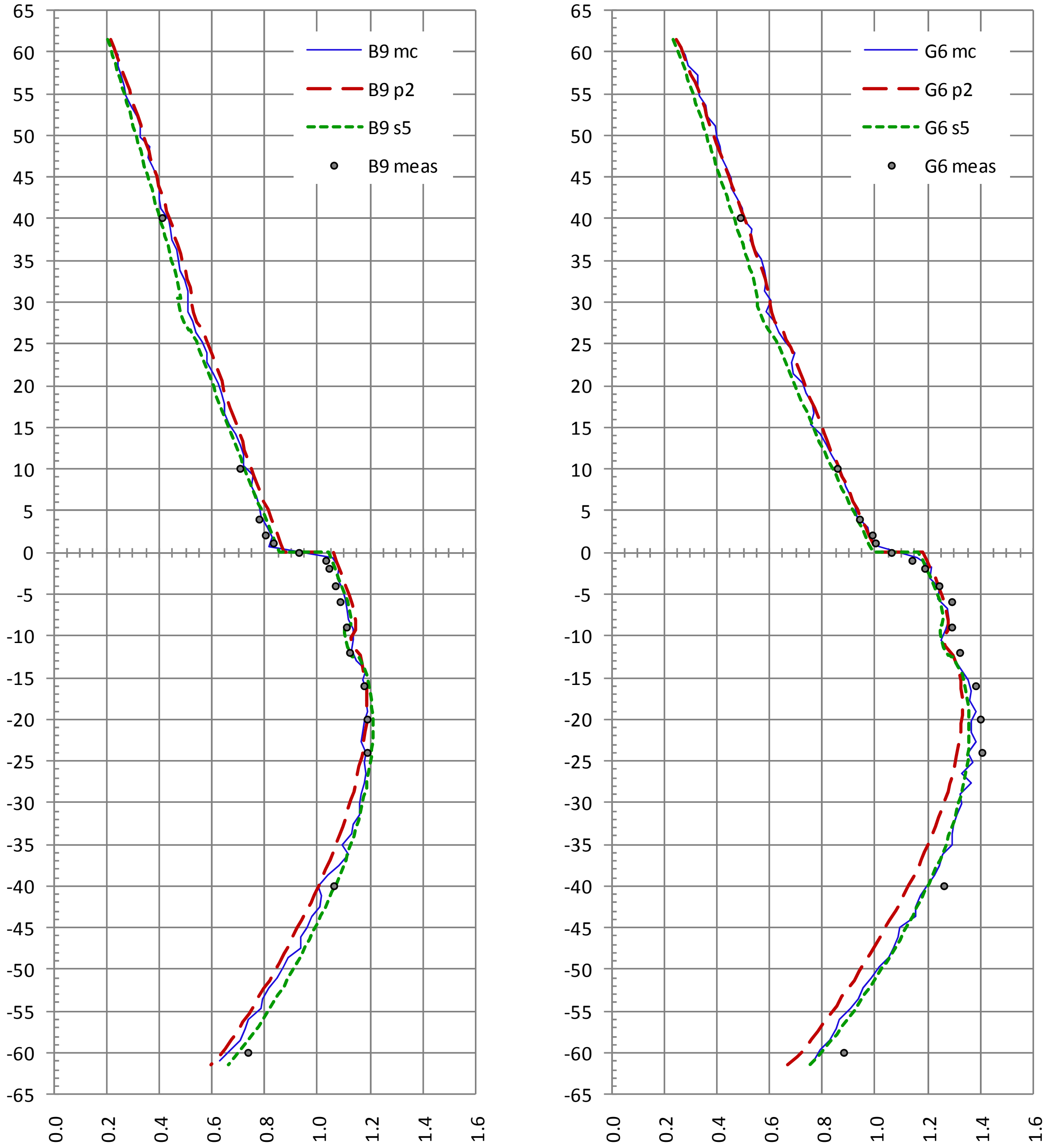

Figure 87 Configuration I-1C: 3D comparison of calculated and measured total-fission rates in pins B9 and G6. The PRESTO-2 results (red dashed line) correspond to programme version 1.15. The effect of the spacers can be seen, at +28.64 cm and, more clearly, at −10.66 cm with respect to the core midplane.

6.8 k-effective

As was done in Sections 4.9 and 5.8 for Configurations I-1A and I-2A, respectively, certain considerations concerning the k-effective obtained in the different calculations performed on Configuration I-1C are discussed here.

Table 35 shows the k-effective values obtained with the different codes and code versions mentioned in this chapter. The MCNPX k-effective corresponds to the case used for the determination of the total-fission rates (see the first footnote in Section 6.3), run with 800 x 10^6 histories.

Table 35 k-effective values for Configuration I-1C. The second column of numbers shows the differences (expressed in pcm) with respect to MCNPX, the k-effective value for which is given in the first row of Column 1, followed in brackets by its 1σ uncertainty (in pcm). Column 3 shows the differences (in pcm), for all calculations with respect to the PRESTO-2-1.13 case.

		Differences (pcm) with respect to:	
	k-effective	MCNPX	PRESTO-2 (v1.13)
MCNPX-2.6b with JEFF-3.1 library	1.00323 (3)	0	-1312
PRESTO-2 (v1.13)	1.01635	1312	0
PRESTO-2 (v1.15)	1.01655	1332	20
SIMULATE-5 (2 groups)	1.01157	834	-478
SIMULATE-5 (5 groups)	1.00959	636	-676
PRESTO-2 (v1.13, no spacer)	1.01823	1500	188
SIMULATE-5 (2 groups, no spacer)	1.01463	1140	-172
SIMULATE-5 (5 groups, no spacer)	1.01268	945	-367

As in the case of Configurations I-1A and I-2A, also for Configuration I-1C, the k-effective values obtained with the deterministic codes are significantly higher than that calculated with MCNPX. Furthermore, as before (Configuration I-1A), the use of 5 energy groups in the SIMULATE-5 calculation reduces the k-effective (by ~200 pcm), as compared with the 2-group case.

On the other hand, in contrast to Configuration I-1A, the k-effective of the SIMULATE-5 2-group calculation is about 500 pcm lower than that of the PRESTO-2 reference case (it was only about 80 pcm lower in the case of Configuration I-1A; see Table 16).

As expected, the difference between the k-effective values obtained with the two PRESTO-2 versions is small (20 pcm).

It is seen that SIMULATE-5 agrees better with MCNPX than PRESTO-2. At the same time, the flux curvature also shows better agreement. The fact that the two parameters (k-effective and the flux curvature) are related to the k-infinity of the lattices and the test-zone leakage, suggests that the corresponding modelling of Configuration I-1C is better with C5/S5 than with HE/P2.

Finally, the k-effective results depicted in Table 35 show that the negative reactivity introduced by the spacers is about 120 pcm larger in C5/S5 (~310 pcm) than in HE/P2 (~190 pcm). For C5/S5, the effect of the spacers on k-effective is almost the same for the 2-group and the 5-group calculations.

6.9 Chapter summary and principal messages

In the present chapter, focus was set on the investigation of the total-fission rate axial distribution, although valuable information on the radial behaviour was also obtained. In Configuration I-1C, the interface between two different lattice designs is made coincident with the test-zone midplane, allowing the investigation of the local region where changes in enrichment and gadolinium content takes place. The nine fuel assemblies loaded in the test zone being identical, global radial or azimuthal asymmetries do not occur.

Contrary to the case of the axially uniform Configurations I-1A and I-2A, discussed in the two previous chapters, the modelling of the axial variation of the radial PCRs is very important in Configuration I-1C. For instance, for the most relevant PCR, viz. the side PCR for the epithermal group, the difference between the values at axial levels 3 and 8 is approximately 10%.

Comparisons against LWR-PROTEUS experimental results were made for the nodal codes PRESTO-2 and SIMULATE-5, and also for the stochastic transport code MCNPX. The use of a 3D normalisation scheme, in which the 153 experimental points, as also the corresponding calculated values from MCNPX, PRESTO-2 and SIMULATE-5, were normalized to 1.0, has allowed a simultaneous comparison in the axial and radial directions.

For the 3D comparison over all the 153 measurements, the standard deviations of the C/Es corresponding to MCNPX, PRESTO-2, and SIMULATE-5 are 9.4%, 11.5% and 10.5%, respectively. However, ignoring the most challenging 13 points, the standard deviations are significantly reduced, the values resulting from the comparison of the 140 remaining C/Es being 3.1%, 4.3% and 3.2%, respectively. This can be regarded as good agreement, SIMULATE-5 being almost as accurate as MCNPX, with PRESTO-2 showing somewhat larger deviations.

In general, all calculations reproduce the experimental axial profiles with good accuracy, although some systematic underestimation of the measurements can be observed in the lower part of the test zone, mainly in the case of PRESTO-2.

The gradual transition occurring in the immediate vicinity of the core midplane, accurately predicted by MCNPX, is described by PRESTO-2 and SIMULATE-5 as a pronounced step. Since the function $\xi(z)$ describing the axial dependence of the asymptotic flux within each node is the same for all pins (variable separation for the flux), the effect of the changes in the axial composition of the fuel, which are different for different pins, cannot be exactly accounted for. Furthermore, the strong gradients occurring at the node boundaries that are coincident with the axial discontinuity cannot be captured completely by the combination of exponential shape functions that constitute $\xi(z)$. Finally, the lack of 3D transport information at pellet level, caused by the 2D character of the pin-power maps used in the reconstruction process, contributes significantly to the deviations observed very near the axial discontinuity.

In brief, it has been shown in this chapter that the LWR-PROTEUS experimental results concerning the axial heterogeneity of BWR fuel assemblies provide a valuable platform for assessing the axial modelling capabilities of nodal methodologies with pin-power reconstruction. In this context, the accurate description of the test-zone surroundings by means of adequate PCRs is of particular importance.

Chapter 7

Partial control blade insertion - Configuration I-6A

> *In 1964, the first two Soviet nuclear power plants were commissioned. A 100 MW boiling water graphite channel reactor began operating in Beloyarsk (Urals). In Novovoronezh (Volga region), a new design − a small (210 MW) pressurised water reactor (PWR) known as VVER (veda-vodyanoi energetichesky reaktor - water cooled power reactor) − was built.*

The present chapter addresses the experimental comparisons performed for LWR-PROTEUS Configuration I-6A, which features the partial insertion of the L-shaped hafnium control blade at the north-west corner of the test-zone's central SVEA-96+ assembly.

The experimental set-up is described in Section 7.1, while Section 7.2 presents the characteristics of the HELIOS and PRESTO-2 modelling. In Section 7.3, the representation of the test-zone boundary is addressed. The results of the 3D total-fission C/E comparisons using MCNPX and HELIOS/PRESTO-2 are presented in Section 7.4, general remarks being made in Section 7.5. Section 7.6 shows results obtained with PRESTO-2 version 1.15. A discussion about the k-effective obtained in the different calculations presented in this chapter is given in Section 7.7. Finally, in Section 7.8, a summarising overview of the chapter is made.

7.1 Description of the test zone

In Configuration I-6A, the axial non-uniformity imposed by the partially inserted control blade is investigated. The position of the core midplane is the same as in Configurations I-1A and I-2A, presented in Chapters 4 and 5, i.e. the lower section of the SVEA-96+ fuel assemblies

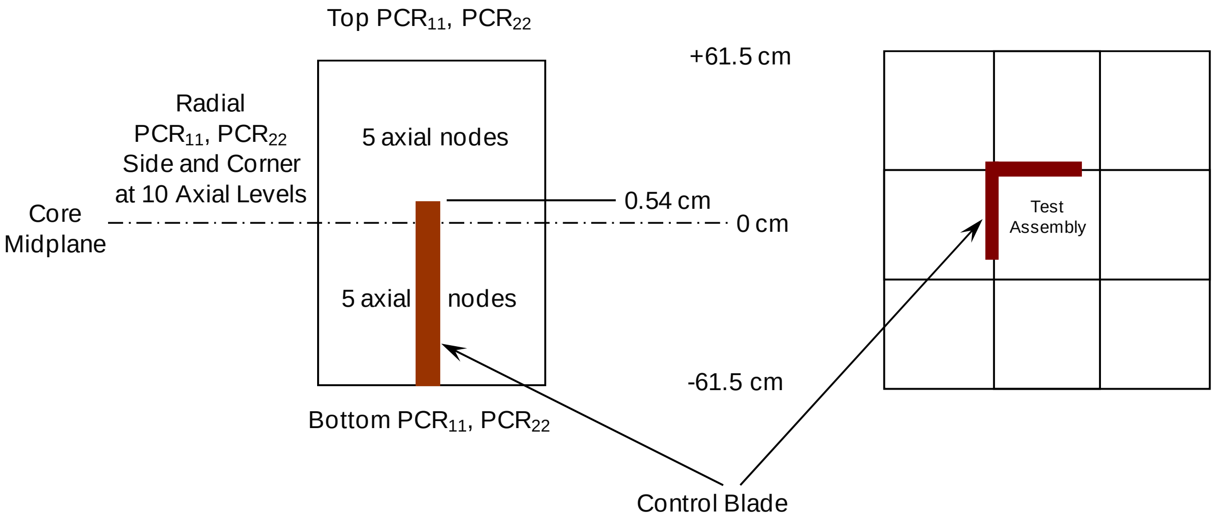

Figure 88 Schematic representation of the test zone in Configuration I-6A, showing the position of the L-shaped control blade.

occupies the entire active length of the test zone. In this case, however, the L-shaped hafnium control blade is inserted with its tip located 0.54 cm above the core mid-plane. Thus, the 6th axial level in the PRESTO-2 nodalisation is partially (only slightly) controlled. This is schematically shown in Figure 88.

As in the case of Configurations I-1A, I-2A and I-1C, the test tank was filled with light water at room temperature. The sub-assembly pressing, described in Section 4.1, was also the same. The experimental inter-assembly distances in Configuration I-6A are shown in Figure 89.

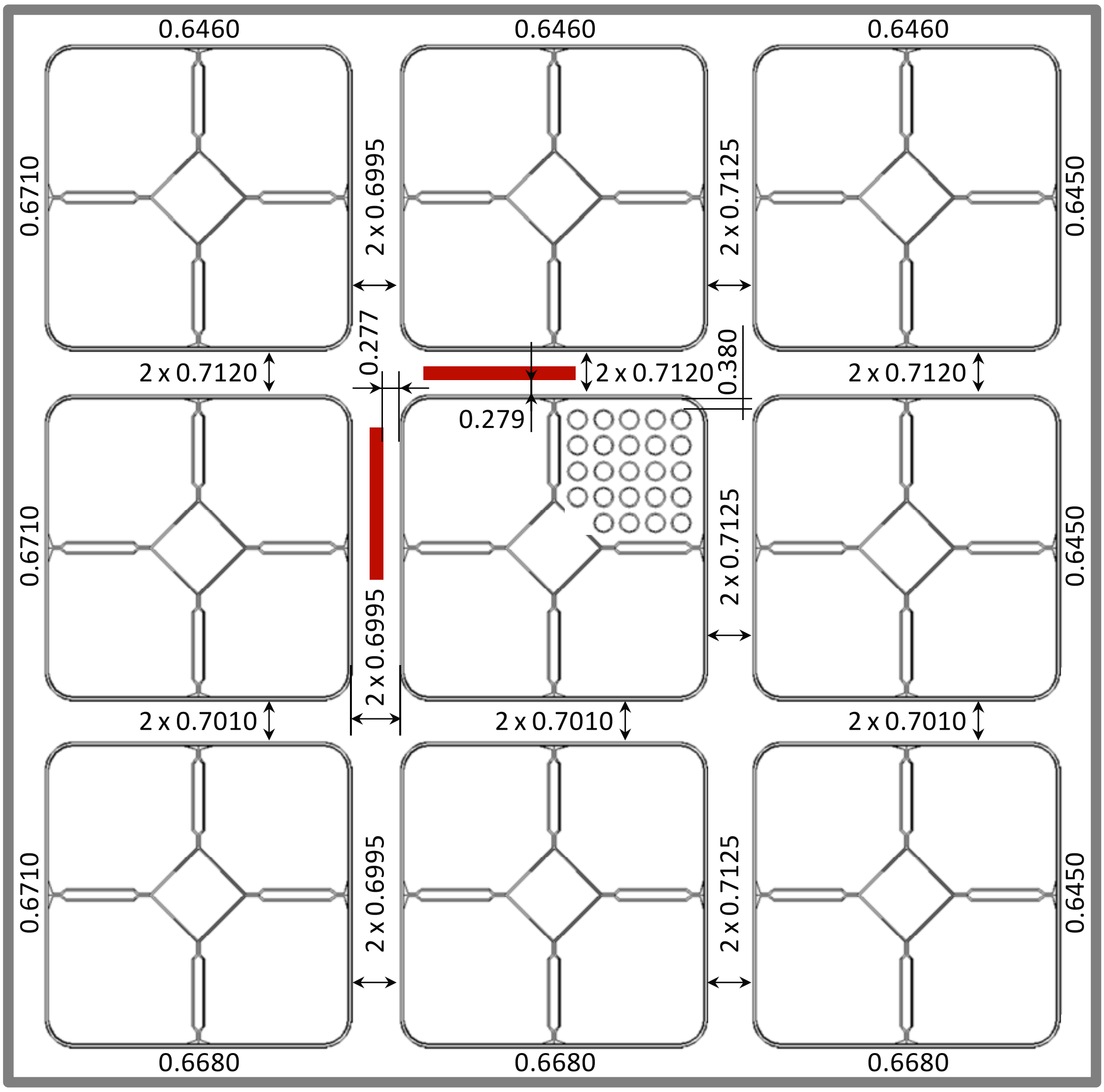

Figure 89 Measured dimensions (cm) in Configuration I-6A. The distance between the outer surface of the cladding of the peripheral pins and the inner wall of the fuel box is 0.380 cm (sub-assembly pressed 0.051 cm towards the central canal). The wings of the control blade are separated from the north and west outer surfaces of the central-assembly fuel box by 0.279 cm and 0.277 cm, respectively.

The measurements were carried out for 13 different fuel pins, with 17 experimental points per pin, distributed axially over the range −65 cm to +55 cm. In Configuration I-6A, the first and second spacers of the SVEA-96+ bundles (counted from the bottom) are located at −29.36 cm and +29.54 cm with respect to the core midplane, respectively.

7.2 Characteristics of the calculational models

7.2.1 Lattice calculations - HELIOS model

The lattice calculations were performed with HELIOS using the modelling features corresponding to the reference case, described in Subsection 4.2.1. For Configuration I-6A, 12 different sets of cross-sections are needed: 9 for the uncontrolled part (one for each fuel assembly, accounting for the measured gaps) and 3 for the controlled part (for assemblies 2 and 4, with one control blade (CB) wing each, and for assembly 5, with two CB wings). Each of the six assemblies that are not affected by the control blade can be described by one single set of cross-sections over the entire length of the test zone. For the controlled lattices, the same considerations concerning the modelling of the L-shaped control blade, as described in Sections 5.1 and 5.2, apply.

As done for Configuration I-1C, the spacers were explicitly modelled (their positions being given in Section 7.1). As before, this has been done following the methodology used in power reactor calculations, i.e. by defining delta parameters representing the spacer (see also Subsection 3.2.2).

7.2.2 Core calculations - PRESTO-2 model

The PRESTO-2 model for the test zone in Configuration I-6A is analogous to that used for Configurations I-1A and I-2A, its fundamental aspects having been discussed in Section 3.3. In this case, the presence of the control blade is described by the definition of two segments of active lengths 62.04 and 60.96 cm, for the controlled and uncontrolled parts of the test zone, respectively. As discussed in Subsection 3.2.2, this modelling feature departs from the normal procedure used in production applications of nodal core simulators. In fact, in a power reactor core, the position of the control blades changes during operation. To allow for this, the effects of the control blade on the lattice parameters (cross-sections, discontinuity factors and pin-power maps) are accounted for by introducing delta-parameters that are calculated as differences between the controlled and uncontrolled states and stored in the XSDB. The nodal core simulator then adds these deltas, according to the type and position of the control blades, to the basic parameters to obtain the controlled values. In the case of LWR-PROTEUS, however, this methodology cannot be applied directly. The reason for this is two-fold. First, and differently from the case of a real, cruciform control blade, the L-shaped control blade in LWR-PROTEUS affects the four fuel assemblies that surround it to different degree. Thus, different delta-control tables, all corresponding to the same control-blade type, must be defined depending on the number of CB wings that each assembly will face. Although possible, this procedure is cumbersome and not really justifiable. Second, the test-zone, being an array of 3x3 assemblies, does not comply with the general lay-out rules of BWR cores, which always have an even number of assembly rows. Hence, specification of the control blade following the standard procedure is not possible in the case of LWR-PROTEUS.

Physically, and despite the modelling differences discussed above, the methodology selected for the calculation of the controlled cases investigated in this thesis, viz. Configurations I-2A and I-6A, leads to the same results as the standard specification of control blades. This is because the HELIOS calculations that define the controlled and uncontrolled lattices are the same as those that would have been used to determine the delta-control parameters.

In agreement with the preservation of the standard modelling features used in power reactor calculations (see Subsection 3.3.2), the axial nodalisation of the test zone is kept independent from the position of the control blade. Thus, the interface between the controlled and uncontrolled lattices occurs 0.54 cm above the interface between the 5th and 6th axial nodes, the latter being coincident with the core midplane.

The elevations of the centres of the first and second spacers with respect to the beginning of the active length in the SVEA-96+ fuel assemblies are 56.44 cm and 115.34 cm, respectively, while the core midplane is at 85.80 cm above the beginning of the SVEA-96+ active length (see Figure 18). Thus, the elevations of the spacers with respect to the bottom of the test zone, as given to PRESTO-2, are:

1st spacer: 56.44 – (85.80-61.5) = 32.14 cm

2nd spacer: 115.34 – (85.80-61.5) = 91.04 cm

which correspond to −29.36 cm and +29.54 cm with respect to the core midplane, respectively.

As discussed in Subsection 3.3.2, the axial nodalisation of the test zone is kept independent of the spacers' positions. The heterogeneous flux solution, as described in Subsection 2.3.2, accounts for the perturbation of the intra-nodal axial flux profile caused by the spacers.

7.3 Test-zone boundary conditions using the 3D MCNPX model

PCRs representing the test-zone surroundings were calculated using a 3D MCNPX model of LWR-PROTEUS for Configuration I-6A, following the methodology described in Subsection 3.6.1. As in the case of Configurations I-1A, I-2A and I-1C, the MCNPX calculations were performed using 200'000 particles and 250 cycles, i.e. 50×10^6 histories[48].

7.3.1 PCRs for PRESTO-2

The procedure used for the calculation of the radial PCRs needed for PRESTO-2 in Configuration I-6A is identical to that described in Subsection 4.3.1 for the case of Configuration I-1A. The PCRs for PRESTO-2 in Configuration I-6A, for 1.84 eV thermal cut-off energy, are shown in Table 36, the approximate 1σ statistical relative errors in % being shown in brackets[49].

7.3.2 Axial behaviour of the radial PCRs

As in the case of Configuration I-1C, in which the different lattice designs of the upper and lower segments of the SVEA-96+ assemblies produced a significant axial dependence of the radial PCRs, the presence of the control blade also leads to a strong axial dependence of the

---

[48] As in the case of Configuration I-1C, for the comparison of the total-fission rate, the number of particles and cycles was increased to 10^6 and 800, respectively. This was done to improve the statistical accuracy in the small volumes used to tally the total-fission rate at pellet level.

[49] The PCR relative errors are propagated from the 1σ statistical uncertainties of the MCNPX current tallies. Although these uncertainties are slightly dependent on the axial level, a common single value, representing all levels, is defined to characterise the accuracy of the calculated PCRs.

PCRs in Configuration I-6A. This can be observed in Table 36, and also in Figure 90, where the corresponding PCR values are presented graphically.

Table 36 PCRs for PRESTO-2 in Configuration I-6A, derived from the partial currents obtained in the 3D whole-reactor MCNPX calculation. The figures in brackets are the approximate 1σ statistical relative errors in %. As in the case of production applications at KKL, the HELIOS/PRESTO-2 calculations were performed using a thermal cut-off energy of 1.84 eV.

Configuration I-6A Upper limit (eV)	PCR_{11} $20x10^6$		PCR_{22} 1.84	
Axial direction at top	0.777 (0.05)		0.938 (0.1)	
Radial direction 1σ error (%)	Side (0.05)	Corner (0.3)	Side (0.2)	Corner (1.0)
Axial level 10	0.998	1.040	0.388	0.424
Axial level 9	1.005	1.041	0.387	0.425
Axial level 8	1.014	1.050	0.387	0.422
Axial level 7	1.022	1.058	0.388	0.418
Axial level 6	1.030	1.064	0.389	0.419
Axial level 5	1.047	1.073	0.393	0.421
Axial level 4	1.066	1.082	0.396	0.422
Axial level 3	1.076	1.090	0.398	0.424
Axial level 2	1.077	1.088	0.400	0.428
Axial level 1	1.069	1.078	0.403	0.438
Axial direction at bottom	0.839 (0.05)		0.959 (0.1)	

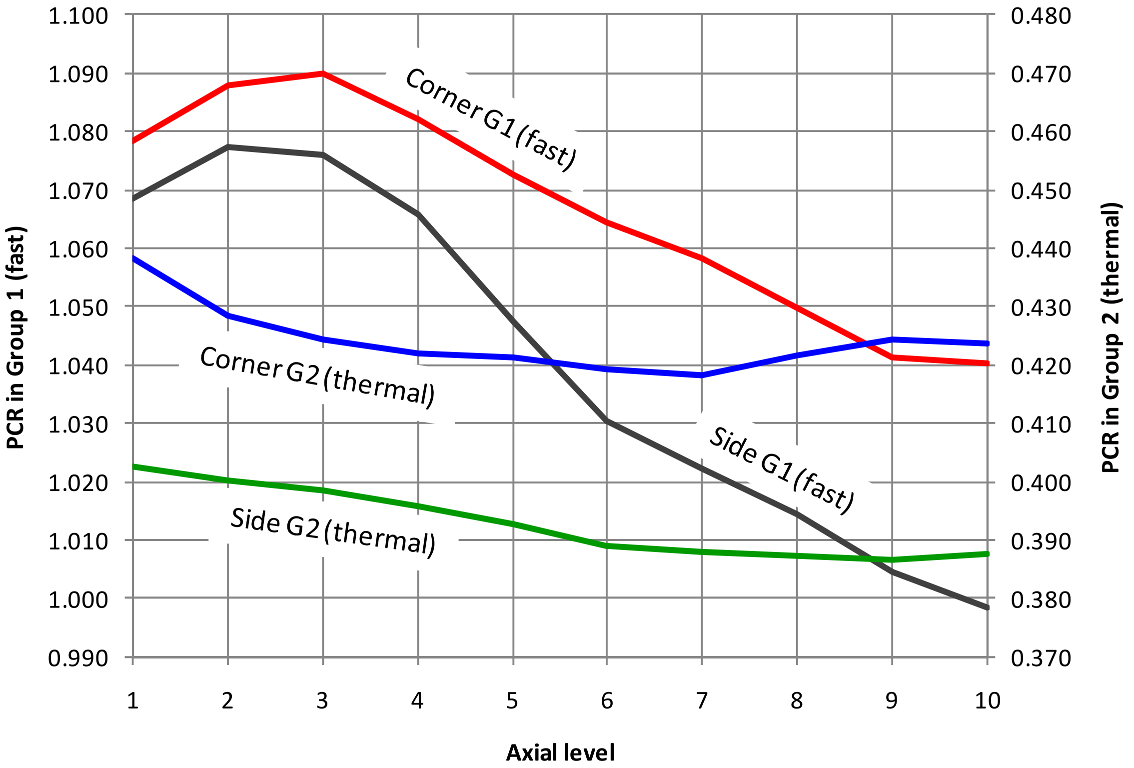

Figure 90 Axial variation of the radial PCRs in Configuration I-6A, as derived from the partial currents obtained in the 3D whole-reactor MCNPX calculation. The numerical values are shown in Table 36.

The axial variation of the PCRs in Configuration I-6A reflects the effect of the partially inserted control blade. For instance, below the core midplane, the reactivity of the test zone is much lower than in the upper part. Thus, the contribution of the PROTEUS driver zones to the neutron balance in the test zone is stronger in this region, which results in larger radial PCRs, particularly in the epithermal energy group. This behaviour is analogous to that observed in Configuration I-1C (see Subsection 6.3.3), where the axial variation of the PCRs was caused by the different material compositions above and below the core midplane. However, one important difference between the two cases needs to be mentioned. In Configuration I-1C, the nine fuel assemblies have the same composition and, consequently, the axial discontinuity affects the periphery of the test zone directly. In Configuration I-6A, on the other hand, the axial discontinuity is restricted to the central part of the test zone (north and west gaps of the central assembly). Hence, with the peripheral fuel assemblies having a decoupling effect, the impact of the axial discontinuity on the PCRs is weaker in Configuration I-6A. This can be observed when comparing Figure 90 with Figure 76. Looking at the side PCRs in group 1, for example, the difference between the values at axial levels 8 and 3 is 1.125−1.016 = 0.109 for Configuration I-1C (Table 28) and 1.014−1.076 = −0.062 for Configuration I-6A (Table 36). Despite this somewhat weaker variation, Figure 90 clearly indicates that, as in the case of Configuration I-1C, accounting for the axial dependence of the PCRs is also very important in Configuration I-6A.

7.3.3 Energy dependence of the partial currents and PCRs

As previously done in Subsections 4.3.4, 5.3.3 and 6.3.4 for Configurations I-1A, I-2A and I-1C, respectively, Figure 91 shows the relative intensity of the partial currents in Configuration I-6A, calculated with the 3D MCNPX model in five energy groups. The values shown have been integrated over the complete test-zone radial boundary, i.e. by summing over all sides and corners and over all axial levels. Shown along with the partial currents are the corresponding PCRs.

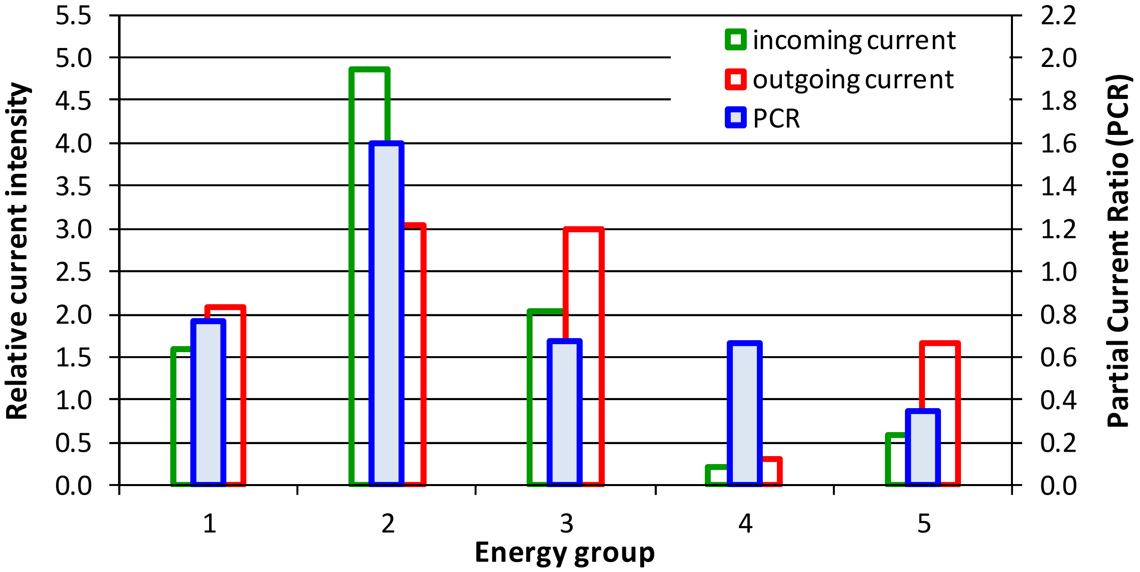

Figure 91 Energy dependence of the radial currents and PCRs in Configuration I-6A (shown in five energy groups), as derived from the partial currents obtained in the 3D whole-reactor MCNPX calculation. The partial currents were integrated over the complete test-zone boundary, i.e. by summing over all sides and corners and over all axial levels.

As mentioned before, the axial dependence of the partial currents, and hence of the PCRs, is very important in Configuration I-6A. Comparing for example the axial levels 8 and 3, as done in Subsection 6.3.4 for Configuration I-1C, the differences in radial coupling discussed before can be seen. For instance, Figure 92 and Figure 93 show the relative partial currents and the PCRs at axial level 8 and 3, respectively, the numerical values of the PCRs being presented in Table 37.

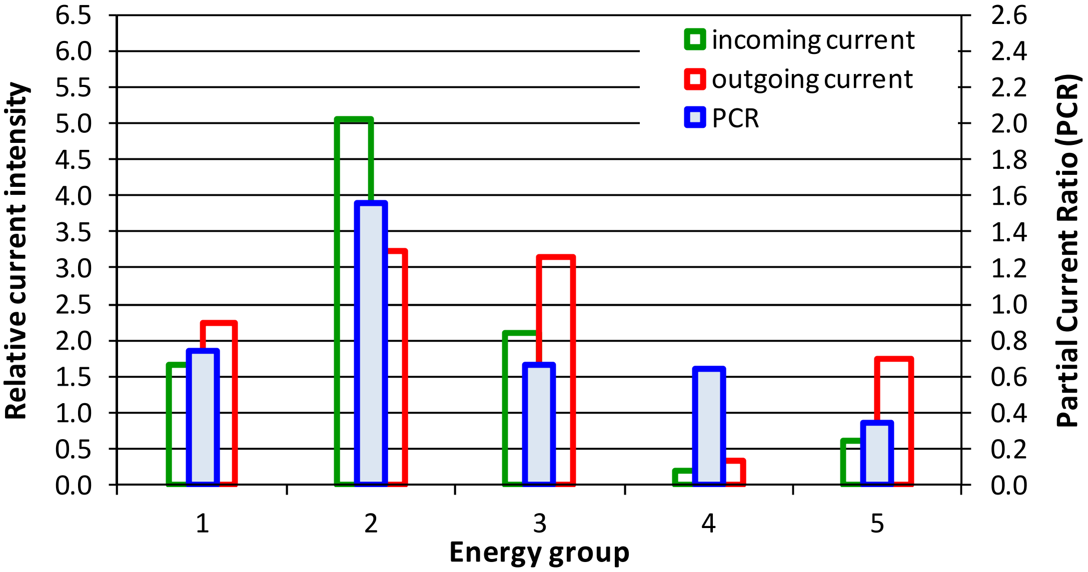

Figure 92 Energy dependence of the radial currents and PCRs in Configuration I-6A in five energy groups, at axial level 8 (middle of the test-zone upper half).

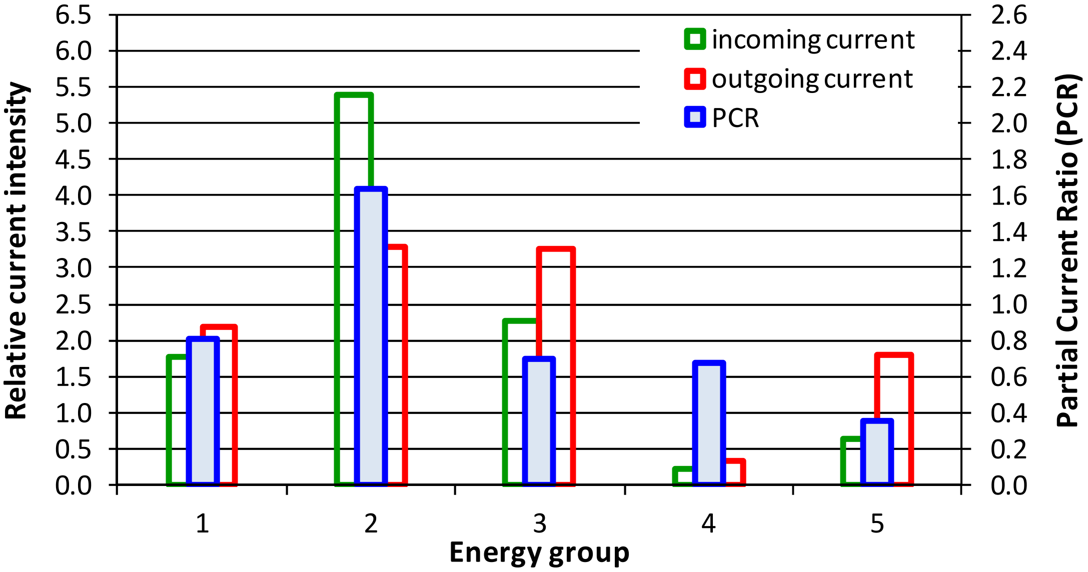

Figure 93 Energy dependence of the radial currents and PCRs in Configuration I-6A in five energy groups, at axial level 3 (middle of the test-zone lower half).

From these pictures, it can be seen that the coupling between the test zone and the surrounding buffer and driver zones is stronger in the lower part of the core (larger PCRs). As discussed in Subsection 7.3.2, this is caused by the presence of the control blade in the bottom half of the test zone.

Table 37 PCRs in Configuration I-6A, derived from the partial currents obtained in the 3D whole-reactor MCNPX calculation. The PCRs are given in the five-group structure shown in Table 7.

Configuration I-6A	5 energy groups				
	PCR_{11}	PCR_{22}	PCR_{33}	PCR_{44}	PCR_{55}
Upper limit (eV)	20×10^6	821×10^3	9119	1.84	0.625
Radial direction side					
Axial level 8	0.737	1.560	0.666	0.646	0.345
Axial level 3	0.808	1.640	0.694	0.672	0.352

As illustration, the axial profiles of the partial currents crossing the radial boundary of the test zone, in two energy groups with 0.625 eV cut-off, are shown in Figure 94. Comparing this figure with Figure 80 (Configuration I-1C), it can be seen that the peaks of the partial current profiles are displaced here towards the upper part of the core.

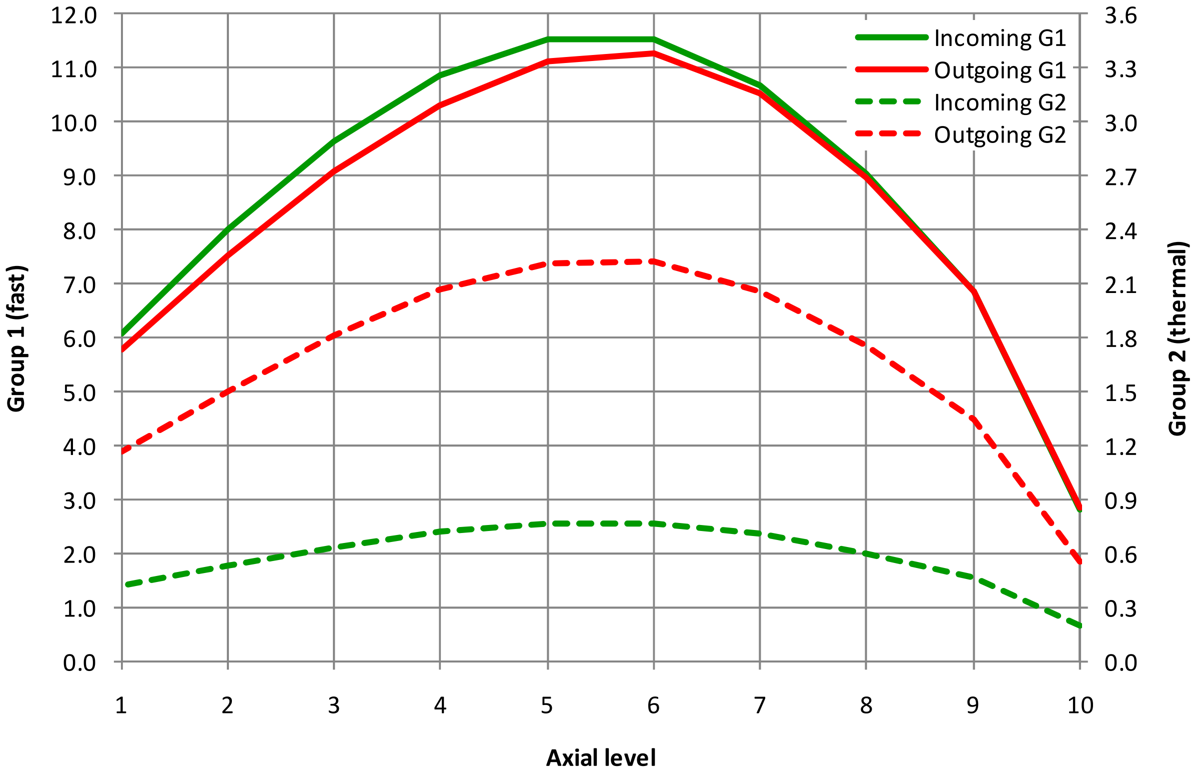

Figure 94 Axial profiles of the radial currents in Configuration I-6A, in two groups with 0.625 eV cut-off energy. The partial currents were integrated over the test-zone boundary at each axial level, i.e. by summing over all sides and corners.

7.3.4 Use of 2D test-zone boundary conditions

In Configuration I-6A, for the reasons discussed in Subsection 7.3.2, axially averaged PCRs cannot be used over the whole test-zone length without the loss of valuable information about the radial leakage. On the other hand, two different sets of PCRs, one for the upper part of the test zone (uncontrolled) and one for the lower part (controlled), could be derived using the corresponding 2D HELIOS models of the whole LWR-PROTEUS reactor. As for all axially heterogeneous configurations, this procedure, although applicable, would lead to a less accurate description of the test-zone boundary.

Thus, in this thesis, the modelling of Configuration I-6A is focussed on the use of 3D PCRs obtained from MCNPX whole reactor calculations. As previously discussed, this provides the most accurate description of the test-zone surroundings that can be used to assess nodal methodologies based on LWR-PROTEUS experimental results.

7.4 3D comparisons of total-fission rates

Analogously to the case of Configuration I-1C (see Section 6.5), the 13*17=221 experimental points measured in Configuration I-6A have been normalized to 1.0, as also have been the corresponding calculated total-fission rates from MCNPX and PRESTO-2. As in the case of Configuration I-2A, and for the same reasons as explained in Chapter 5, CASMO-5/ SIMULATE-5 calculations could not be performed for Configuration I-6A.

The C/Es corresponding to MCNPX and PRESTO-2 are presented and discussed in Subsections 7.4.1 and 7.4.2, respectively, while plots showing the total-fission distribution calculated with the two methodologies, together with the LWR-PROTEUS experimental results, are presented in Subsection 7.4.3. For the plots, the data sets were normalized as described in Section 6.5, the same scale being used in all the graphics in order to facilitate the visual comparison.

As described in Section 3.3 for the case of PRESTO-2, all calculations of total-fission rates, including those performed with MCNPX, cover the axial range ±61.5 cm with respect to the core midplane, the measurements at −65 cm lying, consequently, below the lowest calculated points. However, as can be seen from the plots of the 3D total-fission distribution (see Subsection 7.4.3), the axial profile in the lower part of the test zone shows quite a linear behaviour. Taking advantage of this behaviour, the C/Es at level −65 cm, which are displayed in Table 38 and Table 39 in italics and with a grey background, were obtained using C-values derived by linear extrapolation of the calculated axial profile in each pin[50].

7.4.1 C/E of total-fission distribution for MCNPX results

The C/E values corresponding to the MCNPX calculations are shown in Table 38. For each measured pin, the last four rows show the maximum (Max), minimum (Min), standard deviation (StD), and standard deviation excluding the C/Es at ±1 cm (StD2) respectively, the values corresponding to all pins being given in the last column. Although 17 measurements were made for each fuel pin, the sets of measured points were not the same for all the pins, because of which

---

[50] The extrapolation was done by simply using the two lowermost points of the axial distribution. In the case of MCNPX, due to the stochastic character of the results, this can lead to an increased uncertainty. More elaborated extrapolation procedures, considering more data points, could be applied to reduce this effect. However, for the purpose of the comparisons performed here, this was not considered necessary.

Table 38 contains some empty positions. In Table 38, the extrapolated points at −65 cm, discussed above, have been excluded from the various statistical results.

If one considers all the 221 measured points, the standard deviation of the C/Es is found to be 4.2%. If the 13 extrapolated points at −65 cm are eliminated from the statistics, as is the case in Table 38, the standard deviation of the remaining 208 C/Es (StD) is reduced to 2.3%, which represents a very good agreement. Excluding in addition the 26 points closest to the core midplane, at elevations ±1 cm, the standard deviation of the remaining 182 C/Es (StD2) remains unchanged at 2.3%. Thus, once again, the comparison of the MCNPX results with the LWR-PROTEUS experimental database confirms the ability of the whole-reactor model to predict the total-fission distribution in the central assembly of the test zone with good accuracy, in this case in the presence of the strong axial, radial and azimuthal heterogeneity produced by the presence of the partially inserted, L-shaped control blade. Thus, as in the case of Configuration I-1C, the MCNPX results in Configuration I-6A can be used as a reference for comparisons against other calculations, also for pins that have not been measured, thus extending the range of application of the experimental database.

Table 38 C/E values corresponding to MCNPX for the 221 points (13 pins and 17 axial levels) measured in Configuration I-6A. The empty positions correspond to elevations that, for the given pin, were not measured. In the last four rows, the maximum (Max), minimum (Min), standard deviation (StD) and standard deviation excluding the C/Es at ±1 cm (StD2) are shown for each measured pin (columns 2 to 14), while the values for all pins are shown in the last column. The C/Es corresponding to the extrapolated calculations at -65 cm, displayed in italics with a grey background, were excluded from the various statistical results.

Elev.	J10	J5	J1	I9	G6	E10	E8	D3	C4	B3	A10	A8	A1	All pins
55	0.986	0.960	0.976	0.974	0.973	0.980	0.984	0.978	0.950	0.942	0.985	0.987	0.995	
35	1.002	0.995	0.992	0.990	0.985	1.014	0.993	0.992	0.992	0.970	1.008	0.972	1.002	
25		0.987	0.998	0.975	1.003	1.016	1.000	0.983	0.977	0.971	1.029			
15	1.008	0.999	0.996	0.996	1.011	0.996	1.001	0.992	0.981	0.973	1.022	1.012	1.011	
10		1.008	1.000	1.009	0.997	0.994	1.001	0.997	0.989	0.974	1.031			
5	1.015	1.006	1.009	1.010	1.003	1.003	1.019	0.998	0.991	0.975	1.026	1.011	0.996	
1	*1.067*	*1.047*	*1.008*	*1.039*	*1.024*	*1.025*	*0.995*	*1.016*	*0.985*	*0.973*	*1.045*	*1.004*	*1.010*	*excluded*
-1	*1.040*	*1.023*	*0.992*	*1.016*	*1.009*	*0.998*	*1.004*	*0.992*	*0.992*	*0.980*	*1.045*	*0.999*	*1.011*	*from StD2*
-3	1.036	0.989	0.993	1.002	1.008	0.995	1.018	0.993	0.986	0.977	1.017	1.023	1.010	
-4	1.031											1.013	1.021	
-5	1.012	1.000	0.972	1.023	1.029	1.008	1.000	1.001	0.976	0.966	1.023	0.996	1.014	
-6	1.032											0.988	1.008	
-7	1.046	0.996	0.973	0.988	0.999	1.015	1.004	1.006	0.979	0.971	1.022	0.986	1.001	
-9	1.019	0.972	0.973	0.974	1.027	0.990	0.999	1.011	0.995	0.961	1.020	0.993	1.009	
-11	1.047	0.985	0.968	0.992	1.033	1.017	0.990	0.987	0.972	0.963	1.011	1.014	1.008	
-15	1.018	0.975	0.979	0.978	1.016	0.955	0.987	0.992	0.966	0.963	1.015	0.989	1.007	
-25	1.078	0.974	0.980	1.038	1.001	0.979	1.011	1.003	0.961	0.922	1.023	0.964	0.999	
-45	1.048	0.963	0.967	1.028	1.013	0.972	0.957	0.996	0.978	0.912	0.975	0.987	0.995	
-65	*0.928*	*0.920*	*0.813*	*1.165*	*0.859*	*0.726*	*0.862*	*0.939*	*0.730*	*0.920*	*1.020*	*1.083*	*1.013*	*excluded*
Max	1.078	1.047	1.009	1.039	1.033	1.025	1.019	1.016	0.995	0.980	1.045	1.023	1.021	1.078
Min	0.986	0.960	0.967	0.974	0.973	0.955	0.957	0.978	0.950	0.912	0.975	0.964	0.995	0.912
StD	0.024	0.022	0.014	0.022	0.016	0.019	0.015	0.010	0.012	0.020	0.018	0.016	0.007	0.023
StD2	*0.023*	*0.015*	*0.014*	*0.021*	*0.016*	*0.019*	*0.015*	*0.009*	*0.013*	*0.020*	*0.016*	*0.017*	*0.008*	*0.023*

7.4.2 C/E of total-fission distribution for PRESTO-2 results

The C/E values corresponding to the PRESTO-2 results are, in a manner analogous to that of the previous subsection, depicted in Table 39. Considering all the 221 measured points, the standard deviation of the C/Es is 6.8%. In this case, the 13 C/Es obtained using extrapolated

C-results (marked with a grey background) do not show particularly worse values than the rest. This is because, contrary to the case of MCNPX, the deterministic result shows a smooth profile. In fact, when these 13 points are removed from the statistics, the standard deviation of the remaining 208 C/Es remains practically constant at 6.9%, which for the nodal calculation can be considered as good agreement. On the other hand, as will be discussed in Subsection 7.4.3, the nodal reconstructed values can deviate significantly from the measurements very near the core midplane. Thus, in the case of PRESTO-2, the exclusion from the statistics of the 26 C/Es at elevations ±1 cm leads to significant improvements in the standard deviations (StD2 in Table 39).

Table 39 C/E values corresponding to PRESTO-2 in Configuration I-6A. The layout of this table is identical to that of Table 38.

Elev.	J10	J5	J1	I9	G6	E10	E8	D3	C4	B3	A10	A8	A1	All pins
55	0.921	0.948	0.935	0.966	0.950	0.945	0.964	0.983	0.968	0.949	0.933	0.969	0.951	
35	0.939	0.968	0.950	0.972	0.965	0.962	0.974	0.996	0.983	0.957	0.955	0.979	0.957	
25		0.976	0.956	0.981	0.975	0.975	0.987	1.001	0.993	0.963	0.965			
15	0.956	0.992	0.964	0.996	0.992	0.981	0.995	1.010	1.001	0.980	0.974	1.006	0.964	
10		0.964	0.960	0.987	0.983	0.962	0.990	1.015	1.012	0.995	0.973			
5	0.975	1.013	0.974	1.027	0.997	0.999	1.012	1.010	1.000	0.979	0.983	1.006	0.972	
1	*1.335*	*1.377*	*1.060*	*1.288*	*1.005*	*1.334*	*1.053*	*0.974*	*0.959*	*0.930*	*1.079*	*0.979*	*0.912*	*excluded*
-1	*0.837*	*0.879*	*0.936*	*0.909*	*1.045*	*0.867*	*1.019*	*1.150*	*1.135*	*1.119*	*0.963*	*1.068*	*1.123*	*from StD2*
-3	0.927	0.936	0.933	0.976	1.019	0.945	1.016	1.103	1.098	1.072	0.954	1.044	1.062	
-4	0.939											1.027	1.054	
-5	0.936	0.954	0.921	0.997	1.020	0.956	1.009	1.087	1.070	1.050	0.948	1.025	1.041	
-6	0.955											1.024	1.031	
-7	0.961	0.952	0.914	1.000	1.025	0.967	1.007	1.075	1.068	1.039	0.940	1.015	1.020	
-9	0.960	0.952	0.910	1.007	1.017	0.951	1.013	1.065	1.053	1.028	0.934	1.006	1.018	
-11	0.980	0.958	0.911	1.017	1.022	0.969	1.025	1.067	1.056	1.023	0.937	1.019	1.011	
-15	0.950	0.944	0.913	0.997	1.015	0.944	1.012	1.077	1.058	1.042	0.934	1.012	1.032	
-25	1.021	0.975	0.935	1.032	1.028	0.970	1.032	1.094	1.089	1.036	0.957	1.034	1.052	
-45	1.015	0.976	0.943	1.051	1.041	0.975	1.050	1.120	1.111	1.064	0.962	1.049	1.078	
-65	*1.023*	*0.943*	*0.918*	*0.995*	*0.990*	*0.941*	*1.017*	*1.070*	*1.057*	*0.984*	*0.921*	*0.995*	*1.049*	*excluded*
Max	1.335	1.377	1.060	1.288	1.045	1.334	1.053	1.150	1.135	1.119	1.079	1.068	1.123	1.377
Min	0.837	0.879	0.910	0.909	0.950	0.867	0.964	0.974	0.959	0.930	0.933	0.969	0.912	0.837
StD	0.104	0.108	0.037	0.080	0.027	0.098	0.024	0.053	0.054	0.052	0.035	0.026	0.054	0.069
StD2	*0.030*	*0.020*	*0.022*	*0.024*	*0.027*	*0.016*	*0.023*	*0.046*	*0.046*	*0.041*	*0.016*	*0.022*	*0.041*	*0.045*

7.4.3 3D comparisons

Measured pins J10 and I9

Figure 95 shows the 3D comparison of MCNPX and PRESTO-2 with experiment for pins J10 and I9.

For MCNPX, the agreement between measurement and calculation is very good for both pins, the standard deviation of the C/Es being 2.4% and 2.2%, respectively. The global flux profile is well predicted, both in the upper (uncontrolled) and lower (controlled) test-zone regions. For pin J10 (lattice corner facing the control blade vertex), MCNPX slightly overestimates the total-fission in the controlled part (by approximately 4%, the average of the C/Es over the axial levels −45 cm to +1 cm being 1.039). This reflects the radial behaviour already observed in Configuration I-2A (see Figure 62, right hand side), in which the C/E value for pin J10 is 1.050. For pin I9, which lies one lattice position away from the control blade in both directions, the agreement is better. In this case, the average of the C/Es in the controlled part of the test zone is 1.008 (1.021 in Figure 62). Furthermore, in the vicinity of the axial heterogeneity, i.e. near the core midplane, just above which the tip of the control blade is located, MCNPX accurately reproduces the axial flux gradient. This is an important observation, taking into account the short distance between these two pins and the control blade.

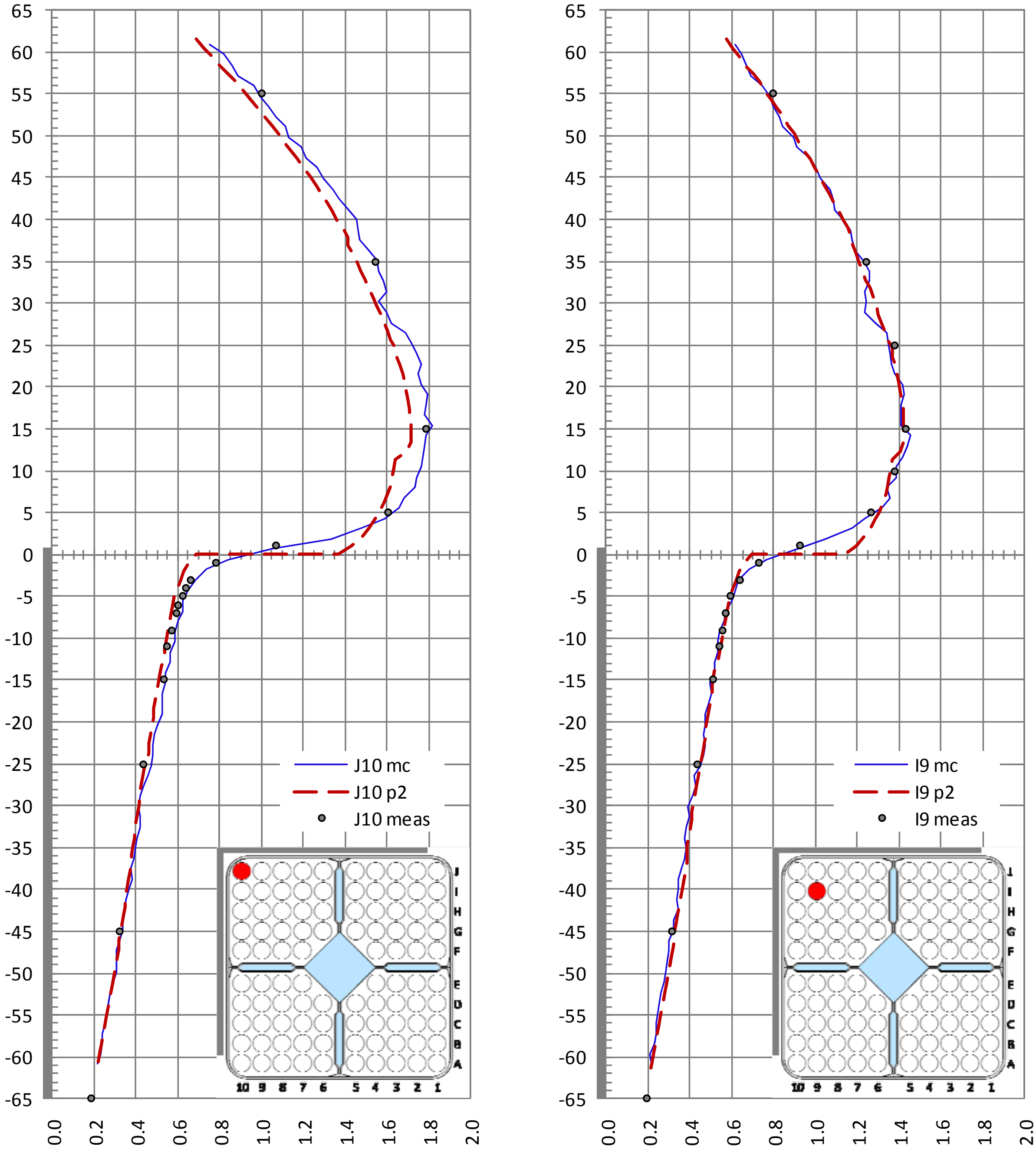

Figure 95 Configuration I-6A: 3D comparison of calculated and measured total-fission rates in pins J10 and I9 for MCNPX (blue line) and PRESTO-2 (red dashed line). All distributions are normalized to 1.0 over the complete 3D set of 221 measured points.

In the case of PRESTO-2, the global flux profile also shows the behaviour previously observed in the radial comparisons in Configurations I-1A (uncontrolled) and I-2A (controlled). For instance, in the upper part of the test-zone, PRESTO-2 underestimates the total-fission in pin J10 by ~5%, the average of the C/Es over the axial levels +5 cm to +55 cm being 0.948, while the C/E in Configuration I-1A is 0.972 for the same pin (see Figure 41, left hand side). In the controlled zone, the average of the C/Es over the axial levels −45 cm to −3 cm is 0.985, the C/E for pin J10 being 0.957 in Configuration I-2A (see Figure 62, left hand side)[51]. For pin I9, as in the case of MCNPX, the global 3D agreement of PRESTO-2 with experiment is better than for pin J10. For pin I9, the average of the C/Es over the axial levels +5 cm to +55 cm is 0.988, while over the axial levels −45 cm to −3 cm it is 1.009. Also these values agree well with those obtained for Configurations I-1A and I-2A, which are 1.005 (Figure 41) and 1.006 (Figure 62), respectively.

Considering the 16 measurements per pin (−65 cm has been excluded), the standard deviations of the C/Es obtained with PRESTO-2 for pins J10 and I9 are 10.4% and 8.0%, respectively. It needs to be noted here that the significantly larger standard deviations for PRESTO-2, compared to MCNPX (2.4% and 2.2%, respectively), are mainly caused by the local differences near the interface between the controlled and uncontrolled nodes. In fact, excluding the two axial levels located at ±1 cm from the statistics, the standard deviations of the PRESTO-2 C/Es reduce to 3.0% and 2.4% for pins J10 and I9, respectively. Doing the same with the MCNPX C/Es, the standard deviations remain, as expected, practically unchanged, at 2.3% and 2.1%, respectively.

It can be seen that the partial insertion of the control blade imposes a strong challenge to the nodal calculation in the vicinity of the core mid-plane. In this region, the function describing the intra-nodal asymptotic flux (which is unique for all pins due to the variable separation for the flux, see Subsection 2.3.2) cannot adequately follow the strong gradient resulting from the axial heterogeneity. For instance, the results of PRESTO-2 reflect the slight insertion (0.54 cm) of the control blade into the 6th axial level through a small step at the interface between the 6th and 7th nodes, located at +12.3 cm (see Figure 95). The major discontinuity, however, is located exactly at the core midplane, which is coincident with the node boundary. It can be observed that, due to the shorter distance between pin J10 and the control blade, the step occurring at the interface between the 5th and 6th axial nodes is more pronounced in this pin than in pin I9. As expected, the MCNPX transport solution, on the other hand, describes the transition with good accuracy.

The depression caused by the spacer located at +29.54 cm can be clearly seen in the MCNPX results shown in Figure 95. As in the case of Configuration I-1C, however, PRESTO-2, does not capture this effect correctly. It will be shown in Section 7.6, that this aspect improves when the latest available PRESTO-2 version, viz. 1.15, is used. On the other hand, due to the relatively low fission rate occurring in the controlled part of the test zone, the effect of the spacer located at −29.36 cm can hardly be observed in either of the calculations.

Measured pins J1 and A10

Pins J1 and A10 are located at the NE and SW corners of the lattice, respectively. Thus, except for the asymmetries in the measured gaps (see Figure 89), the total-fission rate must be the same for these two pins.

Considering 16 axial measurements (i.e. excluding −65 cm), the standard deviations of the MCNPX C/Es for pins J1 and A10 are 1.4% and 1.8%, respectively. When excluding the points at ±1 cm, these remain, as expected, practically unchanged (1.4% and 1.6%). In pin A10, a slight

---

[51] For these comparisons, in order to eliminate the effect of the large deviations occurring very near the nodal interface in Configuration I-6A, the C/Es at ±1 cm were not included in the corresponding axial averages.

overestimation can be observed in the MCNPX results between levels +5 cm and +25 cm, which agrees with the radial results of Configuration I-1A, shown on the right hand side of Figure 41. However, despite these small deviations, the agreement between calculation and measurement is very good for both pins.

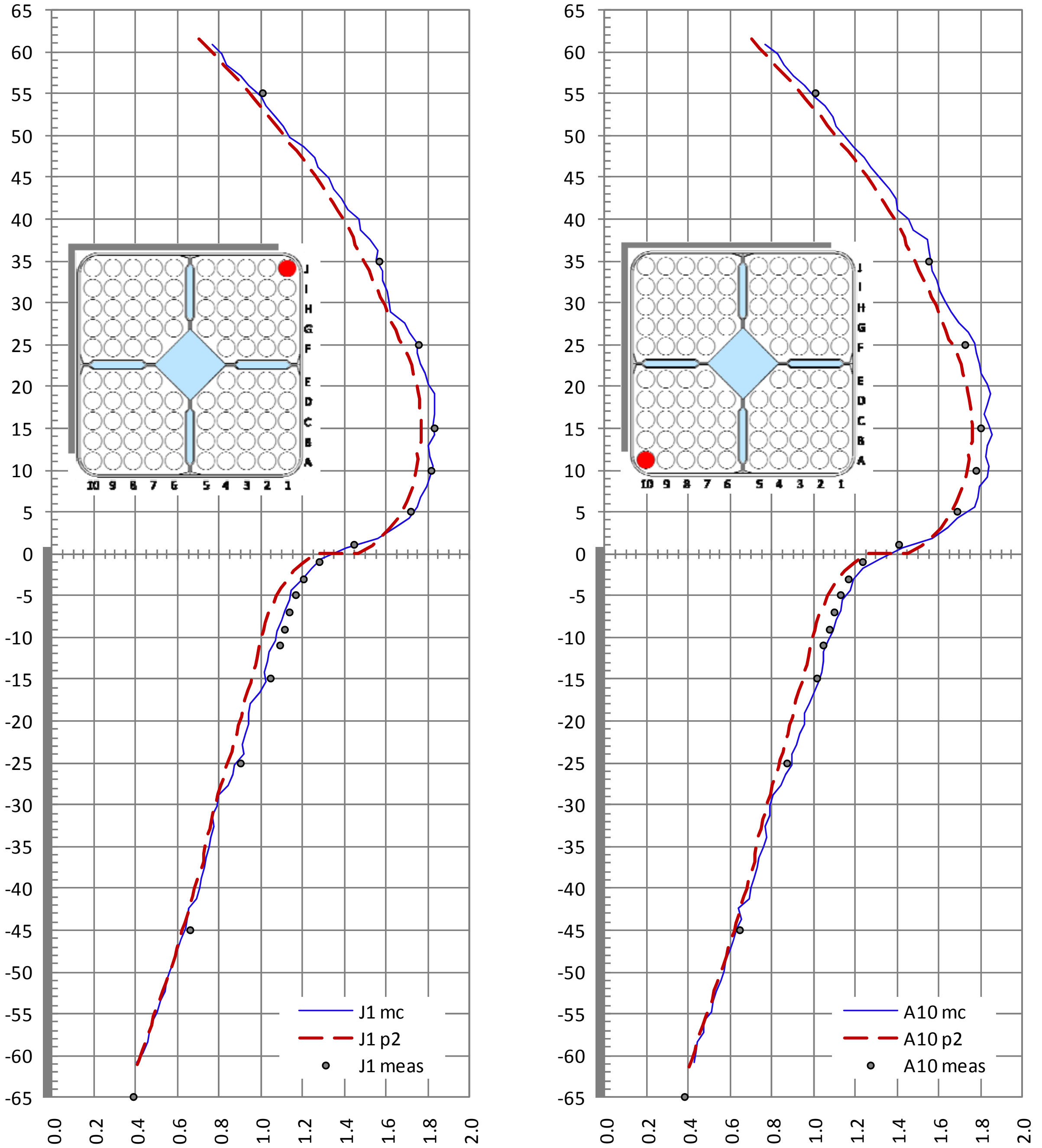

Figure 96 Configuration I-6A: 3D comparison of calculated and measured total-fission rates in pins J1 and A10 for MCNPX (blue line) and PRESTO-2 (red dashed line). All distributions are normalized to 1.0 over the complete 3D set of 221 measured points.

In the case of PRESTO-2, the total-fission rate is underestimated both in the uncontrolled and controlled zones. Thus, for pin J1, the average of the C/Es over the axial levels +5 cm to +55 cm is 0.957, while over the axial levels −45 cm to −3 cm it is 0.922. For pin A10, in turn, the same averages are 0.964 and 0.946, respectively. These results are consistent with the observations made in Chapters 4 and 5 for Configurations I-1A and I-2A, respectively, where the fission rates in these pins were systematically underestimated by PRESTO-2 (see left hand side of Figure 41 and Figure 62). Finally, considering 16 axial measurements as done before, the standard deviations of the PRESTO-2 C/Es for pins J1 and A10 are 3.7% and 3.5%, while by excluding the points at ±1 cm these are reduced to 2.2% and 1.6%, respectively.

Measured pins J5 and E10

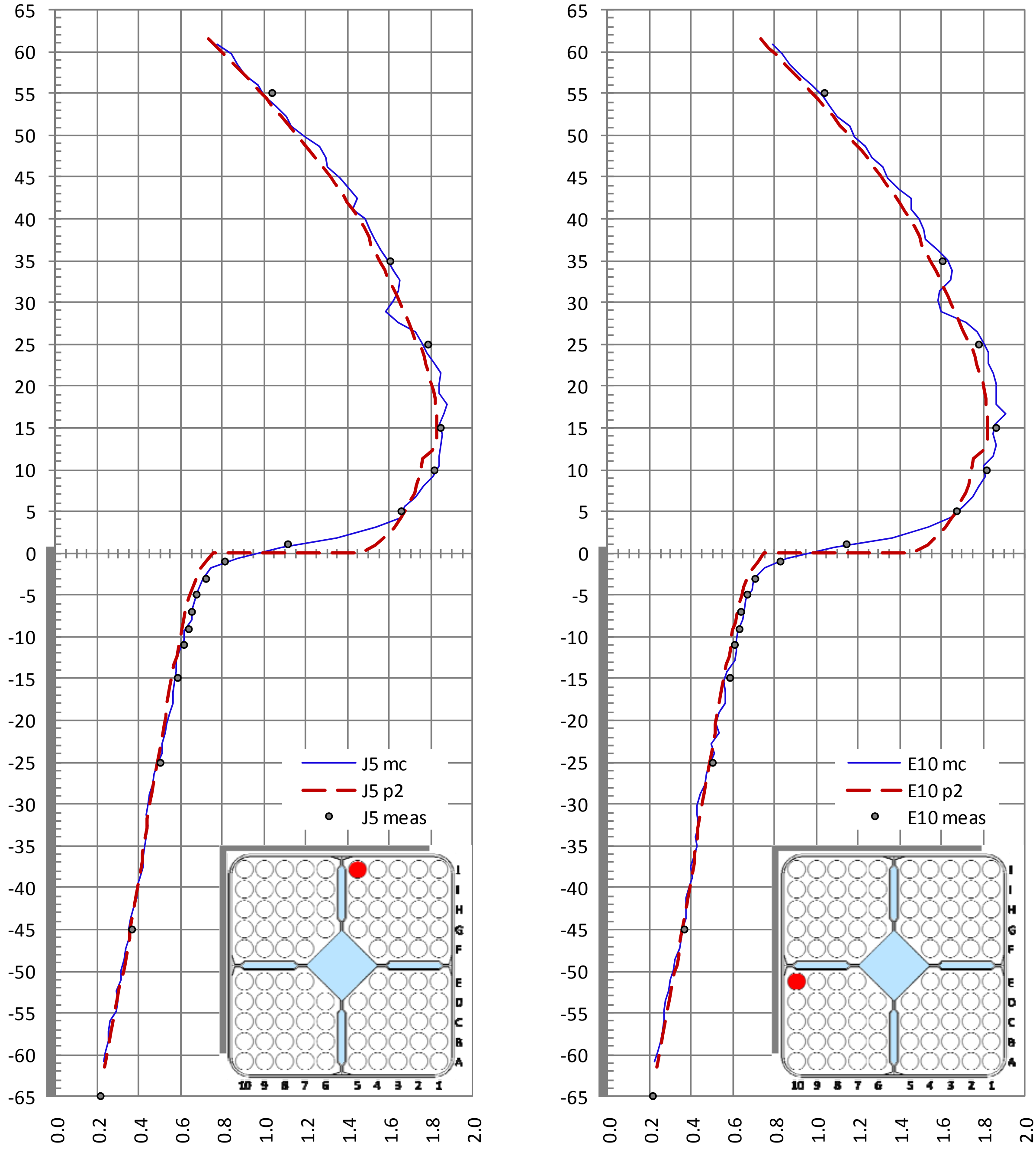

Figure 97 Configuration I-6A: 3D comparison of calculated and measured total-fission rates in pins J5 and E10 for MCNPX (blue line) and PRESTO-2 (red dashed line). All distributions are normalized to 1.0 over the complete 3D set of 221 measured points.

The 3D comparison of MCNPX, PRESTO-2 and experiment for pins J5 and E10 is shown in Figure 97. As in the case of pins J1 and A10, discussed above, these two pins occupy symmetrical lattice positions. Thus, except for the asymmetries occurring in the measured gaps (see Figure 89), their total-fission rates must be the same.

The underestimation of about 4.5% shown by PRESTO-2 in the lower (controlled) part of the test zone agrees with the results obtained for the reference case in Configuration I-2A (see Subsection 5.5.1). In the upper (uncontrolled) part of the test zone, the underestimation of the total-fission rate by PRESTO-2 for pins J5 and E10 (~2.5%) is smaller than for pins J1 and A10 (~3.5%). A similar qualitative behaviour was observed in the comparisons made in Configuration I-1A (see Subsection 4.5.1), although in that case the underestimation for pins J5 and E10 did not exceed 1.0%.

As for all pins lying close to the control blade, the discussion made above in connection with the PRESTO-2 behaviour at the core midplane can also be applied to pins J5 and E10.

Considering the 16 axial measurements, the standard deviations of the MCNPX C/Es for pins J5 and E10 are 2.2% and 1.9%, respectively. In the case of PRESTO-2, these are 10.8% and 9.8%, while by excluding the points at ±1 cm the latter are reduced to 2.0% and 1.6%, respectively.

Measured pins G6 and E8

These two pins occupy central lattice positions and, hence, are only weakly affected by the presence of the control blade. The results of the 3D comparisons of MCNPX, PRESTO-2 and experiment are shown in Figure 98. It can be seen that the global agreement is very good over the entire test-zone length.

Considering the 16 axial measurements, the standard deviations of the C/Es obtained with MCNPX are 1.6% and 1.5% for pins G6 and E8, respectively. In the case of PRESTO-2, these are 2.7% and 2.4%, respectively. For both pins, the axial variation of the total-fission rate near the core midplane is relatively smooth. In consequence, the exclusion of the two points at ±1 cm does not lead to a reduction in the standard deviation of the C/Es, neither for MCNPX nor for PRESTO-2, which can be seen by comparing the corresponding StD and StD2 values in Table 38 and Table 39, respectively.

A particular behaviour of the PRESTO-2 total-fission axial profile, similar to that noted in the 3D comparisons for Configuration I-1C (see Subsection 6.5.4), is observed at core midplane in pin G6. Also here, the transition between axial nodes 5 and 6 (whose interface coincides with the core midplane) shows a singular feature, viz. a step variation. Because of this step, the value of the reconstructed total-fission rate immediately below the core midplane is larger than that immediately above it. As in the case of Configuration I-1C, this unphysical behaviour is caused by the combined effect of the variable separation for the flux (equation {30}) and the use of 2D pin-power maps for the pin-power reconstruction (see also the discussion made in Subsection 6.5.4 and Section 6.6, which can also be applied here, while keeping in mind the fact that the axial heterogeneity is being caused by the presence of the partially inserted control blade).

One other interesting observation must be added to the present discussion. As can be seen in Figure 98, the sign (or direction) of the step in the total-fission axial profile for pin E8 is the opposite to that for pin G6. Although much smaller in magnitude, this step corresponds qualitatively to the behaviour observed in the first six pins discussed above, which are all located closer to the control blade. Now, pin E8 is one lattice pitch closer to the nearest control blade wing than pin G6. This suggests that for pins that are located at larger distances from the control blade, a similar “inverse” step as observed for pin G6 should be expected. It will be shown in the following that this is in fact the case.

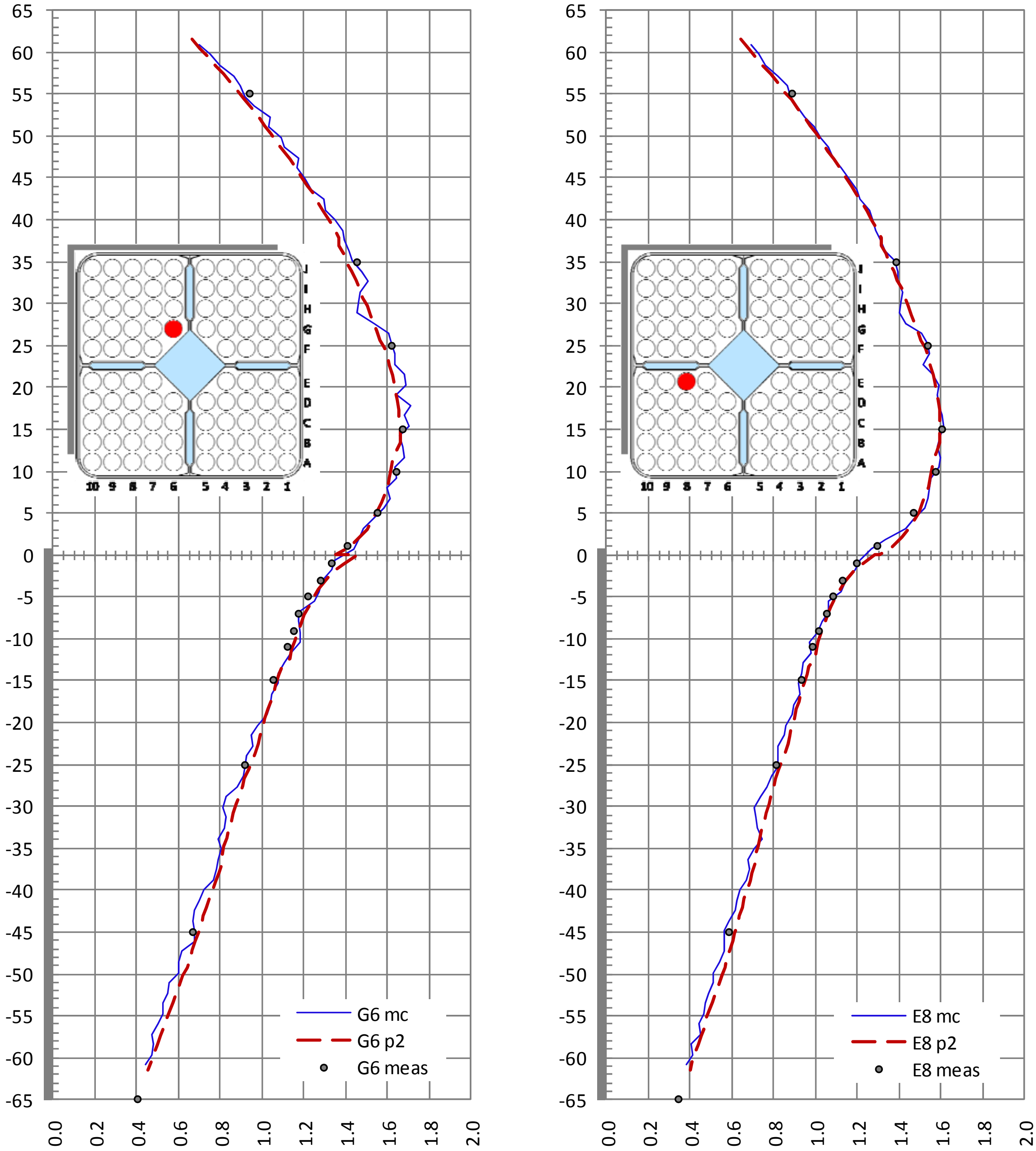

Figure 98 Configuration I-6A: 3D comparison of calculated and measured total-fission rates in pins G6 and E8 for MCNPX (blue line) and PRESTO-2 (red dashed line). All distributions are normalized to 1.0 over the complete 3D set of 221 measured points.

Measured pins D3 and C4

The results for pins D3 and C4 are shown in Figure 99. These two pins occupy symmetrical lattice positions in the central part of the SE sub-assembly. Thus, the effect of the asymmetries occurring in the measured gaps (see Figure 89) can be expected to be negligible. The agreement of MCNPX with experiment is seen to be very good over the entire test-zone length.

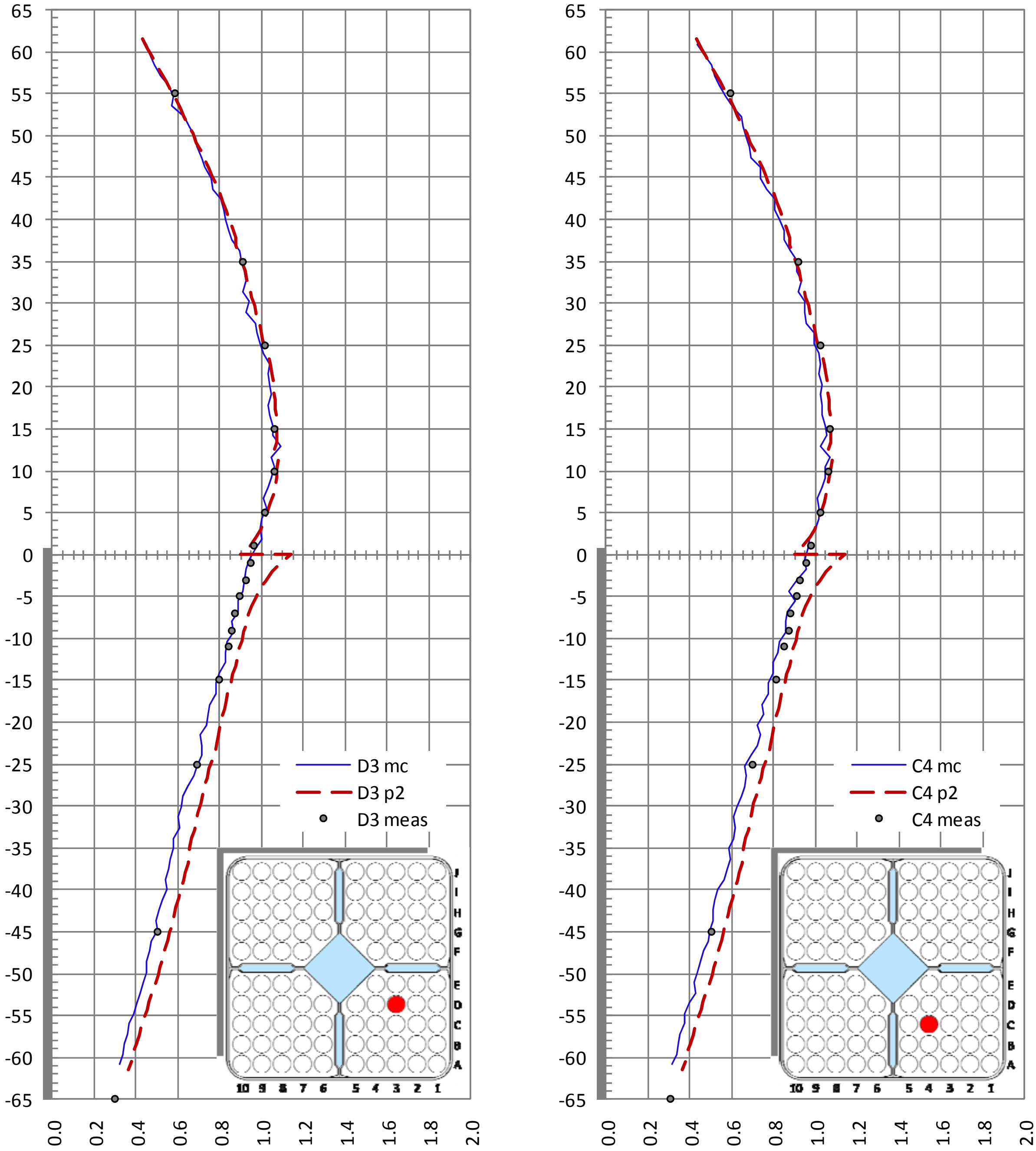

Figure 99 Configuration I-6A: 3D comparison of calculated and measured total-fission rates in pins D3 and C4 for MCNPX (blue line) and PRESTO-2 (red dashed line). All distributions are normalized to 1.0 over the complete 3D set of 221 measured points.

For PRESTO-2, however, the agreement is good in the upper (uncontrolled) part of the test zone, while a clear overestimation is observed in the lower (controlled) part. Once more, this behaviour is consistent with the results of the radial comparisons in Configurations I-1A and

I-2A, shown on the left hand side of Figure 42 and Figure 63, respectively. In particular, the overestimation, in Configuration I-2A, of the total-fission rate in pins that are distant from the control blade (which is clearly seen in Figure 63) can also be observed here.

As anticipated earlier, the axial total-fission profiles for pins D3 and C4 show significant "inverse" steps in the transition between the axial nodes 5 and 6 at the core midplane. Here, the impact of the variable separation used for the asymptotic flux description is seen most clearly. Contrary to the case of Configuration I-1C, the axial dependence of the flux in Configuration I-6A is globally dependent on the radial position, being governed by the flux gradient imposed by the presence of the control blade. Hence, the assumption made in equation {30} of a separable z-dependence, valid for any (x,y), is less accurate.

Considering, as before, 16 axial measurements, the standard deviations of the C/Es obtained with MCNPX are 1.0% and 1.2% for pins D3 and C4, respectively, while for PRESTO-2 these are 5.3% and 5.4%, respectively. For the latter, the "inverse" steps in the axial total-fission rate profiles worsen the agreement near the core midplane. Thus, the exclusion of the two points at ±1 cm leads to an improvement in the standard deviation of the C/Es, the StD2 values becoming 4.6% for both pins.

Measured pins B3 and A8

As in the case of pins D3 and C4, discussed in the previous subsection, pins B3 und A8 are located far from the immediate influence of the control blade, thus showing a similar behaviour at core midplane. Also, some overestimation of the total-fission rate in the lower part of the test zone is observed for both pins (in relative sense being stronger for B3 than for A8; see Table 39), although it has less magnitude than in pins D3 and C4. Furthermore, pin B3 contains 3.95% gadolinium, so that its power is significantly lower.

The results of the 3D comparisons of total-fission rates between MCNPX, PRESTO-2 and experiment are shown in Figure 100. The standard deviations for MCNPX of the C/Es in pins B3 and A8 are 2.0% and 1.6%, respectively, while for PRESTO-2 these are 5.2% and 2.6%, respectively. Excluding the two points at ±1 cm, these values remain unchanged for MCNPX (see StD2 in Table 38), while for PRESTO-2 they are reduced to 4.1% and 2.2%, respectively (see Table 39).

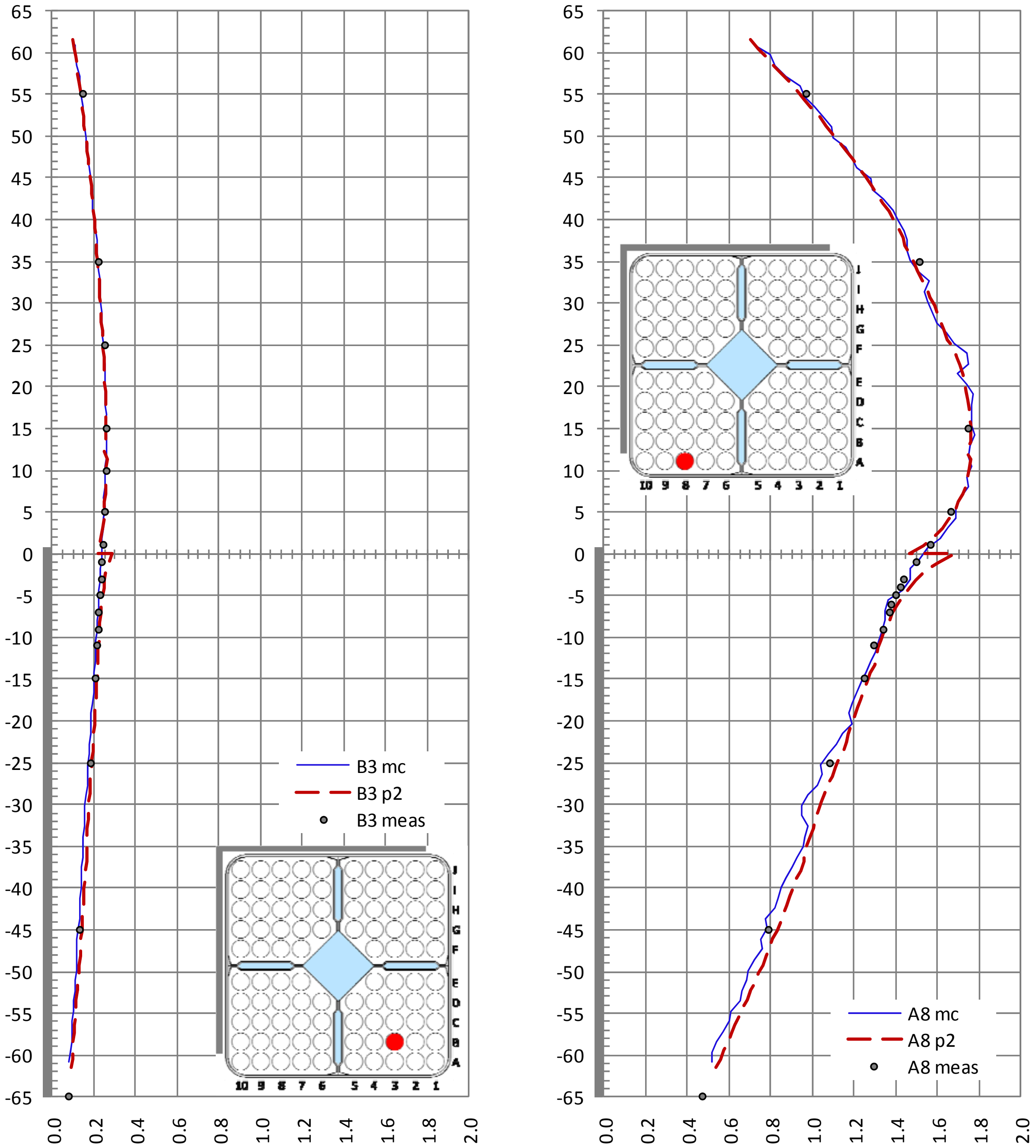

Figure 100 Configuration I-6A: 3D comparison of calculated and measured total-fission rates in pins B3 and A8 for MCNPX (blue line) and PRESTO-2 (red dashed line). All distributions are normalized to 1.0 over the complete 3D set of 221 measured points.

Measured pin A1

Pin A1 is located at the largest distance with respect to the control blade vertex, viz. at the opposite lattice corner. In it, the unphysical behaviour caused by the combined effect of the variable separation of the flux (equation {30}) and the use of 2D pin-power maps for the pin-power reconstruction (see also Subsection 6.5.4 and Section 6.6), is manifested with strongest intensity.

The 3D comparisons of total-fission rates between MCNPX, PRESTO-2 and experiment are shown in Figure 101. Considering 16 axial elevations, the standard deviations are 0.7% and 5.4% for MCNPX and PRESTO-2, respectively. Excluding the two points at ±1 cm, StD2 remains unchanged for MCNPX (see Table 38), while for PRESTO-2 it reduces to 4.1% (see Table 39).

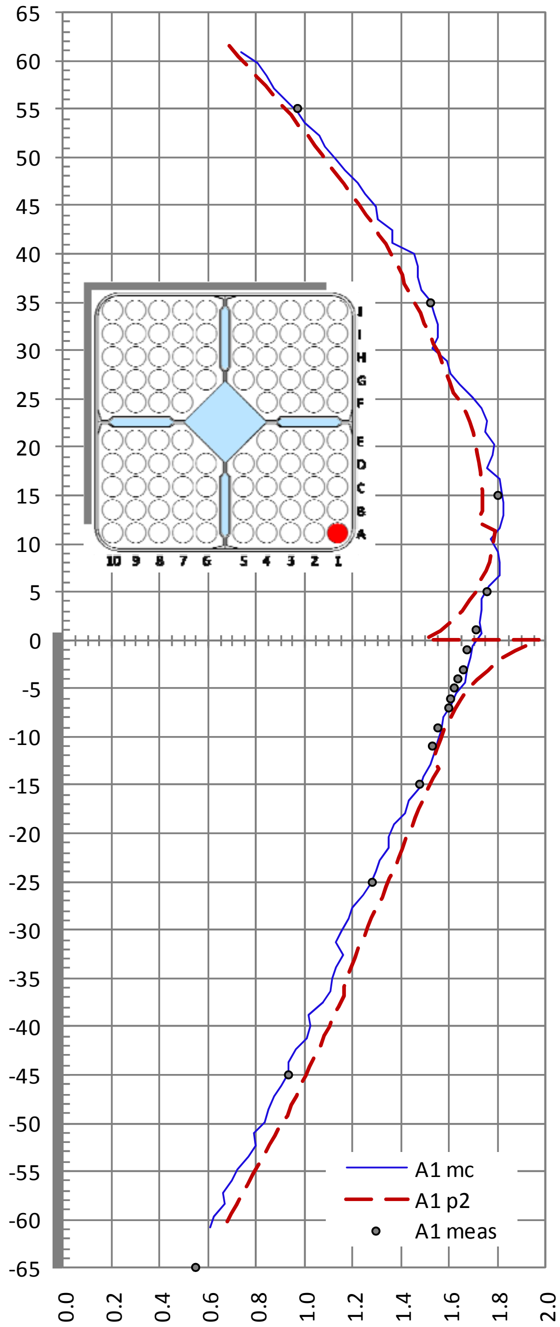

Figure 101 Configuration I-6A: 3D comparison of calculated and measured total-fission rates in pin A1. The distance to the control blade being maximum, the "inverse" step at the transition between the axial nodes 5 and 6 at the core midplane is strongest.

7.5 General remarks concerning the 3D comparisons in Configuration I-6A

The 3D whole-reactor MCNPX model predicts the measured total-fission rate distribution with very good accuracy. Considering the set of 13x16 measurements (the extrapolated values at ±65 cm being excluded), the standard deviation of the C/Es is 2.3%. The transport calculation also delivers accurate results in the challenging region near the tip of the control blade. In fact, if the two C/Es at ±1 cm distance from the core midplane are excluded from the statistics, the standard deviation remains unchanged (see Table 38).

Disregarding the axial region very near the core midplane (consequently, very near the tip of the control blade), also the PRESTO-2 model predicts the measured total-fission rate distribution with good accuracy. Thus, excluding the two points at ±1 cm, the standard deviation calculated over the 3D distribution of 14x13 = 182 C/Es is 4.5% which, for a nodal methodology with pin-power reconstruction, can be regarded as a good result, especially in the challenging conditions occurring in Configuration I-6A.

Very near the core midplane, however, larger deviations occur for the PRESTO-2 results. Thus, when including the two points at ±1 cm in the analysis, the standard deviation increases to 6.9%. As discussed before, these larger deviations are caused by the combined effect of the variable separation of the flux (equation {30}) and the use of 2D pin-power maps for the pin-power reconstruction. Moreover, the strong gradients occurring at the node boundaries near the axial discontinuity[52] for pins that are close to the control blade cannot be captured completely by the exponential shape functions describing the homogeneous flux (see also Subsections 2.3.1 and 2.3.2). As can clearly be seen for pins J10 and I9 in Figure 95, and for pins J5 and E10 in Figure 97, PRESTO-2 strongly overestimates the measurements immediately above the core midplane, while it significantly underestimates them immediately below it. For pins that are distant from the control blade, on the other hand, the situation is reversed. In them, the appearance of the unphysical “inverse” step, discussed in the previous subsections, produces significant underestimations immediately above the interface between the controlled (axial level 5) and the (almost) uncontrolled (axial level 6) nodes, while immediately below this interface, the opposite occurs.

It will be discussed later, in Chapter 9, that the above mentioned local inaccuracies may have an impact on the monitoring of thermal parameters in power reactor applications. However, since the relative average power in controlled assemblies is relatively low, such assemblies are in general not limiting. The situation may become more critical when the control blade is withdrawn after a long period of insertion. In such cases, the cumulative effect of ^{239}Pu build-up may have a significant impact on the linear heat generation rate (LHGR) distribution. The maximum value could then possibly occur in an assembly that was controlled previously and shows inaccuracies in the region where the control blade tip was located.

Finally, it is worth underlining the magnitude of the local discrepancies in the total-fission rate calculated with PRESTO-2 near the nodal interface at core midplane in Configuration I-6A. From Table 39, it can be seen that for pins facing the control blade, such as J10, J5 and E10, the overestimation at axial level +1cm is more than 33% (almost 38% in pin J5). At axial level −1 cm, on the other hand, the underestimation lies in the range of ~12% to 16% for these three pins. For pin A1, at the opposite corner of the lattice, the underestimation at level +1 cm is almost 9%, while the overestimation at −1 cm is ~12%.

7.6 Use of PRESTO-2-1.15

As in the case of Configuration I-1C (see Section 6.7), the PRESTO-2 calculations for Configuration I-6A were repeated using the presently latest released version of the programme, viz. PRESTO-2-1.15. As mentioned before, this new version includes improvements in the modelling of the axial flux dependence that result in a better capture of local effects such as the

---

[52] It should be recalled that the tip of the control blade in Configuration I-6A is placed 0.54 cm above the core midplane, i.e. is not exactly coincident with the nodal interface between the 5th and 6th axial levels.

depression caused by the presence of spacer grids. The deviations discussed in Section 7.5, however, are basic to the nodal methodology with pin-power reconstruction as used in PRESTO-2 and, although showing a slight improvement, still remain. Figure 102 shows, for example, the 3D comparisons of total-fission rates between MCNPX, PRESTO-2 and experiment for pins I9 and E8, while Figure 103 does the same for pins D3 and A1.

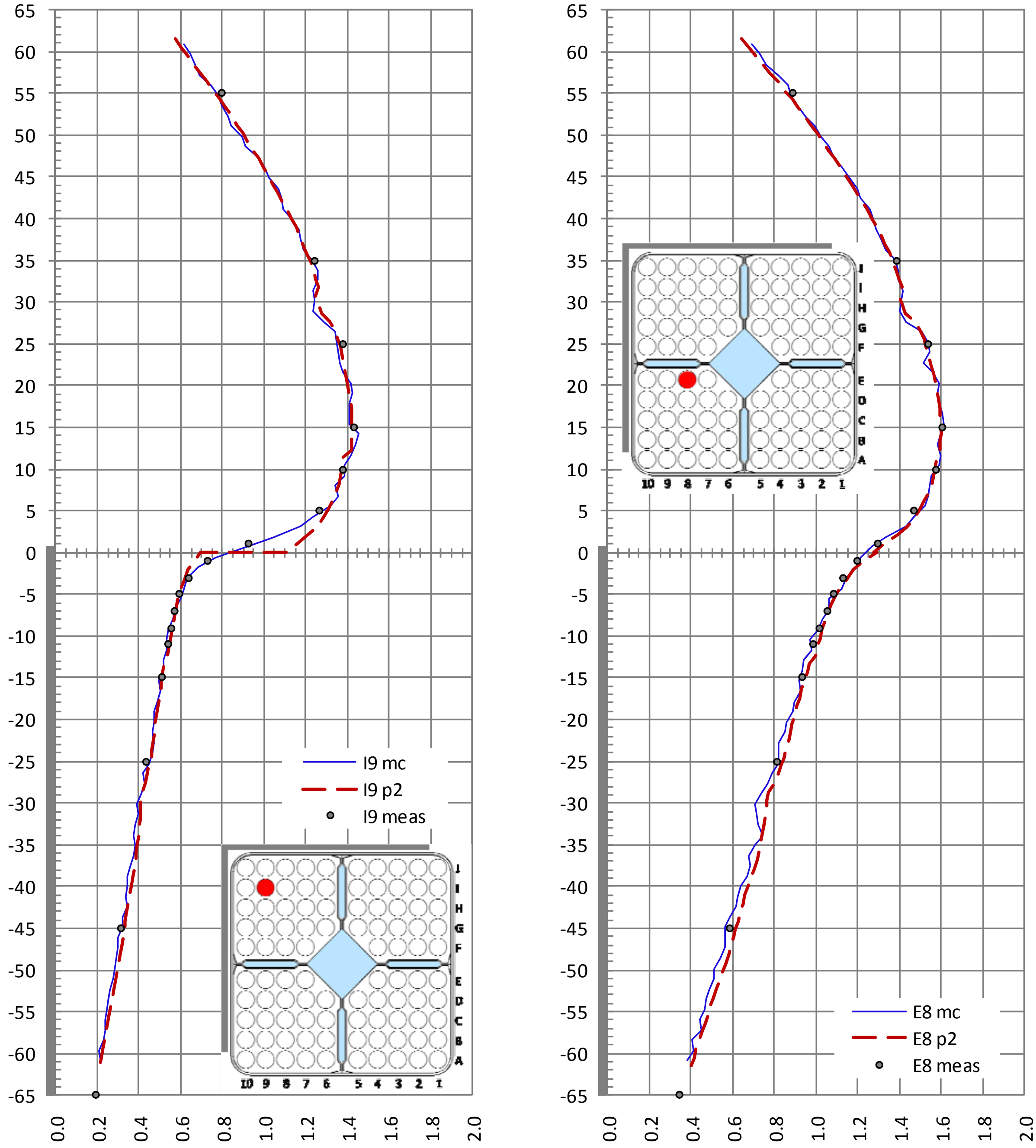

Figure 102 Configuration I-6A: 3D comparison of calculated and measured total-fission rates in pins I9 and E8 for MCNPX (blue line) and PRESTO-2 (red dashed line). The PRESTO-2 results correspond to programme version 1.15.

The C/E results for all pins are presented in Table 40. Considering 16 axial elevations, the standard deviation of the 3D comparison with experiment over all pins (208 points) is 6.6%, i.e. 0.3% lower than with PRESTO-2-1.13 (see Table 39). When excluding the two elevations at ±1 cm, however, the value (StD2) remains unchanged at 4.5%. Thus, although the graphical comparisons show that the flux depression at the spacer grid elevations is better described by PRESTO-2-1.15, the slight reduction in the standard deviation over all C/Es is due to small improvements in the agreement near the core midplane (there are no measured points at the spacer locations). Such an improvement can be observed for pin E8, for example, by comparing Figure 102 with Figure 98.

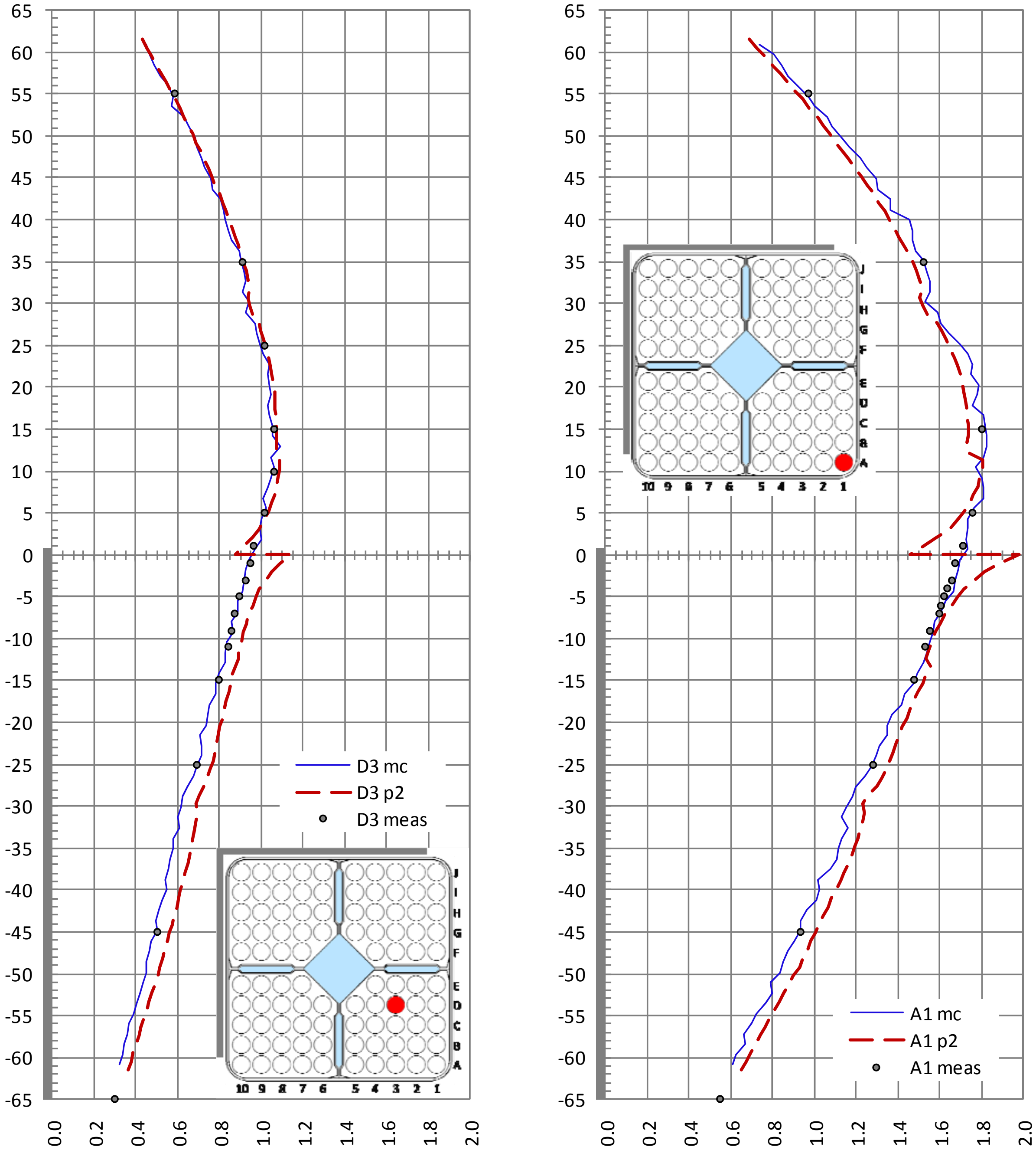

Figure 103 Configuration I-6A: 3D comparison of calculated and measured total-fission rates in pins D3 and A1 for MCNPX (blue line) and PRESTO-2 (red dashed line). The PRESTO-2 results correspond to programme version 1.15.

Comparing Table 40 with Table 39, it can be seen that, for pins facing the control blade (such as J10, J5 and E10), PRESTO-2-1.15 agrees at +1 cm about 3% better with experiment than PRESTO-2-1.13. At axial level −1 cm, on the other hand, the underestimation in these pins remains practically unchanged. For pin A1, at the opposite corner of the lattice, the underestimation at level +1 cm increases by ~3% (reaching almost 12%), while the overestimation at −1 cm (~12%) is unchanged.

Table 40 C/E values corresponding to PRESTO-2 in Configuration I-6A. The results correspond to code version 1.15. The layout of this table is identical to that of Table 38.

Elev.	J10	J5	J1	I9	G6	E10	E8	D3	C4	B3	A10	A8	A1	All pins
55	0.920	0.948	0.934	0.965	0.949	0.944	0.964	0.983	0.967	0.949	0.933	0.968	0.950	
35	0.949	0.978	0.960	0.982	0.975	0.973	0.985	1.006	0.993	0.969	0.965	0.989	0.967	
25		0.978	0.958	0.983	0.978	0.978	0.989	1.004	0.996	0.964	0.967			
15	0.957	0.993	0.964	0.996	0.991	0.981	0.996	1.009	1.001	0.980	0.974	1.006	0.964	
10		0.973	0.970	0.997	0.993	0.971	1.000	1.025	1.022	1.006	0.983			
5	0.977	1.015	0.976	1.029	1.000	1.001	1.015	1.013	1.003	0.983	0.986	1.009	0.974	
1	*1.294*	*1.334*	*1.027*	*1.247*	*0.974*	*1.292*	*1.020*	*0.942*	*0.929*	*0.901*	*1.046*	*0.948*	*0.884*	*excluded*
-1	*0.836*	*0.881*	*0.938*	*0.911*	*1.046*	*0.868*	*1.021*	*1.152*	*1.137*	*1.123*	*0.964*	*1.069*	*1.125*	*from StD2*
-3	0.926	0.936	0.934	0.976	1.020	0.947	1.018	1.104	1.100	1.076	0.955	1.045	1.063	
-4	0.938											1.028	1.055	
-5	0.935	0.955	0.921	0.997	1.021	0.957	1.010	1.089	1.071	1.051	0.949	1.026	1.041	
-6	0.954											1.025	1.032	
-7	0.959	0.952	0.914	1.001	1.025	0.968	1.008	1.077	1.069	1.040	0.941	1.016	1.020	
-9	0.959	0.952	0.911	1.007	1.018	0.951	1.014	1.065	1.053	1.028	0.935	1.007	1.018	
-11	0.978	0.959	0.911	1.017	1.023	0.970	1.026	1.068	1.056	1.023	0.937	1.020	1.012	
-15	0.951	0.944	0.913	0.997	1.015	0.945	1.012	1.078	1.059	1.042	0.934	1.013	1.033	
-25	1.026	0.981	0.941	1.037	1.034	0.976	1.038	1.100	1.095	1.041	0.962	1.039	1.058	
-45	1.018	0.979	0.945	1.054	1.043	0.978	1.052	1.122	1.113	1.064	0.962	1.051	1.079	
-65	*1.028*	*0.943*	*0.911*	*1.000*	*0.990*	*0.960*	*1.008*	*1.073*	*1.060*	*1.035*	*0.924*	*0.997*	*1.051*	*excluded*
Max	1.294	1.334	1.027	1.247	1.046	1.292	1.052	1.152	1.137	1.123	1.046	1.069	1.125	1.334
Min	0.836	0.881	0.911	0.911	0.949	0.868	0.964	0.942	0.929	0.901	0.933	0.948	0.884	0.836
StD	0.095	0.098	0.031	0.070	0.028	0.088	0.021	0.057	0.057	0.055	0.028	0.030	0.058	0.066
StD2	*0.031*	*0.022*	*0.023*	*0.024*	*0.026*	*0.016*	*0.022*	*0.045*	*0.046*	*0.040*	*0.018*	*0.022*	*0.041*	*0.045*

7.7 k-effective

For completeness, Table 41 shows the k-effective values obtained with the different programmes and programme versions used for modelling Configuration I-6A. As in the case of Configuration I-1C, the MCNPX k-effective corresponds to the case used for the determination of the total-fission rates (see footnote in Section 7.3), run with 800 x 10^6 histories.

Table 41 k-effective values for Configuration I-6A. The second column of numbers shows the differences (expressed in pcm) with respect to MCNPX, the k-effective value for which is given in the first row of Column 1, followed in brackets by its 1σ uncertainty (in pcm). Column 3 shows the differences (in pcm), for all calculations with respect to the PRESTO-2-1.13 case.

		Differences (pcm) with respect to:	
	k-effective	MCNPX	PRESTO-2 (v1.13)
MCNPX-2.6b with JEFF-3.1 library	1.00320 (2)	0	-720
PRESTO-2 (v1.13)	1.01040	720	0
PRESTO-2 (v1.15)	1.01040	720	0
PRESTO-2 (v1.13, no spacer)	1.01210	890	170

As already observed in the case of Configurations I-1A, I-2A and I-1C, also for Configuration I-6A the k-effective value calculated with PRESTO-2 is significantly higher than that obtained with MCNPX. This, and some other aspects concerning the k-effective behaviour in the deterministic calculations, have been discussed in the three previous chapters (see Sections 4.9, 5.8 and 6.8). A deeper analysis, as mentioned before, would fall outside the scope of the present thesis, and will therefore be omitted.

7.8 Chapter summary and principal messages

The impact of partially inserted control blades constitutes an important issue in the neutronic analysis of BWR cores. In this chapter, the LWR-PROTEUS experimental results on Configuration I-6A, corresponding to the partial insertion of a L-shaped hafnium control blade in the test zone, were used as basis for the assessment of PRESTO-2 nodal reconstructed results and also, as a complement, transport results obtained with MCNPX.

For HELIOS/PRESTO-2, the radial behaviour of the total-fission rate in the uncontrolled and controlled zones of Configuration I-6A can be correlated with previous observations made for the axially uniform configurations I-1A and I-2A, respectively. For instance, an underestimation of the corner pins is observed in the upper part of the test zone while, in the lower part, significant deviations occur due to the use of reflective boundary conditions in the lattice calculations and the use of azimuthally uniform PCRs. Thus, in the lower part, the total-fission rates of the measured pins are systematically overestimated in the south-east quadrant of the assembly. This radial asymmetry, which is caused by the control blade presence, is comparable to that occurring in Configuration I-2A. Despite the fact that this systematic trend could have largely been corrected by defining PMCFs, as was done in the case of Configuration I-2A, an equivalent correction has not been introduced here. The reason for this is that, in the present chapter, focus was set on the 3D behaviour of the total-fission rate calculated by PRESTO-2, without the a-posteriori application of correction factors. The specific radial aspects related to the use of PMCFs have been addressed in detail in Chapter 5, for the case of the fully-controlled Configuration I-2A.

The control blade being partially inserted, its presence produces, in addition to the radial asymmetry in the lower part of the test zone, a significant axial dependence of the total-fission distribution. As a consequence, accounting for the axial variation of the radial PCRs is very important in the case of Configuration I-6A.

In order to preserve the radial information while focusing on the axial behaviour, a 3D normalisation, analogous to that used for Configuration I-1C, was also applied here. Thus, the complete set 221 experimental points was normalized to 1.0, as also were the corresponding sets of calculated total-fission rates obtained with MCNPX and PRESTO-2. For the same reasons as explained in connection with Configuration I-2A, calculations for Configuration I-6A using the code system CASMO-5/SIMULATE-5 could not be performed.

Excluding the 13 extrapolated calculations at ±65 cm, the standard deviations over the remaining 208 points of the 3D C/E distributions are 2.3% and 6.9%, for MCNPX and PRESTO-2, respectively. Ignoring the points located immediately above and below the core midplane (at ±1 cm), the standard deviation of the MCNPX C/Es remains unchanged, while that corresponding to PRESTO-2 drops significantly to 4.5%.

These comparisons show that the agreement of the PRESTO-2 nodal reconstructed total-fission rates with the experimental results is good, except for the two levels located very near the interface between the 5th and 6th axial nodes. As in the case of Configuration I-1C, and for the same reasons, the nodal reconstructed axial profile cannot accurately follow the steep gradient caused by the transition between the controlled and uncontrolled parts of the test zone. Instead, a step is observed in the axial dependence of the flux. Due to the significant axial asymmetry occurring in Configuration I-6A, the impact of the variable separation of the 3D flux and the use of 2D pin power maps produces a conspicuous “inverse” step at core midplane for pins that are far from the control blade.

In brief, the comparisons of PRESTO-2 with the LWR-PROTEUS experimental results obtained in Configuration I-6A show that nodal methodologies with pin power reconstruction can adequately model the 3x3 array of fuel assemblies in the presence of a partially inserted L-shaped control blade, the significant axial and radial asymmetries being described with good accuracy.

Chapter 8

Partial length rods - Configurations III-1 and III-2

Around the world, most countries have chosen light water reactor designs for their nuclear power programmes. Today, about 60% of the world's nuclear electricity is produced by PWRs and 21% by BWRs.

The LWR-PROTEUS Phase III investigations performed on SVEA-96 Optima2 BWR fuel assemblies, featuring partial length rods (PLRs), are presented in this chapter.

A brief introduction to the particular characteristics of this fuel assembly design is given in Section 8.1. Section 8.2 describes the relevant characteristics of the experimental set-ups (Configurations III-1 and III-2), the calculational models (HELIOS/PRESTO-2 and CASMO-5/SIMULATE-5) being presented in Section 8.3. Section 8.4 addresses the determination of the test-zone boundary conditions by means of 3D MCNPX calculations, while considerations concerning the potential use of 2D HELIOS calculations for the determination of the PCRs are made in Section 8.5. The results of the comparisons of total-fission rates between PRESTO-2, SIMULATE-5, MCNPX and experiment are presented, for the radial direction and in 3D, in Sections 8.6 and 8.7, respectively. Selected results obtained using PRESTO-2 version 1.15 are shown and discussed in Section 8.8. In Section 8.9, general observations concerning the radial and 3D comparisons are made, while a brief discussion concerning the k-effective values obtained in the different calculations is given in Section 8.10. Finally, Section 8.11 summarises the messages derived from the investigations presented in this chapter.

8.1 General aspects concerning BWR fuel assemblies with PLRs

About 20 years ago, the nuclear industry started developing boiling water reactor (BWR) fuel designs with partial length rods (PLRs), with the purpose of improving the dry-out performance and the shut-down margin of the core. Since the PLRs have a reduced length, their lattice position, in each case, is occupied by moderator above the tip of the rod. All these assembly designs thus have in common a reduced number of fuel rods in their upper part.

An axial segment exists in each fuel rod where the cladding allocates a free volume for the fission gases (plenum). In the SVEA-96 Optima2 design, used in the LWR-PROTEUS Phase III experiments, this segment is located at the top of the pellet column, lying for full length rods (FLRs) outside the active length of the core. For PLRs, however, the plenum is located within the active zone of the assembly, thus having an impact on the total-fission rate distribution[53].

The SVEA-96 Optima2 BWR fuel assembly is a further development of the SVEA-96 design. In order to improve the dry-out behaviour of the fuel and the shut-down margin of the

---

[53] In some designs (e.g. ATRIUM from AREVA), the plenum of the PLRs is located at the bottom of the assembly, i.e. in a low power region of the core, but still within the active length of the FLRs.

core, some of the fuel rods have been shortened allowing moderator to fill the corresponding lattice positions. As an additional effect, due to the reduced pressure drop in the upper part of the assembly, the core stability is also improved. A negative impact of the introduction of PLRs is the more positive isothermal temperature coefficient (ITC), which in some situations can be significantly positive and must be accordingly accounted for during reactor start-up.

A simplified cross-view of the SVEA-96 Optima2 fuel assembly is shown in Figure 104. As in the SVEA-96+ case, the assembly consists of an array of 10x10 fuel pins, with a water canal occupying 4 lattice positions in the centre of the assembly and four water wings that subdivide the array in four quadrants. These water structures are designed to contain non-boiling water during normal operation, providing increased moderation in the upper part of the assembly. In its bottom section, the assembly contains 96 fuel rods. At roughly 1/3 of the active height, the four corner pins end, being replaced by moderator. These are referred to as 1/3 PLRs. The 92 fuel pin section extends up to roughly 2/3 of the active height, where eight further fuel rods end. These rods are adjacent to the central water canal and are referred to as 2/3 PLRs. The remaining 84 fuel rods extend to the complete active length of the assembly and are the FLRs. At the top of the enriched pellet column, the PLRs contain two pellets of natural uranium, followed by a plenum volume to allocate the fission gases released during burnup.

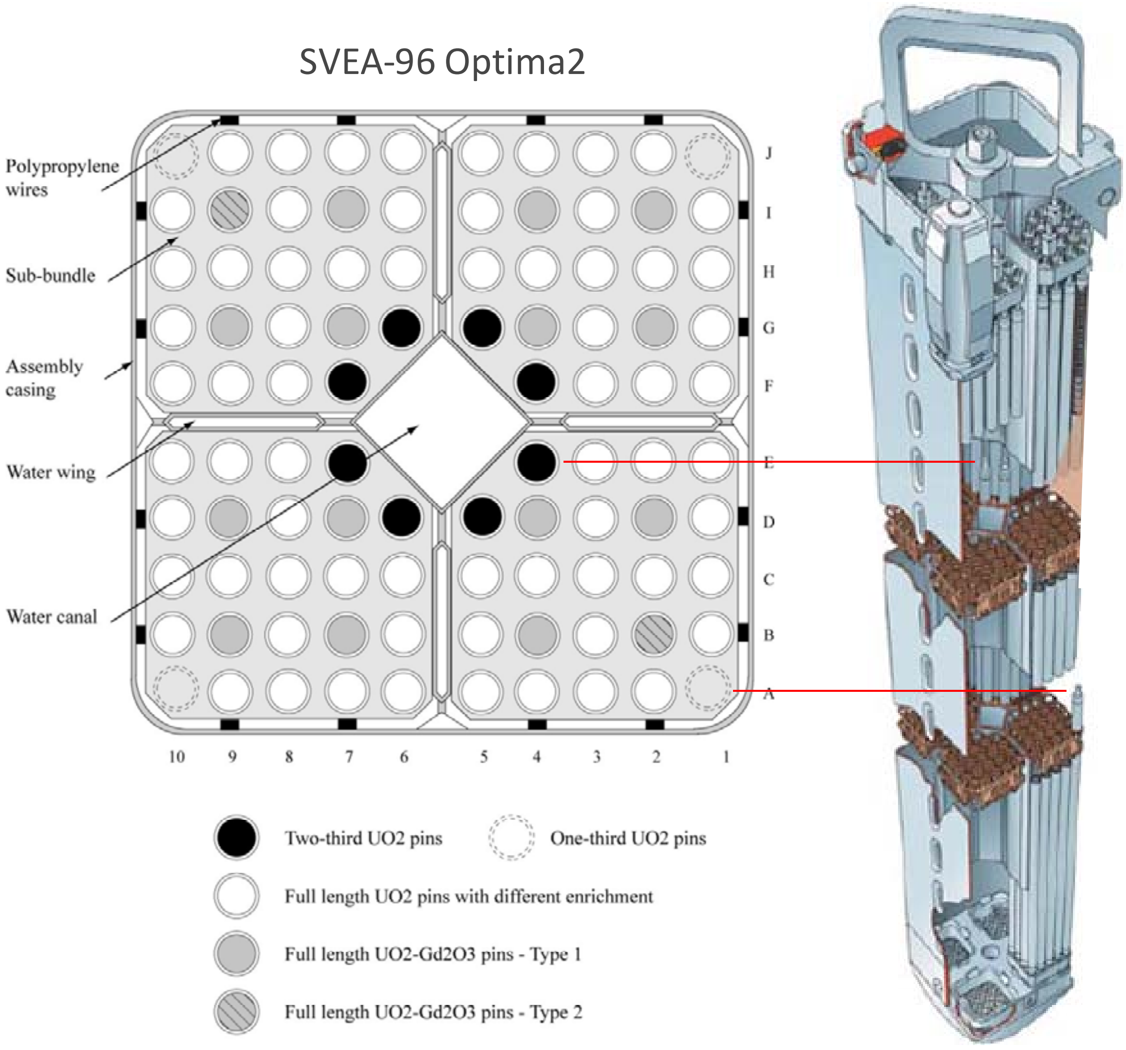

Figure 104 Schematic view of a SVEA-96 Optima2 BWR fuel assembly, showing in particular the lattice positions occupied by the 1/3-length and 2/3-length PLRs. The positions of the Gd pins correspond to the particular KKL nuclear design loaded in the central position of the test zone.

8.2 Description of the test zones

Since the most recent modern BWR fuel assembly designs all contain PLRs, there is interest in evaluating the accuracy of the nodal pin-reconstruction methodology in the prediction of local pin-powers in the presence of axial discontinuities caused by this type of rods.

In the LWR-PROTEUS Phase-III experiments, the test zone consists of 9 full-size SVEA-96 Optima2 fuel assemblies positioned as shown in Figure 105. The central assembly (KKL e20-2), where the measurements were made, has an average enrichment of 4.18 w/o U235 and contains 16 fuel rods with 5.0 w/o gadolinium. The eight peripheral assemblies (KKL e18-1) have 4.02 w/o U235 and contain 12 fuel rods with 4.0 w/o gadolinium. Further details about the axial zoning of these fuel assemblies have been given in Section 2.5 (see, in particular, Figure 17).

As in the Phase I configurations, presented in Chapters 4 to 7, the 3x3 array of fuel assemblies has a nominal pitch of 15.24 cm, equal to the assembly pitch of the KKL core, in which all four inter-assembly gaps have the same nominal width. The external side dimension of the fuel box is 13.86 cm, leading to a nominal gap width of 0.69 cm. In the present experiments, as for all configurations discussed before, the assemblies are slightly displaced, leading to deviations in the gap size with respect to the nominal value. The measured distances between the fuel box of the central assembly and the boxes of its neighbours are shown in Figure 106 and Figure 107 for Configurations III-1 and III-2 respectively. The same distances are summarized in Table 42, which also shows the average half gaps used for the reflected assembly model with half-lattice symmetry (see also Section 8.3).

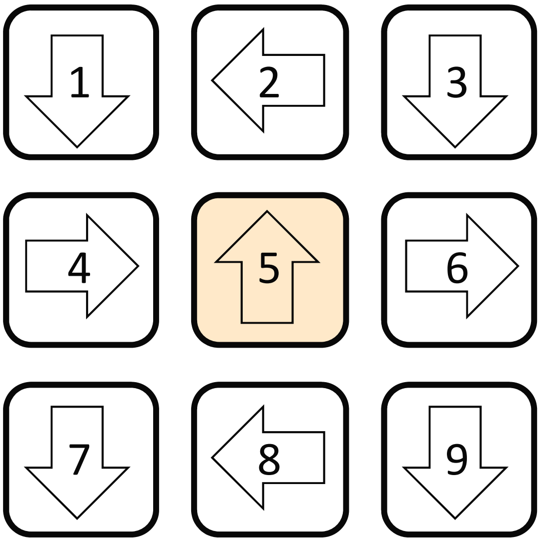

Figure 105 Test zone arrangement in Configurations III-1 and III-2, with the 3x3 array of SVEA-96 Optima2 fuel assemblies. The central assembly belongs to the KKL reload batch e20-2, the eight peripheral ones to reload batch e18-1.

Table 42 Measured distances (cm) between the fuel box of the central assembly and the boxes of its neighbours, and average half-gaps used in the reflected assembly calculations.

	Configuration III-1 (1/3 PLR)				Configuration III-2 (2/3 PLR)			
	West	North	East	South	West	North	East	South
Measured distance	1.323	1.286	1.423	1.498	1.321	1.295	1.412	1.487
Half-gap	0.661	0.643	0.711	0.749	0.661	0.647	0.706	0.744
Average half-gap	0.652		0.730		0.654		0.725	

Also as before, the four sub-bundles were pressed towards the centre of the assembly, in order to simulate the displacement of the fuel pins caused by the forces imposed by the coolant flow, which is assumed to take place in the reactor core under power conditions. To do this, the sub-bundles of the central assembly were pressed 0.5 mm, in x and y directions, by means of polypropylene wires placed between the spacers and the fuel box, as shown in Figure 104. This was done in both Configurations III-1 and III-2. The sub-bundles in the eight peripheral assemblies, in turn, were also pressed, in this case by 0.17 mm and 0.32 mm for Configurations III-1 and III-2, respectively, as summarized in Table 43[54].

Table 43 Measured displacements of the sub-bundles with respect to the nominal lattice positions (sub-bundle pressing). All displacements are directed towards the central water canal.

	Configuration III-1 (1/3 PLR)		Configuration III-2 (2/3 PLR)	
	Central	Peripheral	Central	Peripheral
Measured displ. (cm)	0.050	0.017	0.050	0.032

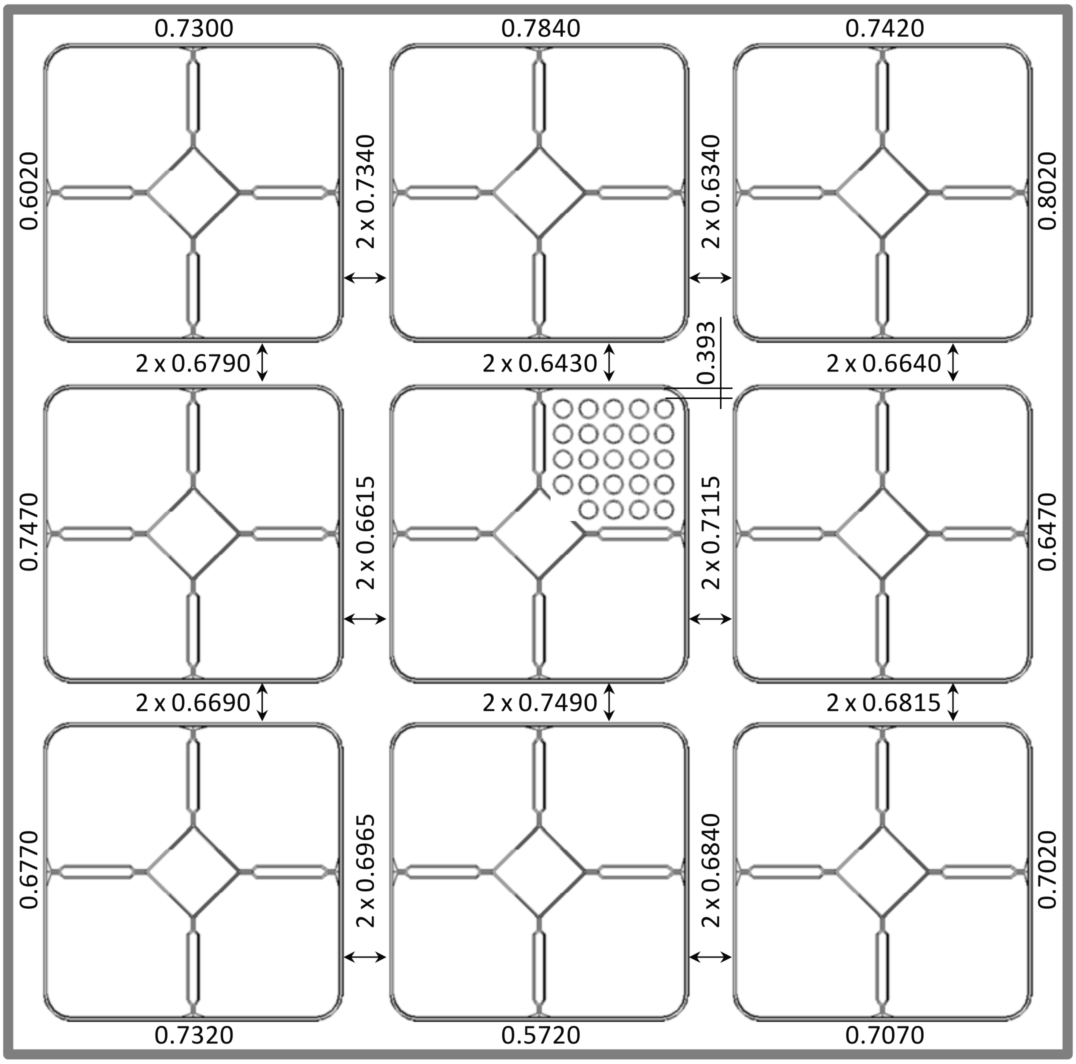

Figure 106 Measured dimensions (cm) in Configuration III-1. In the central assembly, the distance between the outer surface of the cladding of the corner pins and the inner wall of the fuel box is 0.393 cm (sub-channel pressed 0.050 cm towards the central canal). In the peripheral assemblies, this distance is 0.360 cm (sub-channel pressed 0.017 cm towards the central canal).

---

[54] For the peripheral assemblies, the displacements describing the sub-bundle pressing have not been explicitly measured. In this case, the sub-bundles were tied together only at the top, the displacements of 0.17 and 0.32 mm having been derived by linear interpolation under the assumption that they occupy the corresponding nominal positions at the bottom.

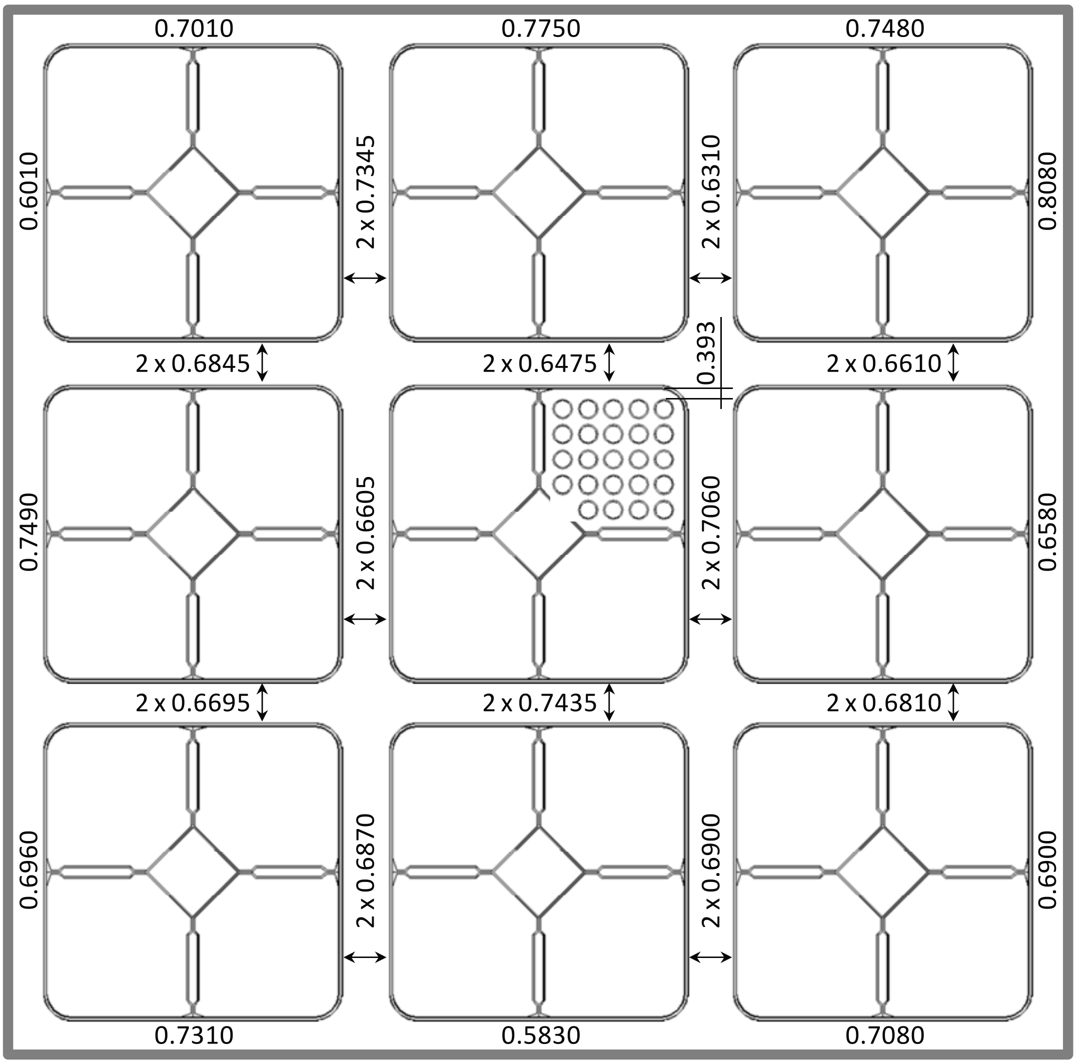

Figure 107 Measured dimensions (cm) in Configuration III-2. In the central assembly, the distance between the outer surface of the cladding of the corner pins and the inner wall of the fuel box is 0.393 cm (sub-channel pressed 0.050 cm towards the central canal). In the peripheral assemblies, this distance is 0.375 cm (sub-channel pressed 0.032 cm towards the central canal).

The measurements were done in the central fuel assembly at different axial positions. For the 3D comparisons, pins of particular interest were selected: in Configuration III-1 (1/3 PLRs), these are the 3 fuel rods surrounding the PLR at each lattice corner (in total 12 pins). In configuration III-2 (2/3 PLRs), 7 PLRs and 7 neighbouring FLRs (in total 14 pins) were measured. For all pins covering the complete test zone length, the measurements were done at 19 axial levels, although at slightly different positions in each configuration. For the 7 PLRs measured in configuration III-2, the measurements covered the 8 lowermost elevations of the axial-level set.

In addition, with the aim of gathering more detailed radial information, additional pins were measured for each configuration at two axial positions with respect to the core midplane: in III-1, −9 cm (76 pins) and +21 cm (72 pins), in III-2, −15 cm (74 pins) and +25 cm (67 pins). These elevations were selected in order to impose an adequate distance between the points of measurement and the test-zone midplane, such that the radial distributions were not perturbed by the axial heterogeneities caused by the PLR tips.

In contrast to the Phase I configurations investigated in this thesis, for which light water at room temperature was used as moderator, Configurations III-1 and III-2 feature a mixture of H_2O and D_2O, also at room temperature, chosen to simulate the numerical density of hydrogen in water at power-reactor operating temperature.

For this mixture, the numerical densities and weight fractions of hydrogen (H), deuterium (D) and oxygen (O), used for the MCNPX, HELIOS and CASMO-5 calculations, have been calculated as follows.

The volume fraction of D_2O in the mixture is 33.7%. Thus, recalling that the densities of H_2O and D_2O at room temperature (20°C) are 0.9982 and 1.1056 g/cm^3, respectively, the density of the mixture is given by:

$$\rho_{mixture} = 0.9982 \cdot (1 - 0.337) + 1.1056 \cdot 0.337 = 1.0344\, g/cm^3$$

Further, the molecular weights of H_2O and D_2O being 18 and 20 g/mol, respectively, the molecular weight of the mixture is:

$$A_{mixture} = 18 \cdot (1 - 0.337) + 20 \cdot 0.337 = 18.674\, g/mol$$

From this, the numerical density of the “molecules” representing the mixture is given by:

$$N_{mixture} = \frac{1.0344\, g/cm^3}{18.674\, g/mol} = 0.0554 \frac{mol}{cm^3} = 0.0333 \cdot 10^{24} \frac{1}{cm^3} = 0.0333 \frac{1}{cm \cdot barn}$$

where the Avogadro number $N_A = 6.02 \cdot 10^{23}\, 1/mol$ was used to obtain the number of molecules per cm^3.

Thus, the numerical densities of hydrogen, deuterium and oxygen are:

$$N_H = 0.0333 \cdot 2 \cdot 0.663 = 4.42 \cdot 10^{-2}\, (cm \cdot barn)^{-1}$$

$$N_D = 0.0333 \cdot 2 \cdot 0.337 = 2.24 \cdot 10^{-2}\, (cm \cdot barn)^{-1}$$

$$N_O = 0.0333 \cdot 1 \cdot 1.000 = 3.33 \cdot 10^{-2}\, (cm \cdot barn)^{-1}$$

while the weight fractions of the elements in the mixture are given by[55]:

$$[w/o]_H = 2 \cdot 0.663/18.674 = 7.101\, \%$$

$$[w/o]_D = 4 \cdot 0.337/18.674 = 7.219\, \%$$

$$[w/o]_O = 16 \cdot 1.0/18.674 = 85.680\, \%$$

In the SVEA-96 Optima2 fuel assemblies, aiming to mitigate the impact of the moderator-to-fuel ratio increase that takes place at the end of the pellet column in the PLRs, the uppermost two pellets of those rods are replaced by two natural uranium pellets. The effect of these two pellets on the global properties of the assembly is relatively small, and accordingly, these are not explicitly modelled in production calculations for the NPP. In this thesis, however, to study the local behaviour of the flux in the vicinity of the axial discontinuity, the two natural uranium

---

[55] For the generation of the case matrix required by SIMULATE-5, CASMO-5 calculates the density of coolant and moderator by using internal steam tables for light water. Thus, in order to obtain the correct numerical densities for hydrogen, deuterium and oxygen, the corresponding weight fractions were multiplied by the ratio between the mass densities of the mixture and of light water (1.0344/0.9982). The resulting weight fractions (7.358, 7.481 and 88.788, for H, D and O, respectively) were then specified in the CASMO-5 cards COO and MOD.

pellets have been considered explicitly. The axial zoning of the fuel is depicted in Figure 17 (see Section 2.5).

In Configurations III-1 and III-2, the core midplane was made coincident with the elevation of the interface between the enriched pellets and the two natural uranium pellets at the top of the active columns of the 1/3 and 2/3 partial length rods, respectively.

As in the cases of Configurations I-1C and I-6A, spacers have been explicitly modelled in the two Phase-III configurations presented here. The heights and axial positions of the spacers in the SVEA-96 Optima2 fuel assemblies (both central and peripheral) are shown in Table 44, the corresponding elevations with respect to the bottom of the test zone being given in Table 45.

Table 44 Spacer heights and axial positions (in cm) for the SVEA-96 Optima2 fuel assemblies. The distances are measured from the beginning of the assembly active length to the midplane of the spacer.

Spacer (from bottom)	1	2	3	4	5	6	7	8
Height	2.6	2.6	2.6	2.6	2.6	2.6	2.6	2.6
Elevation from bottom of fuel assembly active length	46.24	90.54	134.84	179.14	223.44	267.74	312.04	356.34

Table 45 Spacer elevations (in cm) for Configurations III-1 and III-2. The distances are measured from the bottom plane of the test zone (upper row) and from the core midplane (lower row).

Configuration	−	III-1			III-2			−
Spacer (order in test zone)	1(−)	2(1)	3(2)	4(3)	5(1)	6(2)	7(3)	8(−)
Elev. from bottom of TZ Elev. from core midplane	Outside the TZ	26.04 −35.46	70.34 8.84	114.64 53.14	33.94 −27.56	78.24 16.74	122.54 61.04	Outside the TZ

8.3 Characteristics of the calculational models

8.3.1 Lattice calculations – HELIOS model

The HELIOS model used for the lattice calculations in Configurations III-1 and III-2 follows the same basic principles already described in connection with the Phase I calculations (viz. Configurations I-1A, I-2A, I-1C and I-6A), described in Chapters 4 to 7. In particular, the modelling features that characterise the reference case described in Subsection 4.2.1 are also used here. However, three important differences have been introduced in the Phase III cases:

1) Differently from Phase-I, where all the measured inter-assembly gaps were explicitly accounted for by means of individual cross-section sets in each assembly of the test zone, Configurations III-1 and III-2 were modelled using identical peripheral assemblies. Thus, for each configuration, cross-section sets were defined for each axial zone (lattice) of the central assembly and for each axial zone of the (common) peripheral one (see Figure 17). This procedure was selected in order to avoid the large number of lattices that would have been needed to model each peripheral assembly with its particular gaps.

2) While for the peripheral assemblies the nominal gap size was selected (as in the KKL core, where the narrow and wide gaps are equal), for the central assembly an average of the half inter-assembly distances in each direction has been used to define the narrow and wide gaps. This procedure was intentionally chosen so as to conform as much as possible to the situation occurring in the production calculations and, at the same time, to account for the slightly displaced coordinates of the central assembly in the experiment. The half-gap sizes used in the reflected lattice calculations for the central assembly in Configurations III-1 and III-2 are shown in Table 42.
3) Instead of full-lattice geometry, as employed in Phase I, the Phase III HELIOS calculations have been performed in half-lattice geometry, making use of the diagonal symmetry, and, as consequence, losing a certain additional detail in the modelling of the experimental gaps.
4) The thermal cut-off energy of the two-group lattice parameters was set to 0.625 eV (instead of 1.84 eV, as in the Phase I calculations). This has been done for compatibility with standard applications of CASMO-5/SIMULATE-5, the cut-off energy 1.84 eV being particular to the KKL HELIOS/PRESTO-2 production XSDB (see also Subsection 3.2.2). As discussed in Subsection 4.5.2, the impact of the thermal cut-off energy on the calculated total-fission rate distribution is small.

Thus, for each configuration, 14 lattices have been calculated with HELIOS, seven for each assembly type (see also Table 46 and Figure 17), and stored in a cross-section data bank. The appropriate data are then retrieved with PRESTO-2 according to the axial position of the test tank, in order to reflect the test-zone axial composition in each configuration (III-1 or III-2).

8.3.2 Core calculations - PRESTO-2 model

The PRESTO-2 modelling of Configurations III-1 and III-2 follows the same principles discussed earlier for the Phase I configurations. The pin-power maps and discontinuity factors, which have been calculated by HELIOS in half-symmetry, are automatically expanded to full-assembly geometry, so that no special input is needed in this respect. As for all the nodal calculations presented in this thesis, the axial discretisation consists of ten uniform nodes, 12.3 cm high, five of which are placed at each side of the test-zone midplane. On the other hand, the axial segmentation of the fuel assembly is specifically described by defining the length of the material regions constituting the test zone in each configuration. Thus, as in the normal case of power reactor modelling, the material boundaries are in general not coincident with the nodal interfaces (with the exception of the interface between the 5th and 6th axial levels at core midplane, which is intentionally placed at the interface between the enriched and the natural-uranium pellets). Further details concerning the test-zone composition are given below, while the PCRs describing the test-zone boundary at the different axial levels will be presented in Section 8.4.

As mentioned in Section 8.2, the core midplane in Configurations III-1 and III-2 was made coincident with the interface between the enriched pellets and the two natural uranium pellets at the top of the active column of the 1/3 and 2/3 partial length rods, respectively. Accordingly, the values for the lengths of the fuel segments, as modelled in PRESTO-2, are those shown in Table 46 (see also Figure 17).

Table 46 Lengths (cm) of the fuel segments in the test-zone model of PRESTO-2. Since the lattice data in Configurations III-1 and III-2 differ (due to different gap sizes in the central assembly and different sub-assembly pressing in the peripheral ones), the data was stored in two different XSDBs. Hence, the same lattice names could be used for both configurations. "Unat" denotes natural uranium in the PLR positions.

Configuration III-1 (1/3 PLR)				Configuration III-2 (2/3 PLR)			
Number of lattice positions occupied by fuel, plenum and moderator (F/P/M)	Lattice name		Length (cm)	Number of lattice positions occupied by fuel, plenum and moderator (F/P/M)	Lattice name		Length (cm)
	Centre	Periphery			Centre	Periphery	
–	–	–	–	84/0/12	KKL126	KKL096	38.45
–	–	–	–	84/8/4	KKL127	KKL097	21.05
–	–	–	–	92/0/4 Unat	KKLnc2	KKLnp2	2.0
92/0/4	KKL128	KKL098	46.35	92/0/4	KKL128	KKL098	61.50
92/4/0	KKL129	KKL099	13.15	–	–	–	–
96/0/0 Unat	KKLnc1	KKLnp1	2.0	–	–	–	–
96/0/0	KKL130	KKL100	61.50	–	–	–	–

8.3.3 Lattice calculations - CASMO-5 model

For the modelling of Configurations III-1 and III-2 with CASMO-5, the same methodology and options as applied in the calculations for Phase I (Configurations I-1A and I-1C) have been used (see Section 3.4).

The inter-assembly gaps for the central assembly are the same as in the HELIOS calculations (see Table 42), which, as discussed in Subsection 8.3.1, are also performed in half-lattice symmetry. Also as in the case of HELIOS, the eight peripheral fuel assemblies are calculated using nominal gap widths.

As done for the configurations in Phase I (see Subsection 3.4.4), cards LDX and LDY have been used to specify the displacements of the pin coordinates caused by the sub-channel pressing (see Table 43). In the case of the SVEA-96 Optima2 fuel assembly, in which the pin pitch is not regular over the entire lattice, the LDX/LDY cards carry, in addition, the information needed to determine the exact position of each pin.

Two cross-section data banks were generated with CMSLINK for SIMULATE-5: a 5-group XSDB, with the group structure shown in Table 5, and a 2-group XSDB, with a thermal cut-off energy of 0.625 eV.

8.3.4 Core calculations - SIMULATE-5 model

The SIMULATE-5 model for Configurations III-1 and III-2 is basically the same as that used for Configurations I-1A and I-1C, its fundamental aspects being discussed in Section 3.5. As in the case of PRESTO-2, the axial composition of the fuel and the spacer positions were specified explicitly. These are shown in Table 46 and Table 45, respectively. As done for all previous configurations, the calculations were performed in 2 and 5 energy groups.

8.4 Test-zone boundary conditions using the 3D MCNPX model

The PCRs for Configurations III-1 and III-2 have been calculated using a 3D MCNPX model of the LWR-PROTEUS reactor, as done before, following the methodology described in Subsection 3.6.1. In this case, however, the calculations were performed using 10^6 particles and 800 cycles, i.e. 8×10^8 histories, for both the calculation of the PCRs and for the determination of the pellet-wise total-fission rates[56].

Differently from the approach used for the calculations in Phase I, in which the test-zone perimeter at each axial level was subdivided in 48 segments to capture the spatial dependence of the radial PCRs, a single PCR per axial level and energy group is defined here, the partial currents being tallied, for this purpose, over each complete side of the test zone. Thus, in the case of Configurations III-1 and III-2, the side and corner PCRs, as defined in PRESTO-2 (see Figure 30), are replaced by a single PCR, which is valid for the complete boundary slice corresponding to each particular axial level. Thus, for these configurations, the radial PCRs used in PRESTO-2 and in SIMULATE-5 are the same.

It is worth to recall here, that the comparisons performed on Configuration I-1A (see Subsection 4.5.3) have shown that, for azimuthally uniform configurations, the subdivision of the radial boundary into sides and corners has almost no impact on the calculated total-fission distribution. Thus, the use of a single PCR per axial level and energy group in Configurations III-1 and III-2 is well justified.

8.4.1 PCRs for PRESTO-2

Consistently with the lattice parameters, the 2-group PCRs were calculated for a cut-off energy of 0.625 eV. The radial PCRs at each axial level, and the axial PCRs at the test-zone top and bottom planes, are shown in Table 47.

---

[56] This has no special significance for the PCRs, for which 200’000 particles and 250 cycles (as used in the Phase I calculations) are sufficient. In the Phase III calculations, however, the same run was used for the determination of both the PCRs and the total-fission rate distribution in the central assembly.

Table 47 PCRs for PRESTO-2 in Configurations III-1 and III-2, derived from the partial currents obtained in the 3D whole-reactor MCNPX calculation. The approximate 1σ statistical relative errors are lower than 0.05% in all cases. The thermal cut-off energy is 0.625 eV.

Configuration		III-1 (1/3 PLR)		III-2 (2/3 PLR)	
		PCR$_{11}$	PCR$_{22}$	PCR$_{11}$	PCR$_{22}$
Axial direction at top		0.789	0.920	0.798	0.929
Radial direction	Axial level 10	0.981	0.377	1.047	0.391
	Axial level 9	0.984	0.367	1.054	0.382
	Axial level 8	0.989	0.364	1.057	0.376
	Axial level 7	0.990	0.364	1.052	0.377
	Axial level 6	0.987	0.371	1.039	0.372
	Axial level 5	0.976	0.374	1.016	0.369
	Axial level 4	0.972	0.372	1.006	0.367
	Axial level 3	0.969	0.374	1.000	0.368
	Axial level 2	0.959	0.376	0.986	0.368
	Axial level 1	0.942	0.383	0.968	0.376
Axial direction at bottom		0.869	0.960	0.867	0.961

8.4.2 PCRs for SIMULATE-5

In addition to the 2-group structure with a cut-off energy of 0.625 eV, the PCRs to be used in SIMULATE-5 are defined in 5 energy groups, the group boundaries being given in Table 7. The PCRs corresponding to Configurations III-1 and III-2 are shown in Table 48 and Table 49, respectively[57].

Table 48 PCRs for SIMULATE-5 in Configuration III-1, derived from the partial currents obtained in the 3D whole-reactor MCNPX calculation. The group boundaries correspond to those given in Table 7.

Configuration III-1 (1/3 PLR)		5 energy groups					2 energy groups	
		PCR$_{11}$	PCR$_{22}$	PCR$_{33}$	PCR$_{44}$	PCR$_{55}$	PCR$_{11}$	PCR$_{22}$
Upper limit (eV)		20x10^{6}	821x10^{3}	9119	1.84	0.625	20x10^{6}	0.625
Axial dir. at top		0.635	0.826	0.864	0.848	0.920	0.789	0.920
Radial direction	Axial level 10	0.793	1.434	0.650	0.657	0.377	0.981	0.377
	Axial level 9	0.786	1.438	0.664	0.664	0.367	0.984	0.367
	Axial level 8	0.786	1.442	0.672	0.669	0.364	0.989	0.364
	Axial level 7	0.787	1.442	0.676	0.673	0.364	0.990	0.364
	Axial level 6	0.781	1.431	0.677	0.679	0.371	0.987	0.371
	Axial level 5	0.760	1.414	0.675	0.678	0.374	0.976	0.374
	Axial level 4	0.754	1.410	0.673	0.672	0.372	0.972	0.372
	Axial level 3	0.752	1.406	0.669	0.669	0.374	0.969	0.374
	Axial level 2	0.745	1.395	0.657	0.659	0.376	0.959	0.376
	Axial level 1	0.731	1.370	0.643	0.650	0.383	0.942	0.383
Axial dir. at bottom		0.792	0.881	0.912	0.913	0.960	0.869	0.960

---

[57] As mentioned earlier, the 2-group PCRs are the same for PRESTO-2 and SIMULATE-5.

Table 49 PCRs for SIMULATE-5 in Configuration III-2, derived from the partial currents obtained in the 3D whole-reactor MCNPX calculation. The group boundaries correspond to those given in Table 7.

	Configuration III-2 (2/3 PLR)	5 energy groups					2 energy groups	
		PCR$_{11}$	PCR$_{22}$	PCR$_{33}$	PCR$_{44}$	PCR$_{55}$	PCR$_{11}$	PCR$_{22}$
	Upper limit (eV)	20x10^{6}	821x10^{3}	9119	1.84	0.625	20x10^{6}	0.625
	Axial dir. at top	0.643	0.833	0.872	0.855	0.929	0.798	0.929
Radial direction	Axial level 10	0.891	1.524	0.677	0.687	0.391	1.047	0.391
	Axial level 9	0.887	1.532	0.695	0.699	0.382	1.054	0.382
	Axial level 8	0.885	1.535	0.705	0.704	0.376	1.057	0.376
	Axial level 7	0.880	1.524	0.705	0.704	0.377	1.052	0.377
	Axial level 6	0.858	1.510	0.698	0.699	0.372	1.039	0.372
	Axial level 5	0.827	1.477	0.688	0.689	0.369	1.016	0.369
	Axial level 4	0.812	1.463	0.683	0.681	0.367	1.006	0.367
	Axial level 3	0.805	1.455	0.677	0.677	0.368	1.000	0.368
	Axial level 2	0.792	1.440	0.663	0.665	0.368	0.986	0.368
	Axial level 1	0.778	1.414	0.648	0.656	0.376	0.968	0.376
	Axial dir. at bottom	0.788	0.878	0.910	0.919	0.961	0.867	0.961

8.4.3 Axial behaviour of the radial PCRs

As in the cases of Configurations I-1C and I-6A (see Subsections 6.3.3 and 7.3.2, respectively) the axial variation of the PCRs in Configurations III-1 and III-2 reflects the different reactivity of the lattices on both sides of the test-zone midplane. For instance, for both configurations, the reactivity of the lower part of the test-zone is higher than that of the upper part. This can be seen in Table 50, where the k-infinity values obtained with HELIOS are shown for all lattices (except for those containing the natural uranium pellets at the PLR tips).

Table 50 k-infinity values obtained with HELIOS for Configurations III-1 and III-2. The average inter-assembly half-gaps of Table 42 have been used for the central assembly, while the peripheral assemblies were modelled, as mentioned in Section 8.3, with nominal gaps. The values of the sub-channel pressing used for each configuration are given in Table 43.

	Peripheral (KKL e18-1)		Central (KKL e20-2)	
Configuration	Lattice	k-infinity	Lattice	k-infinity
III-2 (2/3 PLR)	KKL096 KKL097 KKL098	1.09871 1.10584 1.14595	KKL126 KKL127 KKL128	0.99532 0.99965 1.04013
III-1 (1/3 PLR)	KKL098 KKL099 KKL100	1.14626 1.14294 1.15298	KKL128 KKL129 KKL130	1.04011 1.03874 1.05830

Thus, the contribution of the PROTEUS buffer and driver zones to the neutron balance in the test zone is stronger in the region above the core midplane, which results in larger epithermal radial PCRs for that region. This behaviour is similar to that observed in Configuration I-1C (see

Subsection 6.3.3), where the axial variation of the PCRs was caused by the different material compositions above and below the core midplane. Although the magnitude of the differences between the PCRs in the upper and lower part of the test zone are smaller in Configurations III-1 and III-2 than in Configuration I-1C, these differences can be qualitatively correlated with the k-infinity values of the assembly lattices in an analogous way[58]. For instance, Table 51 shows a comparison of the epithermal PCRs (above 0.625 eV) at axial levels 8 and 3 for Configurations I-1C, III-1 and III-2. It can be seen, that the ratio of the PCRs at axial levels 8 and 3 follows the trend of the k-infinity values in the corresponding lattices[59].

Table 51 Comparison of the epithermal PCRs (above 0.625 eV) at axial levels 8 and 3 for Configurations I-1C, III-1 and III-2.

	Configuration I-1C	Configuration III-1	Configuration III-2
Level 8	1.108	0.989	1.057
Level 3	1.009	0.969	1.000
Level 8 / Level 3	1.098	1.021	1.057
(k-inf. lev. 8 – k-inf. lev. 3) (pcm)	−6497	−672	−4724

The PCRs presented in Table 47 are plotted as a function of the elevation in Figure 108. As in the cases of Configurations I-1C and I-6A (see Figure 76 and Figure 90, respectively), it can be seen that, for Configurations III-1 and III-2, an appropriate modelling of the axial dependence of the PCRs is important.

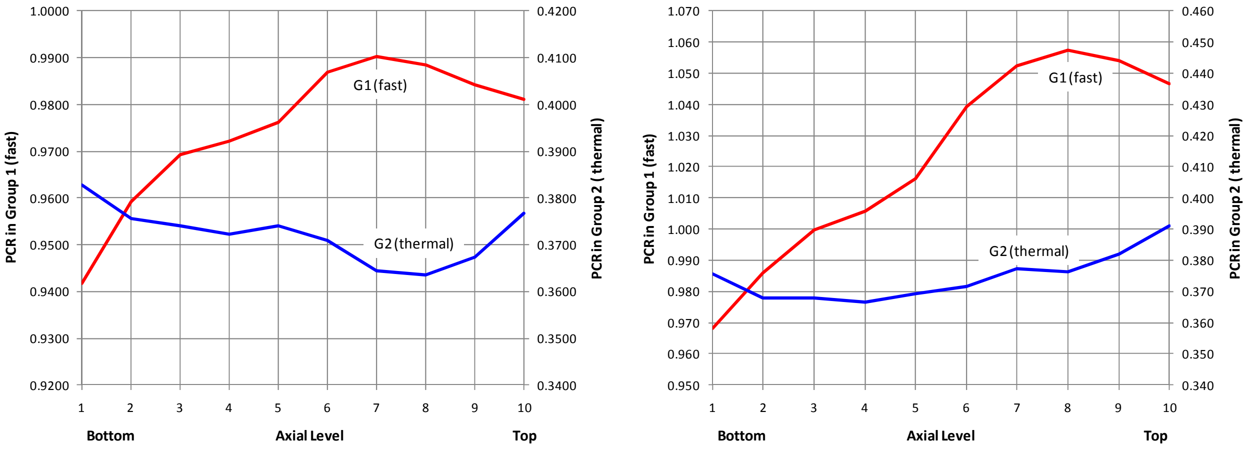

Figure 108 Axial variation of the two-group PCRs for Configuration III-1 (left) and Configuration III-2 (right). The numerical values are shown in Table 47.

---

[58] Strictly speaking, for the comparison of the relative reactivity behaviour of the LWR-PROTEUS test zone in the different cases, the migration area M^2 (see equation {45}) should also be taken into account. With the H_2O/D_2O mixture having been used as moderator in Phase III, M^2 is about 20% larger than in Phase I, where H_2O was used. However, for the purpose of the present discussion, it is the ratio between the properties of the upper and lower test-zone halves (for each configuration independently) which is important. For Configurations III-1 and III-2, the M^2 values of the lattices located on the two sides of the test-zone midplane differ only by ~0.9% and ~2.2%, respectively, M^2 following, qualitatively, the same trend as k-infinity. Hence, for the analysis of the axial profiles of the radial PCRs, it is sufficient to consider the relative k-infinity behaviour.

[59] For Configurations III-1 and III-2, the k-infinity values of the peripheral assemblies are shown, these being the most representative for the test zone reactivity and its impact on the PCRs.

8.4.4 Energy dependence of the partial currents and PCRs

As previously done in Subsections 4.3.4, 5.3.3, 6.3.4 and 7.3.3 for Configurations I-1A, I-2A, I-1C and I-6A, respectively, the relative intensity of the MCNPX calculated, 5-group partial currents and PCRs corresponding to Configurations III-1 and III-2, are presented and discussed below.

Energy dependence in Configuration III-1

Figure 109 shows the energy dependence of the partial currents and PCRs for Configuration III-1. In this figure, as before, the currents are integrated over the complete test-zone radial boundary, i.e. by summing over all sides and axial levels.

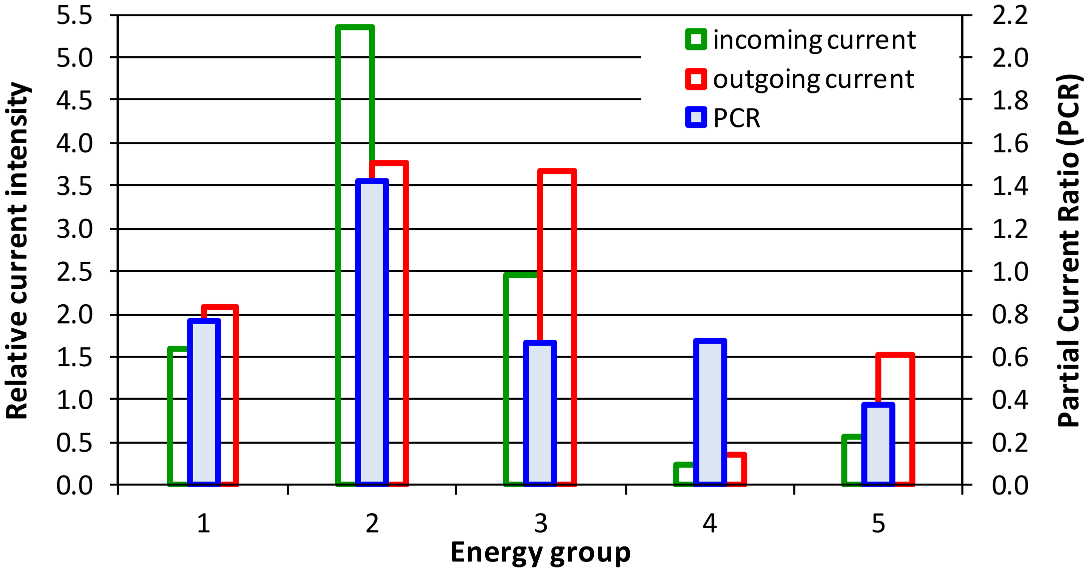

Figure 109 Energy dependence of the radial currents and PCRs in Configuration III-1 in five energy groups, derived from the partial currents obtained in the 3D whole-reactor MCNPX calculation. The partial currents were integrated over the complete test-zone boundary, i.e. were summed over all sides and axial levels.

As done before for the axially heterogeneous configurations (I-1C and I-6A), plots have been considered in analogy to Figure 109 while focusing on two particular axial levels instead of the whole test-zone length. Thus, Figure 110 and Figure 111 show the partial currents and the PCRs for Configuration III-1 at the axial levels 8 and 3, respectively. As discussed above, the difference between the epithermal PCRs at these two axial levels lies in the order of 2% (see Table 51). This relatively weak axial dependence is also observed for the PCRs in 5 energy groups. The magnitude of the partial currents themselves, on the other hand, shows a stronger axial variation, which is displayed (for simplicity, in two energy groups) in Figure 112. It is seen that, for the epithermal group, the partial currents at level 8 are approximately 25% lower than those at level 3. This axial dependency of the partial currents reflects, to some extent, the axial variation of the neutron flux in the test zone.

At this point, a distinction between the cases of Configurations I-1C and III-1 (and also III-2, which will be discussed later) should be made. It needs to be noted, in this context, that in Configuration I-1C the number of fuel rods is the same over the entire test-zone length and that the nine fuel assemblies that constitute the test zone have identical design. Thus, in this case, the axial variation of the partial currents closely follows the profile of the total-fission rate (compare, for instance, Figure 80 in Subsection 6.3.4 with Figure 82 in Subsection 6.5.4). In Configuration III-1, on the other hand, the four corner pins vanish in the upper part of the test zone, thus reducing the average fuel density in that region. Consequently, compared with the lower part of the test zone (and its surroundings in the radial direction), the average total-fission rate in the upper part, und thus the corresponding partial currents, decreases more strongly than the total-fission rate in each individual pin. This effect can be observed by comparing the axial profile of the partial currents at the test-zone boundary, shown in Figure 112, with the global curvature of the total-fission rate profiles, which will be presented in Subsection 8.7.1.

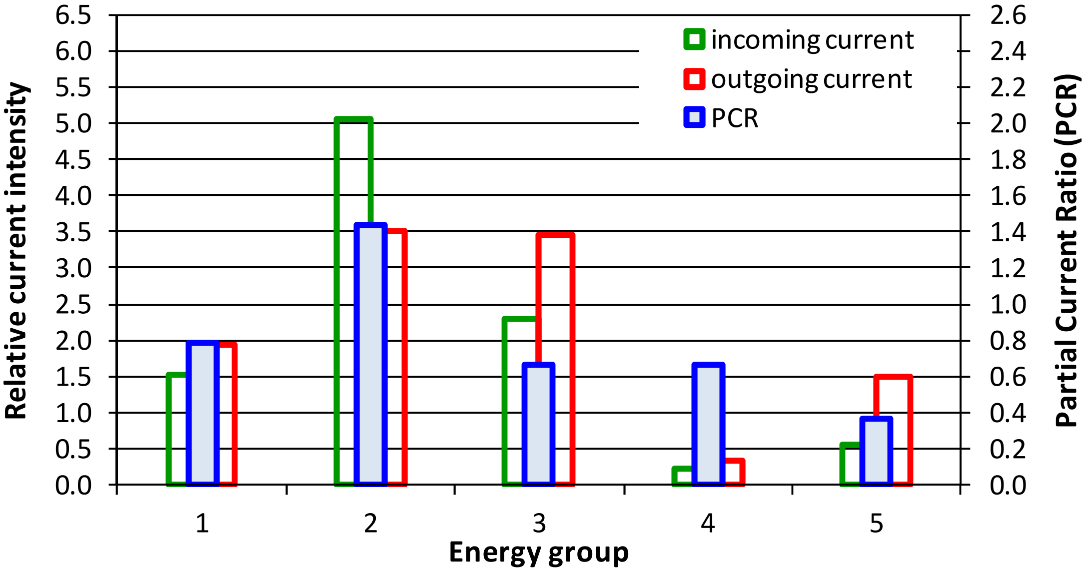

Figure 110 Energy dependence of the radial currents and PCRs in Configuration III-1 in five energy groups, at axial level 8 (middle of the test-zone upper half).

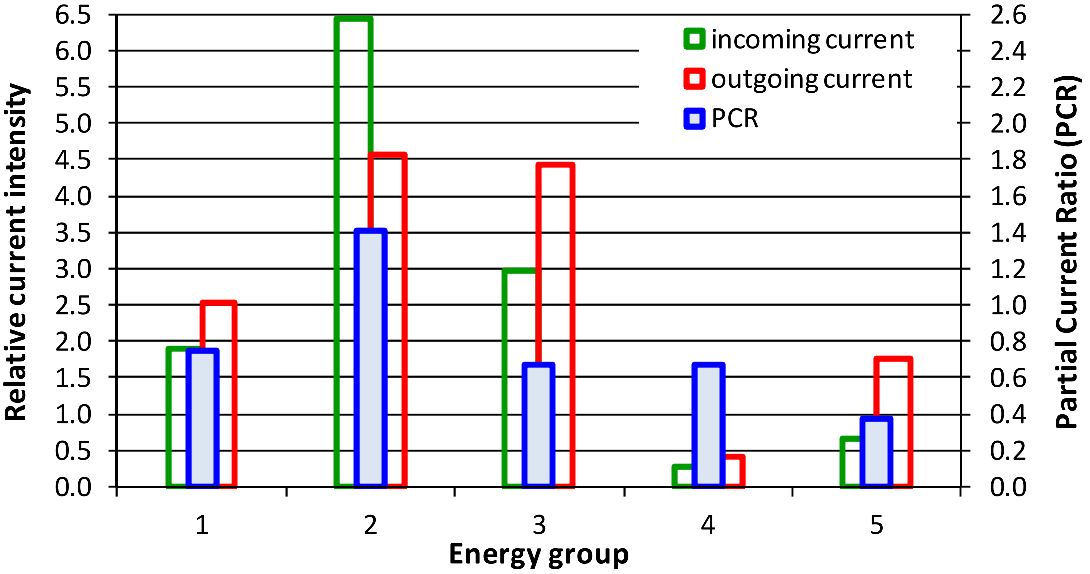

Figure 111 Energy dependence of the radial currents and PCRs in Configuration III-1 in five energy groups, at axial level 3 (middle of the test-zone lower half).

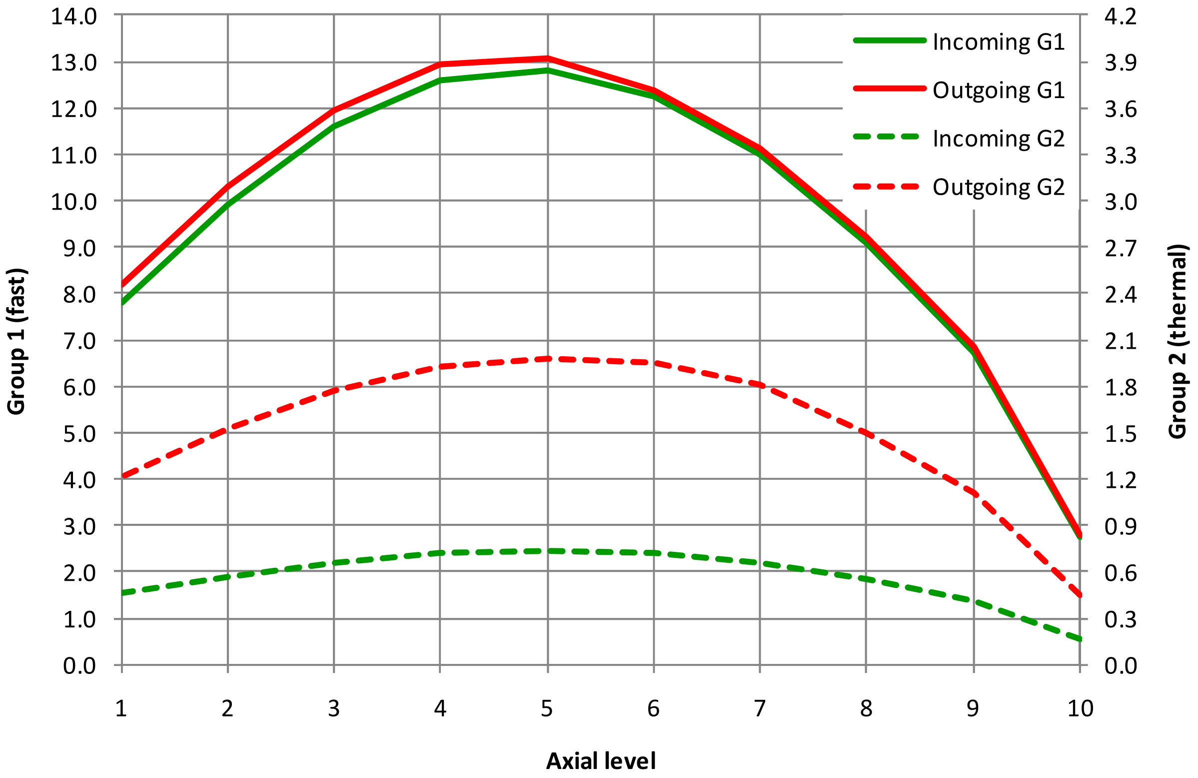

Figure 112 Axial profile of the radial currents in Configuration III-1, in two groups with 0.625 eV cut-off energy. The partial currents were integrated over the test-zone boundary at each axial level, i.e. were summed over all sides.

Energy dependence in Configuration III-2

The behaviour of the partial currents and the PCRs in Configuration III-2 is basically the same as in Configuration III-1. The partial currents integrated over the complete test-zone radial boundary and the corresponding PCRs are shown in Figure 113, while Figure 114 and Figure 115 show the results for nodal axial levels 8 and 3, respectively.

As discussed above in connection with Configuration III-1, the axial profile of the partial currents in Configurations III-2 shows a stronger dependence on the elevation than does the total-fission rate in the individual pins. This can be observed by comparing Figure 116 with the global curvature of the total-fission rate profiles, which will be presented in Subsection 8.7.2. As discussed before, this effect is related to the different number of fuel rods on the two sides of the core midplane. In the case of Configuration III-2, there are 8 PLRs involved (in comparison to the 4 involved in Configuration III-1). Thus, the axial dependence of the partial currents is stronger in Configuration III-2 than in Configuration III-1. Another aspect contributing to the same effect, and in addition also impacting the PCRs, is the relatively large difference in the k-infinity values of the upper and lower lattices in Configuration III-2 (see Table 51), the ratio between the PCRs in levels 8 and 3 being 1.057.

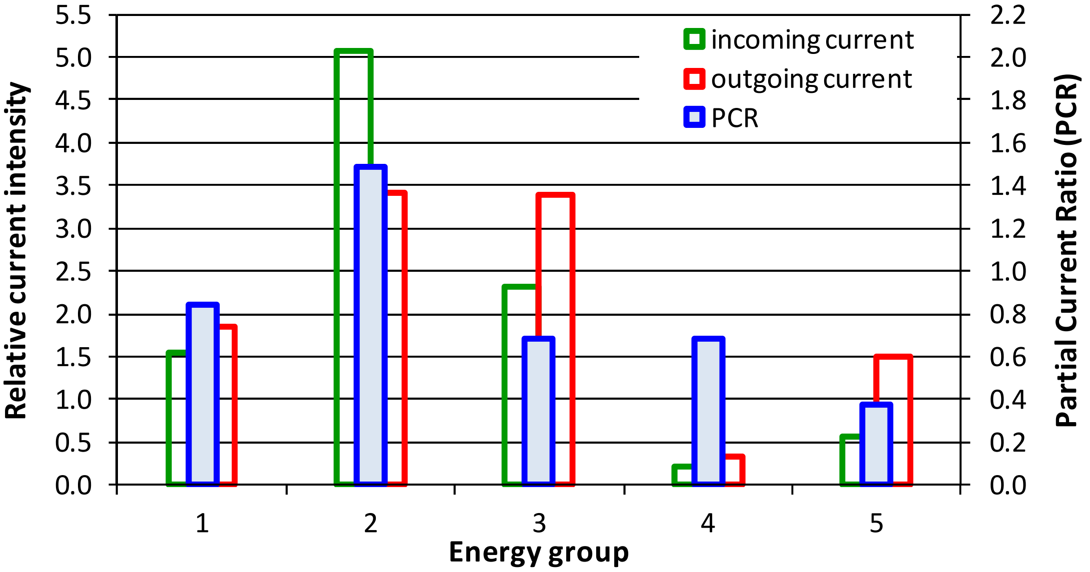

Figure 113 Energy dependence of the radial currents and PCRs in Configuration III-2 in five energy groups, derived from the partial currents obtained in the 3D whole-reactor MCNPX calculation. The partial currents were integrated over the complete test-zone boundary, i.e. were summed over all sides and axial levels.

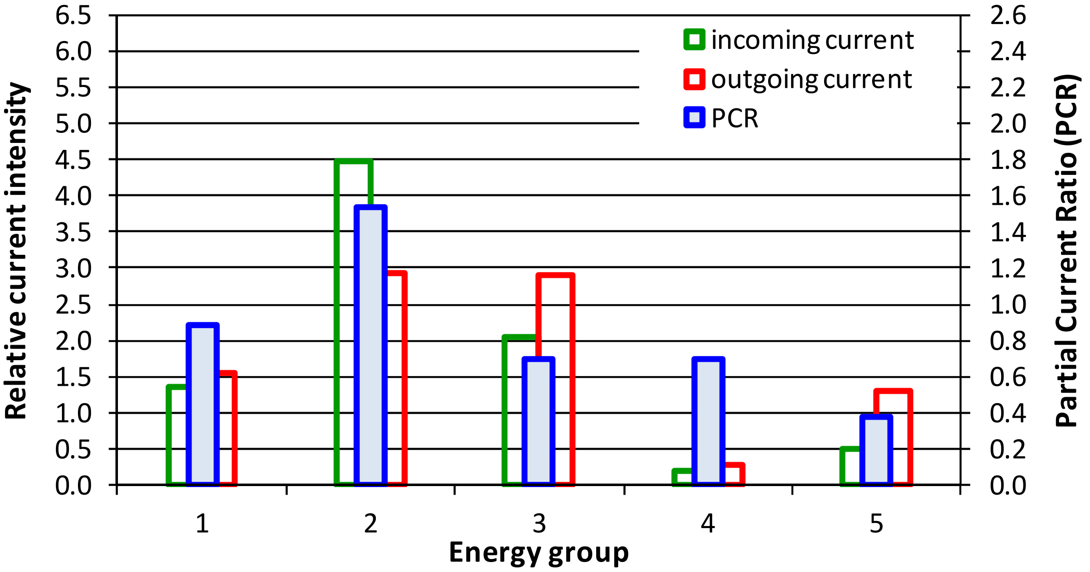

Figure 114 Energy dependence of the radial currents and PCRs in Configuration III-2 in five energy groups, at axial level 8 (middle of the test-zone upper half).

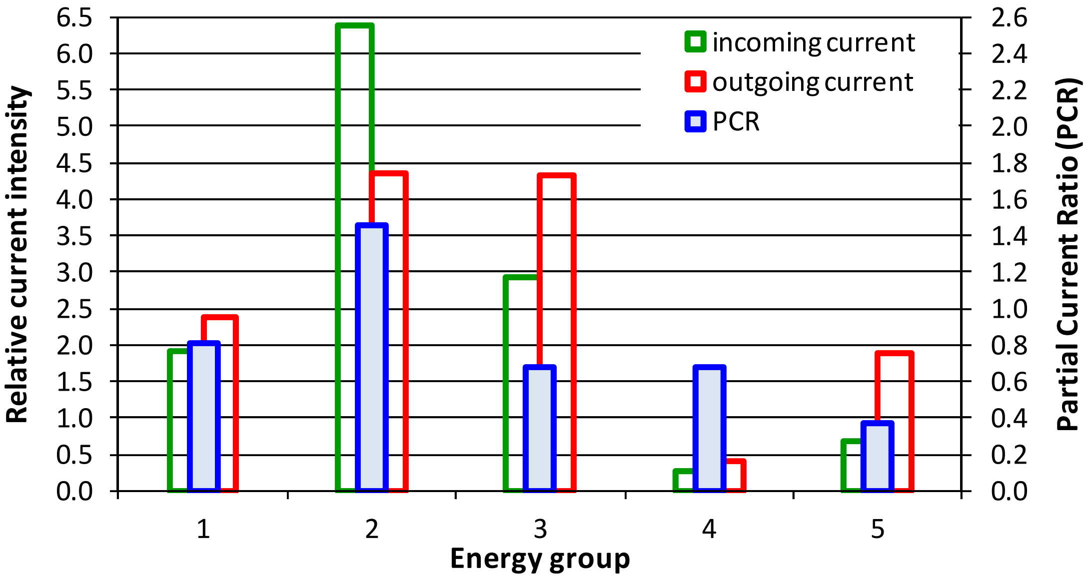

Figure 115 Energy dependence of the radial currents and PCRs in Configuration III-2 in five energy groups, at axial level 3 (middle of the test-zone lower half).

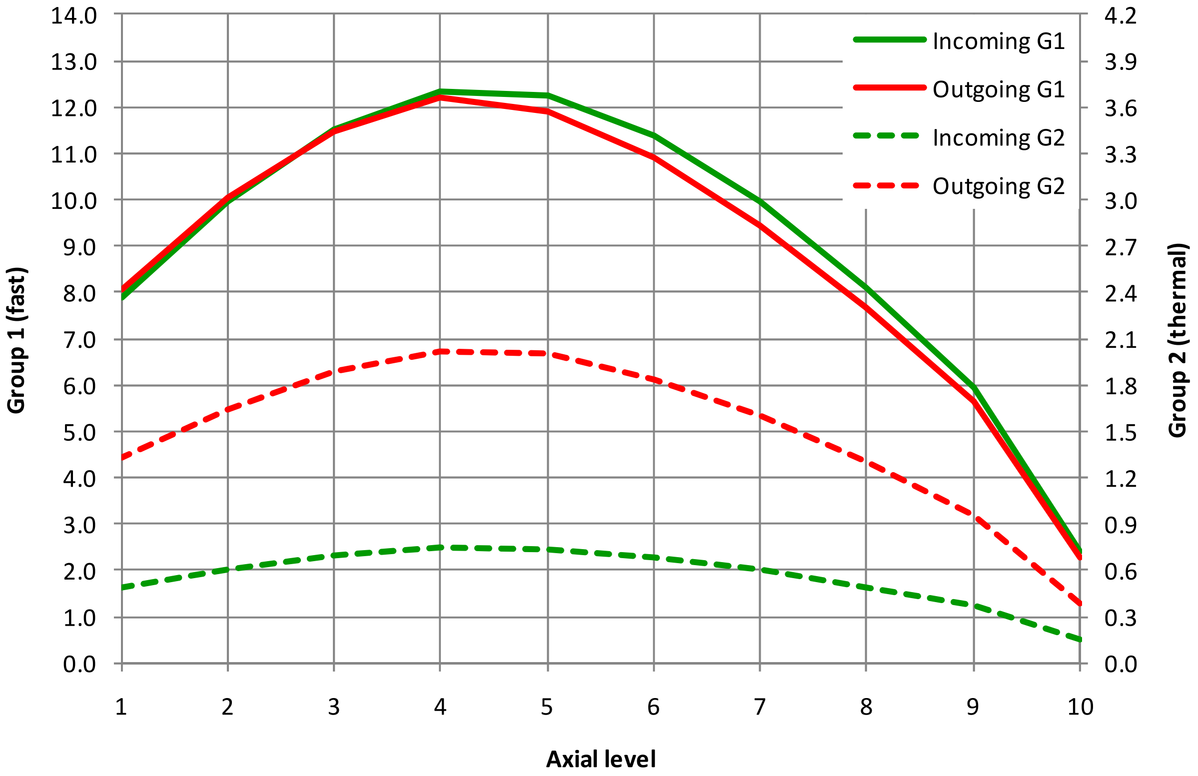

Figure 116 Axial profile of the radial currents Configuration III-2, in two groups with 0.625 eV cut-off energy. The partial currents were integrated over the test-zone boundary at each axial level, i.e. were summed over all sides.

8.5 Use of 2D test-zone boundary conditions

Based on the results presented in Section 8.4, and for the same reasons as discussed in Subsection 6.3.3 concerning Configuration I-1C, axially averaged PCRs cannot be used over the entire test-zone length in Configurations III-1 and III-2 without the lost of valuable information about the radial leakage. Although the use of a 2D PCR methodology could be probably acceptable for the upper part of Configuration III-1, where the axial variation of the epithermal PCR lies in a band of ~1% (see the LHS of Figure 108), it would certainly lead to larger deviations in the lower part, the effect being even more pronounced in Configuration III-2. Thus, in this thesis, the 3D PCR methodology has been consistently applied to both configurations.

8.6 Radial comparisons of total-fission rates

As mentioned in Section 8.2, two kinds of total-fission rate measurements were performed for Configurations III-1 and III-2. In the first, a relatively large number of pins (about 70 in each configuration) were measured at two axial positions, in order to provide detailed information in the radial direction. Second, selected pins were measured at several elevations, allowing the characterisation of the individual axial profiles. In the two following subsections, the calculated values of reconstructed total-fission rates obtained with MCNPX, HELIOS/PRESTO-2 and CASMO-5/SIMULATE-5 (with 5 energy groups) are compared radially with the experimental results, the corresponding 3D comparisons being addressed in Section 8.7.

8.6.1 Radial comparisons in Configuration III-1

The C/E values corresponding to the radial comparisons on Configuration III-1 are shown in Figure 117, Figure 118 and Figure 119 for MCNPX, PRESTO-2 and SIMULATE-5, respectively. In each figure, the left hand side corresponds to the measurements performed at a distance of −9 cm from the core midplane (96-fuel-pin section), the right hand side showing the comparisons at +21 cm (92-fuel-pin section). In these figures, the number under each C/E corresponds to its absolute error expressed in permille. The measured and calculated total-fission rate distributions have been normalised to 1.0, as described for the case of Configuration I-1A in Section 4.5 (see equation {47}).

Differently from the approach used for Configurations I-1A and I-2A (see Sections 4.5 and 5.5, respectively), in which the variance of the MCNPX results was intentionally ignored in the error bands of the corresponding C/Es, the stochastic 1σ uncertainty of the reaction rate tallies has now been accounted for. Thus, in the MCNPX results reported here, the absolute error of the C/Es corresponds to the propagation of the experimental percental error ε_E and the calculated percental error ε_C. The uncertainties corresponding to the input data (e.g. dimensions, compositions, temperatures, etc.) are, however, not propagated. Under these assumptions, the absolute error of the C/Es is given by:

$$e_{\left(\tilde{C}/_{\tilde{E}}\right)} = 0.01 \cdot \sqrt{(\varepsilon_E^2 + \varepsilon_C^2)} \cdot \tilde{C}/\tilde{E} \qquad \{49\}$$

In the PRESTO-2 and SIMULATE-5 calculations, on the other hand, no stochastic uncertainties exist. Also here, the uncertainties corresponding to the input data are not accounted for. Hence, for the comparisons with the nodal reconstructed values, the absolute error of the C/Es are given by equation {48} of Section 4.5.

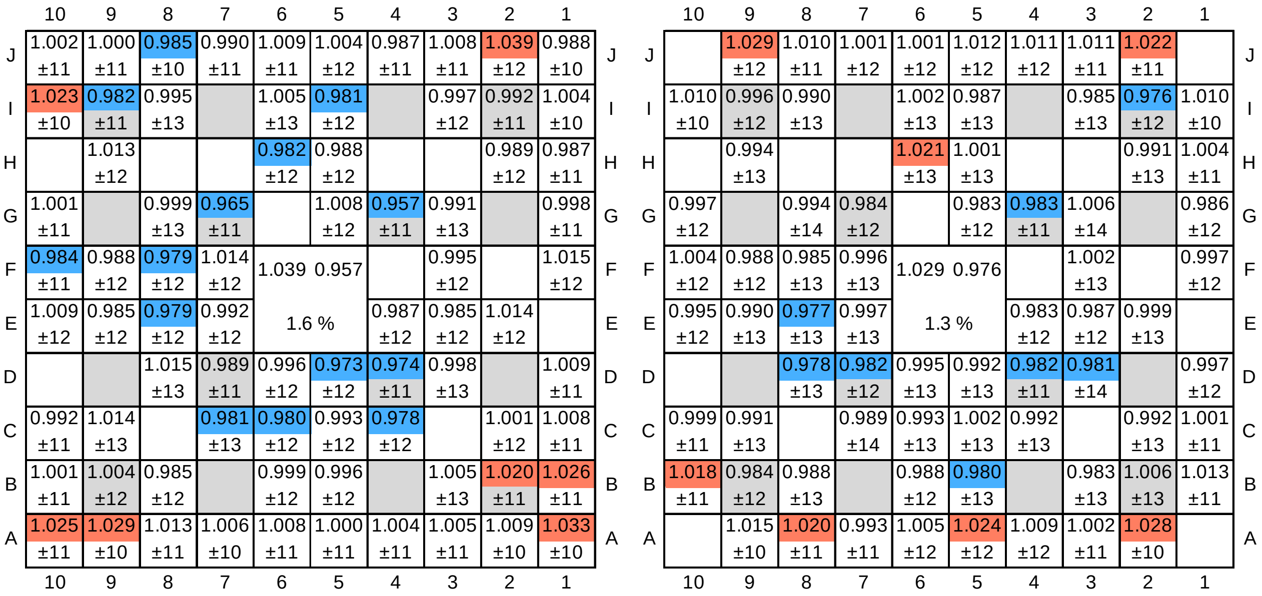

	10	9	8	7	6	5	4	3	2	1	
J	1.002 ±11	1.000 ±11	0.985 ±10	0.990 ±11	1.009 ±11	1.004 ±12	0.987 ±11	1.008 ±11	1.039 ±12	0.988 ±10	J
I	1.023 ±10	0.982 ±11	0.995 ±13		1.005 ±13	0.981 ±12		0.997 ±12	0.992 ±11	1.004 ±10	I
H		1.013 ±12			0.982 ±12	0.988 ±12			0.989 ±12	0.987 ±11	H
G	1.001 ±11		0.999 ±13	0.965 ±11		1.008 ±12	0.957 ±11	0.991 ±13		0.998 ±11	G
F	0.984 ±11	0.988 ±12	0.979 ±12	1.014 ±12	1.039	0.957		0.995 ±12		1.015 ±12	F
E	1.009 ±12	0.985 ±12	0.979 ±12	0.992 ±12	1.6 %		0.987 ±12	0.985 ±12	1.014 ±12		E
D			1.015 ±13	0.989 ±11	0.996 ±12	0.973 ±12	0.974 ±11	0.998 ±13		1.009 ±11	D
C	0.992 ±11	1.014 ±13		0.981 ±13	0.980 ±12	0.993 ±12	0.978 ±12		1.001 ±12	1.008 ±11	C
B	1.001 ±11	1.004 ±12	0.985 ±12		0.999 ±12	0.996 ±12		1.005 ±13	1.020 ±11	1.026 ±11	B
A	1.025 ±11	1.029 ±10	1.013 ±11	1.006 ±10	1.008 ±11	1.000 ±11	1.004 ±11	1.005 ±11	1.009 ±10	1.033 ±10	A
	10	9	8	7	6	5	4	3	2	1	

	10	9	8	7	6	5	4	3	2	1	
J		1.029 ±12	1.010 ±11	1.001 ±12	1.001 ±12	1.012 ±12	1.011 ±12	1.011 ±11	1.022 ±11		J
I	1.010 ±10	0.996 ±12	0.990 ±13		1.002 ±13	0.987 ±13		0.985 ±13	0.976 ±12	1.010 ±10	I
H		0.994 ±13			1.021 ±13	1.001 ±13			0.991 ±13	1.004 ±11	H
G	0.997 ±12		0.994 ±14	0.984 ±12		0.983 ±12	0.983 ±11	1.006 ±14		0.986 ±12	G
F	1.004 ±12	0.988 ±12	0.985 ±13	0.996 ±13	1.029	0.976		1.002 ±13		0.997 ±12	F
E	0.995 ±12	0.990 ±13	0.977 ±13	0.997 ±13	1.3 %		0.983 ±12	0.987 ±12	0.999 ±13		E
D			0.978 ±13	0.982 ±12	0.995 ±13	0.992 ±13	0.982 ±11	0.981 ±14		0.997 ±12	D
C	0.999 ±11	0.991 ±13		0.989 ±14	0.993 ±13	1.002 ±13	0.992 ±13		0.992 ±13	1.001 ±11	C
B	1.018 ±11	0.984 ±12	0.988 ±13		0.988 ±12	0.980 ±13		0.983 ±13	1.006 ±13	1.013 ±11	B
A		1.015 ±10	1.020 ±11	0.993 ±11	1.005 ±12	1.024 ±12	1.009 ±12	1.002 ±11	1.028 ±10		A
	10	9	8	7	6	5	4	3	2	1	

Figure 117 C/E maps corresponding to MCNPX in Configuration III-1 (1/3 PLRs). The LHS and RHS show the results at −9 cm and +21 cm, respectively. The number under each C/E value corresponds to its absolute error expressed in permille, according to equation {49}. The red colour indicates positions where C/E minus the absolute error exceeds 1.005. The blue colour indicates positions where the C/E plus the absolute error is less than 0.995. The pin cells containing gadolinium are identified by a grey background. In the place occupied by the central water hole, the maximum, minimum and standard deviation of the C/E distribution are shown.

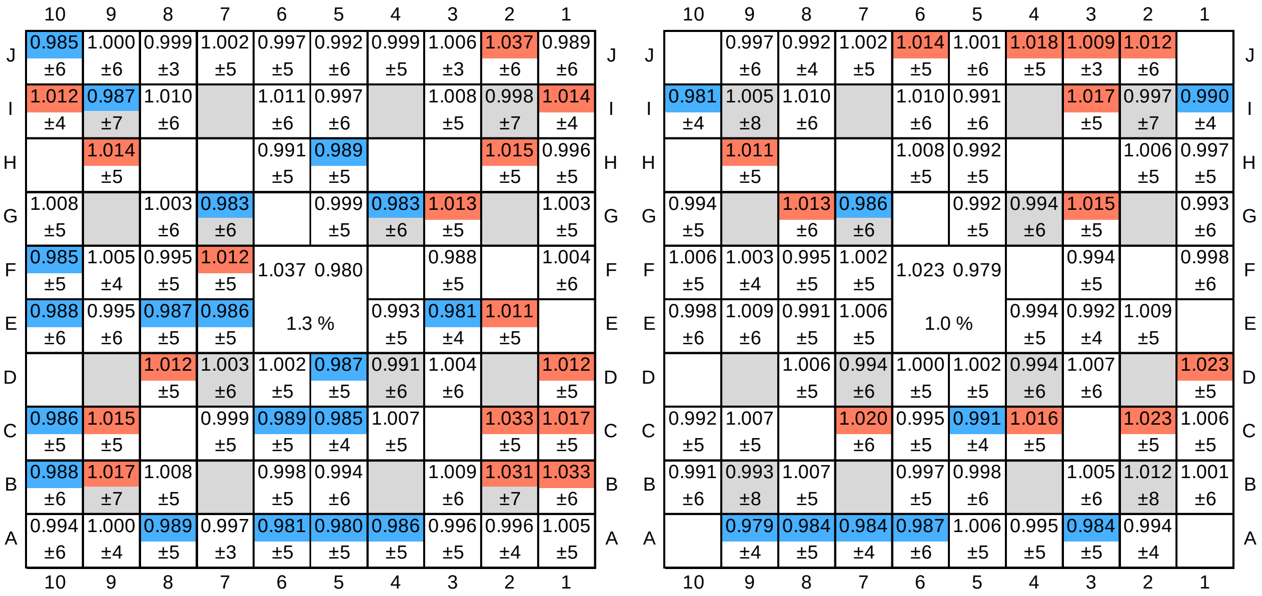

	10	9	8	7	6	5	4	3	2	1	
J	0.985 ±6	1.000 ±6	0.999 ±3	1.002 ±5	0.997 ±5	0.992 ±6	0.999 ±5	1.006 ±3	1.037 ±6	0.989 ±6	J
I	1.012 ±4	0.987 ±7	1.010 ±6		1.011 ±6	0.997 ±6		1.008 ±5	0.998 ±7	1.014 ±4	I
H		1.014 ±5			0.991 ±5	0.989 ±5			1.015 ±5	0.996 ±5	H
G	1.008 ±5		1.003 ±6	0.983 ±6		0.999 ±5	0.983 ±6	1.013 ±5		1.003 ±5	G
F	0.985 ±5	1.005 ±4	0.995 ±5	1.012 ±5	1.037	0.980		0.988 ±5		1.004 ±6	F
E	0.988 ±6	0.995 ±6	0.987 ±5	0.986 ±5	1.3 %		0.993 ±5	0.981 ±4	1.011 ±5		E
D			1.012 ±5	1.003 ±6	1.002 ±5	0.987 ±5	0.991 ±6	1.004 ±6		1.012 ±5	D
C	0.986 ±5	1.015 ±5		0.999 ±5	0.989 ±5	0.985 ±4	1.007 ±5		1.033 ±5	1.017 ±5	C
B	0.988 ±6	1.017 ±7	1.008 ±5		0.998 ±5	0.994 ±6		1.009 ±6	1.031 ±7	1.033 ±6	B
A	0.994 ±6	1.000 ±4	0.989 ±5	0.997 ±3	0.981 ±5	0.980 ±5	0.986 ±5	0.996 ±5	0.996 ±4	1.005 ±5	A
	10	9	8	7	6	5	4	3	2	1	

	10	9	8	7	6	5	4	3	2	1	
J		0.997 ±6	0.992 ±4	1.002 ±5	1.014 ±5	1.001 ±6	1.018 ±5	1.009 ±3	1.012 ±6		J
I	0.981 ±4	1.005 ±8	1.010 ±6		1.010 ±6	0.991 ±6		1.017 ±5	0.997 ±7	0.990 ±4	I
H		1.011 ±5			1.008 ±5	0.992 ±5			1.006 ±5	0.997 ±5	H
G	0.994 ±5		1.013 ±6	0.986 ±6		0.992 ±5	0.994 ±6	1.015 ±5		0.993 ±6	G
F	1.006 ±5	1.003 ±4	0.995 ±5	1.002 ±5	1.023	0.979		0.994 ±5		0.998 ±6	F
E	0.998 ±6	1.009 ±6	0.991 ±5	1.006 ±5	1.0 %		0.994 ±5	0.992 ±4	1.009 ±5		E
D			1.006 ±5	0.994 ±6	1.000 ±5	1.002 ±5	0.994 ±6	1.007 ±6		1.023 ±5	D
C	0.992 ±5	1.007 ±5		1.020 ±6	0.995 ±5	0.991 ±4	1.016 ±5		1.023 ±5	1.006 ±5	C
B	0.991 ±6	0.993 ±8	1.007 ±5		0.997 ±5	0.998 ±6		1.005 ±6	1.012 ±8	1.001 ±6	B
A		0.979 ±4	0.984 ±5	0.984 ±4	0.987 ±6	1.006 ±5	0.995 ±5	0.984 ±5	0.994 ±4		A
	10	9	8	7	6	5	4	3	2	1	

Figure 118 C/E maps corresponding to PRESTO-2 in Configuration III-1 (1/3 PLRs). The LHS and RHS show the results at −9 cm and +21 cm, respectively. The number under each C/E value corresponds to its absolute error expressed in permille, according to equation {48}. The colour convention is the same as in Figure 117.

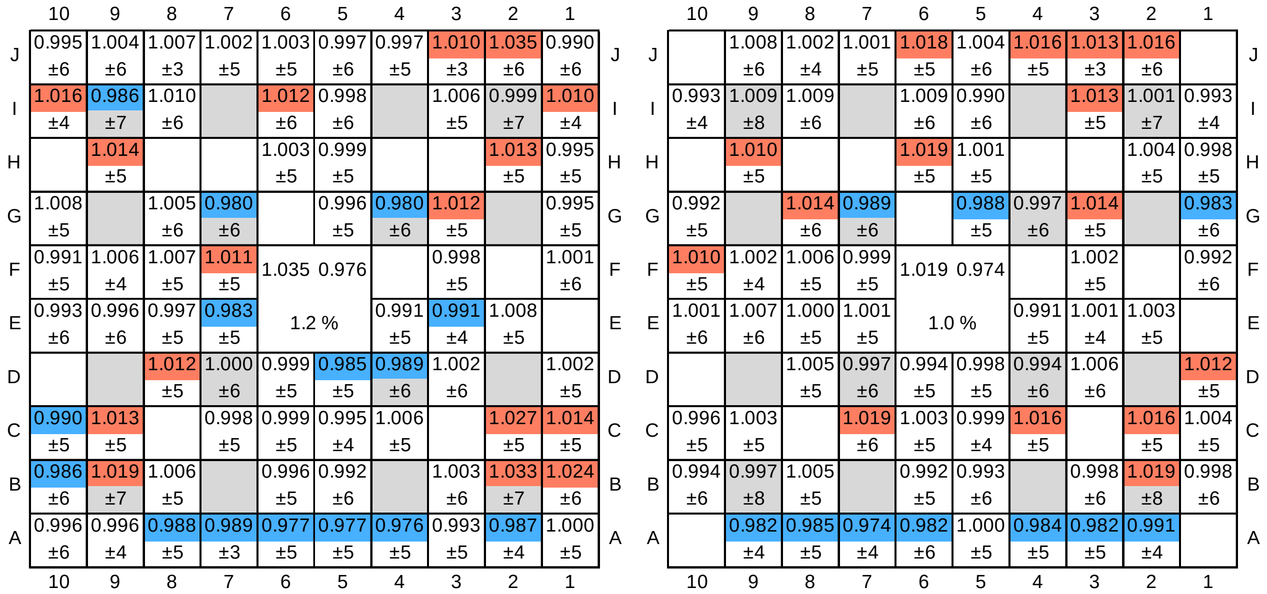

	10	9	8	7	6	5	4	3	2	1	
J	0.995 ±6	1.004 ±6	1.007 ±3	1.002 ±5	1.003 ±5	0.997 ±6	0.997 ±5	1.010 ±3	1.035 ±6	0.990 ±6	J
I	1.016 ±4	0.986 ±7	1.010 ±6		1.012 ±6	0.998 ±6		1.006 ±5	0.999 ±7	1.010 ±4	I
H		1.014 ±5			1.003 ±5	0.999 ±5			1.013 ±5	0.995 ±5	H
G	1.008 ±5		1.005 ±6	0.980 ±6		0.996 ±5	0.980 ±6	1.012 ±5		0.995 ±5	G
F	0.991 ±5	1.006 ±4	1.007 ±5	1.011 ±5	1.035	0.976		0.998 ±5		1.001 ±6	F
E	0.993 ±6	0.996 ±6	0.997 ±5	0.983 ±5	1.2 %		0.991 ±5	0.991 ±4	1.008 ±5		E
D			1.012 ±5	1.000 ±6	0.999 ±5	0.985 ±5	0.989 ±6	1.002 ±6		1.002 ±5	D
C	0.990 ±5	1.013 ±5		0.998 ±5	0.999 ±5	0.995 ±4	1.006 ±5		1.027 ±5	1.014 ±5	C
B	0.986 ±6	1.019 ±7	1.006 ±5		0.996 ±5	0.992 ±6		1.003 ±6	1.033 ±7	1.024 ±6	B
A	0.996 ±6	0.996 ±4	0.988 ±5	0.989 ±3	0.977 ±5	0.977 ±5	0.976 ±5	0.993 ±5	0.987 ±4	1.000 ±5	A
	10	9	8	7	6	5	4	3	2	1	

	10	9	8	7	6	5	4	3	2	1	
J		1.008 ±6	1.002 ±4	1.001 ±5	1.018 ±5	1.004 ±6	1.016 ±5	1.013 ±3	1.016 ±6		J
I	0.993 ±4	1.009 ±8	1.009 ±6		1.009 ±6	0.990 ±6		1.013 ±5	1.001 ±7	0.993 ±4	I
H		1.010 ±5			1.019 ±5	1.001 ±5			1.004 ±5	0.998 ±5	H
G	0.992 ±5		1.014 ±6	0.989 ±6		0.988 ±5	0.997 ±6	1.014 ±5		0.983 ±6	G
F	1.010 ±5	1.002 ±4	1.006 ±5	0.999 ±5	1.019	0.974		1.002 ±5		0.992 ±6	F
E	1.001 ±6	1.007 ±6	1.000 ±5	1.001 ±5	1.0 %		0.991 ±5	1.001 ±4	1.003 ±5		E
D			1.005 ±5	0.997 ±6	0.994 ±5	0.998 ±5	0.994 ±6	1.006 ±6		1.012 ±5	D
C	0.996 ±5	1.003 ±5		1.019 ±6	1.003 ±5	0.999 ±4	1.016 ±5		1.016 ±5	1.004 ±5	C
B	0.994 ±6	0.997 ±8	1.005 ±5		0.992 ±5	0.993 ±6		0.998 ±6	1.019 ±8	0.998 ±6	B
A		0.982 ±4	0.985 ±5	0.974 ±4	0.982 ±6	1.000 ±5	0.984 ±5	0.982 ±5	0.991 ±4		A
	10	9	8	7	6	5	4	3	2	1	

Figure 119 C/E maps corresponding to SIMULATE-5 (with 5 energy groups) in Configuration III-1 (1/3 PLRs). The LHS and RHS show the results at −9 cm and +21 cm, respectively. The number under each C/E value corresponds to its absolute error expressed in permille, according to equation {48}. The colour convention is the same as in Figure 117.

At both elevations, the radial agreement of the three calculations with experiment is good. For the 96-fuel-pins section at −9 cm, the standard deviations of the C/Es obtained with MCNPX, PRESTO-2 and SIMULATE-5 are 1.6%, 1.3% and 1.2%, respectively. For the 92-fuel-pins section at +21 cm, an even slightly better agreement is observed for the three codes, the corresponding standard deviations being 1.3%, 1.0% and 1.0%, respectively.

The ~0.3% larger standard deviation of MCNPX compared with both nodal codes can be partially attributed to the statistical variance of the total-fission rate tallies ($1\sigma \approx 1\%$). Concerning this, reference is made to the fact that, in all the comparisons on Configurations III-1 and III-2 the calculated values correspond to the individual tallies (1.23 cm long) at the elevations in question. In fact, as discussed in Section 4.5 for the case of Configuration I-1A, this leads to somewhat larger variances compared to the case of axially averaged tallies (see Figure 40 and compare, for instance, the right hand sides of Figure 41 and Figure 42).

For PRESTO-2 and SIMULATE-5, the small systematic deviations observed in the peripheral pins are principally due to the use of average measured gap-sizes in the lattice calculations for the central assembly (which have been performed in half-geometry, see Section 8.2). Thus, the south and west gaps being narrower in the model than in the experiment (see Table 42), the corresponding sides of the assembly tend to be underestimated, while the opposite is observed for the north and east sides.

It is also worth mentioning that MCNPX slightly underestimates the total-fission rates in the gadolinium pins, while PRESTO-2 and SIMULATE-5, on the other hand, agree quite well with the measurements. This aspect will be discussed in greater detail in Section 8.9.

8.6.2 Radial comparisons in Configuration III-2

For Configuration III-2, which concerns the 2/3 PLRs section, an analogous procedure has been followed. Figure 120, Figure 121 and Figure 122 show the C/E distributions corresponding to MCNPX, PRESTO-2 and SIMULATE-5, respectively. In each figure, the left hand side corresponds to the measurements performed at a distance of −15 cm from the core midplane (92-fuel-pin section), while the right hand side shows the comparisons at +25 cm (84-fuel-pin section). The normalisation of the experimental and calculated total-fission distributions, the structure of the pin-wise C/E maps and the calculation of the absolute error of the C/Es are analogous to those described in Subsection 8.6.1.

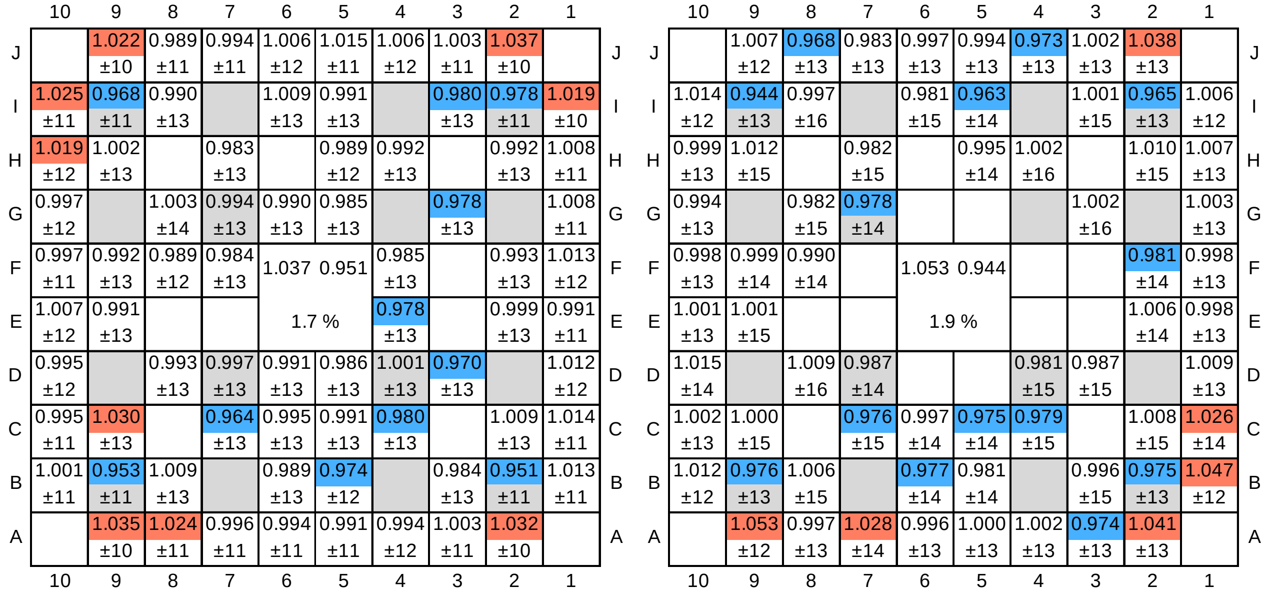

	10	9	8	7	6	5	4	3	2	1	
J		1.022 ±10	0.989 ±11	0.994 ±11	1.006 ±12	1.015 ±11	1.006 ±12	1.003 ±11	1.037 ±10		J
I	1.025 ±11	0.968 ±11	0.990 ±13		1.009 ±13	0.991 ±13		0.980 ±13	0.978 ±11	1.019 ±10	I
H	1.019 ±12	1.002 ±13		0.983 ±13		0.989 ±12	0.992 ±13		0.992 ±13	1.008 ±11	H
G	0.997 ±12		1.003 ±14	0.994 ±13	0.990 ±13	0.985 ±13		0.978 ±13		1.008 ±11	G
F	0.997 ±11	0.992 ±13	0.989 ±12	0.984 ±13	1.037	0.951	0.985 ±13		0.993 ±13	1.013 ±12	F
E	1.007 ±12	0.991 ±13			1.7 %		0.978 ±13		0.999 ±13	0.991 ±11	E
D	0.995 ±12		0.993 ±13	0.997 ±13	0.991 ±13	0.986 ±13	1.001 ±13	0.970 ±13		1.012 ±12	D
C	0.995 ±11	1.030 ±13		0.964 ±13	0.995 ±13	0.991 ±13	0.980 ±13		1.009 ±13	1.014 ±11	C
B	1.001 ±11	0.953 ±11	1.009 ±13		0.989 ±13	0.974 ±12		0.984 ±13	0.951 ±11	1.013 ±11	B
A		1.035 ±10	1.024 ±11	0.996 ±11	0.994 ±11	0.991 ±11	0.994 ±12	1.003 ±11	1.032 ±10		A
	10	9	8	7	6	5	4	3	2	1	

	10	9	8	7	6	5	4	3	2	1	
J		1.007 ±12	0.968 ±13	0.983 ±13	0.997 ±13	0.994 ±13	0.973 ±13	1.002 ±13	1.038 ±13		J
I	1.014 ±12	0.944 ±13	0.997 ±16		0.981 ±15	0.963 ±14		1.001 ±15	0.965 ±13	1.006 ±12	I
H	0.999 ±13	1.012 ±15		0.982 ±15		0.995 ±14	1.002 ±16		1.010 ±15	1.007 ±13	H
G	0.994 ±13		0.982 ±15	0.978 ±14				1.002 ±16		1.003 ±13	G
F	0.998 ±13	0.999 ±14	0.990 ±14		1.053	0.944			0.981 ±14	0.998 ±13	F
E	1.001 ±13	1.001 ±15			1.9 %				1.006 ±14	0.998 ±13	E
D	1.015 ±14		1.009 ±16	0.987 ±14			0.981 ±15	0.987 ±15		1.009 ±13	D
C	1.002 ±13	1.000 ±15		0.976 ±15	0.997 ±14	0.975 ±14	0.979 ±15		1.008 ±15	1.026 ±14	C
B	1.012 ±12	0.976 ±13	1.006 ±15		0.977 ±14	0.981 ±14		0.996 ±15	0.975 ±13	1.047 ±12	B
A		1.053 ±12	0.997 ±13	1.028 ±14	0.996 ±13	1.000 ±13	1.002 ±13	0.974 ±13	1.041 ±13		A
	10	9	8	7	6	5	4	3	2	1	

Figure 120 C/E maps corresponding to MCNPX in Configuration III-2 (2/3 PLRs). The LHS and RHS show the results at −15 cm and +25 cm, respectively. The number under each C/E value corresponds to its absolute error expressed in permille, according to equation {49}. The colour convention is the same as in Figure 117.

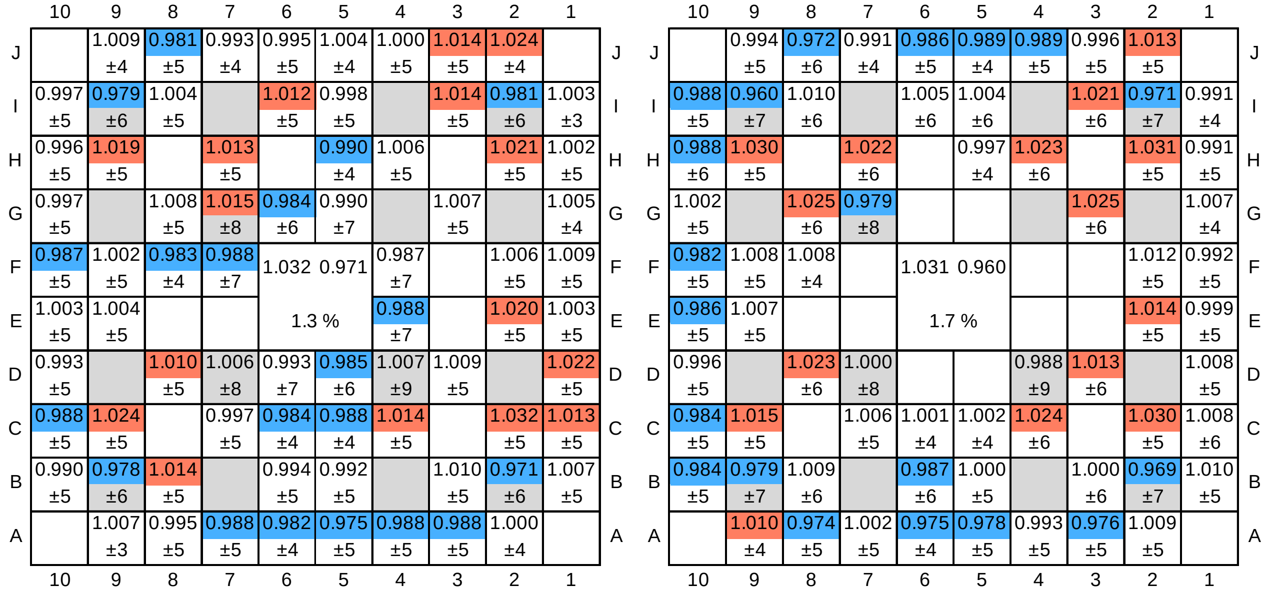

	10	9	8	7	6	5	4	3	2	1	
J		1.009 ±4	0.981 ±5	0.993 ±4	0.995 ±5	1.004 ±4	1.000 ±5	1.014 ±5	1.024 ±4		J
I	0.997 ±5	0.979 ±6	1.004 ±5		1.012 ±5	0.998 ±5		1.014 ±5	0.981 ±6	1.003 ±3	I
H	0.996 ±5	1.019 ±5		1.013 ±5		0.990 ±4	1.006 ±5		1.021 ±5	1.002 ±5	H
G	0.997 ±5		1.008 ±5	1.015 ±8	0.984 ±6	0.990 ±7		1.007 ±5		1.005 ±4	G
F	0.987 ±5	1.002 ±5	0.983 ±4	0.988 ±7	1.032	0.971	0.987 ±7		1.006 ±5	1.009 ±5	F
E	1.003 ±5	1.004 ±5			1.3 %		0.988 ±7		1.020 ±5	1.003 ±5	E
D	0.993 ±5		1.010 ±5	1.006 ±8	0.993 ±7	0.985 ±6	1.007 ±9	1.009 ±5		1.022 ±5	D
C	0.988 ±5	1.024 ±5		0.997 ±5	0.984 ±4	0.988 ±4	1.014 ±5		1.032 ±5	1.013 ±5	C
B	0.990 ±5	0.978 ±6	1.014 ±5		0.994 ±5	0.992 ±5		1.010 ±5	0.971 ±6	1.007 ±5	B
A		1.007 ±3	0.995 ±5	0.988 ±5	0.982 ±4	0.975 ±5	0.988 ±5	0.988 ±5	1.000 ±4		A
	10	9	8	7	6	5	4	3	2	1	

	10	9	8	7	6	5	4	3	2	1	
J		0.994 ±5	0.972 ±6	0.991 ±4	0.986 ±5	0.989 ±4	0.989 ±5	0.996 ±5	1.013 ±5		J
I	0.988 ±5	0.960 ±7	1.010 ±6		1.005 ±6	1.004 ±6		1.021 ±6	0.971 ±7	0.991 ±4	I
H	0.988 ±6	1.030 ±5		1.022 ±6		0.997 ±4	1.023 ±6		1.031 ±5	0.991 ±5	H
G	1.002 ±5		1.025 ±6	0.979 ±8				1.025 ±6		1.007 ±4	G
F	0.982 ±5	1.008 ±5	1.008 ±4		1.031	0.960			1.012 ±5	0.992 ±5	F
E	0.986 ±5	1.007 ±5			1.7 %				1.014 ±5	0.999 ±5	E
D	0.996 ±5		1.023 ±6	1.000 ±8			0.988 ±9	1.013 ±6		1.008 ±5	D
C	0.984 ±5	1.015 ±5		1.006 ±5	1.001 ±4	1.002 ±4	1.024 ±6		1.030 ±5	1.008 ±6	C
B	0.984 ±5	0.979 ±7	1.009 ±6		0.987 ±6	1.000 ±5		1.000 ±6	0.969 ±7	1.010 ±5	B
A		1.010 ±4	0.974 ±5	1.002 ±5	0.975 ±4	0.978 ±5	0.993 ±5	0.976 ±5	1.009 ±5		A
	10	9	8	7	6	5	4	3	2	1	

Figure 121 C/E maps corresponding to PRESTO-2 in Configuration III-2 (2/3 PLRs). The LHS and RHS show the results at −15 cm and +25 cm, respectively. The number under each C/E value corresponds to its absolute error expressed in permille, according to equation {48}. The colour convention is the same as in Figure 117.

Also in this case, the radial agreement with experiment is seen to be good for all calculations. For the 92-fuel-pin section at −15 cm, the standard deviations of the C/Es obtained with MCNPX, PRESTO-2 and SIMULATE-5 are 1.7%, 1.3% and 1.3%, respectively, while for the 84-fuel-pin section at +25 cm, the values are 1.9%, 1.7% and 1.4%, respectively.

In general, the observations made for Configuration III-1 (see Subsection 8.6.1) are also applicable to Configuration III-2. Also in this case, the C/E distributions obtained with MCNPX show slightly (~0.2% to ~0.4%) larger standard deviations compared to those obtained with PRESTO-2 and SIMULATE-5. Furthermore, analogous observations concerning the C/Es in the peripheral and gadolinium pins can be made (see also Section 8.9).

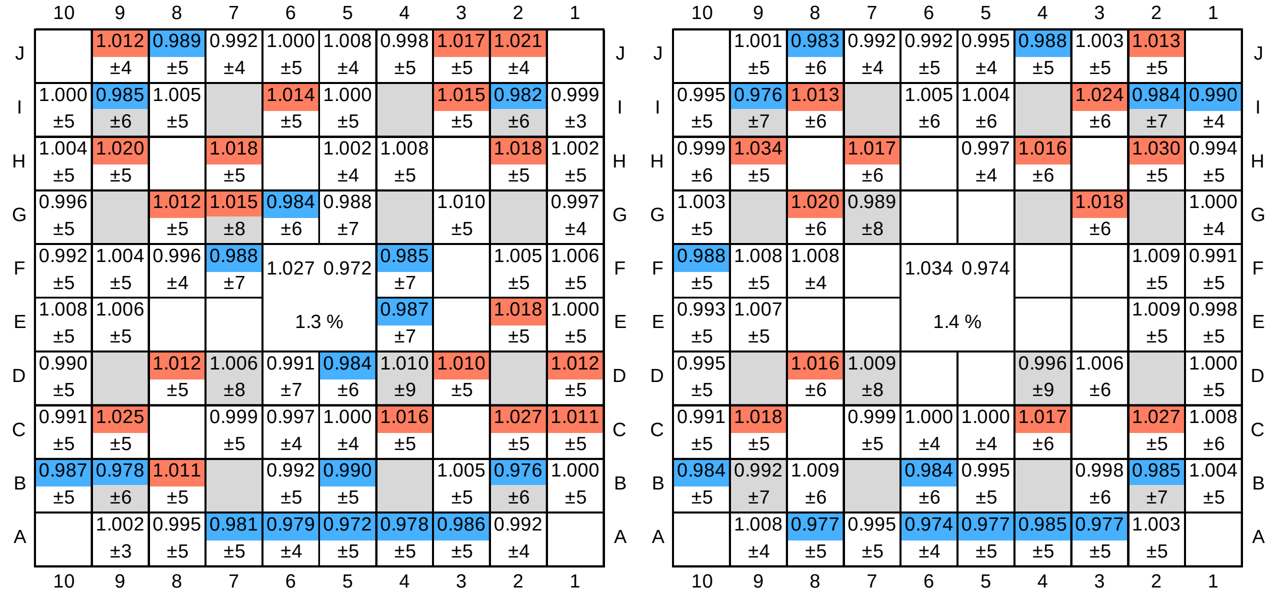

	10	9	8	7	6	5	4	3	2	1	
J		1.012 ±4	0.989 ±5	0.992 ±4	1.000 ±5	1.008 ±4	0.998 ±5	1.017 ±5	1.021 ±4		J
I	1.000 ±5	0.985 ±6	1.005 ±5		1.014 ±5	1.000 ±5		1.015 ±5	0.982 ±6	0.999 ±3	I
H	1.004 ±5	1.020 ±5		1.018 ±5		1.002 ±4	1.008 ±5		1.018 ±5	1.002 ±5	H
G	0.996 ±5		1.012 ±5	1.015 ±8	0.984 ±6	0.988 ±7		1.010 ±5		0.997 ±4	G
F	0.992 ±5	1.004 ±5	0.996 ±4	0.988 ±7	1.027	0.972	0.985 ±7		1.005 ±5	1.006 ±5	F
E	1.008 ±5	1.006 ±5			1.3 %		0.987 ±7		1.018 ±5	1.000 ±5	E
D	0.990 ±5		1.012 ±5	1.006 ±8	0.991 ±7	0.984 ±6	1.010 ±9	1.010 ±5		1.012 ±5	D
C	0.991 ±5	1.025 ±5		0.999 ±5	0.997 ±4	1.000 ±4	1.016 ±5		1.027 ±5	1.011 ±5	C
B	0.987 ±5	0.978 ±6	1.011 ±5		0.992 ±5	0.990 ±5		1.005 ±5	0.976 ±6	1.000 ±5	B
A		1.002 ±3	0.995 ±5	0.981 ±5	0.979 ±4	0.972 ±5	0.978 ±5	0.986 ±5	0.992 ±4		A
	10	9	8	7	6	5	4	3	2	1	

	10	9	8	7	6	5	4	3	2	1	
J		1.001 ±5	0.983 ±6	0.992 ±4	0.992 ±5	0.995 ±4	0.988 ±5	1.003 ±5	1.013 ±5		J
I	0.995 ±5	0.976 ±7	1.013 ±6		1.005 ±6	1.004 ±6		1.024 ±6	0.984 ±7	0.990 ±4	I
H	0.999 ±6	1.034 ±5		1.017 ±6		0.997 ±4	1.016 ±6		1.030 ±5	0.994 ±5	H
G	1.003 ±5		1.020 ±6	0.989 ±8				1.018 ±6		1.000 ±4	G
F	0.988 ±5	1.008 ±5	1.008 ±4		1.034	0.974			1.009 ±5	0.991 ±5	F
E	0.993 ±5	1.007 ±5			1.4 %				1.009 ±5	0.998 ±5	E
D	0.995 ±5		1.016 ±6	1.009 ±8			0.996 ±9	1.006 ±6		1.000 ±5	D
C	0.991 ±5	1.018 ±5		0.999 ±5	1.000 ±4	1.000 ±4	1.017 ±6		1.027 ±5	1.008 ±6	C
B	0.984 ±5	0.992 ±7	1.009 ±6		0.984 ±6	0.995 ±5		0.998 ±6	0.985 ±7	1.004 ±5	B
A		1.008 ±4	0.977 ±5	0.995 ±5	0.974 ±4	0.977 ±5	0.985 ±5	0.977 ±5	1.003 ±5		A
	10	9	8	7	6	5	4	3	2	1	

Figure 122 C/E maps corresponding to SIMULATE-5 (with 5 energy groups) in Configuration III-2 (2/3 PLRs). The LHS and RHS show the results at −15 cm and +25 cm, respectively. The number under each C/E value corresponds to its absolute error expressed in permille, according to equation {48}. The colour convention is the same as in Figure 117.

The radial comparisons for Configurations III-1 and III-2 underline the good performance of both nodal codes in predicting the pin-wise total-fission rate in configurations without strong radial heterogeneities[60]. In these cases, similar standard deviations are obtained for the C/E distributions as were obtained for Configuration I-1A (see Chapter 4), for which the values corresponding to PRESTO-2 and SIMULATE-5 are 1.3% (Figure 42) and 1.1% (Figure 54), respectively. Slightly larger values are observed, however, in the case of MCNPX, for which the standard deviation of the C/Es in Configuration I-1A is 1.3% (Figure 42).

In the above context, it should be borne in mind that the measurements in Configuration I-1A have been made at the core midplane, where the neutron flux has zero axial gradient, while in Configurations III-1 and III-2 they were performed at both sides of the test-zone midplane. Another difference worth mentioning is that, in Configuration I-1A, the nine fuel assemblies constituting the test zone are identical, while in Configurations III-1 and III-2 the eight peripheral assemblies have a different nuclear design and feature different sub-channel pressings compared to the central assembly. Moreover, the lattice calculations for the peripheral assemblies have been performed, as mentioned in Section 8.3, using nominal instead of

---

[60] In Phase III, the test zone contains two different assembly types (central and peripheral), this heterogeneity being azimuthally symmetric and much less pronounced than that imposed by the L-shaped control blade in the controlled configurations, viz. I-2A and I-6A.

measured gaps. The comparisons presented here demonstrate that these aspects have, in fact, very little impact on the quality of the results.

8.7 3D comparisons of total-fission rates

As mentioned in Section 8.2, 12 pins in Configuration III-1 and 14 pins in Configuration III-2 were measured at different elevations, thus allowing the characterisation of the axial total-fission rate profile in each pin. In this thesis, to obtain the 3D distributions needed for the comparisons, the individual axial profiles have been superimposed onto the radial distributions measured at the lower elevations mentioned before, viz. −9 cm in Configuration III-1 and −15 cm in Configuration III-2. For the latter, the choice of the lower elevation was made in order to allow the inclusion of the 7 PLRs which were also axially measured. For consistency, the lower elevation was then used in Configuration III-1 as well, although in this case no axial measurements on the PLRs were included in the experimental data set. Subsequently, the 3D sets of experimental points have been normalized to 1.0, as also have been the calculated values from MCNPX, PRESTO-2 and SIMULATE-5 for the same set of measured positions. This 3D normalisation procedure is analogous to that used in the cases of Configurations I-1C and I-6A (see Sections 6.5 and 7.4, respectively).

Figure 123 shows the pins that were axially measured in Configurations III-1 (left) and III-2 (right). These pins were selected to study the axial perturbations caused by the PLRs. As before, the use of MCNPX as reference (3D transport) calculation offers the possibility of extending the comparisons to other pins in the lattice.

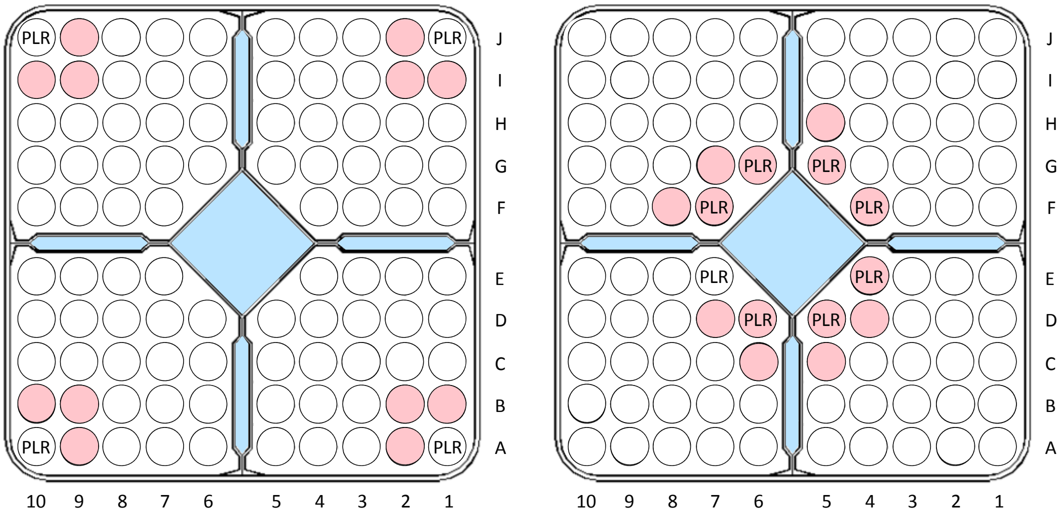

Figure 123 Pins that were measured axially in Configurations III-1 (left) and III-2 (right).

8.7.1 3D comparisons in Configuration III-1

In Configuration III-1, 19 measurements were made for each of the 12 pins shown on the left hand side of Figure 123, covering the axial range −24 cm to +36 cm relative to the core midplane. The resulting 3D distribution of the 12x19=228 experimental values, normalised as described above, was compared against the results obtained with MCNPX, PRESTO-2 and SIMULATE-5, the corresponding C/E values being presented in Table 52, Table 53 and Table 54, respectively. The 3D agreement between calculation and measurement is seen to be good for all three codes, the standard deviations of the complete distribution of C/Es being 2.1%, 2.7% and 2.0% for MCNPX, P2 and S5, respectively. Axial plots showing the calculated and measured total-fission rates in selected pins, are presented in the following.

Table 52 C/E values corresponding to MCNPX for the 228 points (12 pins and 19 axial levels) measured in Configuration III-1. In the last three rows, the maximum, minimum and standard deviation of the C/Es for each measured pin (columns 2 to 13) and for all the measurements considered together (last column) are shown.

Elev.	A2	B1	A9	B10	J2	I1	J9	I10	B2	B9	I2	I9	All
36	0.981	1.029	1.006	0.992	1.029	0.994	1.017	1.011	1.009	0.983	0.960	0.969	
26	1.000	1.026	1.012	0.997	1.014	0.995	0.992	1.017	0.985	0.980	0.961	0.949	
23	0.996	1.029	1.006	0.974	1.006	0.992	1.008	1.008	1.002	0.972	0.960	0.949	
21	0.995	1.016	1.002	0.987	1.022	1.000	1.006	1.010	1.009	0.988	0.957	0.961	
18	0.990	1.016	0.987	0.985	1.037	0.996	0.985	1.019	0.986	0.988	0.964	0.957	
16	0.996	1.016	1.012	0.994	1.021	0.975	0.985	1.004	1.003	0.988	0.971	0.952	
14	0.989	1.037	1.016	0.988	1.031	0.995	1.003	1.017	1.000	0.972	0.982	0.954	
12	1.011	1.033	1.001	0.979	1.036	1.006	1.003	1.009	1.007	0.985	0.986	0.962	
10	1.000	1.014	0.990	0.987	1.017	1.007	1.013	0.995	1.009	0.992	0.980	0.960	
8	0.993	1.017	0.981	0.970	1.009	0.982	1.000	0.997	0.997	1.006	0.971	0.958	
6	1.007	1.024	1.010	0.996	1.026	1.005	1.000	1.005	1.002	0.996	0.975	0.953	
4	1.015	1.034	1.010	0.998	1.035	1.007	1.011	1.026	0.988	0.996	0.966	0.959	
2	1.000	1.020	1.003	0.995	1.032	1.000	0.999	1.018	1.010	1.002	0.991	0.968	
0	0.981	1.023	0.995	0.987	1.025	0.998	0.990	1.010	1.002	0.969	0.968	0.953	
-2	0.985	1.018	0.991	0.961	1.003	0.995	0.992	0.994	1.010	0.988	0.960	0.945	
-4	0.972	1.027	0.984	0.980	1.016	0.987	0.996	0.986	1.020	0.994	0.959	0.961	
-9	0.988	1.005	1.008	0.980	1.017	0.984	0.980	1.003	0.999	0.984	0.972	0.962	
-14	0.991	1.010	0.992	0.962	1.001	0.996	0.980	1.001	1.007	0.993	0.960	0.960	
-24	0.991	1.013	0.997	0.984	0.999	0.985	0.967	0.982	1.000	1.006	0.947	0.956	
Max	1.015	1.037	1.016	0.998	1.037	1.007	1.017	1.026	1.020	1.006	0.991	0.969	1.037
Min	0.972	1.005	0.981	0.961	0.999	0.975	0.967	0.982	0.985	0.969	0.947	0.945	0.945
StD	0.011	0.009	0.010	0.011	0.012	0.009	0.013	0.011	0.009	0.011	0.011	0.006	0.021

Table 53 C/E values corresponding to PRESTO-2 for the 228 points (12 pins and 19 axial levels) measured in Configuration III-1. In the last three rows, the maximum, minimum and standard deviation of the C/Es for each measured pin (columns 2 to 13) and for all the measurements considered together (last column) are shown.

Elev.	A2	B1	A9	B10	J2	I1	J9	I10	B2	B9	I2	I9	All
36	0.963	0.995	0.974	0.951	1.003	0.983	0.973	0.985	0.997	0.985	0.964	0.959	
26	0.968	0.998	0.970	0.958	1.007	0.981	0.969	0.980	0.991	0.988	0.970	0.952	
23	0.950	0.986	0.954	0.943	0.998	0.967	0.953	0.965	1.000	0.981	0.967	0.952	
21	0.949	0.990	0.954	0.948	0.998	0.967	0.961	0.968	1.002	0.984	0.964	0.957	
18	0.957	0.991	0.962	0.954	0.998	0.974	0.962	0.972	0.991	0.982	0.961	0.954	
16	0.970	1.003	0.972	0.965	1.014	0.984	0.972	0.981	0.996	0.977	0.964	0.956	
14	0.979	1.019	0.987	0.976	1.025	0.998	0.990	0.996	0.994	0.983	0.965	0.951	
12	0.991	1.025	0.989	0.977	1.033	1.003	0.994	1.003	1.006	0.982	0.981	0.955	
10	0.997	1.031	0.999	0.988	1.041	1.016	0.998	1.007	1.028	1.009	0.993	0.976	
8	0.993	1.028	0.998	0.980	1.038	1.011	1.000	1.011	1.014	1.008	0.989	0.974	
6	0.980	1.009	0.985	0.970	1.023	1.000	0.988	0.990	1.012	1.012	0.983	0.970	
4	0.980	1.015	0.984	0.974	1.032	1.003	0.988	0.995	0.998	0.995	0.978	0.976	
2	1.008	1.049	1.013	1.005	1.054	1.020	1.014	1.019	1.007	0.999	0.983	0.968	
0	1.007	1.054	1.016	1.019	1.064	1.031	1.017	1.031	1.029	1.013	0.988	0.988	
-2	0.998	1.043	1.005	0.992	1.049	1.021	1.002	1.020	1.053	1.034	1.013	1.007	
-4	1.006	1.047	1.008	1.000	1.053	1.023	1.014	1.025	1.048	1.037	1.015	1.004	
-9	1.013	1.051	1.017	1.005	1.055	1.032	1.017	1.029	1.048	1.035	1.015	1.004	
-14	1.007	1.056	1.021	1.003	1.061	1.032	1.011	1.029	1.044	1.040	1.015	1.011	
-24	1.003	1.049	1.020	0.999	1.050	1.027	1.008	1.023	1.043	1.033	1.015	1.001	
Max	1.013	1.056	1.021	1.019	1.064	1.032	1.017	1.031	1.053	1.040	1.015	1.011	1.064
Min	0.949	0.986	0.954	0.943	0.998	0.967	0.953	0.965	0.991	0.977	0.961	0.951	0.943
StD	0.021	0.025	0.022	0.022	0.023	0.022	0.021	0.022	0.022	0.022	0.020	0.021	0.027

Table 54 C/E values corresponding to SIMULATE-5 for the 228 points (12 pins and 19 axial levels) measured in Configuration III-1. In the last three rows, the maximum, minimum and standard deviation of the C/Es for each measured pin (columns 2 to 13) and for all the measurements considered together (last column) are shown.

Elev.	A2	B1	A9	B10	J2	I1	J9	I10	B2	B9	I2	I9	All
36	0.980	1.014	0.997	0.976	1.029	1.006	1.006	1.018	1.036	1.015	0.994	0.992	
26	0.986	1.015	0.992	0.980	1.029	1.003	0.996	1.008	1.026	1.015	0.997	0.984	
23	0.977	1.014	0.986	0.976	1.033	1.000	0.995	1.007	1.035	1.015	1.000	0.985	
21	0.975	1.016	0.986	0.980	1.032	0.999	1.002	1.008	1.039	1.017	0.997	0.990	
18	0.980	1.014	0.991	0.982	1.027	1.002	0.999	1.009	1.024	1.009	0.987	0.985	
16	0.987	1.020	0.995	0.987	1.037	1.007	1.002	1.012	1.024	1.000	0.986	0.976	
14	0.963	1.003	0.973	0.964	1.012	0.985	0.982	0.988	1.024	1.012	0.993	0.978	
12	0.973	1.006	0.975	0.964	1.021	0.989	0.987	0.996	1.034	1.008	1.006	0.984	
10	0.964	0.998	0.971	0.961	1.013	0.987	0.978	0.986	1.025	1.002	0.986	0.972	
8	0.961	0.995	0.971	0.954	1.011	0.983	0.979	0.990	1.012	1.002	0.983	0.971	
6	0.978	1.006	0.989	0.975	1.028	1.004	0.999	1.002	1.028	1.025	0.996	0.988	
4	0.986	1.022	0.996	0.987	1.045	1.016	1.007	1.015	1.021	1.017	1.000	1.001	
2	0.994	1.034	1.005	0.997	1.046	1.012	1.013	1.018	1.031	1.022	1.006	0.992	
0	0.976	1.021	0.990	0.994	1.037	1.004	0.998	1.012	1.034	1.014	0.989	0.989	
-2	0.973	1.017	0.985	0.974	1.030	1.001	0.989	1.007	1.038	1.016	0.995	0.988	
-4	0.981	1.021	0.988	0.982	1.034	1.003	1.001	1.012	1.033	1.021	1.000	0.988	
-9	0.988	1.026	0.997	0.987	1.036	1.012	1.005	1.017	1.034	1.020	1.000	0.987	
-14	0.984	1.032	1.001	0.986	1.042	1.013	1.000	1.018	1.037	1.026	1.002	0.995	
-24	0.985	1.030	1.006	0.987	1.037	1.013	1.003	1.017	1.039	1.025	1.008	0.994	
Max	0.994	1.034	1.006	0.997	1.046	1.016	1.013	1.018	1.039	1.026	1.008	1.001	1.046
Min	0.961	0.995	0.971	0.954	1.011	0.983	0.978	0.986	1.012	1.000	0.983	0.971	0.954
StD	0.009	0.011	0.011	0.011	0.010	0.010	0.010	0.010	0.007	0.008	0.007	0.008	0.020

Measured pin J9

The axial plots of calculated and measured total-fission rates in pin J9 are depicted in Figure 124. On the left hand side, the complete axial range (-61.5 cm to +61.5 cm) is shown. In order to enhance the visualisation of the axial profiles near the core midplane, a zoom of the axial region between -28 cm and +28 cm is given on the right hand side of the figure.

MCNPX and SIMULATE-5 are seen to predict the global profile of the measured total-fission rate with good accuracy. Also the perturbation produced by the proximity of the PLR at lattice position J10 is appropriately captured by these two codes. In particular, on the RHS of Figure 124, the effect of the plenum and the two natural-uranium pellets (see Figure 17) present in the neighbouring pin J10 can be clearly identified, as also the depression caused by the presence of the spacer (2.6 cm high) centred at 8.84 cm (see Table 45).

In the case of PRESTO-2, somewhat larger deviations are observed in the global profile, with a slight underestimation in the upper part of the test zone. Also the local effects of the plenum, natural uranium and spacer are less accurately captured than with MCNPX and SIMULATE-5. However, as will be shown in Section 8.8, the local agreement improves when PRESTO-2 version 1.15 is used. The agreement of the global curvature with experiment, on the other hand, does not depend on the programme version used.

The standard deviations of the C/Es for pin J9 are, for MCNPX (Table 52), PRESTO-2 (Table 53) and SIMULATE-5 (Table 54), 1.3%, 2.1% and 1.0%, respectively.

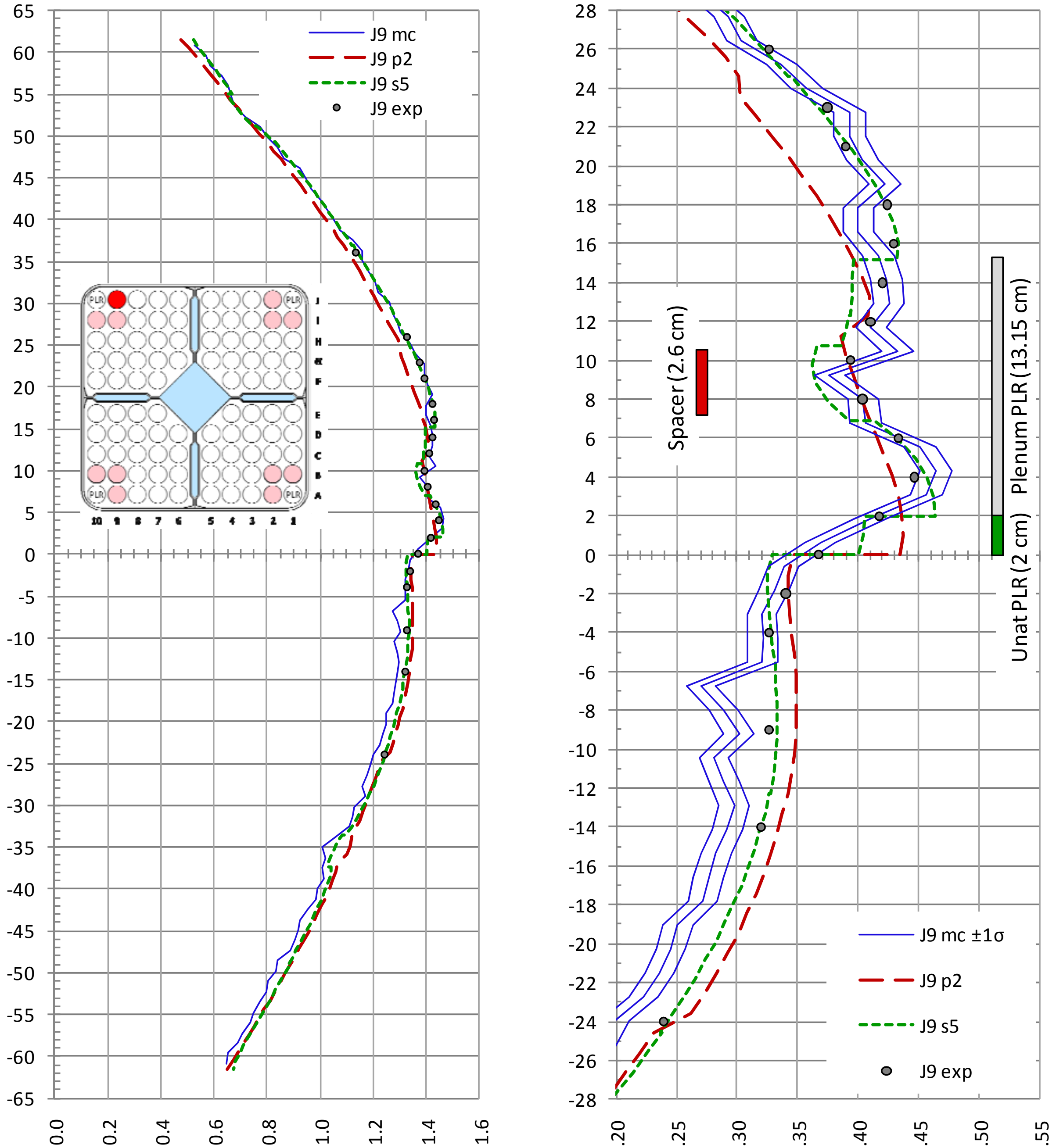

Figure 124 Configuration III-1: 3D comparison of calculated and measured total-fission rates in pin J9 for MCNPX (blue line), PRESTO-2 (red dashed line) and SIMULATE-5 (green dotted line). All distributions are normalized to 1.0 over the complete 3D set of 228 measured points. The dots represent the experimental values. On the right hand side, a zoom of the axial region between -28 cm and +28 cm from the core midplane is shown. For MCNPX, the “most probable” results are represented by the middle line, while the lines on both sides represent the (±1σ) uncertainty band.

Measured pin J2

Apart from the slight radial overestimation shown by all three codes (which is also observable in Figure 117, Figure 118 and Figure 119), the 3D results for pin J2 show a similar behaviour as compared to that of pin J9. Thus, the same observations as made above for pin J9 are also applicable to this pin[61]. The axial plots of calculated and measured total-fission rates in pin J2 are shown in Figure 125. The standard deviations of the C/Es for this pin are 1.2%, 2.3% and 1.0% for MCNPX, PRESTO-2 and SIMULATE-5, respectively.

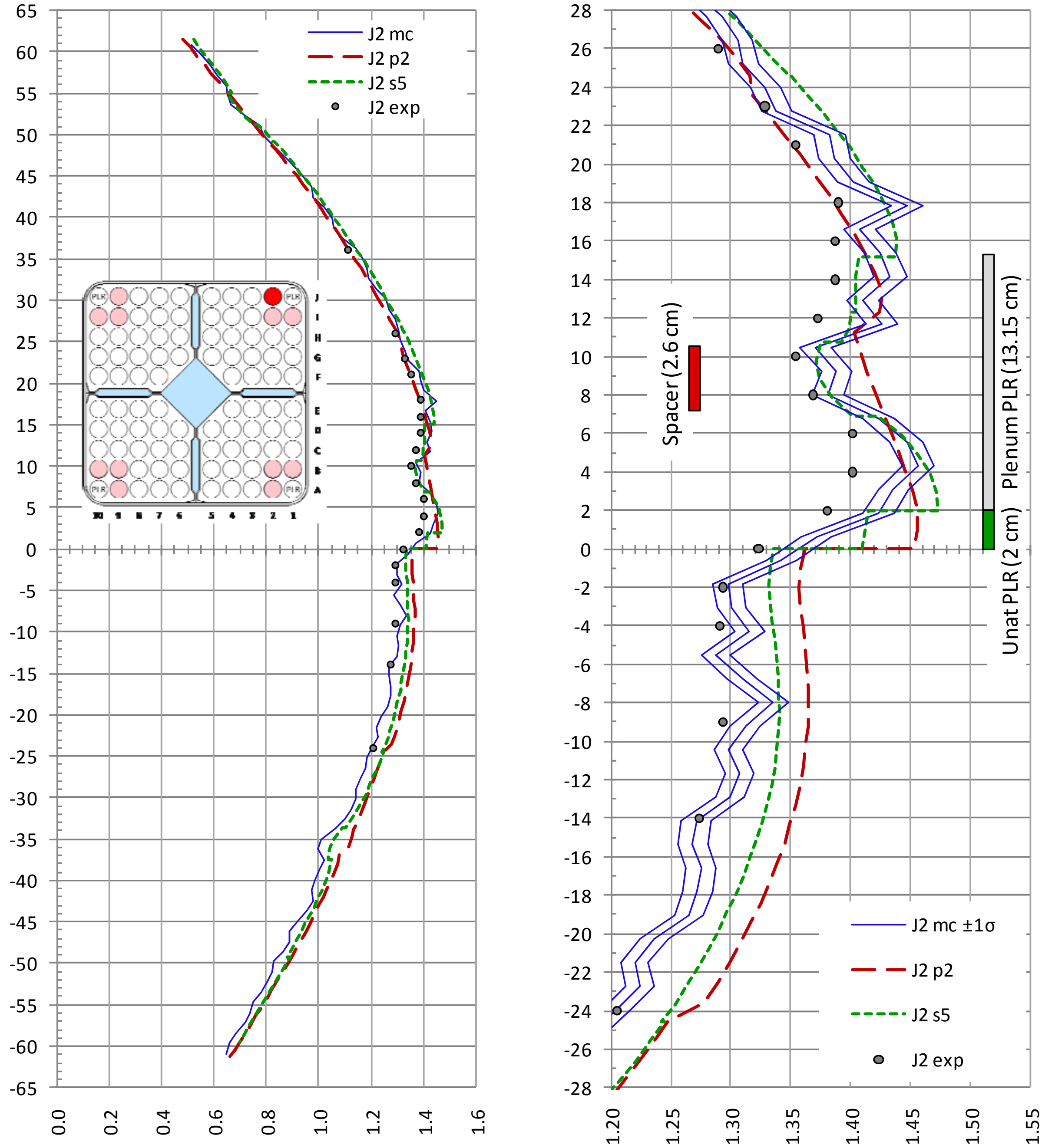

Figure 125 Configuration III-1: 3D comparison of calculated and measured total-fission rates in pin J2 for MCNPX (blue line), PRESTO-2 (red dashed line) and SIMULATE-5 (green dotted line).

---

[61] When comparing the 2D and 3D results, one important aspect must be remembered: the normalisation of the radial maps has been done using the complete set of radial measurements (e.g. 76 for the case of Configuration III-1 at −9 cm), while the 3D distributions were normalised over the complete set of axial measurements over all pins (228 points). Thus, the values of the C/Es obtained from the 3D distributions at −9 cm do not exactly match with those of the 2D maps.

Measured pin B10

Figure 126 shows the axial plots of calculated and measured total-fission rates in pin B10. For this pin, MCNPX and SIMULATE-5 predict somewhat lower values compared with the measurements, although the differences are quite small. PRESTO-2 agrees well in the lower part of the test zone, showing some underestimation in the upper part. Concerning the local behaviour, the same observations can be made here as done above for pin J9.

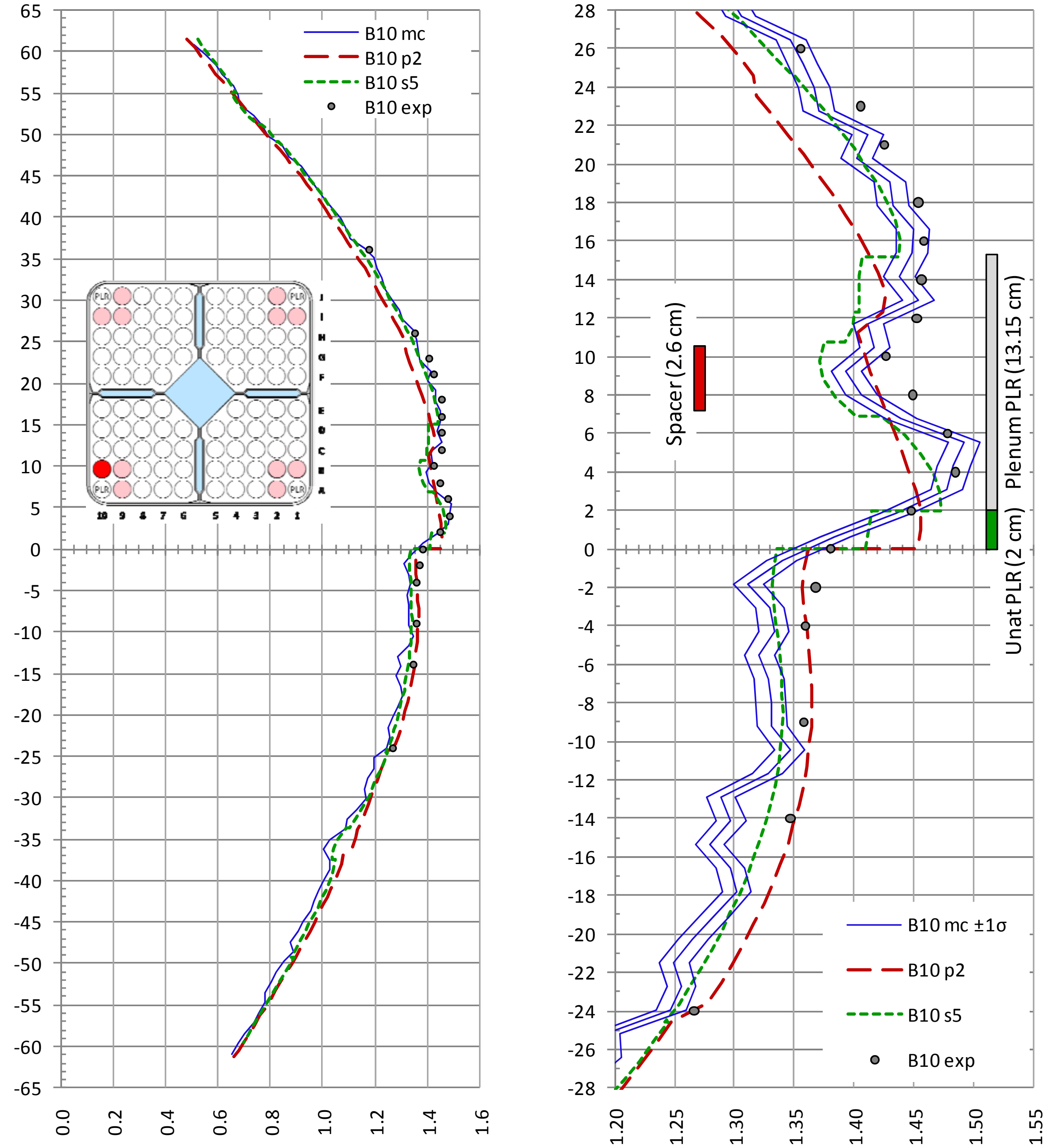

Figure 126 Configuration III-1: 3D comparison of calculated and measured total-fission rates in pin B10 for MCNPX (blue line), PRESTO-2 (red dashed line) and SIMULATE-5 (green dotted line).

The standard deviations of the C/Es for pin B10 are 1.1%, 2.2% and 1.1% for MCNPX, PRESTO-2 and SIMULATE-5, respectively. The remaining axially measured uranium pins show, as expected, a very similar behaviour.

Measured pins I9 and B2

For pins containing gadolinium (5.0 w/o in this case), the total-fission rate in the fresh fuel is so much lower, as compared with the regular uranium pins, that plots on the same scale do not provide any significant information. Figure 127 shows a zoomed view of the central part of the 3D plots for pins I9 and B2, in which a good axial agreement is observed for MCNPX and SIMULATE-5, although slight radial deviations occur. In the case of PRESTO-2, a clear step is observed at the nodal interface at core midplane, the origin of which can be attributed to the same effects as discussed in Section 6.6 for the case of Configuration I-1C.

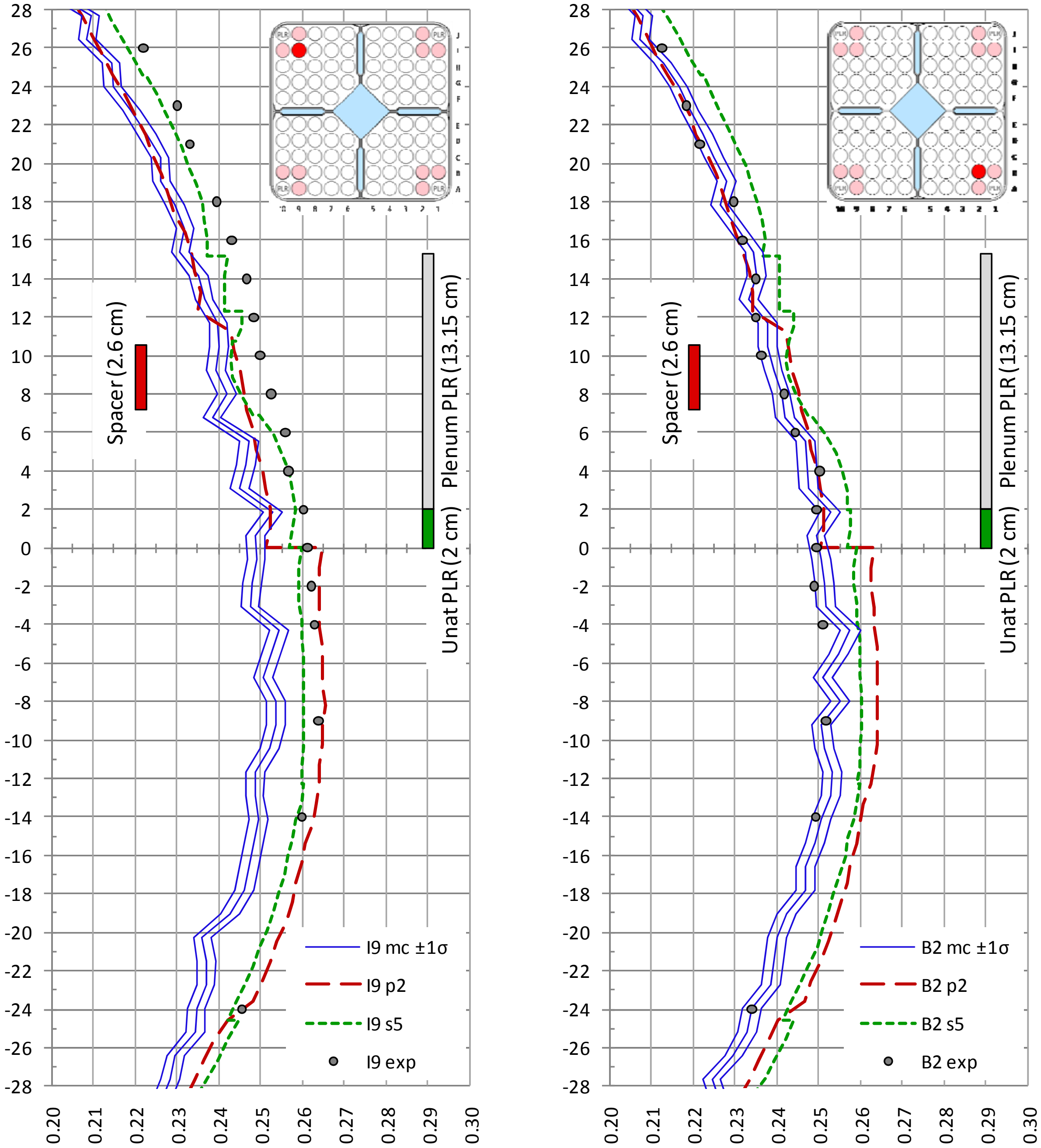

Figure 127 Configuration III-1: 3D comparisons of calculated and measured total-fission rates in pins I9 and B2 for MCNPX (blue line), PRESTO-2 (red dashed line) and SIMULATE-5 (green dotted line). Since these two pins contain gadolinium (5.0 w/o), their total-fission rates are relatively low, and the scale of the abscissas has been zoomed accordingly.

The standard deviations of the C/Es for MCNPX, PRESTO-2 and SIMULATE-5 are, respectively, 0.6%, 2.1% and 0.8% (pin I9) and 0.9%, 2.2% and 0.7% (pin B2).

Non-measured pins J10 and J8

As mentioned before, the availability of a validated MCNPX (transport) reference solution for the 3D total-fission rate distribution allows one to extend the comparison to pins and elevations that lie outside the measured domain. This is particularly important in the case of

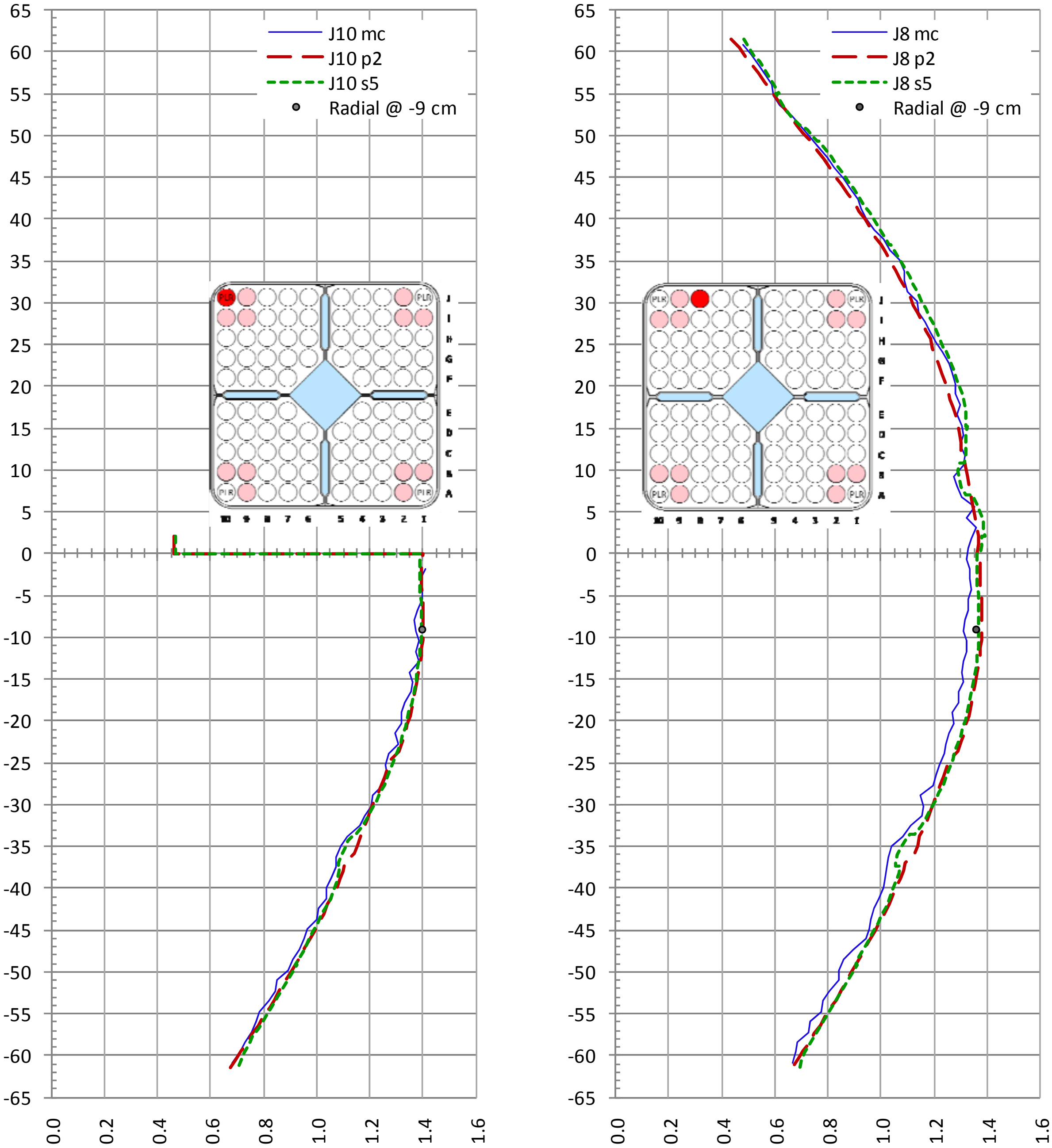

Figure 128 Configuration III-1: 3D comparison of calculated total-fission rates in pins J10 and J8 for MCNPX (blue line), PRESTO-2 (red dashed line) and SIMULATE-5 (green dotted line). The results of the radial measurements performed at −9 cm are also included (black dots). For pin J10, the MCNPX results are shown up to the elevation −2 cm, i.e. the 2 cm natural uranium segment is not included in this profile.

Configurations III-1 and III-2, for which the axial measurements were limited to pins neighbouring the PLRs. In this frame, it is interesting to see the behaviour of pins located in other regions of the lattice. Figure 128, for instance, shows the comparisons in pins J10 and J8, the experimental results corresponding to the radial measurements at −9 cm also being shown. Here it is seen that, for pin J8, MCNPX shows a conspicuous underestimation of the measurement. This effect can also be observed on the left hand side of Figure 117, where the C/E value for pin J8 is found to be 0.985.

In general, however, the 3D agreement between MCNPX, PRESTO-2 and SIMULATE-5 for these two pins is seen to be good, as also is the agreement with the results of the radial measurements. The strong reduction of the total-fission rate in the 2 cm natural uranium segment at the tip of the PLR at position J10 can be clearly seen. As in previous cases, MCNPX and SIMULATE-5 capture the effect of the spacers with good accuracy, while PRESTO-2 (version 1.13) shows practically no impact. As will be seen in Section 8.8, this aspect improves with the use of PRESTO-2 version 1.15.

Non-measured pins E4 and F7

As shown in Figure 123, the pins measured in Configuration III-1 were concentrated at the corner regions of the lattice, surrounding the PLRs. This selection was made setting focus on the accurate characterisation of the total-fission axial profile in the vicinity of the PLR-tips, which was the principal aim of these measurements. For the 3D comparison of calculated distributions, however, the normalisation to the measured points then results in an overweighting of the corner regions, which could lead to systematic deviations in other regions of the lattice (e.g. near the water canal). This effect, however, is not observed, which underlines the good 3D agreement between the different calculations. For instance, Figure 129 shows the comparisons for pins E4 and F7 (both adjacent to the central water canal), for which a similar 3D agreement as for the measured pins (all located near the corners of the assembly), can be seen.

For PRESTO-2, the axial heterogeneity imposed by the PLRs, which are in reality too distant to affect the local flux profile in pins E4 and F7, produces a discontinuity at the interface of the axial nodal levels 5 and 6 (coincident with the core midplane), and also at the interface of the axial nodal levels 6 and 7 (located at +12.3 cm). As will be shown in Section 8.8, this fictitious behaviour, which is related to the flux axial reconstruction process, is significantly reduced when version 1.15 of PRESTO-2 is used.

For pins E4 and F7, the 3D agreement between the two nodal codes and MCNPX is good, as also is the agreement between the three codes and the radial measurements at −9 cm.

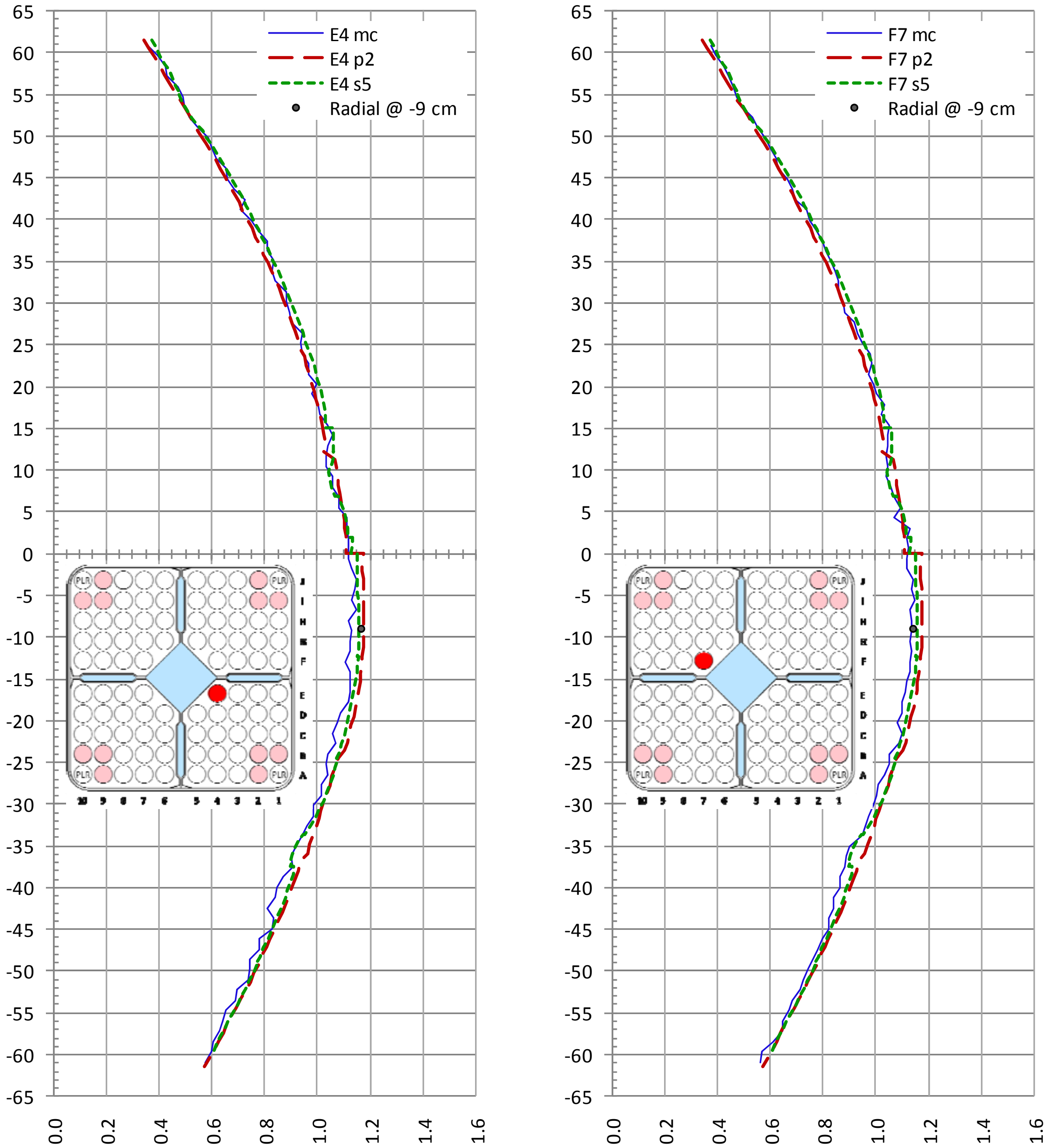

Figure 129 Configuration III-1: 3D comparison of calculated total-fission rates in pins E4 and F7 for MCNPX (blue line), PRESTO-2 (red dashed line) and SIMULATE-5 (green dotted line). The results of the radial measurements performed at −9 cm are also included (black dots).

Non-measured pins D3 and C3

Figure 130 shows the comparisons of calculated total-fission rates for pins D3 and C3. For pin D3, the radial measurement at −9 cm is also shown. For pin C3, on the other hand, no measurement is available.

In general, the same observations can be made as those for pins E4 and F7. The agreement between the three codes is seen to be good, PRESTO-2 still showing a discontinuity at core midplane, although smaller than noted previously.

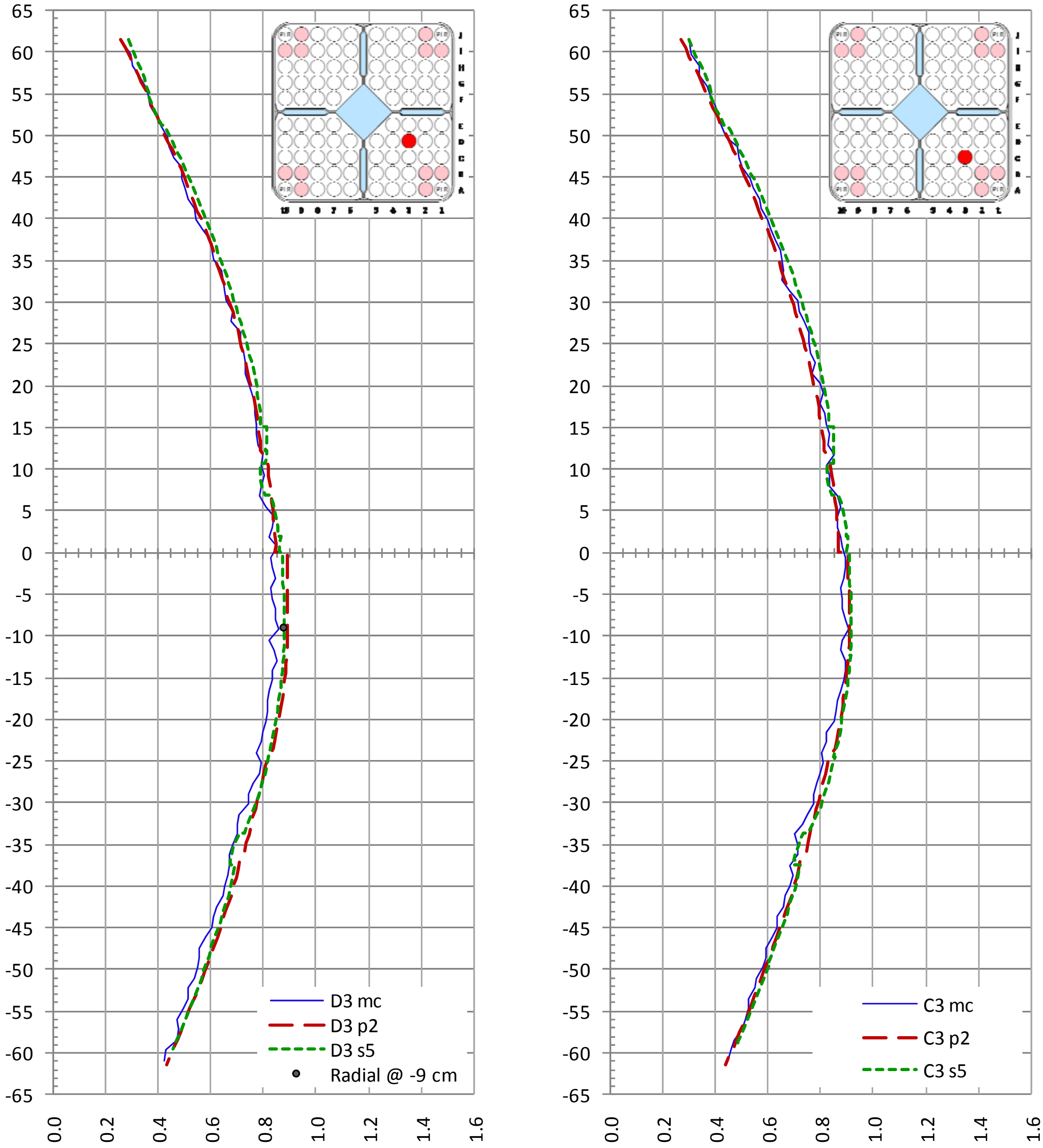

Figure 130 Configuration III-1: 3D comparison of calculated total-fission rates in pins D3 and C3 for MCNPX (blue line), PRESTO-2 (red dashed line) and SIMULATE-5 (green dotted line). For pin D3, the result of the radial measurement performed at −9 cm is also included (black dot).

8.7.2 3D comparisons in Configuration III-2

In Configuration III-2, axial measurements were made for each of the 14 pins shown on the right hand side of Figure 123. For the 7 FLRs, 19 measurements covering the axial range from

−30 cm to 30 cm, relative to the core midplane, were made, while the 7 PLRs were measured at the 8 lowermost elevations, between −30 cm and −4 cm. In this thesis, the resulting 3D

Table 55 C/E values corresponding to MCNPX for the 189 points (7 FLR at 19 axial levels and 7 PLRs at 8 axial levels) measured in Configuration III-2. In the last three rows, the maximum, minimum and standard deviation of the C/Es for each measured pin (columns 2 to 15) and for all the measurements considered together (last column) are shown.

Elev.	C5	H5	C6	F8	D4	D7	G7	E4	F4	D5	G5	D6	G6	F7	All
30	1.019	1.032	1.019	1.023	1.019	1.019	1.028								
25	1.002	1.028	1.025	1.012	1.014	1.013	1.010								
20	1.025	1.011	1.023	1.021	1.013	1.020	1.034								
15	1.029	1.024	1.015	1.033	1.013	1.015	1.017								
10	1.008	1.000	1.007	1.016	1.019	1.028	1.001								
7	0.998	1.017	1.001	1.007	0.996	0.993	1.005								
5	1.015	0.995	1.015	1.006	1.016	1.023	1.024								
3	1.027	1.019	1.011	1.012	1.005	1.000	1.000								
1	1.041	1.021	1.001	1.002	0.997	1.000	1.001								
0	1.036	1.022	0.996	1.015	1.002	1.007	1.012								
-2	0.990	0.981	1.001	0.975	1.000	1.021	0.981								
-4	1.007	1.007	1.005	1.000	0.996	0.990	1.010	0.997	1.023	0.992	1.015	1.012	0.994	1.010	
-6	0.985	0.982	1.002	0.988	0.995	1.013	0.987	0.974	0.978	1.008	1.004	0.996	0.983	0.988	
-8	0.989	0.989	0.993	1.001	0.991	0.987	1.006	0.971	0.997	0.984	1.009	0.991	0.982	0.977	
-10	0.981	0.991	0.992	0.977	0.992	1.002	0.995	0.994	1.002	1.010	0.998	0.986	0.999	0.986	
-12	0.996	0.994	1.001	0.978	0.992	1.001	0.996	0.983	0.983	0.990	0.992	0.997	0.983	0.990	
-15	0.993	0.992	0.997	0.991	1.004	0.999	0.997	0.980	0.988	0.988	0.988	0.994	0.993	0.986	
-20	0.999	1.003	0.996	0.989	0.990	0.988	1.017	0.979	1.006	1.001	1.006	0.993	0.980	0.993	
-30	1.008	0.982	0.995	1.012	0.994	1.004	0.994	1.010	0.994	0.987	1.006	1.000	0.994	0.971	
Max	1.041	1.032	1.025	1.033	1.019	1.028	1.034	1.010	1.023	1.010	1.015	1.012	0.999	1.010	1.041
Min	0.981	0.981	0.992	0.975	0.990	0.987	0.981	0.971	0.978	0.984	0.988	0.986	0.980	0.971	0.971
StD	0.018	0.017	0.010	0.016	0.010	0.012	0.014	0.013	0.014	0.010	0.009	0.008	0.007	0.012	0.014

Table 56 C/E values corresponding to PRESTO-2 for the 189 points (7 FLR at 19 axial levels and 7 PLRs at 8 axial levels) measured in Configuration III-2. In the last three rows, the maximum, minimum and standard deviation of the C/Es for each measured pin (columns 2 to 15) and for all the measurements considered together (last column) are shown.

Elev.	C5	H5	C6	F8	D4	D7	G7	E4	F4	D5	G5	D6	G6	F7	All
30	0.981	0.977	0.970	0.977	0.983	0.978	0.986								
25	0.965	0.965	0.965	0.965	0.957	0.963	0.948								
20	0.947	0.948	0.948	0.946	0.958	0.961	0.960								
15	0.969	0.966	0.971	0.968	0.954	0.953	0.952								
10	0.991	0.988	0.986	0.988	1.009	1.020	1.014								
7	0.991	0.992	0.990	0.988	1.004	1.010	1.009								
5	1.002	0.997	1.001	0.990	1.016	1.021	1.014								
3	1.022	1.024	1.019	1.022	1.008	1.002	1.004								
1	1.078	1.075	1.076	1.074	1.013	1.015	1.009								
0	1.056	1.043	1.035	1.042	1.026	1.036	1.028								
-2	1.003	0.999	1.001	0.998	1.028	1.032	1.034								
-4	1.011	1.009	1.002	0.997	1.020	1.017	1.025	1.013	1.020	1.011	1.022	1.019	1.006	1.007	
-6	1.007	1.006	1.004	1.000	1.026	1.033	1.018	1.010	1.004	1.015	1.011	1.014	0.992	1.008	
-8	1.005	1.006	1.001	0.996	1.014	1.021	1.027	1.003	1.001	1.008	1.006	1.009	0.997	0.996	
-10	1.002	1.003	0.998	0.997	1.017	1.021	1.012	1.002	1.002	1.006	1.004	1.006	0.998	1.000	
-12	1.003	1.004	0.999	0.994	1.014	1.017	1.014	1.003	1.001	1.004	1.005	1.005	0.990	1.001	
-15	0.998	0.999	0.994	0.992	1.017	1.015	1.024	0.997	0.996	0.994	1.000	1.002	0.993	0.997	
-20	0.994	0.992	0.989	0.984	1.007	1.013	1.011	0.989	1.003	0.996	0.998	1.000	0.981	0.994	
-30	0.985	0.985	0.985	0.982	0.989	0.992	0.998	0.985	0.985	0.986	0.982	0.989	0.970	0.978	
Max	1.078	1.075	1.076	1.074	1.028	1.036	1.034	1.013	1.020	1.015	1.022	1.019	1.006	1.008	1.078
Min	0.947	0.948	0.948	0.946	0.954	0.953	0.948	0.985	0.985	0.986	0.982	0.989	0.970	0.978	0.946
StD	0.030	0.028	0.027	0.028	0.024	0.025	0.026	0.010	0.010	0.010	0.011	0.009	0.011	0.009	0.023

Table 57 C/E values corresponding to SIMULATE-5 for the 189 points (7 FLR at 19 axial levels and 7 PLRs at 8 axial levels) measured in Configuration III-2. In the last three rows, the maximum, minimum and standard deviation of the C/Es for each measured pin (columns 2 to 15) and for all the measurements considered together (last column) are shown.

Elev.	C5	H5	C6	F8	D4	D7	G7	E4	F4	D5	G5	D6	G6	F7	All
30	1.028	1.024	1.018	1.025	1.033	1.029	1.038								
25	1.026	1.022	1.021	1.022	1.016	1.022	1.007								
20	0.992	0.994	0.994	0.994	1.020	1.026	1.025								
15	0.994	0.971	0.976	0.976	0.990	0.990	0.991								
10	1.002	1.002	0.999	1.003	1.024	1.029	1.024								
7	1.004	1.007	1.005	1.004	1.017	1.021	1.020								
5	1.015	1.012	1.016	1.006	1.028	1.033	1.026								
3	1.034	1.037	1.032	1.037	1.021	1.012	1.014								
1	1.036	1.034	1.035	1.034	0.999	1.001	0.994								
0	1.029	1.017	1.011	1.018	1.008	1.016	1.010								
-2	0.994	0.993	0.995	0.993	1.005	1.013	1.014								
-4	1.004	1.004	0.998	0.993	1.001	1.001	1.009	0.995	0.999	0.994	1.002	0.998	0.988	0.990	
-6	1.002	1.002	1.001	0.997	1.008	1.018	1.003	0.993	0.986	0.998	0.993	0.996	0.976	0.992	
-8	1.003	1.006	1.000	0.996	1.000	1.009	1.016	0.989	0.985	0.994	0.990	0.993	0.984	0.983	
-10	1.002	1.004	0.999	0.999	1.003	1.010	1.001	0.990	0.988	0.994	0.990	0.992	0.987	0.989	
-12	1.005	1.007	1.001	0.997	1.001	1.006	1.003	0.992	0.988	0.993	0.992	0.992	0.980	0.991	
-15	1.003	1.005	1.000	0.999	1.014	1.010	1.018	0.990	0.988	0.987	0.991	0.994	0.987	0.991	
-20	1.001	1.000	0.998	0.994	1.005	1.010	1.009	0.984	0.997	0.991	0.992	0.994	0.978	0.991	
-30	0.996	0.996	0.998	0.995	1.002	1.004	1.010	0.984	0.982	0.985	0.980	0.986	0.971	0.978	
Max	1.036	1.037	1.035	1.037	1.033	1.033	1.038	0.995	0.999	0.998	1.002	0.998	0.988	0.992	1.038
Min	0.992	0.971	0.976	0.976	0.990	0.990	0.991	0.984	0.982	0.985	0.980	0.986	0.971	0.978	0.971
StD	0.014	0.015	0.014	0.016	0.011	0.011	0.011	0.004	0.006	0.004	0.006	0.004	0.006	0.005	0.015

distribution of 7x19+7x8=189 experimental values, normalised as described in Subsection 8.7.1 for Configuration III-1, but now using the radial distribution at axial level -15 cm (74 measurements), was compared against the results obtained with MCNPX, PRESTO-2 and SIMULATE-5. The corresponding C/E values are presented in Table 55, Table 56 and Table 57, respectively. The 3D agreement between calculation and measurement is seen to be good for all three codes, the standard deviations of the complete distribution of C/Es being 1.4%, 2.3% and 1.5% for MCNPX, PRESTO-2 and SIMULATE-5, respectively. Axial plots showing the calculated and measured total-fission rates in selected pins are presented below.

Measured pin F8

Figure 131 shows the axial plots of calculated and measured total-fission rates in pin F8. On the left hand side, the complete axial range (−61.5 cm to +61.5 cm) is covered, while a zoom of the axial region between −32 cm and +32 cm is given on the right hand side of the figure, enhancing the visualisation of the axial profiles near the core midplane.

In the region below the core midplane, all three calculations show a very good agreement with the experimental results. In the upper part of the test zone, MCNPX and SIMULATE-5 predict the global profile of the measured total-fission rate with good accuracy. The perturbation produced by the proximity of the PLR at lattice position F7 is appropriately captured by these two codes. In particular, the effect of the plenum and the two natural-uranium pellets (see Figure 17) present in the neighbouring pin F7 can be clearly identified on the RHS of Figure 131.

In the case of PRESTO-2, a trend to underestimate the measurements in the upper part of the test zone is observed, with a deviation of −5.4% at +20 cm (see Table 56). In particular, the PRESTO-2 total-fission rate profile is depressed at axial level 7 (+12.3 to +24.6 cm), above and below which it approaches the MCNPX and SIMULATE-5 results more closely.

The depression in the total-fission rate caused by the presence of the spacers (2.6 cm high) centred at −27.56 cm and +16.74 cm (see Table 45) can be observed in the MCNPX and SIMULATE-5 results. As before, PRESTO-2 (version 1.13) does not capture this detail. The somewhat longer depression observed in the axial profile of SIMULATE-5, as compared with the height of the spacers, is due to the flux axial discretisation, which is set to 1 cm (~one pellet).

The standard deviations of the C/Es for pin F8 are, for MCNPX (Table 55), PRESTO-2 (Table 56) and SIMULATE-5 (Table 57), 1.6%, 2.8% and 1.6%, respectively.

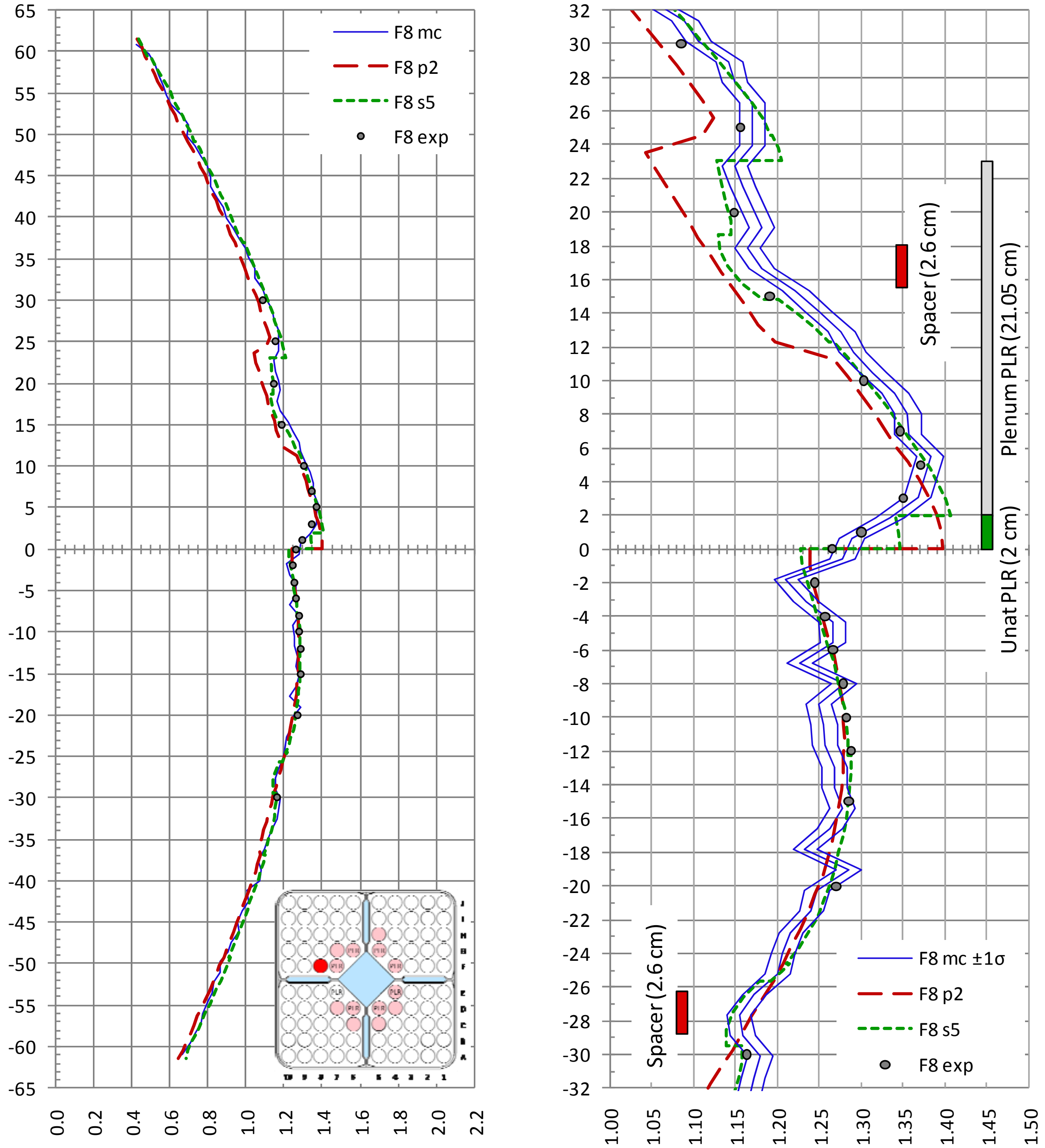

Figure 131 Configuration III-2: 3D comparison of calculated and measured total-fission rates in pin F8 for MCNPX (blue line), PRESTO-2 (red dashed line) and SIMULATE-5 (green dotted line). All distributions are normalized to 1.0 over the complete 3D set of 189 measured points. The dots represent the experimental values. On the right hand side, a zoom of the axial region between -32 cm and +32 cm from the core midplane is shown. For MCNPX, the "most probable" results are represented by the middle line, while the lines on both sides represent the (±1σ) uncertainty band.

Measured pin C5

Figure 132 shows the axial plots of calculated and measured total-fission rates in pin C5. This pin shows, as expected, a behaviour quite similar to that of pin F8. Thus, the same observations can be made as above. The standard deviations of the C/Es for pin C5 are 1.8%, 3.0% and 1.4% for MCNPX, PRESTO-2 and SIMULATE-5, respectively.

The two remaining axially measured pins that occupy analogous positions, viz. H5 and C6, show, once again, a very similar behaviour. Thus, no explicit comparisons are presented for these pins.

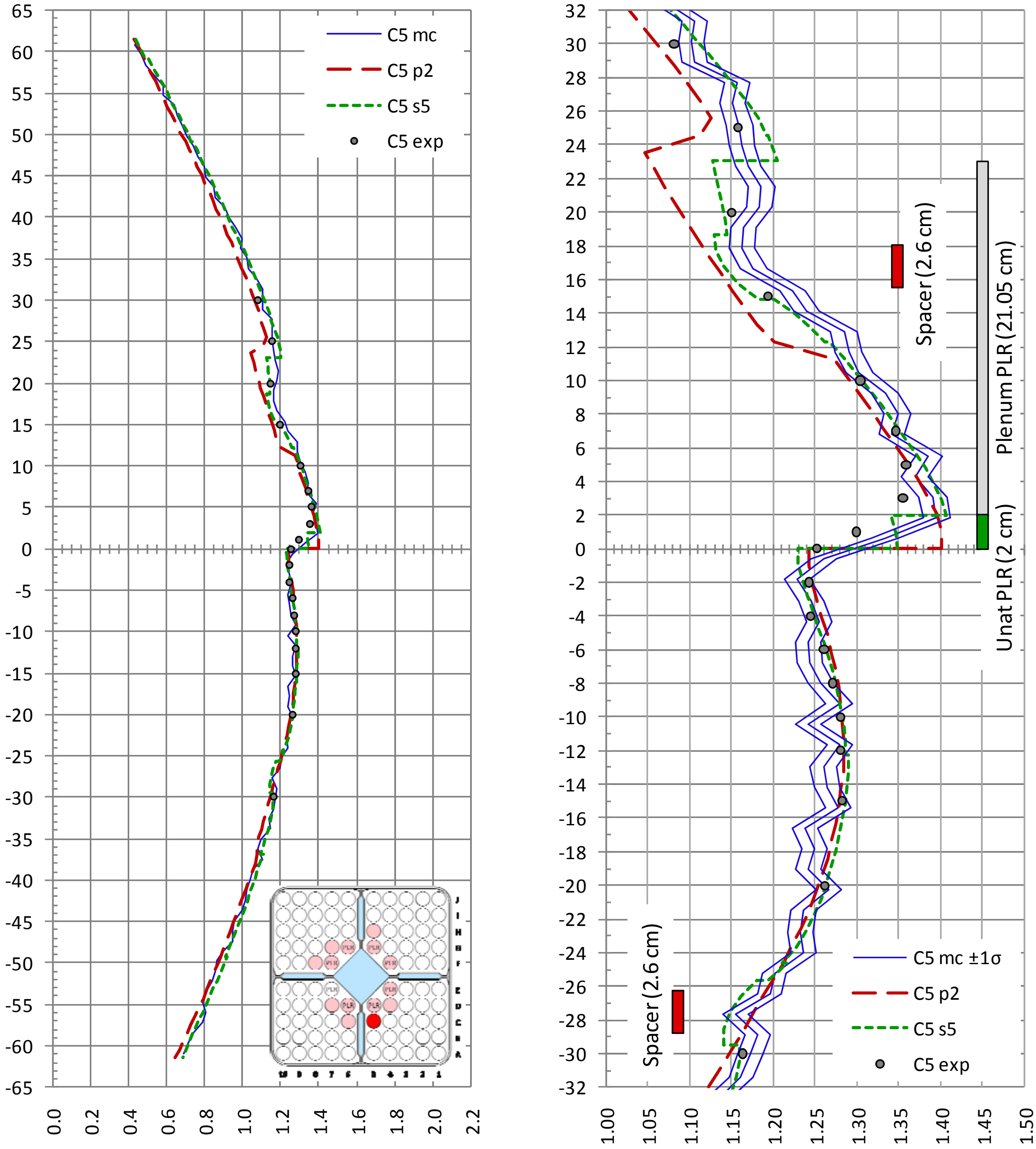

Figure 132 Configuration III-2: 3D comparison of calculated and measured total-fission rates in pin C5 for MCNPX (blue line), PRESTO-2 (red dashed line) and SIMULATE-5 (green dotted line).

Measured pins G7 and D4

These two pins contain 5.0 w/o Gd_2O_3 and experience therefore very low total-fission rates. Figure 133 shows a zoomed view of the central part of the 3D plots for pins G7 and D4. The agreement of MCNPX and SIMULATE-5 with the measurements is seen to be very good. PRESTO-2 slightly overestimates the total-fission rate below the test-zone midplane, while showing a small underestimation in the upper part of the axial range.

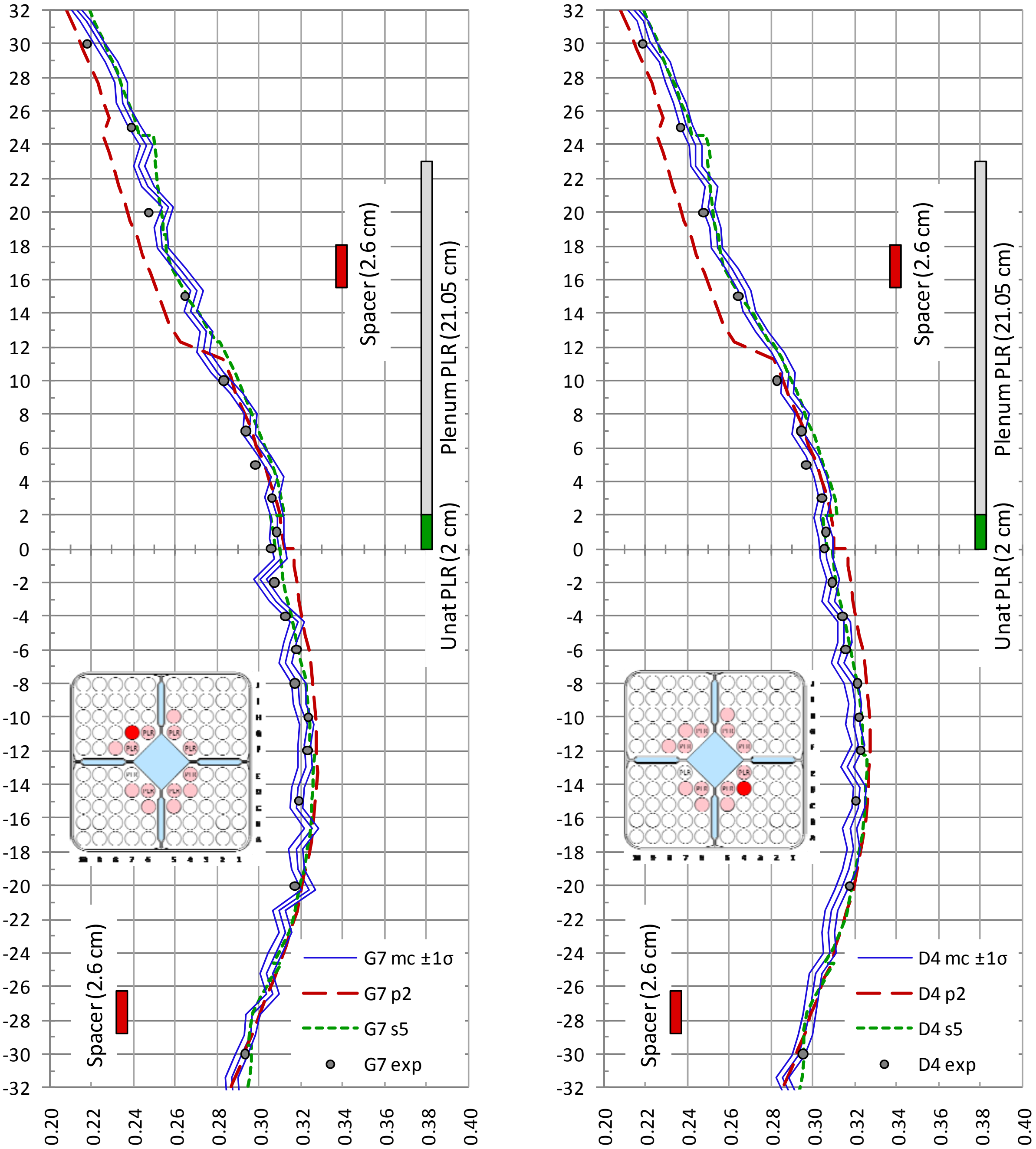

Figure 133 Configuration III-2: 3D comparisons of calculated and measured total-fission rates in pins G7 and D4 for MCNPX (blue line), PRESTO-2 (red dashed line) and SIMULATE-5 (green dotted line). Since these two pins contain gadolinium (5.0 w/o), their total-fission rates are relatively low, and the scale of the abscissas has been zoomed accordingly.

The standard deviations of the C/Es for MCNPX, PRESTO-2 and SIMULATE-5 are, respectively, 1.4%, 2.6% and 1.1% (pin G7) and 1.0%, 2.4% and 1.1% (pin D4).

Measured pins G5 and D6

The comparisons for these two PLRs of 2/3 length are shown in Figure 134. The agreement of all calculations with the measurements is seen to be good. The strong reduction of the total-fission rate in the 2 cm natural uranium segment at the tip of the PLRs can be clearly seen. The standard deviations of the C/Es for MCNPX, PRESTO-2 and SIMULATE-5 are, respectively, 0.9%, 1.1% and 0.6% (pin G5), and 0.8%, 0.9% and 0.4% (pin D6).

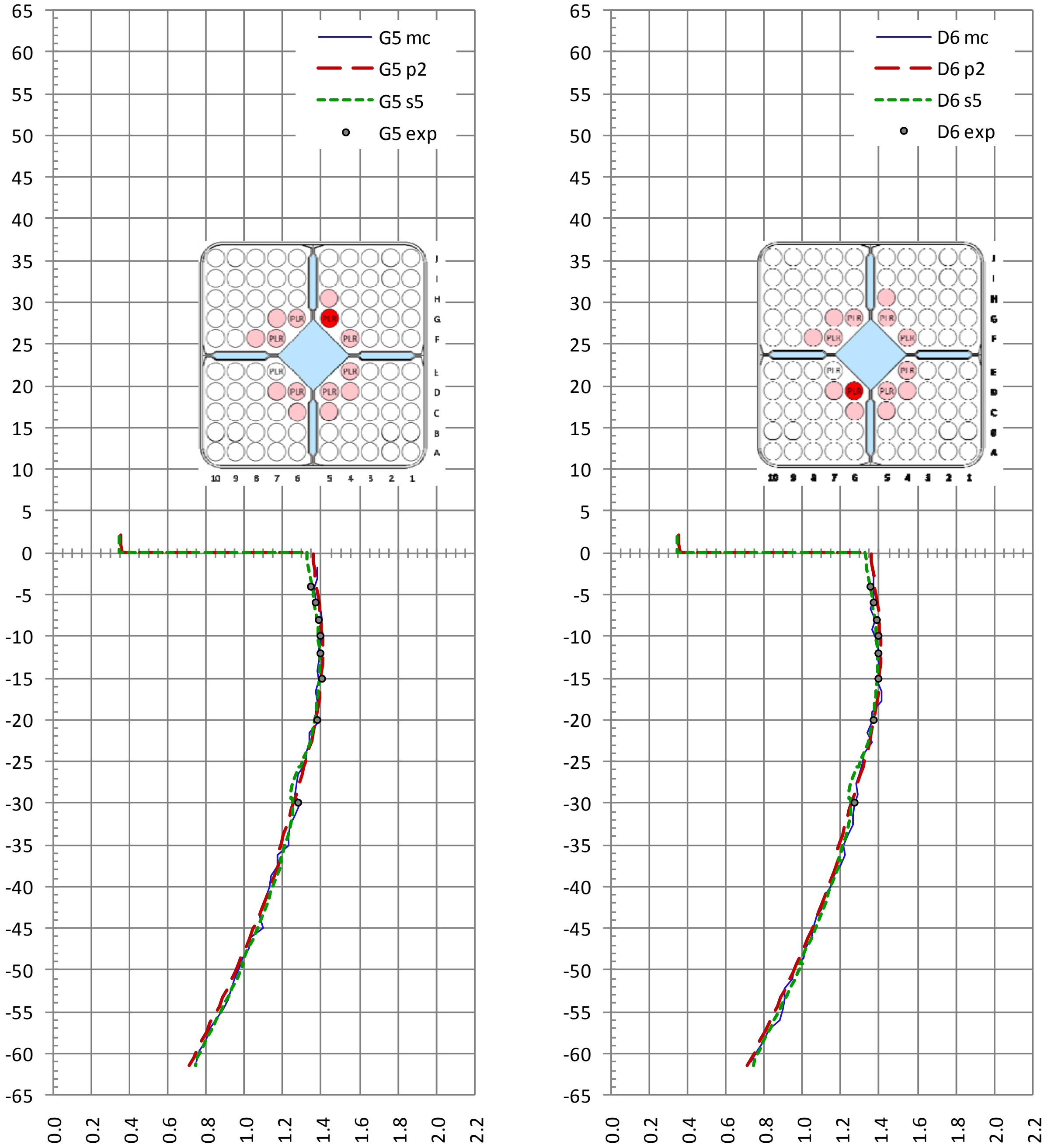

Figure 134 Configuration III-2: 3D comparison of calculated and measured total-fission rates in pins G5 and D6 for MCNPX (blue line), PRESTO-2 (red dashed line) and SIMULATE-5 (green dotted line). The MCNPX results are shown up to the elevation −2 cm, i.e. the 2 cm natural uranium segment is not included in the corresponding profiles.

The five remaining axially measured PLRs, viz. F7, G6, F4, E4 and D5, show, as expected, a very similar behaviour. Thus, no explicit comparisons are presented for these pins.

Non-measured pins I10, B1, J6 and B3

As done before, it is interesting to study the agreement between calculations for pins that have not been axially measured, e.g. pins I10 and B1 in Figure 135. Moreover, the comparison of the calculated 3D total-fission rate distributions with the radial measurements performed at specific elevations, for example −15 cm in this case, also provides valuable information.

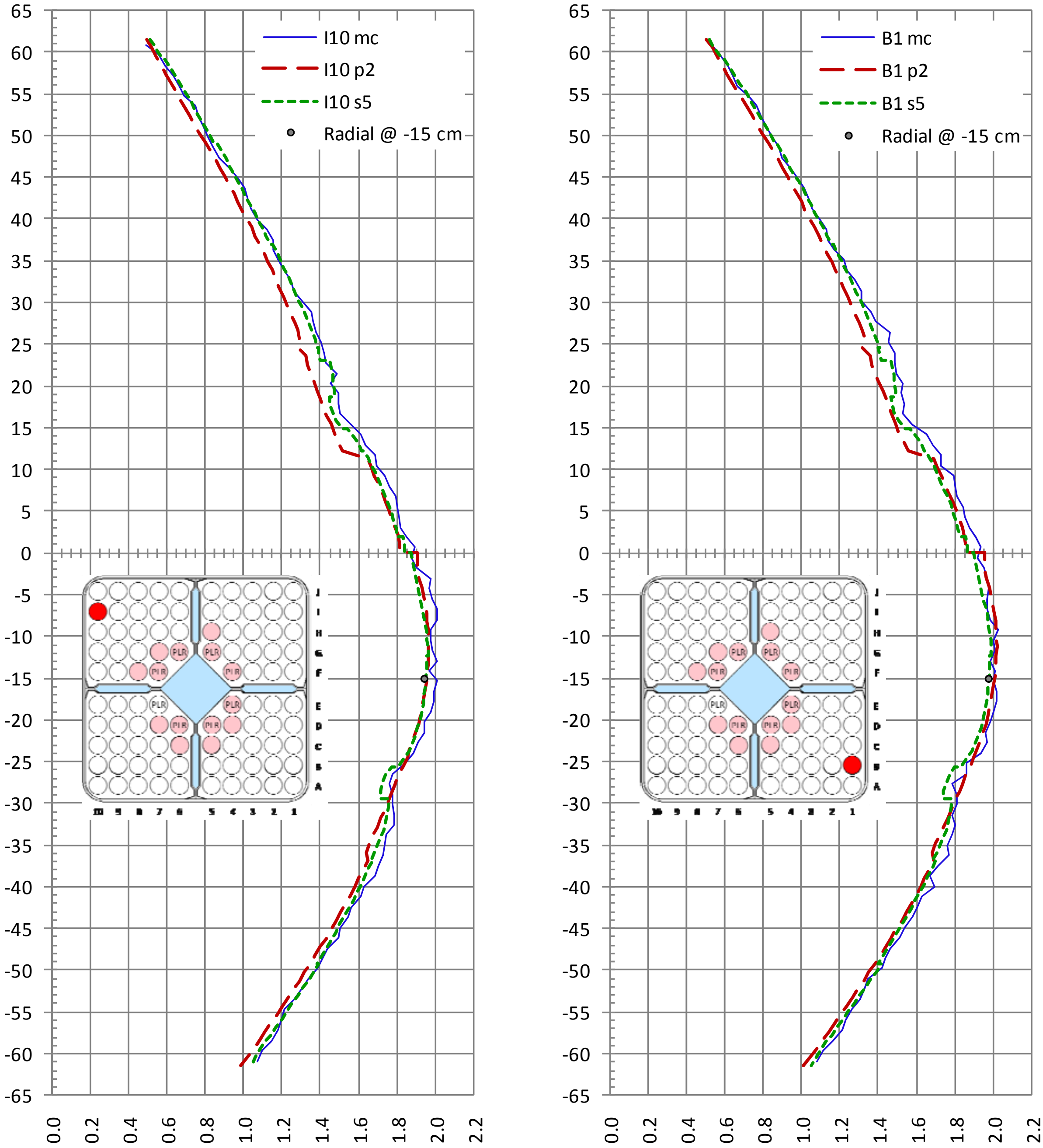

Figure 135 Configuration III-2: 3D comparison of calculated total-fission rates in pins I10 and B1 for MCNPX (blue line), PRESTO-2 (red dashed line) and SIMULATE-5 (green dotted line). The results of the radial measurements performed at −15 cm are also included (black dots).

As in the case of pins E4 and F7 in Configuration III-1, pins I10 and B1 occupy lattice positions that are far from the pins where the axial measurements in Configuration III-2 were made. Thus, global trends could have an amplifying impact on these pins. However, as has been the case in Configuration III-1, such an effect is not observed, the 3D agreement between the different calculations being equally good for these pins as for those on which the measurements were done. The same observation can be made for non-measured pins that are somewhat closer to the measured ones, in peripheral or internal lattice positions, as can be seen for pins J6 and B3, respectively, in Figure 136. As before, this demonstrates the good global results obtained with the three codes analysed in this research.

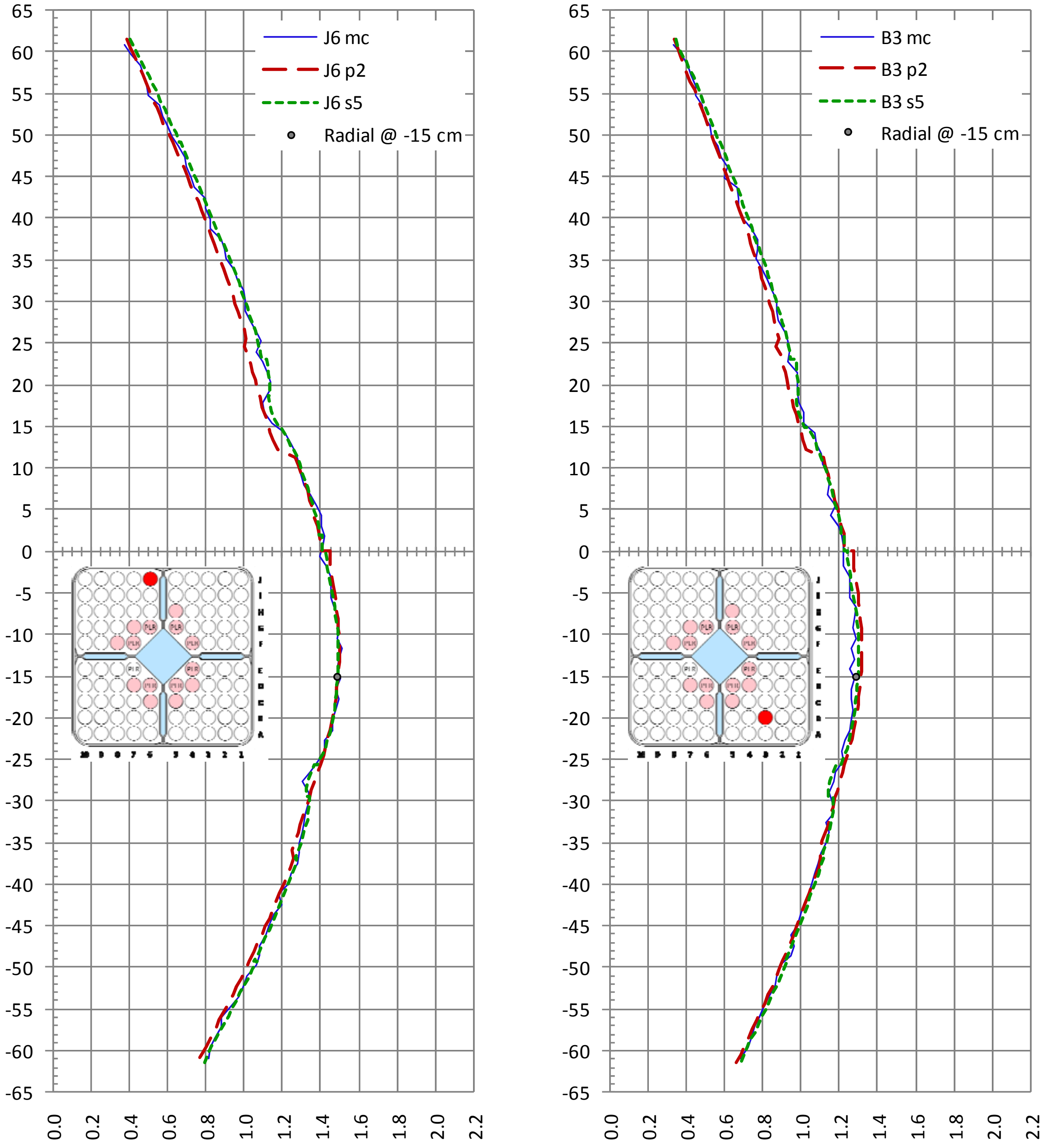

Figure 136 Configuration III-2: 3D comparison of calculated total-fission rates in pins J6 and B3 for MCNPX (blue line), PRESTO-2 (red dashed line) and SIMULATE-5 (green dotted line). The results of the radial measurements performed at −15 cm are also included (black dots).

8.8 Use of PRESTO-2-1.15

As mentioned before, the latest released version of programme PRESTO-2, viz. version 1.15, features improvements in the axial flux reconstruction methodology compared with its predecessors. Thus, as done previously for Configurations I-1C (see Section 6.7) and I-6A (see Section 7.6), comparisons have been made with experiment for Configurations III-1 and III-2 using PRESTO-2 version 1.15, instead of version 1.13. The results of these comparisons are shown and discussed in the following subsections.

8.8.1 3D comparisons in Configuration III-1

Concerning the global behaviour of the 3D total-fission distribution, both PRESTO-2 versions show, as expected, similar results. However, a slightly larger standard deviation of the C/E distribution is observed for all pins when using PRESTO-2-1.15, as can be seen by comparing Table 58 (version 1.15) with Table 53 (version 1.13). The standard deviation of the 3D C/E distribution increases by 0.1%, from 2.7% to 2.8%.

Table 58 C/E values corresponding to PRESTO-2 (version 1.15) for the 228 points (12 pins and 19 axial levels) measured in Configuration III-1.

Elev.	A2	B1	A9	B10	J2	I1	J9	I10	B2	B9	I2	I9	All
36	0.963	0.996	0.975	0.952	1.004	0.983	0.973	0.986	0.997	0.988	0.968	0.959	
26	0.969	0.999	0.971	0.959	1.008	0.983	0.969	0.980	0.993	0.988	0.970	0.955	
23	0.954	0.990	0.958	0.947	1.002	0.971	0.957	0.969	1.003	0.984	0.970	0.956	
21	0.952	0.993	0.957	0.952	1.002	0.970	0.965	0.971	1.006	0.988	0.968	0.961	
18	0.958	0.992	0.964	0.955	0.999	0.975	0.963	0.972	0.993	0.982	0.961	0.956	
16	0.965	0.998	0.967	0.959	1.008	0.979	0.967	0.976	0.991	0.973	0.960	0.950	
14	0.978	1.018	0.986	0.975	1.024	0.997	0.988	0.995	0.993	0.981	0.963	0.949	
12	0.990	1.023	0.988	0.975	1.032	1.002	0.992	1.002	1.005	0.981	0.980	0.955	
10	0.983	1.017	0.986	0.974	1.027	1.002	0.985	0.993	1.016	0.995	0.979	0.964	
8	0.969	1.003	0.974	0.957	1.013	0.987	0.976	0.987	0.990	0.984	0.965	0.951	
6	0.984	1.012	0.989	0.974	1.027	1.004	0.992	0.994	1.016	1.016	0.987	0.974	
4	0.988	1.024	0.993	0.982	1.040	1.012	0.996	1.003	1.005	1.003	0.987	0.983	
2	1.015	1.057	1.020	1.012	1.061	1.027	1.021	1.026	1.012	1.006	0.990	0.976	
0	1.020	1.067	1.028	1.032	1.077	1.043	1.029	1.044	1.042	1.023	0.998	0.999	
-2	0.998	1.043	1.005	0.992	1.049	1.021	1.001	1.019	1.054	1.032	1.011	1.004	
-4	1.005	1.046	1.008	1.000	1.053	1.023	1.013	1.024	1.048	1.038	1.016	1.004	
-9	1.012	1.051	1.016	1.004	1.054	1.031	1.016	1.029	1.048	1.034	1.014	1.004	
-14	1.006	1.055	1.020	1.003	1.060	1.032	1.011	1.029	1.044	1.039	1.014	1.011	
-24	1.009	1.055	1.026	1.005	1.056	1.033	1.014	1.029	1.048	1.039	1.021	1.007	
Max	1.020	1.067	1.028	1.032	1.077	1.043	1.029	1.044	1.054	1.039	1.021	1.011	1.077
Min	0.952	0.990	0.957	0.947	0.999	0.970	0.957	0.969	0.990	0.973	0.960	0.949	0.947
StD	0.022	0.026	0.024	0.024	0.024	0.024	0.022	0.024	0.023	0.023	0.021	0.023	0.028

Figure 137 shows the total-fission rate comparisons over the axial region -28 cm to +28 cm for pins J9 and J2, using PRESTO-2-1.15. These plots can be compared with the right hand sides of Figure 124 (pin J9) and Figure 125 (pin J2), both showing PRESTO-2-1.13 results. In all these figures, the MCNPX and SIMULATE-5 results are identical.

It can be seen, from Figure 137, that PRESTO-2-1.15 correctly captures the effect of the spacer, which represents an improvement with respect to version 1.13.

In the axial region affected by the 2 cm natural uranium segment, located at the tip of the PLRs, PRESTO-2-1.15 predicts a peak in the total-fission axial profile, contradicting the evidence provided by the experimental results. This behaviour, which is not shown by version 1.13 (see Figure 124 and Figure 125), cannot be physically explained, and is partially responsible for the slightly larger standard deviations mentioned at the beginning of this subsection.

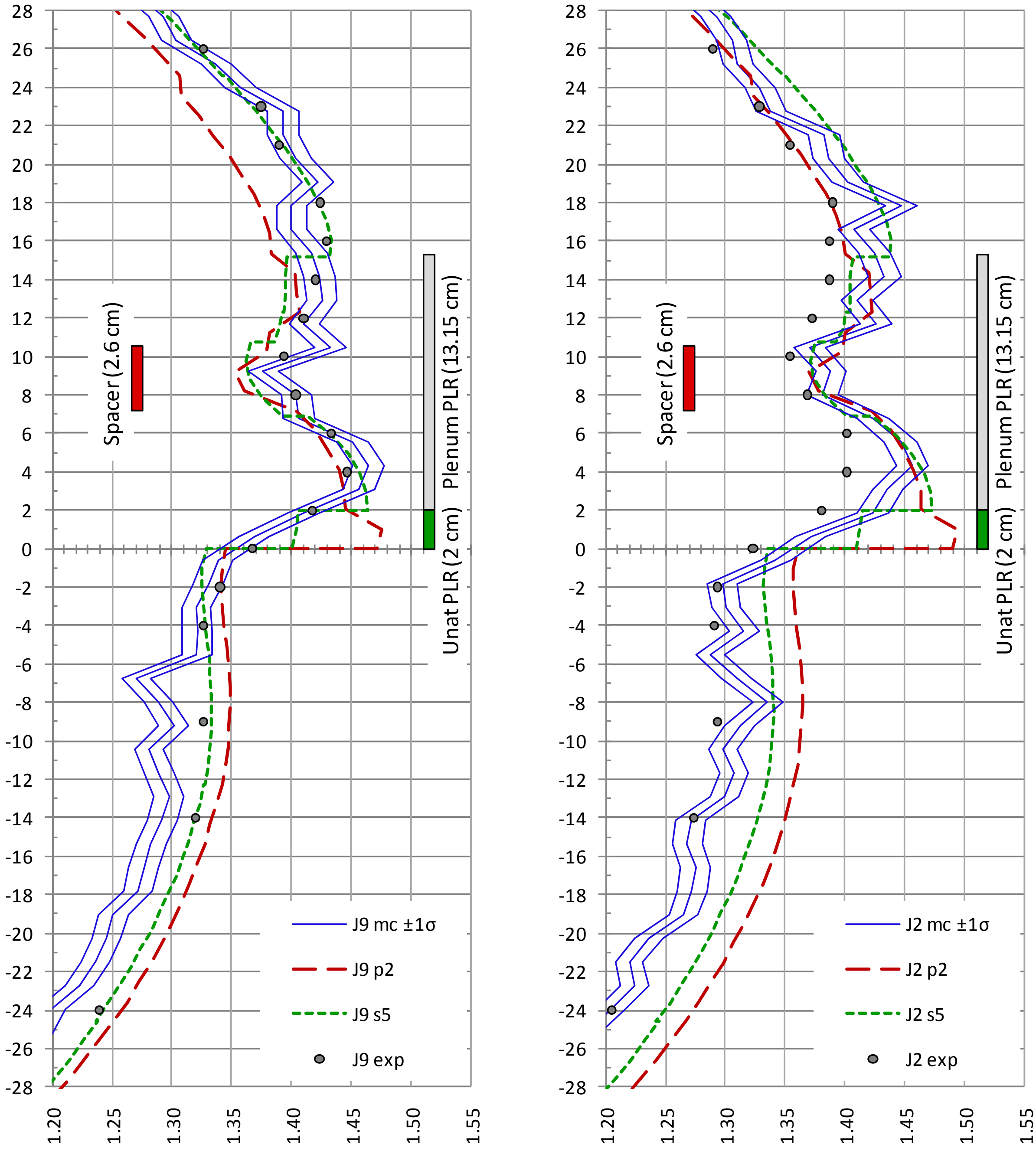

Figure 137 Configuration III-1: 3D comparison of calculated and measured total-fission rates in pins J9 and J2 for MCNPX (blue line), PRESTO-2-1.15 (red dashed line) and SIMULATE-5 (green dotted line).

In general, and disregarding the local effect mentioned above, PRESTO-2-1-15 delivers an improved description of the axial flux profile compared with PRESTO-2-1.13. For instance, Figure 138 shows the 3D results for pins E4 and F7, obtained using PRESTO-1.15. Comparing these with Figure 129, it can be seen that the discontinuity shown by PRESTO-1.13 at the level of the core midplane is reduced for both pins, while at the same time the depressions caused by the presence of the spacers can now be identified. On the other hand, as mentioned before, the global behaviour of the calculated total-fission rate distribution does not change significantly, although a small worsening of the standard deviation is observed for almost all pins when version 1.15 is used.

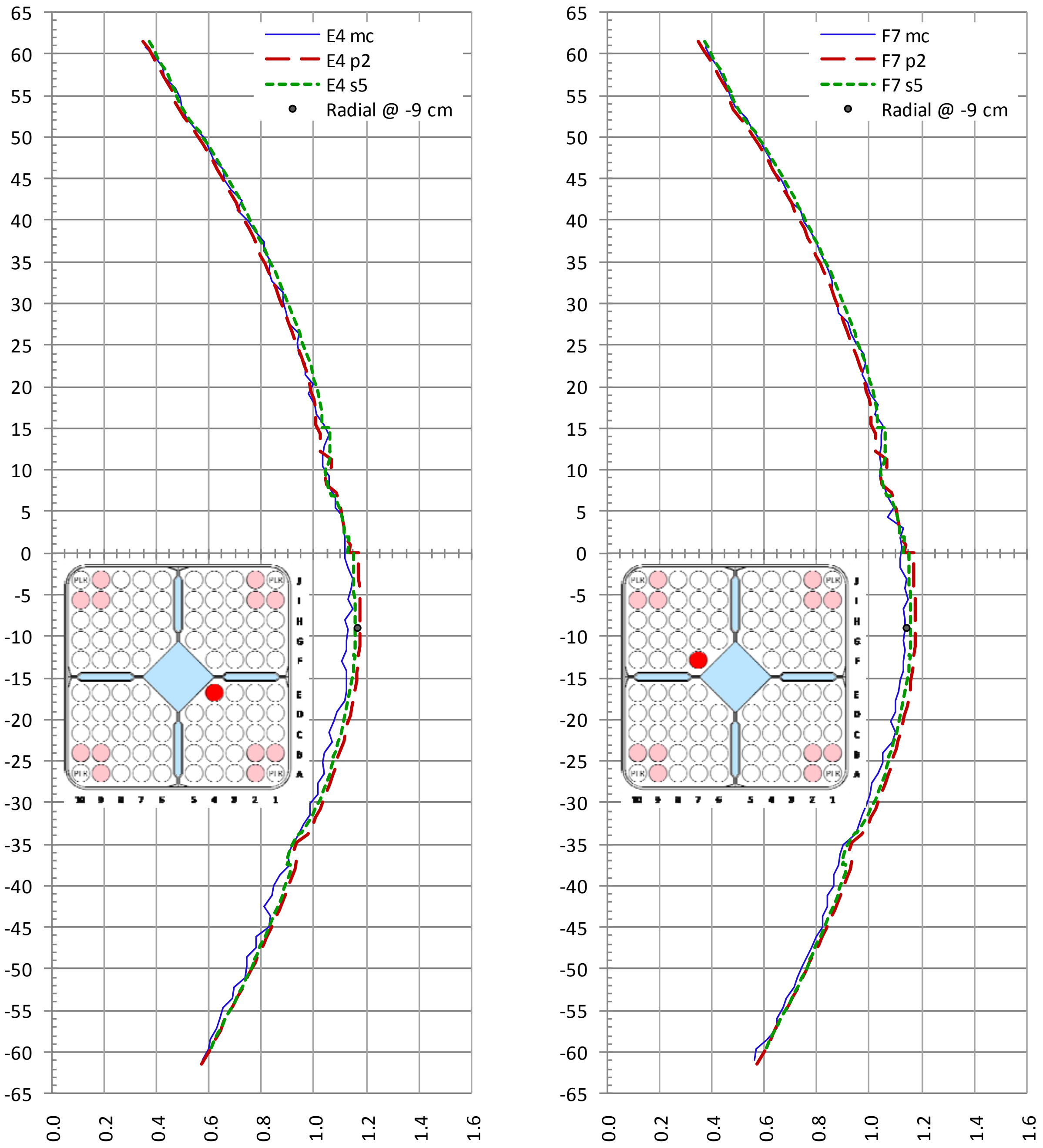

Figure 138 Configuration III-1: 3D comparison of calculated total-fission rates in pins E4 and F7 for MCNPX (blue line), PRESTO-2-1.15 (red dashed line) and SIMULATE-5 (green dotted line). The results of the radial measurements performed at −9 cm are also included (black dots).

8.8.2 3D comparisons in Configuration III-2

Similar observations can be made from the use of PRESTO-2-1.15 in Configuration III-2. The 3D distribution of C/Es (Table 56) remains practically unchanged, in line with the very small variations observed in the case of Configuration III-1 (in Configuration III-2, however, the standard deviation of the 3D C/E distribution remains unchanged at 2.3%).

Concerning the local behaviour of the axial profiles, Figure 139 shows comparisons of the total-fission rate over the axial region −32 cm to +32 cm for pins F8 and C5, using PRESTO-2 version 1.15. These plots can be compared with the right hand sides of Figure 131 (pin F8) and Figure 132 (pin C5), showing the corresponding results obtained with PRESTO-2-1.13.

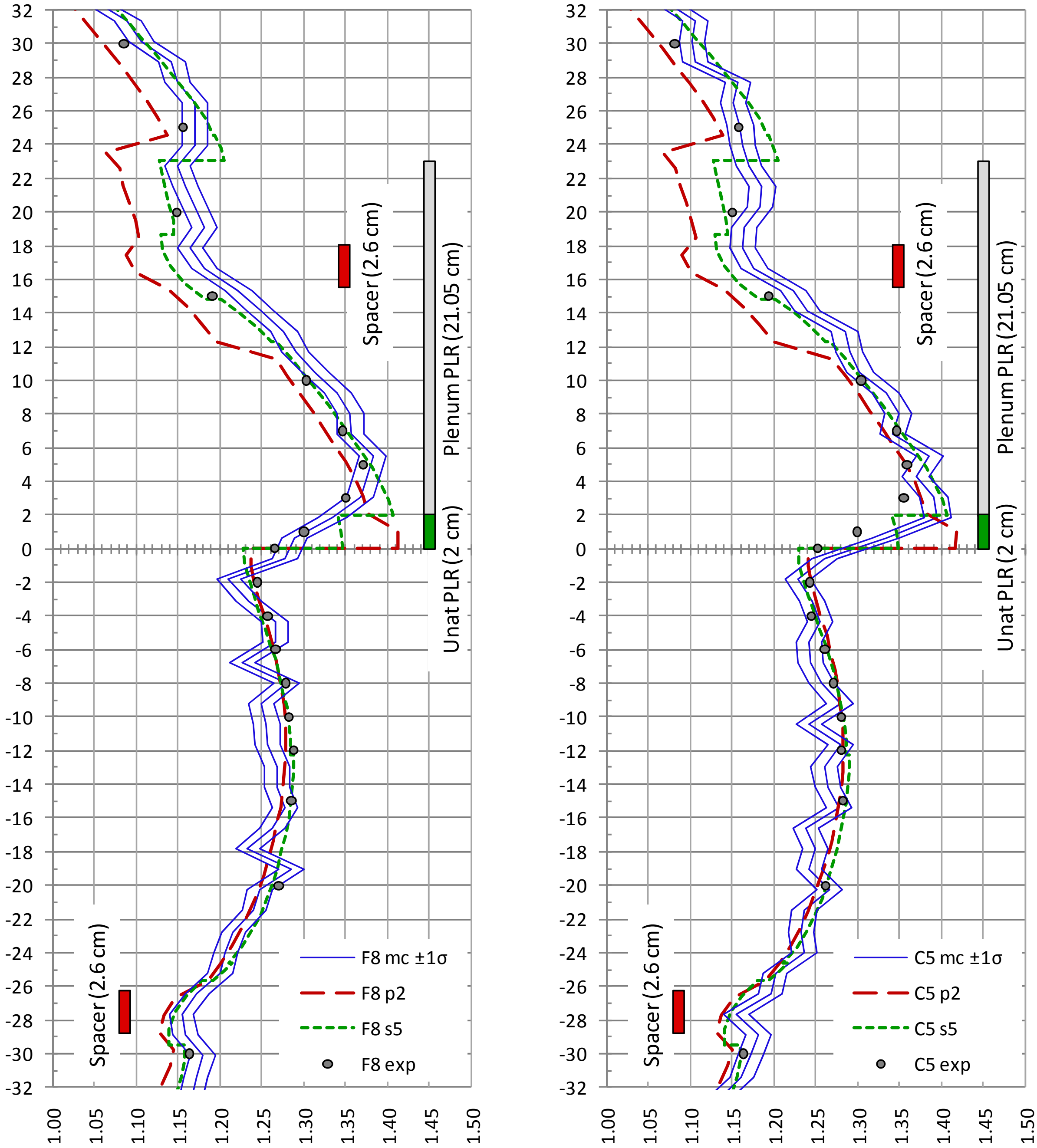

Figure 139 Configuration III-2: 3D comparison of calculated and measured total-fission rates in pins F8 and C5 for MCNPX (blue line), PRESTO-2-1.15 (red dashed line) and SIMULATE-5 (green dotted line).

In a qualitative sense, the same differences between the two PRESTO-2 versions, presented in Section 8.8.1 for Configuration III-1, are also observed here. These concern the effects of the spacers and the natural uranium pellets, respectively, and the corresponding previous discussions apply.

8.9 General remarks

8.9.1 Radial comparisons in Configurations III-1 and III-2

The radial comparisons of total-fission rates presented in Subsections 8.6.1 and 8.6.2 show that the nodal diffusion codes investigated, viz. PRESTO-2 and SIMULATE-5, can reproduce the LWR-PROTEUS experimental results for Configurations III-1 and III-2 with good accuracy, the standard deviations of the radial C/E distributions being of the same order of those obtained with the transport code MCNPX. These results agree with the observations made in Chapter 4, for the case of Configuration I-1A, and demonstrate that, also in the case of reduced moderation (mixture of H_2O and D_2O) and for significantly different nuclear designs in the central and peripheral assemblies composing the test zone, the nodal methodologies with pin-power reconstruction provide very satisfactory agreement with experiment.

One specific aspect worth discussing here is the comparison between calculations and measurements for pins containing gadolinium. Table 59 shows the C/E values, averaged over all measured gadolinium pins, for each of the two sets of radial measurements performed in Configurations III-1 and III-2, together with the corresponding results obtained in the axially uniform Configurations I-1A and I-2A (Subsections 4.5.1 and 5.5.1, respectively). For each case, the number of fuel pins present in the lattice are shown, thus giving an indication of the moderator-to-fuel ratio prevailing at the corresponding elevations. Complementing this information, the spectral indexes (ϕ_2/ϕ_1), as calculated by PRESTO-2, for a cut-off energy of 1.84 eV, are also presented[62].

As can be seen, when the spectral index decreases, i.e. the spectrum becomes harder, the C/Es tend to increase (get closer to 1). In agreement with the observations previously made for Configuration I-1A (see Section 4.5.1), this behaviour may indicate an overestimation of the flux depression occurring in the gadolinium pins, which becomes less important for harder spectra. This observation agrees with that made for Configuration I-2A (see Subsection 5.5.2), in which the spectrum hardens due to the presence of the control blade.

For the interpretation of the results presented in Table 59, however, one should bear in mind that the moderator in Phase I was light water, while for Phase III a mixture of light and heavy water was used. Furthermore, the concentration of Gd_2O_3 differs between the assembly types used in the two different phases. Hence, rather than considering Table 59 as a whole, it is more

---

[62] In Table 59, the P2 C/E values for Configurations I-1A and I-2A, and the S5 value for Configuration I-1A, correspond to the results at core midplane, while the MCNPX values are axial averages over the entire pin length. The difference between these two approaches is very small (see Section 4.5). As mentioned before, the P2 calculations for Phase III were performed using a cut-off energy of 0.625 eV, while for Phase I the cut-off was 1.84 eV. As discussed in Subsection 4.5.2, this also has an insignificant impact on the total-fission rate distribution. All S5 results correspond to calculations performed with five energy groups. As previously mentioned (see Subsection 2.4.4), the C5/S5 route could not be applied to LWR-PROTEUS configurations with the L-shaped control blade inserted. Thus, no S5 results are available for Configuration I-2A.

appropriate to compare the variation of C/E, with the spectral index, for the two phases separately. Doing this, it can be clearly seen that, in each case, the reduction of the spectral index leads to improvements in the agreement between calculation and experiment for the gadolinium pins. This observation applies to all three codes analysed. However, it needs to be mentioned that, in Configurations III-1 and III-2, while MCNPX slightly underestimates the total-fission rates in the gadolinium pins, PRESTO-2 and SIMULATE-5 appear to agree quite well with the measurements.

Table 59 Average C/E values for the gadolinium pins measured in Configurations I-1A, I-2A, III-1 and III-2. The different cases are listed in order of decreasing spectral index, an indicator of the spectrum hardness (a lower spectral index indicates a harder spectrum).

				Average C/E for the gadolinium pins		
Conf.	Elevation (axial level)	Number of fuel pins	Spectral index	MCNPX	PRESTO-2	SIMULATE-5
I-1A	midplane (5)	96	0.36	0.975	0.975	0.974
I-2A	midplane (5)	96	0.29	0.986	0.996	not available
III-2	+25 cm (8)	84	0.26	0.972	0.978	0.990
	−15 cm (4)	92	0.23	0.977	0.991	0.993
III-1	+21 cm (7)	92	0.22	0.989	0.999	1.002
	−9 cm (5)	96	0.20	0.986	1.001	1.000

8.9.2 3D comparisons in Configurations III-1 and III-2

Also concerning the 3D total-fission rate distributions, the results of the comparisons with experiment are quite satisfactory for the three codes investigated. In particular, SIMULATE-5 shows an accuracy similar to MCNPX. PRESTO-2, on the other hand, leads to somewhat larger global deviations, showing also some difficulty to capture the local effects of the axial heterogeneities related to the presence of the PLRs. Some improvement in this respect is obtained by using the latest PRESTO-2 release, version 1.15, instead of version 1.13. In particular, the effect of spacers is better captured and the non-physical steps occurring at the test zone midplane for specific pins are significantly reduced.

As mentioned before, in addition to the 5-group results presented in this chapter for SIMULATE-5, results have also been obtained for Configurations III-1 and III-2 using S5 with 2 energy groups. Table 60 shows the standard deviations for the various radial and 3D comparisons. The differences between the two sets of calculations are seen to be indeed quite small, a presentation of the standard deviations with 3 significant digits being necessary to see the changes.

Table 60 Standard deviations (in %) of the total-fission C/E distributions in Configurations III-1 and III-2, corresponding to SIMULATE-5 with 2 and 5 energy groups, respectively

Configuration	Comparison	2 groups	5 groups
III-1	radial +21 cm	1.03	1.03
	radial −9 cm	1.25	1.21
	3D (228 points)	2.12	1.96
III-2	radial +25 cm	1.33	1.35
	radial −15 cm	1.28	1.28
	3D (189 points)	1.42	1.48

Finally, while interpreting the 3D comparisons presented in this chapter, one particular aspect should be borne in mind. This is that the relative number of measurements performed in the upper and lower test-zone regions are significantly different in the two configurations, which results in a different weighting in the 3D normalisation process. Table 61 shows the number of experimental points lying above, at, and below the test zone midplane in Configurations III-1 and III-2.

Table 61 Number of measurements performed above, at, and below the core midplane in Configurations III-1 and III-2.

	Configuration III-1	Configuration III-2
above TZ midplane	156	63
at TZ midplane	12	7
below TZ midplane	60	119
Total	228	189

As can be seen in Table 61, most measurements were made in the upper part of the test zone for Configuration III-1, while the reverse is the case for Configuration III-2. This fact explains the generally better 3D agreement observed in the upper and lower parts of the test zone for the comparisons in Configuration III-1 and III-2, respectively.

8.10 k-effective

As for the previously analysed configurations, the investigation of the k-effective behaviour does not constitute the primary aim of the present research; however, it provides a useful consistency check. Thus, some observations concerning the k-effective obtained in the different calculations performed for Configurations III-1 and III-2 will be discussed here.

Table 62 and Table 63 show, for Configurations III-1 and III-2, respectively, the k-effective values obtained with the different codes and code versions used in this thesis. The MCNPX k-effective values correspond to the cases used for the determination of the PCRs and the total-fission rates, in which 800 x 10^6 histories were run.

Table 62 k-effective values obtained for Configuration III-1. For MCNPX, the 1σ uncertainty (in pcm) is given in brackets. “Unat” denotes natural uranium (two uppermost pellets in the PLRs) .

		Differences (pcm) with respect to:	
	k-effective	MCNPX	PRESTO-2 (v1.13)
MCNPX-2.6b with JEFF-3.1 library	1.00482 (3)	0	-923
PRESTO-2 (v1.13)	1.01405	923	0
PRESTO-2 (v1.15)	1.01405	923	0
SIMULATE-5 (2 groups)	1.00187	-295	-1218
SIMULATE-5 (5 groups)	1.00080	-402	-1325
PRESTO-2 (v1.13, no Unat)	1.01444	39	Differences (pcm) with respect to the base cases with modelled Unat pellets in the PLR tips.
SIMULATE-5 (2 groups, no Unat)	1.00226	39	
SIMULATE-5 (5 groups, no Unat)	1.00120	40	

Table 63 k-effective values obtained for Configuration III-2. For MCNPX, the 1σ uncertainty (in pcm) is given in brackets. “Unat” denotes natural uranium (two uppermost pellets in the PLRs).

		Differences (pcm) with respect to:	
	k-effective	MCNPX	PRESTO-2 (v1.13)
MCNPX-2.6b with JEFF-3.1 library	1.00606 (2)	0	-974
PRESTO-2 (v1.13)	1.01580	974	0
PRESTO-2 (v1.15)	1.01579	973	-1
SIMULATE-5 (2 groups)	1.00049	-557	-1531
SIMULATE-5 (5 groups)	1.00096	-510	-1484
PRESTO-2 (v1.13, no Unat)	1.01680	100	Differences (pcm) with respect to the base cases with modelled Unat pellets in the PLR tips
SIMULATE-5 (2 groups, no Unat)	1.00153	104	
SIMULATE-5 (5 groups, no Unat)	1.00209	113	

As previously observed for the LWR-PROTEUS Phase I configurations, also in Phase III PRESTO-2 calculates larger k-effective values than MCNPX, the differences being ~920 pcm and ~970 pcm for Configurations III-1 and III-2, respectively. SIMULATE-5, on the other hand, calculates k-effective values quite close to 1 for both configurations. Thus, the differences between the k-effective values obtained with SIMULATE-5 (with 2 energy groups) and PRESTO-2 are significantly larger (−1218 pcm for Configuration III-1 and −1531 pcm for Configuration III-2) than, for example, for Configuration I-1C (−478 pcm; see Table 35 in Section 6.8).

Table 62 and Table 63 show that the negative reactivity introduced by the 2 natural uranium pellets located at the tip of the PLRs is about 40 pcm in Configuration III-1 (4 PLRs) and about 100 pcm in Configuration III-2 (8 PLRs), the results obtained with PRESTO-2 and SIMULATE-5 being quite similar.

The SIMULATE-5 calculations presented in this thesis show that passing from 2 to 5 energy groups generally improves the k-effective results, i.e. the 5-group nodal diffusion model produces k-effective values which are closer to 1 (with the exception of Configuration III-2, for which the k-effective values do not exceed 1 by more than 100 pcm for both group structures). Recalling the results shown in Table 16 and Table 35, the SIMULATE-5 (5-group) k-effective values for Configurations I-1A and I-1C, 1.00825 and 1.00959, respectively, reflect an adequate neutron balance calculation also for these cases.

These observations suggest that, at least in conjunction with CASMO-5/SIMULATE-5, the methodology of representing the outer PROTEUS reactor regions (buffer, drivers and reflector) by means of appropriate PCRs, is adequate also from the point of view of the reactor criticality, the overestimation of k-effective being somewhat larger in the case of HELIOS/PRESTO-2.

8.11 Chapter summary and principal messages

Currently, partial length rods are a standard feature of most modern BWR fuel designs, aimed at improving the critical power ratio and the shutdown margin of the reactor core. At the tip of these rods, 3D local perturbations of the neutron flux occur, especially in the transition region between fuel, fission-gas plenum and coolant. These heterogeneities affect the neutron flux, and hence the total-fission rate distribution, in the fuel rods that are close to the PLRs.

The principal aim of the investigations presented in this chapter has been to assess the ability of nodal methodologies with pin-power reconstruction, in particular HELIOS/PRESTO-2 and CASMO-5/SIMULATE-5, to predict the local total-fission rate distribution in the vicinity of the heterogeneities imposed by the presence of PLRs. Furthermore, it has been the intention to demonstrate, as in the case of the Phase I configurations presented in the previous chapters, that the modelling of the LWR-PROTEUS Phase III configurations carried out in this thesis is appropriate for the mentioned purpose.

The results of the experimental comparisons have confirmed once more that the performance of the nodal methodologies in predicting the global distribution of the total-fission rate is indeed satisfactory. Considering Configurations III-1 and III-2 together, the standard deviations of the radial C/E distributions lie between 1.0% and 1.7% for PRESTO-2, and between 1.0% and 1.4% for SIMULATE-5, which represent a remarkable agreement. In the case of MCNPX, the corresponding standard deviations lie within the band 1.3% to 1.9%.

Good agreement with experiment is also observed in the 3D comparisons. For PRESTO-2, the standard deviations are 2.7% and 2.3% for Configurations III-1 and III-2, respectively, while for SIMULATE-5 the corresponding values are 2.0% and 1.5%. These results are very satisfactory for the nodal methodologies, the standard deviations being comparable to those obtained with MCNPX, viz. 2.1% and 1.4%, respectively.

Three-dimensional local effects are well predicted by SIMULATE-5, which shows an accuracy level approaching that of MCNPX. Both codes properly describe the singularities caused by the natural uranium pellets and the plenum regions present at the top of the PLRs, closely reproducing the experimental results. Also the effect of the spacers is adequately described by the two codes.

PRESTO-2, on the other hand, shows a more restricted capability to calculate the local flux distribution in the presence of strong axial heterogeneities, both concerning the effects of the PLRs and the spacers, these aspects being partially improved in version 1.15 of the code. Despite this slight weakness, the PRESTO-2 results can be considered as good, the global behaviour being only marginally less accurate than that of SIMULATE-5.

Finally, it may be concluded that, also for the case of Configurations III-1 and III-2 of the LWR-PROTEUS experimental programme, the representation of the test-zone surroundings by means of Partial Current Ratios (PCRs) obtained from MCNPX 3D transport calculations provides an adequate platform for the assessment of nodal codes used in BWR core monitoring and design. The particular features of these two configurations, viz. the use of a mixture of D_2O and H_2O as moderator, and the existence of two different assembly designs (peripheral and central) in the test zone, are treated quite adequately by the present methodology.

Chapter 9

Principal messages and suggestions for future research

By the late 1990s, the first third-generation reactor − Kashiwazaki-Kariwa 6, a 1350 MWe Advanced BWR – was commissioned in Japan. In 2004, the first of the so-called Generation III+ units was ordered by Finland, a 1600 MWe European PWR (EPR). A similar unit is planned for France, as the first step of a full fleet replacement there. In the USA, the 2005 Energy Policy Act provided incentives for establishing new-generation power reactors there.

In this last chapter, a summary is provided of the various investigations performed in the present thesis, and possible paths for further research are identified.

Section 9.1, while briefly recalling the main aim of this doctoral research, summarises its principal findings, including conclusions about the calculational accuracies obtained in the different cases investigated. In Section 9.2, the advantages and limitations of using the LWR-PROTEUS experimental database for the assessment of industrial 3D nodal codes are discussed. Considerations concerning the relevance of the current experimental comparisons to the practical situation of BWR cores under normal operation are presented in Section 9.3. Finally, suggestions for further research are made in Section 9.4.

9.1 Principal findings and conclusions

The assessment of calculational methodologies based on experimental evidence gained in critical facilities is a fundamental aspect of reactor physics. Although comparisons between different, independent calculations (for example benchmark exercises) are very useful for evaluating the plausibility of specific results, experimental comparisons remain the only means of confirming that the calculations reflect reality with appropriate accuracy. Thus, integral experiments, such as those performed under the LWR-PROTEUS experimental programme, provide highly valuable information for the necessary assessment process.

Whereas considerable validation work has been previously performed in comparing a variety of 2D assembly codes with experimental results such as those from the LWR-PROTEUS programme, little experience exists concerning the deployment of such databases for the validation of 3D codes used for the design and monitoring of commercial LWR cores, in particular nodal core simulators.

In this thesis, comparisons have been made of nodal reconstructed, pin-wise total-fission rate distributions against measurements carried out in several different LWR-PROTEUS configurations. Two independent industrial code systems, viz. HELIOS/PRESTO-2 and CASMO-5/SIMULATE-5, have been deployed for this purpose. Both these code systems are widely used in the nuclear industry for the monitoring and design of nuclear power plants, and have proven to provide a very fast and accurate solution of the global 3D power distribution in the reactor core, in the context of both PWR and BWR applications.

Within this frame, the aim of the present doctoral research has been two-fold. First, the feasibility of modelling the different LWR-PROTEUS configurations by means of 3D nodal simulators designed for power reactors has been investigated, the demonstration of the applicability of the LWR-PROTEUS experimental database for the assessment of such codes being the principal result. These aspects, which constitute an important part of the present research, are discussed in the next section. Second, the developed methodology has been applied to study the behaviour of the two mentioned code systems in the presence of strong local heterogeneities, of the type which occur in actual BWR cores, both in the radial and axial directions. The principal conclusions derived from these investigations – viz. the two- and three-dimensional comparisons of calculated total-fission rate distributions against experimental results performed in the different LWR-PROTEUS configurations − are presented below.

Uniform case – Configuration I-1A

For the uniform test-zone arrangement of Configuration I-1A (Chapter 4), the nodal reconstructed total-fission rate distributions show similar radial agreements with experiment as the 3D transport whole-reactor MCNPX model, the values of the standard deviation of the C/E distributions being 1.1%, 1.3% and 1.1% for MCNPX, PRESTO-2 and SIMULATE-5, respectively.

The only systematic effects observed (a ~2.5% underestimation of the total-fission rate in the pins containing gadolinium and in the pins located at the lattice corners) have their origin in the lattice calculations and are not a consequence of the nodal calculation. In the case of C5/S5, the agreement in the corner pins is about 1% better than for HE/P2, while the gadolinium pins are underestimated by ~3%.

In addition to the radial results, the verification of the test-zone axial flux curvature has shown a very good agreement between all three calculations and experiment (measurements performed with a miniature fission chamber moved axially over the test-zone height at lattice position E2).

The good agreement of the nodal, pin-reconstructed results with experiment indicate that the representation of the test zone surroundings by means of Partial Current Ratios (PCRs) is quite adequate. In the case of Configuration I-1A, it has been found that the radial PCRs are relatively uniform, in both the azimuthal and the axial directions, which is consistent with the uniform character of this particular configuration. However, it also indicates that the PROTEUS concept of a test zone surrounded by a buffer, two driver zones and a reflector, is very successful in providing conditions for the test region that are only weakly dependent on the surroundings and can, therefore, be quite easily modelled. Moreover, in the case of the present experiments, the eight peripheral assemblies of the test-zone's 3x3 arrangement represent a very efficient additional decoupling feature for the central assembly (where the measurements have been made) from the external zones of the reactor.

In brief, it can be concluded that, for the simple case of a uniform array of axially uniform fuel assemblies, the LWR-PROTEUS experimental results are reproduced by the nodal methodologies with very good accuracy, equivalent to that achievable with high-order transport methods.

Fully inserted control blade – Configuration I-2A

For the reasons mentioned in Chapter 2, the CASMO-5/SIMULATE-5 route could not be applied to LWR-PROTEUS configurations with the L-shaped control blade inserted; hence, the following summary concerns only HELIOS/PRESTO-2 results.

In the case of Configuration I-2A (Chapter 5), in which the L-shaped control blade is fully inserted in the north-west gap of the central assembly, the radial agreement between the HE/P2 calculation and experiment worsens, compared with Configuration I-1A, from 1.3% to 3.2%, due to the steep, asymmetric flux gradients caused by the control blade. For MCNPX, on the other hand, the corresponding standard deviation is 1.3%, similar to that of Configuration I-1A (1.1%).

Two main effects can be identified from the comparisons on Configuration I-2A. First, the C/E distribution shows a clear radial tilt along the NW-SE diagonal of the central fuel assembly. Second, the zero-current assumption, implicit in the 2D reflected assembly calculations, leads to the systematic underestimation of pins located near the control blade tips (which reaches ~9% for the SW and NE corner pins), these deviations being caused by the presence of the fictitious blades introduced by the reflective boundary condition.

The first of the effects mentioned above is caused by the pronounced radial tilt that the L-shaped control blade imposes across the test zone and, in particular, across the central fuel assembly. In this case, the PRESTO-2 requirement of azimuthally uniform PCRs (called albedos in PRESTO-2) cannot capture the azimuthal dependence of the partial currents entering and exiting the test zone. By applying Pin Map Correction Factors (PMCFs)[63], which partially compensate the effect of these asymmetries on the total-fission distribution across the test-zone central assembly, the standard deviation in Configuration I-2A is reduced from 3.2% to 2.8%.

The second effect is a consequence of the use of reflective boundary conditions in the lattice calculations and cannot be avoided as long this approximation is used (which is always the case for the generation of cross-section data banks for reactor calculations)[64].

As in the case of Configuration I-1A, the verification of the axial flux curvature over the test-zone length in Configuration I-2A has shown a very good agreement between calculation and experiment[65], for both MCNPX and PRESTO-2.

Finally, it can be concluded that for the fully controlled case of Configuration I-2A, the nodal methodology of PRESTO-2 reproduces the experimental total-fission results with acceptable accuracy, although unavoidable approximations made in the modelling produce some systematic deviations in the C/E distribution, which are not observed, as expected, in the MCNPX high-order transport results.

---

[63] These correction factors are derived from two HELIOS calculations performed over the 3x3 test zone. In one calculation, the PCRs used in PRESTO-2 are used as boundary conditions; in the other, a finer discretised set (both in space and energy) is used. All these PCRs are derived from the 3D MCNPX modelling of the whole reactor. The PMCFs are defined as the ratio of the pin-power maps calculated by HELIOS in these two situations, and are applied by simply multiplying them with the reconstructed total-fission distribution calculated by PRESTO-2.

[64] It should be mentioned here that, for the particular case of a BWR with all control rods inserted, the reflective boundary approximation reflects in fact the real situation. However, during operation, only few control blades are (partially) inserted into the core, for which the depression caused by the reflected blades in the lattice calculation is, in fact, fictitious.

[65] In this case, two axial measurements were made: a gamma-scanning of pin J1 and a TIP (Traversing In-Core Probe) traverse along the inter-assembly gap facing pin position A1.

Enrichment boundary – Configuration I-1C

In Configuration I-1C (Chapter 6), the interface between two different lattice designs is made coincident with the test-zone midplane, allowing the investigation of the local region where the axial change of enrichment and gadolinium content takes place.

Experimental comparisons have been made mainly for the nodal codes PRESTO-2 and SIMULATE-5, but MCNPX results were also considered. In this case, the comparisons are three-dimensional, i.e. describe the radial and axial agreement simultaneously. The most relevant aspect considered is, however, the characterisation of the axial behaviour, principally near the fuel composition boundary.

Considering all the measured points, the standard deviations of the 3D C/E comparisons are 9.4%, 11.5% and 10.5% for MCNPX, PRESTO-2, and SIMULATE-5, respectively. However, significant deviations occur only within a short distance from the nodal interface in pins showing large composition differences on the two sides of the core midplane, the axial shapes being well predicted in most cases (see plots for individual pins in Chapter 6). When excluding 13 points showing large deviations (which are not relevant for the characterisation of the overall agreement; see Section 6.5 for details), the standard deviations are significantly reduced for all three calculations, the values resulting from the comparison of the 140 remaining C/Es being 3.1%, 4.3% and 3.2% for MCNPX, PRESTO-2 and SIMULATE-5, respectively.

For pins showing significantly different total-fission rates on the two sides of the core midplane, the experimentally observed gradual transition, accurately captured by MCNPX, is described by PRESTO-2 and SIMULATE-5 as a pronounced step. This is a consequence of the use of a unique function $\xi(z)$ describing the axial dependence of the asymptotic flux within each node for all pins, combined with the lack of 3D transport information at pellet level (caused by the 2D character of the pin-power maps used in the reconstruction process).

In general, it has been found that all calculations reproduce the experimental axial profiles with good accuracy, although some systematic underestimation of the measurements can be observed in the lower part of the test zone. This underestimation is most pronounced in the case of PRESTO-2, but is also observed for MCNPX and SIMULATE-5.

Partially inserted control blade – Configuration I-6A

The partial insertion of a control blade, investigated in Configuration I-6A (Chapter 7) is one of the most challenging conditions for the nodal diffusion methodologies. In this case, strong flux gradients occur in both (axial and radial) directions. As in the case of Configuration I-2A, the CASMO-5/SIMULATE-5 route could not be applied; hence, once again, the following observations concern only HELIOS/PRESTO-2 results.

The 3D comparisons show that the agreement of the nodal reconstructed total-fission rates with experiment is good. Excluding 39 points which are not relevant for the characterisation of the overall agreement (at ±1 cm and -65 cm from the core midplane; see Section 7.4 for details), the standard deviations resulting from the comparison of the 182 remaining C/Es are 2.3% and 4.5% for MCNPX and PRESTO-2, respectively.

In a global sense, PRESTO-2 tends to overestimate the total-fission rate in the SE quadrant of the assembly for the lower (controlled) half of the test zone. This is in agreement with the observations made for the fully-controlled case of Configuration I-2A. In the upper (uncontrolled) part, on the other hand, the corner pins seem to be underestimated by PRESTO-2, as has been observed for Configuration I-1A.

At local level, it is found that the nodal reconstructed axial profile cannot accurately follow the steep gradient caused by the transition between the controlled and uncontrolled parts of the test zone. Due to the significant radial and axial asymmetry occurring in Configuration I-6A, the variable separation of the 3D asymptotic flux and the use of 2D pin power maps produce a step in the axial dependence of the flux, and also a conspicuous "inverse" step at core midplane for pins that are far from the control blade. Thus, for the two measurements located very near the interface between the 5th and 6th axial nodes, large C/E deviations are obtained. These, however, improve markedly only a few centimetres away from the nodal interface.

To conclude, it should be underlined that, considering the challenging conditions caused by the partial insertion of the L-shaped control blade, PRESTO-2 predicts the total-fission rate at pellet level with good accuracy. In the case of MCNPX, the agreement is, as expected, very good.

Partial length rods – Configurations III-1 and III-2

In Phase III of the LWR-PROTEUS experimental programme, SVEA-96 Optima2 fuel assemblies, featuring partial length rods (PLRs) of two different lengths, were investigated. The moderator used for filling the test tank was a mixture of D_2O and H_2O, especially selected to simulate the moderating properties of light water at BWR operational temperature. Configurations III-1 and III-2 (Chapter 8) concern the measurements aimed to characterise the flux behaviour in the vicinity of the tips of the 1/3 and 2/3 length-rods, respectively.

The results of the comparisons have shown that, also in these configurations, the performance of the nodal methodologies in predicting the global distribution of total-fission is very satisfactory. Considering Configurations III-1 and III-2 together, the standard deviations of the radial C/E distributions lie between 1.0% and 1.7% for PRESTO-2, and between 1.0% and 1.4% for SIMULATE-5, which can be regarded as a very good agreement. In the case of MCNPX, the corresponding standard deviations lie within the band 1.3% to 1.9%.

Also for the 3D distribution of the total-fission rate, the agreement of all calculations with experiment is good. For PRESTO-2, the standard deviations are 2.7% and 2.3% for Configurations III-1 and III-2, respectively, while for SIMULATE-5 the corresponding values are 2.0% and 1.5%. These results are very satisfactory for nodal methodologies, with only the PRESTO-2 standard deviations being slightly larger than those obtained with MCNPX, viz. 2.1% and 1.4% for Configurations III-1 and III-2, respectively.

SIMULATE-5 predicts the local three-dimensional effects caused by the PLRs with an accuracy similar to that of MCNPX, both codes properly describing the singularities caused by the natural uranium pellets and the plenum regions present at the top of the PLRs. Also the effect of the spacers is adequately captured by the two codes. A somewhat greater difficulty in predicting the local flux distribution in the presence of strong axial heterogeneities is observed in the case of PRESTO-2, these aspects being partially improved if the latest available version of the code (1.15) is used.

As an additional observation, for Configurations III-1 and III-2 (moderated by a mixture of D_2O and H_2O), the systematic underestimation of the total-fission rate in the gadolinium pins observed for Configuration I-1A (moderated by H_2O), is reduced. The reason for this can be attributed to the spectrum hardening, by which the relative importance of the absorptions in the gadolinium isotopes decreases in the case of the Phase III configurations (see also Section 8.9 for further details). Interesting is to note that it is under such "low moderation" conditions (the D_2O/H_2O mixture simulates, for instance, the case of zero void fraction at operating temperature) that the gadolinium is depleted in a power reactor core. From this point of view, a good experimental agreement for the total-fission rate in the case of Configurations III-1 and III-2 is a welcome result.

Closing remarks

An overview of the agreement obtained between calculations and experiment, represented by the standard deviations of the C/E values, is given for the different configurations in Table 64.

Table 64 Summary of the standard deviations of the C/E distributions for the total-fission rate obtained in the different experimental comparisons performed in this thesis. For the radial comparisons in Configurations III-1 and III-2, the values corresponding to the measurements performed in the lower/upper test-zone halves are shown. For the reasons mentioned in Chapter 2, the C5/S5 route could not be applied to configurations with the L-shaped control blade inserted.

	Radial (%)			Three-dimensional (%)		
Conf.	MCNPX	PRESTO-2	SIMULATE-5 (5 groups)	MCNPX	PRESTO-2	SIMULATE-5 (5 groups)
I-1A	1.1	1.3	1.1	–	–	–
I-2A	1.3	3.2	–	–	–	–
I-1C	–	–	–	3.1	4.3	3.2
I-6A	–	–	–	2.3	4.5	–
III-1	1.6 / 1.3	1.3 / 1.0	1.2 / 1.0	2.1	2.7	2.0
III-2	1.7 / 1.9	1.3 / 1.7	1.3 / 1.4	1.4	2.3	1.5

Overall, it is seen that the two nodal code systems investigated are capable of reproducing the LWR-PROTEUS experimental results with good accuracy, both for the radial and for the 3D comparisons. Significant deviations occur almost exclusively within a short distance from the nodal interface, in cases with strong gradients across the core midplane. The axial shapes of the total-fission rate distributions are well predicted in most cases, as can be seen from the plots presented in Chapters 6 to 8. In particular, it should be mentioned that the comparisons of MCNPX with experiment show standard deviations that are only slightly better than those obtained with HELIOS/PRESTO-2 and CASMO-5/SIMULATE-5, suggesting that the nodal methodologies, with the exception of very localised effects, are able to produce results with accuracies similar to that of high-order transport calculations[66].

---

[66] As complementary information, it can be mentioned that a single MCNPX calculation for the whole PROTEUS reactor (with 800×10^6 neutron histories) needs approximately 9 hours of run time on the computer cluster at the Swiss National Supercomputing Centre (CSCS), while using 265 processors in parallel. The same calculation would take, in very approximate terms, about 2400 hours, i.e. 100 calendar days, running on a single CPU. On the other hand, a PRESTO-2 or SIMULATE-5 calculation of the test zone (90 nodes), takes approximately 3 seconds running on one single (equivalent) CPU (one requires in this case, however, the pre-calculation of the lattice data describing the fuel assemblies, as also of the PCR matrices representing the PROTEUS reactor's outer zones).

Thus, the investigations performed in this thesis allow one to conclude that, for the conditions under which the measurements were done, the code systems HELIOS/PRESTO-2 and CASMO-5/SIMULATE-5 predict the total-fission rate distribution at pellet level with good accuracy. Furthermore, the results also confirm that the basic methodology used in this thesis, viz. describing the LWR-PROTEUS test zone by means of a 3D nodal core simulator, while representing the surroundings of the nodal domain by means of Partial Current Ratios, is quite appropriate. Finally, and probably most important, this research demonstrates that the LWR-PROTEUS experimental database, as such, constitutes an easily applicable and very valuable basis for the validation and assessment of 3D nodal methodologies with pin-power reconstruction, this specific aspect being discussed in greater detail in the next section.

9.2 Suitability of LWR-PROTEUS for the assessment of nodal codes

Considering the very heterogeneous character of the PROTEUS reactor (see Section 2.5 for details), it is evident that the whole-reactor modelling, with full geometrical and material detail, can be accomplished adequately only by applying transport methodologies, either deterministic or stochastic, and by using codes featuring fully flexible geometrical capabilities. This is the case, for instance, for the HELIOS (2D) and MCNPX (3D) whole-reactor models of LWR-PROTEUS, both presented in Chapter 3.

The application of nodal diffusion methodologies to the LWR-PROTEUS experiments, on the other hand, becomes possible only if the calculated domain is restricted to the 3x3 array of BWR fuel assemblies constituting the test zone. In fact, it is just in this domain that the nodal codes can be applied in a manner that resembles the modelling of an actual BWR core. This aspect has been fundamental in defining the goal of the present research, viz. to validate the nodal methodologies while keeping the modelling options as close as possible to those used in power reactor applications[67].

Thus, the basic issue of representing the PROTEUS external zones (buffer, driver regions and reflector) by means of suitable boundary conditions applied to the test zone has had to be given due importance. In the present research, this has been accomplished by defining Partial Current Ratios (PCRs) for each interface between the test zone and its surroundings. Since the PCRs are defined in terms of the ratio between the incoming and outgoing partial currents for each energy group, the PCRs are diagonal matrices, all their energy-transfer (non-diagonal) components being equal to zero. Furthermore, since the partial currents that cross the test-zone boundaries are dependent on all the reactor zones, they can only be obtained by means of whole-reactor calculations. It should be underlined here that the PCR matrices have been calculated specifically for each individual configuration and, as such, reflect not only the test-zone composition but also the specific fuel loading in the reactor’s driver zones (see Section 3.6 for further details).

In this thesis, the PCRs have been primarily determined, for each individual configuration, by means of 3D MCNPX calculations of the entire reactor. Although costly in terms of computer resources, this approach has enabled one to account for the axial variation of the currents crossing the test-zone faces in the radial direction, this variation being important for the

---

[67] For example, the nine fuel assemblies have been subdivided in 10 practically cubic axial nodes, disregarding the axial composition of the test zone, while the corresponding lattice data were obtained from (almost) standard lattice calculations.

investigation of the 3D behaviour of the total-fission rate distributions in axially non-uniform cases. In addition, the 3D MCNPX model allows the determination of axial PCRs for the top and bottom faces of the test zone, which are needed to close the nodal domain. However, as an alternative approach, PCRs obtained by means of 2D HELIOS calculations of the entire LWR-PROTEUS reactor have also been applied. It has been found that the 2D modelling is quite adequate for axially uniform configurations (such as I-1A and I-2A), while for configurations with axial heterogeneities, the 3D dependence of the PCRs certainly affects the calculated results.

However, despite the relative importance of determining appropriate PCRs to characterise the test-zone boundaries, the present research has shown that the fission rate distribution in the test-zone central assembly is relatively independent of the outer zones of the reactor. Thus, for example, using 2D HELIOS PCRs (instead of 3D MCNPX) does not change the C/E distribution significantly for axially uniform configurations, although this does have a noticeable impact on the calculated k-effective value. Furthermore, it has been found that refining the azimuthal discretisation of the PCRs hardly affects the results for configurations with azimuthal symmetry, although this aspect becomes more important if strong asymmetries (such as those caused by the presence of the L-shaped control blade) occur[68]. Concerning the energy discretisation of the PCRs, the results show that changing the number of energy groups from 2 to 5 has no significant impact on the calculated total-fission distribution.

Despite its excellent general applicability, there are two particularities of the LWR-PROTEUS experimental database that can produce difficulties for the modelling of controlled configurations when using industrial nodal codes. First, with the test zone consisting of a 3x3 array of fuel assemblies, one does not have the situation corresponding to the standard lay-out of BWR cores, for which the number of assembly rows is always even (a control blade is located at the centre of the core, and there is one control blade associated with each group of 2x2 assemblies). Second, the L-shaped control blade (especially fabricated for LWR-PROTEUS) differs significantly from the actual, cruciform control blades in BWRs. There are these two features which, although unavoidable considering the space constraints of the PROTEUS test zone, complicate investigation of the controlled configurations in certain cases. For instance, for code systems featuring a high level of automatism (i.e. requiring only basic engineering data from the user, while assuming most system features implicitly), modelling the experimental setup may become impossible. In this thesis, this has been the case for the application of CASMO-5/SIMULATE-5 to Configurations I-2A and I-6A. In the case of HELIOS/PRESTO-2, on the other hand, the modelling of the controlled configurations could be carried out with relative ease, thanks to the large degree of freedom that this code system offers to the user, not only with respect to the system geometry but also concerning the data transfer between the lattice and the nodal codes (in particular, the configuration of the cross-section data bank).

To conclude, the results obtained in this research show that, in a general sense, the basic strategy adopted for the LWR-PROTEUS programme, viz. performing reaction rate measurements in the central element of a 3x3 array of BWR fuel assemblies, is very effective in terms of providing conditions that are only weakly dependent on the surroundings. Thus, the definition of diagonal PCR matrices, with a relatively coarse spatial and energetic discretisation,

---

[68] It has been also shown, however, that the effect of the azimuthal asymmetry of the boundary conditions can be significantly compensated by defining pin map correction factors (PMCFs), which are calculated as the ratio of two 2D HELIOS calculations for a model of the 3x3 test zone using specific PCR (albedo) boundary conditions. One should bear in mind, in this context, that the need for these corrections is caused by the input limitations of the nodal codes, viz. that the PCRs must be the same on all the faces (and corners) of the system radial boundary.

is quite adequate for modelling the test zone with nodal methodologies. For the investigation of radial effects, for example, not even a 3D MCNPX model is needed for obtaining the PCRs, 2D whole-reactor calculations with HELIOS being sufficient for the purpose. Such robust behaviour underlines the excellent applicability of the LWR-PROTEUS database for the type of assessment carried out in this research.

9.3 Relevance for nuclear power plant surveillance and design

Although the principal interest from the industrial point of view concerns the determination of the calculation uncertainties under the conditions occurring in a power reactor core, it is obvious that these conditions cannot be fully reproduced in experiments performed in a zero-power critical facility. Instead, simplified and accurately characterised experimental configurations need to be used, from which the behaviour expected to occur in the power reactor environment can be assessed as closely as possible. In this section, the relevance of the messages obtained from the present research is discussed from the point of view of the surveillance and design of power reactor cores. This is done by interpreting the impact of some of the currently observed individual effects on related uncertainties encountered in actual power reactor situations. In this context, the cases of channel bowing and sub-assembly pressing are discussed in particular.

9.3.1 General remarks

It has been seen that the steep gradients occurring in the vicinity of axial heterogeneities can lead to C/E values that, in a local sense, differ significantly from 1.0. Although, in such cases, the deviations in the total-fission rate may reach 100%, the effect remains strongly local and has only a small impact on the calculated Linear Heat Generation Rate (LHGR)[69].

As shown and discussed in Chapter 7, the variable separation of the function describing the 3D asymptotic flux can lead, for the case of the partial insertion of a control blade, to unphysical results near the axial interface of the controlled and uncontrolled nodes. This effect, in the form of an “inverse” step observed in pins that are distant from the control blade, may lead to some overestimation of the LHGR below the tip of the control blade (see, for instance, Figure 101), which would represent a conservative behaviour. However, it may also cause an underestimation above the control blade tip, which would be non-conservative. In any case, as mentioned before, since it is only a small part of the node height which is affected, the impact on the LHGR is small. Moreover, since controlled fuel assemblies develop a reduced power, the deviations occurring at pins belonging to such assemblies are usually not crucial from the point of view of the monitoring of thermal parameters in the core.

An important remark must be made in connection with the accumulative effect of burnup. In fact, modern nodal simulators with pin-power reconstruction capabilities calculate the fuel exposure at pin-nodal level, in some cases using a microscopic depletion model[70]. The pin burnup is calculated for each pin of each node by integrating the pin-power over time. Hence,

---

[69] For core surveillance, the LHGR is averaged, for each pin in the lattice, over the height of an axial node.

[70] This is the case, for instance, for SIMULATE-5. In PRESTO-2, on the other hand, the cross-section model is purely macroscopic (i.e. is based exclusively on macroscopic cross-sections calculated at lattice level).

deviations in the pin-power distribution may cause deviations in the pin-burnup values. In controlled cases, in addition, a second effect must be accounted for. The spectral hardening caused by the presence of the control blade enhances the build-up of ^{239}Pu. This leads to a greater increase in the local power when the blade is withdrawn. Hence, uncertainties in the pin-power, and consequently in the pin-burnup, can have an enhanced impact in controlled cases.

The operational limit for the LHGR, specified through so-called TMOL (Thermal Mechanical Operating Limit) tables, is a decreasing function of local burnup. Thus, the FLPD (Fraction of Limiting Power Density), which is the ratio between the actual LHGR and the TMOL, has a double dependence on the calculated pin-power distribution.

Another important parameter which is constantly monitored during the operation of a BWR is the Critical Power Ratio (CPR), which is the ratio between the assembly power which leads to dry-out and the actual power developed by the fuel assembly. In most current-day methodologies used for the CPR calculation in BWRs, the nodal reconstructed pin-power distribution provided by the 3D core simulator is not directly used. Assembly peaking factors are accounted for by means of so-called R- or K-factor tables, which are evaluated based on 2D lattice calculations. Thus, the uncertainties discussed above have no direct impact on the calculated CPR distribution. There are, nevertheless, recent methodologies that make direct use of the 3D pin-power distribution calculated by the nodal code. For these, the impact of the uncertainty of the pin-power distribution on the calculated CPR can vary, depending on the exact methodology in question.

It is important to recall, in the context of this general discussion, that – as mentioned in Section 9.1, – the axial and radial shapes of the three-dimensional total-fission distributions are well predicted in most calculations. This is an important observation concerning the monitoring of operational limits in power reactors, for which the power peaking factors play a fundamental role.

9.3.2 Uncertainties in the characterisation of the power reactor core

While the characterisation of BWR assemblies in an experimental facility such as PROTEUS can be accomplished quite precisely, uncertainties cannot be avoided in the characterisation of their geometry and material composition under the actual operating conditions of a power reactor core, principally at local fuel-pellet level. Thus, pressure and temperature gradients affect the nominal geometry of the fuel assemblies. Furthermore, the neutron fluence accumulated during fuel exposure, particularly in cases showing conspicuous fluence gradients, impacts the material growth and hence the assembly geometry. In addition, the nodal distribution of coolant (moderator) density, which is a result of the core thermal-hydraulic calculation, is also affected by a certain level of uncertainty. In fuel assemblies of SVEA-type, moreover, the flow (and hence the power) distribution across the four sub-assemblies also plays an important role. At a more detailed level, one has the radial distribution of the coolant density inside each individual sub-assembly, which is treated in a simplified manner in the lattice calculations via the assumption that the coolant is homogeneously distributed over the entire inter-pin space. Also important is the distribution of temperatures, mainly in the fuel but also in the coolant and structural materials. Fabrication tolerances add uncertainties in the geometry and composition of the core, while fluctuations in the different operational parameters measured at the plant, and the accuracy of such measurements, contribute to uncertainties in characterising the core operational conditions themselves. Finally, uncertainties on the local fuel exposure distribution also affect the overall accuracy in the characterisation of the power reactor core.

Among the above types of effects, those for which certain insights have been obtained from the present research are the ones related to geometrical uncertainties, viz. assembly box bowing and sub-assembly pressing. The corresponding aspects are discussed in the following. A quantification of the impact of the other effects is a topic that clearly falls outside the scope of this thesis. Corresponding investigations are one of the recommendations for further work, as presented in Section 9.4.

Channel bowing

It has been shown (see Subsection 4.5.5) that a 0.3 mm change in the inter-assembly half-gap size leads to an approximately 1% difference in the total-fission rate for pins adjacent to the gap. It is a known fact that BWR assembly boxes experience a certain bowing during their lifetime in the reactor. The actual bowing of every particular assembly box in the core is not known, but measurements may be made on a certain number of assemblies, normally with different exposures, in order to characterise the effect in a statistical way[71]. Furthermore, two adjacent assemblies may feature bowing in additive or subtractive directions, this aspect being strongly dependent on the core loading pattern. In this frame, it is reasonable to assume that the deviations of the inter-assembly gap widths follow a normal distribution law. The experience shows, that typical channel bowing distributions have average absolute values that lie within the band ~0.5 to ~1.5 mm (deviation of the half-gap width with respect to its nominal value), although significant variations may occur between different plants and fuel assembly types[72]. Assuming a channel bowing distribution with a most probable value of zero (as mentioned before, bowing may occur in both directions)[73] and a 1σ standard deviation of ~1.0 mm (uncertainty in the half-gap width), a 1σ uncertainty of ~3.3% in the pin-power distribution may be deducted as the effect of the channel bowing on the relative position of the pins in the core[74].

Sub-assembly pressing

Furthermore, pins in SVEA-type fuel assemblies may be displaced, with respect to their nominal lattice positions, due to the forces imposed by the coolant flow on the four sub-assemblies in which they are arranged (sub-assembly pressing). Contrary to the case of channel bowing, the sub-assembly pressing has a systematic character, the displacement being oriented towards the centre of the assembly. As shown for the case of Configuration I-1A (see Subsection

---

[71] Semi-empirical methods exist, which, making use of fluence gradients across the assembly while considering the fuel box material properties, give an estimation of the expected channel bowing. Although these methods may provide an additional source of data for the characterisation of the channel bowing distribution in the core, measurements constitute the only source of accurate data, corresponding experimental campaigns being regularly conducted in many power plants.

[72] There are elaborate methods to estimate the statistical behaviour of channel bowing in BWRs, by means of which different probability distributions can be defined, depending on assembly properties such as burnup, box material and core position history. Furthermore, the effect of bowing on the gap size depends on the elevation. For the present discussion, however, it is sufficient to assume a single representative value for the channel-bowing related 1σ standard deviation (this is also done in industrial applications).

[73] Channel bowing distributions can also have mean values different from zero. In these cases, systematic effects may need to be considered.

[74] One should bear in mind that the sensitivities observed in the present calculations correspond to full-density moderator at room temperature, the values corresponding to two-phase flow under operating conditions being expected to be different.

4.5.6), a sub-assembly pressing of ~0.5 mm can affect the total-fission rate of the pins near the central water canal by up to ~4%. Assuming a normal distribution of sub-assembly pressing, with a most probable value of ~0.5 mm[75] and a 1σ standard deviation of ~0.2 mm[76], a 1σ uncertainty of ~1.6 % in the pin-power distribution may be assumed as the effect of the sub-assembly pressing on the relative position of the pins in the core.

It should be borne in mind that, in practice, the lattice calculations are performed using nominal dimensions. As such, in principle, a pin-dependent bias should be imposed on the calculated pin-power distribution to correct for the systematic effect of the sub-assembly pressing. For Configuration I-1A, for example, the impact of using nominal pin coordinates (instead of the experimental 0.51 mm pressing) has been found to vary between −2.6% and 4.3% for the different pins. Under power reactor conditions, however, the corresponding pin-dependent biases may be significantly different.

Combined uncertainty of channel bowing and sub-assembly pressing

Under the justifiable assumption that the uncertainties mentioned above can be considered to be statistically independent, the 1σ uncertainty on the pin-power distribution in an operating power reactor core, due to the two effects together, is given by:

$$\sigma_{bow+press} \cong \sqrt{3.3^2 + 1.6^2} = 3.7\%$$

This result suggests that attempting to determine the pin-power distribution in the power reactor core with an accuracy better than ~4% would not bring a real benefit, since it is simply not possible to characterise the geometry of the system with the required precision. Comparing this value with the standard deviations presented in Table 64, it can be concluded that the nodal methodologies investigated in this thesis effectively determine the pin-power distribution with an accuracy that is clearly within this uncertainty range[77].

Overall uncertainty

The overall situation concerning the sources of calculational uncertainty under the conditions occurring in a power reactor core is depicted in Figure 140. As mentioned earlier, it is beyond the scope of the present research to provide a quantification for all the indicated effects. Nevertheless, it is quite clear that the net uncertainty on the pin-power distribution in the power reactor core will be larger than that obtained from the combined effect of just the channel bowing and sub-assembly pressing. However, it should be noted that several of these uncertainties are correlated and will thus lead to a combined variance which is smaller than the sum of the individual variances.

---

[75] It should be noted that this is just an estimated representative value. In practice, the sub-assembly pressing varies, depending on effects such as the active channel coolant flow and the axial position in the assembly.

[76] No specific data are available concerning the dispersion of the sub-channel pressing distribution. The value of 0.2 mm for the 1σ standard deviation is again only an estimation made for this discussion.

[77] Although the standard deviations for Configurations I-1C and I-6A slightly exceed 4% for PRESTO-2, this statement can certainly be considered valid in a general sense.

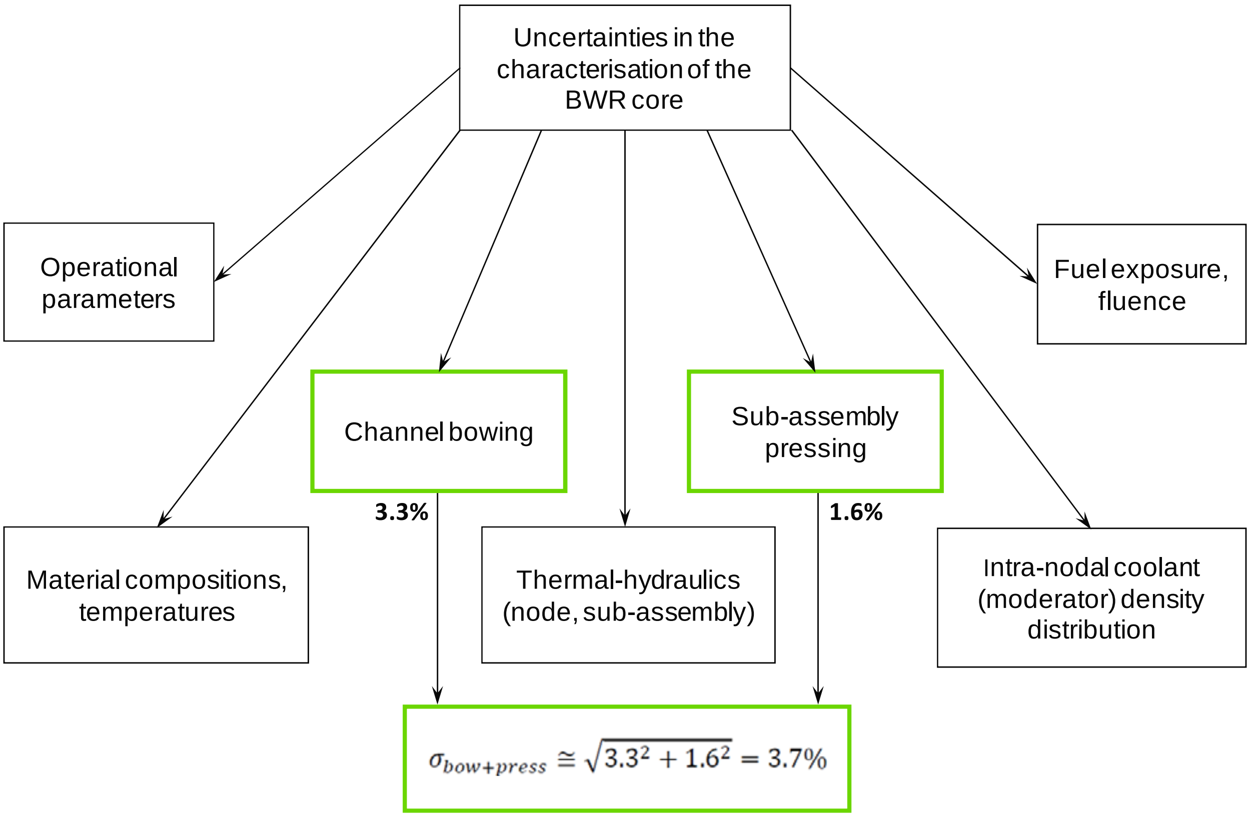

Figure 140 Schematic showing the various sources of uncertainty in the characterisation of a BWR core for the determination of the local power distribution. The two currently considered effects, viz. channel bowing and sub-assembly pressing, are indicated with the green boxes, the corresponding combined uncertainty amounting to about 4%.

9.3.3 Conclusion regarding the accuracy of nodal methodologies

The above considerations lead to the conclusion that the accuracy of the investigated nodal methodologies, as appraised by the current research, is quite appropriate for the determination of the pin-power distribution in power reactor cores. In other words, the level of predictability of results for the “clean” experimental conditions of LWR-PROTEUS clearly satisfies the accuracy level that is practically achievable in nuclear power plants.

9.4 Suggestions for future investigations

The present doctoral research has, on the basis of the LWR-PROTEUS database, targeted a quantitative assessment of the performance of two different 3D core simulators, in terms of their capability to predict local power distributions at pellet level. Besides this main objective, and as means to achieving it, a work environment featuring a relatively high level of automatism has been developed. In fact, from the very outset, considerable attention has been paid to the development of procedures, scripts and macros, with the purpose of automating the data processing. This early decision proved quite advantageous, allowing the investigation of a large number of sensitivity cases with affordable effort. While several sensitivity studies have been presented and discussed in this thesis, others could be conducted as further investigations, employing basically the same methodology. Examples of such sensitivity studies are:

a) Sensitivity to the axial nodalisation.
b) Impact of the basic cross-section libraries.
c) Sensitivity of the axial dependence of the radial PCRs to variations in the tally discretisation used in MCNPX.
d) Additional validation of the PCR-methodology, by means of comparisons between MCNPX and nodal reconstructed results for the peripheral assemblies of the LWR-PROTEUS test zone.
e) Sensitivity to the neutronic models used for the nodal diffusion calculations.

Other areas of research, with the potential of achieving further in-depth understanding of local power monitoring issues in BWR power reactor cores, are:

1) Quantitative investigation of the sources of uncertainty – other than those considered currently – which affect the accuracy of predicted power distributions. The impact of the different individual effects indicated schematically in Figure 140, i.e. of the corresponding variances on the overall uncertainty in predicting local power, is of fundamental importance for nuclear power plant operators. This field of research includes aspects related not only to neutronics, but also to thermal-hydraulics and materials behaviour.

2) Development of an alternative methodology to describe the spatial dependence of the 3D homogeneous flux, such as to eliminate the assumption of variable separation.

   Basically, this implies finding a true three-variable-function $\phi^{hom}(x,y,z)$, describing the intra-nodal homogeneous (asymptotic) flux, which would replace the present representation given by the separation $\psi(x,y)+\xi(z)$. This would require the definition of a pin-wise axial shape for the pin-power reconstruction. Presently, a single axial power profile is used for all pins in the node. The use of 3D transport methodologies for the determination of pin-wise axial form factors is one possible way of addressing this challenging issue.

3) Investigation of the use of radial leakage information at lattice level, for the determination of leakage-corrected discontinuity factors.

   From the nodal calculation, node- and face-average fluxes, as well as face-average partial currents, are known for each node in the core. This information could be used to perform lattice calculations such that the standard (reflected, no-leakage) boundary conditions are replaced by 2D PCRs. The homogeneous flux in the lattice could then be solved using a diffusion algorithm similar to that used in the 3D nodal calculation. The knowledge of the homogeneous and heterogeneous (transport) flux at the lattice boundaries would allow the calculation of leakage-corrected radial discontinuity factors, which could be fed back to the

3D nodal calculation. Alternatively, the homogeneous flux solution in the lattice could be replaced by the homogeneous flux obtained in the 3D calculation, scaled to the corresponding level using the node-average flux. This approximation is based on the assumption that the use of PCRs in the lattice calculation leads to a homogeneous flux in the lattice which accounts for the leakage in the same way as does the homogeneous flux in the nodal calculation. Either of the two approaches would lead to an iterative process between the lattice and nodal calculations. This could, in principle, be replaced by a parametric table look-up concept to avoid excessive consumption of computer resources.

Radial leakage considerations are important concerning strong heterogeneities caused by different nuclear properties in adjacent assemblies, for example due to burnup or the presence of MOX.

4) Application of the developed methodology to the assessment of other core simulators used in the industry.

The methodology employed in this thesis can clearly be applied to basically any 3D nodal core simulator, provided the specification of axially-dependent radial-albedo boundary conditions is accepted by the code. Furthermore, for the investigation of configurations in which the L-shaped control blade is inserted, the code system (lattice and nodal codes) must allow modelling a L-shaped control blade (not only a full cruciform blade), while also allowing the specification of BWR control elements in a core geometry consisting of an odd number of assembly rows. In these cases, the characterisation of the test-zone boundary can be improved if the nodal code allows the specification of azimuthally variable albedo matrices (PCRs) in the radial direction.

An additional area of interest could be the study of the impact of uncertainties in the reconstructed pin-power distribution on TIP (Traversing In-Core Probe) and LPRM (Local Power Range Monitor) detector readings.

TIP detectors are usually gamma-chambers that can be moved axially along steel tubes, placed in the narrow-narrow gap corners at specific radial positions in a BWR core. They provide a 3D picture of the gamma field, which can be correlated with the 3D power distribution. This correlation is governed by the contribution of each pin to the total gamma flux at the detector location. Normally, all the pins belonging to the four assemblies that surround the detector are accounted for, an importance function describing the contribution of each pin to the total gamma field. This contribution is composed mainly of three components: prompt (fission) gamma-rays, delayed (fission-product decay) gamma-rays and gamma-rays created by radiative capture in the fuel. The sources of the first two components are located in the pin where the fissions take place while, for the third, the gamma-rays originate in pins where the neutrons (that were born in other pins) are captured. Calculations performed with MCNPX have shown [41] that the third component contributes significantly to the total gamma flux at the location of the detector. Thus, the detector signals depend on the pin-power distribution of the surrounding assemblies, the contributions being important even for pins lying at relatively large distances from the detector. The investigation of the impact of pin-power uncertainties on TIP detector signals could thus be of significance for the surveillance of power reactor cores.

Similar investigations could be conducted to assess the behaviour of LPRMs. In BWRs, these detectors are located at the same radial positions as the TIP strings; they, however, occupy four fixed axial positions. The LPRMs are fission chambers and, unlike the gamma-TIPs, have a response linked directly to the neutron field. The impact of pin-power uncertainties on LPRM readings would thus be quite different from that on TIP signals.

Closing words

On the basis of experimental results obtained in the LWR-PROTEUS programme, this doctoral research provides valuable evidence of the ability of nodal diffusion methodologies with pin-power reconstruction to accurately predict the 3D local power distribution in BWR fuel assemblies, even in the presence of strong radial and axial heterogeneities. The extensive LWR-PROTEUS experimental database offers, in this frame, an appropriate platform for the assessment and appraisal of such methodologies.

References

[1] Outline History of Nuclear Energy, World Nuclear Association, http://www.world-nuclear.org/info.

[2] F. Giust, D. Greiner, C. Vidal, "BWR Core Monitoring without LPRM Adaption". Fourth American Nuclear Society International Topical Meeting on Nuclear Plant Instrumentation, Controls and Human-Machine Interface Technologies (NPIC&HMIT 2004), Columbus, Ohio (2004).

[3] T. Williams, "Experimental test matrix for the BWR phase (EGL/ABB) of the LWR-PROTEUS experiments". Internal PSI report AN-41-98-04, Paul Scherrer Institute (1998).

[4] T. Williams, R. Chawla, P. Grimm, O. P. Joneja, R. Seiler, A. Ziver, "New experiments at a zero-power facility using power reactor fuel". Proceedings of International Conference on the Physics of Nuclear Science and Technology, Long Island, USA (1998).

[5] A. Ziver, R. Brogli, R. Chawla, P. Grimm, H. Hager, R. Seiler, T. Williams, "Planning calculations for new LWR-experiments at the PROTEUS facility". Proceedings of Annual Meeting on Nuclear Technology ‘97, Aachen, Germany. (1997)

[6] M. Murphy, A. Lüthi, R. Seiler, P. Grimm, O. P. Joneja, A. Meister, R. van Geemert, F. Jatuff, R. Brogli, R. Jacot-Guillarmod, T. Williams, S. Helmersson, R. Chawla, "Neutronics investigations for the lower part of a Westinghouse SVEA-96+ assembly". Nucl.Sci.Eng. 141, 32-45 (2002).

[7] M. Plaschy, F. Jatuff, P. Grimm, F. Tani, R. Jacot-Guillarmod, F. Giust, J. Krouthén, R. Chawla, "Comparisons of Deterministic Neutronic Calculations with Monte Carlo Results for an Advanced BWR Fuel Assembly with Hf Control Blades". J. Nucl. Sci. Technol., Vol. 43, No. 11, 1298-1310 (2006).

[8] M. Plaschy, M. Murphy, F. Jatuff, A. Lüthi, P. Grimm, R. Jacot-Guillarmod, F. Giust, U. Bergmann, S. Helmersson, R. Seiler, J. Krouthén, R. Chawla, "Experimental Validation of Reaction Rate Distributions for a SVEA-96+ BWR Assembly with Hafnium Control Blades". J. Nucl. Sci. Technol., Vol. 46, No. 9, 933-943 (2009).

[9] F. Jatuff, P. Grimm, R. van Geemert, M. Murphy, R. Seiler, R. Brogli, F. Giust, R. Jacot-Guillarmod, T. Williams, S. Helmersson, R. Chawla, "Validation of Axial Pin Power Distributions in a 10x10 BWR Assembly across an Enrichment Boundary under Full-Density Water Moderation Conditions". *Ann. Nucl. Energy* 30, 911-930 (2003).

[10] M. Tohjoh, M. Watanabe, A. Yamamoto, "Three-dimensional pin power reconstruction for the axially heterogeneous region in BWR". *Ann. Nucl. Energy* 33, 242-251 (2006).

[11] R.J.J. Stamm’ler, M.J. Abbate, "Methods of steady-state reactor physics in nuclear design". ISBN 0-12-663320-7 © 1983, Academic Press Inc. (London) Ltd.

[12] P. Reuss, "Neutron Physics". ISBN 978-2-7598-0041-4 © 2008, EDP Sciences (France).

[13] A. Hébert, "Applied Reactor Physics". ISBN 978-2-553-01436-9 © 2009, Presses Internationales Polytechniques (Québec).

[14] J.J. Duderstadt, L.J. Hamilton, "Nuclear Reactor Analysis". ISBN 0471223638 © 1976, John Wiley & Sons.

[15] K.S. Smith, "An analytical nodal method for solving the two-group, multidimensional, static and transient neutron diffusion equations". Department of Nuclear Engineering Thesis, M.I.T., Cambridge, Mass. (March 1979).

[16] M. Clark, Jr. and K. F. Hansen, "Numerical Methods of Reactor Analysis". Academic Press, New York, N.Y. (1964).

[17] S. Børresen, "A simplified, coarse-mesh, three-dimensional diffusion scheme for calculating the gross power distribution in a boiling water reactor". Nucl. Sci. Eng. 44, 37-43 (1971).

[18] PRESTO-2 Models Manual, Studsvik Scandpower.

[19] K.S.Smith, "Spatial homogenization methods for light water reactor analysis". PhD Thesis, M.I.T., Cambridge, Mass. (June 1980).

[20] K. Koebke, "A new approach to homogenization and group condensation". Paper presented at the IAEA Thechnical Committee Meeting on Homogenisation Methods in Reactor Physics, Lugano, Switzerland. (November 1978).

[21] HELIOS Models Manual, Studsvik Scandpower.

[22] E. Villarino, R. Stamm'ler, "The heterogeneous response method in slab geometry". Ann. of Nucl. Energy 11, 429-440 (1984).

[23] M. Edenius, et al., "CASMO-3 User's Manual", Rev. 3. STUDSVIK/NFA-89-3, Studsvik of America (1993).

[24] J. Rhodes, et al., "CASMO-4 User's Manual", Rev. 4. SSP-01/400, Studsvik Scandpower (2004).

[25] J. Rhodes, K. Smith, D. Lee, "CASMO-5 Development and Applications". PHYSOR-2006, ANS Topical Meeting on Reactor Physics, Vancouver, Canada, September 10-14, (2006).

[26] D. Dean, et al., "SIMULATE-3 - Advanced Three-Dimensional Two-Group Reactor Analysis Code". SSP-95/15 Rev. 3, Studsvik Scandpower (2005).

[27] S-Ö Lindahl, "SIMULATE-5 Overview". STUDSVIK/SSP-10/120, Rev.0 (2010).

[28] Pelowitz D. (editor), "MCNPX User's Manual", Version 2.5.0. (2005).

[29] R.J.J. Stamm'ler, A. Ferri, E. Villarino, J. Casal, 2005. HELIOS Methods (Version 1.9). Studsvik Scandpower.

[30] Børresen S., Lindahl S.Ö., Patiño N., Oña C., 2006. PRESTO-2 Methods (Version 1.13)", Studsvik Scandpower.

[31] SSP-07/431, "CASMO5 / CASMO5-M User's Manual", (2010), restricted distribution. For general programme description see: http://www.studsvikscandpower.com/nuclear-reactor-analysis-software/casmo-5.

[32] PSI Report AN-41-99-29, "Post-Calculation Data-Sheets for Configuration 1A of the LWR-Proteus Experimental Programme", 23.12.1999.

[33] O. P. Joneja, M. Plaschy, F. Jatuff, A. Lüthi, M. Murphy, R. Seiler, R. Chawla, "Validation of an MCNP4B Whole-Reactor Model for LWR-PROTEUS using ENDF/B-V, ENDF/B-VI and JEF-2.2 Cross-Section Libraries". Ann. Nucl. Energy 28, 701-713 (2001).

[34] L.E. Strawbridge and R.F. Barry, 1965. "Criticality Calculations for Uniform Water-Moderated Lattices". Nucl. Sci. Eng. 23, 58-73.

[35] P. Grimm, personal communication.

[36] G. Perret et al., "Impact of New Gadolinium Cross Sections on Reactor Rate Distributions in 10x10 BWR Assemblies". Nucl. Sci. Eng. 163, 17-25 (2009).

[37] C. Pralong, "Investigation of Within-Pin Reaction Rate Distributions in a Highly Heterogeneous BWR Fuel Assembly", These N° 2663 (2002), École Polytechnique Fédérale de Lausanne.

[38] M. Plaschy, M. Murphy, F. Jatuff, R. Seiler, R. Chawla, 2006. "Experimental critical loadings and control rod worths in LWR-PROTEUS configurations compared with MCNPX results". Proceedings of PHYSOR-2006, International Conference on Reactor Physics, Vancouver, Canada.

[39] T. Bahadir, S-Ö. Lindahl, S.P. Palmtag. "SIMULATE-4 Multigroup Nodal Code with Microscopic Depletion Model". American Nuclear Society Topical Meeting in Mathematics & Computation, Avignon, France, September 12-15, 2005.

[40] I. Remec, J. C. Gehin, P. D'hondt, E. Sartori. "OECD/NEA KRITZ-2 UO2 and MOX Benchmarks". PHYSOR 2002, Seoul, Korea, October 7-10, 2002.

[41] R. Fridström. "Response of the Gamma TIP Detectors in a Nuclear Boiling Water Reactor". MSc. thesis UPTEC F10 042, Uppsala University, Sweden, June 2010.

Acknowledgements

I wish to express my gratitude to École Polytechnique Fédérale de Lausanne, Paul Scherrer Institute, Axpo Kernenergie AG and Studsvik Scandpower for making possible the realisation of this research.

In particular, I would like to underline my recognition and gratitude to:

Prof. Rakesh Chawla, my thesis director, for his constant support and guidance from the very early stages of this work.

Peter Grimm, my technical advisor, for the numerous technical discussions, valuable comments and suggestions.

Dr. Tony Williams, head of the Nuclear Fuel Department, Axpo Kernenergie, and former project leader at Paul Scherrer Institute, for allowing me the use of part of my working time for this research, thus making possible the realisation of this thesis.

Jan Krouthén, head of the Incore Fuel Management Section, Axpo Kernenergie, for providing me the flexibility needed for the simultaneous accomplishment of my duties related to production work.

Dr. Sten-Örjan Lindahl, reactor physics expert, Studsvik Scandpower, for his valuable advice on the use of the CASMO-5/SIMULATE-5 code system, and the preparation of a special version of SIMULATE-5 for application in this thesis.

Dr. Fabian Jatuff, head of the Nuclear Fuel Department, Kernkraftwerk Gösgen, and former head of the Experimental Reactor Physics Group at Paul Scherrer Institute, for his support and numerous discussions concerning experimental and theoretical reactor physics.

Mike Murphy, former head of the Experimental Reactor Physics Group, Paul Scherrer Institute, for his readiness to clarify details of the experimental campaigns.

Dr. Gregory Perret, presently head of the Experimental Reactor Physics Group, Paul Scherrer Institute, and Dr. Michael Plaschy, for fruitful discussions concerning the MCNPX modelling.

Flavio Dante Giust

Curriculum Vitae

Date of birth: 27 November 1961
Place of birth: Buenos Aires, Argentina
Nationality: Italy and Argentina

Education :
October 2006-Present
Doctoral School - Program in Energy
Ecole polytechnique fédérale de Lausanne (EPFL)
Lausanne, Switzerland

August 1983-July1987:
Nuclear Engineering
Balseiro Institute - Bariloche, Argentina

April 1981-July 1983:
Electronics Engineering
Two years required for admission to Balseiro Institute
University of Buenos Aires - Buenos Aires, Argentina

1975-1980:
Technical High School, Electromechanics
Philips Technical School - Buenos Aires, Argentina

Certificates and Degrees:
Nuclear Engineer (1987)
Technician in Electromechanics (1980)

Languages: English, German, Norwegian, Italian, Spanish

PROFESSIONAL EXPERIENCE

Axpo Kernenergie AG, Switzerland 25 September 2009 - Present
Nordostschweizerische Kraftwerke AG (NOK), Switzerland 1 April 2003 - 25 Sep. 2009

Same duties as in period 1 June 2000 - 31 March 2003 at EGL.
Incore fuel management for the Beznau Nuclear Power Plant (KKB).
Project management and deputy section head.

Elektrizitäts-Gesellschaft Laufenburg AG (EGL), Switzerland 1 June 2000 - 31 March 2003

Methods responsible physicist.
Supervision of the calculational methods used for incore fuel management and core monitoring at the Leibstadt Nuclear Power Plant (KKL). Verification and validation of calculational models.
Implementation and Software Configuration Management of calculational schemes.

BWR thermal-hydraulics development.
Thermal-hydraulics modelling and supervision.
Implementation of correlations for Critical Power Ratio (CPR) monitoring.
Follow-up of the development activities of vendors and software providers.

Reactor physics.
Studies related to special situations concerning 2D XS calculations.

Plant operation support related to special events and projects.

Studsvik Scandpower AS, Norway 1 April 1998 - 31 May 2000

Nuclear engineering, principal consultant.

Reactor physics.
Model development for PWR, BWR and VVER applications.
User training and application support to BWR utilities.

Quality assurance and software configuration management.
Responsible for installation, testing and distribution of software for nuclear applications.

Scandpower AS, Norway 1 April 1989 - 31 March 1998

Nuclear engineering, principal consultant.

Reactor physics.
Co-development of cross-section library generator for the HELIOS lattice code.
Application and maintenance of lattice physics related programmes.
Nuclear data generation models for LWR 3D steady-state applications and transient analysis.

BWR thermal-hydraulics.
Steady-state thermal-hydraulic models for advanced fuel designs.
Development of the thermal-hydraulic module of code CM_PRESTO.

Dynamics.
Stability analysis of the Ringhals-1 plant.
Application of code RAMONA-3B.

Application support to BWR utilities on neutronics- and thermal-hydraulics-related issues.

Bariloche Nuclear Research Centre, Argentina 1986 - 1989

Development of the resonance and burnup calculation modules of the cross-section generation code HERMET, aimed at the calculation of heterogeneous cells and lattices in Material Testing Reactor (MTR) geometry (Nuclear Engineering Thesis Work).

Neutronic studies on high flux reactor designs.
Development and maintenance of computer code systems used in the reactor physics group.

TEACHING EXPERIENCE

Swiss Federal Institute of Technology Zürich (ETHZ), Switzerland Feb.-March 2009-2011

Master of Science in Nuclear Engineering - Lecturer in Special Topics in Reactor Physics.

Balseiro Institute, Argentina August 1986-February 1989

Teaching assistant in the areas of:
nuclear reactor theory,
nuclear reactor analysis and calculations.

Co-advisor for nuclear engineering thesis work in the areas of:
development of a fuel element calculation code for research reactors,
development and application of nodal transport methods.

University of Buenos Aires, Argentina March-June 1983

Teaching assistant in elementary physics.

Philips Technical School, Argentina April-November 1979

Teaching assistant in laboratory of electrical measurements.

SCHOLARSHIPS

Comisión Nacional de Energía Atómica (CNEA) - Instituto Balseiro. August 1983
Duration: 4 years.

Philips Argentina. Duration: 6 years. March 1975

SPECIAL COURSES ATTENDED

"Frédéric Joliot / Otto Hahn - Summer School on Nuclear Reactors, August 2008
Physics, Fuels and Systems", "The Role of Experiments in Nuclear Reactor Simulation and Analysis". EPFL Doctoral Course EY-F03.
Aix-en-Provence, France. 20.-29.08.2008. 3 credits. Duration: 47 hours.

"Materials for Nuclear Fission Reactors", EPFL Doctoral Course EY-F02, January 2008
PSI, Switzerland. 20.09.2007-20.12.2007. 3 credits. Duration: 36 hours.

"Frédéric Joliot / Otto Hahn - Summer School on Nuclear Reactors, September 2007
Physics, Fuels and Systems", "Sustainability of Nuclear Energy - Gen-IV, Partitioning and Transmutation, Waste Management". EPFL Doctoral Course EY-F03. Forschungszentrum Karlsruhe, Germany. 29.08.-07.09.2007.
3 credits. Duration: 43 hours.

"Radiation and Radioisotope Applications", EPFL Doctoral Course PY-031, February 2007
PSI, Switzerland. 26.10.2006-08.02.2007. 3 credits. Duration: 42 hours.

"MCNPX Introductory Workshop", Los Alamos National Laboratory, Paris, January 2007
France. 29.01.-02.02.2007. EPFL Doctoral Course. 2 credits. Duration: 5 days.

Initial Reactor Engineering Qualification Training - RETAQS Inc. Sep. 2002, Dec. 2002
BWR SNE qualification program. Lewisville, Texas. Duration: 25 days.

Thermohydraulic Behavior in Pressure Vessels and Piping Systems. April 2002
F.J. Moody. KKL. Duration: 2 days.

BWR Stability. March 2002
GSE Systems. KKM. Duration: 3 days.

SCIENTIFIC MEETINGS ATTENDED

ICONE18, 18th International Conference on Nuclear Engineering, Xi'an, China, May 17-21, 2010.

NURETH-13, 13th International Topical Meeting on Nuclear Reactor Thermal-Hydraulics, Kanazawa, Japan, September 27 - October 2, 2009.

PHYSOR-2008, International Conference on Reactor Physics, Nuclear Power: A Sustainable Resource, Interlaken, Switzerland, September 14-19, 2008.

M&C 2005, International Topical Meeting on Mathematics and Computation, Avignon France, 11.-15. September 2005.

PHYSOR-1990, International Conference on the Physics of Reactors: Operation, Design and Computation, Marseille, France, April 23-27, 1990.

XVI Scientific Meeting of AATN (Asociación Argentina de Tecnología Nuclear), Mendoza Argentina, November 1988.

XV Scientific Meeting of AATN (Asociación Argentina de Tecnología Nuclear), Bariloche Argentina, November 1987.

PUBLICATIONS

M.J. Abbate, M.M. Sbaffoni, F.D. Giust, "Pre-Processing and Processing of Nuclear Data". Exercise Practice Guide. Instituto Balseiro (1986).

F.D. Giust, "Desarrollo de un Sistema de Cálculo Neutrónico para Combustibles MTR". Trabajo Especial en Ingeniería Nuclear. Instituto Balsiro (1987).

F.D. Giust, C.A. Lecot, E.A. Villarino, "HERMET - Código de Cálculo Neutronico de Celda para Combustibles MTR". Asociación Argentina de Tecnología Nuclear, S.C. de Bariloche, (November 1987).

H. Blaumann, O. Calzetta, G. Gennuso, C. Gho, F. Giust, F. Leszcynski, "Estudio de Factibilidad de la Transformación del Reactor RA-6 en un Reactor de Alto Flujo". Asociación Argentina de tecnología Nuclear, Mendoza, (November 1988).

F.D. Giust, B. Melkerson, L. Moberg, E. Rolstad, E. Rudbäck, "Out-of-Phase Azimuthal Oscillations in the Ringhals-1 BWR Reactor-Measurements, Data Analysis and Qualification of a Predictive RAMONA Model". 28th ASME/AIChE/ANS National Heat Transfer Conference, San Diego, California, (August 1992).

F.D. Giust, "HELIOS: Examples of Benchmarking". Reactor Physics Calculations in the Nordic Countries, Helsinki/Espoo, Finland, 8 - 9 May 1995.

B.T. Adams, L. Moberg, R.J.J. Stamm'ler, A. Ferri, F.D. Giust, "Validation of the Helios Cross Section Model of Dodewaard for use with the Ramona-3B Coupled Thermal Hydraulic and Neutronic Code". Technical Report IRI-131-97-004, Delft University of Technology, The Netherlands, April 1997.

F.D. Giust, M.M. Sobieska, R.J.J. Stamm'ler, "HELIOS: Benchmarking against Hexagonal TIC Lattices". 7th Symposium on VVER Reactor Physics and Reactor Safety, Hörnitz by Zittau, Germany, 23 - 26 September 1997.

R.J.J. Stamm'ler, F.D. Giust, S. Børresen, "HELIOS/PRESTO-2: Application of Advanced Methods in BWRs". Fachtagung der KTG-Fachgruppen Brennelemente und Reaktorphysik und Berechnungsmethoden, 3 - 4 February 1998.

F. Jatuff, P. Grimm, R. van Geemert, M. Murphy, R. Seiler, R. Brogli, F. Giust, R. Jacot-Guillarmod, T. Williams, S. Helmersson, and R. Chawla, "Validation of Axial Pin Power Distributions in a 10x10 BWR Assembly across an Enrichment Boundary under Full-Density Water Moderation Conditions". Annals of Nuclear Energy 30 (2003) 911-930.

F. Giust, D. Greiner, C. Vidal, "BWR Core Monitoring without LPRM Adaption". Forth American Nuclear Society International Topical Meeting on Nuclear Plant Instrumentation, Controls and Human-Maschine Interface Technologies (NPIC&HMIT 2004), Columbus, Ohio, September 2004.

F. Jatuff, F. Giust, J. Krouthén, S. Helmersson, R. Chawla, "Effects of Void Uncertainties on the Void Reactivity Coefficient and Pin Power Distributions for a 10x10 BWR Assembly". Annals of Nuclear Energy 33 (2006) 119-125.

M. Plaschy, F. Jatuff, P. Grimm, F. Tani, R. Jacot-Guillarmod, F. Giust, J. Krouthén, R. Chawla, "Comparisons of Deterministic Neutronic Calculations with Monte Carlo Results for an Advanced BWR Fuel Assembly with Hf Control Blades". Journal of Nuclear Science and Technology, Vol. 43, No. 11, pp. 1298-1310, 2006.

M. Plaschy, M. Murphy, F. Jatuff, A. Lüthi, P. Grimm, R. Jacot-Guillarmod, F. Giust, U. Bergmann, S. Helmersson, R. Seiler, J. Krouthén, R. Chawla, "Experimental Validation of Reaction Rate Distributions for a SVEA-96+ BWR Assembly with Hafnium Control Blades". Journal of Nuclear Science and Technology, Vol. 46, No. 9, pp. 933-943, 2009.

F. Jatuff, G. Perret, M. Murphy, F. Giust, R. Chawla, "Void reactivity coefficient benchmark results for a 10 x 10 BWR assembly in the full 0–100% void fraction range". Annals of Nuclear Energy 36 (2009) 853–858.

F. Giust, P. Grimm, F. Jatuff, R. Chawla, "Comparison of reconstructed radial pin total fission rates with experimental results in full scale BWR fuel elements". PHYSOR-2008, International Conference on Reactor Physics, Nuclear Power: A Sustainable Resource, Interlaken, Switzerland, September 14-19, 2008.

F. Giust, P. Grimm, R. Chawla, "Experimental comparisons of 3D reconstructed pin-power distributions in full-scale BWR fuel assemblies". ICONE18, 18th International Conference on Nuclear Engineering, Xi'an, China, May 17-21, 2010.

F. Giust, P. Grimm, R. Chawla, "Experimental validation of radial reconstructed pin-power distributions in full-scale BWR fuel assemblies with and without control blade". Ann. Nucl. Energy 37 (2010) 1629–1639.

F. Giust, P. Grimm, R. Chawla, "Experimental Comparisons of 3D Reconstructed Pin-Power Distributions in Full-Scale BWR Fuel Assemblies". Journal of Engineering for Gas Turbines and Power, Vol. 133, (2011).